Transactions of the ASME

Journal of Heat Transfer

Published Quarterly by The American Society of Mechanical Engineers
VOLUME 104 • NUMBER 4 • NOVEMBER 1982

Journal of Heat Transfer (ISSN 0022-1481) is edited and published quarterly at the offices of The American Society of Mechanical Engineers, *United Engineering Center*, 345 E. 47th St., New York, N. Y. 10017. ASME-TWX No. 710-581-5267, New York. Second-class postage paid at New York, N.Y., and at additional mailing offices.

CHANGES OF ADDRESS must be received at Society headquarters seven weeks before they are to be effective. Please send old label and new address.

PRICES: To members, $36.00, annually; to *nonmembers*, $72.00. *Single copies*, $24.00 *each*. Add $5.00 for postage to countries outside the United States and Canada.

INDEXED by the Engineering Index, Inc.

ANNOUNCEMENTS

TECHNICAL PAPERS

(Contents Continued on Page 586)

TECHNICAL NOTES

(Contents Continued on Page 615)

(Contents Continued)

Radiative Transfer in Packed Fluidized Beds: Dependent Versus Independent Scattering

M. Q. Brewster

C. L. Tien
Fellow ASME

Department of Mechanical Engineering,
University of California,
Berkeley, Calif. 94720

Experimental measurements are compared with theoretical predictions for radiative transfer in suspensions of 11.0 μ dia Dow latex particles using 0.6328 μ He-Ne laser light. Both absorbing and nonabsorbing particles are studied with particle volume fraction ranging from 0.01 to 0.7 (close-packed). Predictions based on the classical assumptions that particles act as independent point scatterers are shown to give close agreement with experimental data even for close-packed conditions, as long as the interparticle clearance is greater than about 0.3 wavelengths. Evidence is presented indicating that interparticle spacing measured in wavelengths is the most critical parameter to gauge the importance of dependent scattering and that high particle concentration alone is no indication that scattering is dependent. The results have direct application to the design of packed/fluidized bed systems wherein thermal radiation is a significant heat transfer mode.

Introduction

Many modern technologies and industrial processes utilize packed and fluidized beds of particles which operate at temperatures high enough or pressures low enough that thermal radiation is a significant mechanism of heat transfer. Among these are coal combustors, chemical reactors, and cryogenic microsphere insulations. Since these systems are characterized by relatively high particle concentrations, the unresolved issue of dependent versus independent scattering of radiation [1-3] has consistently hampered their design and optimization, which could result in substantial energy savings.

The classical theory of radiative transfer in particulate media is based on the assumption that the particles are separated by very large distances (relative to the particle diameter) and therefore act as independent point scatterers (Fig. 1(*a*)). Hence, the Mie solution [1, 2] for scattering by a single homogeneous sphere can be employed to define the radiative properties in the transfer theory. Dependent scattering, on the other hand, is said to occur when the particle spacing becomes so small that the interaction of individual particles with radiation begins to be influenced by the close proximity of neighboring particles (Fig. 1(*b*)). Under these circumstances, a rigorous analysis utilizing electromagnetic theory (comparable to the Mie theory) is not feasible. Nevertheless, it is still of prime importance from both fundamental and practical viewpoints to be able to characterize the limit(s) of independent scattering theory and thereby be able to predict under what conditions dependent scattering will be appreciable.

Initially, the limit of independent theory was suggested as occurring at some maximum value of the particle concentration or particle volume fraction, f_v, which is also equivalent to δ/d, the ratio of center-to-center particle spacing to diameter. The two can be related by the formula for a rhombohedral array, which gives the maximum concentration for a given spacing, $\delta/d \simeq 0.905/f_v^{1/3}$. Thus, tentative limiting values ranging from $f_v = 0.05$. to 0.30 (or $\delta/d = 2.5$ to 1.3) were put forth [4-7]. Since the value of f_v (typically 0.3-0.6) in packed and fluidized beds nearly always exceeds these limits, the occurrence of dependent scattering in packed/fluidized beds has been a foregone conclusion [8]. Subsequently, in an important step forward, the particle

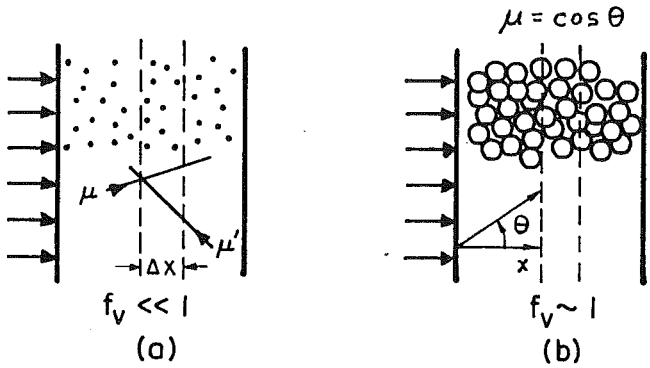

Fig. 1 Schematic illustrations of (*a*) independent and (*b*) dependent multiple scattering

spacing measured in wavelengths, c/λ, was also employed to correlate dependent scattering effects. Using multiple wavelengths, particle sizes, and concentrations, so that a range of values for δ/d and c/λ could be tested experimentally, Hottel et al. [9] found that dependent scattering effects were actually better correlated by c/λ than δ/d (or f_v). Furthermore, the values $f_v = 0.27$ ($\delta/d = 1.4$) and $c/\lambda = 0.3$ were suggested as simultaneous limits of independent theory [9, 10].

The preceding experimental studies collectively suffer two limitations. First, only nonabsorbing particles have been tested. Second, and more important, particle diameters have been restricted to the neighborhood of 1 μ or less, placing the particle size parameter $x (= \pi d/\lambda)$, in the so-called Mie range ($x \sim 1$). By testing only particles in the Mie range it is difficult to establish sufficiently wide ranges of f_v (or δ/d) and c/λ to assess their relative roles in the occurrence of dependent scattering independently.

In this paper, results are presented of both experimental and theoretical studies of radiative transfer among closely spaced, uniform spheres. Large particles ($x >> 1$) are emphasized (*i*) to simulate typical radiative conditions in packed/fluidized beds and (*ii*) to allow further independent testing of the relative roles of f_v and c/λ in the phenomenon of dependent scattering, which has not been possible in previous studies using smaller particles. Both absorbing and nonabsorbing particles are considered and the particle spacing is varied from the independent regime ($f_v < 0.1$) to packed conditions ($f_v = 0.7$). For theoretical predictions, independent

Contributed by the Heat Transfer Division and presented at the Joint AIAA/ASME Fluids, Plasma, Thermophysics, and Heat Transfer Conference, St. Louis, Missouri, June 7-11, 1982. Manuscript received by the Heat Transfer Division February 8, 1982.

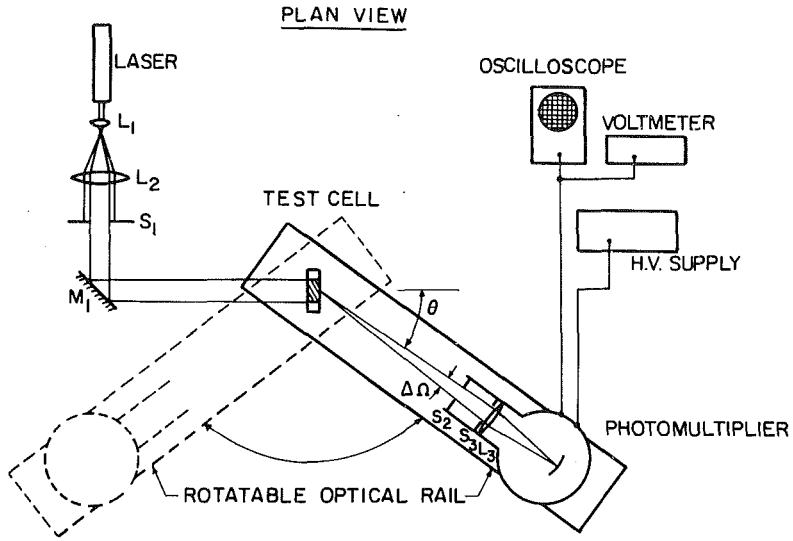

Fig. 2 Experimental apparatus

scattering is assumed, and, to the extent that extraneous sources of error have been minimized, discrepancies between experimental and theoretical results are taken as indicative of the occurrence of dependent scattering.

Experimental System

Rectangular spectrophotometer cells (1 cm by 5 cm) with pathlength ranging from 0.1 mm to 1.0 mm were filled with aqueous suspensions of polydivinyl benzene particles manufactured by Dow Chemical Company. The mean particle diameter, as measured by a scanning electron microscope, was 11.15 μ, with a standard deviation of 1.66 μ. These particles, which are nonabsorbing to visible light, were made absorbing by a dyeing process which implanted blue dye deeply and uniformly in the particles. While the refractive index of the undyed particles is well-known (approximately 1.6 in air and 1.2 in water at visible wavelengths) the complex component introduced by dyeing had to be determined experimentally. This was done by making transmission measurements on dye solutions which had the same concentration of dye as the solution used to color the particles, assuming that the concentration in the particles reached the equilibrium value of the solution. The real part of the refractive index was assumed to remain unchanged.

A He-Ne laser beam (circularly polarized with wavelength 0.6328 μ) was directed normally at the cell (Fig. 2). The scattered light was measured using an RCA-4526 photomultiplier tube mounted on an optical rail which was made to pivot in a circular arc with the test cell at the center. Thereby, the azimuthally symmetric radiation field could be measured by traversing a single plane. The diameter of the incident beam was made at least five times larger than the test cell pathlength in order to approximate a one-dimensional plane-parallel medium. Details of the equipment may be found in [11].

Analysis

For analysis, the medium is treated as a pseudo-continuum (Fig. 1(*a*)). An energy balance on a beam of radiation with intensity I traversing a plane-parallel one-dimensional elemental volume Δx in the direction μ, results in the transfer equation [11, 12][1]

$$\mu \frac{\partial I(x,\mu)}{\partial x} = -[\sigma(\mu)+a(\mu)]I + \frac{1}{2}\int_{-1}^{1} \sigma(\mu')I(x,\mu')p(\mu,\mu')d\mu' \quad (1)$$

which must be supplemented by the scattering coefficient, σ, the absorption coefficient, a, and the scattering phase function, p. Strictly speaking, σ, a, and p are properties of Δx which is mathematically passed to the limit $\Delta x \to 0$. In order to express σ, a, and p in terms of the corresponding properties of

[1] Polarization effects, which have been shown to be negligible at sufficiently large optical thicknesses ($\tau_0 \gtrsim 1$) [9] are ignored.

Nomenclature

a = absorption coefficient
b = collimated back-scatter fraction
B = diffuse back-scatter fraction
c = inter-particle clearance, $\delta - d$
C = cross-section factor
d = particle diameter
f_v = particle volume fraction
i = $\sqrt{-1}$
I = intensity, watts/sr cm^2 μ
I_0 = incident intensity, watts/cm^2 μ
L = slab thickness
n = real part of refractive index, $\tilde{n} = n - i\kappa$
p = scattering phase function
R = bi-directional reflectance, $\pi I(0,\mu)/I_0$
T = bi-directional transmittance, $\pi I(\tau_0,\mu)/I_0$
x = particle size parameter, $\pi d/\lambda$ or slab coordinate
Δx = elemental slab volume
δ = center-to-center particle spacing
ϵ = emissivity
Θ = particle scattering angle from incidence
θ = polar angle of slab
κ = imaginary part of refractive index, $\tilde{n} = n - i\kappa$
λ = wavelength of radiation
λ_0 = wavelength of radiation in vacuum
μ = cos θ, also micron
σ = scattering coefficient
τ = optical depth, $(\sigma + a)x$
τ_0 = $(\sigma + a)L$
ψ = azimuthal angle of slab
ω = single scattering albedo, $\sigma/(\sigma + a)$

Subscripts

eff = effective quantity
λ = monochromatic
e,s,a = extinction, scattering, absorption
a,w,g = air, water, glass
u = unscattered

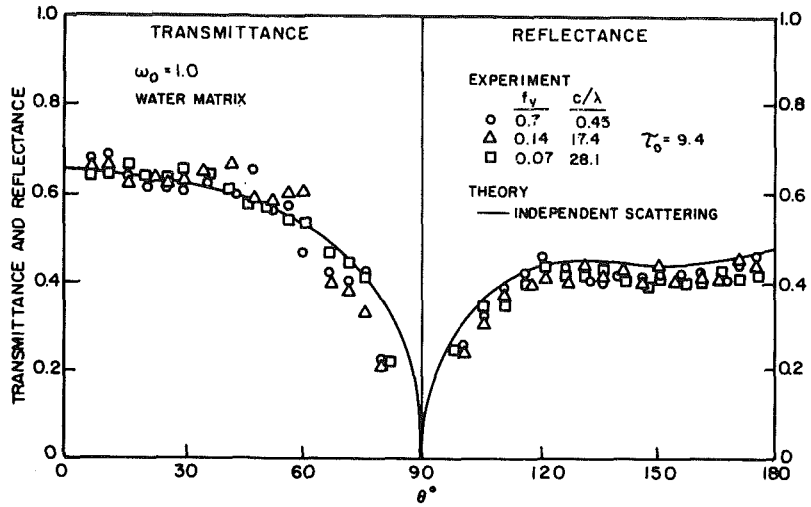

Fig. 3 Effect of particle concentration at large c/λ ($d = 11.15\ \mu$, $n_p = 1.21$, $\lambda_0 = 0.6328\ \mu$, $n_w = 1.332$)

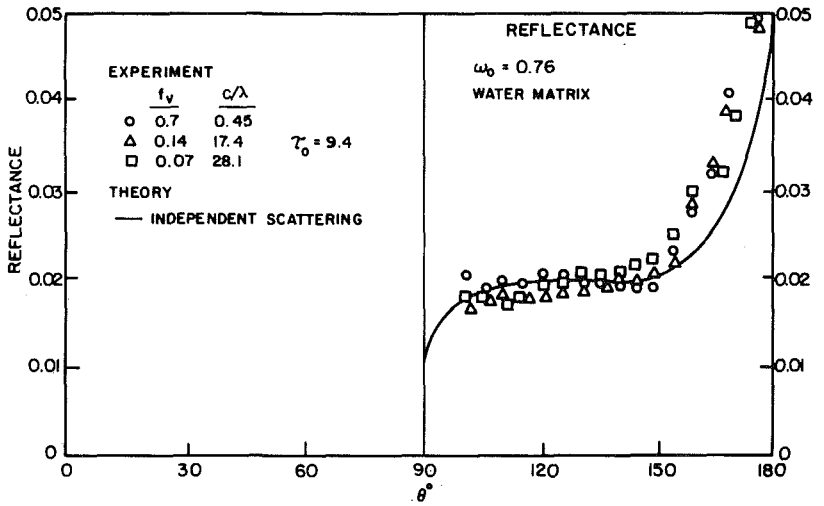

Fig. 4 Effect of particle concentration at large c/λ ($d = 11.15\mu$, $\tilde{n}_p = 1.21 + i\,0.0013$)

the particles in Δx, it is necessary to assume that they act as independent point scatterers ($f_v << 1$). Assuming a monodispersion of spherical particles, the radiative properties can then be expressed as [3]

$$\sigma = C_s N = 1.5 Q_s f_v / d \tag{2a}$$

$$a = C_a N = 1.5 Q_a f_v / d \tag{2b}$$

$$p(\mu\mu') = \frac{1}{2\pi}\int_0^{2\pi} p\{\Theta(\mu,\psi;\mu',\psi')\}d\psi' \tag{2c}$$

where N is the particle number density, $C_{s,a}$ are the single scattering and absorption cross sections, $Q_{s,a}$ the corresponding efficiencies, and $p(\Theta)$ is the single scattering phase function. The single scatter properties Q_s, Q_a, and $p(\theta)$ are given by either the laws of geometric optics ($x >> 1$) or the Mie equations ($x \sim 1$). (See [1] or [2] for a complete treatment of single scattering.) Regarding the assumption of monodispersity, it should be noted that this assumption does not greatly affect the accuracy of the theoretical results due to the fact that at large values of x, the scattering properties are relatively constant. The same, of course, would not be true for particles in the Mie range where scattering properties are very strong functions of the assumed mean particle diameter.

The solution of the transfer equation, modified to account for Fresnel reflection at the boundaries by the glass slides, follows closely the development of [13] using the method of discrete ordinates and is outlined adequately in that work. However, special treatment of the phase function was necessary due to the extreme forward scattering for large particles (see the Appendix).

Discussion of Results

To test the importance of particle concentration f_v in the occurrence of dependent scattering, a set of experiments was devised in which f_v was varied from a very low value ($f_v = 0.07$), indisputably in the independent scattering regime, to the maximum value ($f_v = 0.7$) occurring at close-packed conditions. As the value of f_v was increased, the test cell pathlength was proportionately decreased to keep the optical depth τ_0 constant. Thereby, each set of experimental data corresponded to only one independent scattering theoretical curve. Those results are presented in Fig. 3 for nonabsorbing spheres and Fig. 4 for absorbing spheres. As can be seen, dependent scattering effects are plainly absent, even at close-packed conditions. It should also be pointed out, though, that due to the relatively large particle diameter ($d = 11.15\mu, x = 73.7$), smallest value of wavelength spacing parameter c/λ (occurring at $f_v = 0.7$) was 0.45, well above Hottel's recommended critical value of 0.3.

A contrasting situation is presented in Fig. 5, where smaller particles ($d = 0.10\ \mu$) were tested and therefore lower values of

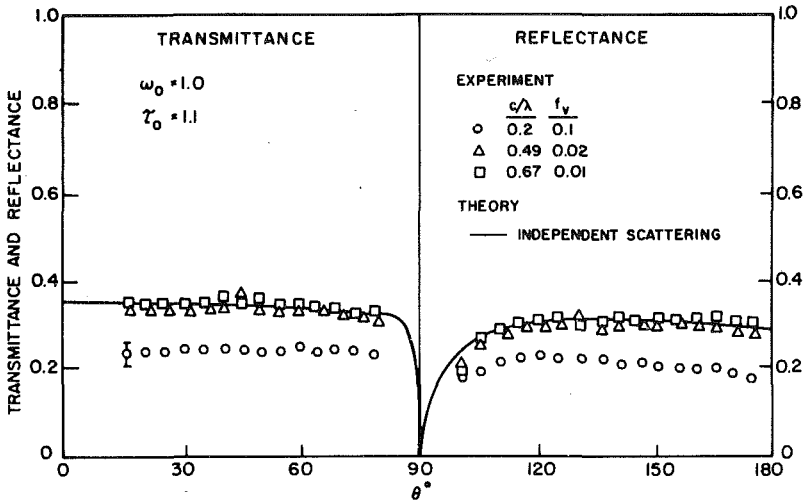

Fig. 5 Effect of small c/λ ($d = 0.1\ \mu$, $n_p = 1.21$, $x = 0.66$)

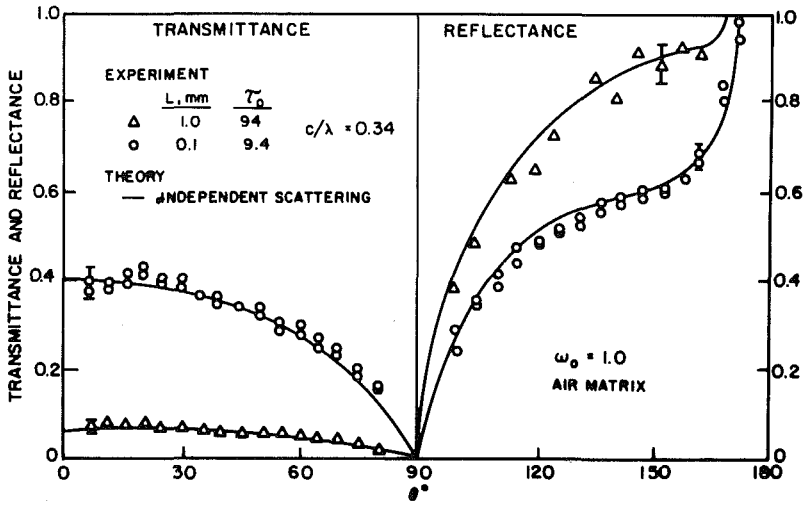

Fig. 6 Effect of optical thickness ($d = 11.15\mu$, $f_v = 0.7$, $n_p = 1.61$)

c/λ could be achieved. Notice that the data represented by circles in Fig. 5 for $c/\lambda = 0.2$ readily exhibit dependent scattering effects even though the value of f_v is only 0.1, while the data corresponding to $c/\lambda = 0.49$ evidence no significant departure from independent scattering theory. Further tests using large particles confirmed the use of $c/\lambda = 0.3$ as a criterion for determining the onset of dependent scattering.

In Fig. 6 the particles were allowed to settle ($f_v = 0.7$) and the water evaporate so that the surrounding fluid matrix was air. In air, since the speed of light is greater, the value of c/λ decreased from 0.45 (for the water matrix) to 0.34. Yet, within experimental error, the independent assumption was still found to be valid. Figures 7 and 8 also present similar results for dyed particles, demonstrating the effect of absorption.

Comparison with Packed Bed Studies

The results of this investigation indicate that if particle clearance exceeds 0.3 wavelengths, dependent scattering is negligible. A comparative study was made to determine if this conclusion is supported by previous investigations of radiation in packed beds. Comparison with the theoretical study of Chan and Tien [8], which assumed a cubic lattice arrangement of the particles in order to calculate the radiative properties, revealed that while general trends with varying particle emmissivity, etc., were similar, the corresponding transmitted and reflected energy fluxes from a slab of particles were different by as much as an order of magnitude. This discrepancy, however, could very well be due to their assumption of a cubic particle array, since they reported substantial disagreement between their own predictions and experimental results of Chen and Churchill [14] anyway.

In the experimental vein, the most suitable work for comparison here is that of Chen and Churchill [14] because it appears to be the only experimental study in which radiation has been completely separated from the conduction contribution. Using the familiar two-flux model and properties as outlined in the Appendix, results of independent scattering theory are compared in Fig. 9 with Chen and Churchill's experimental results for both glass and steel spheres. Considering the uncertainty in the particle properties, especially for the steel spheres, the agreement seen in Fig. 9 is very encouraging.

Independent scattering theory was also compared with the numerous conduction-radiation cell models reviewed by Vortmeyer [15], which utilize an effective radiative conductivity, k_r, and found to consistently predict high values of k_r. This is not seen, however, as a contradiction to the independent scattering assumption for the reason that when conduction is also present, it is a very difficult and complex problem to distinguish between what is radiative heat flux and what is conductive heat flux. For example, at very high temperatures, most of the heat conducted through a particle will be radiated from the back side to the next particle. It is

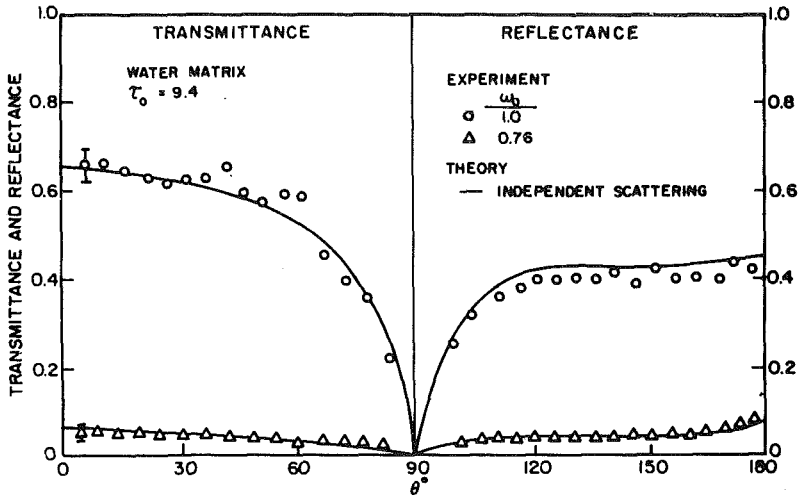

Fig. 7 Effect of absorption in water matrix ($d = 11.15\ \mu$, $f_v = 0.7$, $c/\lambda = 0.45$, for circles $n_p = 1.21$, for triangles $\bar{n}_p = 1.21 + i\,0.0013$)

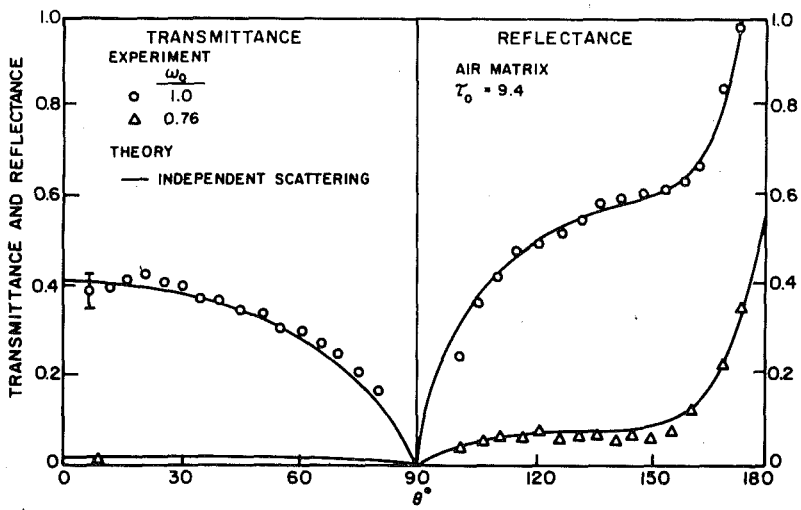

Fig. 8 Effect of absorption in air matrix ($d = 11.15\ \mu$, $f_v = 0.7$, $c/\lambda = 0.34$, for circles $n_p = 1.61$, for triangles $\bar{n}_p = 1.61 + i\,0.0016$)

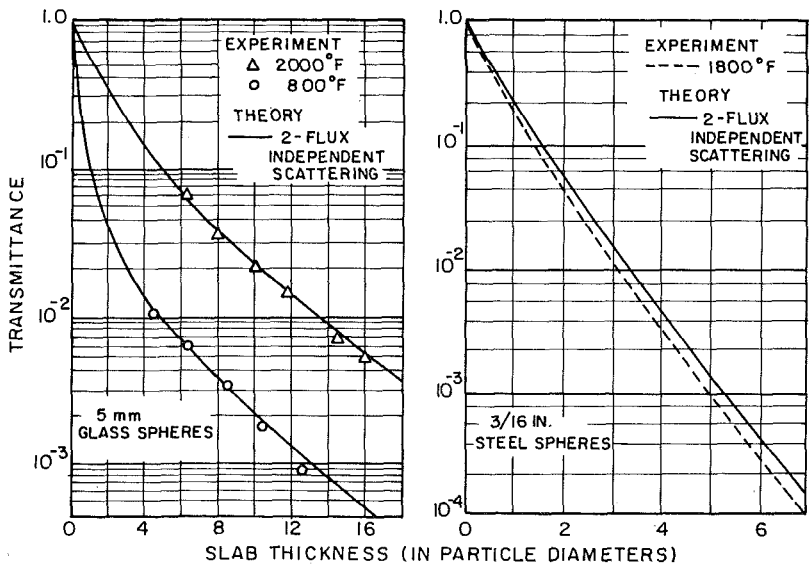

Fig. 9 Comparison of independent scattering theory with experiments of Chen and Churchhill [14]

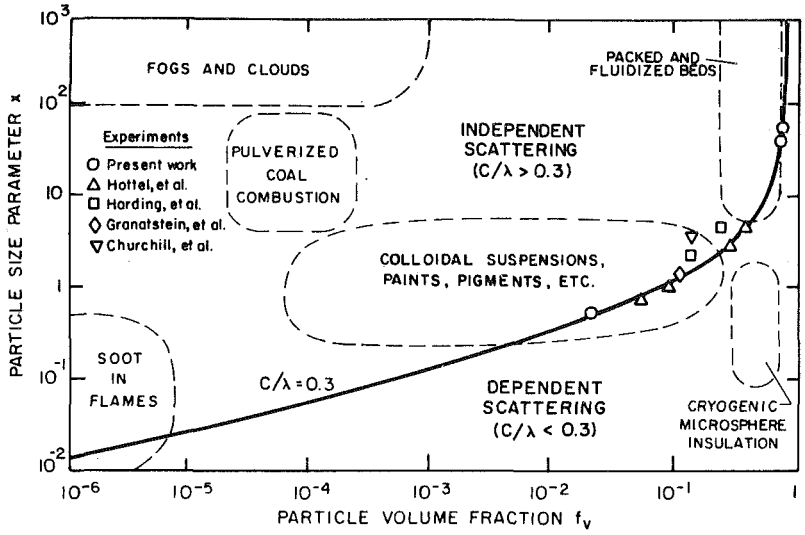

Fig. 10 Independent and Dependent scattering regimes: x versus f_v (experimental points are limit of independent theory)

mainly a matter of choice whether that heat flux is called radiative or conductive since it is actually both modes in series. The important point is that independent scattering theory accounts for it as radiative flux (through the assumption of local thermodynamic equilibrium) while conduction-radiation cell models either include it in the conduction contribution or obscure the issue. Therefore, theoretical predictions of k_r are understandably larger than those of cell models. More work is still needed in the area of design and analysis of practical packed/fluidized beds to unravel the complicated coupling between radiation, conduction, and convection of heat in those systems.

The findings of this study can be usefully displayed as in Fig. 10, where the particle size parameter x is plotted verses f_v and the approximate domains of different radiative scattering systems included. The curve $c/\lambda = 0.3$ demarcates the independent scattering regime ($c/\lambda > 0.3$) from the dependent regime ($c/\lambda < 0.3$) and is given by the equation

$$x = \pi\left(\frac{c}{\lambda}\right)\frac{f_v^{1/3}}{0.905 - f_v^{1/3}}, \quad \frac{c}{\lambda} = 0.3 \tag{3}$$

where use has been made of the rhombohedral correlation for random particle spacing. Various limits of independent scattering, as reported by other investigators, are also included in Fig. 10. Notice that these points (excluding the present work) tend to cluster around values of x between 1 and 10, such that the variation among the different values of f_v at which dependent effects were noticed might easily be interpreted as being within the realm of experimental error. This leads to the erroneous conclusion that the approximate condition $0.1 < f_v < 0.3$ marks the limit of independent scattering. If such were the case, packed and fluidized beds would certainly fall in the dependent regime. However, by extending the range of values of x which were tested experimentally, it has been shown here that the domain of packed and fluidized beds, for the most part, actually falls well in the independent scattering regime.

Summary and Conclusions

The classical theory of independent multiple scattering actually incorporates two distinct assumptions: (*i*) the particles act as point scatterers in that distances separating the particles are much greater than the particle dimensions, ($\delta/d >> 1$ or $f_v << 1$) and (*ii*) the interaction of individual particles with incident radiation is independent of, that is, uninfluenced by, the presence of neighboring particles ($c/\lambda >> 1$). With this in mind, it would therefore seem logical that the domain of validity of the independent scattering theory be defined in terms of two separate criteria, namely, f_v less than some critical value of c/λ greater than some critical value. The interesting result of experimental investigation, however, is that c/λ alone monitors the onset of dependent scattering ($c/\lambda \sim 0.3$) and that f_v (or δ/d) is irrelevant indicating that the point geometry assumption (*i*) is only an artifice in the derivation of the theory and not crucial to its application or validity.

The implications of these results for the design and analysis of packed and fluidized beds are far-reaching and only yet in the initial stages of being explored. Since most packed/fluidized beds systems of engineering interest fall in the independent scattering regime, radiative transfer in such systems can now be calculated with confidence using only first principles and fundamental optical properties. For those systems, such as cryogenic microsphere insulations, which exhibit dependent scattering, it is recommended to use the empirical correlation of Hottel et al. [9]

$$\log_{10}\log_{10}(Q_s/Q_{s_{\text{eff}}}) = 0.25 - 5.1(c/\lambda)$$

to calculate an effective dependent scattering efficiency, $Q_{s_{\text{eff}}}$. And for the absorption efficiency and phase function, although there is yet no experimental justification, it is recommended to simply retain the single scatter quantities because in the limit, as close-packed particles are compressed and form a homogeneous medium, it is only the scattering property which is lost – the absorbing nature of the material, if present initially in the particles, still remains.

References

1 Van de Hulst, H. C., *Light Scattering By Small Particles*, Wiley, 1957, p. 5 and p. 114.

2 Kerker, M., *The Scattering of Light and Other Electromagnetic Radiation*, Academic Press, New York, 1969.

3 Siegel, R., and Howell, J. R., *Thermal Radiation Heat Transfer*, McGraw-Hill, 1972, pp. 662-669.

4 Churchhill, S. W., Clark, G. C., and Sliepcevich, C. M., "Light Scattering by Very Dense Monodispersions of Latex Particles," *Discussions of the Faraday Society*, No. 30, 1960, p. 192.

5 Blevin, W. R., and Brown, W. J., "Effects of Particle Separation on the Reflectance of Semi-Infinite Diffusers," *J. Opt. Soc. Am.*, Vol. 51, 1961, pp. 129-134.

6 Granatstein, V. L., Rhinewine, M., Levine, A. M., Feinstein, D. L., Mazuroski, M. J., and Piech, K. R., "Multiple Scattering of Laser Light from a Turbid Medium," *App. Opt.*, Vol. 11, 1972, pp. 1217-1224.

7 Harding, R. H., Golding, B., and Morgen, R. A., "Optics of Light-Scattering Films. Study of Effects of Pigment Size and Concentration," *J. Opt. Soc. Am.*, Vol. 50, 1960, pp. 446-455.

8 Chan, C. K., and Tien, C. L., "Radiative Transfer in Packed Spheres," ASME JOURNAL OF HEAT TRANSFER, Vol. 96, 1974, pp. 52–58.
9 Hottel, H. C., Sarofim, A. F., Dalzell, W. H., and Vasalos, I. A., "Optical Properties of Coatings. Effect of Pigment Concentration," *AIAA Journal*, Vol. 9, 1970, pp. 1895–1898.
10 Hottel, H. C., Sarofim, A. F., Vasalos, I. A., and Dalzell, W. H., "Multiple Scatter: Comparison of Theory with Experiment," ASME JOURNAL OF HEAT TRANSFER, Vol. 92, 1970, pp. 285–291.
11 Brewster, M. Q., "Radiative Transfer in Packed and Fluidized Beds," Ph.D thesis in Mechanical Engineering, University of California, Berkeley, 1981.
12 Chandrasekhar, S., *Radiative Transfer*, Dover, 1960, p. 13.
13 Hottel, H. C., Sarofim, A. F., Evans, L. B., and Vasalos, I. A., "Radiative Transfer in Anisotropically Scattering Media: Allowance for Fresnel Reflection at the Boundaries," ASME JOURNAL OF HEAT TRANSFER, Vol. 90, 1968, pp. 56–62.
14 Chen, J. C., and Churchhill, S. W., "Radiant Heat Transfer in Packed Beds," *AIChE Journal*, Vol. 9, 1963, pp. 35–41.
15 Vortmeyer, D., "Radiation in Packed Solids," *Proceedings of the Sixth International Heat Transfer Conference*, Toronto, 1978, pp. 525–539.

APPENDIX

Due to large size of the particles used in this study, the phase function could not be represented by a series of Legendre polynominals with a reasonable number of terms as is customarily done in the case of smaller particles, and thus the integration of $p(\Theta)$ over azimuthal angle ψ could not be avoided. (Note that Θ, the scattering angle of a single particle is not θ the polar angle of the plane-parallel geometry). Therefore integrating over the appropriate limits,

$$p(\mu,\mu') = \frac{1}{\pi}\int_0^{\pi} p\{\Theta(\mu,\mu';\psi)\}\,d\psi \tag{A1}$$

where

$$\cos\Theta = \mu\mu' + (1-\mu^2)^{1/2}(1-\mu'^2)^{1/2}\cos(\psi-\psi') \tag{A2}$$

gives

$$p(\mu,\mu') = \frac{1}{\pi}\int_{\Theta_0}^{\Theta_\pi} \frac{p(\Theta)\sin\Theta\, d\Theta}{[(1-\mu^2)(1-\mu'^2)-(\cos\Theta-\mu\mu')^2]^{1/2}} \tag{A3}$$

with

$$\cos\Theta_0 = \mu\mu' + (1-\mu^2)^{1/2}(1-\mu'^2)^{1/2} \tag{A4}$$

and

$$\cos\Theta_\pi = \mu\mu' - (1-\mu^2)^{1/2}(1-\mu'^2)^{1/2} \tag{A5}$$

Because the denominator of the integrand in (A3) goes to zero at the bounds (A4) and (A5), ordinary numerical integration was impractical. Instead the integral was performed analytically over each small interval $\Delta\Theta$ assuming $p(\Theta)$ to be constant over the interval. The use of one degree intervals resulted in sufficiently accurate representation of $p(\mu,\mu')$.

The Two-Flux Model

Based on the assumption of semi-isotropic intensities, I^+ and I^-, the familiar two-flux equations

$$\frac{dI^+}{dx} = -(\tilde{\sigma}+\tilde{a})I^+ + \tilde{\sigma}I^- \tag{A6}$$

$$-\frac{dI^-}{dx} = -(\tilde{\sigma}+\tilde{a})I^- + \tilde{\sigma}I^+ \tag{A7}$$

with boundary conditions $I^+(0) = 1$, $I^-(L) = 0$, result in the expressions for transmittance (T) and reflectance (R).

$$T = \frac{2\beta}{(1+\beta^2)\sinh(\gamma L) + 2\beta\cosh(\gamma L)} \tag{A8}$$

$$R = \frac{(1-\beta^2)\sinh(\gamma L)}{(1+\beta^2)\sinh(\gamma L) + 2\beta\cosh(\gamma L)} \tag{A9}$$

where $\beta = [\tilde{a}/(\tilde{a}+2\tilde{\sigma})]^{1/2}$, $\gamma = [\tilde{a}(\tilde{a}+2\tilde{\sigma})]^{1/2}$, $\tilde{a} = 2a$, $\tilde{\sigma} = 2\beta\sigma$, and $B = 1/2\int_0^1\int_{-1}^0 p(\mu,\mu')\,d\mu'$ is the back-scatter fraction.

For large opaque spheres the efficiency factors are [3] $Q_a = \epsilon_\lambda$, $Q_s = 1-\epsilon_\lambda$ and the phase function is $p(\Theta) = 1$ (giving $B = 0.5$) of the spheres are specularly reflecting and the specular reflectivity is assumed uniform with direction, and

$$p(\Theta) = \frac{8}{3\pi}(\sin\Theta - \Theta\cos\Theta)$$

(giving $B = 0.667$) if the spheres reflect diffusely.

For large transparent spheres the absorption and scattering efficiencies can, of course, be taken as zero and one, respectively, while the phase function must be determined by ray tracing (see [1] or [11]).

In the examples cited in the text the following properties were assumed.

Steel spheres: $\epsilon_\lambda = 0.4$, $0<\lambda<\infty$, diffusely reflecting

Glass spheres: $\epsilon_\lambda = 0.03$, $0<\lambda<2.7\mu$, smooth transparent

$\epsilon_\lambda = 0.9$, $2.7\mu<\lambda<\infty$, specularly reflecting

The fact that absorption is so small for the glass spheres below 2.7 μ allows the phase function to be calculated as for transparent sphere in that region. Assuming a real refractive index of $n = 1.5$ resulted in $B = 0.265$ for that wavelength region.

The Effect of Molecular Gas Absorption on Radiative Heat Transfer With Scattering

R. O. Buckius
Associate Professor,
Department of Mechanical
and Industrial Engineering,
University of Illinois at Urbana-Champaign,
Urbana, Ill. 61801
Assoc. Mem. ASME

Radiative heat transfer in an isotropically scattering and nongray absorbing planar medium is investigated. General wide-band absorption quantities, including the effects of gray absorption and scattering by the scattering components and nongray absorption by the gaseous components, are considered. Analysis for the reflection, transmission, and emission from isothermal layers is presented. Numerical calculations are presented for the wide-band absorption quantities in the high-pressure limit. The effects of the scattering and absorption properties on the wide band absorption quantities are discussed.

Introduction

Radiative heat transfer in many practical engineering situations must include general nongray absorption by the gaseous constituents and scattering by the particulates. Many radiation calculations neglect scattering, which is an accurate assumption when the characteristic length of the scattering components is small relative to the dominant wavelengths. The emphasis of the problem is then placed on the spectral dependence of the absorbing components. The other limit in radiation calculations is the situation of dominant scattering where the absorption can be neglected or considered independent of wavelength over a spectral interval. The equation of transfer including all scattering contributions must then be solved for the particular geometry in question. This work considers the effects of nongray absorption by molecular gases and isotropic scattering.

The basic method is solving radiative heat transfer problems where there are rapid changes in the absorption spectra and significant scattering contributions is to solve the equation of transfer for each wave number and integrate over all wave numbers. Generally, the absorption spectra of the gases are divided into a number of spectral intervals and the solution to the equation of transfer is obtained for the specified absorption coefficient and scattering properties [1-3]. The solution to the equation of transfer is valid for these specific properites and must be repeated for each set of radiative properties in each spectral interval. An alternate approach is to determine all the possible path lengths of photon travel and use these photon path lengths to include absorption [4]. This last approach can easily include any nongray absorption yet requires the solution for the distribution of photon path lengths.

Radiative heat transfer in a planar medium with exponential wide-band absorption has been investigated by Edwards [5, 6]. The usefulness of the slab-band absorptance for molecular gas radiation without scattering is clearly demonstrated. The objective of this paper is to consider the effects of scattering and molecular gas radiation for a plane parallel layer. Numerical solutions are presented for the radiative heat flux and intensities.

Formulation

The planar medium investigated is an isothermal homogeneous layer at T_0 which scatters isotropically and absorbs spectrally. The absorption and scattering by the scattering constituents are independent of wave number or gray, and the molecular gas absorption is banded. Blackbody radiation at a temperature T_1 is incident at $\kappa=0$, and the boundary at $\kappa=\kappa_L$ is transparent. The resulting expressions for the intensities for this isothermal medium are [7]

$$i_\nu^+(\kappa_\nu,\mu)=i_{\nu b}(T_1)e^{-\kappa_\nu/\mu}+(1-\omega_\nu)i_{\nu b}(T_0)(1-e^{-\kappa_\nu/\mu}) + \frac{\omega_\nu}{2}\int_0^{\kappa_\nu}\frac{G_\nu(\kappa_\nu')}{2\pi}e^{-(\kappa_\nu-\kappa_\nu')/\mu}\frac{d\kappa_\nu'}{\mu} \quad (1a)$$

$$i_\nu^-(\kappa_\nu,-\mu)=(1-\omega_\nu)i_{\nu b}(T_0)[1-e^{-(\kappa_{\nu L}-\kappa_\nu)/\mu}] + \frac{\omega_\nu}{2}\int_{\kappa_\nu}^{\kappa_{\nu L}}\frac{G_\nu(\kappa_\nu')}{2\pi}e^{-(\kappa_\nu'-\kappa_\nu)/\mu}\frac{d\kappa_\nu'}{\mu} \quad (1b)$$

where the average incident intensity is $G_\nu(\kappa_\nu)=2\pi\int_{-1}^{1} i_\nu(\kappa_\nu,\mu')d\mu'$. The solution for the intensity is completed with the expression for the average incident intensity. From the definition of $G_\nu(\kappa_\nu)$, the governing equation is

$$\frac{G_\nu(\kappa_\nu)}{2\pi}=i_{\nu b}(T_1)E_2(\kappa_\nu)+(1-\omega_\nu)i_{\nu b}(T_0)\cdot [2-E_2(\kappa_\nu)-E_2(\kappa_{\nu L}-\kappa_\nu)] + \frac{\omega_\nu}{2}\int_0^{\kappa_{\nu L}}\frac{G_\nu(\kappa_\nu')}{2\pi}E_1(|\kappa_\nu-\kappa_\nu'|)d\kappa_\nu' \quad (2)$$

The preceding expressions include the spectral variation of all the constituents within the medium. The positive and negative heat flux, $q_\nu^+(\kappa_\nu)$ and $q_\nu^-(\kappa_\nu)$, are determined directly from the intensities.

Total expressions for the intensity and heat flux are obtained by integrating the above equations over all wave numbers. The scattering constituents with gray extinction have an optical depth denoted as $\kappa_S[=(\alpha_S+\sigma)y]$ and a single scattering albedo denoted as $\omega_S[=\sigma/(\alpha_S+\sigma)]$. The incorporation of the spectral gaseous absorption is denoted with a subscript, ν, and is included through $\gamma\,(=\alpha_\nu/(\alpha_S+\sigma))$. Note that the optical depth including gaseous and particulate constituents is $\kappa_\nu=\kappa_S(1+\gamma)$ and the albedo is $\omega_\nu=\omega_S/(1+\gamma)$. The total intensity and heat flux are represented by $i_\nu^\pm(\kappa_S,\mu,\kappa_{SL},\omega_S,\gamma)$ and $q_\nu^\pm(\kappa_S,\kappa_{SL},\omega_S,\gamma)$, respectively, where the dependences are explicitly denoted. The gray absorption and scattering by the scattering constituents are the base values for the quantities and the band absorption depletes the total values.

The exponential wide-band absorption is used to include the gaseous absorption. The three parameter per band description

Contributed by the Heat Transfer Division for publication in the JOURNAL OF HEAT TRANSFER. Manuscript received by the Heat Transfer Division July 27, 1981. Paper No. 81-HT-61.

is expressed as $A_i^*(\kappa_H, \eta_b)$ where κ_H is the optical depth at band head or center and η_b is the effective broadening parameter. The third parameter is the exponential decay width ω_{bi}. Regional expressions for the exponential band model are available [6] yet for many heat-transfer problems, a simplified model is applicable. In the large pressure limit ($\eta_b \to \infty$), an explicit expression for the absorption coefficient is obtained as

$$\kappa_{\nu i} = \kappa_H \kappa_\nu^* \tag{3}$$

where

$$\kappa_\nu^* = \exp[-(\nu_i - \nu)/\omega_{bi}], \nu < \nu_i \tag{4}$$

A discussion of the extensive applicability of this representation for various conditions is given in reference [5]. There it is noted that symmetrical bands can be approximated with this representation.

The scattering wide-band absorption quantities are defined as the difference between the total quantity including only gray scattering constituents (gray absorption and scattering) and the total quantity with both gray and wide-band absorption. A boundary source is considered and the medium is assumed to be at zero temperature. The wide band is assumed to be sufficiently narrow so that the Planck function can be removed from all integrals and evaluated at the band head or center. The total intensity for a single band, i, is defined as

$$i_i^{\pm *}(\kappa_S, \mu, \kappa_{SL}, \omega_S, \kappa_{HL}) = \frac{1}{i_{\nu_i b}(T_1)} \int_0^\infty [i_\nu^\pm(\kappa_S, \mu, \kappa_{SL}, \omega_S, \gamma = 0) - i_\nu^\pm(\kappa_S, \mu, \kappa_{SL}, \omega_S, \gamma)] d\left(\frac{\nu}{\omega_{bi}}\right) \tag{5}$$

and the heat flux is

$$q_i^{\pm *}(\kappa_S, \kappa_{SL}, \omega_S, \kappa_{HL}) = \frac{1}{\pi i_{\nu_i b}(T_1)} \int_0^\infty [q_\nu^\pm(\kappa_S, \kappa_{SL}, \omega_S, \gamma = 0) - q_\nu^\pm(\kappa_S, \kappa_{SL}, \omega_S, \gamma)] d\left(\frac{\nu}{\omega_{bi}}\right) \tag{6}$$

where the η_b is not denoted since the results presented are applicable only in the limit $\eta_b \to \infty$. Equations (5) and (6) are transformed using equation (4) to yield

$$i_i^{\pm *}(\kappa_S, \mu, \kappa_{SL}, \omega_S, \kappa_{HL}) = \frac{1}{i_{\nu_i b}(T_1)} \int_0^1 \left[i_\nu^\pm(\kappa_S, \mu, \kappa_{SL}, \omega_S, 0) - i_\nu^\pm(\kappa_S, \mu, \kappa_{SL}, \omega_S, \gamma) \right] \frac{d\kappa_\nu^*}{\kappa_\nu^*} \tag{7}$$

and

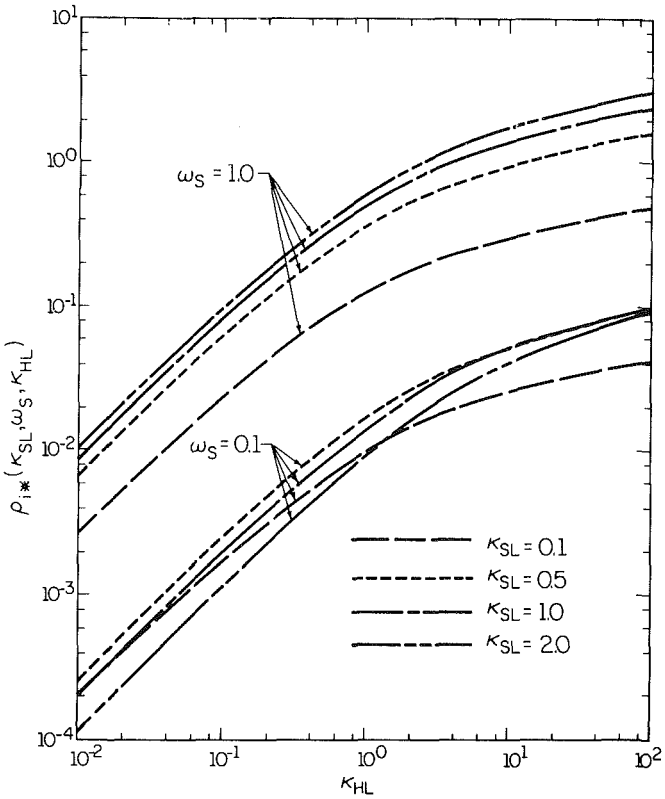

Fig. 1 Hemispherical wide-band absorption for reflection

$$q_i^{\pm *}(\kappa_S, \kappa_{SL}, \omega_S, \kappa_{HL}) = \frac{1}{\pi i_{\nu_i b}(T_1)} \int_0^1 \left[q_\nu^\pm(\kappa_S, \kappa_{SL}, \omega_S, 0) - q_\nu^\pm(\kappa_S, \kappa_{SL}, \omega_S \gamma) \right] \frac{d\kappa_\nu^*}{\kappa_\nu^*} \tag{8}$$

The radiative heat flux and intensity that exit the plane layer are also expressed as the reflectance and the transmittance. Considering the boundary source problem, the directional spectral reflectance and transmittance are given as

$$\rho_\nu'(\mu, \kappa_{SL}, \omega_S, \gamma) = \frac{i_\nu^-(0, \mu, \kappa_{SL}, \omega_S, \gamma)}{i_{\nu b}(T_1)} \tag{9a}$$

and

$$\tau_\nu'(\mu, \kappa_{SL}, \omega_S, \gamma) = \frac{i_\nu^+(\kappa_{SL}, \mu, \kappa_{SL}, \omega_S, \gamma)}{i_{\nu b}(T_1)} \tag{9b}$$

Nomenclature

A_i^* = wide-band absorption
E_n = exponential integrals
G = average incident intensity
$i^\pm$ = intensity
$i_i^{\pm *}$ = scattering-band absorption intensity
$q^\pm$ = heat flux
$q_i^{\pm *}$ = scattering-band absorption heat flux
S_ν = source function
T = temperature
y = distance
α = absorption coefficient
γ = $\alpha_\nu/(\alpha_S + \sigma)$
γ_E = Euler's constant
ϵ = emittance
ϵ_i^* = wide-band absorption for emission
η_b = pressure broadening parameter
θ = angle
κ_ν = optical depth, $(\gamma + 1)\kappa_S$
κ_S = $(\alpha_S + \sigma)y$
κ_H = optical depth at band head or center
μ = cos θ
ν = wavenumber
ρ = reflectance
ρ_i^* = wide-band absorption for reflection
σ = scattering coefficient, Stefan-Boltzmann constant
τ = transmittance
τ_i^* = wide-band absorption for transmission
ω = scattering albedo
ω_S = $\sigma/(\alpha_S + \sigma)$
ω_{bi} = exponential decay width

Subscripts

b = blackbody or band parameter
i = band number
L = total layer thickness
S = scattering
ν = wavenumber dependent
$*$ = dimensionless
0,1,2 = positions

Superscripts

$\pm$ = positive or negative direction
$'$ = directional

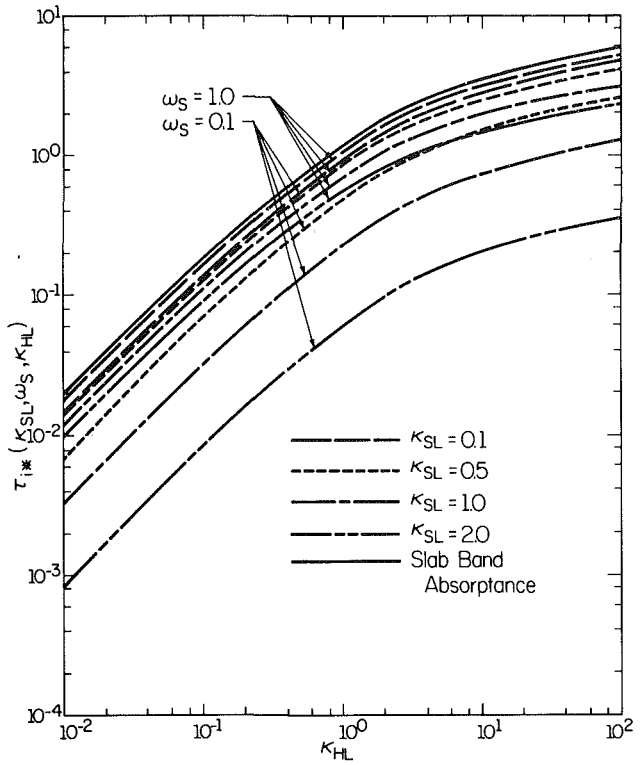

Fig. 2 Hemispherical wide-band absorption for transmission

The hemispherical spectral reflectance and transmittance are

$$\rho_\nu(\kappa_{SL},\omega_S,\gamma) = \frac{q_\nu^-(0,\kappa_{SL},\omega_S,\gamma)}{\pi i_{\nu b}(T_1)} \tag{10a}$$

and

$$\tau_\nu(\kappa_{SL},\omega_S,\gamma) = \frac{q_\nu^+(\kappa_{SL},\kappa_{SL},\omega_S,\nu)}{\pi i_{\nu b}(T_1)} \tag{10b}$$

The corresponding emission from an isothermal layer at T_1 without boundary incidence is obtained directly from these quantities. The directional spectral emittance is given by

$$\epsilon_\nu'(\mu,\kappa_{SL},\omega_S,\gamma) + \rho_\nu'(\mu,\kappa_{SL},\omega_S,\gamma) + \tau_\nu'(\mu,\kappa_{SL},\omega_S,\gamma) = 1 \tag{11}$$

and the hemispherical spectral emittance is given as

$$\epsilon_\nu(\kappa_{SL},\omega_S,\gamma) + \rho_\nu(\kappa_{SL},\omega_S,\gamma) + \tau_\nu(\kappa_{SL},\omega_S,\gamma) = 1 \tag{12}$$

The total intensity and heat flux exiting a plane layer for a single wide band can be expressed in terms of the reflectance and transmittance. The directional wide band absorption for reflection and transmission are obtained from equations (7) and (9),

$$\rho_i'^*(\mu,\kappa_{SL},\omega_S,\kappa_{HL}) = i_i^{-*}(0,\mu,\kappa_{SL},\omega_S,\kappa_{HL})$$
$$= \int_0^1 \left[\rho_\nu'(\mu,\kappa_{SL},\omega_S 0) - \rho_\nu'(\mu,\kappa_{SL},\omega_S,\gamma)\right] \frac{d\kappa_\nu^*}{\kappa_\nu^*} \tag{13a}$$

and

$$\tau_i'^*(\mu,\kappa_{SL},\omega_S,\kappa_{HL}) = i_i^{+*}(\kappa_{SL},\mu,\kappa_{SL},\omega_S,\kappa_{HL})$$
$$= \int_0^1 \left[\tau_\nu'(\mu,\kappa_{SL},\omega_S,0) - \tau_\nu'(\mu,\kappa_{SL},\omega_S,\gamma)\right] \frac{d\kappa_\nu^*}{\kappa_\nu^*} \tag{13b}$$

The hemispherical wide-band absorption for reflection and transmission are given with equations (8) and (10) as

$$\rho_i^*(\kappa_{SL},\omega_S,\kappa_{HL}) = q_i^{-*}$$
$$(0,\kappa_{SL},\omega_S,\kappa_{HL}) = \int_0^1 \left[\rho_\nu(\kappa_{SL},\omega_S,0) - \rho_\nu(\kappa_{SL},\omega_S,\gamma)\right] \frac{d\kappa_\nu^*}{\kappa_\nu^*} \tag{14a}$$

and

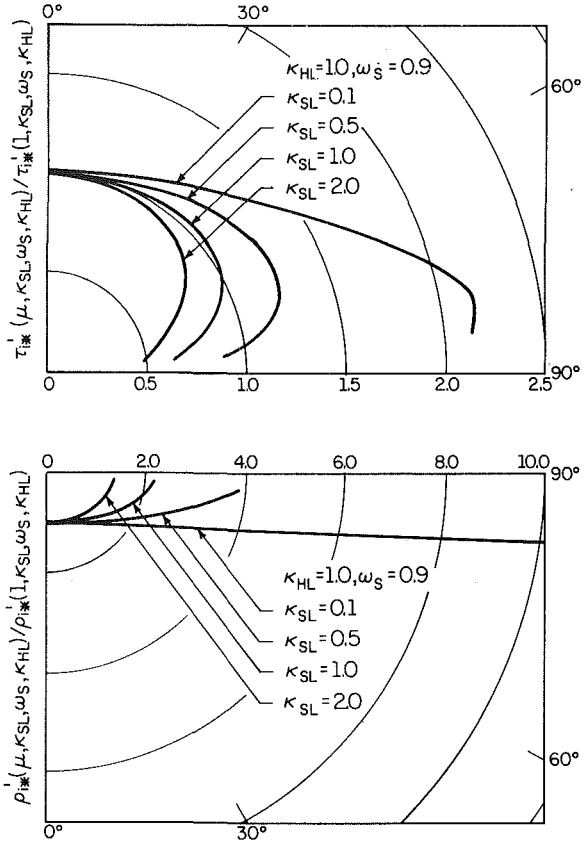

Fig. 3 Effect of κ_{SL} on the directional wide-band absorption for transmission and reflection

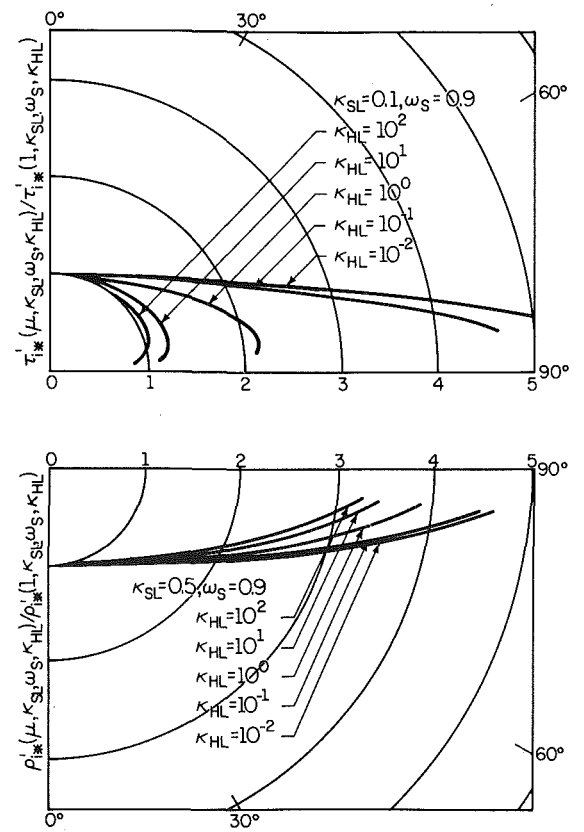

Fig. 4 Effect of κ_{HL} on the directional wide-band absorption for transmission and reflection

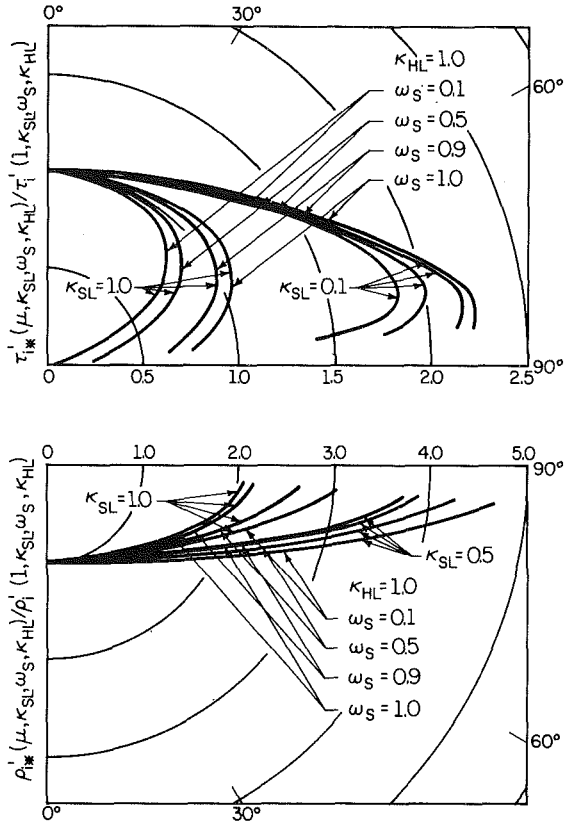

Fig. 5 Effect of ω_S on the directional wide-band absorption for transmission and reflection

$$\tau_i^*(\kappa_{SL},\omega_S,\kappa_{HL}) = q_i^{+*}(\kappa_{SL},\kappa_{SL},\omega_S,\kappa_{HL})$$
$$= \int_0^1 \left[\tau_\nu(\kappa_{SL},\omega_S,0) - \tau_\nu(\kappa_{SL},\omega_S,\gamma)\right] \frac{d\kappa_\nu^*}{\kappa_\nu^*} \quad (14b)$$

The total emission for a single wide band from an isothermal layer is obtained directly from equations (11-14). The directional wide-band absorption for the emission is

$$\epsilon_i'^*(\mu,\kappa_{SL},\omega_S,\kappa_{HL}) = \int_0^1 \left[\epsilon_\nu'(\mu,\kappa_{SL},\omega_S,0) - \epsilon_\nu'(\mu,\kappa_{SL},\omega_S,\gamma)\right] \frac{d\kappa_\nu^*}{\kappa_\nu^*}$$
$$= -\rho_i'^*(\mu,\kappa_{SL},\omega_S,\kappa_{HL}) - \tau_i'^*(\mu,\kappa_{SL},\omega_S,\kappa_{HL}) \quad (15)$$

and the hemispherical wide-band absorption for emission is

$$\epsilon_i^*(\kappa_{SL},\omega_S,\kappa_{HL}) = \int_0^1 \left[\epsilon_\nu(\kappa_{SL},\omega_S,0) - \epsilon_\nu(\kappa_{SL},\omega_S,\gamma)\right] \frac{d\kappa_\nu^*}{\kappa_\nu^*}$$
$$= -\rho_i^*(\kappa_{SL},\omega_S,\kappa_{HL}) - \tau_i^*(\kappa_{SL},\omega_S,\kappa_{HL}) \quad (16)$$

Thus the emission from an isothermal layer is obtained directly from the reflectance and transmittance for the boundary source problem.

The total quantities defined in the previous paragraphs incorporate the nongray gaseous absorption and gray scattering for a single wide band. The radiant heat flux at the walls of the plane layer for the realistic multiband situation is evaluated from these quantities. If the walls of the medium are black at T_1 and T_2 and the medium is isothermal at T_0, then the radiant flux incident on the wall at $\kappa_S = 0$ is

$$q^-(0,\kappa_{SL},\omega_S,\gamma) = \tau_\nu(\kappa_{SL},\omega_S,0)\sigma T_2^4 + \epsilon_\nu(\kappa_{SL},\omega_S,0)\sigma T_0^4$$
$$+ \rho_\nu(\kappa_{SL},\omega_S,0)\sigma T_1^4 - \sum_{i=1}^{n} \omega_{bi}[\tau_i^*(\kappa_{SL},\omega_S,\kappa_{HL})\pi i_{\nu_i b}(T_2)$$
$$+ \epsilon_i^*(\kappa_{SL},\omega_S,\kappa_{HL})\pi i_{\nu_i b}(T_0) + \rho_i^*(\kappa_{SL},\omega_S,\kappa_{HL})\pi i_{\nu_i b}(T_1)] \quad (17)$$

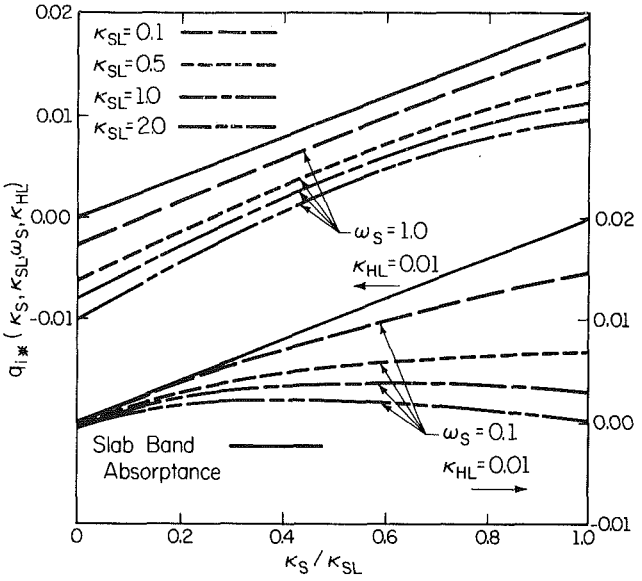

Fig. 6(a) Wide-band absorption heat flux verses κ_S with κ_{HL} = 0.01

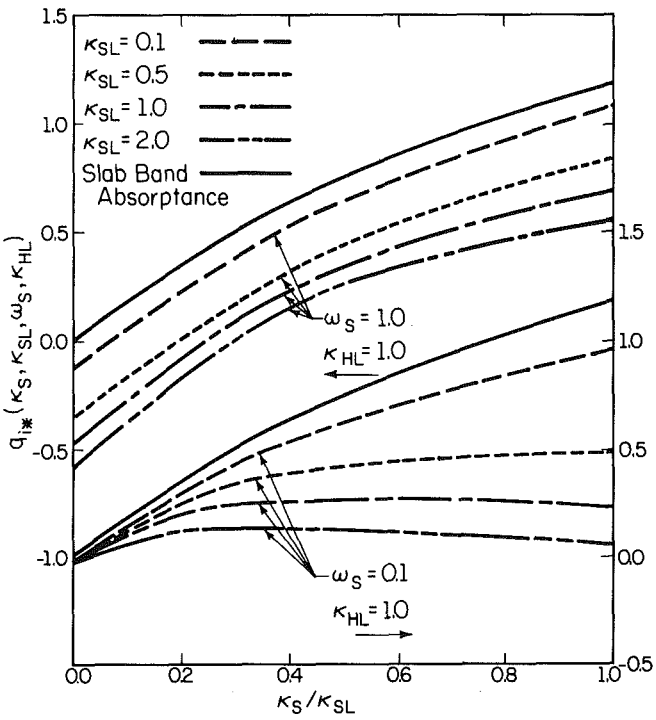

Fig. 6(b) Wide-band absorption heat flux verses κ_S with κ_{HL} = 1.0

where the first three terms on the right-hand side are the gray contributions and summation includes the gaseous effects of n bands. The gray transmittance and reflectance have been presented in reference [8]. The radiant heat flux is then

$$q(0,\kappa_{SL},\omega_S,\gamma) = q^+(0,\kappa_{SL},\omega_S,\gamma) - q^-(0,\kappa_{SL},\omega_S,\gamma)$$
$$= \sigma T_1^4 - q^-(0,\kappa_{SL},\omega_S,\gamma) \quad (18)$$

The scattering wide-band absorption quantities are functions of three variables $-\omega_S$, κ_{SL}, and κ_{HL}. Limiting expressions in various regions of these variables are possible. In the nonscattering limit as $\omega_S \to 0$ for a medium at zero temperature, the positive heat flux is

Table 1 $\rho_i'^*(1\kappa_{SL}\omega_S\kappa_{HL})$

κ_{SL}	0.1				0.5				1.0				2.0			
ω_S	1.0	0.9	0.5	0.1	1.0	0.9	0.5	0.1	1.0	0.9	0.5	0.1	1.0	0.9	0.5	0.1
$\rho_\nu'(1,\kappa_{SL},\omega_S,0)$ / κ_{HL}	0.0477	0.0421	0.0217	0.0041	0.2025	0.1690	0.0730	0.0120	0.3413	0.2674	0.0991	0.0150	0.5175	0.3617	0.1128	0.0163
0.01	0.0011	0.00097	0.00045	0.000075	0.0039	0.0030	0.0010	0.00014	0.0062	0.0042	0.0011	0.00013	0.0089	0.0047	0.00080	0.00008
0.1	0.0100	0.0086	0.0040	0.00069	0.0361	0.0282	0.0098	0.0013	0.0574	0.0398	0.0103	0.0012	0.0833	0.0449	0.0078	0.00082
1.0	0.0569	0.0495	0.0243	0.0043	0.2245	0.1796	0.0668	0.0097	0.3630	0.2618	0.0752	0.0095	0.5240	0.3058	0.0613	0.0068
10.0	0.1534	0.1346	0.0678	0.0124	0.6284	0.5135	0.2058	0.0317	1.0327	0.7759	0.2524	0.0348	1.5096	0.9623	0.2384	0.0297
100.0	0.2611	0.2297	0.1169	0.0216	1.0871	0.8961	0.3703	0.0586	1.8043	1.3791	0.4740	0.0681	2.6734	1.7710	0.4854	0.0646

Table 2 $\tau_i'^*(1,\kappa_{SL},\omega_S,\kappa_{HL})$

κ_{SL}	0.1				0.5				1.0				2.0			
ω_S	1.0	0.9	0.5	0.1	1.0	0.9	0.5	0.1	1.0	0.9	0.5	0.1	1.0	0.9	0.5	0.1
$\tau_\nu'(1,\kappa_{SL},\omega_S,0)$ / κ_{HL}	0.9523	0.9468	0.9265	0.9089	0.7975	0.7654	0.6742	0.6175	0.6587	0.5916	0.4461	0.3792	0.4825	0.3565	0.1893	0.1421
0.01	0.0102	0.0100	0.0095	0.0091	0.0102	0.0093	0.0072	0.0062	0.0101	0.0081	0.0049	0.0038	0.0100	0.0059	0.0021	0.0014
0.1	0.0986	0.0972	0.0925	0.0890	0.0977	0.0896	0.0701	0.0607	0.0959	0.0780	0.0475	0.0374	0.0930	0.0557	0.0206	0.0140
1.0	0.7818	0.7741	0.7471	0.7255	0.7266	0.6795	0.5588	0.4945	0.6728	0.5700	0.3765	0.3041	0.5947	0.3869	0.1626	0.1140
10.0	2.7710	2.7510	2.6794	2.6193	2.4108	2.2921	1.9698	1.7818	2.0822	1.8290	1.3127	1.0949	1.6500	1.1576	0.5613	0.4104
100.0	4.9631	4.9304	4.8125	4.7120	4.2464	4.0541	3.5222	3.2037	3.5981	3.1909	2.340	1.9681	2.7597	1.9782	0.9972	0.7375

$$q_\nu^+(\kappa_S,\kappa_{SL},\omega_S=0,\gamma=0)=2\pi i_{\nu b}(T_1)E_3(\kappa_S) \tag{19}$$

for no gaseous absorption and

$$q_\nu^+(\kappa_S,\kappa_{SL},\omega_S=0,\gamma)=2\pi i_{\nu b}(T_1)E_3(\kappa_S+\kappa_H\kappa_{\nu H}) \tag{20}$$

including gaseous absorption. The scattering wide-band absorption for the positive heat flux is then given in equation (8) as

$$q_i^{+*}(\kappa_S,\kappa_{SL},0,\kappa_H)=2\int_0^1 [E_3(\kappa_S) - E_3(\kappa_S+\kappa_H\kappa_\nu^*)]\frac{d\kappa_\nu^*}{\kappa_\nu^*} \tag{21}$$

This expression yields the linear result of $2\,\kappa_{HL}E_2(\kappa_S)$ for κ_{HL} small and the limit for κ_{HL} large could not be obtained in closed-form. In the limit of $\kappa_{SL}\to 0$, equation (21) yields the slab band absorption [5]

$$q_i^{+*}(0,0,0,\kappa_H)=1n(\kappa_H)+E_1(\kappa_H)+\gamma_E+\frac{1}{2}-E_3(\kappa_H) \tag{22}$$

Exact limiting expressions for the spectral radiative heat flux including scattering at finite and large ω_S have been obtained [9, 10] yet the forms do not permit convenient closed-form solutions for the scattering wide-band absorption quantities.

Results and Discussion

The determination of the total quantities in equations (7) and (8) requires the numerical evaluation of the spectral or gray intensity and radiative heat flux. The solution for the average incident intensity in equation (2) is obtained by the method of successive approximation [7, 11]. This result is then used in equation (1) to evaluate the spectral intensity and then the heat flux. The integral in equation (2) contains a singular kernel which was evaluated by the method of singularity subtraction [12]. The integrations in optical depth were performed by improved Gaussian quadratures of order 40 [13]. The integrals over κ_ν^* in equation (7) and (8) were evaluated by Gaussian quadratures of a maximum order of 25 [14]. The results for the transmittance and reflectance were compared with those in reference [8]. The directional and hemispherical values indicated a maximum difference of less than 0.1 percent even for $\kappa_{SL}=10.0$ and $\omega_S=1.0$. Computations were also compared to the results for radiative equilibrium [15] up to $\kappa_{SL}=30.0$ and the maximum difference was 0.4 percent.

The normal and hemispherical values of the wide-band absorption quantities exiting the layer are presented in Tables 1–4. The corresponding values for the reflection and transmission quantities without gaseous absorption are also given. The hemispherical wide-band absorption for reflection and transmission are also plotted in Figs. 1 and 2, respectively. The reflection-band absorption is strongly dependent upon the scattering contribution since the quantity would be zero if $\omega_S=0$. The value decreases by more than an order of magnitude as ω_S decreases from 1.0 to 0.1. For conservative scattering, the reflection-band absorption increases with increasing κ_{SL}, and the increase with increasing κ_{HL} is similar to the dependence of the slab-band absorption. The small albedo results indicate a clear shifting of the transistion (from the linear to logarithmic asymptotes) to larger κ_{HL} as κ_{SL} increases.

The transmission-band absorption (Fig. 2) shows a strong albedo dependence yet not of the magnitude observed in reflection. The effect of ω_S decreases as κ_{SL} decreases since the scattering contribution are reduced. In the limit of no

Table 3 $\rho_i^*(\kappa_{SL},\omega_S,\kappa_{HL})$

κ_{SL}	0.1				0.5				1.0				2.0			
ω_S	1.0	0.9	0.5	0.1	1.0	0.9	0.5	0.1	1.0	0.9	0.5	0.1	1.0	0.9	0.5	0.1
$\rho_v(\kappa_{SL},\omega_S,0)$ / κ_{HL}	0.0843	0.0744	0.0384	0.0072	0.2958	0.2475	0.1077	0.0178	0.4466	0.3527	0.1342	0.0208	0.6099	0.4372	0.1451	0.0216
0.01	0.0026	0.0023	0.0011	0.00019	0.0064	0.0051	0.0018	0.00025	0.0084	0.0058	0.0016	0.00019	0.0101	0.0055	0.0010	0.00011
0.1	0.0230	0.0200	0.00962	0.0017	0.0593	0.0468	0.0168	0.0024	0.0780	0.0549	0.0150	0.0019	0.0940	0.0521	0.0099	0.0011
1.0	0.1203	0.1052	0.0522	0.0094	0.3555	0.2863	0.1093	0.0162	0.4861	0.3549	0.1064	0.0139	0.5942	0.3567	0.0778	0.0091
10.0	0.2966	0.2605	0.1319	0.0242	0.9543	0.7831	0.3186	0.0498	1.3632	1.0344	0.3480	0.0492	1.7360	1.1372	0.3036	0.0397
100.0	0.4869	0.4286	0.2188	0.0405	1.6250	1.3439	0.5619	0.0898	2.3724	1.8299	0.6480	0.0952	3.1039	2.1120	0.6206	0.0861

Table 4 $\tau_i^*(\kappa_{SL},\omega_S,\kappa_{HL})$

κ_{SL}	0.1				0.5				1.0				2.0			
ω_S	1.0	0.9	0.5	0.1	1.0	0.9	0.5	0.1	1.0	0.9	0.5	0.1	1.0	0.9	0.5	0.1
$\tau_v(\kappa_{SL},\omega_S,0)$ / κ_{HL}	0.9157	0.9060	0.8704	0.8397	0.7042	0.6599	0.5350	0.4580	0.5534	0.4748	0.3067	0.2319	0.3901	0.2656	0.1071	0.0659
0.01	0.0172	0.0168	0.0155	0.0146	0.0134	0.0120	0.0085	0.0068	0.0115	0.0089	0.0046	0.0032	0.0097	0.0054	0.0015	0.00083
0.1	0.1608	0.1576	0.1466	0.1381	0.1263	0.1133	0.0814	0.0654	0.1076	0.0845	0.0443	0.0307	0.0903	0.0512	0.0147	0.0081
1.0	1.0748	1.0585	1.0010	0.9537	0.8429	0.7700	0.5834	0.4804	0.6989	0.5696	0.3243	0.2314	0.5514	0.3372	0.1095	0.0623
10.0	3.0822	3.0439	2.9065	2.7902	2.3900	2.2183	1.7501	1.4756	1.9211	1.6139	0.9914	0.7326	1.4219	0.9252	0.3417	0.2037
100.0	5.1875	5.1271	4.9089	4.7222	4.0101	3.7369	2.9817	2.5301	3.1942	2.7065	1.6976	1.2664	2.3186	1.5364	0.5882	0.3554

scattering, the slab-band absorptance is obtained which is indicated in the figure.

The directional distributions of the exiting quantities are presented in Figs. 3 to 5. The directional results are given relative to the normal value which have been given in Tables 1 and 2. The larger changes in the wide band absorption for transmittance and reflectance occur at small κ_{SL}'s. Figure 3 shows these variations as well as the significant changes for the reflectance quantity. The wide band absorption quantities became more uniform in angle as the scattering optical depth increases because the intensity distribution itself becomes more uniform. An increase in the wide-band optical depth reduces the wide-band absorption variation with angle as indicated in Fig. 4. If the scattering optical depth is increased beyond those presented, the distributions show less dependence upon κ_{HL} and are also less dependent upon angle. The effect of the scattering albedo is closely coupled with the scattering optical depth since these quantities control the scattering processes. Figure 5 indicates the large variations at small optical depths. The wide band absorption for transmission show large variations with large scattering albedos and a decrease as the albedo decreases. The wide band absorption for reflection exhibits the opposite trend. Note that all the distributions are presented relative to the normal value so that the magnitude of the wide band absorption quantities is assessed by use of the entries in Tables 1 and 2.

The internal distribution of the wide-band absorption heat flux is presented in Fig. 6. This heat flux is

$$q_i^*(\kappa_S,\kappa_{SL},\omega_S,\kappa_{HL}) = q_i^{+*}(\kappa_S,\kappa_{SL},\omega_S,\kappa_{HL}) - q_i^{-*}(\kappa_S,\kappa_{SL},\omega_S,\kappa_{HL})$$

The slab-band absorptance prediction as given in equation (22) is also presented. This nonscattering result has no contribution in the negative direction and, therefore, increases from zero to the value at κ_{HL}. All the scattering results have a negative contribution to the heat flux and exhibit negative values at $\kappa_S = 0$. These negative values are greatest for large albedos and large scattering optical depths where the negative contribution is significant. The wide-band absorption heat flux for $\omega_s = 1.0$ has the same trends with κ_S/κ_{SL} as the slab-band absorptance, i.e., linear at small κ_{HL} (Fig. 6(*a*)) shifting to logarithmic at larger κ_{HL} (Fig. 6(*b*). As ω_S decreases, the wide band absorption heat flux tends to level off and then decrease as κ_S increases. This occurs since the absorption of the positive heat flux exhibits an increase and then a decrease as κ_S/κ_{SL} increases. The wide-band absorption heat flux decreases because the scattering heat flux decreases as κ_S/κ_{SL} increases, and the gaseous absorption increase does not offset this trend. Note that the magnitudes and trends are much different for wide-band absorption quantities than the slab-band absorptance.

Conclusions

General wide-band absorption quantities for a planar medium have been defined. The effects of molecular gas absorption have been included for an isotropically scattering problem. Exact solutions have been presented for the intensity and heat flux for a single wide band. Analysis has also been given for the computation of the directional and total emission from an isothermal layer. The effects of multiband problems can also be determined from the results presented. The directional and hemispherical quantities have indicated the importance of scattering properties on both the exiting intensities and heat flux as well as the internal distributions.

Acknowledgment

This work was supported in part by the National Science Foundation under Grant No. MEA-8109250.

References

1 Viskanta, R., and Toor, J. S., "Radiant Energy Transfer in Waters," *Water Resources Res.*, Vol. 8(*d*), 1972, pp. 595–608.

2 Korb, G., and Zdunkowski, W., "Distribution of Radiative Energy in Ground Fog," *Tellus*, Vol. 12, 1970, pp. 298–320.

3 Lenoble, J., "Absorption Lines in the Radiation Scattered by a Planetary Atmosphere," *J. Quant. Spectroscopy and Radiative Transfer*, Vol. 8, 1968, pp. 641–654.

4 Buckius, R. O., and Fernandez-Fraga, A., "The Optical Path Length Approach to Radiation Heat Transfer with Isotropic Scattering and Gaseous Absorption," *J. Quant. Spectroscopy and Radiative Transfer*, Vol. 24, 1980, pp. 1–13.

5 Edwards, D. K., and Balakrishnan, A., "Slab Band Absorptance for Molecular Gas Radiation," *J. Quant. Spectroscopy and Radiative Transfer*, Vol. 12, 1972, pp. 1379–1387.

6 Edwards, D. K., "Molecular Gas Band Radiation," *Adv. Heat Transfer*, Vol. 12, 1976, pp. 115–193.

7 Sparrow, E. M., and Cess, R. D., *Radiation Heat Transfer*, Hemisphere Publishing Corporation, McGraw-Hill, New York, 1978.

8 Crosbie, A. L., "Apparent Radiative Properties of an Isotropically Scattering Medium on a Diffuse Substrate," ASME JOURNAL OF HEAT TRANSFER, Vol. 101, 1979, pp. 68–75.

9 Crosbie, A. L., "Emittance of an Isothermal, Isotropically Scattering Medium," *AIAA Journal*, Vol. 11 (8), 1973, pp. 1203–1205.

10 Crosbie, A. L., "Reflection Function for an Isotropically Scattering Finite Medium," *AIAA Journal*, Vol. 11 (10), 1973, pp. 1448–1450.

11 Crosbie, A. L., Merriam, R. L., and Viskanta, R., "Application of Sokolov's Method to Problems of Radiative Transfer," *J. Quant. Spectroscopy and Radiative Transfer*, Vol. 8, 1968, pp. 1609–1613.

12 Hartree, D. R., *Numerical Analysis*, Oxford University Press, London, 1958.

13 Kronrod, A. S., *Nodes and Weights of Quadrature Formulas*, Consultants Bureau, New York, 1965.

14 Stroud, A. H., and Secrest, D., *Gaussian Quadrature Formulas*, Prentice-Hall, Englewood Cliffs, N.J., 1966.

15 Heaslet, M. A., and Warming R. F., "Radiative Transport in an Absorbing Planar Medium II. Predictions of Radiative Source Function," *International Journal of Heat and Mass Transfer*, Vol. 10, 1967, pp. 1413–1427.

Attenuation of Thermal Radiation by Pulverized Coal and Char

W. L. Grosshandler
Associate Professor,
Department of Mechanical Engineering,
Washington State University,
Pullman, Wash. 99164
Mem. ASME

S. L. P. Monteiro
Department of Physics,
Washington State University,
Pullman, Wash. 99164

The absorption and scattering of thermal radiation within a dilute cloud of pulverized coal and char is investigated. Results are presented of monochromatic absorptivity measurements on particles 50–150 μm in diameter under conditions representative of the early pyrolysis zone of a combustion chamber. No dependence of absorptivity on coal composition could be discerned for the three lignite and bituminous coals selected. A slight increase in monochromatic absorptivity with temperature and extent of char was observed. For the spectral region investigated, 1.2–5.3 μm, an empirical equation of the form $\alpha_\lambda = 0.78 + 0.18/\lambda^{1/2}$ was found to represent the data for all coals and chars within 5 percent. A single total hemispherical absorptivity of 0.89 is recommended for heat-transfer calculations in pulverized coal and char clouds if the particles can be assumed to act as Mie scatters, and if the volume fraction of ash and soot particles is small.

Introduction

Combustion of coal dust suspensions can occur in both desirable and undesirable situations. It is desirable to have pulverized coal as a fuel, primarily in large furnaces, but also in advanced design MHD generators, gas turbines, and Diesel engines. It is undesirable to have ignition of coal dust suspensions in mining or coal processing operations, with the ultimate hazard being a disastrous explosion. In both controlled and uncontrolled combustion the primary driving force is the transfer of heat from the exothermic oxidation back to the unheated fuel. Conduction, convection, and radiation all play a role in this process; but because of the nature of the suspension, the temperature of the products, and the speed of the combustion reaction, radiation is often the dominant mode of heat transfer. Thermal radiation is also the primary mechanism of energy transfer from the burning coal particle cloud to the water-cooled walls of a boiler furnace because of the large enclosure dimensions, relatively low gas velocities, and high temperature.

Within a suspension of particulate matter, thermal radiation can be either enhanced or attenuated, depending upon the size and concentration of particulates, the temperature distribution, and the radiative properties of the matter. Even for a pure material such as carbon, the specification of the pertinent radiative properties is not straightforward. The crystalline structure of the carbon and the surface conditions can greatly affect the spectral emissivity. For example, Kibler et al. [1] reported that the A-face of pyrolytic graphite has about double the emissivity of the C-face in the near infrared for temperatures above 1800 K. For a heterogeneous substance such as coal, the difficulties are multiplied since the particulate cloud can be made up of varying fractions of unreacted coal, char, ash, and soot, each of which has its own optical properties dependent upon wavelength, temperature and particle size. Viskanta et al. [2] have recently examined the importance of some of these parameters (mean particle radius, size distribution, temperature, back-scatter) for polydispersions of various coals and fly-ash using a numerical model with average spectral properties.

Research into the optical properties of carbonaceous materials extends back to work done by Senftleben and Benedict [3] in which they measured the reflectivity of electrode carbon in the infrared wavelengths. Whitson [4] has compiled comprehensive data from more recent measurements of the refractive index and emissivity of graphite and carbonaceous material at high temperatures. The results of over twenty-five references are summarized in graphical and tabular form for the spectral region between 0.4 and 12.5 μm. Blokh [5] has reviewed the results of many experiments on bulk coal, soot, and pulverized coal. Using Mie theory, the absorption and scattering coefficients of different coals were calculated as a function of particle size.

As an indication of the variation in properties between coal and ash, Sato and Kunitomo [6] estimated their total emissivities to be 0.83 and 0.58, respectively, at moderate temperatures. The strong spectral dependence of the emissivity of Al_2O_3, a significant component of boiler ash, is given in the handbook by Whitson [4]. The total emissivity changes from about 0.75 at room temperature to less than 0.40 above 1200 K [7].

The optical constants of polished specimens of several coals have been determined by Foster and Howarth [8]. They measured significant differences between the spectral refractive index for coal and polycrystalline graphite. Little work has been reported on the monochromatic properties of coal in pulverized form, or the effect of heating the coal. This study was undertaken to determine the absorptive properties of different coals under conditions similar to the early pyrolysis zone of a pulverized coal furnace. Three different coal types were investigated: a bituminous, a sub-bituminous, and a lignite. Particle diameters were typical of furnace operation, ranging between 40 and 150 μm. Chars formed from the coal were conditioned up to 1200 K. Spectral measurements were made of the absorptivity in the wavelength region between 1.2 and 5.3 μm, the region corresponding to over 80 percent of the radiant energy from a blackbody at temperatures ranging from 1400 to 2400 K.

The theoretical background on thermal radiation attenuation is briefly reviewed in the next section. With this background, the design of an experimental facility in which to determine the spectral absorptivity of coal and char particles is discussed. The results of the experimental measurements are then presented. In the final section, the importance of scattering to the attenuation process is investigated.

Theoretical Background

On a monochromatic basis, the change in intensity of a beam of radiation in a given angle in space is determined by the solution of the equation of transfer ([9], Ch. 14])

Contributed by the Heat Transfer Division for publication in the JOURNAL OF HEAT TRANSFER. Manuscript received by the Heat Transfer Division December 14, 1981. Paper No. 81-HT-23.

$$\frac{dI_\lambda}{dl} = -(K_a + K_s) I_\lambda + K_a I_{b\lambda}$$

$$+ \frac{K_s}{4\pi} \int_{\Omega_i} I_\lambda(\Omega_i)\, \Phi(\lambda, \Omega, \Omega_i)\, d\Omega_i \qquad (1)$$

The importance of individual terms in this equation vary with the physical properties of the medium and the size of the particles in the medium relative to the wavelength of radiation, as characterized by the size parameter, $2\pi r/\lambda$.

For particles not too closely spaced (distance between centers greater than $3r$ [10]), the effect of a cloud of particles can be found by summing over all individual particles. In the large size parameter limit, the absorption coefficient becomes

$$K_a = \int_0^\infty N(r)\, A(r)\, \alpha_\lambda\, dr = \alpha_\lambda \tilde{A} \qquad (2)$$

where α_λ is the hemispherical spectral absorptivity of the particles, $N(r)$ is the particle size frequency distribution per unit volume, and $A(r)$ is the effective geometric cross section of the particles. The particle cross section per unit volume, $\tilde{A}$, is defined by

$$\int_0^\infty N(r)\, A(r)\, dr.$$

The integral term in equation (1) accounts for all scattering into the line-of-sight. For large specularly reflecting particles, the scatter is predominantly in the forward direction, so that the final term becomes approximately $K_s I_\lambda$. (The extent to which this is true for coal dust is explored in a later section.) If the particles can be assumed to both emit and absorb radiation equally from all angles, equation (1) can be written

$$\frac{dI_\lambda}{dl} = -\alpha_\lambda \tilde{A} I_\lambda + \alpha_\lambda \tilde{A} I_{b\lambda} \qquad (3)$$

Solving for the individual particle absorptivity in an isothermal, homogeneous cloud,

$$\alpha_\lambda = -\frac{1}{\tilde{A}L} ln\left[\frac{I_{b\lambda} - I_\lambda(L)}{I_{b\lambda} - I_\lambda(0)}\right] \qquad (4)$$

If the particle cross section per unit volume, the total path-length, L, and the temperature are known, then the particle hemispherical spectral absorptivity can be easily determined by measuring I_λ at $l = 0$ and L. This is the basis of the procedure used in the experimental facility described next.

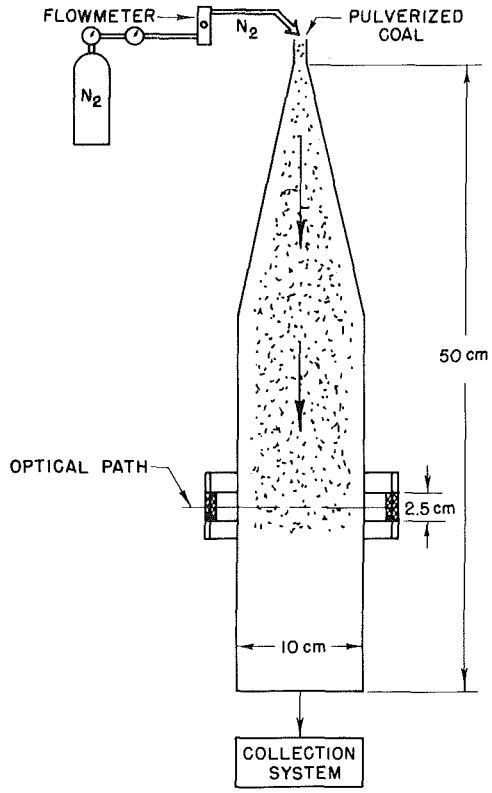

Fig. 1 Test chamber configuration

Experimental Apparatus

The experiment was carried out in a sealed steel chamber 50-cm high, 10.2-cm deep, and 2.5-cm wide. Pulverized coal was fed in vertically from the top of the chamber. The optical path was along the depth, 10.2-cm long. At each end of the optical path an Irtran infrared transparent window was attached (see Fig. 1). The stainless steel chamber served as a heat exchanger as well as to maintain the samples in an inert atmosphere. Three chromel/alumel thermocouples were

Nomenclature

$A(r)$ = projected area of particles of radius r
$\tilde{A}$ = total particle cross-sectional area per unit volume of cloud
A_c = cross-sectional area of duct
a = curve-fitting constant, equation (8)
b = curve-fitting constant, equation (8)
c = proportionality constant, equation (6)
C_1, C_2 = Planck's first and second radiation constants
F_i = normalized size frequency distribution function
I_λ = monochromatic intensity
$I_{b\lambda}$ = monochromatic blackbody intensity
K_a = monochromatic absorption coefficient
K_s = monochromatic scattering coefficient
l = distance along optical path
L = total length of optical path
$\dot{m}_p$ = mass flow rate of particles
n = curve-fitting constant, equation (8), or real part of refractive index
$\tilde{n}$ = complex refractive index, $n - i\kappa$
$N_i, N(r)$ = number of particles of given radius per unit volume of cloud
r, r_i = particle radius
T_s = radiation source temperature
u_p = absolute particle velocity
v_p = particle specific volume
α = total hemispherical absorptivity of solid material
α_λ = monochromatic-hemispherical absorptivity of solid material
θ = scattering angle
κ = imaginary part of refractive index
$\Gamma(n)$ = gamma function
λ = wavelength
ρ_λ = monochromatic-hemispherical reflectivity of solid material
σ = Stefan-Boltzmann constant
Φ = phase function for scattering
Ω = solid angle

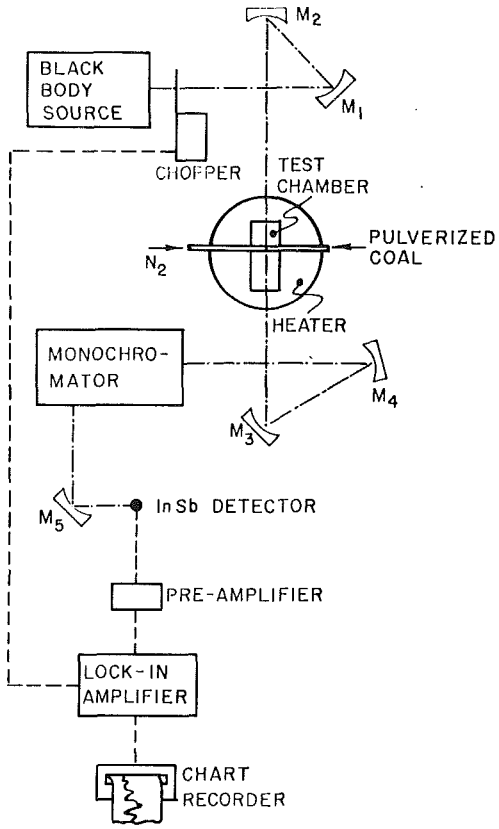

Fig. 2 Top view of test chamber showing optical path

located inside the test chamber just below the optical path. These measured the test chamber temperature close to the wall, a quarter, and a half of the way along the optical path. Temperature variations of less than ±5 K were measured, allowing the assumption of isothermal conditions to be made. At the bottom of the chamber a collecting filter received the pulverized coal for mass and size distribution determination. Coal was fed by a Vibra-screw auger feeder to the top of the chamber. Dry inert nitrogen gas transported the coal and served, by varying its flow rate, as a control on the sample density as the cloud moved down past the windows through the optical path. The nitrogen line was equipped with a pressure gage and a calibrated rotameter for volume flow rate determination.

The stainless steel chamber was located inside a propane-fired furnace, internally lined with a zirconia casting and externally insulated with a Cotronics ceramic blanket. The two Irtran windows provided optical access to the chamber. Approximately 30 cm of the coal feeding line was also within the furnace, flowing counter to the exhaust, thus increasing the heat-exchanging length. This precaution was taken to ensure that the sample would be at the desired temperature as it passed through the optical path.

The radiation source was a blackbody cavity manufactured by Infrared Industries (Model 263). A mechanical chopper (PAR Model 125-A) was used in conjunction with a lock-in amplifier (PAR Model 120). The monochromator used was a 1/4 meter Spex with two different gratings, covering the whole spectral region scanned by the Judson series 10 InSb detector (i.e., 1.2 to 5.3 μm). To ensure spectral consistency, data points were taken with each grating in the overlapping region. The gratings were adjusted using the harmonics of a He-Ne laser. The estimated half-width of the signal at the output of the monochromator was .01 μm or less. The collection optics had an included angle of 12 deg.

Figure 2 is a schematic of the optical path passing through the test chamber. Radiation from the infrared source was chopped and then focused with front-surfaced mirrors M1 and M2 in the experimental chamber. The chopping was necessary to improve the signal-to-noise-ratio and to reject emission by the surrounding chamber and coal particle cloud for the high-temperature measurements. Within the experimental chamber, one could control the cloud density by adjusting the mass flow rate of pulverized coal, the size distribution, and the volume flow of nitrogen. A thin cloud was always used, with density varying typically from 0.0002 to 0.001 g/cc (volume fraction between 0.00014 and 0.0007).

The optical components were purged with dry nitrogen, but some atmospheric CO_2 and H_2O were still present. To take into consideration the atmospheric absorption within the spectral region studied, the monochromator was fixed at a specific wavelength and the signal recorded with no coal present. Keeping all conditions constant, pulverized coal was then fed into the chamber, creating additional absorption. The stronger signal (without coal) was proportional to the incident radiation on the cloud, while the weaker signal (passing through the coal cloud) showed the coal absorption in addition to any previous atmospheric absorption. When the blackbody emission is eliminated, equation (4) involves only the ratio of the intensities, so that atmospheric absorption is automatically discounted. A typical run consisted of a steady signal (noise < 1/2 percent) corresponding to the source output at the selected wavelength, attenuated by the prevailing circumstances, followed by a drop in signal when the coal feeder was turned on. The coal attenuated signal showed a maximum noise of 5 percent due to fluctuations in the cloud density. Cases with larger fluctuations were rejected as unreliable. The time constant in the lock-in amplifier was kept at 1 s in all runs, maintaining a standard cutoff of very short term fluctuations in cloud density.

An important part of the experiment was the sample preparation. Mechanical sieving gave good results with 8 in. dia sieves as small as 45 μm (325 mesh) if batches of 50 gm of well dried pulverized coal were used. Moisture tends to conglomerate the particles, and consequently small particles would stay together with the large fraction. An aerodynamical separator was also used with equivalent results in a much shorter time. To determine the particle size distribution, a Coulter counter was used. This instrument determines the size of small particles by measuring the capacitance variations as the particles pass through a small aperture. Fifty thousand particles can be easily counted this way in approximately 15 min., giving a very good statistical distribution.

The char was prepared from the presieved coal samples. The test chamber, itself, served to devolatize the coal. With the temperature set at the desired level between 600 and 1200 K, the particles, suspended in dry nitrogen, were allowed to pass through the heated chamber. The transit time was about 10 s at the elevated temperatures. The partially devolatized char was recovered, and the process repeated three times. A size distribution measurement was made after the final pass, and this material was used in all the char measurements.

Experimental Results

The blackbody emission from the particle cloud was eliminated in the experimental measurements by mechanically chopping the incident radiation, and by amplifying only the synchronized transmitted intensity. Thus, the particle spectral-hemispherical absorptivity could be determined using equation (4), which becomes

$$\alpha_\lambda = -ln\,[I_\lambda\,(L)/I_\lambda(0)]/\tilde{A}L \qquad (5)$$

The pathlength, L, is fixed at 10.2 cm, the intensity ratio is the

primary dependent variable which is measured, and $\tilde{A}$ is an experimental variable which can be computed from the cloud density.

$\tilde{A}$ is evaluated by a discrete sum with sixteen terms, the number of channels in the Coulter counter which furnishes the particle size frequency distribution, F_i. (A typical distribution is shown in Fig. 3.). The particle number density, N_i, in each discrete radius increment, r_i, is directly proportional to F_i, so that

$$\tilde{A} = \sum_{i=1}^{16} cF_i r_i^2 \tag{6}$$

where c is a constant of proportionality and πr_i^2 is the cross-sectional area of the assumed spherical particles. The conservation of mass flowing through the test section was used to evaluate c in terms of the coal mass flow rate, $\dot{m}_p$, the coal particle specific volume, v_p, the absolute particle velocity, u_p, and the cross-sectional area of the duct, A_c. The result is

$$c = \dot{m}\, v_p / \left(A_c u_p \sum_i F_i \frac{4}{3} \pi r_i^3 \right) \tag{7}$$

Maximum random errors of less than 5 percent were associated with $\dot{m}_p$, v_p, and u_p. A_c was fixed by the experiment and F_i and r_i were based upon a large statistical average. Replication of experiments for a fixed wavelength, coal-type, and temperature was used to keep uncertainty in the computed value of α_λ within ± 3 percent. Details on computing $\tilde{A}$ and a more complete discussion of errors can be found in the dissertation by Monteiro [11] and the paper by Monteiro and Grosshandler [12].

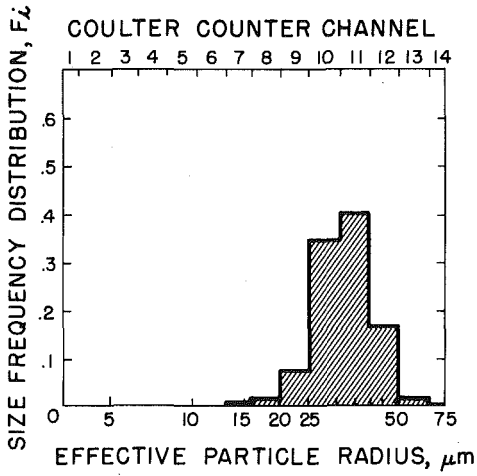

Fig. 3 Typical size frequency distribution for lignite coal as determined from Coulter particle counter

Table 1 Experimental parameters

Parameter	Range
wavelength, μm	1.2–5.3
coal types	3 (see Table 2)
temperature, K	300–1200
coal mass flow rate, g/s	0.06–0.15
particle cloud density, g/cm^3	0.0002–0.001
particle solid density, g/cm^3	1.4
nitrogen speed, cm/s	1.4–8.8
measured intensity ratio, $I_\lambda(l)/I_\lambda(0)$	0.60–0.85
blackbody source temperature	1200 K

Table 1 shows the range of variation of the principal parameters used during the experiment. Of particular interest were the effects of wavelength, coal type, and the temperature on the particle absorptivity. The composition of the three coals tested, before charring, is given in Table 2.

The wavelength effect on the spectral absorptivity was found to be appreciable. Figure 4 shows the experimentally determined particle spectral-hemispherical absorptivity as a function of wavelength, with all coal types plotted in a single curve. The temperature is 300 K. The figure indicates a general decrease in the absorptivity from about 0.95 at 1 μm down to about 0.87 at a wavelength of 4 μm. There is no statistically significant difference among the three coal types, in spite of the 50 percent increase in ash content between the lignite and the bituminous coal. This is not too surprising considering recent measurements [13] of coal ash deposits, indicating that their emissivity is close to that measured in the present work.

The effect of temperature, or degree of charring, is demonstrated in Fig. 5. Changing the temperature does not change the general spectral trend of the absorptivity for the lignite coal and char. There is a noticeable increase in absorption by the higher temperature, more highly devolatized char. This is consistent with a decrease in hydrogen content and increase in porosity of the charred material. (Inspection of the charred material under an electron microscope [11] revealed that the particles were sponge-like, with fewer jagged edges than the parent coal particles.) The least squares plot of the 300 and 900 K temperature measurements may not be significantly different, but the 5 percent increase in absorptivity at the short wavelengths for the 1200 K char is larger than the estimated uncertainty of 3 percent in the data.

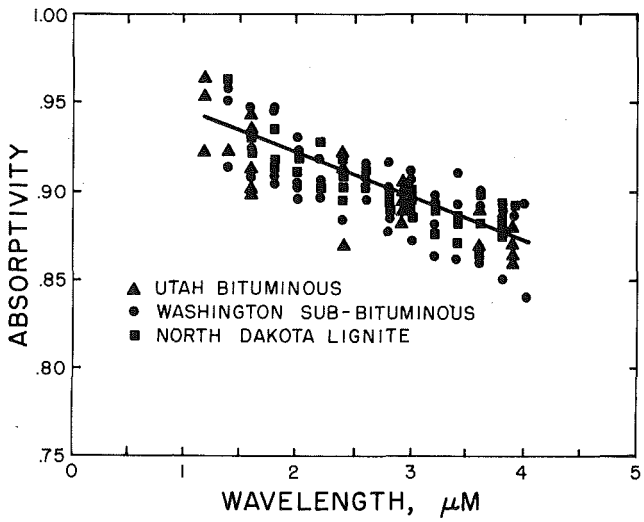

Fig. 4 Monochromatic absorptivity of three different coals at room temperature

Table 2 Coal analysis

Designation	Type	C/H atom ratio	Ash, % dry wt.	Carbon, % dry wt.	Moisture, % as received
I	Utah bituminous	1.10	17.4	66	3.4
II	North Dakota lignite	1.22	11.4	63	29.8
III	Washington sub-bituminous	1.29	14.9	65	7.0

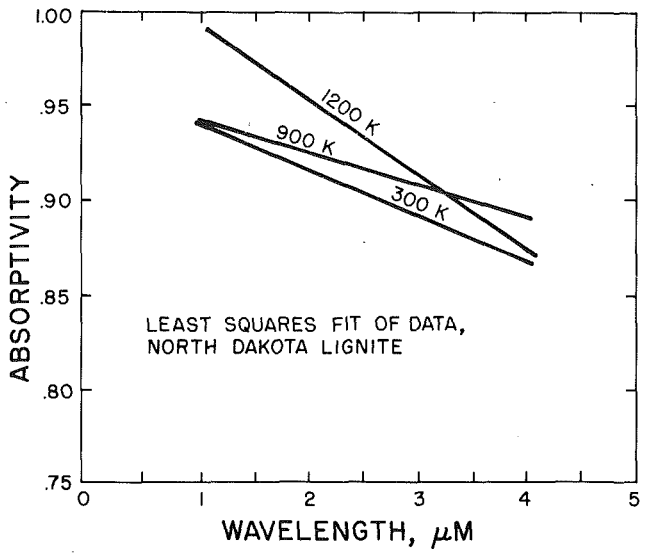

Fig. 5 Effect of temperature on monochromatic absorptivity

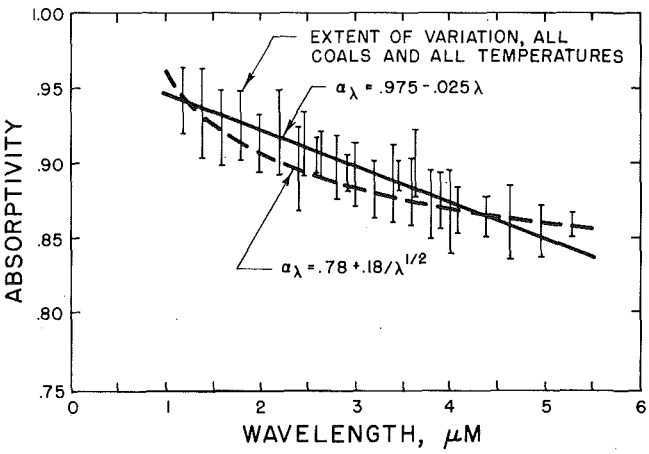

Fig. 6 Correlations of all spectral absorptivity data for three types of coal and char, and temperatures between 300 and 1200 K

The absorptivity data from all temperature conditions and all coal types and chars is plotted versus wavelength on a single curve in Fig. 6. The extent of measurement fluctuations for all of these cases is indicated for each spectral region investigated. The data can be correlated with a polynomial of the general form

$$\alpha_\lambda = a + b\lambda^n \tag{8}$$

where a, b, and n are constants. For a simple linear expression, it is found that the spectral absorptivity can be represented by $\alpha_\lambda = 0.975 - 0.025\lambda$ in the spectral region between 1.0 and 5.3 μm. Close inspection of th data, however, suggests that the absorptivity levels off after 4 μm, so that a preferred expression is

$$\alpha_\lambda = 0.78 + 0.18/\lambda^{1/2} \tag{9}$$

This expression is shown plotted as the dashed line in Fig. 6. The spectral reflectivity, $\rho_\lambda = 1 - \alpha_\lambda$, is compared in Fig. 7 with the results of Foster and Howarth [8] for a low ash coal (dot-dash curve) and polycrystalline graphite (solid curve). It should be pointed out that Foster and Howarth used specimens of polished lump coal and graphite for their reflectivity measurements. Their spectral reflectivity measurements agree well with the present results for wavelengths between 1 and 2 μm. At 5 μm, however, the reflectivity of the particulate matter is about 0.15, which is twice what Foster and Howarth calculated. A recalculation,

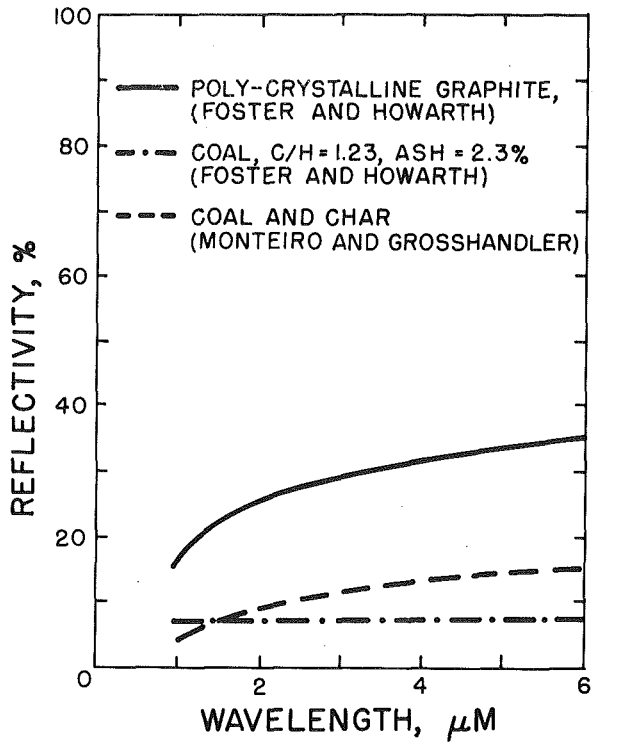

Fig. 7 Monochromatic hemispherical reflectivity of coal and char compared to results of Foster and Howarth [8] for polished bulk specimens of coal and graphite

though, based on their own data indicates that their curve may be in error, and a value of ρ_λ closer to 0.12 may be more appropriate.

The total hemispherical absorptivity is defined as the source spectral-distribution function weighted average of the spectral-hemispherical absorptivity. For a gray or blackbody source at T_s, this is written

$$\alpha(T_s) = \int_0^\infty \frac{\alpha_\lambda I_{b\lambda}(T_s)\, d\lambda}{\sigma T_s^4/\pi} \tag{10}$$

Using equation (8) for α_λ, the integral can be broken into two terms, with the first term integrating exactly to "a." The second term, involving the coefficient b, becomes

$$\frac{\pi}{\sigma T_s^4}\int_0^\infty b\lambda^n I_{b\lambda} d\lambda \cong \frac{\pi}{\sigma T_s^4}\int_0^\infty \frac{2C_1 b\lambda^n}{\lambda^5 \exp(C_2/\lambda T_s)}\, d\lambda \tag{11}$$

Planck's blackbody distribution function, $I_{b\lambda}$, has been approximated by Wien's distribution in (11), which is reasonable for the temperature-wavelength region of interest in furnace calculations ([9], Ch. 2). Equation (11) can be integrated analytically, with the result that the total hemispherical absorptivity is

$$\alpha(T_s) = a + \frac{2\, bC_1 \Gamma(4-n)}{\sigma C_2^{4-n} T_s^{\,n}} \tag{12}$$

The gamma function, Γ, depends upon the order of the wavelength dependence, n, in equation (8).

For the negative half-order dependence given in equation (9), the total hemispherical absorptivity becomes

$$\alpha(T_s) = 0.78 + 0.00269\, T_s^{1/2} \tag{13}$$

This is a weak dependence upon the source temperature. For conditions typical of furnace combustion, between 1200 and 2200 K, α is bounded between 0.87 and 0.91. The linear relation plotted in Fig. 6 yields results which are only 1 per cent higher. It should be pointed out that neither of these

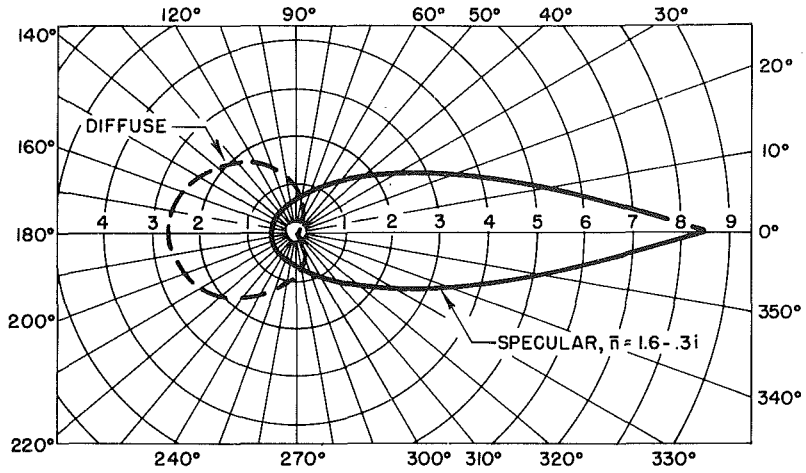

Fig. 8 Scattering phase functions comparing diffuse and specular spheres. Total hemispherical reflectivity equals 0.12

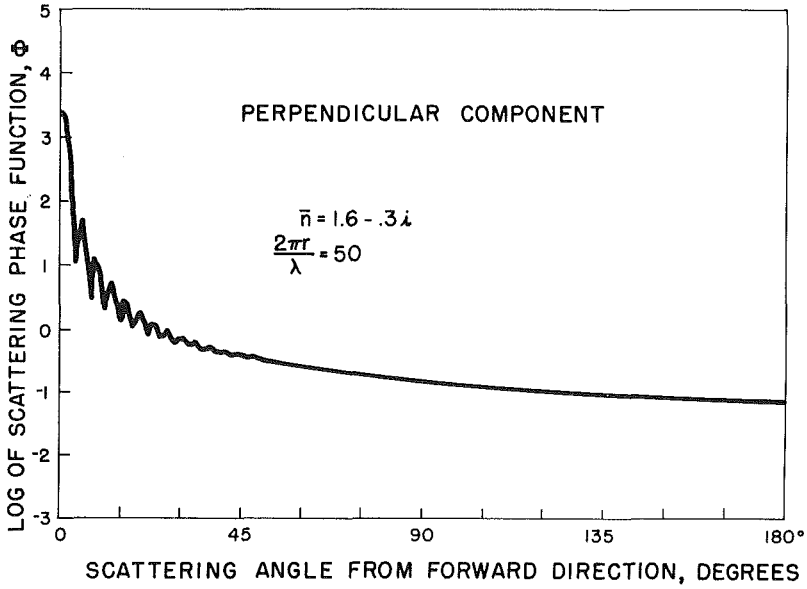

Fig. 9 Mie scattering phase function for coal with index of refraction equal to 1.6 − 0.3i and a size parameter of 50. Perpendicularly polarized component shown.

algebraic expressions predict the actual spectral behavior for wavelengths in the visible or far infrared region. In one case, the spectral absorptivity exceeds 1.0 for $\lambda < .67$ μm, and in the other, α_λ becomes negative for $\lambda > 39$ μm. However, since about 90 percent of all radiant energy within a furnace at 1500 K is located between 1.0 and 6.0 μm, the nonphysical aspects of the data correlation should not have a significant effect on the absorptivity. Thus, it appears that for the range of conditions investigated, a single value of total hemispherical absorptivity equal to 0.89 is sufficient for reasonably accurate coal and char cloud absorption calculations.

Scattering in Coal Particle Clouds

The reliability of the experimental results presented depends upon the accuracy of the assumptions used in arriving at equation (3). In general, radiation can be refracted, diffracted, or reflected from an optically large particle. Important assumptions that have been made are that all the refracted radiation is absorbed, all the diffracted radiation directed into the forward direction, and all of the reflection is also forward. One can be convinced of the appropriateness of these assumptions by examining each of these processes in order.

A fraction of the radiation which is refracted into the coal particle will be absorbed before it passes through to the far surface of the particle. The fraction which is transmitted can then undergo reflection or refraction at the second interface. This phenomena can be important in individual particles of small or moderate optical depth, as determined by Simpson [14] in his ray-tracing study of heavy fuel oils. The absorption coefficient of coal can be estimated from the data of Foster and Howarth [8] to be about 1.9×10^6 m^{-1} at a wavelength of 3 μm; so that for a particle diameter of 10 μm, less than 10^{-8} of the incident radiation will penetrate to the far surface. The remainder is absorbed.

The scattering efficiency due to diffraction is equal to one. When the size parameter is greater than 30, the phase function for diffraction drops below .004 for angles greater than 12 deg off of the forward direction ([9], p. 584). What these two facts imply is that if the collection optics encompass all of the radiation passing through a coal/char particle cloud within 12 deg of the forward direction, then the out-scatter along the line-of-sight will be balanced by the in-scatter represented by

the diffraction contribution to the integral in equation (1). Since the size parameters used in the experiment are mostly greater than 50, and since the collection optics encompass a cone angle of 12 deg, it is appropriate to treat diffraction as was done in developing equation (3).

The directional distribution of radiation reflected from a large spherical particle is strongly dependent upon the surface condition. The surface will be optically smooth (specular) if the average roughness and pore size are significantly less than the wavelength of radiation; say, of the order of 0.5 μm. The spectrum investigated went up to 5.3 μm, so that a random roughness or pore size above 10μm would lead to a diffuse surface on a particle greater than 60μm in diameter. Crevices of the order of tens of micrometers were observed over a portion of the surface of the coal particles [11]. Heating the coal to the highest temperature increased the number of pores in the submicron to 10 micrometer range, but neither material could be classified by their electronmicrographs as being solely specular or diffuse. Figure 8 compares the phase functions for the two limiting cases, computed from the equations in any of a number of textbooks (e.g., [9], Ch. 16). In the large particle limit, neither diffuse nor specular reflection depend upon diameter. The diffuse phase function is also independent of the optical properties of the material. The specular phase function is based upon a typical coal refractive index of $\tilde{n} = 1.6 - 0.3i$ [8], for which the hemispherical reflectivity can be calculated to be 0.12. While the specular phase function is not as sharply peaked as that for diffraction, it is still predominantly in the forward direction. In contrast, diffuse scatter is predominantly in the backward direction, with no component for $\theta = 0$ deg. From equation (1), then, the effect is to increase attenuation of the incident radiation by reflection, and to contribute nothing along the line-of-sight with the integral term. The absorptivity as calculated by equation (4) is, thus, an upper limit on the true particle absorptivity if the particle surface is diffuse to any degree.

Viskanta et al. [2] estimated the effect of backward scatter on the overall absorptance of a polydispersion of bituminous coal in a plane layer. They found about a 5 percent decrease in effective absorptance if the particles were assumed to scatter isotropically rather than predominantly in the forward direction when the volume fraction was equal to that used in the present work. The size distribution used in their calculations had a mean radius of only 6.1 μm, so that it is impossible to compare quantitatively the results of their estimates with our experiments. However, their estimates are consistent with the statement regarding the measured particle absorptivity as being an upper limit.

The Mie theory can be applied if the particles are assumed to be true specular, spherical reflectors. The numerical code of Grehan and Gousbet [15] was used to estimate the directional intensity scattered by Mie-type coal particles with the same refractive index as used above. Figure 9 is a plot of the phase function for the perpendicular component of intensity for a size parameter of 50. The phase function, on the ordinate, is reduced about three orders-of-magnitude by an angle θ from the forward direction (plotted along the abscissa) of 15 deg. If the intensity is integrated over the solid angle viewed by the detector, using this phase function, it is found that 0.990 of all the scattered radiation is collected by the optics. Similar calculations on both the parallel and perpendicular components for size parameters between 26 and 256 indicate that over 98 percent of the scattered radiation is incident on the detector.

Therefore, it can be concluded that the assumption of forward scatter is as reliable as the assumption that the coal and char behave as specular, spherical scattering centers. To the extent that some of the particles act in a diffuse manner, the reported absorptivities are upper limits.

Summary and Conclusions

The spectral absorptivity of pulverized coal and char in the near infrared has been studied. Measurements were made with particle sizes between 50 and 150 μm suspended in an inert nitrogen cloud. The coal rank and ash content were varied, and chars were formed at temperatures up to 1200 K. The results can be summarized as follows:

1 Pulverized coal and char absorb from 85 to 95 percent of the radiation between 1.2 and 5.3 μm.

2 The spectral absorptivity decreases with increasing wavelength, and can be approximated by the relation $\alpha_\lambda = 0.78 + 0.18/\lambda^{1/2}$.

3 No effect on the absorptivity was found due to coal rank or ash content.

4 The absorptivity increases slightly with the extent of charring at temperatures above 900 K.

Radiation is only one phenomena which must be considered in engineering calculations of heat transfer in coal-fired furnaces and combustors, so that a simple total hemispherical absorptivity applicable to all coals and chars is highly desirable. Based upon the findings of the present study it is recommended that a value of 0.89 be used in regions of the flame where the coal and char contribute significantly more to the solids volume fraction than either soot or ash.

Acknowledgment

This work has been completed with the assistance of a research grant from the National Science Foundation, ENG77-06099. Support has also been provided by the Department of Mechanical Engineering of Washington State University.

References

1 Kibler, G. M., Lyon, T. F., Linevsky, M. J., and De Santis, V. J., "Refractory Materials Research," WADD TR-60-646, Part IV, Materials Lab., Wright-Patterson AFB, Ohio, Aug. 1964.

2 Viskanta, R., Ungan, A., and Mengüc, M. P., "Predictions of Radiative Properties of Pulverized Coal and Fly-Ash Polydispersions," 20th National Heat Transfer Conference, ASME Paper No. 81-HT-24, Milwaukee, Aug. 1981.

3 Senftleben, H., and Benedict, E., "Uber die Optischen Konstanten und die Strahlungsgestze der Kohle," *Annalen der Physik,* ser 4, Vol. 54, 1917, p. 65.

4 Whitson, M. E., "Handbook of the Infrared Optical Properties of Al_2O_3, Carbon, MgO, and ZrO_2, Vol. I," AD/A-013 722, The Aerospace Corporation, El Segundo, Calif., June 1975.

5 Blokh, A. G., "Problem of Flame as a Disperse System," in *Heat Transfer in Flames*, Scripta Book Co., Washington, D.C., 1974, p. 111.

6 Sato, T., and Kunitomo, T., "Radiation from Fine Particle Clouds in High Temperature Combustion Gas," *Memoirs of the Faculty of Engineering, Kyoto University*, Vol. XXVII, Part 1, Jan. 1965.

7 Touloukian, Y. W., *Thermophysical Properties of High Temperature Solid Materials*, Vol. 4, MacMillan, New York, 1967.

8 Foster, P. J., and Howarth, C. R., "Optical Constants of Carbons and Coals in the Infrared," *Carbon*, Vol. 6, 1968, pp. 719–729.

9 Siegel, R., and Howell, J. R., *Thermal Radiation Heat Transfer*, 2nd ed., McGraw-Hill, 1981.

10 Van der Hulst, H. C., *Light Scattering by Small Particles*, John Wiley and Sons, New York, 1957.

11 Monteiro, S. L. P., "On the Spectral Emissivity of Polydispersion — Applications to Coal," PhD dissertation, Physics Department, Washington State University, 1981.

12 Monteiro, S. L. P., and Grosshandler, W. L., "On the Spectral Emissivity of Pulverized Coal and Char," 20th National Heat Transfer Conference, ASME Paper No. 81-HT-23, Milwaukee, Aug. 1981.

13 Goetz, G. J., Nsakala, N. Y., and Borio, R. W., "Development of Method for Determining Emissivities and Absorptivities of Coal Ash Deposits," ASME *Journal of Engineering for Power*, Vol. 101, 1979, pp. 607–614.

14 Simpson, H. C., "Combustion of Droplets of Heavy Liquid Fuels," ScD thesis, Chemical Engineering, MIT, 1954.

15 Grehan, G., and Gouesbet, G., "The Computer Program 'SUPERMIDI' for Mie Theory Calculations, Without 'Practical' Size nor Refractive Index Limitations," Laboratorie de Thermodynamique, Universite de Rouens, Report TTI/GG/79/03/20, 1979.

Combined Conductive and Radiative Heat Transfer in an Absorbing, Emitting, and Scattering Cylindrical Medium

R. Fernandes
Visiting Assistant Professor,
Aerospace, Mechanical,
and Nuclear Engineering,
University of Oklahoma,
Norman, Okla. 73019

J. Francis
Professor,
Aerospace, Mechanical,
and Nuclear Engineering,
University of Oklahoma,
Norman, Okla. 73019.
Mem. ASME

The purpose of this study was to formulate and solve the problem of transient combined conduction and radiation in a grey absorbing, emitting, and scattering medium of cylindrical geometry. The medium is bounded by grey diffuse surfaces at known temperatures. The problem was solved by the Galerkin finite element method using linear interpolating functions. The transient terms were handled using the Crank-Nicolson scheme with the time steps chosen to avoid temperature fluctuations at early times. The results were compared with exact solutions for the extreme cases, i.e., pure conduction and radiative equilibrium. Results are also compared with an approximate solution for the case of combined conduction and radiation. The effects of various parameters on the solutions are presented in tabular as well as graphical forms. The results obtained compare well with the exact solutions. The Galerkin finite element technique is well suited to this problem because of the ease with which integrals with variable limits can be handled.

Introduction

With the advent of the recent energy crisis and rapidly spiraling energy prices, conservation of energy has become a primary concern. One of the many ways to reduce consumption of energy is the use of insulation to reduce heat transfer. However, the analysis of heat transfer through some insulating materials is rendered difficult because of the combination of simultaneous conductive, convective, and radiative heat transfer. The combination of these three modes vastly increases the complexity of the analysis of any system, and, consequently, makes the modeling of any real system much more difficult. There are many practical problems where these combined mode studies must be addressed. We have chosen to investigate the cylindrical geometry problem for an insulating material in the annular region between two concentric right circular cylinders. This geometry has applications ranging from the obvious insulation on a pipe or insulation on cylindrical vessels to the rather complex hot wire thermal conductivity apparatus. For many insulating materials the heat transfer by convection is negligible. In this study the problem of combined conduction and radiation in a cylindrical medium with known temperatures on the boundaries is investigated.

Combined conduction and radiation in a medium has been analyzed by numerous authors using various geometries. Viskanta and Merriam [1] studied the problem for a spherical geometry using various boundary conditions. Fernandes, Francis, and Reddy [2], as well as Viskanta [3] have been among the many authors who have studied the problem of combined conduction and radiation for the planar geometry. Chang and Smith [4] have studied the transient and steady-state problem using the Eddington approximation for a medium between coaxial cylinders, while Howell [5] solved the steady-state problem using exchange factors. Saito et al. [6] investigated the hot wire method analytically and experimentally with combined conductive and radiative heat transfer. A number of solutions [7–10] were obtained which considered radiative equilibrium for the cylindrical geometry. Of these only the solutions obtained by Perlmutter and Howell [10] can be considered the most accurate. Azad and Modest [13] have solved the problem of heat transfer by radiative in a solid cylinder. Wu et al. [14] have described a system in radiative equilibrium using a finite element formulation. The results were linked with a second finite-element model, which included conduction for the planar geometry.

This paper presents an exact formulation and solution using finite elements to the problem of combined conduction and radiation in a long concentric annular medium with known temperatures at the boundaries. The medium is considered to be isotropically scattering, absorbing, and emitting with diffuse boundaries.

Analysis

The problem will be formulated using the procedure of Kesten [11] or Kuznetsov [12]. For the cylindrical geometry infinitely long in the z-direction, the intensity, I, depends on the radius, r, polar angle, θ', and the azimuthal angle, γ. The following notation will be used to specify the angles shown in Fig. 1:

β = horizontal projection of the acute angle between the direction of intensity and a line from the point of entry into the medium to the center of the cylinder

γ = horizontal projection of the angle measured clockwise from the radius to the direction of the intensity

θ = angle between the direction of the intensity and the outward drawn normal to the surface

α = angle between the ray and the horizontal

The integrated intensity

$$G_\nu(r) = \int_\omega I d\omega = 2\int_0^{\pi/2}\int_0^{2\pi} I_\nu \cos\alpha d\gamma d\alpha \tag{1}$$

The net radiative flux directed radially outward is given by

$$q_\nu(r) = \int_\omega I_\nu \cos\theta d\omega = -2\int_0^{\pi/2}\int_0^{2\pi} I_\nu \cos^2\alpha \cos\gamma d\gamma d\alpha \tag{2}$$

The transport equation using the coordinates shown in Fig. 1. for a material with refractive index, n, is given by

$$\frac{dI_\nu}{ds} = -\beta_\nu I_\nu + \kappa_\nu n^2 I_{b\nu} + \frac{\sigma_\nu}{4\pi} G_\nu \tag{3}$$

where $\beta_\nu = \sigma_\nu + \kappa_\nu$

G_ν = integrated intensity defined in equation (1)

Contributed by the Heat Transfer Division for publication in the JOURNAL OF HEAT TRANSFER. Manuscript received by the Heat Transfer Division December 14, 1981.

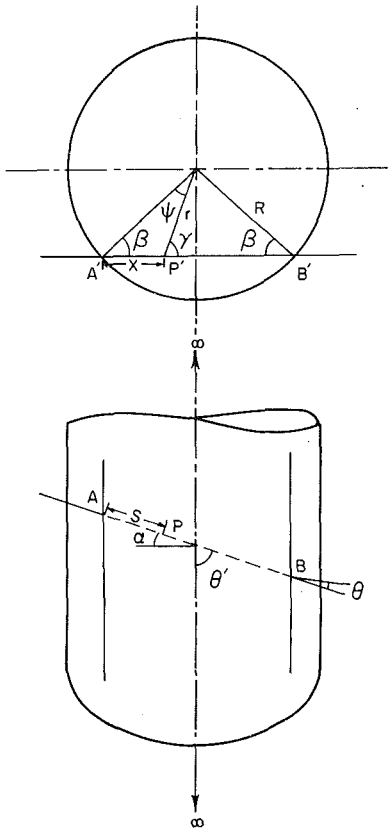

Fig. 1 Coordinate geometry (inner cylinder of radius r_0 has not been shown for clarity)

and $I_{b\nu}$ is the black body intensity or Planck's function. From Fig. 1, it is seen that

$$ds = \frac{dx}{\cos\alpha} \tag{4}$$

$$r^2 = x^2 + R^2 - 2xR\cos\beta \tag{5}$$

The transport equation will be rewritten by denoting I_ν^- as the intensity in the range $0 \le x \le R\cos\alpha$ and I_ν^+ as the intensity in the range $R\cos\beta \le x \le 2R\cos\beta$. While I^+ and I are defined in terms of the location from the outer cylinder it should be noted that these are equivalent to the notation used in planar problems indicating positive and negative directions.

From Fig. 1 we obtain

$$r \sin\gamma = R \sin\beta \text{ for } 0 \le \gamma < \pi \tag{6}$$

We now divide the annular region into one in which the rays intercept the inner cylinder, subscripted 1, and a region in which rays to not intercept the inner cylinder, subscripted 2. Utilizing the above equation and assuming gray and temperature independent properties, we can rewrite equation (3) as

$$\frac{dI^-}{dr^*} - \frac{r^*}{F(r^*,\beta)\cos\alpha} I^- = -\frac{(1-\omega_0)r^* n^2 I_b}{F(r^*,\beta)\cos\alpha} - \frac{\omega_0 r^* G}{4\pi F(r^*,\beta)\cos\alpha} \tag{7}$$

and

$$\frac{dI^+}{dr^*} + \frac{r^*}{F(r^*,\beta)\cos\alpha} I^+ = \frac{(1-\omega_0)r^* n^2 I_b}{F(r^*,\beta)\cos\alpha} + \frac{\omega_0 r^* G}{4\pi F(r^*,\beta)\cos\alpha} \tag{8}$$

where $F(r^*,\beta) = [r^{*2}\sin^2\beta]^{1/2}$.

By solving equations (7) and (8) and using the following conditions at $r^* = R^* I_1^- = I^-(R^*) = I_2^-$, at $r^* = r_0^* I_1^+ = I_1^+(r_0^*)$ and at $r^* = R^*\sin\beta I_2^+(R^*\sin\beta) = I_2^-(R^*\sin\beta)$ we obtain

Nomenclature

C_p = specific heat at constant pressure
G = incident radiation or irradiation
I = radiative intensity
k = thermal conductivity
n = refractive index
N = conduction radiation parameter
q = radiative heat flux
q'' = conductive plus radiative heat flux
r = radius
r_0 = inner radius
R = outer radius
s = coordinate along the ray
t = time
T = temperature
T_{outer} = temperature at the outside radius
T_{inner} = temperature at the inner radius
x = coordinate along the horizontal projection of the ray
α = thermal diffusivity and angle between a ray and the horizontal
β = extinction coefficient and angle
γ = local azimuthal angle
ϵ = emissivity
θ = outward drawn normal to the cylindrical surface
θ' = polar angle
κ = asborption coefficient
ν = frequency
ρ = density
σ = scattering coefficient
σ_s = Stefan-Boltzmann constant
τ = optical distance
Φ,ϕ = radiation potential
Ψ = azimuthal angle
ω = solid angle
$\omega_0 = \dfrac{\sigma}{\beta}$ = albedo

Nondimensional Variables

$\eta = \dfrac{G}{n^2\sigma_s T^4_{\text{reference}}}$

$Q_r = \dfrac{q}{n^2\sigma_s T^4_{\text{reference}}}$

$N = \dfrac{k\beta}{4n^2\sigma_s T^3_{\text{reference}}}$

Ψ = interpolating function and $\dfrac{q''}{k\beta T_{\text{reference}}}$

$\Phi,\phi = \dfrac{\pi I}{n^2\sigma_s T^4_{\text{reference}}}$

$r^* = \beta r$
$r_0^* = \beta r_0$
$R^* = \beta R$
$t^* = \dfrac{k\beta^2 t}{\rho C_p}$
$T^* = \dfrac{T}{T_{\text{reference}}}$
$x^* = \beta x$
$\tau = R^* - r_0^*$

Subscripts

ν = monochromatic
b = black body
e = element
r = radiative

Superscripts

$*$ = dimensionless
1,2 = node index

$$I_1^-(r^*,\alpha,\beta)=\exp\left[\frac{F(r^*,\beta)}{\cos\alpha}\right]\left\{I^-(R^*)\exp\left[\frac{-R^*\cos\beta}{\cos\alpha}\right]+\int_{r^*}^{R^*}\frac{\left\{(1-\omega_0)n^2I_b(r')+\frac{\omega_0}{4\pi}G(r')\right\}r'}{F(r',\beta)\cos\alpha}\exp\left[-\frac{F(r',\beta)}{\cos\alpha}\right]dr'\right\} \quad (9)$$

for $0\le\beta<\sin^{-1}r_0/R$

$$I_2^-(r^*,\alpha,\beta)=\exp\left[\frac{F(r^*,\beta)}{\cos\alpha}\right]\left\{I^-(R^*)\exp\left[\frac{-R^*\cos\beta}{\cos\alpha}\right]+\int_{r^*}^{R^*}\frac{\left\{(1-\omega_0)n^2I_b(r')+\frac{\omega_0}{4\pi}G(r')\right\}r'}{F(r',\beta)\cos\alpha}\exp\left[-\frac{f(r',\beta)}{\cos\alpha}\right]dr'\right\} \quad (10)$$

for $\sin^{-1}r_0/R\le\beta<\sin^{-1}r/R$

$$I_1^+(r^*,\alpha,\beta)=\exp\left[\frac{F(r^*,\beta)}{\cos\alpha}\right]\left\{I_1^+(r_0{}^*)\exp\left[\frac{F(r_0{}^*,\beta)}{\cos\alpha}\right]+\int_{r_0{}^*}^{r^*}\frac{\left\{(1-\omega_0)n^2I_b(r')+\frac{\omega_0}{4\pi}G(r')\right\}R''}{F(r',\beta)\cos\alpha}\exp\left[\frac{F(r',\beta)}{\cos\alpha}\right]dr'\right\} \quad (11)$$

for $0\le\beta<\sin^{-1}r_0{}^*/R^*$

$$I_2^+(r^*,\alpha,\beta)=\exp\left[-\frac{F(r^*,\beta)}{\cos\alpha}\right]\left\{I^-(R^*)\exp\left[\frac{-R^*\cos\beta}{\cos\alpha}\right]+\int_{R\sin\beta}^{R^*}\frac{\left\{(1-\omega_0)n^2I_b(r')+\frac{\omega_0}{4\pi}G(r')\right\}r'}{F(r',\beta)\cos\alpha}\exp\left[-\frac{F(r',\beta)}{\cos\alpha}\right]dr'+\int_{R^*\sin\beta}^{r^*}\frac{\left\{(1-\omega_0)n^2I_b(r')+\frac{\omega_0}{4\pi}G(r')\right\}r'}{F(r',\beta)\cos\alpha}\exp\left[\frac{F(r',\beta)}{\cos\alpha}\right]dr'\right\} \quad (12)$$

for $\sin^{-1}r_0{}^*/R^*\le\beta<\sin^{-1}r^*/R^*$

Because of symmetry, equation (1) may be written as

$$G(r^*)=4\int_0^{\pi/2}\int_0^{\pi/2}(I^++I^-)\cos\alpha d\gamma d\alpha$$

which in nondimensional form becomes:

$$\eta(r^*)=\frac{4R^*}{\pi}\Phi^-(R^*)\int_0^{\pi/2}\int_0^{\sin^{-1}\frac{r^*}{R^*}}\frac{\cos\alpha\cos\beta}{F(r^*,\beta)}\exp\left[\frac{F(r^*,\beta)-R^*\cos\beta}{\cos\alpha}\right]d\beta d\alpha$$

$$+\frac{4R^*}{\pi}\int_0^{\pi/2}\int_0^{\sin^{-1}\frac{r^*}{R^*}}\int_{r^*}^{R^*}\frac{\cos\beta}{F(r^*,\beta)}\frac{\left\{(1-\omega_0)T^{*4}(r')+\frac{\omega_0}{4}\eta(r')\right\}}{F(r',\beta)}r'\exp\left[\frac{F(r^*,\beta)-F(r',\beta)}{\cos\alpha}\right]dr'd\beta d\alpha$$

$$+\frac{4R^*}{\pi}\Phi_1+(r_0{}^*)\int_0^{\pi/2}\int_0^{\sin^{-1}\frac{r_0{}^*}{R^*}}\frac{\cos\alpha\cos\beta}{F(r^*,\beta)}\exp\left[\frac{F(r_0{}^*,\beta)-F(r^*,\beta)}{\cos\alpha}\right]d\beta d\alpha$$

$$+\frac{4R^*}{\pi}\int_0^{\pi/2}\int_0^{\sin^{-1}\frac{R^*}{r_0{}^*}}\frac{\cos\beta}{F(r',\beta)}\frac{\left\{(1-\omega_0)T^{*4}(r')+\frac{\omega_0}{4}\eta(r')\right\}}{F(r',\beta)}r'\exp\left[\frac{F(r',\beta)-F(r^*,\beta)}{\cos\alpha}\right]dr'd\beta d\alpha$$

$$+\frac{4R^*}{\pi}\Phi^-(R^*)\int_0^{\pi/2}\int_{\sin^{-1}\frac{r_0{}^*}{R^*}}^{\sin^{-1}\frac{r^*}{R^*}}\frac{\cos\alpha\cos\beta}{F(r^*,\beta)}\exp\left[-\frac{F(r^*,\beta)+R^*\cos\beta}{\cos\alpha}\right]d\beta d\alpha$$

$$+\frac{4R^*}{\pi}\int_0^{\pi/2}\int_{\sin^{-1}\frac{r_0{}^*}{R^*}}^{\sin^{-1}\frac{r^*}{R^*}}\int_{R^*\sin\beta}^{R^*}\frac{\cos\beta}{F(r^*,\beta)}r'\frac{\left\{(1-\omega_0)T^{*4}(r')+\frac{\omega_0}{4}\eta(r')\right\}}{F(r',\beta)}\exp\left[-\frac{F(r^*,\beta)+F(r',\beta)}{\cos\alpha}\right]dr'd\beta d\alpha$$

$$+\frac{4R^*}{\pi}\int_0^{\pi/2}\int_{\sin^{-1}\frac{r_0{}^*}{R^*}}^{\sin^{-1}\frac{r^*}{R^*}}\int_{R^*\sin\beta}^{r^*}\frac{\cos\beta}{F(r^*,\beta)}r'\frac{\left\{(1-\omega_0)T^{*4}(r')+\frac{\omega_0}{4}\eta(r')\right\}}{F(r',\beta)}\exp\left[\frac{F(r',\beta)-F(r^*,\beta)}{\cos\alpha}\right]dr'd\beta d\alpha \quad (13)$$

where $\Phi_1{}^+(r_0{}^*)$ and $\Phi^-(R^*)$ are the dimensionless intensities at the boundaries.

From equation (2) the expression for radiative flux directed radially outward in nondimensional form is

$$Q_r(r^*)=\frac{4R^*}{\pi r^*}\int_0^{\pi/2}\int_0^{\sin^{-1}\frac{r_0{}^*}{R^*}}\{\phi_1{}^+(r^*,\alpha,\beta)-\phi_1{}^-(r^*,\alpha,\beta)\}\cos^2\alpha\cos\beta d\beta d\alpha$$

$$+\frac{4R^*}{\pi r^*}\int_0^{\pi/2}\int_{\sin^{-1}\frac{r_0^*}{R^*}}^{\sin^{-1}\frac{r^*}{R^*}}\{\phi_2{}^+(r^*,\alpha,\beta)$$

$$-\phi_2{}^-(r^*,\alpha,\beta)\}\cos^2\alpha\cos\beta d\beta d\alpha \tag{14}$$

The energy equation

$$\rho C_p\frac{\partial T}{\partial t}+\nabla\cdot(-k\nabla T+q)=0$$

written in nondimensional form becomes

$$-\frac{\partial T^*}{\partial t^*}+\frac{\partial^2 T^*}{\partial r^{*2}}+\frac{1}{r^*}\frac{\partial T^*}{\partial r^*}=\frac{1}{4N}\frac{\partial Q_r}{\partial r^*}+\frac{1}{4N}\frac{Q_r}{r^*} \tag{15}$$

Substituting equation (14) into the above equation we obtain the following equation:

$$-\frac{\partial T^*}{\partial t^*}+\frac{\partial^2 T^*}{\partial r^{*2}}+\frac{1}{r^*}\frac{\partial T^*}{\partial r^*}=\frac{(1-\omega_0)}{N}\left\{T^{*4}(r^*)-\frac{\eta(r^*)}{4}\right\} \tag{16}$$

Boundary Conditions. Most insulating materials have surfaces which appear rough when compared to wavelengths in which heat transfer by radiation dominates. As a result we can associate an effective diffuse reflectance with the two surfaces of our cylindrical geometry. Thus, assuming diffuse surfaces of reflectances ρ_1 and ρ_2, the boundary conditions ($\Phi^-(R^*)$ and $\Phi_1{}^+(r_0{}^*)$ can be obtained as follows:

At the outer radius, R^*:

$$\pi I^-(R^*)=(1-\rho_1)[\text{Emitted Flux}]+\rho_1[\text{Incident Flux}]$$

or

$$\pi I^-(R^*)=(1-\rho_1)\pi n^2 I_{\text{outer}}$$

$$+4\rho_1\int_0^{\pi/2}\int_0^{\sin^{-1}\frac{r_0{}^*}{R^*}} I_1{}^+(R^*,\alpha,\beta)\cos^2\alpha\cos\beta d\beta d\alpha$$

$$+4\rho_1\int_0^{\pi/2}\int_{\sin^{-1}\frac{r_0{}^*}{R^*}}^{\pi/2} I_2{}^+(R^*,\alpha,\beta)\cos^2\alpha\cos\beta d\beta d\alpha$$

In nondimensionalized form this becomes:

$$\Phi^-(R^*)=(1-\rho_1)T^{*4}{}_{\text{outer}}+\frac{4\rho_1}{\pi}\int_0^{\pi/2}\int_0^{\sin^{-1}\frac{r_0{}^*}{R^*}}$$

$$\cos^2\alpha\cos\beta\exp\left[\frac{1}{\cos\alpha}\{F(r_0{}^*,\beta)-R^*\cos\beta\}\right]$$

$$\Phi_1{}^+(r_0{}^*)d\beta d\alpha+\frac{4\rho_1}{\pi}\int_0^{\pi/2}\int_0^{\sin^{-1}\frac{r_0{}^*}{R^*}}\int_{r_0{}^*}^{R^*}$$

$$\frac{\cos\alpha\cos\beta\left\{(1-\omega_0)T^{*4}(r')+\frac{\omega_0}{4}\eta(r')\right\}}{F(r',\beta)}r'$$

$$\exp\left[\frac{1}{\cos\alpha}\{F(r',\beta)-R^*\cos\beta\}\right]dr'd\beta d\alpha$$

$$+\frac{4\rho_1}{\pi}\int_0^{\pi/2}\int_{\sin^{-1}\frac{r_0{}^*}{R^*}}^{\pi/2}\cos^2\alpha\cos\beta$$

$$\exp\left[\frac{-2R^*\cos\beta}{\cos\alpha}\right]\Phi^-(R^*)d\beta d\alpha$$

$$+\frac{4\rho_1}{\pi}\int_0^{\pi/2}\int_{\sin^{-1}\frac{r_0{}^*}{R^*}}^{\pi}\int_{R^*\sin\beta}^{R^*}\cos\alpha\cos\beta$$

$$\frac{\left\{(1-\omega_0)T^{*4}(r')+\frac{\omega_0}{4}\eta(r')\right\}}{F(r',\beta)}r'\exp\left[\frac{-R^*\cos\beta}{\cos\alpha}\right]$$

$$\left\{\exp\left[\frac{F(r',\beta)}{\cos\alpha}\right]+\exp\left[\frac{-F(r',\beta)}{\cos\alpha}\right]\right\}dr'd\beta d\alpha \tag{17}$$

Similarly the other boundary condition can be obtained as follows:

$$\Phi_1^+(r_0{}^*)=(1-\rho_2)T^{*4}{}_{\text{inner}}+\frac{4R^*\rho_2}{\pi r_0{}^*}$$

$$\int_0^{\pi/2}\int_0^{\sin^{-1}\frac{r_0{}^*}{R^*}}\cos^2\alpha\cos\beta$$

$$\exp\left[\frac{1}{\cos\alpha}\{F(r_0{}^*,\beta)-R^*\cos\beta\}\right]\Phi^-(R^*)d\beta d\alpha$$

$$+\frac{4R^*\rho_2}{\pi r_0{}^*}\int_0^{\pi/2}\int_0^{\sin^{-1}\frac{r_0{}^*}{R^*}}\int_{r_0{}^*}^{R^*}\cos\alpha\cos\beta$$

$$\frac{\left\{(1-\omega_0)T^{*4}(r')+\frac{\omega_0}{4}\eta(r')\right\}}{F(r',\beta)}r'$$

$$\exp\left[\frac{1}{\cos\alpha}\{F(r_0{}^*,\beta)-F(r',\beta)\}\right]dr'd\beta d\alpha \tag{18}$$

Equations (16) and (13), along with the boundary conditions given by equations (17) and (18), are an exact formulation of the problem for diffuse boundary surfaces. The Galerkin finite element method was used to solve this problem.

Heat Flux. The total heat flux, $q''=-kdT/dr+q$, which in dimensionless form (at $r^*=r_0{}^*$) is given by

$$\Psi_{r^*=r_0{}^*}=-\frac{dT^*}{dr^*}\,r^*=r_0{}^*+\frac{1}{4N}Q_{r0} \tag{19}$$

where

$$Q_{r0}=\frac{4R^*}{\pi r_0{}^*}\int_0^{\pi/2}\int_0^{\sin^{-1}\frac{r_0{}^*}{R^*}}\cos^2\alpha\cos\beta\{\phi_1{}^+(r_0{}^*,\alpha,\beta)$$

$$-\phi_1{}^-(r_0{}^*,\alpha,\beta)\}d\beta d\alpha$$

Finite Element Formulation

The finite element procedure is to divide the radial domain $r_0{}^*$ to R^* in to a finite number of elements. The unknown functions $T^*(r^*)$ and $\eta(r^*)$ are approximated over each element in the form

$$T_e(r^*)=\sum_{i=1}^{2}\psi_e{}^{(i)}(r^*)T_e{}^{(i)} \tag{20}$$

and

$$\eta(r^*)=\sum_{i=1}^{2}\psi_e{}^{(i)}(r^*)\eta_e{}^{(i)}$$

where $\psi_e{}^{(i)}$ are linear interpolating functions, the subscript "e" applies to an element, e, and the superscript, i, denotes the node index. Linear interpolating polynominals are chosen for this problem since they represent the simplest functions which satisfy the conditions for completeness and compatability. The expressions for $\psi_e{}^{(1)}$ and $\psi_e{}^{(2)}$ are given as

$$\psi_e{}^{(1)}(r^*)=\frac{r_e{}^{*(2)}-r^*}{r_e{}^{*(2)}-r_e{}^{*(1)}} \tag{21}$$

and

$$\psi_e{}^{(2)}(r^*)=\frac{r^*-r_e{}^{*(1)}}{r_e{}^{*(2)}-r_e{}^{*(1)}}$$

where $r_e{}^{(1)}$ represents the location of the first node of element, e, and $r_e{}^{*(2)}$ represents the location of the second node of element, e.

The integral terms integrated with respect to r^* and r' are represented by a summation of integrals over the individual elements in the radial domain $r_0{}^*$ to R^*. Substitution of the assumed form of the unknown functions, i.e., equation (20), into the governing equations, multiplication by the interpolating functions $\Psi_e{}^{(j)}(r^*)$, $j=1, 2$, and integrating over the individual elements, constitutes the Galerkin formulation. More details of this formulation are available in reference [2].

Some terms in the governing equations which are integrated with respect to r' do not have limits which coincide with the nodes of the elements. An example of such terms are those whose lower limits are $R^*\sin\beta$.

If $R^*\sin\beta$ lies within some element, say e, it is easily shown that

$$\int_{R^*\sin\beta}^{r_e{}^{(2)}} \eta dr = \int_{R^*\sin\beta}^{r_e{}^{(2)}} \sum_{i=1}^{2} \eta_e{}^{(i)} \psi_e{}^{(i)}(r) dr \tag{22}$$

where the superscripts (1) and (2) are the nodes of element, e, and $\Psi_e{}^{(i)}(r)$, $i=1, 2$ are the interpolating functions for element, e.

The assembled equations along with the boundary conditions

$$\text{at } r^* = r_0{}^* \quad T^* = T_{\text{inner}}{}^*$$

and

$$\text{at } r^* = R^* \quad T^* = T_{\text{outer}}{}^* \tag{23}$$

can now be solved for the steady state problem by any suitable method.

Formulation of the Transient Term. The method used to evaluate the transient term in equation (16) is the Crank-Nicolson scheme.

A computer program was written to solve both the steady-state and transient problems. Since the equations are nonlinear, an iterative procedure was used. A linear solution for T^* was assumed, and thereby T^{*4} was evaluated. The resulting equations were solved and the new value of T^* compared with the initial guess. If convergence to within 0.001 was not obtained for T^*, the system of equations was solved again updating T^*, and hence T^{*4}, as the initial guess. After T^* converged the results were printed.

Numerical Approximations to the Integrals

Before obtaining a solution to the problem given a particular set of parameters, a number of integrals need to be evaluated. One method of evaluating integrals consists of employing a Gauss quadrature. The Gauss quadrature has been used to evaluate all the integrals in the study. Some of the integrals have one or more singularities at the limits. The integrals themselves exist but the integrands approach infinity at one or more limits. While evaluating the integrals it was found that they were highly sensitive to any change in the quadrature used for the variable β, but not sensitive to the change in quadrature of the other variables, namely r^*, r', and α. Thus in order to improve the answers, the limits on β were divided into two equal parts and a six point quadrature applied over each part. A four point quadrature was used for the integrals with respect to r^*, r', and α. On comparing solutions for the radiative equilibrium case ($N=0$) with those obtained by the Monte Carlo technique [10] good results were obtained for the cases involving black surfaces, i.e., $\epsilon_1=\epsilon_2=1$. But the results for surface emissivities other than 1 were extremely poor. The difficulty arises in the singularities of the integrals. By observing the integrals in the expressions for the irradiation η and the boundary terms $\bar{\Phi}(R^*)$ and $\Phi_1{}^+(r_0{}^*)$, we recognize that some integrands are singular at the limits of β or r' or both. Since the integrals were sensitive to the quadrature on β, they were approximated by the largest value of the exponential term in the integrand near the singularity in β. Thus any approximations with respect to singularities in r' were ignored. It should be noted that because the Gauss quadrature is used the integrands do not approach infinity since the function is never evaluated at the limits. Using this procedure, the finite element and Monte Carlo compared favorably for all radiative equilibrium cases.

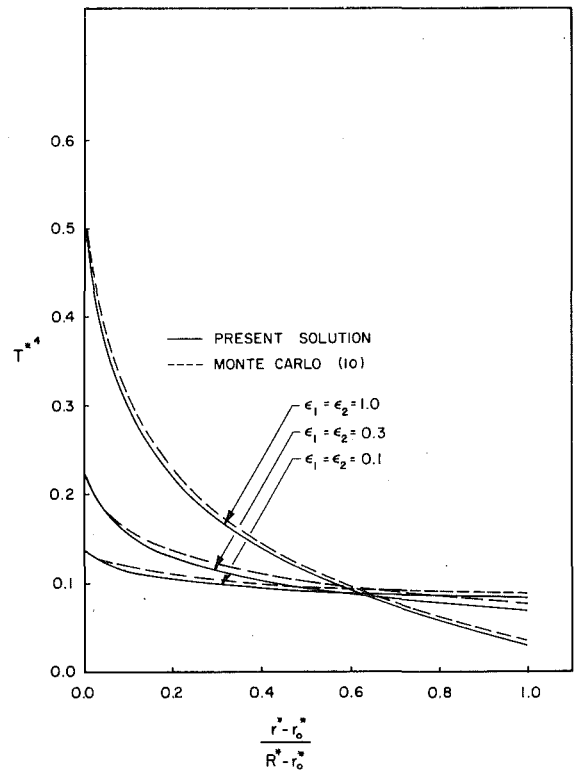

Fig. 2 Radiative equilibrium for $T^*_{\text{inner}}=1.0$, $T^*_{\text{outer}}=0.0$ $r_0{}^*/R^*=0.1$ and optical depth $R^*-r_0{}^*=2$

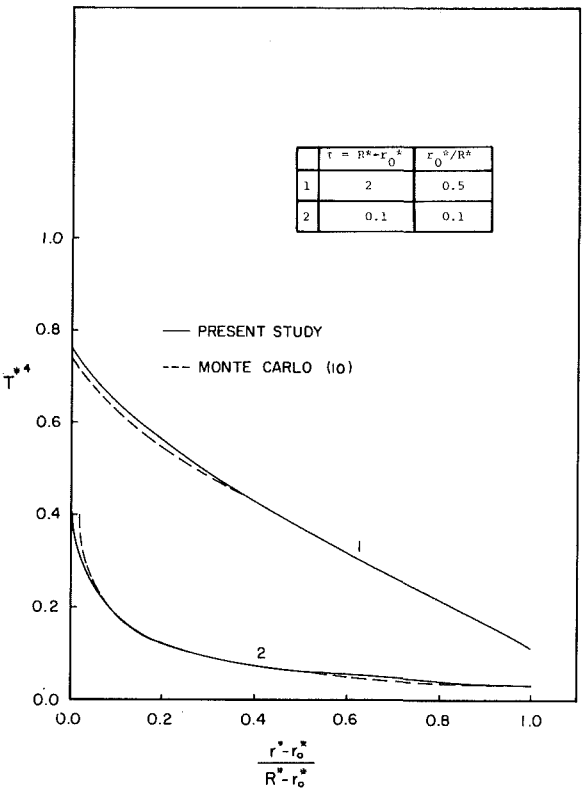

Fig. 3 Radiative equilibrium for $T^*_{\text{inner}}=1.0$, $T^*_{\text{outer}}=0.0$ and $\epsilon_1=\epsilon_2=1.0$

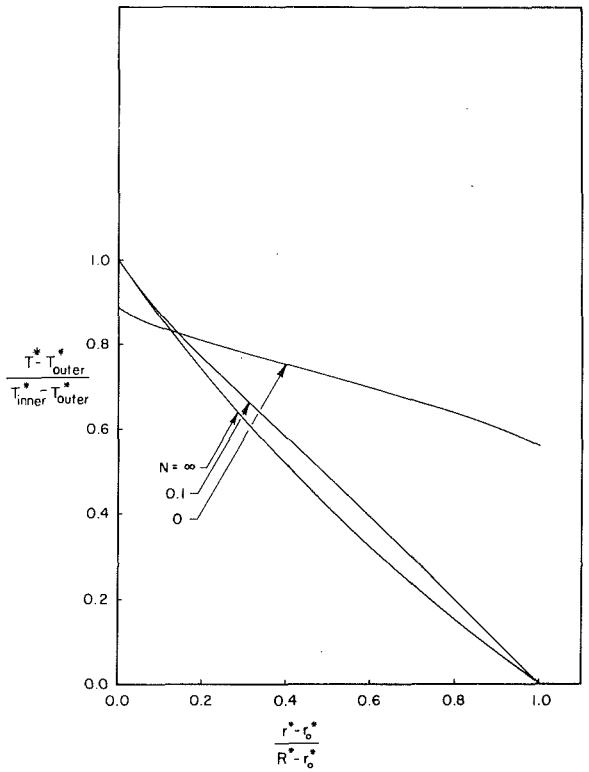

Fig. 4 Effect of the parameter N on temperature distribution for $\omega_0 = 0.5$, $\epsilon_1 = \epsilon_2 = 1.0$, $T^*_{inner} = 1.0$, $T^*_{outer} = 0.1$, $r_0{}^* = 1.0$ and $R^* = 2.0$

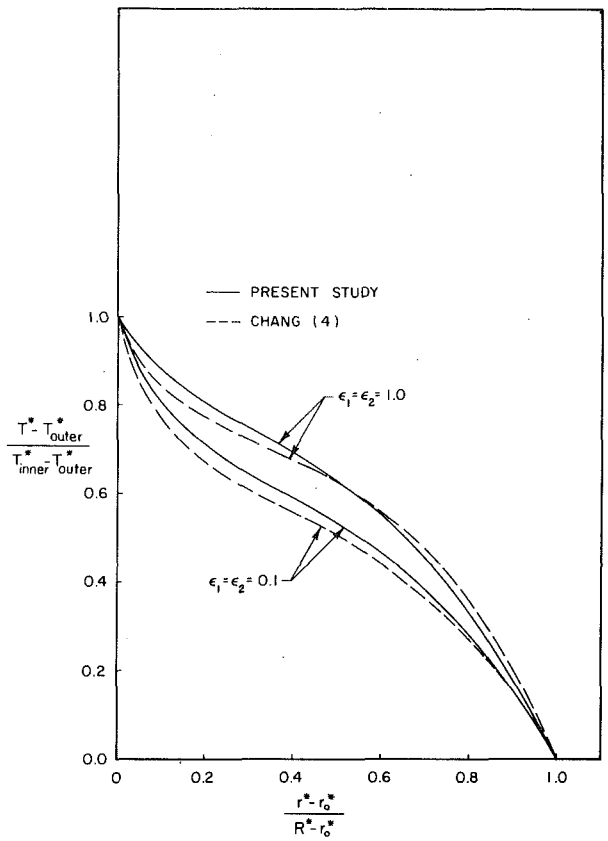

Fig. 6 Steady-state temperature profiles for $N = 0.03$, $\omega_0 = 0$ $r_0{}^* = 1.0$, $R^* = 2.0$, $T^*_{inner} = 1.0$, and $T^*_{outer} = 0.1$

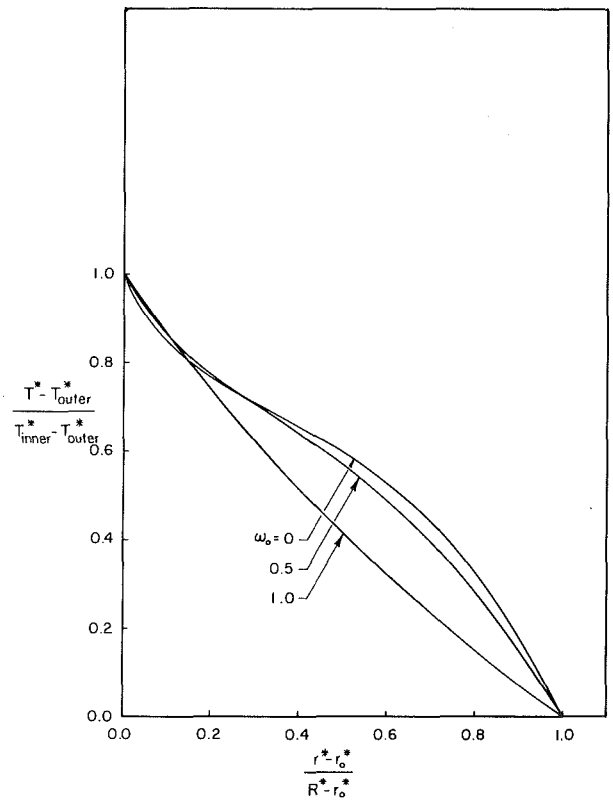

Fig. 5 Effect of scattering on temperature distribution for $\epsilon_1 = \epsilon_2 = 0.5$, $N = 0.03$, $T^*_{inner} = 1.0$, $T^*_{outer} = 0.1$, $r_0{}^* = 1.0$ and $R^* = 2.0$

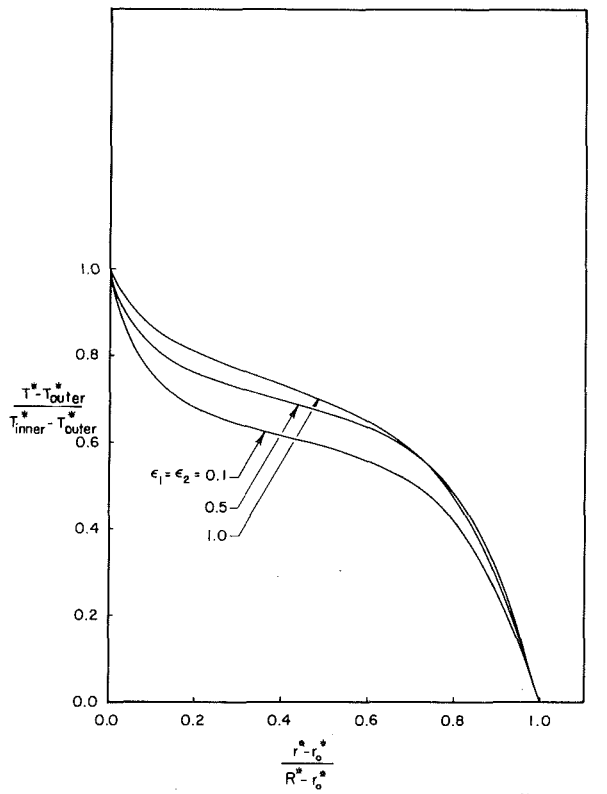

Fig. 7 Effect of surface emmisivity on temperature distribution for $N = 0.01$, $\omega_0 = 0$, $T^*_{inner} = 1.0$, $T^*_{outer} = 0.1$, $r_0{}^* = 1.0$ and $R^* = 2.0$

Results

Known exact solutions for the problem of combined conduction and radiation in the cylindrical geometry exist only for the extreme cases, i.e., conduction only or radiative equilibrium. Pure conduction is a trivial problem, and the results can be readily verified by consideration of the cases where $\omega_0 = 1$.

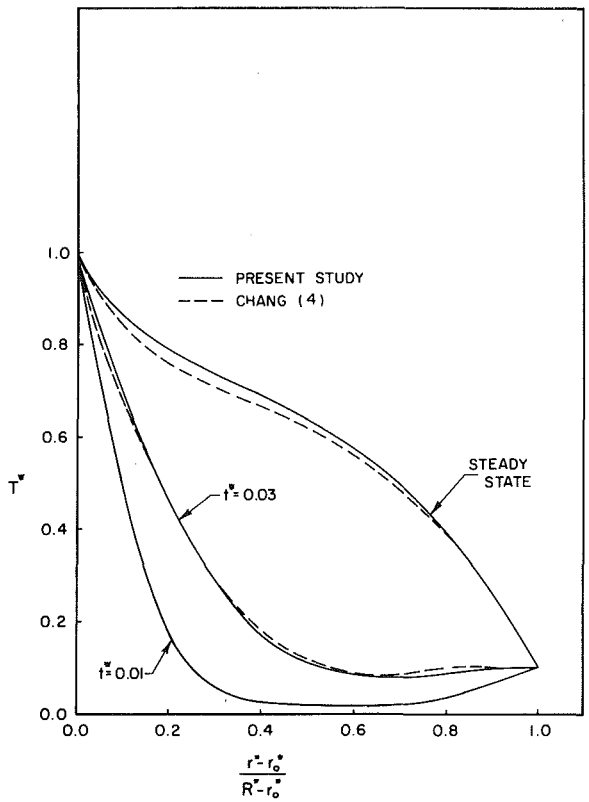

Fig. 8 Transient temperature profiles for combined conduction and radiation $\omega_0 = 0$, $N = 0.03$, $\epsilon_1 = \epsilon_2 = 0.5$ $r_0{}^* = 1.0$, $R^* = 2.0$, $T^*_{\text{inner}} = 1.0$, $T^*_{\text{outer}} = 0.1$, and $T^*_{\text{initial}} = 0.0$

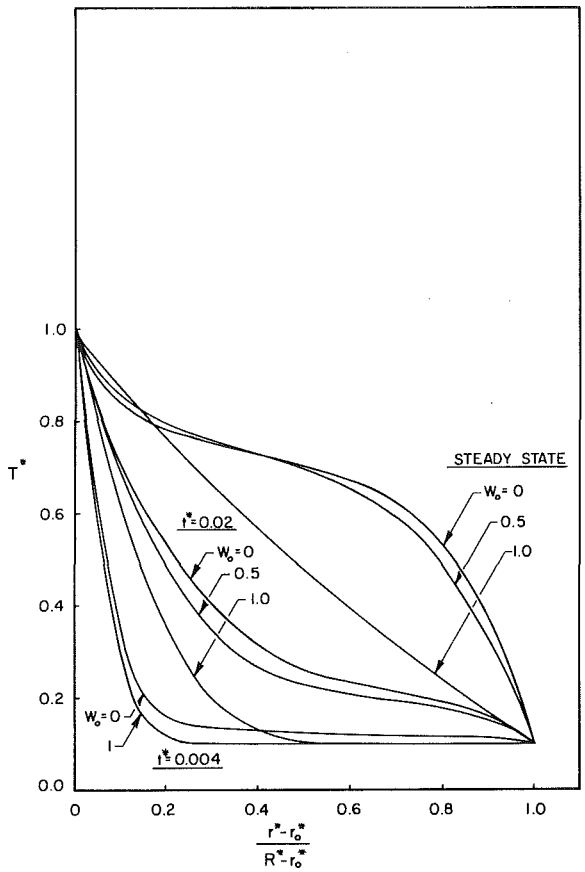

Fig. 9 Effect of scattering on transient temperature distribution for $N = 0.01$, $\epsilon_1 = \epsilon_2 = 0.5$, $r_0{}^* = 1.0$, $R^* = 2.0$, $T^*_{\text{inner}} = 1.0$, $T^*_{\text{outer}} = 0.1$, and $T^*_{\text{initial}} = 0.1$

Table 1 Heat-transfer rates for surface emissivities of 0.1

$r_0 = 1.0$	$R^* = 2.0$	$T_{\text{inner}}{}^* = 1.0$	$T_{\text{outer}}{}^* = 0.1$	$\epsilon_1 = \epsilon_2 = 0.1$
		$\left.\frac{dT^*}{dr^*}\right\|_{r^*=r_0{}^*}$	$Q_r\|_{r^*=r_0{}^*}$	Ψ
		$N = 0.5$		
0		−1.388	0.076	1.426
0.5		−1.348	0.079	1.387
1.0		−1.298	0.062	1.329
		$N = 0.1$		
0		−1.731	0.076	1.921
0.5		−1.541	0.079	1.738
1.0		−1.298	0.062	1.454
		$N = 0.5$		
0		−2.118	0.076	2.500
0.5		−1.769	0.079	2.164
1.0		−1.298	0.062	1.608

Table 2 Heat-transfer rates for surface emissivities of 0.5

$T^*_{\text{inner}} = 1.0$	$T^*_{\text{outer}} = 0.1$	$\epsilon_1 = \epsilon_2 = 0.5$	$r_0{}^* = 1.0$	$R^* = 2.0$
ω_0	$dT^*/dr^*\|_{r=r_0{}^*}$		$Q_r\|_{r=r_0{}^*}$	Ψ
		$N = 0.5$		
0.0	−1.333		0.379	1.523
0.5	−1.307		0.383	1.498
1.0	−1.298		0.340	1.468
		$N = 0.1$		
0.0	−1.499		0.372	2.430
0.5	−1.363		0.378	2.308
1.0	−1.298		0.340	2.148
		$N = 0.05$		
0.0	−1.728		0.368	3.566
0.5	−1.464		0.373	3.330
1.0	−1.298		0.340	2.998

Table 3 Heat-transfer rates for surface emissivities of 1.0

$T^*_{inner} = 1.0$	$T^*_{outer} = 0.1$	$\epsilon_1 = \epsilon_2 = 1.0$	$r_0^* = 1.0$	$R^* = 2.0$
	$\left.dT^*/dr^*\right\|_{r=r_0^*}$		$\left.Q_r\right\|_{r=r_0^*}$	
ω_0				Ψ
		$N = 0.5$		
0	−1.274		0.773	1.660
0.5	−1.270		0.765	1.653
1.0	−1.298		0.702	1.649
		$N = 0.1$		
0	−1.273		0.748	3.144
0.5	−1.212		0.751	3.088
1.0	−1.298		0.702	3.053
		$N = 0.05$		
0	−1.366		0.731	5.019
0.5	−1.218		0.738	4.907
1.0	−1.298		0.702	4.808

Radiative equilibrium solutions were compared with those obtained by the Monte Carlo technique [10]. Figure 2 shows results obtained by the finite element and Monte Carlo methods for various surface emissivities. In Fig. 3 the two methods were compared for black surfaces and different radius ratios and optical depths. The radial domain was divided into twenty equal elements. The results compare well with those obtained by the Monte Carlo technique.

Combined conduction and radiation solutions were compared with those obtained by Chang [4]. Although Chang's solution is based on an Eddington's first approximation model of radiation heat transfer, it is one of the few known solutions that exists for this problem even though scattering is omitted. The steady-state results are compared in Fig. 6, while the transient case is compared in Fig. 8. The radial domain was divided into nineteen elements of which twelve closest to the inner cylinder were of length 0.025, and the remaining seven were of length 0.10.

Figure 4 shows the effect of the conduction radiation parameter, N, on the temperature distribution. N equal to infinity heat transfer by conduction only, and thus we expect a log curve. $N = 0$ implies heat transfer by radiation only, and we would expect temperature slip at the boundary.

Figure 4 shows the effect of scattering on the temperature distribution. For $\omega_0 = 1$, the medium does not absorb but only scatters radiation, and this we would expect a log curve. For other values of ω_0 the medium absorbs incident radiation.

Figure 7 shows the effect of surface emissivity on the temperature distribution. It is seen that the initial slope of the temperature increases with decrease in emissivity.

Figure 9 shows the effect of scattering on the transient temperature distribution. Nineteen elements were used of sizes 0.025 and 0.1, and the time step was selected to avoid any temperature fluctations at early times. On the average the time required to achieve steady state is $t^* = 1.0$.

Table 1, 2, and 3 present results for the conductive, radiative, and total heat flux at the inner cylinder. It is seen that descreasing N increases the conductive and total heat flux. Decreasing the surface emissivities reduces the radiative heat flux. The conductive fluxes obtained in these tables are solved as part of the system of equations rather than being calculated after the temperatures profiles are obtained.

Conclusions

This study, has solved the problem of combined conduction and radiation in an absorbing, emitting, and scattering medium of cylindrical geometry bounded by grey surfaces at known temperatures. Solutions compare well with known exact solutions of limiting cases, i.e., pure conduction and radiative equilibrium. The authors believe that the finite-element technique is well suited for the problem because of the ease with which integrals with variable limits can be handled and the accuracy with which the conductive flux can be evaluated for the steady-state case. Another advantage lies in the fact that the elements do not have to be of equal length and the programming was such that very few changes needed to be made to change the length of each element or to increase the number of elements. Nineteen or twenty elements were found to be sufficient for reasonable accuracy.

References

1 Viskanta, R., and Merriam, R. L., "Heat Transfer by Combined Conduction and Radiation between Concentric Spheres Separated by a Radiating Medium," ASME JOURNAL OF HEAT TRANSFER, May 1968, pp. 248–256.

2 Fernandes, R., Francis, J., and Reddy, J. N., "A Finite Element Approach to Combined Conductive and Radiative Heat Transfer in a Planar Medium," *AIAA Progress Series in Astronautics and Aeronautics*, Vol. 78, *Heat Transfer and Thermal Control*, pp. 92–109.

3 Viskanta, R., "Heat Transfer by Conduction and Radiation in Absorbing and Scattering Materials," ASME JOURNAL OF HEAT TRANSFER, Series C, Vol. 87, Feb. 1965, pp. 143–150.

4 Chang, Y., and Smith, R. S., "Steady and Transient Heat Transfer by Radiation and Conduction in a Medium Bounded by Two Coaxial Cylindrical Surfaces," *International Journal of Heat and Mass Transfer*, Vol. 13, 1970, pp. 69–80.

5 Howell, J. R., "Determination of Combined Conduction and Radiation of Heat Through Absorbing Media by the Exchange Factor Approximation," *Chemical Engineering Progress Symposium Series*, Vol. 61, No. 59, 1965.

6 Saito, A., Mani, N., and Venart, J. E. S., "Combined Transient Conduction/Radiation Effects with the Line Source Technique of Measuring Thermal Conductivity," presented at the 16th National Heat Transfer Conference, St. Louis, Mo., Aug. 8–11, 1976, Paper No. 76—CSME/CSChE-6.

7 Bayazitoglu, Y., and Higenyi, J., "Higher-Order Differential Equations of Radiative Transfer: P_3 Approximation," *AIAA Journal*, Vol. 17, Apr. 1979, pp. 424–431.

8 Modest, M. F., and Stevens, D. S., "Two Dimensional Radiative Equilibrium of a Gray Medium between Concentric Cylinders," *Jour. of Quant. Spect. and Rad. Trans.*, Vol. 19, 1978, pp. 353–365.

9 Olfe, D. B., "Application of the Modified Differential Approximation to Radiative Transfer in a Gray Medium between Concentric Cylinders and Spheres," *Jour. of Quan. Spect. and Rad. Trans.*, Vol. 8, Mar. 1968, pp. 899–907.

10 Perlmutter, M., and Howell, J. R., "Radiant Transfer through a Grey Gas between Concentric Cylinders using Monte Carlo," ASME JOURNAL OF HEAT TRANSFER, Vol. 86, Feb. 1964, pp. 165–179.

11 Kesten, A. S., "Radiant Heat Flux Distribution in a Cylindrically-Symmetric Nonisothermal Gas with Temperature—Dependent Absorption Coefficient," *J. Quant. Spect. and Rad. HT*, Vol. 8, 1968, pp. 419–434.

12 Kuznetsov, Ye S., "Temperature Distribution in an Infinite Cylinder and in a Sphere in a State of Monochromatic Radiative Equilibrium," *Jour. of USSR Computational Mathematics and Mathematical Physics*, Vol. 2, 1963, pp. 230–254.

13 Azad, F. H., and Modest, M. F., "Evaluation of the Radiative Heat Flux in Absorbing, Emitting and Linear-Anistropically Scattering Cylindrical Media," ASME JOURNAL OF HEAT TRANSFER, Vol. 103, May 1981, pp. 350–356.

14 Wu, S. T., Ferguson, R. E., and Altgilbers, L. L., "Application of Finite-Element Techniques to the Interaction of Conduction and Radiation in a Partcipating Medium," *AIAA Progress Series and Astronautics and Aeronautics*, Vol. 78, *Heat Transfer and Thermal Control*, pp. 61–91.

Evaluation of Coefficients for the Weighted Sum of Gray Gases Model

T. F. Smith
Professor.
Mem. ASME

Z. F. Shen
Research Assistant.

J. N. Friedman
Research Assistant.

University of Iowa,
Iowa City, Iowa 52242

The weighted sum of gray gases model postulates that total emissivity and absorptivity may be represented by the sum of a gray gas emissivity weighted with a temperature dependent factor. The gray gas emissivity is expressed in terms of a temperature-independent absorption coefficient, absorbing gas partial pressure, and path length. The weighting factors are given by polynomials in gas temperature with associated polynomial coefficients. For absorptivity, a second polynomial for the irradiation temperature is introduced. A regression scheme is employed to fit the model to total emissivity and absorptivity values obtained from the exponential wide-band model. Absorption and polynomial coefficients are reported for carbon dioxide, water vapor, and mixtures of these gases. The model with these coefficients more accurately represents the total properties over a wider range of temperatures and partial pressure-path length products than previously available coefficients.

Introduction

Evaluation of radiant exchange within a gas as well as between a gas and surrounding surfaces may be accomplished by the zone method [1]. The zone method is attractive since the computational effort associated with the spectral and spatial integrations common to radiant exchange analyses is minimized by introduction of the weighted sum of gray gases model for the radiative properties of total emissivity and absorptivity. This model represents these properties by a summation of a number of terms, each given by the multiplication of a weighting factor and a gray emissivity. The weighting factors are expressed in terms of polynomials in temperature with associated coefficients. Gray gas emissivities are expressed in terms of a temperature independent gray gas absorption coefficient and the product of the partial pressure of the absorbing gas and path length. Total emissivity and absorptivity may then be evaluated once absorption and polynomial coefficients are available.

In several energy systems, radiant exchange in gases resulting from combustion of a hydrocarbon fuel is to be evaluated. The systems generally exist at a total pressure of one atmosphere and exhibit temperatures ranging from about 600 to 2400 K. The gases contain carbon dioxide and water vapor where the radiant participation by these gases depends on several parameters of which gas and irradiation temperatures, total and absorbing gas partial pressures, and path lengths are the most important. Partial pressures of carbon dioxide and water vapor are near 0.1 atm for stoichiometric combustion of oil and 0.1 and 0.2 atm, respectively, for stoichiometric combustion of methane [2]. The path length range is approximately 0.1 to 10 m as characteristic of combustion chambers and boilers. The partial pressure-path length products, therefore, acquires values from 0.01 to 10 atm-m. Values for absorption and polynomial coefficients must be available for these cited parameteric ranges as well as for carbon dioxide, water vapor, and mixtures of these gases.

Absorption and polynomial coefficients are available from several sources [3–9]. Coefficients reported in [3–7] are applicable for $P_w/P_c = 1$. In addition, coefficients were also presented in [4–6] for $P_w/P_c = 2$. For these coefficients, $P_c = 0.1$ atm and $P_T = 1$ atm. Linear and third-order polynomials were utilized in [4–6] and [3, 7], respectively. Two gray gas components were found adequate in [4, 6] whereas three components were employed in [3, 5–7]. A second order polynomial and six gray gas components were utilized for carbon dioxide in [8]. Four gray gases were employed in [9] for water vapor. Incorporation of four or more gray gases in the zone method may result in significant computational effort. Since the temperature and partial pressure-path length product ranges varied over which the coefficients are applicable, it is not meaningful to compare the magnitudes of the absorption and polynomial coefficients, the order of polynomials, as well as the number of gray gas components and emissivities. There exists, therefore, a lack of well-defined and representative coefficients for employment in the weighted sum of gray gases model. This deficiency is partially attributed to the absence of representative total emissivity and absorptivity values.

The objective of this investigation is to develop a set of absorption and polynomial coefficients for the weighted sum of gray gases model. Emphasis is placed on acquiring coefficients for carbon dioxide and water vapor, as well as mixtures of these gases for a wide range of partial pressure-path length products and temperatures. This investigation also examines the number of gray gas components and polynomial orders required to represent the total emissivity and absorptivity values, taking into account the intended application of evaluation of radiant exchange. In order to develop these coefficients, total emissivities and absorptivity values must be available. Radiative gas property models capable of yielding total emissivity and absorptivity values are examined first. From this discussion, a model is selected to provide the total properties. Following this, the weighted sum of gray gases model and procedure for computing the coefficients are briefly described. This discussion is then succeeded by that for the results of this investigation.

Radiative Gas Property Models

Radiative gas property models which yield total emissivities and absorptivities may be conveniently classified into four general categories associated with narrow-band models [10], exponential wide-band models [11, 12], weighted sum of gray gases models [3–9], and charts and correlations [1, 2, 10, 11, 13–17]. It should be noted that some methods may rely on results of other models. Comparisons of total emissivities and absorptivities evaluated from the various models are available in [8, 9, 14, 15, 17, 18]. A total emissivity chart prepared by

Contributed by the Heat Transfer Division and presented at the 20th ASME/AIChE National Heat Transfer Conference, Milwaukee, Wisconsin, August 2–5, 1981. Manuscript received by the Heat Transfer Division, October 1, 1981. Paper No. 81-HT-55.

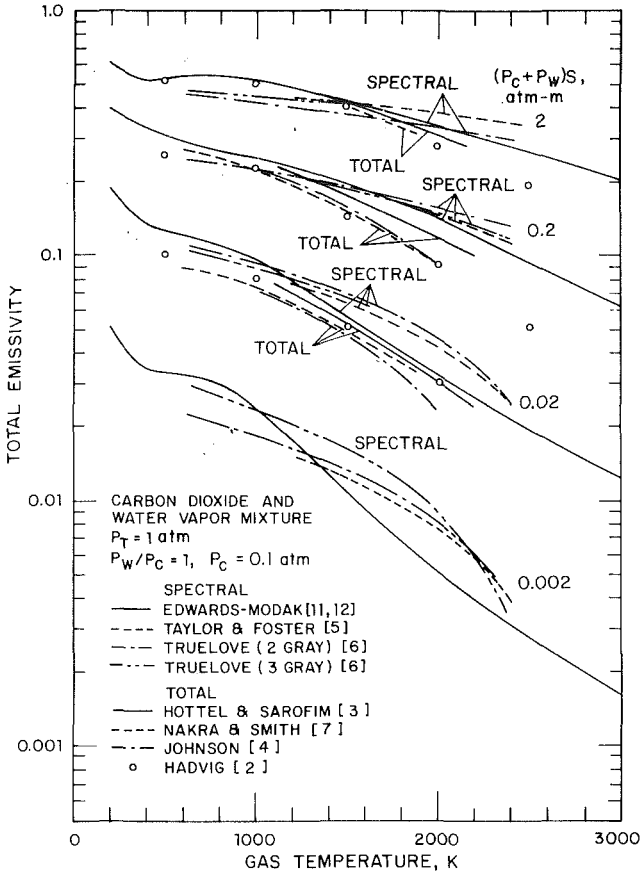

Fig. 1 Emissivities for carbon dioxide and water vapor mixture

De Ris [19] compares emissivities [1, 5, 13, 17] for $P_w/P_c = 1$, $P_c = 0.1$ atm, and $P_T = 1$ atm. Emissivities from [1, 5, 17] are similar at high temperatures. The Leckner [13] and Hottel [1] results are lower at the low and high temperatures, respectively. Other comparisons [18] of models for carbon dioxide [1, 11, 13, 15, 17] and water vapor [1, 10–14, 17] reveal significant differences, particularly for water vapor at high temperatures. Representative comparisons of the models for a carbon dioxide and water vapor mixture are illustrated in Fig. 1 for total emissivity at $P_T = 1$ atm and $P_w/P_c = 1$ with $P_c = 0.1$ atm. Results are subdivided into two general categories related to total emissivities based on spectral models which include narrow and wide-band models [5, 6, 11, 12] and charts [2–4, 7] which yield total emissivities. Emissivities from the Hadvig charts [2] are denoted by data symbols to imply that they are based on total emissivity measurements. At each partial pressure-path length product, two curves related to two and three gray gas components for the Truelove results [6] are illustrated. Other comparisons revealed that results from the Leckner [13] and Modak [17] correlations are similar to those from the Edwards-Modak model [11, 12].

Emissivity results from the total models are in general agreement with each other and with the Hadvig results. The latter finding is expected since these emissivities have a common source, namely, the Hottel charts. The spectral models yield higher emissivities than the total models, particularly at the higher temperatures. This has also been observed by Taylor and Foster [5]. The models attributed to Taylor and Foster [5] as well as Truelove [6] exhibit similar trends with the Truelove two gray term approximation in closer agreement with the Taylor and Foster model which employs three gray terms. Results from these models, particularly at the lower partial pressure-path length products, differ considerably from those of the Edwards-Modak model. Based on these comparisons, the exponential wide-band model with correlation parameters from [11, 12] was selected to provide total emissivities and absorptivities for utilization in this study. It should be noted, however, that considerable differences, particularly at low partial pressure-path length products and high temperatures, exist between the models. Additional studies are needed to rectify these differences and to provide measurements for the total properties.

Weighted Sum of Gray Gases Model

Total emissivity for the weighted sum of gray gases model is evaluated from the following expression

$$\epsilon = \sum_{i=0}^{I} a_{\epsilon,i}(T)\left[1 - e^{-k_i PS}\right] \tag{1}$$

where $a_{\epsilon,i}$ denote the emissivity weighting factors for the i-th gray gas as based on gas temperature, T. The bracketed quantity in equation (1) is the i-th gray gas emissivity with absorption coefficient, k_i, and partial pressure-path length product, PS. For a gas mixture, P is the sum of the partial pressures of the absorbing gases. The weighting factor, $a_{\epsilon,i}$, may be physically interpreted as the fractional amount of black body energy in the spectral regions where gray gas of absorption coefficient, k_i, exists. The absorption coefficient for $i = 0$ is assigned a value of zero to account for windows in the spectrum between spectral regions of high absorption. Since total emissivity is an increasing function of the partial pressure-path length product approaching unity in the limit, the weighting factors must sum to unity and, also, must be positive values. The weighting factor for $i = 0$ is evaluated from

$$a_{\epsilon,0} = 1 - \sum_{i=1}^{I} a_{\epsilon,i} \tag{2}$$

Thus, only I values of the weighting factors need to be determined. A convenient representation of the temperature dependency of the weighting factors is a polynomial of order J-1 given as follows

Nomenclature

a_α, a_ϵ = absorptivity and emissivity weighting factors
b_ϵ = emissivity polynomial coefficients
c_α = absorptivity polynomial coefficients
k_i = absorption coefficients, $(\text{atm-m})^{-1}$
I = number of gray gas components
J = number of temperature polynomial coefficients
K = number of irradiation polynomial coefficients
L = number of partial pressure-path length products
M = number of temperature values
P = pressure, atm
P_c = partial pressure of carbon dioxide, atm
P_T = total pressure, atm
P_w = partial pressure of water vapor, atm
S = path length, m
T = gas temperature, K
T_s = irradiation temperature, K
x = variable
α = total absorptivity
ϵ = total emissivity
σ = root-mean-square error
ϕ = objective function

$$a_{\epsilon,i} = \sum_{j=1}^{J} b_{\epsilon,i,j} T^{j-1} \tag{3}$$

where $b_{\epsilon,i,j}$ are referred to as the emissivity gas temperature polynomial coefficients. The absorption and polynomial coefficients are evaluated by fitting equation (1) to a table of total emissivities. For I gray gases and $J-1$ polynomial order, there are $I(1+J)$ coefficients to be evaluated.

For total absorptivity, the irradiation temperature of surfaces surrounding the gas is also introduced. Hence, the absorptivity is

$$\alpha = \sum_{i=0}^{I} a_{\alpha,i}(T, T_s)\left[1 - e^{-k_i PS}\right] \tag{4}$$

where the absorptivity weighting factors, $a_{\alpha,i}$, are also a function of the surface irradiation temperature, T_s. The weighting factors must all sum to unity and must all be positive. The weighting factor for $i = 0$ is given as

$$a_{\alpha,0} = 1 - \sum_{i=1}^{I} a_{\alpha,i} \tag{5}$$

The dependency of the weighting factors on gas and irradiation temperatures is expressed by polynomials of orders $J-1$ and $K-1$, respectively, as follows

$$a_{\alpha,i} = \sum_{j=1}^{J}\left[\sum_{k=1}^{K} c_{\alpha,i,j,k} T_s^{k-1}\right] T^{j-1} \tag{6}$$

where $c_{\alpha,i,j,k}$ are the absorptivity polynomial coefficients. In order to reduce the computational effort associated with the zone method, the absorption coefficients for total emissivity and absorptivity are taken to be identical. However, the polynomial orders may differ for the two properties. The number of coefficients to be evaluated for total absorptivity is then equal to I^*J^*K.

Procedure

Evaluation of the absorption and polynomial coefficients requires a procedure which fits the model expressions to tabulated values of total emissivity and absorptivity. For future references, the tabulated values are referred to as data. Since the model expressions are nonlinear and there are generally more data values then coefficients to be determined, a curve fitting procedure based on minimization of the error between the model and data values is desired. Furthermore, the procedure should be available on a digital computer in order to reduce the effort required to generate the coefficients and to remove any subjective biasing. These requirements dictate the utilization of some form of a regression analysis.

The procedure employed in this study is the Fletcher-Powell technique [20] for multivariable unconstrained nonlinear problems. The basic idea behind this technique is to minimize the function

$$\phi(x_1, x_2, \ldots, x_n)$$

where ϕ is called the objective function with variables x_n. For the problem of interest, the objective function is defined as

$$\phi = \sum_{l=1}^{L}\sum_{m=1}^{M}\left(\frac{\epsilon_{d,l,m} - \epsilon_{l,m}}{\epsilon_{d,l,m}}\right)^2 \tag{7}$$

where indices l and m represent the partial pressure-path length product and temperature values, respectively, for which emissivity data values $\epsilon_{d,l,m}$ are available. $\epsilon_{l,m}$ corresponds to the emissivity evaluated from the model given by equation (1). A relative error is employed in equation (7) since the emissivities vary over several orders of magnitude for the desired ranges of partial pressure-path length products and temperatures. The objective of the minimization procedure is then to obtain a near zero value for the objective function. The variables are assigned the desired coefficients as follows

$$x_i = k_i; \quad x_{I+j+(i-1)J} = b_{\epsilon,i,j} \tag{8}$$

for $1 \le i \le I$ and $1 \le j \le J$ which yields $I(J+1)$ variables. A more representative indication of the agreement between the model and data is furnished by the root-mean-square (rms) error defined as

$$\sigma = \left[\frac{1}{LM}\phi\right]^{1/2} \tag{9}$$

It was found that the minimization code was faster when the function was defined by equation (7) than by equation (9). The derivatives of the objective function are also required in order to reduce the computational effort and are expressed as

$$\frac{\partial\phi}{\partial x_i} = -2\sum_{l=1}^{L}\sum_{m=1}^{M}\left(\frac{\epsilon_{d,l,m} - \epsilon_{l,m}}{\epsilon_{d,l,m}^2}\right)\frac{\partial\epsilon_{l,m}}{\partial x_i} \tag{10}$$

In terms of the model, the emissivity derivatives can be evaluated utilizing equations (1) and (3).

A computer code [20] was modified [21] to accept the expressions for the present objective function and its derivatives. Similar expressions were utilized for total absorptivity. However, the absorption coefficients in the absorptivity expression were assigned those for the emissivity. Thus, subscript i on x_i acquires values greater than I.

Results and Discussions

Data values for total emissivity and absorptivity of carbon dioxide, water vapor, and mixtures of these gases were generated from the exponential wide-band model for a total pressure of 1 atm and gas temperatures from 600–2400 K with a temperature interval of 50 K. In all cases, the partial pressure-path length product was assigned the sequence of values of 1, 1.4, 2, 3, 4, 5, 6, 7, 8, and 9 over the range of 0.001 to 10.0 atm-m. For carbon dioxide, data values corresponded to the case when the partial pressure of carbon dioxide vanished. Comparisons [22] illustrated that the partial pressure has a negligible influence on emissivity and absorptivity of carbon dioxide for the considered total and partial pressures. However, for water vapor, emissivity and absorptivity illustrated a dependency on partial pressure, and data values were computed for $P_w \to 0$, $= 0.2$, 0.5, and 1.0 atm. For mixtures of carbon dioxide and water vapor with the remaining gas taken to be nitrogen, data values corresponded to $P_w/P_c = 1$ and 2 with $P_c = 0.1$ atm for both ratios. The partial pressure for these mixtures is the sum of that for carbon dioxide and water vapor. Data values for absorptivity were evaluated for irradiation temperatures of 600, 1050, 1500, 1950, and 2400 K.

Plots of emissivity and absorptivity versus gas temperature with parameter of partial pressure-path length product and versus partial pressure-path length product with parameter of gas temperature were prepared to assist in identifying the functional form of the data. For absorptivity, these plots were prepared for each irradiation temperature. Since each data set contained 1517 data values corresponding to 37 gas temperature and 41 partial pressure-path length product values, significant computational effort would be realized in the Fletcher-Powell technique if all data values were employed to generate the coefficients. Thus, some preliminary tests particularly with carbon dioxide emissivity were performed to determine the sensitivity of the curve fitting scheme to the number of data points and their intervals, number of gray gas components, and polynomial order. To perform these tests, it was necessary to develop a sorting routine to extract a subset

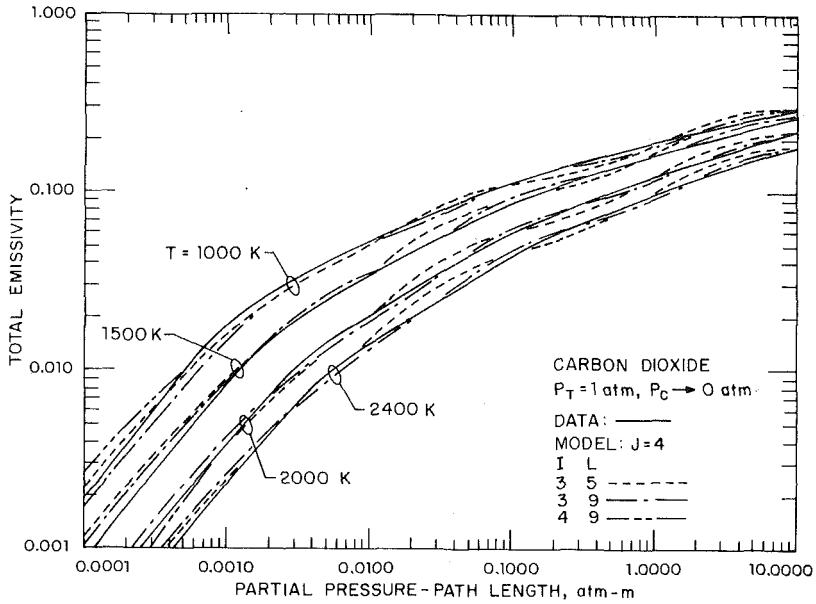

Fig. 2 Emissivity versus partial pressure-path length for carbon dioxide

of values from the set. The extensiveness of these tests precludes presentation of all results and only a summary of the findings is reported with more detailed discussion and results available elsewhere [21].

In order to perform these tests, the number of gray gas components (I) and gas temperature polynomial coefficients (J) were initially taken as 3 and 4, respectively. The effects of these parameters on the accuracy of the model are examined later. From these tests, it was found that a gas temperature interval of 200 K yielding $M = 10$ temperature values could be utilized without loss of accuracy. The influence of the number of partial pressure-path length products was examined by considering the P_cS sequences of 1, 1, and 3, as well as 1, 3, and 6 between 0.001 and 10.0 atm-m yielding $L = 5$, 9, and 13, respectively, in equation (7). The respective subset and set rms errors are 0.042 and 0.080, 0.064, and 0.054, as well as 0.061 and 0.052. An rms error of 0.05 implies an average agreement between the model results and data of 5 percent. The ability of the coefficients to predict emissivities at the intermediate P_cS values is indicated by the set rms errors. It was concluded that the coefficients obtained for $L = 9$ yielded reasonable agreement with the data and computational effort. Thus, $L = 9$ was utilized in the remaining computations.

In conjunction with these tests, the influence of I and J on the curve fitting procedure and errors was also explored. Of course, larger values of I and J would be expected to yield better correlation between the model and data. Cognizance in selecting these values, however, must be made of the intended application to examine radiative transfer with the zone method where significant computational effort would result for the larger values of I and J. Of the two parameters, I would have a greater effect on the computational effort since this parameter dictates the number of direct exchange areas to be evaluated. To examine the influence of I, results were acquired for $I = 2$ and 3 with $J = 5$ and $L = 5$ for both cases where set rms errors were 0.149 and 0.0754, respectively. Thus, in view of the larger error for $I = 2$, this case did not receive additional consideration. To further explore the influence of I, coefficients were generated for $I = 4$ and $J = 4$ with $L = 9$ where subset and set rms errors of 0.043 and 0.039, respectively, are lower than those cited for $I = 3$ and $J = 4$. Comparisons of model results for $I = 3$ and 4 with data values for carbon dioxide are illustrated in Fig. 2, where emissivities are displayed as a function of P_cS with $T = 1000$, 1500, 2000, and 2400 K. It is observed that the lower errors for $I = 4$ are attributed to a better fit at low values of P_cS. It should be noted that data values for P_cS values below 0.001 atm-m are adequately described by the model results. In view of the intended usage of these results, $I = 3$ was selected for further computations.

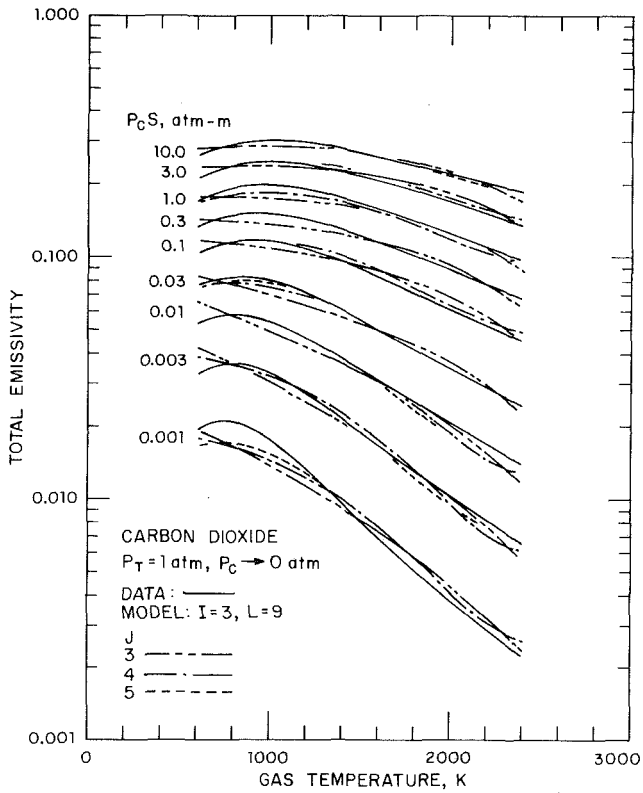

Fig. 3 Influence of polynomial order for carbon dioxide

Selection of the value for J was aided by examination of the temperature behavior of emissivities for carbon dioxide displayed in Fig. 3 where model results correspond to $I = 3$ and $L = 9$ with $J = 3$, 4, and 5. The corresponding subset and set rms errors for $J = 3$ and 5 are 0.086 and 0.073, as well as 0.053 and 0.049 with errors for $J = 4$ cited previously. Thus,

Table 1 Coefficients for emissivity

i	k_i	$b_{\epsilon,i,1}*10^1$	$b_{\epsilon,i,2}*10^4$	$b_{\epsilon,i,3}*10^7$	$b_{\epsilon,i,4}*10^{11}$
			Carbon dioxide, $P_c \to 0$ atm		
1	0.3966	0.4334	2.620	−1.560	2.565
2	15.64	−0.4814	2.822	−1.794	3.274
3	394.3	0.5492	0.1087	−0.3500	0.9123
			Water vapor, $P_w \to 0$ atm		
1	0.4098	5.977	−5.119	3.042	−5.564
2	6.325	0.5677	3.333	−1.967	2.718
3	120.5	1.800	−2.334	1.008	−1.454
			Water vapor, $P_w = 1.0$ atm		
1	0.4496	6.324	−8.358	6.135	−13.03
2	7.113	−0.2016	7.145	−5.212	9.868
3	119.7	3.500	−5.040	2.425	−3.888
			Mixture, $P_w/P_c = 1$		
1	0.4303	5.150	−2.303	0.9779	−1.494
2	7.055	0.7749	3.399	−2.297	3.770
3	178.1	1.907	−1.824	0.5608	−0.5122
			Mixture, $P_w/P_c = 2$		
1	0.4201	6.508	−5.551	3.029	−5.353
2	6.516	−0.2504	6.112	−3.882	6.528
3	131.9	2.718	−3.118	1.221	−1.612

$P_T = 1$ atm, $0.001 \le PS \le 10.0$ atm-m, $600 \le T \le 2400$K

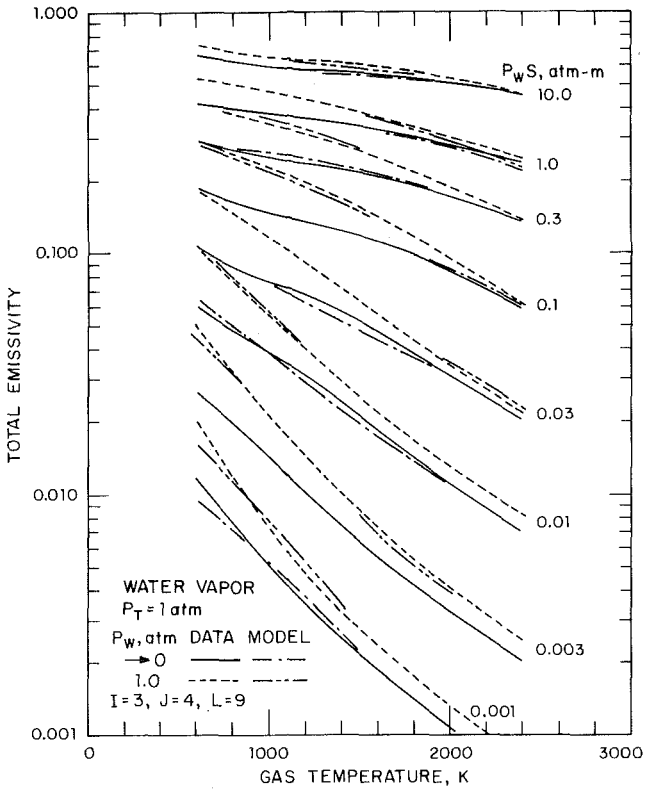

Fig. 4 Emissivity for water vapor

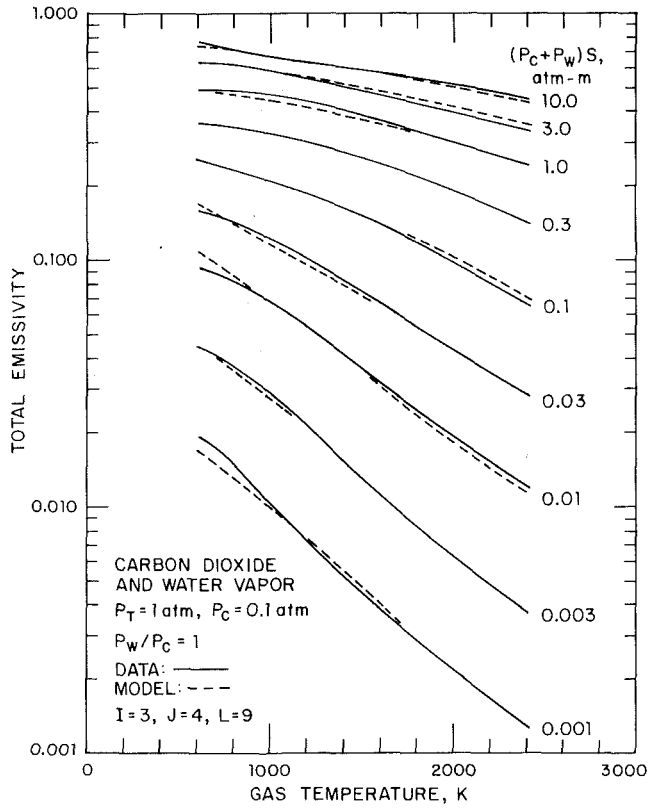

Fig. 5 Emissivity for mixture

as J increases, the agreement between the model and data also increases. From these findings, $J = 4$ was chosen with some accuracy being sacrificed at the lower values of P_cS and T.

A final consideration of these tests concerns the number of decimal digits which must be reported to produce similar results. All calculations were performed utilizing fourteen decimal digits of accuracy. Upon completion of these calculations, the coefficient values were rounded to three and four decimal digits, and rms errors recomputed. It was found that the original results could be reproduced with four decimal digits. Thus, this is the accuracy employed to report the coefficients.

The absorption and polynomial coefficients for carbon dioxide are presented in Table 1 for $I = 3$ and $J = 4$. The absorption coefficients are seen to be of the order of 0.1, 10, and 100 (atm-m)$^{-1}$. This may be interpreted as a real gas being represented by three gray gases corresponding to optically thin, intermediate optical thickness, and optically thick, respectively.

The tests for water vapor were not as extensive as those for carbon dioxide, since water vapor emissivity does not exhibit a similar behavior as that for carbon dioxide at low values of PS and T. From these tests, it was found that values of $I = 3$, $J = 4$, and $L = 9$ produced results in agreement with the data values. This agreement is illustrated in Fig. 4 for $P_w \to 0$ and $= 1.0$ atm. For clarity purposes, results for $P_wS = 3.0$ atm-m are not shown. The respective subset and set rms errors are

Table 2 Coefficients and errors for absorptivity of mixtures

		$c_{\alpha,i,j,k}$			
		$P_w/P_c = 1$			
	k				
i	j	1	2	3	4
1	1	0.55657 E-00	−0.62824 E-03	0.31876 E-06	−0.52922 E-10
2	1	0.16676 E-01	0.15769 E-03	−0.10937 E-06	0.19588 E-10
3	1	0.28689 E-01	0.20697 E-03	−0.17473 E-06	0.37238 E-10
1	2	0.32964 E-03	0.27744 E-06	−0.26105 E-09	0.37807 E-13
2	2	0.50910 E-03	−0.76773 E-06	0.40784 E-09	−0.69622 E-13
3	2	0.24221 E-03	−0.55686 E-06	0.34884 E-09	−0.67887 E-13
1	3	−0.53441 E-06	0.33753 E-09	−0.10348 E-12	0.26027 E-16
2	3	0.37620 E-07	0.18729 E-09	−0.15889 E-12	0.30781 E-16
3	3	−0.19492 E-06	0.36102 E-09	−0.21480 E-12	0.41305 E-16
1	4	0.12381 E-09	−0.90223 E-13	0.38675 E-16	−0.99306 E-20
2	4	−0.32510 E-10	−0.26171 E-13	0.29848 E-16	−0.58387 E-20
3	4	0.41721 E-10	−0.73000 E-13	0.43100 E-16	−0.83182 E-20
		$P_w/P_c = 2$			
1	1	0.59324 E-00	−0.61741 E-03	0.29248 E-06	−0.45823 E-10
2	1	−0.35664 E-01	0.21502 E-03	−0.13648 E-06	0.24284 E-10
3	1	0.12951 E-00	0.54520 E-04	−0.80049 E-07	0.17813 E-10
1	2	0.35739 E-03	0.22122 E-06	−0.26380 E-09	0.45951 E-13
2	2	0.51605 E-03	−0.70037 E-06	0.38680 E-09	−0.70429 E-13
3	2	0.15210 E-03	−0.37750 E-06	0.21019 E-09	−0.36011 E-13
1	3	−0.71313 E-06	0.46181 E-09	−0.70858 E-13	0.38038 E-17
2	3	0.12245 E-06	0.99434 E-10	−0.15598 E-12	0.37664 E-16
3	3	−0.13165 E-06	0.20719 E-09	−0.96720 E-13	0.14807 E-16
1	4	0.17806 E-09	−0.11654 E-12	0.19939 E-16	−0.13486 E-20
2	4	−0.57563 E-10	−0.10109 E-13	0.35273 E-16	−0.89872 E-20
3	4	0.26872 E-10	−0.34803 E-13	0.14336 E-16	−0.19754 E-20

P_w/P_c	Subset σ^*10^2	Set σ^*10^2
1	5.124	4.621
2	4.415	3.909

$P_T = 1$ atm, $P_c = 0.1$ atm, $0.001 \leq (P_c + P_w)s \leq 10.0$ atm-m, $600 \leq T, T_s \leq 2400$ K

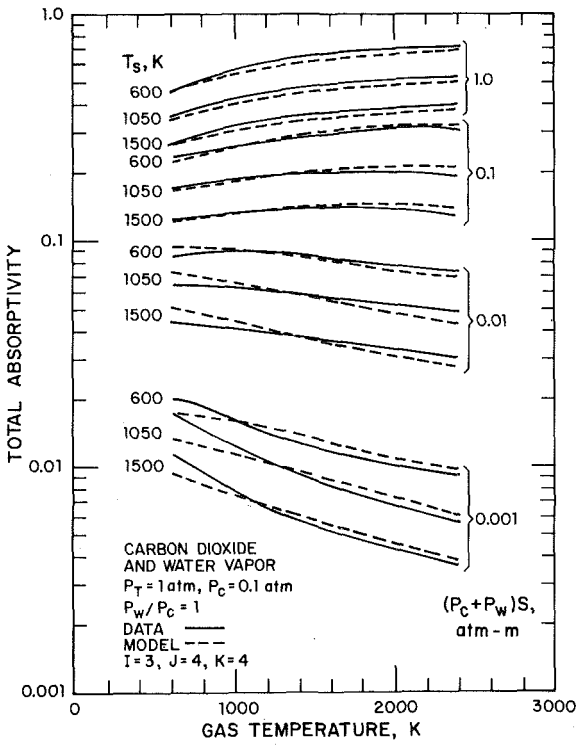

Fig. 6 Absorptivity for mixture

0.040 and 0.035, as well as 0.043 and 0.040. Similar errors were obtained for the other values of P_w. Values for the absorption and polynomial coefficients are reported in Table 1 for $P_w \to 0$ and = 1.0 atm. The agreement between the data values and model results at intermediate P_wS values is similar to that shown in Fig. 2, and the model results may be extended to P_wS values of 0.0001 atm-m without loss of accuracy.

In view of the similarity of results for $P_w/P_c = 1$ and 2, comparisons between data values and model predictions are presented in Fig. 5 only for $P_w/P_c = 1$ with $I = 3$ and $J = 4$. The subset and set rms errors for $P_w/P_c = 1$ and 2 are 0.048 and 0.044 as well as 0.041 and 0.037, respectively. Values for the absorption and polynomial coefficients are reported in Table 1. In general, the absorption coefficients presented by other investigators [3–7] are of similar magnitude.

Comparisons and results reported for total emissivity established that three gray gas components and a third-order gas temperature polynomial yielded model results which adequately represented the data values. These findings were also utilized to compare total absorptivity values from the model. As previously noted, the absorption coefficients for absorptivity were assigned those for emissivity. The number of partial pressure-path length and gas temperature values employed to generate the absorption and gas temperature polynomial coefficients for absorptivity were the same as those for emissivity. It was found that five decimal digits for the irradiation polynomial coefficients must be furnished in order to reproduce an accuracy of four decimal digits for the model results. The additional number of digits for ab-

sorptivity in comparison with the four digits for emissivity is attributed to the errors introduced by the irradiation temperature polynomial.

In view of the amount of results, only representative comparisons are presented. Model results and data values for total absorptivity of a mixture of carbon dioxide and water vapor with $P_w/P_c = 1$ are displayed in Fig. 6. Results for $(P_c + P_w)S = 0.001$, 0.01, 0.1, and 1.0 atm-m are only shown since, for each $(P_c + P_w)S$ value, the influence of the irradiation temperature is illustrated for $T_s = 600$, 1050, and 1500 K. Absorptivity data values are not strongly dependent on gas temperatures particularly for $(P_c + P_w)S$ values between 0.01 and 0.03 atm-m where they are nearly independent of gas temperatures. Based on these findings, Hottel and Sarofim [3] selected a mean gas temperature thereby discarding the gas temperature polynomial in the model expression and reported only polynomial coefficients to describe the effect of the irradiation temperature. This was not undertaken in this study since a wider gas temperature range is of interest. In view of the ranges of the parameters for which the model results are applicable, the agreement between the model and data is acceptable. The irradiation temperature polynomial coefficients $c_{\alpha,i,j,k}$ along with the subset and set errors are furnished in Table 2 for $P_w/P_c = 1$ and 2. The absorption coefficients have been provided in Table 1. The signs and orders of magnitudes for the coefficients are similar for the two values of P_w/P_c. The model results may be extended down to $(P_c + P_w)S = 0.0001$ atm-m.

Conclusions

Coefficients for the weighted sum of gray gases model were evaluated for total emissivity and absorptivity for carbon dioxide, water vapor, and mixtures of these gases. The coefficients are applicable for gas and irradiation tempertures within the range of 600 to 2400 K and partial pressure-path length products from 0.001 to 10.0 atm-m. A regression technique which minimizes the error between the model results and data values of total emissivity and absorptivity was utilized to compute the coefficients. Numerical experiments demonstrated that three gray gas components in conjunction with third-order temperature polynomial yielded models results which adequately predicted the property values. However, particularly at low values of temperatures and partial pressure-path length products, differences between the model results and data values occurred.

Acknowledgments

The authors gratefully acknowledge the financial assistance of the United States Department of Energy, Grant #DE-AC02-79ER10515.A000 for support of this research. Appreciation is also extended to the Graduate College of The University of Iowa for providing computer time. The assistance of P. Hix in preparation of this paper is recognized.

References

1 Hottel, H. C., and Sarofim, A. F., *Radiative Transfer*, McGraw-Hill, 1967.

2 Hadvig, S. A. P., "Gas Emissivity and Absorptivity: A Thermodynamic Study," *J. Inst. Fuel*, Vol. 43, 1970, pp. 129–135.

3 Hottel, H. C., and Sarofim, A. F., "The Effect of Gas Flow Patterns on Radiative Transfer in Cylindrical Enclosures," *International Journal of Heat and Mass Transfer*, Vol. 8, 1965, pp. 1153–1169.

4 Johnson, T. R., "Application of the Zone Method to the Calculation of Heat Transfer from Luminous Flames," Ph.D. thesis, University of Sheffield, 1971.

5 Taylor, P. B., and Foster, P. J., "The Total Emissivities of Luminous and Nonluminous Flames," *International Journal of Heat and Mass Transfer*, Vol. 17, 1974, pp. 1591–1605.

6 Truelove, J. S., *A Mixed Grey Gas Model for Flame Radiation*, United Kingdom Atomic Energy Authority, AERE-R-8494, 1976.

7 Nakra, N. K., and Smith, T. F., "Combined Radiation-Convection for a Real Gas," ASME *Journal of Heat Transfer*, Vol. 99, 1977, pp. 60–65.

8 Farag, I. H., and Allam, K. A., "Gray-Gas Approximation of Carbon Dioxide Standard Emissivity," ASME *Journal of Heat Transfer*, Vol. 103, 1981, pp. 403–405.

9 Farag, I. H., and Allam, K. A., "A Mixed Gray-Gas Model to Calculate Water Vapor Standard Emissivities," ASME Paper No. 81-HT-63, 1981.

10 Ludwig, C. B., Malkmus, W., Reardon, J. E., and Thomson, J. A. L., *Handbook of Infrared Radiation from Combustion Gases*, edited by R. Goulard and J. A. L. Thomson, NASA SP-3080, 1973.

11 Edwards, D. K., "Molecular Gas Band Radiation," *Advances in Heat Transfer*, Vol. 12, 1976, pp. 115–193.

12 Modak, A. T., "Exponential Wide Band Parameters for the Pure Rotational Band of Water Vapor," *J. Quant. Spect. Radiat. Transfer*, Vol. 21, 1979, pp. 131–142.

13 Leckner, B., "Spectral and Total Emissivity of Water Vapor and Carbon Dioxide," *Comb. and Flame*, Vol. 19, 1972, pp. 33–48.

14 Farag, I. H., "Radiative Heat Transmission from Nonluminous Gases: Computational Study of the Emissivities of Water Vapor and Carbon Dioxide," Sc.D. thesis, Chem. Engr., Dept., MIT, 1976.

15 Sarofim, A. F., Farag, I. H., and Hottel, H. C., "Radiative Heat Transmission from Nonluminous Gases. Computational Study of the Emissivities of Carbon Dioxide," *ASME 78-HT-18*, 1978.

16 Bueters, K. Q., Cogole, J. G., and Habelt, W. W., "Performance Prediction of Tangentially Fired Utility Furnances by Computer Model," *Fifteenth Sym. (Int'l.) Comb.*, 1974, pp. 1245–1260.

17 Modak, A. T., "Radiation from Products of Combustion," *Fire Research*, Vol. 1, 1978/79, pp. 339–361.

18 Smith, T. F., and Shen, Z. F., *Total Emissivities and Absorptivities of Carbon Dioxide and Water Vapor*, Division of Energy Engineering, University of Iowa, TR E-TFS-80-002, 1980.

19 De Ris, J., "Fire Radiation — A Review," *Seventeenth Sym. (Int'l.) Comb.*, 1978, pp. 1003–1016.

20 Kuester, J. L., and Mize, J. H., *Optimization Techniques with FORTRAN*, McGraw-Hill, 1973.

21 Smith, T. F., and Shen, F., *Evaluation of Coefficients for the Weighted Sum of Gray Gases Model*, Division of Energy Engineering, University of Iowa, TR E-TFS-80-007, 1980.

22 Smith, T. F., and Shen, F., *Exponential Wide Band Radiative Gas Properties*, Division of Energy Engineering, University of Iowa, TR E-TFS-80-001, 1980.

Combined Radiation-Convection in Gray Fluids Enclosed in Vertical Cavities

G. Lauriat
Assistant Professor,
Laboratoire de Thermique,
CNAM,
75141 Paris, Cedex 03,
France

The interaction of thermal radiation with natural convection in a gray fluid contained inside a cavity is numerically examined. The radiation part of the problem is treated by using the two-dimensional P-1 approximation. The effect of radiation on the conduction, transition, and boundary layer regimes is investigated. The results show that radiation decreases the intensity of the flow at low Rayleigh numbers and, in contrast, leads to an increased flow in convection regimes. The influence of the radiative parameters on the flow and heat transfer is discussed.

Introduction

During the past few decades, numerous investigations have been made of natural convection in enclosures. Most of these studies have considered convection to be the only mode of heat transfer in fluids confined between two isothermal plates. The extension of the problem to include the effects of wall conduction and radiative transfer between the walls has recently been considered [1, 2, 3]. The effect of the radiative properties of the fluid – i.e., absorption, emission and scattering – has been of interest in several papers. For an extensive list of references of natural convection in horizontal semitransparent fluid layer, the reader is referred to the recent article by Hassab and Özisik [4]. These references are devoted to the study of the stability of fluids contained in slots having very large aspect ratios and are restricted to the conduction regime. The interaction of radiation and convection in the boundary layer regime of a vertical cavity has been analytically and experimentally examined by Bratis and Novotny [5]. The experimental data are compared to a boundary layer type analysis in the case of radiating gas at moderate temperature level. Their results indicate that the heat transfer by thermal radiation is important although the relative effect of radiation is much less in magnitude for the vertical case than for the horizontal case [4].

The survey of the foregoing literature reveals that two major effects are predicted: in general, the radiation delays the onset of instability in a slot; and there is an increase in heat flux due to fluid radiation. In conjunction with the variations of the critical Rayleigh number, the magnitude of the velocity of the base flow is reduced [6]. The second effect is accomplished with a tendency to smooth the temperature distribution in the core of the enclosure and to increase the temperature gradient near the boundaries.

On account of the mathematical complexity brought upon by the radiation part of the problem in two-dimensional geometries, approximate analyses have been developed. The most successful technique for a multidimensional radiative heat transfer appears to be the differential formulation or P-1 approximation of the spherical harmonics method which was extended by Traugott [7] in order to allow for the effects of nongrayness of the fluid. One should also mention the method of undetermined parameters considered recently by Yuen and Wong [8] in the case of radiative equilibrium in a rectangular enclosure. However, the extension to nongray fluids seems to be cumbersome and the numerical computations can be quite time-consuming.

The objective of this work is to analyze the influence of the convective and radiative parameters on the conduction regime, on the transverse rolls, and on boundary layer regime.

In order to focus the study on the main features of the interaction, only gray fluids are considered in this paper. Indeed, calculations carried out for real gases enclosed in narrow cavities by using a more exact spectral model have shown that all the general trends obtained with the gray analysis still occur [9].

Formulation

Consider the process of combined natural convection and radiation in a vertical layer of a semitransparent Boussinesq fluid medium enclosed in a cavity with isothermal side walls and adiabatic end walls as shown in Fig. 1. The bounding surfaces are opaque, gray, and diffuse. It is assumed further that the contribution of the radiative stress to the momentum equation is negligible in view of the moderate temperature level of the medium at which the radiation pressure number is very small [10]. Therefore, in the presence of radiation, the continuity and momentum equations are similar. In order to eliminate pressure, these equations are expressed in terms of the vorticity, Ω, and a stream function, ψ. Non-

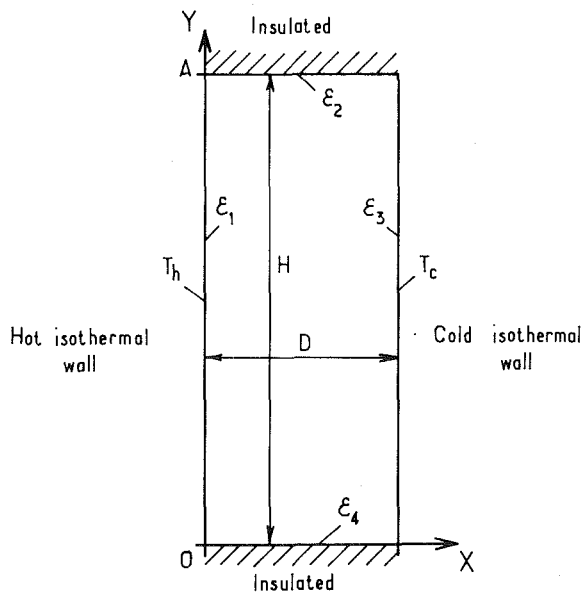

Fig. 1 System configuration and coordinate system

Contributed by the Heat Transfer Division and presented at the AIAA/ASME Fluids, Plasma, Thermophysics, and Heat Transfer Conference, St. Louis, Missouri, June 7-11, 1982. Manuscript received by the Heat Transfer Division April 3, 1981. Paper No. 82-HT-46.

dimensionalizing all variables, the equations governing the fluid motion can be written as

$$\nabla^2\psi = -\Omega \tag{1}$$

$$\frac{\partial\Omega}{\partial t} + u\frac{\partial\Omega}{\partial x} + v\frac{\partial\Omega}{\partial y} = \mathrm{Pr}\,\nabla^2\Omega + \mathrm{RaPr}\frac{\partial\theta}{\partial x} \tag{2}$$

$$\frac{\partial\theta}{\partial t} + u\frac{\partial\theta}{\partial x} + v\frac{\partial\theta}{\partial y} = \nabla^2\theta - \frac{\tau_0}{N}\left(\frac{\partial q_{r,x}}{\partial x} + \frac{\partial q_{r,y}}{\partial y}\right) \tag{3}$$

Where $\tau_0 = \alpha_m D$ is the optical thickness of the fluid layer and $N = \alpha_m\lambda/n^2\sigma T_m^3$ the interaction parameter.

The velocity field is obtained as

$$u = \frac{\partial\psi}{\partial y} \qquad v = -\frac{\partial\psi}{\partial x} \tag{4}$$

The dynamical boundary conditions are given as:

$$\psi = \frac{\partial\psi}{\partial x} = 0 \qquad -\Omega = \frac{\partial^2\psi}{\partial x^2} \qquad \text{at } x = 0,1 \tag{5a}$$

$$\psi = \frac{\partial\psi}{\partial y} = 0 \qquad -\Omega = \frac{\partial^2\psi}{\partial y^2} \qquad \text{at } y = 0,A \tag{5b}$$

The form of these equations can readily be derived following procedures previously used (see [11], for example). It should only be mentioned here that the temperature difference $\Delta T = T_c - T_h$ is chosen as scale factor for temperature and $n^2\sigma T_m^3\Delta T$ as scale factor for the radiative flux.

The energy equation (3) involves the radiative heat flux which will be obtained under the modified P-1 approximation [7]. In terms of the first moment of the intensity, the approximate form of the equation of radiative transfer is

$$\frac{\partial^2 J}{\partial x^2} + \frac{\partial^2 J}{\partial y^2} = 3\tau_0^2(J - 4\theta^4/\theta_m^3) \tag{6}$$

The radiative flux and its divergence are related to J by

$$\frac{\partial J}{\partial x} = -\frac{3\tau_0}{\eta}q_{r,x} \qquad \frac{\partial J}{\partial y} = -\frac{3\tau_0}{\eta}q_{r,y} \tag{7}$$

$$\frac{\partial q_{r,x}}{\partial x} + \frac{\partial q_{r,y}}{\partial y} = -\frac{\eta}{3\tau_0}\nabla^2 J \tag{8}$$

Substituting these relations into the energy equation gives:

$$\frac{\partial\theta}{\partial t} + u\frac{\partial\theta}{\partial x} + v\frac{\partial\theta}{\partial y} = \nabla^2\theta + \frac{\eta}{3N}\nabla^2 J \tag{3b}$$

The set of coupled equations (6) and (3b) requires additional boundary conditions. Following Amlin and Korpela [12], these conditions may be stated for opaque walls as

$$\frac{\partial J(0,y)}{\partial x} = 3\tau_0\lambda_1(J - 4\theta_h^4/\theta_m^3)/\eta \tag{9a}$$

$$\frac{\partial J(1,y)}{\partial x} = -3\tau_0\lambda_3(J - 4\theta_c^4/\theta_m^3)/\eta \tag{9b}$$

and similar relationships at the end walls. In these equations, λ_i characterizes the color of the wall, i, by:

$$\lambda_i = \frac{\epsilon_i}{2(2-\epsilon_i)} \tag{10}$$

ϵ_i being the total hemispherical emissivity of the wall. At the isothermal wall, the thermal boundary conditions remain as

$$\theta_h = 0.5 + \theta_m \quad \text{at } x = 0 \tag{11a}$$

$$\theta_c = -0.5 + \theta_m \quad \text{at } y = 1 \tag{11b}$$

An energy balance at the adiabatic walls yields the thermal conditions as:

$$\frac{\partial\theta}{\partial y} + \frac{\eta}{3N}\frac{\partial J}{\partial y} = 0 \quad \text{at } y = 0,A \tag{12}$$

For perfectly reflecting boundaries, the radiative flux is equal to zero and the equation (12) is reduced to the usual adiabatic condition.

It is apparent from the foregoing system of equations that four additional parameters must be specified, since the effects of radiation depend on N, τ_0, λ_i or ϵ_i, and η. It should be noticed that the present choice of dimensionless quantities just as for a nonradiating fluid leads to an interaction parameter, N, called elsewhere Planck number [6, 12], which charac-

Nomenclature

A = aspect ratio, $A = H/D$
C_p = specific heat at constant pressure
D = width of the cavity
H = height of the cavity
J = dimensionless incident radiation
n = refractive index of the semi-transparent medium
N = conduction-to-radiation parameter, $N = \alpha_m\lambda/n^2\sigma T_m^3$
Nu = Nusselt number
Pr = Prandtl number, $\mathrm{Pr} = \nu/a$
q = heat flux density
q_r = dimensionless radiative heat flux
$q_{r,x}$ = x-component of the dimensionless radiative flux
$q_{r,y}$ = y-component of the dimensionless radiative flux
Ra = Rayleigh number, $\mathrm{Ra} = g\beta\Delta TH^3/a\nu$
t = dimensionless time
T = temperature of the fluid
T_c = temperature of the cold wall
T_h = temperature of the hot wall
T_m = mean temperature, $T_m = (T_c + T_h)/2$
u = x-component of the dimensionless velocity
v = y-component of the dimensionless velocity
x,y = dimensionless coordinates

Greek symbols

α_m = mean extinction coefficient
β = coefficient of thermal expansion
γ = stratification parameter, $\gamma = (\theta_{y,c}\mathrm{Ra}/4)^{0.25}$
ΔT = temperature difference between the isothermal walls
ϵ_i = emissivity of the wall, i
η = nongrayness factor, $\eta = (\kappa_p/\kappa_R)^{1/2}$
κ_p = Planck mean coefficient
κ_R = Rosseland mean coefficient
λ = thermal conductivity of the fluid
λ_i = $= \epsilon_i/2(2-\epsilon_i)$; $i = 1, 4$
ν = kinematic viscosity
θ = dimensionless fluid temperature, $\theta = T/\Delta T$
θ_m = dimensionless mean temperature, $\theta_m = T_m/\Delta T$
$\theta_{x,c}$ = x-temperature gradient at cavity midpoint
$\theta_{y,c}$ = y-temperature gradient at cavity midpoint
ρ_0 = density
σ = Stephan-Boltzmann constant
τ_0 = optical thickness of the fluid, $\tau_0 = \alpha_m H$
ψ = dimensionless stream function
Ω = vorticity

Superscripts

$-$ = mean quantity
$'$ = refers to dimensional quantities

Table 1 Comparison of the solutions ($A=10$, $\mathrm{Ra}=1000$, $N=1$, $\tau_0=1$, $\epsilon_i=1$)

x	0.1	0.3	0.5	0.7	0.9
Pure convection	0.400	0.200	0.	−0.200	−0.400
Analytical [6]	0.364	0.162	0.	−0.162	−0.364
Numerical	0.375	0.191	0.035	−0.133	−0.353

$\theta(x,A/2)-\theta_m$

x	0.1	0.3	0.5	0.7	0.9
Pure convection	−5.830	−6.901	0.	6.901	5.830
Analytical [6]	−5.282	−5.951	0.	5.951	5.282
Numerical	−5.017	−5.902	0.154	5.852	5.251

$v(x,A/2)$

terizes the relative importance of conduction in respect to radiation. It is obvious that such a parameter has only a meaningful physical significance for the conduction regime. Otherwise, it should be preferable to introduce a parameter representing the relative role of radiation to convection [5].

Heat Transfer. The heat is transferred from the hot wall to the cold wall by three modes: diffusion, transport, and radiation. Therefore, the local heat flux through a parallel plane to the side walls can be written as

$$q'(x',y')=-\lambda\frac{\partial T}{\partial x'}+\rho_0 c_p u'(T-T_m)+q'_{r,x'} \tag{13}$$

The average Nusselt number for that plane is defined as

$$\bar{\mathrm{Nu}}(x')=\frac{Q(x')}{\lambda\Delta T/D} \tag{14}$$

Where

$$Q(x')=\frac{1}{H}\int_0^H q'(x',y')dy'$$

The insertion of the nondimensional variables into equation (14) gives

$$\bar{\mathrm{Nu}}(x)=\frac{1}{A}\int_0^A\left(-\frac{\partial\theta}{\partial x}+u(\theta-\theta_m)-\frac{\eta}{3N}\frac{\partial J}{\partial x}\right)dy \tag{15}$$

It should be noted that the Nusselt number for combined radiation-convection can be expressed as the sum of a Nusselt number due to convection and a Nusselt number for radiation [13]. These two components are coupled through the radiation parameters. For adiabatic end walls, the mean heat flux is independent of x and equal to the values at the isothermal walls. Thus,

$$\bar{\mathrm{Nu}}(x)=\bar{\mathrm{Nu}}(0)=\bar{\mathrm{Nu}}(1) \tag{16}$$

Numerical Method

A large number of numerical experiments were carried out by using several finite difference schemes. In order to evaluate these schemes, the test problem was that of pure convection in a cavity of aspect ratio equal to $A=10$. As a result [14], it was concluded that calculations be done with a standard second-order alternating direction implicit (ADI) algorithm for large aspect ratio cavities. The same conclusions are presumed to be applicable when the energy equation is subject to a radiation term. With regard to the radiation part of the problem, equation (6) was recast in transient form and was solved by using an ADI compact fourth-order scheme [15]. Taking into account the form of the boundary conditions of the radiation equation, the size of the relevant matrix system was reduced to a 2×2 bloc tridiagonal form at each step of the iterative procedure by using an accurate relation between the function and its first two derivatives [15].

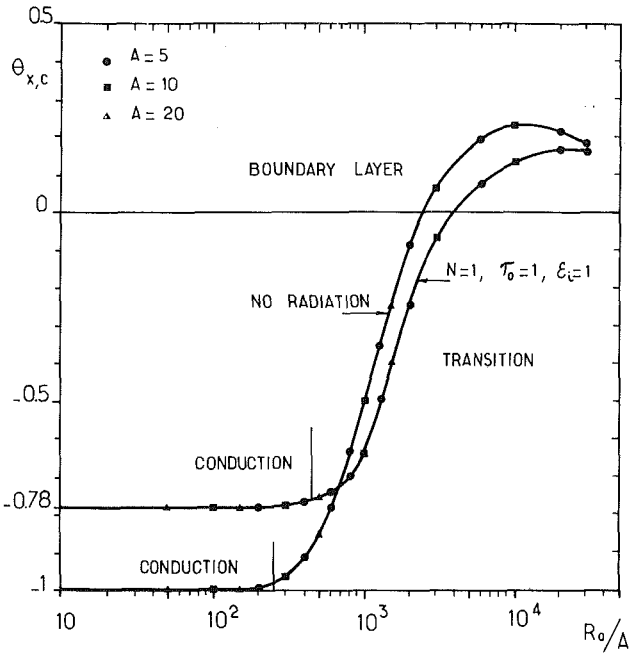

Fig. 2 Horizontal temperature gradient at cavity midpoint versus Ra/A

Since the numerical computations of the mean Nusselt number suffer from inaccuracies of the truncation errors, the equality (16) is generally not satisfied. A check on the accuracy of the numerical procedure was made by monitoring the discrepancies in heat transfer for different vertical planes through the layer. In view of this, solutions have been obtained by using mesh refinements when the Rayleigh number and the interaction were increased.

The computations were carried out on an IBM 370/168 computer. Typical values of CPU-times required for each solution of the equation set (1-3) are given below for a 81×21 grid:

pure convection	: 0.31s
convection + radiation	: 0.46s

Without radiation, the scale of the dimensionless time needed to reach the steady-state solution is of the order of 1/Pr. Consequently, about 700 iterations are required in order to satisfy the convergence criterion if the pure conduction solution ($u=v=0$, linear temperature distribution) is used as an initial guess. It should be noted that the convergence is speeded up under the influence of the radiative transfer or by using the converged solution for a next set of parameters as the initial field for the current set.

Results and Discussions

In this study the Prandtl number was kept fixed at $\mathrm{Pr}=0.7$. The values of the radiative parameters investigated are located in the range of those considered previously [4, 6] and are assumed to be reasonable for gases.

Conduction Regime. According to the approximate analytical solution given by Arpaci and Bayazitoğlu [6], the effects of the coupling between radiation and convection in a slot are to flatten the temperature distributions and to reduce the vertical velocities in the conduction regime. The numerical results agree with this conclusion as seen in Table 1, where values of the temperatures and vertical velocities in the horizontal middle plane are reported for a narrow cavity. A number of other calculations have been made for various sets of the radiation parameters and, as depicted by the analytical

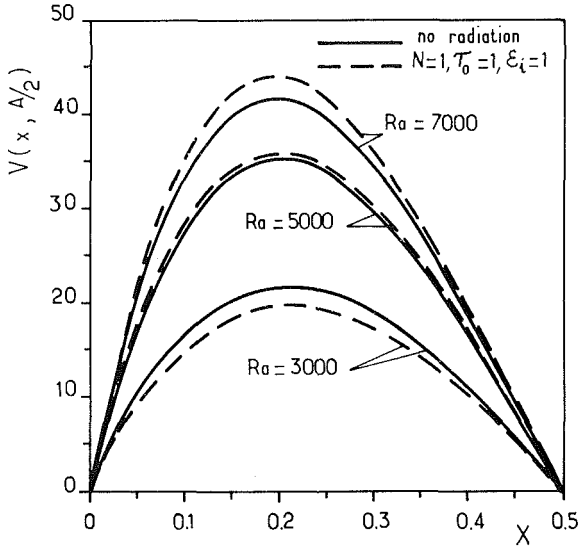

Fig. 3 Vertical velocity profiles on the horizontal mid-plane of the cavity in the transition regime ($A = 5$)

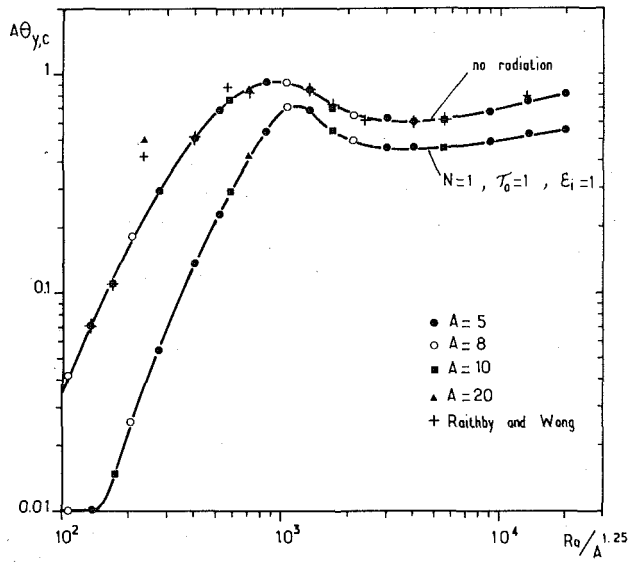

Fig. 4 Vertical temperature gradient at cavity midpoint versus $Ra/A^{1.25}$

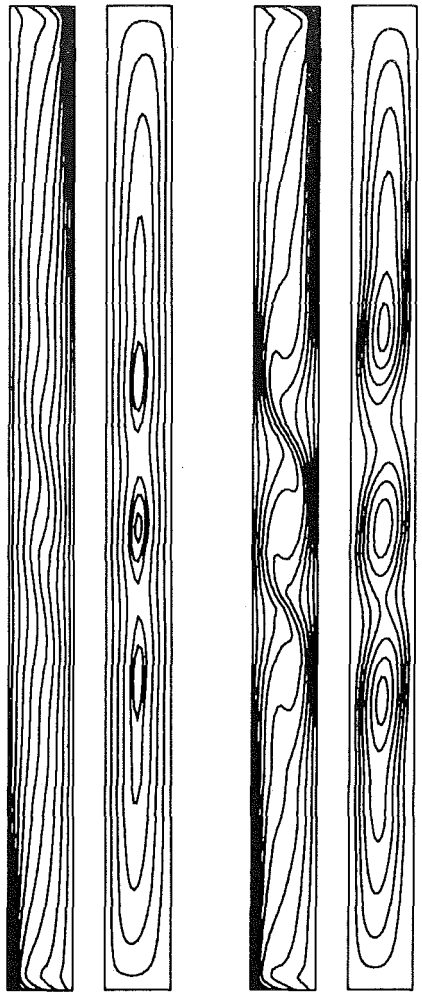

Fig. 5 Streamline and isothermal patterns in a vertical slot ($A = 15$, $N = 1$, $\tau_0 = 1$, $\epsilon_i = 1$).
Contours at: $\theta = 4.5, (0.1), 5.5$
– $Ra = 10^4$: $\psi = 3, 9, 15, 20, 21.5, 31$
– $Ra = 2.5\ 10^4$: $\psi = 7.5, (7.5), 37.5, 42.5, 47.5, 50$

solution, these effects were found to become more significant either by decreasing the interaction parameter, N, or by increasing the optical thickness, τ_0. We may, however, note that two interesting results are provided by the numerical modelling. First, the previous findings are still valid whatever the aspect ratio of the cavity. Second, it appears that the classical centro-symmetry property of the flow due to the form of the boundary conditions is destroyed by the radiation. An appreciable departure from this property can be seen in Table 1, although the values of the radiation parameters are moderate. On the other hand, with the analytical approach the central plane temperature is bound to be equal to θ_m and, consequently, this loss of the centro-symmetry property cannot be obtained. It should be pointed out that the numerical result is in agreement with the solutions obtained in one-dimensional conduction and radiation problems in semitransparent solids where it has been shown that the temperatures in the central region are smoothed and the temperature gradients at both walls are increased.

For this reason, the conductive flux in the core of the flow is substantially less than in nonradiating fluid and the departure of the horizontal temperature gradient at the cavity midpoint from $\theta_{x,c} = -1$ increases as the interaction increases. For example, at moderate values of the radiation parameters it can be seen in Fig. 2 that $\theta_{x,c} = -0.78$.

Transition Regime. For the range of Ra values where conduction plays a significant role in the central part of the cavity, the flow regime was called the transition regime by Eckert and Carlson [16]. This regime can be identified by considering the variation of $\theta_{x,c}$. Following Raithby and Wong [18], the transition regime starts when the temperature gradient breaks away from its value at $Ra = 0$. As in reference [18], we find then by referring to Fig. 2. That the beginning of the transition is $Ra/A \cong 250$ and $Ra/A \cong 450$ in a radiating fluid.

One important feature of the interaction of radiation with convection is the subdivision of the transition regime into two regions as can be seen in Fig. 3: at the lowest Ra values, the vertical velocities in the horizontal middle plane are reduced like in the conduction regime. On the other hand, the result of increases of the Rayleigh number up to $Ra \cong 5000$ is that the differences between the velocities obtained with and without radiation vanish. Further increases produce higher vertical

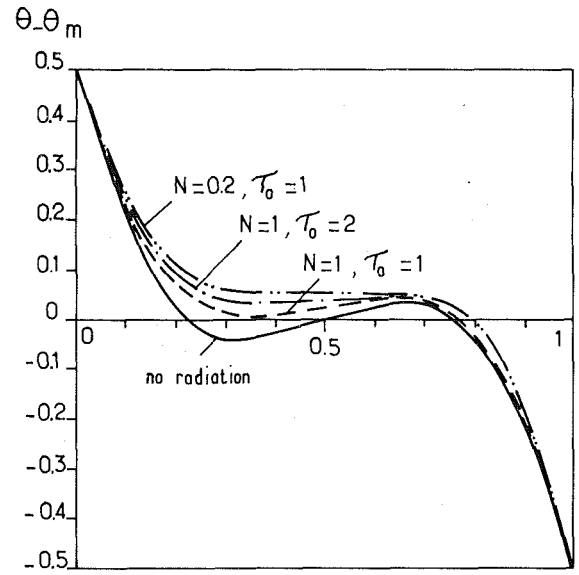

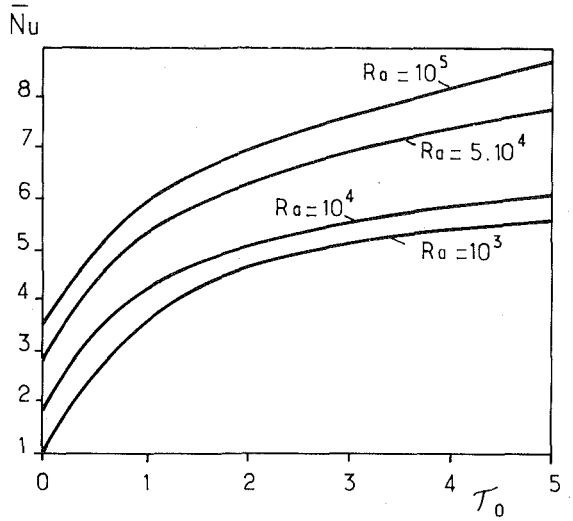

Fig. 7 Average Nusselt number as a function of the optical thickness for various Ra numbers ($A = 6$, $N = 1$, $\epsilon_i = 1$)

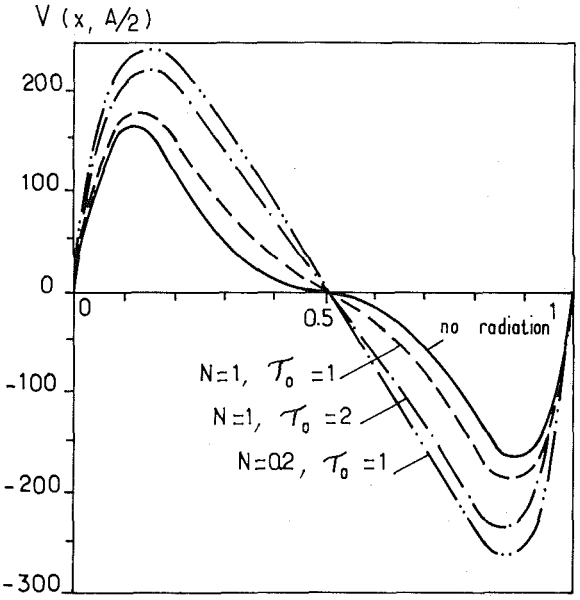

Fig. 6 Temperature distribution and vertical velocity profiles on the horizontal mid-plane of the cavity in the convection regime ($A = 6$, $Ra = 10^5$, $\epsilon_i = 1$)

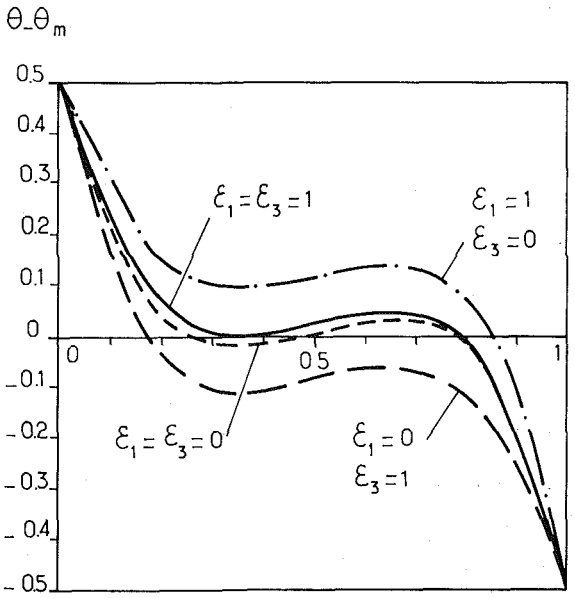

Fig. 8 Effects of the isothermal wall emissivities ϵ_1 and ϵ_3 on the temperature distributions ($A = 6$, $Ra = 10^5$, $\tau_0 = 1$, $N = 1$, $\epsilon_2 = \epsilon_4 = 1$)

velocities and, consequently, more important mass circulation in the cavity. This behavior can be explained qualitatively by referring again to Fig. 2, which shows that the absolute value of the buoyancy term in the transport equation (2) is greater in nonradiating fluid as long as the Rayleigh number is less than approximately 1000A.

For large enough aspect ratios, the base flow may become unstable and the linear stability analyses have shown that stationary multicellular flows occur when the Rayleigh number exceeds a certain magnitude which depends both on A and Pr. In gas-filled cavities, these secondary motions are not possible below $A = 12$ [19] and appear for Rayleigh numbers which correspond to the transition regime when the aspect ratio is not too large (say $A < 20$). In addition, Bergholz [20] has shown that the stratification parameter, γ, is important and determines the nature of the instabilities. For example, at the small values of γ characteristic of the transition regime in narrow cavities, the flow is unstable to stationary disturbances. This parameter is related to the nondimensional vertical temperature gradient in the cavity and the gradient at cavity midpoint, $\theta_{y,c}$, can be obtained by referring to Fig. 4. This figure shows plots of the product $A\theta_{y,c}$ as a function of $Ra/A^{1.25}$ in order to remove the aspect ratio effects [17]. For nonradiating fluid, the agreement between the values given recently by Raithby and Wong [18] with those of the present work is quite good as can be seen in Fig. 4. In the case of a radiating fluid, the values of $A\theta_{y,c}$ are smaller and, consequently, the stratification parameter is reduced. This decrease of γ means that multicellular flows can be generated more easily under the influence of radiation. This is clearly illustrated in Fig. 5 where the isothermal patterns and streamlines are presented at $Ra = 10^4$ and $Ra = 2.5\ 10^4$ for an aspect ratio $A = 15$. Without radiation, the secondary motion appears at Rayleigh numbers slightly greater than $Ra = 10^4$ and has disappeared at $Ra = 2.5 \times 10^4$. This result is in agreement with those presented by Roux et al. [19]: for Rayleigh numbers ranging from $Ra = 7000$ to 30,000, a transition from unicellular to multicellular flow occurs, followed later on by a reverse transition back to unicellular

flow. In a radiating fluid, Fig. 5 shows that the secondary motion is already developed at $Ra = 10^4$ and strengthened at $Ra = 2.5 \times 10^4$. The reverse transition is observed about $Ra = 3.5 \times 10^4$. It should be pointed out here that it is quite difficult to localize these two critical values of the Rayleigh number accurately without using a sufficient grid resolution and higher order accurate numerical methods. Otherwise, the secondary motion can be obscured and a single cell is observed [14]. In this study, it has not been possible to drive solutions to satisfactory convergence when secondary motions occur even by using a fine grid (21×151). However, despite these small numerical oscillations, the results show evidence that radiation accentuates the multicellular structure.

Boundary Layer Regime. From the temperature distributions and velocity profiles carried out for Ra values which correspond to the boundary layer regime in nonparticipating media, two main results can be seen in Fig. 6: first, when the parameter N decreases or when τ_0 increases, the velocities and the thicknesses of the boundary layers are increased. Careful inspection of Fig. 6 shows that the absolute velocities are greater close to the cold wall. This lack of the property of centro-symmetry of the velocity field is emphasized in radiation dominant situations ($N = 0.2$) where the variations of the maximum velocities are substantially greater in proportion than in the conduction regime. Further examinations of Fig. 6 provide the second main results which concern the temperature distributions. The thermal boundary layer grows close to the hot wall when the radiation effects are increased and the horizontal temperature gradient at the center of the cavity is reduced from $\theta_{x,c} = 0.25$ without radiation to zero for $N = 0.2$. In this case, the pure convection solution is greatly affected in the central part of the cavity since the temperature distribution is not only flattened but also shifted upward.

Parametric Study of the Radiation Effects. For moderate optical thickness of the fluid ($\tau_0 = 1$), the error caused by neglecting radiation effects becomes very small when the interaction parameter is greater than $N = 10$. At $Ra = 10^5$, to reduce N from 10 to 0.1 doubles the maximum of the vertical velocity components and leads to a large increase in the heating of the central part of the cavity. In addition, there is a rapid drop-off of the mean Nusselt number for values of the interaction parameter between $N = 0.1$ and $N = 1$. This nonlinear variation of the Nusselt number is indicative of a strengthening of the radiation process which produces a very slow rate of convergence of the numerical procedure. At these low values of N, the convective heat transfer is only significant in the vicinity of the walls while the core is nearly at a uniform temperature close to θ_m.

Next, the effects of the optical thickness, τ_0, on the heat transfer were investigated at various Rayleigh numbers for $N = 1$. In the conduction regime, the results are in accordance with those presented in previous studies. At high Rayleigh numbers, to increase τ_0 produces higher temperatures of the fluid with a negative horizontal temperature gradient and, consequently, the temperature inversion no longer appears in the core. Concerning the vertical velocity profiles, the increasing τ_0 yields similar effects to when radiation becomes stronger by decreasing N as can be seen in Fig. 6.

The next effect of increase in optical thickness is to increase the heat transfer. The behavior of the Nusselt number as a function of τ_0 is shown in Fig. 7 for various Rayleigh numbers. Initially, the curves rise rapidly with τ_0 and a more gradual increase can be observed for τ_0 greater than 2. At low Rayleigh numbers, the Nusselt number tends toward a limit value which can be readily obtained by applying the optically thick limit approximation. In this case, an effective thermal conductivity can be defined by $\lambda_e = \lambda(1 + 16\eta/3N)$ and, on account of the values of η and N, the amount of the optically thick Nusselt number is $\bar{Nu} = 6.33$. In the convection regimes, the limit value is greatly increased since the problem approaches the nonradiating problem with a fictitious Prandtl number equal to $Pr = 0.112$. By using the correlation given by Thomas and de Vahl Davis [17], the $\bar{Nu}$ value should reach about $\bar{Nu} = 11$ for $Ra = 10^5$. Unfortunately, very slow rates of convergence were encountered when the optical thickness is greater than $\tau_0 = 7$, and calculations were stopped before this asymptotic value could be approached.

Finally, Fig. 8 is prepared to illustrate the influence of the hot wall emissivity ϵ_1 and that of the cold wall ϵ_3 on the temperature distribution in the horizontal middle plane. It is obvious that the effects of the radiative transfer are reduced for $\epsilon_1 = \epsilon_3 = 0$ at moderate values of the optical thickness: the temperature distribution and velocity profile look like those obtained in a nonradiating fluid, and the increase of heat transfer is of the order of 10 percent. Next, two other extreme cases were considered. First, if the hot wall is black and the cold wall perfectly white, the core temperatures are shifted upward and, consequently, the maximum vertical velocity is lower near the hot wall than near the cold one. Since there is no radiative transfer at the cold wall, the Nusselt number is lower than for the case of a black cold wall. Second, the decrease of the hot wall emissivity from $\epsilon_1 = 1$ to $\epsilon_1 = 0$ in conjunction with a black cold wall leads to a decrease of the temperature gradient at the hot wall. The vertical velocities are then higher near the hot wall than near the cold one. In these two extreme cases, the differences between the heat transfer coefficients are of the order of 4 percent and it appears that convection compensates for the weakening of the radiation close to the perfectly reflecting wall.

Conclusion

Numerical investigations of heat and momentum transfers by natural convection and radiation in a semitransparent fluid medium inside a cavity were conducted and the following conclusions were obtained:

1 In the conduction regime, the numerical results are in accordance with the predictions of the analytical solution given by Arpaci and Bayazitoğlu [6]: the temperature distributions become S-shaped and the magnitude of the velocities are reduced.

2 On the other hand, the results obtained in the transition regime exhibit an increase of the velocities. For example, at moderate values of the radiation parameters, the limit of the Rayleigh number corresponding to these opposite effects was found to be of the order of $1000A$. In the case of a narrow vertical cavity and in the transition regime, the numerical model predicts that radiation always accentuates the multicellular structure of the flow. This behavior results from a decrease of the thermal stratification.

3 From the temperature distributions and velocity profiles carried out for the Ra values which correspond to the boundary layer regime in a transparent fluid, two main results could be drawn: first, when the radiation effects are increased, the velocities and the thickness of the boundary layers are increased. Second, the inversion of the horizontal temperature distributions in the core disappears in radiation-dominant situations.

4 The results presented here have shown that the radiation highly activates the heat transfer across the cavity.

References

1 Gdalevich, L. B., Nogotov, E. F., and Fertman, V. E., "Effect of Side Walls on Heat Transfer Through a Vertical Air Layer in Laminar Natural Convection," *International Journal of Heat and Mass Transfer*, Vol. 22, 1979, pp. 1601-1606.

2 Balvanz, J. L., and Kuehn, T. H., "Effect of Wall Conduction and Radiation on Natural Convection in a Vertical Slot with Uniform Heat Generation on the Heated Wall," *Natural Convection in Enclosures*. ASME HTD, Vol. 8, 1980, pp. 55-62.

3 Lauriat, G., "A Numerical Study of a Thermal Insulation Enclosure: Influence of the Radiative Transfer," *Natural Convection in Enclosures*, ASME HTD, Vol. 8, 1980, pp. 63-71.

4 Hassab, M. A., and Ozisik, M. N., "Effects of Radiation and Convective Boundary Conditions on the Stability of Fluid in an Inclined Slender Slot," *International Journal of Heat and Mass Transfer*, Vol. 22, 1979, pp. 1095-1105.

5 Bratis, J. C., and Novotny, J. L., "Radiation-Convection Interaction in the Boundary Layer Regime of an Enclosure," *International Journal of Heat and Mass Transfer*, Vol. 17, 1974, pp. 23-36.

6 Arpaci, V. S., and Bayazitoğlu, Y., "Thermal Stability of Radiating Fluids: Asymmetric Slot Problem," *Phys. of Fluids*, Vol. 16, 1973, pp. 589-593.

7 Traugott, S. C., "Radiative Heat-Flux Potential for a Nongrey Gas," *AIAA Journal*, Vol. 4, 1966, pp. 541-542.

8 Yuen, W. W., and Wong, L. W., "Radiative Heat Transfer in a Rectangular Enclosure With Gray Medium," ASME-AICHE Heat Transfer Conference, Orlando, July 1980, ASME Paper No. 80-HT-101.

9 Lauriat, G., "Numerical Study of the Interaction of Natural Convection With Radiation in Nongray Gases in Narrow Vertical Cavity," *Proceedings of the 7th International Heat Transfer Conference*, Paper NC6, 1982.

10 Özisik, M. N., *Radiative Transfer and Interaction with Conduction and Convection*, Wiley, 1973.

11 Mallinson, G. D., and de Vahl Davis, G., "The Method of the False Transient for the Solution of Coupled Elliptic Equations," *Journal of Computational Physics*, Vol. 12, 1973, pp. 435-461.

12 Amlin, D. W., and Korpela, S. A., "Influence of Thermal Radiation on the Temperature Distribution in a Semitransparent Solid," ASME JOURNAL OF HEAT TRANSFER, Vol. 101, 1979, pp. 76-80.

13 Viskanta, R., "Radiation Transfer and Interaction of Convection with Radiation Heat Transfer," *Advances in Heat Transfer*, Vol. 3, 1966, pp. 175-251.

14 Lauriat, G., "Numerical Study of Natural Convection in a Narrow Vertical Cavity: An Examination of High-Order Schemes," ASME-AICHE Heat Transfer Conference, Orlando, July 1980, ASME Paper No. 80-HT-90.

15 Hirsh, R., "Higher-Order Accurate Difference Solution of Fluid Mechanic Problems by a Compact Differencing Technique," *Journal of Computational Physics*, Vol. 19, 1975, pp. 90-109.

16 Eckert, E. R. G., and Carlson, W. O., "Natural Convection in an Air Layer Enclosed Between Two Vertical Plates with Different Temperatures," *International Journal of Heat and Mass Transfer*, Vol. 2, 1961, pp. 106-120.

17 Thomas, R. W., and de Vahl Davis, G., "Natural Convection in Annular and Rectangular Cavities—A Numerical Study," *Proceedings of the Fourth International Conf. on Heat Transfer*, Paris, 1970, N. C. 2-4, pp. 1-11.

18 Raithby, G. D., and Wong, M. H., "Heat Transfer by Natural Convection Across Vertical Air Layers," *Numerical Heat Transfer*, Vol. 4, 1981, pp. 447-457.

19 Roux, B., Grondin, J. C., Bontoux, P., and de Vahl Davis, G., "Reverse Transition from Multicellular to Monocellular Motion in Vertical Fluid Layer," *Physico Chemical Hydrodynamics*, Madrid, 1980.

20 Bergholz, R. F., "Instability of Steady Natural Convection in a Vertical Fluid Layer," *Journal of Fluid Mechanics*, Vol. 84, Part 4, 1978, pp. 743-768.

Fin Geometry for Minimum Entropy Generation in Forced Convection

D. Poulikakos

A. Bejan

Department of Mechanical Engineering,
University of Colorado,
Boulder, Colo. 80309

This paper establishes a theoretical framework for the minimization of entropy generation (the waste of exergy, or useful energy) in extended surfaces (fins). The entropy generation rate formula for a general fin is derived first. Based on this general result, analytical methods and graphic results are developed for selecting the optimum dimensions of pin fins, rectangular plate fins, plate fins with trapezoidal cross section, and triangular plate fins with rectangular cross section.

Introduction

Extended surfaces (fins) constitute one of the most effective design features for promoting heat transfer between a solid surface and a stream of fluid. The importance of this thermal design technique in the general area of heat transfer augmentation and energy conservation is fully recognized by the heat transfer community [1, 2].

The traditional approach to the optimization of fins consists of minimizing the consumption (investment) of fin material for the execution of a specified heat transfer task. More than a half-century ago, Schmidt [3] stated intuitively that a two-dimensional fin must have a parabolic-law pointed cross-sectional profile if it is to require the least material (volume) for a certain heat transfer rate. Schmidt's design principle was later proved by Duffin [4] who relied on the formalism of variational calculus. This design principle has been steadily brought closer to the realities of fin manufacturing and heat exchanger operation by a number of contributors who have analyzed the role of radiation, two-directional heat transfer (curvature), temperature-dependent thermal conductivity and variable heat transfer coefficient (see, for example, references [5–7]). Many of these contributions have been summarized by Kern and Kraus [8]. The essence and practical limitations of this design philosophy are discussed in a recent paper by Kraus and Snider [9].

The objective of this paper is to outline an entirely different approach to the optimization of fins. This approach consists of calculating the entropy generation rate of one fin, and minimizing it systematically.

The first and second laws of thermodynamics, taken together, state that the entropy generated by any engineering system is proportional to the work lost (destroyed) irreversibly by the system. This truth is expressed concisely as the *Gouy-Stodola Theorem* [10]

$$W_{\text{lost}} = T_0 \sum_{\substack{\text{all} \\ \text{system} \\ \text{components}}} S_{\text{gen}} \tag{1}$$

where W_{lost} is the lost available work (lost availability, or lost exergy) [11], T_0 is the absolute temperature of the environment, and S_{gen} is the entropy generated in each compartment of the system. Equation (1) implies that the thermodynamic irreversibility (entropy generation) of each system component contributes to the *aggregate* loss of available work in the system (W_{lost}). For example, in a heat engine the entropy generated in one component (e.g., the condenser) is responsible for a proportional share of the loss in power output from the engine cycle (the lost power is the difference between the theoretical Carnot output and the actual power output). Therefore, it is the engineer's job to focus on each component of the system and, by design, to try to minimize the irreversibility (S_{gen}) of that component.

Heat exchangers serve as components in a wide range of power and refrigeration applications. Therefore, in order to conserve available work (exergy), it is necessary to approach the design of such heat exchangers from the point of view of entropy generation minimization. It is important to go further and focus on the components of heat exchangers and conceptualize the design of each such "building block" for minimum irreversibility.

This paper focuses on the design of fins for minimum entropy generation in forced convection heat transfer. This design philosophy allows us to properly account for the fact that, in addition to enhancing heat transfer, extended surfaces increase fluid friction. The trade-off between heat transfer and fluid friction is a classical dilemma in heat exchanger design [2, 12]: the irreversibility minimization philosophy places this trade-off on a solid foundation, as heat transfer and fluid drag are both mechanisms for entropy generation. In this paper, the competition between enhanced thermal contact and fluid friction is settled when the *heat transfer irreversibility* and the *fluid friction irreversibility* add to yield a minimum rate of entropy generation for the fin.

This paper begins with a derivation of the formula for the rate of entropy generation in an arbitrary fin engaged in forced convection heat transfer. Based on this general result, it is shown how the geometric parameters of common fin shapes can be selected so that the fin saves the most exergy (available work) while performing its specified heat transfer function. For simplicity, throughout most of this study the classical fin heat transfer model [13] is adopted, whereby the fin is slender enough so that the conduction process can be regarded as unidirectional. It is further assumed that the properties of the fin material and those of the external fluid are constant. The external flow is assumed uniform and parallel to the base surface of the fin.

Entropy Generation Due to Convective Heat Transfer From a Single Fin

The entropy generated by a single fin in crossflow can be evaluated based on the general model presented in Fig. 1. Consider, an arbitrary fin suspended in a uniform stream with velocity, U_∞, and temperature, T_∞. The heat transfer, q_B, is driven by the temperature difference between the fin base, T_B, and the free stream, T_∞. In addition, the crossflow arrangement is responsible for a net drag force, F_D, which is transmitted through the fin to the base wall.

As shown in Fig. 1, we choose a control volume which is

Contributed by the Heat Transfer Division for publication in the JOURNAL OF HEAT TRANSFER. Manuscript received by the Heat Transfer Division October 30, 1980.

fixed relative to the fluid. The environment (the wall) "drags" the fin with a speed U_∞ through the stationary fluid, by applying a net force F_D tangentially to the control surface. In the steady state, the first and second laws of thermodynamics dictate, respectively,

$$q_B - q_\infty + F_D U_\infty = 0 \tag{2}$$

$$S_{\text{gen}} = \frac{q_\infty}{T_\infty} - \frac{q_B}{T_B} > 0 \tag{3}$$

where q_∞ is the net heat transfer rate from the control volume to the rest of the fluid, and S_{gen} is the rate of entropy generation associated with the heat and fluid flow arrangement. Combining equations (2) and (3) yields

$$S_{\text{gen}} = \frac{q_B \theta_B}{T_\infty{}^2 (1 + \theta_B / T_\infty)} + \frac{F_D U_\infty}{T_\infty} \tag{4}$$

In this expression θ_B is the temperature difference between the base of the fin and the free stream, $T_B - T_\infty$.

The fin entropy generation rate, (4), is a remarkably simple result which demonstrates that inadequate thermal conductance and fluid friction contribute hand-in-hand to the degrading of fin thermodynamic performance. The first term on the right-hand side of equation (4) represents the entropy generation due to heat transfer across a nonzero temperature difference, while the second term is the entropy generation associated with fluid friction,

$$S_{\text{gen}} = (S_{\text{gen}})_{\text{heat transfer}} + (S_{\text{gen}})_{\text{fluid friction}} \tag{5}$$

Note that the fluid friction entropy generation rate is equal to the mechanical power needed for dragging the fin through the fluid, $F_D U_\infty$, divided by the *absolute* temperature of the fluid.

It is proposed to size an individual fin so that the irreversibility contributed by the fin to the larger system (the heat exchanger) is a minimum. Mathematically, this design approach consists of minimizing expression (4). The power of expression (4) is that it brings together the conflicting issues of excessive thermal resistance versus loss of fluid pumping power: in equation (4), these two effects are weighed relative to one another, not as heat transfer rate versus pumping power (such a comparison would not be appropriate [12]), but as heat transfer irreversibility versus fluid friction irreversibility. It is important to keep in mind that the two

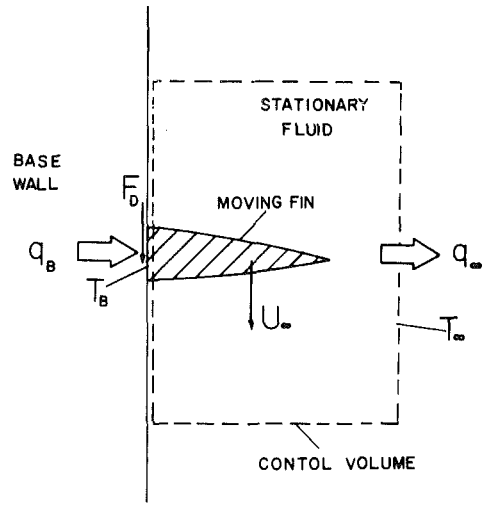

Fig. 1 Schematic of a general fin in a convective heat transfer arrangement

irreversibility contributions, heat transfer and fluid friction (equation (5)), are both relevant only in the case of *forced convection*. This is the case considered in the present paper. In natural convection the designer must be concerned with only the heat transfer part of expression (4): in this case the fluid friction irreversibility is due to the dissipation of work produced not by man, but by the gravity-driven circulation seen as a "heat engine cycle" [14].

An examination of expression (4) leads to the conclusion that in order to minimize the heat transfer contribution to S_{gen} one must minimize the base stream temperature difference, θ_B (note that $(S_{\text{gen}})_{\text{heat transfer}}$ varies monotonically with θ_B). In practical terms, however, to minimize θ_B would imply the use of an infinitely large fin: such a fin would be impractical and thermodynamically undesirable, because an infinitely large fin would have an infinite $(S_{\text{gen}})_{\text{fluid friction}}$, hence, an infinite S_{gen}. We learn that although the fin size influences monotonically the base stream temperature difference, it plays a crucial trade-off role in the thermodynamic performance (S_{gen}).

Nomenclature (cont.)

a = slenderness ratio, L/D, of triangular plate fin (Fig. 2(*d*))
b = breadth of plate fin (Figs. 2(*b*), 2(*c*))
B = fluid friction irreversibility coefficient, equations (11), (19)
B' = fluid friction irreversibility coefficient, equation (25)
B'' = fluid friction irreversibility coefficient, equation (29)
C_D = drag coefficient, equation (12)
C_f = skin friction coefficient, equations (17) and (27)
D = pin diameter (Fig. 2(*a*)), and base width (Fig. 2(*d*))
F_D = drag force
h = heat transfer coefficient
k = thermal conductivity of fluid
L = fin length (Fig. 2)
m = fin conduction parameter, equations (8) and (16)
M = property group, $(k/\lambda)^{1/2}/\text{Pr}^{1/6}$
N_S = entropy generation number, defined in equations (10), (18), (24), and (28)
Nu = Nusselt number
Pr = Prandtl number
q_B = base heat transfer
q_∞ = heat transfer from control volume to remaining fluid (Fig. 1)
R = parameter, equation (26)
Re_j = Reynolds number, jU_∞/ν
S_{gen} = entropy generation rate [W/K]
T_B = absolute temperature of fin base
T_0 = absolute temperature of environment
T_∞ = absolute temperature of free stream
u = parameter, equation (29)
U_∞ = velocity of free stream
v = parameter, equation (20)
W_{lost} = rate of lost available work (exergy, availability), [W]
x = longitudinal coordinate (Fig. 2)
y = transversal coordinate (Fig. 2(*d*))
α = half-angle (Fig. 2(*c*))
γ = slenderness ratio L/D (Fig. 2(*a*)) or L/b (Fig. 2(*b*))
δ = plate thickness (Figs. 2(*b*), 2(*d*))
δ_B = base plate thickness (Fig. 2(*c*))
δ_e = tip plate thickness (Fig. 2(*c*))
θ_B = base-stream temperature difference, $T_B - T_\infty$
λ = thermal conductivity of fin material
μ_e, μ_B = parameters, equation (26)
ν = kinematic viscosity of fluid
ρ = density of fluid

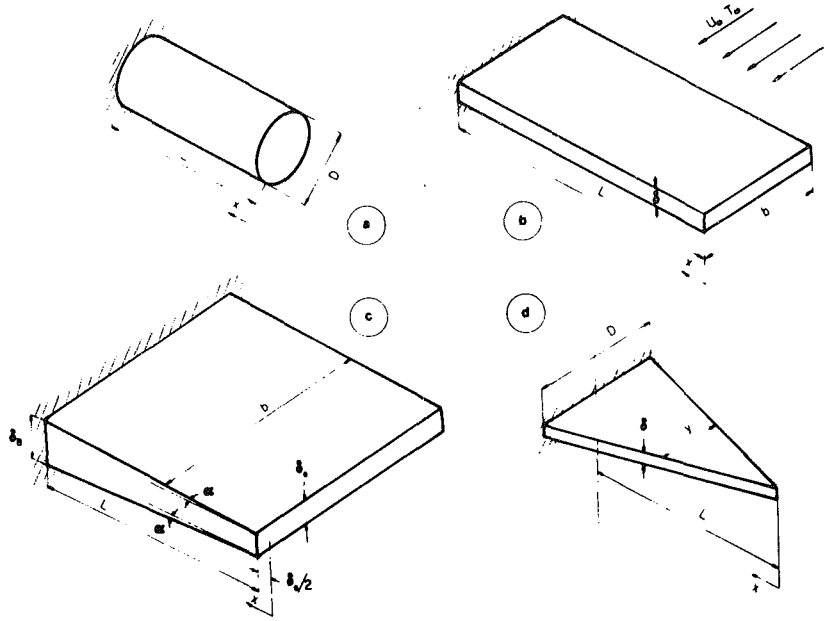

Fig. 2 Four common fin geometries: (*a*) pin fin; (*b*) rectangular plate fin; (*c*) rectangular plate fin of trapezoidal profile; (*d*) triangular plate fin of rectangular profile

In what follows, we examine the fin size trade-off in detail, by minimizing the rate of entropy generation of some of the most common fin geometries encountered in practice. The additional assumption that the temperature difference, θ_B, is small compared with the absolute temperature is made

$$\theta_B << T_\infty \tag{6}$$

This assumption is fully justified in the case of "enhanced thermal contact" applications such as the main counterflow heat exchanger for a helium liquefier, where $\theta_B/T_\infty < 0.1$ [15]. Consequently, the entropy generation expression takes the simpler form

$$S_{\text{gen}} = \frac{q_B \theta_B}{T_\infty{}^2} + \frac{F_D U_\infty}{T_\infty} \tag{7}$$

The size trade-offs presented later in this paper are based on minimizing equation (7) subject to the following constraints:

- constant q_B, T_∞, U_∞
- constant fluid properties

In applications where assumption (6) is not valid, as in the case of steam-to-air heat exchangers, the designer must start with the complete expression, equation (4).

Pin Fins

Consider first the pin fin geometry shown in Fig. 2(*a*). This geometry is one of the simplest, because it depends on only two dimensions: the length, L, and the diameter of the circular cross section, D. According to the unidirectional heat conduction model described in the Introduction, the relationship between base heat flux and base stream temperature difference is [8]

$$\theta_B = \frac{q_B}{\frac{\pi}{4} kD^2 m \tanh(mL)}; m = \left(\frac{4h}{kD}\right)^{1/2} \tag{8}$$

Substituting this expression into equation (7) gives the total entropy generation rate as

$$\frac{S_{\text{gen}}}{} = \frac{q_B{}^2}{\frac{\pi}{2} T_\infty{}^2 (\lambda k)^{1/2} \text{Nu}^{1/2} \text{Re}_D \frac{\nu}{U_\infty} \tanh\left[2\text{Nu}^{1/2}\left(\frac{\lambda}{k}\right)^{1/2} \frac{\text{Re}_L}{\text{Re}_D}\right]} + \frac{\rho \nu^2 U_\infty \text{Re}_L \text{Re}_D C_D}{2T_\infty} \tag{9}$$

where the drag coefficient is $C_D = F_D/(1/2\ \rho\ U_\infty{}^2 DL)$. Since the external flow is assumed known, the Reynolds number is used as dimensionless notation for the two dimensions of the pin fin, $\text{Re}_D = U_\infty D/\nu$, $\text{Re}_L = U_\infty L/\nu$.

In this study, we are adopting the design viewpoint that the "job" of the individual fin is to transfer heat at a specified rate, q_B, from the wall to the known stream, in the least irreversible manner possible (with minimum generation of entropy). Therefore, the *entropy generation number* [16] for this design problem is constructed as

$$N_S = S_{\text{gen}} / \left(\frac{q_B{}^2 U_\infty}{k\ \nu\ T_\infty{}^2}\right) = \frac{(k/\lambda)^{1/2}}{\frac{\pi}{2} \text{Nu}^{1/2} \text{Re}_D \tanh\left[2\text{Nu}^{1/2}\left(\frac{\lambda}{k}\right)^{1/2} \frac{\text{Re}_L}{\text{Re}_D}\right] + \frac{1}{2} BC_D \text{Re}_L \text{Re}_D} \tag{10}$$

where B is a fixed dimensionless parameter that accounts for the importance of fluid friction irreversibility relative to heat transfer irreversibility,

$$B = \rho\ \nu^3 k\ T_\infty / q_B{}^2 \tag{11}$$

Note that parameter B is known as soon as the fluid properties, temperature, and the base heat transfer rate are specified. If the pin fin is slender, the Nusselt number and the drag coefficient can be evaluated from the results developed for a single cylinder in cross flow [17]

$1 < \text{Re}_D < 4$, $\text{Nu} = 0.998\ \text{Re}_D{}^{0.33} \text{Pr}^{1/3}$

$$C_D = 10\ \text{Re}_D{}^{-0.6}$$

$4 < \text{Re}_D < 40$, $\text{Nu} = 0.919\ \text{Re}_D{}^{0.385} \text{Pr}^{1/3}$

$$C_D = 5.484\ \text{Re}_D{}^{-0.246}$$

$40 < \text{Re}_D < 4 \times 10^3$, $\text{Nu} = 0.683\ \text{Re}_D{}^{0.466} \text{Pr}^{1/3}$

$$C_D = 5.484\ \text{Re}_D{}^{-0.246}$$

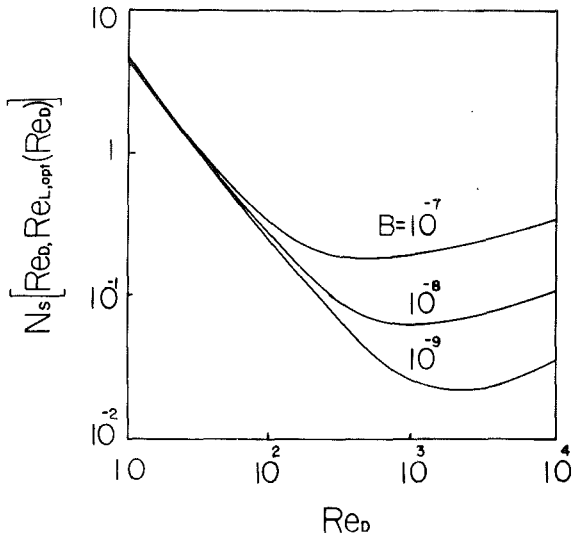

Fig. 3(a) Minimization of entropy generation in a pin fin of optimum length, equation (13) (M = 100)

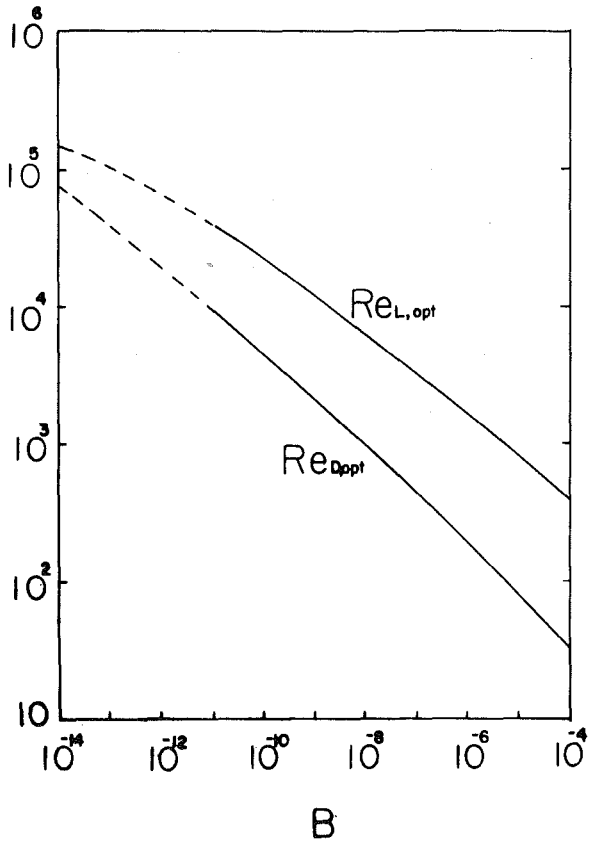

Fig. 3(b) Optimum pin fin diameter and optimum length for absolute minimum irreversibility (M = 100)

$$4\times10^3 < Re_D < 4\times10^4,\ Nu = 0.195\ Re_D^{0.618} Pr^{1/3}$$

$$C_D = 1.1$$

$$4\times10^4 < Re_D < 2\times10^5,\ Nu = 0.0268\ Re_D^{0.805} Pr^{1/3}$$

$$C_D = 1.1 \qquad (12)$$

The entropy generation number, N_S, emerges as a function of five dimensionless groups, two pertaining to fin geometry (Re_L, Re_D), and three accounting for the working fluid and for the fin-stream convective arrangement (Pr, k/λ, B). Minimization of N_S with respect to Re_L is achieved in a straightforward manner by solving $\partial N_S/\partial Re_L = 0$. The optimum pin length calculated in this manner is

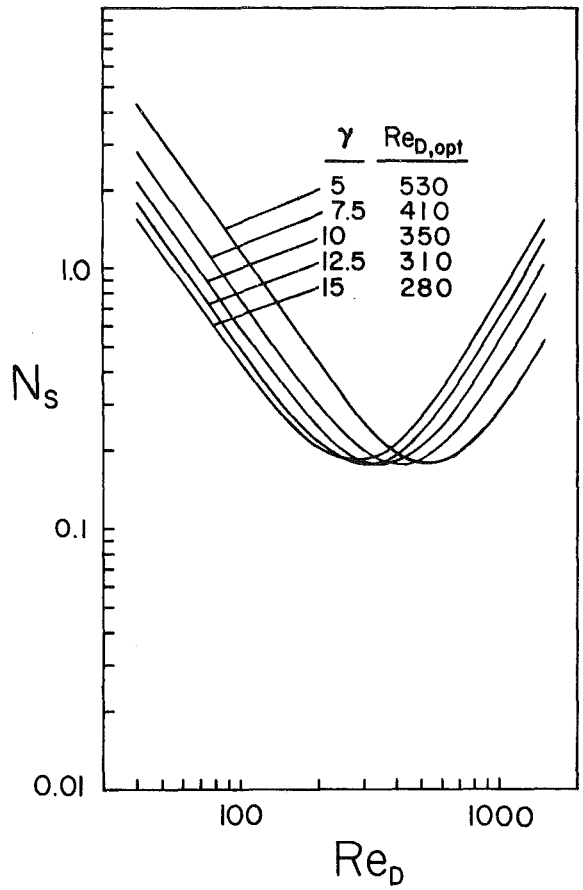

Fig. 4 Thermodynamic optimization of a pin fin subject to fixed slenderness ratio: entropy generation number versus pin diameter ($B = 10^{-7}$, M = 100, range 40 < Re < 4000)

$$Re_{L,opt} = \frac{Re_D}{2Nu^{1/2}} \left(\frac{k}{\lambda}\right)^{1/2} \sinh^{-1}\left[\left(\frac{8}{\pi Re_D{}^3 C_D B}\right)^{1/2}\right] \qquad (13)$$

The engineering significance of result (13) is that the optimum pin length can be calculated immediately, provided Re_D is specified. Substituting equation (13) into equation (10), we obtain the minimum N_S corresponding to optimum pin length, N_S ($Re_{L,opt}$, Re_D). This function was minimized numerically, as shown in Fig. 3(a): the entropy generation number N_S [$Re_{L,opt}$ (Re_D), Re_D] has a clear minimum with respect to pin diameter. Figure 3(b) summarizes our numerical results for optimum pin diameter $Re_{D,opt}$. The same graph shows also the optimum pin length, calculated by substituting $Re_{D,opt}$ into equation (13). The dashed portions of the curves on Fig. 3(b) show the domain in which $L_{opt}/D_{opt} < 5$, i.e., where the "slender pin fin" model [equation (12)] loses its accuracy.

An alternative approach to sizing a pin fin for minimum irreversibility consists of determining the optimum diameter, $Re_{D,opt}$, subject to *fixed slenderness ratio,*

$$\gamma = \frac{L}{D} \qquad (14)$$

This constraint stems from practical limitations encountered in the process of manufacturing a surface covered with a large number of fins. The entropy generation number (10) can be expressed as a function of Re_D and γ,

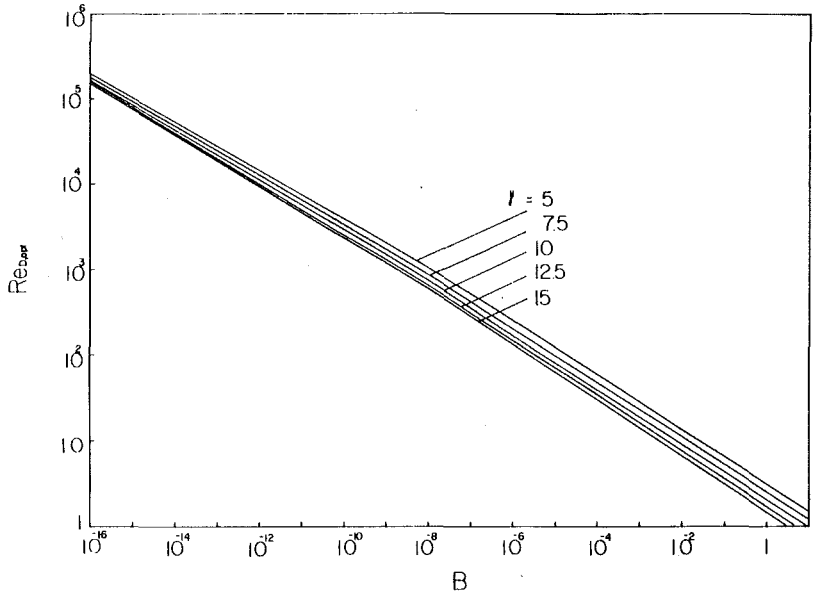

Fig. 5(*a*) Optimum pin diameter versus friction irreversibility parameter $B(M = 100)$

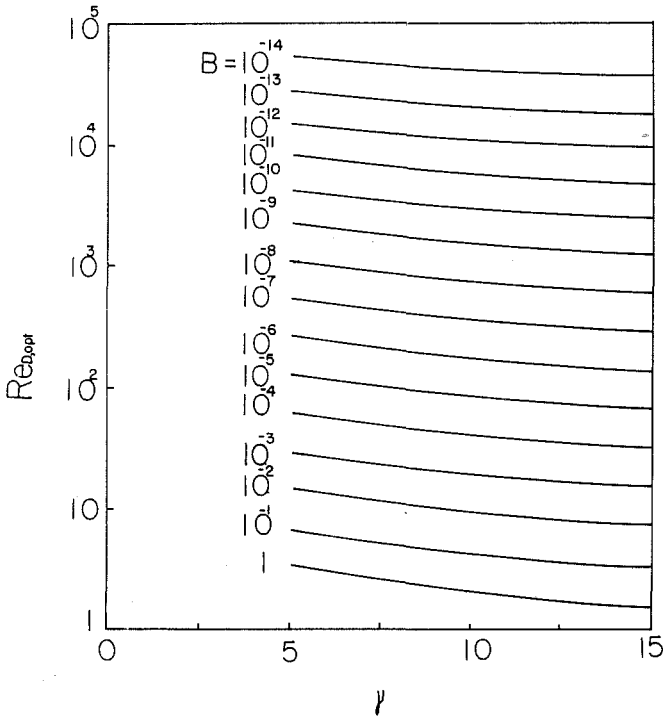

Fig. 5(*b*) Optimum pin diameter versus slenderness ratio ($M = 100$)

$$N_S = \frac{0.77\,M}{\mathrm{Re}_D^{1.23}\tanh\left(\frac{1.65}{M}\mathrm{Re}_D^{0.23}\gamma\right)} + 2.742B\gamma\mathrm{Re}_D^{1.75} \qquad (15)$$

where M is the combined property group $M = (k/\lambda)^{1/2}/\mathrm{Pr}^{1/6}$.

Representative results of the numerical work of minimizing expression (15) are shown in Fig. 4. The entropy generation number, N_S, has a clear minimum with respect to pin diameter, Re_D, when γ, B, and M are fixed. The $N_S - \mathrm{Re}_D$ dependence (Fig. 4) is reported not for design purposes, but to show the designer the "sharpness" of the irreversibility minimum to be achieved through the precise selection of pin diameter.

Figure 4 shows also that the optimum pin diameter, $\mathrm{Re}_{D,\mathrm{opt}}$, increases if the slenderness ratio decreases. This general trend is summarized in Fig. 5(*a*), in the wide range $1 < \mathrm{Re}_D < 10^6$, $10^{-16} < B < 10$ and $5 < \gamma < 15$. When the slenderness ratio is fixed, the optimum pin diameter decreases as B increases (i.e., as the fluid friction irreversibility becomes more important in the irreversibility total, equation (5)). For design purposes, the same information is reported in Fig. 5(*b*) as $\mathrm{Re}_{D,\mathrm{opt}}$ versus γ.

Plate Fins

This section focuses on fin geometries modeled as thin conducting plates parallel to the flow direction. Fins of this type vary widely with respect to the shape and cross section of the surface swept by the flow: in many cases the fin is wide at the base and narrow at the tip, in approximate agreement with Schmidt's principle of material reduction in a fin with fixed heat transfer [3]. Below, we consider the minimum entropy generation design of three frequently used plate fin geometries, illustrated in Figs. 2(*b*), 2(*c*), and 2(*d*).

Rectangular Plate Fin. The simplest plate fin geometry is shown schematically in Fig. 2(*b*). The minimum irreversibility design of this fin requires the selection of three geometric parameters, the length, L, the breadth (length swept by fluid), b, and the plate thickness, δ, where $L >> b >> \delta$. The relationship between heat transfer and base fluid temperature difference is [8]:

$$\theta_B = \frac{q_B}{k\,\delta\,b\,m\tanh(mL)};\; m = \left(\frac{2h}{k\delta}\right)^{1/2} \qquad (16)$$

As in the preceding section, the study is placed in the limit where the plate fin is *slender* ($b << L$); in this limit we rely on laminar heat transfer and skin friction results for two-dimensional flat plates [18]

$$h = 0.664\,\frac{\lambda}{b}\,\mathrm{Re}_b^{1/2}\mathrm{Pr}^{1/3},\; C_f = \frac{F_D}{\rho U_\infty^2 bL} = 1.328\,\mathrm{Re}_b^{-1/2} \qquad (17)$$

Based on equations (16, 17), the entropy generation number for a rectangular plate fin in laminar flow becomes

$$N_S = S_{\mathrm{gen}}/\left(\frac{q_B^2 U_\infty}{k\nu T_\infty^2}\right)$$

$$+\frac{(k/\lambda)^{1/2}}{1.15\,\mathrm{Re}_\delta^{1/2}\mathrm{Re}_b^{3/4}\mathrm{Pr}^{1/6}\tanh(mL)+1.328\,B\,\mathrm{Re}_L\,\mathrm{Re}_b^{1/2}} \quad (18)$$

where

$$B=\rho\,v^3\,k\,T_\infty/q_B{}^2,$$

$$mL=1.15\left(\frac{\lambda}{k}\right)^{1/2}\mathrm{Pr}^{1/6}\mathrm{Re}_L\mathrm{Re}_b{}^{-1/4}\mathrm{Re}_\delta{}^{-1/2} \quad (19)$$

From the outset one notes that the thickness, δ, appears only in the heat transfer term of N_S, equation (18), consequently, Re_δ does not play a trade-off role in the minimization of N_S. Since in most practical applications δ is determined by considerations such as price, availability, and machinability of sheet metal, it makes engineering sense to regard Re_δ as fixed. The minimization of N_S with respect to Re_b and Re_L is achieved by solving the simultaneous set of equations $\partial N_S/\partial\mathrm{Re}_b = 0$ and $\partial N_S/\partial\mathrm{Re}_L = 0$. Eliminating Re_L between these two equations leads to an implicit result of the form

$$v=\left[\frac{\ln[v^{1/2}+(v+1)^{1/2}]}{(1+v)^{1/2}}\right]^{1/2},$$

$$v=(1.328\,B\,\mathrm{Re}_b{}^{3/2}\mathrm{Re}_\delta)^{-1} \quad (20)$$

The numerical solution to equation (20) is $v = 0.7717$. From the system $\partial N_S/\partial\mathrm{Re}_b = 0$ and $\partial N_S/\partial\mathrm{Re}_L = 0$, we conclude that the optimum geometry for minimum entropy generation is explicitly given by

$$\mathrm{Re}_{b,\mathrm{opt}}=0.984B^{-2/3}\mathrm{Re}_\delta{}^{-2/3} \quad (21)$$

$$\mathrm{Re}_{L,\mathrm{opt}}=0.685(k/\lambda)^{1/2}\mathrm{Re}_\delta{}^{1/3}\mathrm{Pr}^{-1/6}B^{-1/6} \quad (22)$$

Dividing equation (22) by equation (21) yields the optimum slenderness ratio of the plate fin

$$\gamma_{\mathrm{opt}}=\left(\frac{L}{b}\right)_{\mathrm{opt}}=0.696\,M\,B^{1/2}\mathrm{Re}_\delta \quad (23)$$

In conclusion, the optimum plate fin dimensions, L and b, can be calculated directly using equations (21) and (22), as soon as the base heat flux (q_B), the flow and the sheet thickness, δ, are known. The optimum length and the optimum breadth both decrease as B increases, in accordance with the trend discovered in the optimization of pin fins (Figs. 3–5). As the plate thickness δ increases, the optimum length increases while the breadth decreases, hence, the optimum slenderness ratio, equation (23), increases.

It is necessary to keep in mind that the formulas (21–23), however convenient, are valid only in the *laminar regime*, $\mathrm{Re}_{b,\mathrm{opt}} < 5 \times 10^5$, and in the *slender shape* limit $\gamma_{\mathrm{opt}} >> 1$. Similar results can be developed numerically for the turbulent regime, by replacing equations (17) with appropriate correlations for turbulent heat transfer and skin friction.

Rectangular Plate Fin of Trapezoidal Profile. A relatively more complex plate fin geometry is represented in Fig. 2(*c*). This time the fin longitudinal section is trapezoidal, again, in the spirit of E. Schmidt's principle of material (volume) minimization [3]. This geometry has another important advantage over the rectangular shape of Fig. 2(*b*): the tapered profile makes trapezoidal fins accessible to metal-cutting operations designed to remove the fin-to-fin material. The minimum entropy generation design of this class of fins can be approached along the same lines as the design of rectangular fins. However, trapezoidal fins have an additional geometric parameter in their constitution, namely, the half-angle, α.

In the interest of brevity, only the key formulas are reported. The entropy generation number can be expressed as

$$N_S=S_{\mathrm{gen}}/\left(\frac{0.614q_B{}^2\left(\frac{k}{\lambda}\right)^{1/2}\mathrm{Re}_b{}^{1/4}}{T_\infty{}^2k\,\mathrm{Pr}^{1/6}}\right)$$

$$=\left[\frac{2\sin\alpha}{\tan\alpha(2\,\mathrm{Re}_L\tan\alpha+\mathrm{Re}_{\delta_e})}\right]^{1/2}$$

$$\left[\frac{I_0(\mu_B)K_1(\mu_e)+I_1(\mu_e)K_1(\mu_B)}{K_1(\mu_e)I_1(\mu_B)-I_1(\mu_e)K_1(\mu_B)}\right]+B'\frac{2\,\mathrm{Re}_L+\mathrm{Re}_{\delta_e}}{2\cos\alpha} \quad (24)$$

where

$$B'=2.164\,\frac{\mathrm{Pr}^{1/6}(k\lambda)^{1/2}\rho\,U_\infty{}^2\nu\,T_\infty}{q_B{}^2\,\mathrm{Re}_b{}^{3/4}} \quad (25)$$

and

$$\mu_e=2R\left[\frac{\delta_e(1-\tan\alpha)}{2\tan\alpha}\right]^{1/2},$$

$$\mu_B=2R\left[\frac{\delta_e(1-\tan\alpha)}{2\tan\alpha}+L+\frac{\delta_e}{2}\right]^{1/2}$$

$$R=\left(\frac{h}{k\sin\alpha}\right)^{1/2} \quad (26)$$

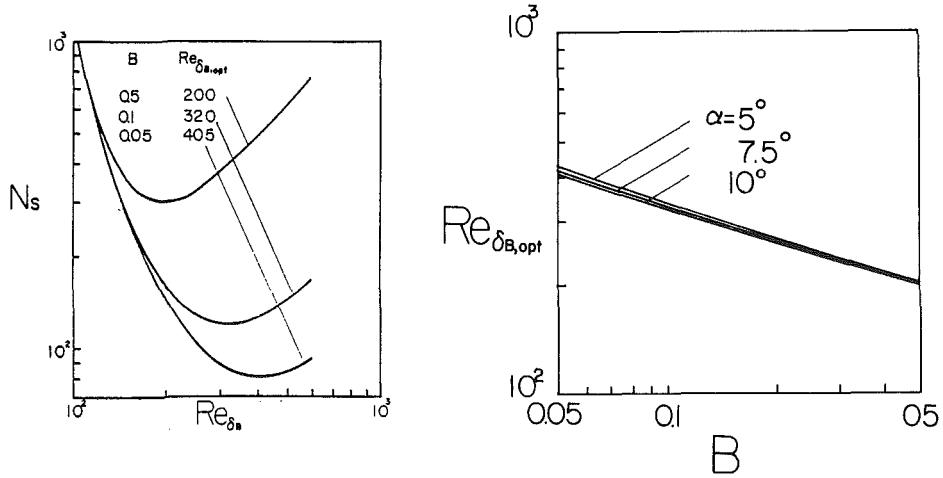

Fig. 6 Thermodynamic optimization of plate fins of trapezoidal profile (α = 10 deg, Re_{δ_e} = 100). Left side: entropy generation number versus geometric aspect ratio. Right side: optimum aspect ratio versus friction irreversibility parameter B'.

As in the preceding example, we have assumed laminar boundary layer flow [18]

$$F_D = C_f \rho U_\infty{}^2 \frac{L + \frac{\delta e}{2}}{\cos \alpha} b, \quad C_f = \frac{1.328}{\mathrm{Re}_b{}^{1/2}},$$

$$h = 0.664 \, \mathrm{Re}_b{}^{1/2} \mathrm{Pr}^{1/3} \frac{\lambda}{b} \tag{27}$$

In addition, the Harper and Brown approximation [8] was employed, whereby the heat transfer from the tip of the fin is taken into account by using the "augmented" fin length $L + \delta_e/2$ in place of L (see Fig. 2(*c*)).

The entropy generation rate (24) depends on four geometric parameters Re_L, Re_b, Re_{δ_e}, and α. Whether or not all four parameters may be considered independent depends on specific circumstances, particularly on the constraints faced by the designer (fixed cost, volume, base area, etc.). In Fig. 6, we show a sample of numerical results obtained in the case when b, δ_e, and α are fixed by design: the only geometric variable in this case is the fin length, L (the dimension perpendicular to the wall). Choosing the optimum Re_L for minimum entropy generation is geometrically equivalent to choosing the optimum base thickness Re_{δ_B} since $\mathrm{Re}_{\delta_B} = \mathrm{Re}_{\delta_e} + 2\,\mathrm{Re}_L \tan \alpha$. The left side of Fig. 6 shows that N_S has a sharp minimum with respect to Re_{δ_B}. The optimum values of base thickness Reynolds number are reported in the right half of Fig. 6 for the case $\mathrm{Re}_{\delta_e} = 100$ in the range 5 deg $\leq \alpha \leq$ 10 deg. We find that the optimum fin size (Re_{δ_B}) decreases as the fluid friction effect (B) becomes more pronounced, in agreement with conclusions reached in previous examples. It is also apparent that in the α range considered, the angle α has a relatively minor impact on the optimum fin size for minimum irreversibility.

Triangular Plate Fin of Rectangular Profile. To the thermodynamic designer, this geometry is challenging due to the absence of convenient correlations for heat transfer and fluid friction in the three-dimensional boundary layer flow which, in most certainty, will cover the triangular faces of the fin. This analytical difficulty can be partially dealt with in the limit $D << L$, where the three-dimensional effects will be minor. In this limit, we can approximately treat the sharp-pointed triangular plate as a flat plate in parallel flow, with the special property that the length swept by the flow (y) is a function of longitudinal position (x). It is worth pointing out that the $D << L$ limit is in full agreement with the unidirectional heat conduction model adopted in the Introduction.

The analytical path leading to the entropy generation rate formula is similar to the method used in the earlier examples. Again, in the interest of brevity, only the key result is reported

$$N_S = S_{\mathrm{gen}} \Big/ \left[\frac{q_B{}^2 U_\infty}{T_\infty{}^2 \nu (k\lambda)^{1/2}} \right]$$

$$= \frac{0.868}{\mathrm{Re}_\delta{}^{1/2} \mathrm{Re}_D{}^{3/4} \mathrm{Pr}^{1/6}} \frac{I_0(u)}{I_1(u)} + 0.885 B'' \, \mathrm{Re}_D{}^{1/2} \mathrm{Re}_L \tag{28}$$

with

$$B'' = \frac{T_\infty \nu^2 (k\lambda)^{1/2} \mu}{q_B{}^2},$$

$$u = 1.536 \left(\frac{\lambda}{k} \right)^{1/2} \mathrm{Pr}^{1/6} \frac{\mathrm{Re}_L}{\mathrm{Re}_D{}^{1/4} \mathrm{Re}_\delta{}^{1/2}} \tag{29}$$

The entropy generation rate depends on three geometric parameters, Re_D, Re_L, and Re_δ. Note that Re_δ does not play a trade-off role, because it appears only in the heat transfer part of expression (28).

Figure 7 presents a sample of optimum fin size results for cases where the triangle aspect ratio $a = L/D$ is fixed. The fin irreversibility, N_S, reaches a clear minimum at a specific value of fin base width, Re_D; the optimum fin size, Re_D, depends on the relative importance of fluid friction irreversibility (B''), on the metal-fluid combination (M), and on the plate thickness (Re_δ). The right-hand side of Fig. 7 is a summary of N_S results obtained for a number of common metal-fluid combinations involving copper, aluminum, water, and air. Regardless of combination, the optimum fin size ($\mathrm{Re}_{D,\mathrm{opt}}$) decreases as the triangular shape of the fin becomes, by design, more slender.

Concluding Remarks

In this paper we have applied the minimization of entropy generation (exergy waste) to the design of extended surfaces. Using the first and second laws of thermodynamics, the entropy generation rate associated with a single fin of unspecified shape and properties was calculated. This general result was then applied to the minimization of irreversibility

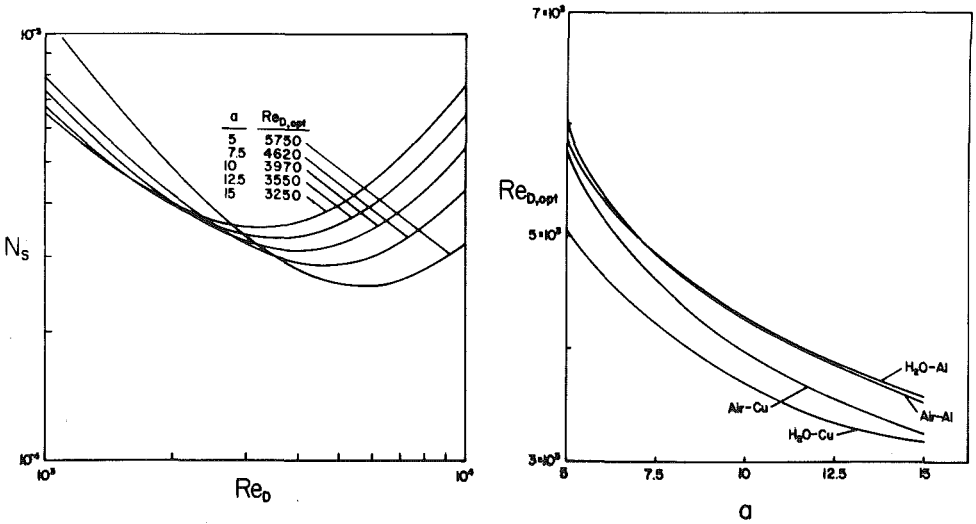

Fig. 7 Thermodynamic optimization of triangular plate fins (Re_δ = 100). Left side: Entropy generation number versus base width (Air-Cu, $B'' = 5 \times 10^{-9}$). Right side: optimum base width versus geometric aspect ratio $a = L/D$. (Air-Cu $B'' = 5 \times 10^{-9}$, Air-Al $B'' = 4 \times 10^{-9}$, H_2O-Cu $B'' = 3.5 \times 10^{-9}$, H_2O-Al $B'' = 2.5 \times 10^{-9}$).

in four of the most frequently used fin shapes. The conclusions of our irreversibility minimization procedure have been reported in analytical or graphical form.

In the analysis of the individual fin we have assumed that the heat transfer rate and the fluid flow parameters are prescribed. This decision is necessary in order to isolate (remove) the fin from the aggregate system (the heat exchanger). It is important to note that heat exchangers, too, are isolated from their respective aggregate systems (power plants) for the purpose of analytical optimization. The decision to isolate a component from the aggregate system leads, necessarily, to the adoption of design constraints around the component. For example, in the design of a heat exchanger we use the notions of "required heat transfer" and "fixed pressure drop;" in the thermodynamic optimization of the fin we have regarded q_B and the flow as fixed. The alternative to optimizing the heat exchanger component-by-component, as in this paper, would be to minimize the irreversibility of the heat exchanger, as a whole. However, this alternative is neither practical nor of fundamental value in view of the diversity of heat exchangers and the large number of geometric features which would have to be optimized simultaneously.

The chief conclusion of this study is that the size of individual fins can be chosen in a way that combines a specified heat transfer function with a desired (optimum) thermodynamic function, namely, the function of conserving exergy. It was also shown that the thermodynamic-optimum fin dimensions can be subjected to additional design constraints, such as the fixed slenderness ratio for pin fins, equation (14). Built into all the analytical and graphic results is the message that the thermodynamic optimization of fins requires a detailed knowledge of the fin-fluid flow interaction. As a first step, we accounted for this interaction by using well-known correlations developed for two-dimensional external flow arrangements. It is felt, however, that much remains to be done experimentally with the objective of documenting the *local* heat transfer and drag characteristics for fins of various shapes bathed by flows of various directions.

As a final comment, we would like to address the issue of thermodynamic optimization versus economic optimization (cost minimization). The former has been the subject of this paper, as applied to the sizing of individual fins engaged in convective heat transfer. The latter is, of course, the philosophy of those who are competitive in the industrial world. The two design philosophies, thermodynamic versus economic, do not necessarily lead to identical fin-sizing decisions. This is due to the fact that the total cost formula for a certain piece of heat exchange equipment contains many items in addition to the cost of lost available work (exergy). However, as the cost of fuel ("bottled exergy") continues to rise and dominate the total cost figure of equipment for power and refrigeration, the thermodynamic optimization philosophy leads to designs which come closer and closer to those demanded by the cost minimization formula. Witness in this regard the development of heat transfer technology for helium refrigeration and large scale superconducting systems, where "good design" has become practically synonymous with "least irreversible design" [19].

It is important to recognize the fundamental value of the exergy-conservation design philosophy relative to the local and temporal character of the economic optimizaton procedure followed by individuals in industry. The *conservation of exergy* is clearly what the heat transfer community must learn first and teach others through its technical journals, if we are to agree on a reasonable course toward fuel-sufficiency in this world [20].

Acknowledgment

This work was sponsored by the Office of Naval Research, The Power Program.

References

1 Bergles, A. E., Webb, R. L., Junkhan, G. H., and Jensen, M. K., "Bibliography on Augmentation of Convective Heat and Mass Transfer," Report HTL-19, ISU-ERI-AMES-79206, Iowa State University, May 1979.

2 Junkhan, G. H., Bergles, A. E., and Webb, R. L., "Research Workshop on Energy Conservation Through Enhanced Heat Transfer," Report HTL-21, ISU-ERI-AMES-80063, Iowa State University, Oct. 1979.

3 Schmidt, E., "Die Wärmeubertragung durch Rippen," *Zeit. d. ver Deutch Ing.*, Vol. 70, 1926, pp. 885–889, and 947–951.

4 Duffin, R. J., "A Variational Problem Relating to Cooling Fins," *Journal of Mathematics and Mechanics*, Vol. 8, 1959, pp. 47–56.

5 Maday, C. J., "The Minimum Weight One-Dimensional Straight Fin," ASME *Journal of Engineering for Industry*, Vol. 96, 1974, pp. 161–165.

6 Guceri, S., and Maday, C. J., "A Least Weight Circular Cooling Fin," ASME *Journal of Engineering for Industry*, Vol. 97, 1975, pp. 1190–1193.

7 Razelos, P., and Imre, K., "The Optimum Dimensions of Circular Fins with Variable Thermal Parameters," ASME JOURNAL OF HEAT TRANSFER, Vol. 102, 1980, pp. 420–425.

8 Kern, D. Q., and Kraus, A. D., *Extended Surface Heat Transfer*, McGraw-Hill, New York, 1972.

9 Kraus, A. D., and Snider, A. D., "New Parametrizations for Heat Transfer in Fins and Spines," ASME JOURNAL OF HEAT TRANSFER, Vol. 102, 1980, pp. 415–419.

10 Szargut, J., "International Progress in Second Law Analysis," *Energy*, Vol. 5, 1980, pp. 709–718.

11 Kestin, J., "Availability: The Concept and Associated Terminology," *Energy*, Vol. 5, 1980, pp. 679–692.

12 Bejan, A., Discussion of a previously published paper, ASME JOURNAL OF HEAT TRANSFER, Vol. 102, 1980, pp. 586, 587.

13 Gardner, K. A., "Efficiency of Extended Surfaces," *Transactions of the ASME*, Vol. 67, 1945, pp. 621–631.

14 Tritton, D. J., *Physical Fluid Dynamics*, Van Nostrand Reinhold, New York, 1980, p. 141.

15 Collins, S. C., "Liquefaction Techniques," Ch. 3 in *Technology of Liquid Helium*, edited by R. H. Kropschot, B. W. Birmingham and D. B. Mann, NBS Monograph 111, Oct. 1968.

16 Bejan, A., "General Criterion for Rating Heat Exchanger Performance," *International Journal of Heat and Mass Transfer*, Vol. 21, 1978, pp. 655–665.

17 Gebhart, B., *Heat Transfer*, McGraw-Hill, New York, 1971, pp. 212–214, 270.

18 Gebhart, B., *op. cit.*, pp. 198, 243.

19 Hubbell, R. H., and Toscano, W. M., "Thermodynamic Optimization of Helium Liquefaction Cycles," *Advances in Cryogenic Engineering*, Vol. 25, 1980, pp. 551–562.

20 Cambel, A. B., "Preface," Second Law Analysis of Energy Devices and Processes, *Energy*, Vol. 5, 1980, pp. III, IV.

Numerical Simulation of Natural Convection in Concentric and Eccentric Horizontal Cylindrical Annuli

C. H. Cho
Graduate student,
Department of Mechanical Engineering.

K. S. Chang
Assoc. Mem. ASME
Associate Professor,
Department of Aeronautical Engineering.

K. H. Park[1]
Korea Advanced Institute
of Science and Technology,
Seoul, Korea

Natural convection heat transfer in concentric and eccentric annuli made of two isothermal horizontal circular cylinders is numerically investigated for Rayleigh numbers less than 5.0×10^4 which is based on the difference of radii. Bipolar coordinates are used for eccentric annuli, and it is found that for very small eccentricity the overall thermal behavior of the annuli exhibits that of the exactly concentric cylinders. The maximum deviation of the local heat-transfer coefficient of the cylinder walls remains, for example, for $\epsilon=0.01$, $R_i/R_0=0.3846$ and $Ra_L=1.0 \times 10^4$, within a meager 5 percent. The parametric effect on the heat-transfer characteristics is discussed with respect to the diameter ratio for concentric cylinders, and eccentricity and azimuthal angular location of the inner cylinder for eccentric annuli. Output is displayed in terms of streamlines, isothermal contours, radial temperature distribution and equivalent thermal conductivities. Convection patterns are explained in detail.

Introduction

Natural convection heat transfer in horizontal enclosures of concentric and eccentric cylindrical annular form has received increased attention due to the interesting feature of the specific heat transport phenomenon and the fundamental importance in practical applications. A very thorough literature survey and comprehensive analysis has been made on the concentric annuli by Kuehn and Goldstein [1, 2]. They have conducted both numerical simulation using finite difference method of relaxation type, and experimental study using Mach-Zehnder interferometer. Application of other type of finite difference method, alternating-direction implicit method, has also been reported by Charrier-Mojtabi et al. [3] in solving the laminar horizontal concentric annuli problem formulated in cylindrical polar coordinates. Recently, flow analysis on concentric annulus has been extended to turbulent natural convection regime, Rayleigh number range $10^6 - 10^7$, using a two-equation turbulence model [4].

For slightly eccentric annular enclosure, Yao [5, 6] has perturbed the solution of concentric annuli to obtain expansion in terms of the double series of eccentricity and Rayleigh number for the case when Ra is small. Experiments have also been conducted using pressure-controlled gas chamber to analyze heat-transfer characteristics in eccentric annuli with relatively large eccentricity [7-9]. Parametric effect on the heat transfer was investigated in these reports for the natural convection which included the unsteady flow regime. Theoretical study, on the other hand, is rare for the eccentric annuli. In reference [9], as a complimentary work of the experimental investigation, the Galerkin finite element method has been applied with isoparametric element to find the conditions for minimum heat loss in annular solar energy receiver geometries.

To treat consistently the concentric and eccentric annuli, two different coordinate systems have been used in the literature. One is the modified bipolar coordinates [12, 14] which degenerate to polar coordinates when the annuli are concentric. The other is the radial coordinate transformation used by Yao [5, 6], which normalizes the distance from the axis of the inner cylinder to the outer cylinder. None of them has singularity at zero eccentricity. However, applications so far have been limited to small eccentricity only.

In the present paper, to extend the existing knowledge on the natural convection heat transfer in the horizonal cylindrical annuli, numerical analysis has been made using finite difference method based on successive-overrelaxation iteration. Concentric and eccentric annuli are treated in a unified manner using the cylindrical bipolar coordinate system. Emphasis is put on the study of changing thermal behavior of the annuli with respect to the diameter ratio of the inner and outer cylinders, eccentricity, and azimuthal angular location of the inner cylinder. Prandtl number is fixed with that of air, 0.706, throughout the study while Rayleigh number is changed to several selected values within the laminar natural convection regime known by the previous experimental study [7].

Derivation of Governing Equations

In the literature, the bipolar coordinate system has been conveniently applied to solve many engineering problems involving tandem spheres or circular cylinders, and eccentric annuli in forced flow [10, 11, 13]. For the natural convection the Boussinesq approximation simplifies the Navier-Stokes equations by neglecting the compressibility effect everywhere except for the buoyancy force terms. Regions of validity of this approximation is presented in [15]. Assuming constant transport properties, one can write respectively the governing equations of the dimensionless stream function, vorticity, and temperature in the cylindrical bipolar coordinate system (ξ,η) as follows:

$$\nabla^2\psi = -\zeta \tag{1}$$

$$\nabla^2\zeta = \frac{1}{\mathrm{Pr}}\left\{\frac{1}{h}\left(U\frac{\partial\zeta}{\partial\xi}+V\frac{\partial\zeta}{\partial\eta}\right)\right\}+$$

$$+\mathrm{Ra}_L\left\{-\left(\sin\theta\frac{\sinh\eta\sin\xi}{a}+\cos\theta\frac{\cosh\eta\cos\xi-1}{a}\right)\frac{\partial\phi}{\partial\xi}\right.$$

[1]Present address: Graduate School, E.N.S.M.A., Poitiers, France

Contributed by the Heat Transfer Division for publication in the JOURNAL OF HEAT TRANSFER. Manuscript received by the Heat Transfer Division November 2, 1981.

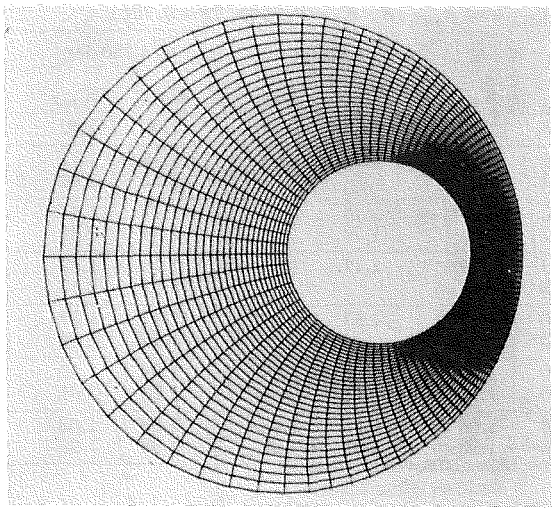

Fig. 1 An example of mesh system in bipolar coordinates

$$-\left(\sin\theta\frac{\cosh\eta\cos\xi-1}{a}-\cos\theta\frac{\sinh\eta\sin\xi}{a}\right)\frac{\partial\phi}{\partial\eta}\Bigg\} \tag{2}$$

$$\nabla^2\phi=\frac{1}{h}\left(U\frac{\partial\phi}{\partial\xi}+V\frac{\partial\phi}{\partial\eta}\right) \tag{3}$$

where

$$\nabla^2=\frac{1}{h^2}\left(\frac{\partial^2}{\partial\xi^2}+\frac{\partial^2}{\partial\eta^2}\right) \tag{4}$$

$$h=\frac{a}{\cosh\eta-\cos\xi} \tag{5}$$

$$U=\frac{1}{h}\frac{\partial\psi}{\partial\eta}\quad\text{and}\quad V=-\frac{1}{h}\frac{\partial\psi}{\partial\xi} \tag{6}$$

The boundary conditions can be written in two different ways depending on the flow domain.

Symmetric twin convective flows:

$$\psi = \zeta=U=0,\frac{\partial V}{\partial\xi}=0,\frac{\partial\phi}{\partial\xi}=0 \text{ on } \xi=0 \text{ and } \xi=\pi\text{(symmetry line)}$$

$$\psi = U=V=0,\phi=1 \text{ on } \eta=\eta_i\text{(inner cylinder)} \tag{7}$$
$$\psi = U=V=0,\phi=0 \text{ on } \eta=\eta_0\text{(outer cylinder)}$$

Nonsymmetric global annular flows:

$$\psi_0 = \psi_{2\pi},\zeta_0=\zeta_{2\pi},\phi_0=\phi_{2\pi} \text{ on } \xi=0 \text{ or } \xi=2\pi \text{ (branch cut)}$$
$$\psi = U=V=0,\phi=1 \text{ on } \eta=\eta_i\text{(inner cylinder)} \tag{8}$$
$$\psi = U=V=0,\phi=0 \text{ on } \eta=\eta_0\text{(outer cylinder)}$$

Of course, the second set of boundary conditions, which includes the periodic condition at branch cut $\xi=0$ or $\xi=2\pi$, could be used for the symmetric flow too, but only with the solution domain doubled unnecessarily. The vorticity function on the solid wall is successively evaluated to second-order accuracy by using the values of stream function in previous iteration, following the usual tested formula [16]:

$$\zeta_w^{k+1}=\frac{1}{h^2}\cdot\frac{7\psi_w^k-8\psi_{w+1}^k+\psi_{w+2}^k}{2(\Delta\eta)^2}+0(\Delta\eta^2)$$

for the outer cylinder, and

$$\zeta_w^{k+1}=\frac{1}{h^2}\cdot\frac{7\psi_w^k-8\psi_{w-1}^k+\psi_{w-2}^k}{2(\Delta\eta)^2}+0(\Delta\eta^2)$$

for the inner cylinder.

Computational Procedure

One of the mesh systems possible in the bipolar coordinate system is shown in Fig. 1, where the radial-like curves represent constant angles in angular ξ-coordinate, and the eccentric circles stand for η-constant lines. By changing the size and radial location of the inner circle and by rotating the whole system with respect to the direction of gravity force, variation in diameter ratio of the two circles, eccentricity, and azimuthal position of the inner cylinder were easily obtained.

The partial differential equations were finite-differenced using central difference schemes for all of the derivatives. Since diffusion plays as important a role as convection for transport of thermal energy in the present problem, central difference approximation was favored for the convection terms to avoid parasitic effect which might be introduced if the upwind scheme had been used. The resultant difference equations were put in the form convenient for iteration in the successive overrelaxation method. The relaxation factors used were, 1.35, 1.2, and 0.5 for ϕ,ψ, and ζ, respectively, for

Nomenclature

a = a constant in the bipolar coordinate system, equal to half of the distance between two poles
c = distance between centers of circular cylinders in eccentric annuli
g = gravitational acceleration
h = metric coefficient, defined in equation (5)
x,y = rectangular Cartesian coordinates
K_ϵ = specific conductivity, the pure-conduction heat transfer for an eccentric annulus divided by that of an equivalent concentric annulus
$K_{eq,c}$ = local equivalent thermal conductivity for concentric cylinders
$\bar{K}_{eq,\epsilon}$ = the first overall equivalent thermal conductivity, the overall natural convection heat transfer scaled by the pure-conduction heat transfer possible for the same geometry
$\bar{K}_{eq,c}$ = $\bar{K}_{eq,\epsilon}\times K_\epsilon$, the second overall equivalent thermal conductivity, based on the pure-conduction heat transfer of an equivalent concentric annulus
L = $R_0 - R_i$, radius difference of the two cylinders
Pr = Prandtl number, ν/α
R = radial coordinate measured from the center for the concentric annuli
R_i/R_0 = radii of the inner and outer circular cylinders
Ra_L = $g\beta L^3(T_i-T_0)/\nu\alpha$, Rayleigh number based on reference length, L
T_i,T_0 = constant temperatures of the inner and outer cylinders, respectively
U,V = contravariant velocity components in ξ- and η-direction
ϵ = c/L, eccentricity
ν = kinematic viscosity
α = thermal diffusivity
ξ,η = Bipolar coordinates defined by $x+iy=ia\cot 1/2(\eta+i\xi)$
θ = angle between x-direction and the gravity force $\mathbf{g}$
θ_p = the azimuthal angle of the inner eccentric cylinder
ψ = dimensionless stream function, scaled by α
ζ = dimensionless vorticity function, scaled by α/L^2
ϕ = $(T-T_0)/(T_i-T_0)$, dimensionless temperature

Table 1 The overall equivalent thermal conductivity $\bar{K}_{eq,\epsilon}$ and $\bar{K}_{eq,c}$ ($R_i/R_0 = 0.3846$, Pr = 0.706)

Eccentricity ϵ	Specific conductivity K_ϵ	$\theta_p = 0$ deg		$\theta_p = 45$ deg		$\theta_p = 90$ deg		$\theta_p = 135$ or 225		$\theta_p = 180$ deg		Ra_L
		$\bar{K}_{eq,\epsilon}$	$\bar{K}_{eq,c}$	$\bar{K}_{eq,\epsilon}$	$\bar{K}_{eq,c}$	$\bar{K}_{eq,\epsilon}$	$\bar{K}_{eq,c}$	$\bar{K}_{eq,\epsilon}$	$\bar{K}_{eq,c}$	$\bar{K}_{eq,\epsilon}$	$\bar{K}_{eq,c}$	
0.900	2.226	1.04	2.32	1.05	2.34	1.08	2.40	1.09	2.43	1.08	2.40	10^3
0.750	1.482	1.06	1.57	1.07	1.59	1.11	1.65	1.14	1.69	1.16	1.72	10^3
		1.37	2.03	-	-	1.47	2.18	-	-	1.62	2.40	10^4
0.623	1.260	1.07	1.35	1.08	1.36	1.12	1.41	1.16	1.46	1.17	1.47	10^3
		1.45	1.83	1.48	1.86	1.57	1.98	1.70	2.14	1.75	2.21	10^4
0.500	1.144	1.08	1.24	1.08	1.24	1.13	1.29	1.17	1.34	1.18	1.32	10^3
		1.55	1.77	-	-	1.69	1.93	-	-	1.85	2.12	10^4
0.250	1.031	1.08	1.11	1.08	1.11	1.10	1.13	1.37	1.17	1.17	1.17	10^3
		1.79	1.85	-	-	1.90	1.96	-	-	1.99	2.05	10^4
0.100	1.005	1.08	1.09	1.08	1.09	1.09	1.10	1.08	1.09	1.09	1.10	10^3
		1.93	1.94	-	-	1.96	1.97	-	-	2.00	2.01	10^4
0.010	1.000	1.08	1.08	1.08	1.08	1.08	1.08	1.08	1.08	1.08	1.08	10^3
		1.98	1.98	1.98	1.98	1.98	1.98	1.98	1.98	1.98	1.98	10^4

Rayleigh numbers of the order of 10^4; they were increased to higher values for lower Rayleigh numbers. Uniform meshes in ξ- and η- direction have been used in the computation, with increased number of grid points assigned for higher Rayleigh numbers. The method became unstable when the diagonal dominancy of the locally linearized coefficient matrix of the finite difference equations was broken. For the cases when the diameter ratio of the inner and outer cylinders was very small, when the eccentricity was near its extremum 1 and when Ra_L was increased to a large value which was beyond the experimentally known laminar flow regime, the solution diverged. Also, for zero eccentricity the method failed because of the coordinate singularity. However, for very small values of eccentricity, for example, at $\epsilon = 0.01$, the overall thermal behavior of the annulus has exhibited that of the exactly concentric cylinders, with maximum deviation of the local heat-transfer coefficient on the cylinder walls remaining within a meager 5 percent. This observation has made it possible to extrapolate with confidence the heat-transfer characteristics of the concentric annuli from the results obtained in the bipolar coordinate system for small eccentricity.

During the computation, because of the slow rate of convergence for the stream function and vorticity compared with that of temperature function, iteration was performed in a weighted cyclic pattern as ψ-ζ-ψ-ζ-ϕ. The convergence criteria needed for termination of the computation were preassigned as

$$\|\psi\|_2 < 10^{-3}, \|\phi\|_2 < 10^{-3} \text{ and } \|\zeta\|_2 < 10^{-2}$$

The output has been displayed in terms of isotherms, streamlines, radial temperature distribution, and equivalent thermal conductivities. The last variable in the above is defined as the overall heat transfer scaled by the pure-conduction heat transfer that would be obtained either for the specific eccentric annulus or for an equivalent concentric annulus. Different notations are reserved for the above two equivalent conductivities: the former denoted by $\bar{K}_{eq,\epsilon}$ and the latter by $\bar{K}_{eq,c}$. The former is an indicator of relative importance of convection over conduction in the given eccentric annulus, while the latter could be used for direct comparison of performance among various annuli of different eccentricity. The two variables are interconvertible by making a table of a third variable namely the specific conductivity, K_ϵ, which refers to the ratio of pure-conduction heat transfer of an eccentric annulus and that of an equivalent concentric annulus. It is readily obtained, since for pure conduction exact temperature solution is known and the isotherms are identical with the coordinate lines η = constant. The above three conductivities K_ϵ, $K_{eq,\epsilon}$ and $K_{eq,c}$ are calculated and listed in Table 1 for seven different values of eccentricity and

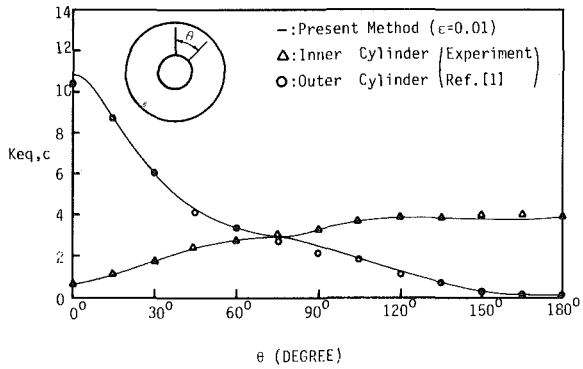

Fig. 2 Local heat-transfer coefficient for a concentric annulus: $Ra_L = 5 \times 10^4$, $R_i/R_0 = 0.3846$

for two different Rayleigh numbers, $Ra_L = 1.0 \times 10^3$ and 1.0×10^4.

The computer used for calculation was Cyber-174 at the computer center in KAIST. CPU time needed for individual calculation depended greatly on the accuracy of the initial guess for the solution. For 24 × 30 mesh points, time needed for $Ra_L = 4.8 \times 10^4$ was slightly less than half an hour in CPU time, when the data converged at $Ra = 1.0 \times 10^4$ were used as initial input. The CPU time increased, in general, with higher Rayleigh numbers and with higher upper eccentricities.

Results and Discussion

To demonstrate that the bipolar coordinate system can be used to produce reliable result for the concentric annulus, a test run was made for $Ra_L = 5 \times 10^4$ and $R_i/R_0 = 0.3846$ by using a very small eccentricity $\epsilon = 0.01$. The calculated local equivalent thermal conductivity is shown in Fig. 2 in comparison with the experimental data drawn from reference [1]. The agreement is excellent for both outer and inner cylinders, the maximum local discrepancy which occurs at the top of the outer cylinder being less than 5 percent, as stated in the previous section.

In Figs. 3(*a*)-3(*c*), the isotherms are presented for a high Rayleigh number flow, $Ra_L = 4.8 \times 10^4$, Pr = 0.706, along with the interferogram analogs available from [7] for comparison. In these plots the diameter ratio is taken uniform as $R_i/R_0 = 0.3846$ but the eccentricity is varied to three distinct values of $\epsilon = 0.652$ upper, $\epsilon = 0.01$ and $\epsilon = 0.623$ lower, respectively. Each closed curve in the plots on the left hand side represents an isothermal line with step temperature increment by the amount $\Delta\phi = 0.05$ toward the inner cylinder. The overall qualitative agreement is again very distinguished. It is readily observable which part of the inner or outer

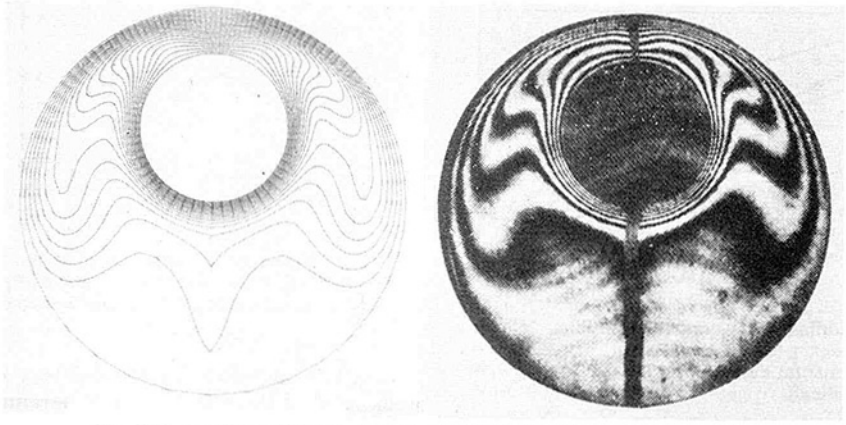

Fig. 3(*a*) Isothermal lines for an eccentric annulus: left, present method ($\Delta\phi = 0.05$); right, from [6], ($Ra_L = 4.8 \times 10^4$, $R_i/R_0 = 0.3846$, $\epsilon = 0.652$ upper vertical)

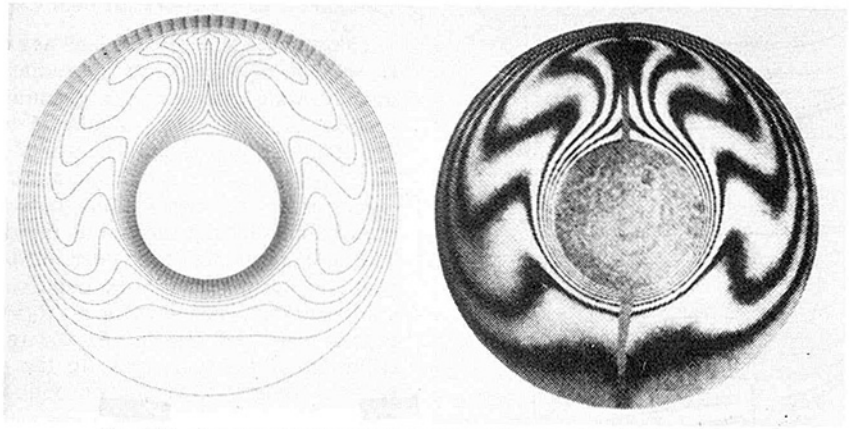

Fig. 3(*b*) Isothermal lines for an concentric annulus: left, present method ($\Delta\phi = 0.05$), $\epsilon = 0.01$); right, from [6], ($Ra_L = 4.8 \times 10^4$, $R_i/R_0 = 0.3846$

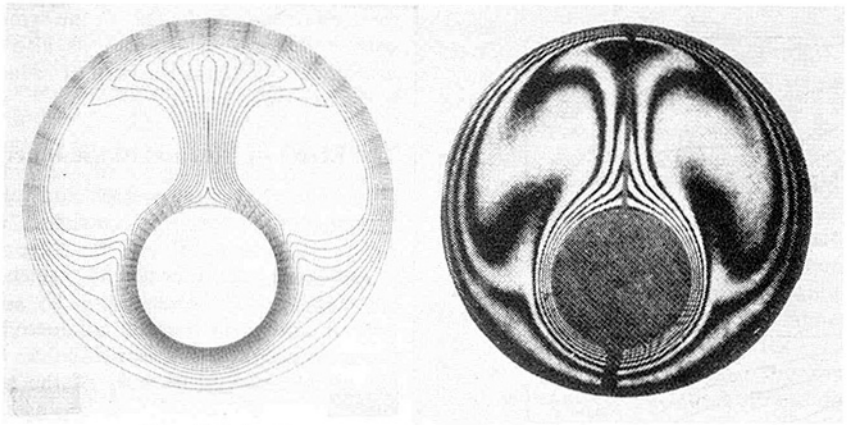

Fig. 3(*c*) Isothermal lines for an eccentric annulus: left, present method ($\Delta\phi = 0.05$); right, from [6], ($Ra_L = 4.8 \times 10^4$, $R_i/R_0 = 0.3846$, $\epsilon = 0.623$ lower vertical)

cylinder has high heat-transfer coefficient, simply by locating those regions where the thermal boundary layer is well-developed from the given temperature contours. In Fig. 3(*a*), where $\epsilon = 0.652$, the upper eccentricity of the inner cylinder has caused a relatively narrow gap near the top of the annular enclosure in which no evidence of plume development is found above the heated inner cylinder. Instead, near the top of the vertical line of symmetry in the narrow gap, a local region of conduction-dominated heat transfer is produced, a phenomenon which is usually found at the bottom portion of the annulus where the flow is inert and stably stratified. Also, it reduces relative contribution of convection, thus the overall heat-transfer coefficient $\bar{K}_{eq,\epsilon}$ for the annulus of high eccentricity is lowered. Such an observation is quantitatively supported by the radial temperature distribution shown in Fig. 4, where along the radial line $\theta = 0$ deg the temperature curve is a nearly-straight line of negative unit slope. It is interesting to note here that the calculated results in Fig. 4 suggest slightly higher conduction effect than the measured in this particular region. Near the bottom of the annulus around $\theta = 150$ and 180 deg, better resolution is observed in the theory than in the experiment. In the bottom portion, the temperature curves are straight outward beginning from $(R - R_i)/(R_0 - R_i) = 0.2$, revealing dominance of conduction outside of the boundary layer, again. In contrast to the annulus of upper large eccentricity, Figs. 3(*b*) and 3(*c*) exhibit

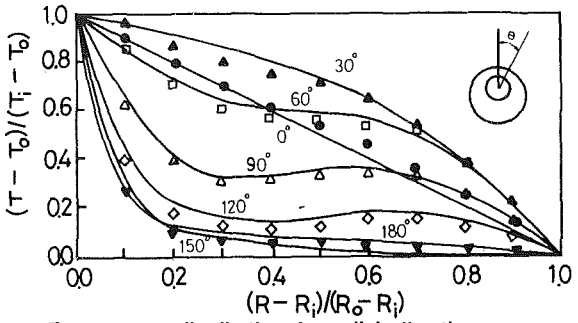

Fig. 4 Temperature distribution in radial directions: __ present method; •(0 deg), ▲(30 deg), □(60 deg), △(90 deg), ◇(120 deg), ▽(150 and 180 deg) from experimental data [6] ($Ra_L = 4.8 \times 10^4$, $R_i/R_0 = 0.3846$, $\epsilon = 0.652$ upper vertical)

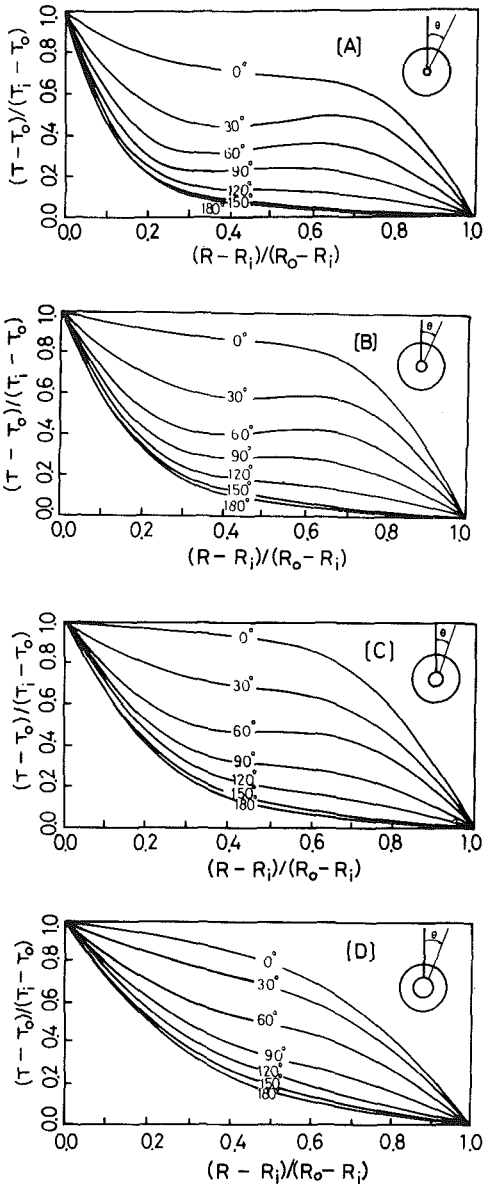

Fig. 5 Radial temperature distribution for concentric annuli: R_i/R_0 = 0.2(A), 0.4(B), 0.6(C), and 0.8(D); $Ra_L = 1.0 \times 10^4$

well-defined plumes that are shed from the inner cylinder and impinge on the top of the outer cylinder. The thermal boundary layers are well developed along the entire surface of the inner cylinder, and along much of the outer cylinder excluding the part of surface submerged in the inert fluid layer at the bottom. For the case of lower eccentricity (Fig. 3(*c*)),

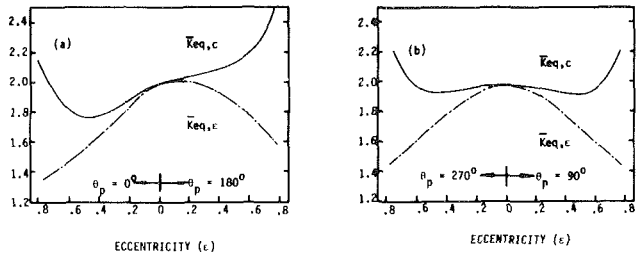

Fig. 6 Eccentricity dependence of the overall equivalent thermal conductivities: $Ra_L = 1.0 \times 10^4$ and $R_i/R_0 = 0.3846$, (*a*) along the line of symmetry, (*b*) along the centered horizontal line

the plume development is noted very salient. Attention is now directed to the effect of some parametric variables for lower Rayleigh number flows which is not much discussed in the literature.

The Effect of Radius Ratio for Concentric Cylinders

Taking fixed parameter values as $\epsilon = 0.01$, $Ra_L = 1.0 \times 10^4$, $Pr = 0.706$, a variation in the radius ratio of the inner and outer cylinder was made to examine its effect on the convection heat transfer. Figure 5 represents temperature distribution along radial lines for $R_i/R_0 = 0.2$, 0.4, 0.6, and 0.8. The four different temperature plots A, B, C, and D demonstrate that temperature curves and their slope have reduced angular dependence as the radius ratio is increased. The temperature inversion phenomenon, that is the fluid layer near the warmer surface becomes cooler than that near the colder surface, is distinct for $R_i/R_0 = 0.2$ and 0.4, but not for higher values of R_i/R_o. As the radius ratio grows, contribution of the convection to the overall heat transfer is reduced contrary to the role of conduction, the curves for high radius ratio being in tendency for gathering around the pure-conduction diagonal line of negative unit slope. Another observation was made from the calculated streamline contours, not shown here, that the centers of the twin vortices are lowered to the middle half in the symmetric annular passages with higher radius ratio. It is also directly related to the aforementioned phenomenon of reduced angular dependence in the narrowed annuli.

The Effect of Position of the Inner Eccentric Cylinder

In Table 1, the overall equivalent conductivities are presented for various eccentricities with fixed aspect ratio $R_i/R_0 = 0.3846$ and $Pr = 0.706$. Pure conduction heat transfer is increased with eccentricity, which is revealed by the increasing specific conductivity K_ϵ as a function of ϵ. The overall equivalent thermal conductivity $\bar{K}_{eq,\epsilon}$ is decreased as the eccentricity grows when $\epsilon > 0.5$, which is true in general for all angular position θ_p of the eccentric inner cylinder. Interpretation is as follows: because of the narrowed gap in the large eccentric annulus thermal convection by large recirculating vortices becomes more and more difficult in contrast to the growing influence of the thermal conduction. For example, for $Ra_L = 1.0 \times 10^4$ the maximum value of $\bar{K}_{eq,\epsilon}$ occurs at about $\epsilon = 0.10$ in lower position when the inner cylinder is moved along the symmetry line. For the same Rayleigh number, maximum $\bar{K}_{eq,\epsilon}$ is identified with the concentric annulus when the inner cylinder is moved along the horizontal line passing through the center of the outer cylinder ($\theta_p = 90$ or 270 deg; see Figs. 6(*a*) and 6(*b*)). Contrary to $\bar{K}_{eq,\epsilon}$, the second equivalent conductivity, $\bar{K}_{eq,c}$, has highest value near the extreme eccentricity due to the large contribution of thermal conduction. When the inner cylinder is moved down from the top extremum position following the vertical symmetry line, $\bar{K}_{eq,c}$ is decreased somewhat before it begins to increase steadily. The point of minimum $\bar{K}_{eq,c}$

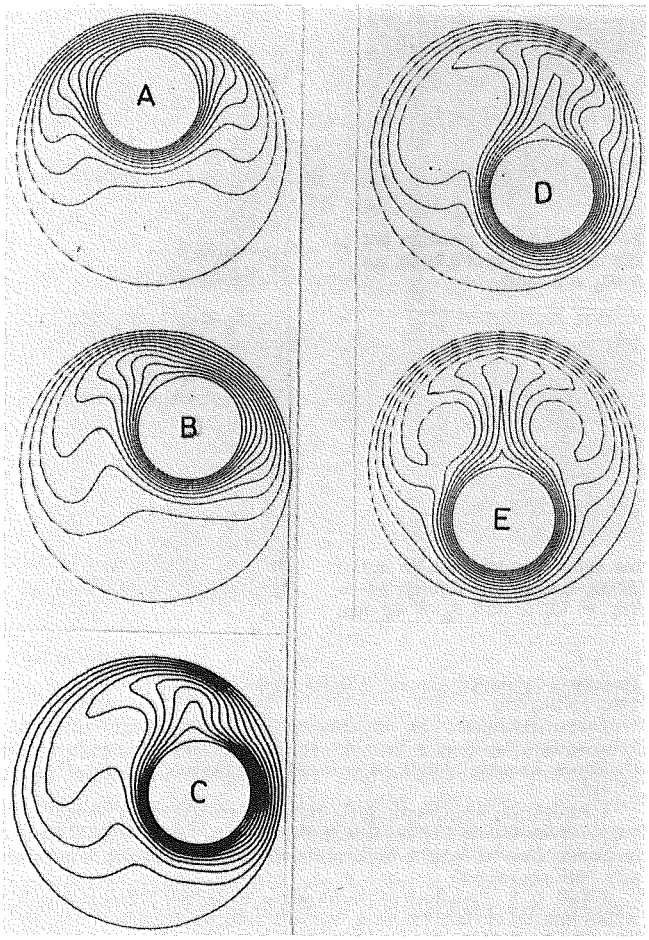

Fig. 7(*a*) Isotherms for annuli of the same eccentricity but in different angular positions: θ_p = 0 deg(A), 45 deg(B), 90 deg(C), 135 deg(D) and 180 deg (E); $\Delta\phi$ = 0.01 (Ra_L = 1.0 × 10^4, ϵ = 0.623, R_i/R_0 = 0.3846)

occurs near $\epsilon = 0.01$, $\theta_p = 0$ deg for $Ra_L = 1.0 \times 10^3$ and near $\epsilon = 0.50$, $\theta_p = 0$ deg for $Ra_L = 1.0 \times 10^4$. The existence of minimum value for $\bar{K}_{eq,c}$ reflects the fact that away from the conduction-dominant extremum positions some distance is needed for the inner cylinder to move down along the line of symmetry until convection assumes an active role in the overall heat transfer. These results are graphically represented in Fig. 6(*a*). For $Ra_L = 1.0 \times 10^4$, the value of $\bar{K}_{eq,c}$ decreases by 7 percent as the inner cylinder at $\epsilon = 0.01$ is moved up to $\epsilon = 0.623$ in the upper position and increases by 11 percent as it is moved down to $\epsilon = 0.623$ in the lower position. These changes are very similar to those observed by Kuehn and Goldstein experimentally [7].

For fixed eccentricity $\epsilon = 0.623$, the inner cylinder is moved circumferentially now. One can read from Table 1 that, by increasing θ_p both overall equivalent conductivities $\bar{K}_{eq,\epsilon}$ and $\bar{K}_{eq,c}$ monotonously increase with azimuthal angle for 0 deg $\leq \theta_p \leq$ 180 deg. This clearly indicates that the role of convection increases with higher θ_p. As θ_p is changed from 0 to 180 deg the increase in $\bar{K}_{eq,\epsilon}$ or $\bar{K}_{eq,c}$ is 10 percent for $Ra_L = 1.0 \times 10^3$ and as much as 20 percent for $Ra_L = 1.0 \times 10^4$. Detailed isotherms and streamlines are presented in Fig. 7(*a*) and 7(*b*), respectively. In the narrowest part of the gap, the conduction-dominancy is readily recognizable from the isotherm plots. Also, as seen from the streamline contours, more and more fluid is mobilized in the convection currents with increasing θ_p to deliver thermal energy from the inner heated cylinder to the colder outer cylinder. It is noted that the positional influence on the heat transfer is felt more strongly from the isotherm plots than from the streamlines, since the temperature inversion phenomenon becomes very distinguished as θ_p is increased.

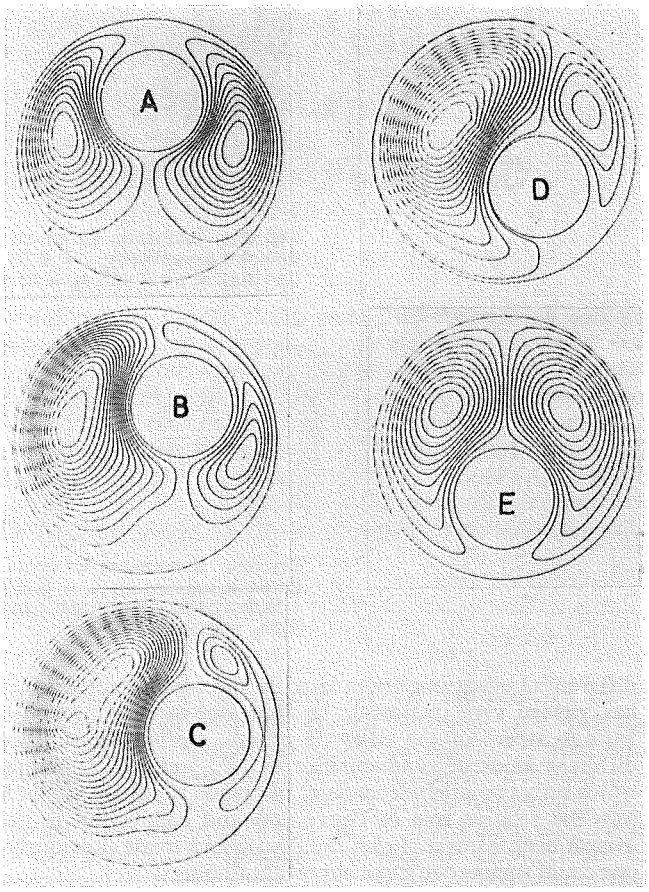

Fig. 7(*b*) Streamlines for annuli of the same eccentricity but in different angular positions: θ_p = 0 deg(A), 45 deg(B), 90 deg(C), 135 deg(D), and 180 deg(E); $\Delta\psi$ = 0.88(A), 0.88(B) 1.11(C), 1.72(D), and 1.99(E) (Ra_L = 1.0 × 10^4, ϵ = 0.623, R_i/R_0 = 0.3846)

In Figs. 8(*a*) and 8(*b*) the angular position is fixed this time along the horizontal line ($\theta_p = 90$ deg) and different eccentricities are considered as $\epsilon = 0.25$, 0.50, 0.65, and 0.75. These cases are denoted respectively by from A to D in the isothermal contours of Fig. 8(*a*) and streamline plots of Fig. 8(*b*). The remarkable process of vortex splitting by the approaching cylinders is sequentially observed in Fig. 8(*b*). For the high eccentricity the conduction-dominating flow region at the narrowest gap of the annuli becomes locally stagnant, which results in splitting of the core of the vortex in the constricted region into two subvortices rotating in the same direction. At first, the vortex core only is halvened, but as the gap is further narrowed local stagnant region grows large enough to bisect the whole vortex even much before the two cylinders come into contact. In the wider part of the eccentric annulus the vortex current is slowed down and location of its core is lowered as eccentricity is increased. From the plot of overall equivalent thermal conductivities $\bar{K}_{eq,\epsilon}$ and $\bar{K}_{eq,c}$ in Fig. 6(*b*), we can observe that the relative role of convection is steadily decreased with higher eccentricity, whereas the overall heat transfer is changed to increasing pattern after a slight decrease near $\epsilon = 0.50$. This is again surely due to the contribution of conduction for increased eccentricities. It is noted that the decreased degree of plume development and temperature inversion with higher eccentricities, as seen in Fig. 8(*a*), and the slowed-down stream speed together with the vortex halvening seen in Fig. 8(*b*) are all consistently related with the magical interaction between the conduction and the convection discussed so far.

Concluding Remarks

The finite-difference solution of the system of partial

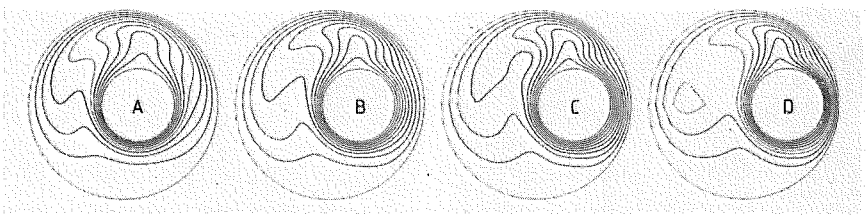

Fig. 8(*a*) Isotherms for annuli in the same angular position but of different eccentricity; ϵ = 0.25(A), 0.50(B), 0.65(C), and 0.75(D); $\Delta\phi$ = 0.11 ($Ra_L = 1.0 \times 10^4$, θ_p = 90 deg, R_i/R_0 = 0.3846)

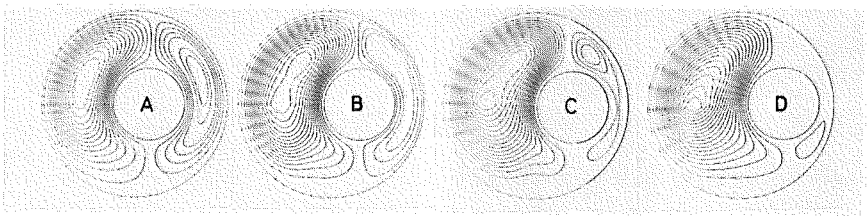

Fig. 8(*b*) Streamlines for annuli in the same angular position but of different eccentricity: ϵ = 0.25(A), 0.50(B), 0.65(C) and 0.75(D); $\Delta\psi$ = 1.16(A) 1.09(B), 1.11(C) and 1.44(D) ($Ra_L = 1.0 \times 10^4$, θ_p = 90 deg, R_i/R_0 = 0.3846)

differential equations formulated in the bipolar coordinates has yielded very interesting laminar Bousssinesq flows for various aspect of the eccentric annuli. Definition of three different kinds of conductivities K_ϵ, $\bar{K}_{eq,\epsilon}$ and $\bar{K}_{eq,c}$ among which only two are independent, has made it possible to look into the relative role of convection and conduction in the overall heat transfer. From the discussions made previously, one could summarize some important findings:

1 The bipolar coordinate system can be used for very small eccentricity to obtain the thermal characteristic of concentric cylinders which is useful for engineering applications.

2 For fixed eccentricity and aspect ratio R_i/R_0, the overall heat transfer is increased due to the expanded convection as the azimuthal angle θ_p of the inner cylinder is increased.

3 For a fixed aspect ratio, when the inner cylinder is moved outward from a concentric position along a horizontal line ($\theta_P = 90$ deg), convection heat transfer decreases contrary to the conduction heat transfer which grows with a faster rate. Consequently, $\bar{K}_{eq,\epsilon}$ decreases and $\bar{K}_{eq,c}$ increases with the eccentricity.

4 As the inner cylinder is moved downward along a vertical symmetry line, for $Ra_L = 1.0 \times 10^4$ and $R_i/R_0 = 0.3846$ the maximum of $\bar{K}_{eq,c}$ occurs at about $\epsilon = 0.10$ on $\theta_p = 180$ deg and the minimum of $\bar{K}_{eq,c}$ occurs at about $\epsilon = 0.50$ along $\theta_p = 0$ deg.

5 For concentric annuli, larger diameter ratio means decreased angular dependence of the local thermal characteristics.

References

1 Kuehn, T. H., and Goldstein, R. J., "An Experimental and Theoretical Study of Natural Convection in the Annulus Between Horizontal Concentric Cylinders," *Journal of Fluid Mechanics*, Vol. 74, 1976, pp. 695-719.

2 Kuehn, T. H., and Goldstein, R. J., "A Parametric Study of Prandtl Number and Diameter Ratio Effects on Natural Convection Heat Transfer in Horizontal Cylindrical Annuli," ASME JOURNAL OF HEAT TRANSFER, Vol. 102, 1980, pp. 768-770.

3 Charrier-Mojtabi, M. C., Mojtabi, A., and Caltagirone, J. P., "Numerical Solution of a Flow due to Natural Convection in Horizontal Cylindrical Annulus," ASME JOURNAL OF HEAT TRANSFER, Vol. 101, 1979, pp. 171-173.

4 Farouk, B., and Guceri, S. I., "Laminar and Turbulent Natural Convection in the Annulus Between Concentric Cylinders," in *Symposium Volume on Natural Convection*, 20th National Heat Transfer Conference, Milwaukee, Wis. 1981, pp. 143-150.

5 Yao, L. S., "Analysis of Heat Transfer in Slightly Eccentric Annuli," ASME JOURNAL OF HEAT TRANSFER, Vol. 102, 1980. pp. 270-284.

6 Yao, L. S., and Chen, F. F., "Effects of Natural Convection in the Melted Region Around a Heated Horizontal Cylinder," ASME JOURNAL OF HEAT TRANSFER, Vol. 102, 1980, pp. 667-672.

7 Kuehn, T. H., and Goldstein, R. J., "An Experimental Study of Natural Convection Heat Transfer in Concentric and Eccentric Horizontal Cylindrical Annuli," ASME JOURNAL OF HEAT TRANSFER, Vol. 100, 1978, pp. 635-640.

8 Sande, E. Van de, and Hamer, B. J. G., "Steady and Transient Natural Convection in Enclosures Between Horizontal Circular Cylinders," *International Journal of Heat Mass Transfer*, Vol. 22, 1979, pp. 361-370.

9 Ratzel, A. C., Hickox, C. E., and Gartling, D. K., "Techniques for Reducing Thermal Conduction and Natural Convection Heat Losses in Annular Receiver Geometries," ASME JOURNAL OF HEAT TRANSFER, Vol. 101, 1979. pp. 108-113.

10 Aminzadeh, K., Al Taha, T. R., Cornish, A. R. H., Kolansky, M. S., and Pfeffer, R., "Mass Transport Around Two Spheres at Low Reynolds Numbers," *International Journal of Heat Mass Transfer*, Vol. 17, 1974, pp. 1425-1436.

11 Snyder, W. T., and Goldstein, G. A., "An Analysis of Fully Developed Laminar Flow in an Eccentric Annulus," *AIChE Journal*, Vol. 11, 1965, pp. 462-467.

12 Wood, W. W., "The Asymptotic Expansion at Large Reynolds Numbers for Steady Motion Between Non-Coaxial Rotating Cylinders," *Journal of Fluid Mechanics*, Vol. 3, 1957, pp. 159-175.

13 Launder, B. E., and Ying, W. M., "Numerical Solutions of Flow Between Rotating Cylinders," *Journal of Mechanical Engineering Science*, Vol. 14, 1972, pp. 400-403.

14 Launder, B. E., and Ying, W. M., "Laminar Heat Transfer In Rotating Eccentric Annuli," Journal of Mechanical Engineering Science," Vol. 16, No. 5, 1974, pp. 306-309.

15 Gray, D. D., and Giorgini, A., "The Validity of the Boussinesq Approximation for Liquids and Gases," *International Journal of Heat Mass Transfer*, Vol. 19, 1976, pp. 545-551.

16 Roache, P. J., *Computational Fluid Dynamics*, Hermosa Publisher, 1972, Albuquerque, New Mexico.

Laminar and Turbulent Natural Convection in the Annulus Between Horizontal Concentric Cylinders

B. Farouk,
Assistant Professor,
Mechanical Engineering and Mechanics Department,
Drexel University,
Philadelphia, Pa. 19104
Assoc. Mem. ASME

S. I. Güçeri,
Associate Professor,
Mechanical and Aerospace Engineering Department,
University of Delaware,
Newark, Del. 19711

Numerical solutions are presented for the steady-state, two-dimensional natural convection in the annulus between two horizontal concentric cylinders which are held at different constant temperatures. Solutions for the laminar case are obtained up to Rayleigh number (based on gap width, L) of 10^5. Turbulent flow results are presented for the Rayleigh number range of $10^6 - 10^7$. the k-ϵ turbulence model has been applied to obtain the results. Buoyancy effects on the turbulence structure are also accounted for. The results for both the laminar and turbulent cases are in good agreement with available experimental data and other solutions in the literature. All results presented are for the outer cylinder diameter to inner cylinder diameter ratio of 2.6.

Introduction

Natural convection in concentric annuli has been the subject of interest of many researchers due to its various applications in engineering devices including the receivers of some focusing solar collectors. The problem was investigated experimentally by Liu et al. [1], Lis [2], and Grigull and Hauf [3] among others [4, 5]. Photographs showing the dependence of the flow patterns on the Grashof number and diameter ratio were presented by Powe, Carley and Bishop [6]. The analytical solutions available in the literature are generally valid for small Rayleigh numbers [7, 8]. More recently Jischke and Farschi [9] have used boundary-layer theory to analyze the flow in the laminar regime. Raithby and Hollands [10] have considered the high Rayleigh number boundary-layer limit with a conduction-layer model. Their empirical analysis correlates data quite well, but it gives no information about the flow and temperature fields. Kuehn and Goldstein also obtained experimental data by optical methods and obtained theoretical results numerically [11, 12]. Numerical results were presented only for the laminar case up to a Rayleigh number (based on gap width, L) of 10^5. An outside diameter to inside diameter ratio of 2.6 was used in these solutions. The diameter ratio is significant as previous studies have suggested [6], since the flow patterns are dependent on it, especially when the flow undergoes transition from laminar to turbulent.

In the present study, numerical solutions are presented for the steady-state, two-dimensional natural convection in the annulus between two horizontal concentric cylinders. Solutions are presented over a wide range of Rayleigh numbers which encompasses both the laminar and turbulent flow situations. For the laminar case, the problem consists of solution of the three elliptic partial differential equations (i.e., vorticity, stream function, and temperature) in a two-dimensional space with specified boundary conditions [13]. Solutions for the laminar case are obtained up to a Rayleigh number of 10^5 for air. Previous experimental studies [2, 11] have suggested that turbulence sets in when the Rayleigh number exceeds the above value. A two-equation $(k-\epsilon)$ turbulence model has been used here to predict the natural convective flow in the annulus for Rayleigh numbers above 10^5. The $k-\epsilon$ model, proposed first by Launder and Spalding [14], has been applied previously to calculate forced and boundary layer flows with success. Relatively less work has been done in predicting buoyancy driven recirculating turbulent flows numerically [15]. In the model used, turbulence is characterized by transport equations for time-averaged k, the turbulent kinetic energy and ϵ, its rate of dissipation. The equations for the time-averaged stream function, vorticity, and temperature along with the differential equations for k and ϵ are solved simultaneously in the same manner as for the laminar case [16].

An outside diameter to inside diameter ratio of 2.6 and air properties at atmospheric pressure were used in the following calculations. The applicability of the method used is, however, not limited to the above cases.

Problem Statement

Prediction of natural convection in a two-dimensional cylindrical annuli requires the solution of coupled partial differential equations. In the laminar flow regime, these equations are obtained from the conservation of mass, momentum, and energy principles. In the turbulent flow, two additional equations, k^* and ϵ^* are considered [14, 16]. By using the stream function-vorticity formulation, the five governing equations can all be represented as a single elliptic equation in the following form [17]:

$$a^\phi\left[\frac{\partial}{\partial r^*}\left(\phi\frac{\partial\psi^*}{\partial\theta}\right)-\frac{\partial}{\partial\theta}\left(\phi\frac{\partial\psi^*}{\partial r^*}\right)\right]-\left[\frac{\partial}{\partial r^*}\left(b^\phi r^*\frac{\partial(c^\phi\phi)}{\partial r^*}\right)+\frac{\partial}{\partial\theta}\left(\frac{b^\phi}{r^*}\frac{\partial(c^\phi\phi)}{\partial\theta}\right)\right]=-r^*d^\phi \quad (1)$$

where the expressions in the first set of brackets on the left hand side of the equation represent the convective terms. The remaining part of this side represents the diffusion terms and the right hand side shows the source/sink terms. The laminar flow regime is described by three equations, ϕ representing the dependent variables ψ^*, ω^*, and T^*. For the turbulent flow regime, ϕ represents the time-averaged values of ψ^*, ω^*, T^*, k^*, and ϵ^*, thus five equations need be solved. In generating these equations from equation (1), the multipliers a^ϕ, b^ϕ, c^ϕ and d^ϕ take appropriate expressions as summarized in Table 1. For laminar regime, μ_t^* is set equal to zero in the expressions

Contributed by the Heat Transfer Division and presented at the 20th ASME/AIChE National Heat Transfer Conference, Milwaukee, Wisconsin, August 2-5, 1981. Manuscript received by the Heat Transfer Division April 6, 1981.

Table 1 Coefficients for the flow equations

ϕ	a^ϕ	$b^{\phi a}$	c^ϕ	d^ϕ
ψ^*	0	1	1	$-\omega^*$
ω^*	1	1	$1+\mu_t^*$	$-\mathrm{Gr}\left[\frac{\partial T^*}{\partial r^*}\sin\theta+\frac{1}{r^*}\frac{\partial T^*}{\partial\theta}\cos\theta\right]$
T^*	1	$\frac{1}{\mathrm{Pr}}+\frac{\mu_t^*}{\sigma_T}$	1	0
k^*	1	$1+\frac{\mu_t^*}{\sigma_k}$	1	S_k
ϵ^*	1	$1+\frac{\mu_t^*}{\sigma_\epsilon}$	1	S_ϵ

[a] $\sigma_k = 1.$, $\sigma_\epsilon = 1.3$, $\sigma_T = 1.$ [14]

and only the first three equations are considered. For turbulent regime, even though the two-dimensional mean motion is studied, the fluctuating components of velocities in all three dimensions were taken into account. In this case, σ_T, σ_k, and σ_ϵ are the turbulent Prandtl numbers for $\bar{T}$, k and ϵ, respectively. The source terms S_k and S_ϵ for the k^* and ϵ^* equations for buoyancy driven recirculating flow (in polar coordinates) are given by

$$S_k = -\mu_t^*\left\{2\left(\frac{\partial v_r^*}{\partial r^*}\right)^2+2\left(\frac{\partial v_\theta^*}{r^*\partial\theta}\right)^2+2\left(\frac{v_r^*}{r^*}\right)^2+\left[r^*\frac{\partial}{\partial r^*}\left(\frac{v_\theta^*}{r^*}\right)+\frac{\partial v_r^*}{r^*\partial\theta}\right]^2\right\}+\mathrm{Gr}\,\frac{\mu_t^*}{\sigma_T}\left[\frac{\partial T^*}{r^*\partial\theta}\sin\theta-\frac{\partial T^*}{\partial r^*}\cos\theta\right]+\epsilon^* \quad (2)$$

$$S_\epsilon = -C_1\mu_t^*\frac{\epsilon^*}{k^*}\left\{2\left(\frac{\partial v_r^*}{\partial r^*}\right)^2+2\left(\frac{\partial v_\theta^*}{r^*\partial\theta}\right)^2+2\left(\frac{v_r^*}{r^*}\right)^2+\left[r^*\frac{\partial}{\partial r^*}\left(\frac{v_\theta^*}{r^*}\right)+\frac{\partial v_r^*}{r^*\partial\theta}\right]^2\right\}+C_3\mathrm{Gr}\,\frac{\mu_t^*}{\sigma_T}\,\frac{\epsilon^*}{k^*}\left[\frac{1}{r^*}\frac{\partial T^*}{\partial\theta}\sin\theta-\frac{\partial T^*}{\partial r^*}\cos\theta\right]+C_2\frac{\epsilon^{*2}}{k^*} \quad (3)$$

The effect of buoyancy on the creation of turbulence energy is taken into account by the second term in the expression for S_k.

The empirical constants are taken as $C_1 = 1.44$ and $C_2 = 1.92$ [14]. C_3 is taken as being equal to C_1 by assuming similar contributions from buoyancy and gradient production terms, and a sensitivity study on C_3 is presented later.

Boundary Conditions

Solution of elliptic equations requires that the boundary conditions be specified along the entire boundary which encloses the flow field. The inner cylinder is considered to be held at a uniform temperature, T_i, and the outer cylinder at a uniform temperature T_0 such that $T_i > T_o$. Because of the geometry considered a vertical symmetry plane exists and the problem is solved only for the vertical half plane. The stream function is constant along each wall, as well as along the lines of symmetry. Since no flow enters or escapes from the enclosure, the stream function is set equal to zero on all the boundaries. The vorticity is zero on the symmetry lines. It is assumed that at the lines of symmetry the angular derivatives of the temperature vanish.

For ψ^*, ω^*, and T^*, the same boundary conditions are used for laminar and turbulent regimes, except for the latter, time-averaged quantities are considered instead.

The complete set of boundary conditions used in generating the results are given in Table 2 [11, 13, 15, 18].

Solution Procedure

Both for the laminar and turbulent cases, the equations of the previous sections are transformed into difference equations by using a finite difference method presented by Gosman et al. [17].

A grid is established by dividing the region in the r and θ directions. For the laminar flow predictions a grid of 25 × 51 ($r \times \theta$) was considered while for the turbulent flow cases a

Nomenclature

C_1, C_2, C_3 = empirical turbulence model constants
C_μ = constant of proportionality, equals 0.09
c_p = specific heat at constant pressure
D_o, D_i = outer and inner cylinder diameters
g = acceleration of gravity
h_i = local heat-transfer coefficient on inner cylinder $q_{w_i}/(T_i - T_0)$
h_o = local heat-transfer coefficient on outer cylinder $q_{w_0}/(T_i - T_0)$
k = turbulent kinetic energy = $(1/2)(\overline{v_r'^2 + v_\theta'^2 + v_z'^2})$
k^* = $L^2 k/\nu^2$
L = gap width $(D_0 - D_i)/2$
q_w = heat flux from cylinder surface
r = radial coordinate
r^* = r/L
Ra_L = Rayleigh number, based on gap width, $\rho^2 g\beta L^3 (T_i - T_0)c_p/\mu\lambda$
T = temperature, $\bar{T} + T'$
T_i = temperature of inner cylinder
T_o = temperature of outer cylinder
T^* = $(\bar{T} - T_0)/(T_i - T_0)$
v_r = radial velocity component, $\bar{v}_r + v_r'$
v_r^* = Lv_r/ν
v_θ = circumferential velocity component, $\bar{v}_\theta + v_\theta'$
v_θ^* = Lv_θ/ν
v_z = velocity component in the axial direction, $0 + v_z'$

Greek Letters

β = thermal coefficient of volume expansion
ϵ = dissipation rate of turbulent kinetic energy
ϵ^* = $L^4\epsilon/\nu^3$
θ = circumferential (angle) coordinate
λ = thermal conductivity
λ_{eq} = local equivalent conductivity, $h_i D_i \ln(D_o/D_i)/2\lambda$ for inner cylinder, $h_o D_o \ln(D_o/D_i)/2\lambda$ for outer cylinder
$\bar{\lambda}_{eq}$ = average equivalent conductivity
ϕ = a dependent variable
μ = molecular viscosity;
μ_t = turbulent viscosity, $C_\mu\rho\frac{k^2}{\epsilon}$
μ_t^* = μ_t/μ
ρ = density
ν = dynamic viscosity
ψ = stream function, $\bar{\psi} + \psi'$
ψ^* = ψ/μ
ω = vorticity, $\bar{\omega} + \omega'$
ω^* = $L^2\omega/\nu$

Table 2 Summary of the boundary conditions

Variable	Inner cylinder	Symmetry plane	Outer cylinder
ψ^*	$\psi^* = 0$	$\psi^* = 0$	$\psi^* = 0$
ω^*	$\omega^* = -\dfrac{2\psi^{*a}}{(\Delta r^*)^2}$	$\omega^* = 0$	$\omega^* = -\dfrac{2\psi^{*a}}{(\Delta r^*)^2}$
T^*	$T^* = 1$	$\dfrac{\partial T^*}{\partial \theta} = 0$	$T^* = 0$
k^*	$k^* = 0$	$\dfrac{\partial k^*}{\partial \theta} = 0$	$k^* = 0$
ϵ^{*b}	$\epsilon_p^* = \dfrac{C_\mu^{3/4}}{\kappa}\dfrac{k_p^{*3/2}}{\Delta r^*}$	$\dfrac{\partial \epsilon^*}{\partial \theta} = 0$	$\epsilon_p^* = \dfrac{C_\mu^{3/4}}{\kappa}\dfrac{k_p^{*3/2}}{\Delta r^*}$

[a] ψ^* is to be evaluated at Δr^* into the fluid.
[b] Subscript p represents the nearest grid point from the wall. κ is the von Karman constant and is equal to 0.42.

denser grid of 41 × 51 was used. Because of the large gradients occurring near the inner and outer walls, the node spacing in the r-direction near the walls is reduced by a factor of 2 as compared to the central region.

The calculations were performed on a Burroughs B7700 digital computer. To obtain convergence, about 300 iterations were needed for the laminar cases and about 600 iterations for the turbulent flow predictions with CPU times of 15 and 50 min, respectively. For higher Rayleigh numbers, the solutions of the previous case were used as initial values in the iterative process. Due to the relatively large variations during initial iterations for k^* and ϵ^* under-relaxation had to be used to obtain converged solutions [17]. An under-relaxation factor of .5 was found to be satisfactory. No under or over-relaxation factor was used for any of the other variables.

Results and Discussion

Initially, solutions were obtained for the laminar case, which could be directly compared with previously published results. Once the validity of the approach was established, the $k-\epsilon$ turbulence model was applied to the similar flow situations with higher Rayleigh numbers. The sufficiency of grid sizing and suitability of the approach were determined by generating data which agree with experimental and other theoretical methods available in the literature for similar flow problems.

The flow and heat transfer results can be divided into several regimes. Below a Rayleigh number of 10^2 the velocities are too small to affect the temperature distribution, which remains essentially as in pure conduction. A transition region exists for Rayleigh numbers between 10^2 and 3×10^4. Since the laminar flow case is documented [11], the stream lines and isotherms are presented for a single case of Ra = 10^4 in Figs. 1(*a*) and 1(*b*), respectively, to demonstrate the applicability of the numerical scheme and for qualitative comparison. The radial temperature inversion appears, suggesting the seperation of the inner and outer cylinder thermal boundary layers. Previous experimental observations [6] suggest that near a Rayleigh number of 10^5 for air at this diameter ratio the crescent-shaped flow pattern is characterized by oscillations about the longitudinal axis; therefore, the results obtained during this study for $Ra_L = 10^5$ can be viewed as the time-averaged values. Unlike in reference [11], convergence was obtained for $Ra_L = 10^5$ with air. This could be due to the upwind difference treatment of the convective terms which is known to give better convergence than the central difference schemes [17]. Heat transfer results are presented in terms of the local equivalent conductivity, which is defined as the ratio of the thermal conductivity that a

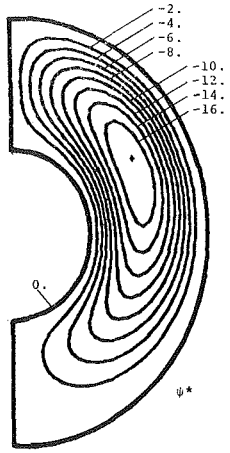

Fig. 1(*a*) Streamlines in laminar flow for $Ra_L = 10^4$, Pr = 0.721, D_o/D_i = 2.6, $\Delta\psi^* = -2.0$

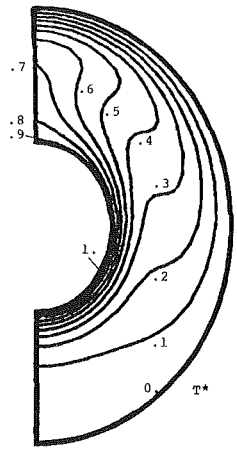

Fig. 1(*b*) Isotherms in laminar flow for $Ra_L = 10^4$, Pr = 0.721, D_o/D_i = 2.6, $\Delta T^* = 0.1$

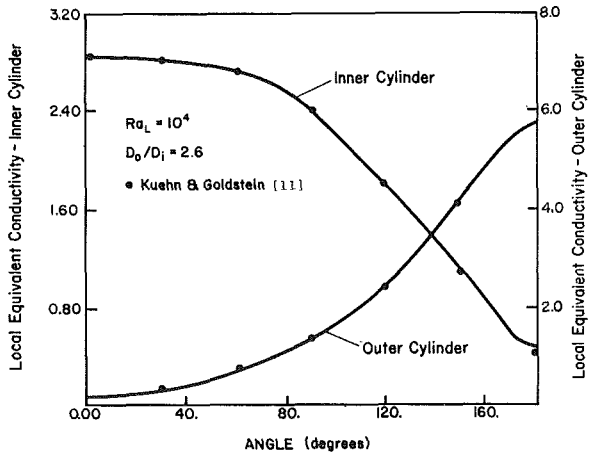

Fig. 2 Distribution of local equivalent conductivities for the inner and outer cylinders; $Ra_L = 10^4$, Pr = 0.721, $D_o/D_i = 2.6$

motionless fluid in the gap must have to transmit the same amount of heat as the moving test fluid to the actual thermal conductivity of the test fluid. Figure 2 shows the distribution of local equivalent thermal conductivities for the inner and outer cylinders at $Ra_L = 10^4$, along with previously reported data [11]. Having thus established the validity for the scheme for laminar flow, the $k-\epsilon$ model was then applied for turbulent flow predictions.

All of the results are described only on a semicircular region since the problem is symmetric. The results are obtained up to

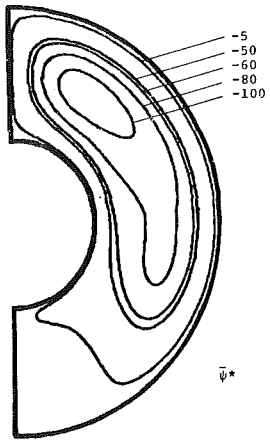

Fig. 3 Streamlines in turbulent flow for $Ra_L = 10^6$, Pr = 0.721, D_o/D_i = 2.6

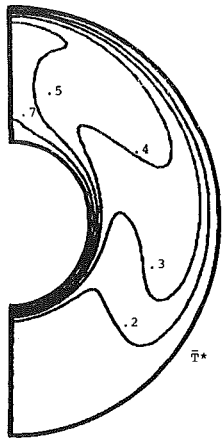

Fig. 3(*b*) Isotherms in turbulent flow for $Ra_L = 10^6$, Pr = 0.721, D_o/D_i = 2.6

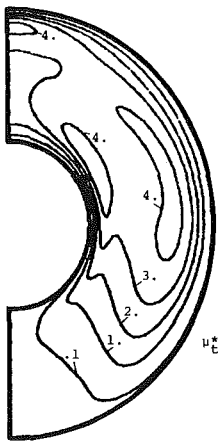

Fig. 4(*a*) Constant turbulent viscosity lines for $Ra_L = 10^6$, Pr = 0.721, D_o/D_i = 2.6

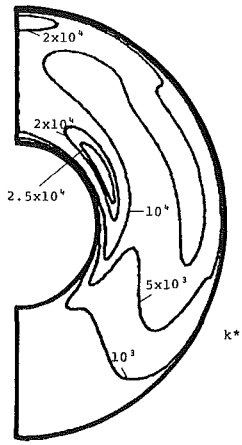

Fig. 4(*b*) Constant turbulent kinetic energy lines for $Ra_L = 10^6$ Pr = 0.721, D_o/D_i = 2.6

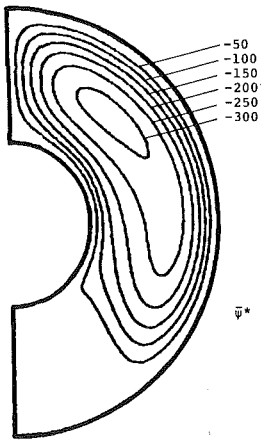

Fig. 5(*a*) Streamlines in turbulent flow for $Ra_L = 10^7$, Pr = 0.721, D_o/D_i = 2.6

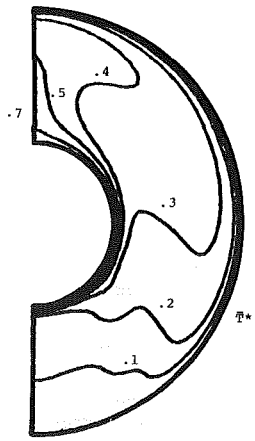

Fig. 5(*b*) Isotherms in turbulent flow for $Ra_L = 10^7$, Pr = 0.721, D_o/D_i = 2.6

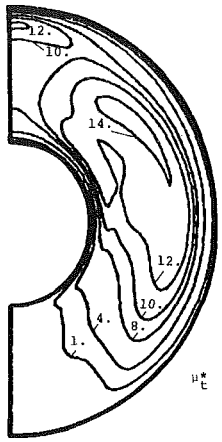

Fig. 6(*a*) Constant turbulent viscosity lines for $Ra_L = 10^7$, Pr = 0.721, $D_o/D_i = 2.6$

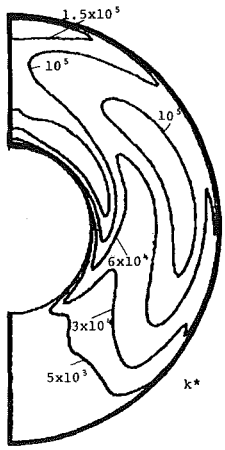

Fig. 6(*b*) Constant turbulent kinetic energy lines for $Ra_L = 10^7$, Pr = 0.721, $D_o/D_i = 2.6$

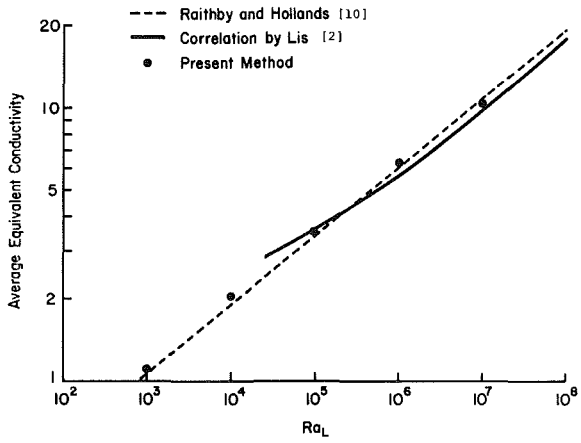

Fig. 7 Average equivalent conductivity as a function of Rayleigh number

a Rayleigh number of 10^7 with $D_o/D_i = 2.6$ and Pr = 0.721. Time-averaged stream function, temperature, turbulent viscosity, and turbulent kinetic energy results are shown in Figs. 3(*a*), 3(*b*), 4(*a*), and 4(*b*), respectively, for $Ra_L = 10^6$ and Figs. 5(*a*), 5(*b*), 6(*a*), and 6(*b*), respectively, for $Ra_L = 10^7$

The two-dimensional recirculation patterns are similar to those obtained in the laminar results. However, the location of the maximum value of the stream function moves further upward. The profiles in Figs. 3(*a*) and 5(*a*) show, respectively, thin boundary layers compared to the size of the gap and the

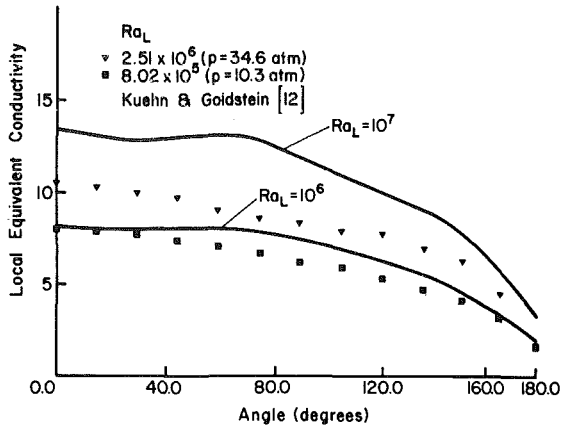

Fig. 8 Distribution of local equivalent conductivities for the inner cylinder, (turbulent regime), Pr = 0.721, $D_o/D_i = 2.6$

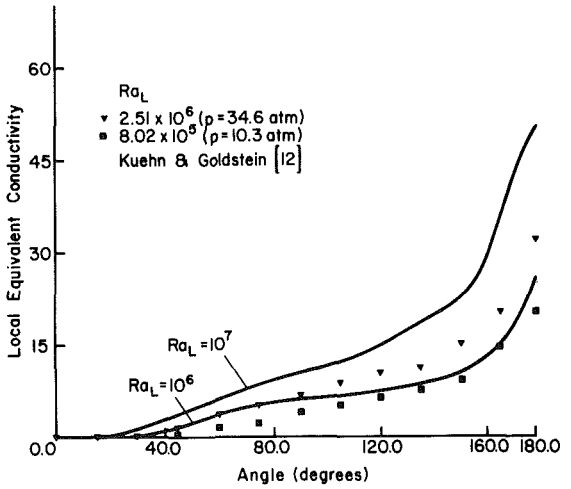

Fig. 9 Distribution of local equivalent conductivities for the outer cylinder, (turbulent regime), Pr = 0.721, $D_o/D_i = 2.6$

continued presence of the temperature inversion in the center, although this is not as pronounced as at lower Rayleigh numbers. The above observations are consistent with previous experimental work in this Rayleigh number range [12]. The velocities at the bottom of the annulus are very low compared to the velocities at the middle and top regions. At $Ra_L = 10^6$, the maximum value of the turbulent viscosity is about four times the molecular viscosity and at $Ra_L = 10^7$ is about fourteen times as large. The turbulent viscosity is only significant in the top half of the annulus. The flow is thus not completely turbulent in the whole annulus for Rayleigh numbers between 10^6 and 10^7, because the regions of significant turbulent viscosity are limited.

As seen in Figs. 4(*b*) and 6(*b*), the values of k^* are large along the plume and very low at the bottom of the annulus. The relative importance of the two sources of turbulent kinetic energy, shear and buoyancy, becomes evident from these figures. The ϵ^* distribution in the field is not presented as its value can be readily obtained from its definition once the values μ_t^* and k^* are known (except at regions very close to the wall).

The heat transfer results were obtained in a similar way as for laminar flow. Figure 7 shows the present numerical results for a Rayleigh number range of $10^3 - 10^7$ for $D_o/D_i = 2.6$ and Pr = 0.721. Two previously obtained correlations are shown for comparison. The present results agree well with the correlation of Lis [2] and the conduction boundary-layer model developed by Raithby and Hollands [10].

Figures 8 and 9 show the distributions of local equivalent

Table 3 Results of sensitivity study for C_3 Ra = 10^6

C_3	$\bar{\lambda}_{eq}$	ψ^*_{min}	$\mu^*_{t\,max}$	k^*_{max}	ϵ^*_{max}
1.44[a]	6.31	−109.4	4.32	2.35×10^4	1.14×10^7
$C_3+20\%$	+3.95%	+4.98%	+31.1%	+15.2%	+1.29%
$C_3+10\%$	+1.70%	+2.19%	+11.1%	+4.69%	+0.51%
$C_3-10\%$	−2.21%	−1.77%	−2.79%	−3.53%	−1.94%
$C_3-20\%$	−4.77%	−3.02%	−7.60%	−5.81%	−3.89%

[a]The reference value for C_3, i.e., $C_3 = C_1$

thermal conductivities for the inner and outer cylinders, respectively, in the turbulent regime. Essentially, the results follow the distributions similar to that for the laminar case. The presence of turbulence, however (e.g., in the upper corner near the outer cylinder), causes substantially higher heat transfer in certain regions. Experimental results of Kuehn and Goldstein [12] are also included for the purpose of qualitative comparison only, since those data are for pressurized nitrogen where as the results presented here are obtained using the properties of air at atmospheric conditions.

A sensitivity study was carried out in order to determine the effects of the model constant, C_3, on the calculated results. The other coefficients were not included, since they have been optimized against experiments for forced flows and used with a reasonable degree of success by several previous investigators [14, 17]. The results of varying the constant C_3 by ± 10 percent and ± 20 percent (from the reference value of $C_3 = C_1$) are shown in Table 3. The effect of variation of C_3 on the mean equivalent conductivity, minimum stream function, maximum turbulent viscosity, maximum turbulent kinetic energy, and maximum dissipation rate is shown. It is observed that the effect on the heat transfer results and streamlines are slight. The effect on the turbulent quantities is quite strong. This is especially true when $C_3 > C_1$. However, $C_3 > C_1$ is not recommended for use in this problem because near the top and the bottom regions the boundary layers become close to being horizontal. A sensitivity study for C_3 was reported for the rectangular enclosure problem with similar observation [15]. For the present case, the location of occurrence of the maximum turbulent quantities did not change appreciably with the variation of C_3.

With this study, the use of a finite difference technique in solving recirculating natural convection and application of the $k-\epsilon$ model is demonstrated. A finer grid is required for predicting the flows with still higher Rayleigh numbers since the boundary layers close to the walls become thinner. Appropriate wall-functions for these types of flows would help in obtaining results without invoking excessive computer time [19]. Further work in this area is under consideration.

References

1 Liu, C. Y., Mueller, W. K., and Landis, F., "Natural Convection Heat Transfer in Long Horizontal Annuli," *International Developments in Heat Transfer*, ASME, 1961, pp. 976–984.

2 Lis, J., "Experimental Investigation of Natural Convection Heat Transfer in Simple and Obstructed Horizontal Annuli," *Proceedings of the 3rd International Heat Transfer Conference*, Paper No. 61, Vol. 2, 1966, pp. 196–204.

3 Grigull, U., and Hauf, W., "Natural Convection in Horizontal Cylindrical Annuli," *Proceedings of 3rd International Heat Transfer Conference*, Vol. 2, 1966, pp. 182–195.

4 Kraussold, H., "Wärmeabgabe von Zylindrischen Flüssigkeitsschichten bei Natüralicher Konvektion," Forsch, *Feb.d. Ingenieururwesen*, 5(4), 1934, pp. 186–191.

5 Beckman, W., "Die Wärmeubertragung in Zylindrischen Gasschichten bei Natürlicher Konvektion," Forsch, *Feb.d. Ingenieurwesen*, 2(5), 1931, pp. 165–178.

6 Powe, R. E., Carley, C. T., and Bishhop, E. H., "Free Convection Flow Patterns in Cylindrical Annuli," ASME JOURNAL OF HEAT TRANSFER, Aug. 1969, pp. 310–314.

7 Mack, L. R., and Bishop, E. H., "Natural Convection Between Horizontal Concentric Cylinders for Low Rayleigh Numbers," *Quart. J. Mech. Appl. Math.*, Vol. 21, 1968, pp. 223–241.

8 Hodnett, P. F., "Natural Convection Between Horizontal Heated Concentric Circular Cylinders," *J. Appl. Math. Phys.*, Vol. 24, 1973, pp. 507–516.

9 Jischke, M. C., and Farschi, M., "Boundary Layer Regime for Laminar Free Convection Between Horizontal Circular Cylinders," ASME JOURNAL OF HEAT TRANSFER, Vol. 102, May 1980, pp. 228–235.

10 Raithby, G. D., and Hollands, K. G. T., "A General Method of Obtaining Approximate Solutions to Laminar and Turbulent Free Convection Problems," *Advances in Heat Transfer*, Vol. 11, 1975, pp. 266–317.

11 Kuehn, T. H., and Goldstein, R. J., "An Experimental and Theoretical Study of Natural Convection in the Annulus Between Horizontal Concentric Cylinders," *Journal of Fluid Mechanics*, Vol. 75, 1976, pp. 695–719.

12 Kuehn, T. H., and Goldstein, R. J., "An Experimental Study of Natural Convection Heat Transfer in Concentric and Eccentric Horizontal Cylindrical Annuli," ASME JOURNAL OF HEAT TRANSFER, Vol. 100, 1978, pp. 635–640.

13 Farouk, B., and Güceri, S. İ., "Natural Convection From a Horizontal Cylinder-Laminar Regime," ASME JOURNAL OF HEAT TRANSFER, Vol. 103, 1981, pp. 522–527.

14 Launder, B. E., and Spalding, D. B., "The Numerical Computation of Turbulent Flows," *Computer Methods in Applied Mechanics and Engineering*, Vol. 3, 1974, pp. 269–289.

15 Fraikin, M. P., Portier, J. J., and Fraikin, C. J., "Application of a k-ϵ Turbulence Model to an Enclosed Buoyancy Driven Recirculating Flow," ASME/AIChE National Heat Transfer Conference, Orlando, Fla., July 1980, ASME Paper No. 80-HT-68.

16 Farouk, B., and Güceri, S. İ., "Natural Convection From a Horizontal Cylinder—Turbulent Regime," submitted for publication, ASME JOURNAL OF HEAT TRANSFER.

17 Gosman, A. D., Pun, W. M., Runchal, A. K., Spalding, D. B., and Wolfshtein, M. W., *Heat and Mass Transfer in Recirculating Flows*, Academic Press, London, 1969.

18 Spalding, D. B., "Turbulence Models (2nd Issue)," Imperial College of Science and Technology, London, Heat Transfer Section Report, HTS/76/17, Jan. 1977.

19 Spalding, D. B., Personal communications, Aug. 1980.

Vortex Instability of Free Convection Flow Over Horizontal and Inclined Surfaces

T. S. Chen
Mem. ASME

K. L. Tzuoo

Department of Mechanical and Aerospace Engineering, University of Missouri-Rolla, Rolla, Mo. 65401

The vortex instability characteristics of laminar free convection flow over horizontal and inclined isothermal surfaces are studied analytically by linear theory. As a prelude to the analysis, the effects of the angle of inclination on the main flow and thermal fields are re-examined by a new approach. Numerical results are presented for wall shear stress, surface heat transfer, neutral stability curve, and critical Grashof number for Prandtl numbers of 0.7 and 7 over a wide range of angles of inclination, ϕ, from the horizontal. It is found that as the angle of inclination increases the rate of surface heat transfer increases, whereas the susceptibility of the flow to the vortex mode of instability decreases. The present study provides new vortex instability results for small angles of inclination ($\phi \leq 30$ deg) and more accurate results for large angles of inclination ($\phi \geq 30$ deg) than previous studies. The present results are also compared with available wave instability results.

Introduction

It is now well established from experimental and analytical studies that laminar free convection flow over an inclined, upward-facing heated plate is unstable to both vortex and wave modes of disturbances (see, for example, [1-12]). The instability of the flow that occurs as the result of a secondary flow in the form of longitudinal vortex rolls is due to the presence of a buoyancy force component that acts in the direction normal to the plate. The experimental work of Lloyd and Sparrow [2] on free convection flow over inclined, upward-facing heated plates in water showed that instability of the flow is of the Tollmien-Schlichting wave mode for inclination angles of less than 14 deg from the vertical, whereas the mode of instability is characterized by the longitudinal vortex rolls for inclination angles in excess of 17 deg from the vertical. For angles between 14 and 17 deg, both modes of instability were found to coexist in this zone of continuous transition.

The experimental finding of Sparrow and co-workers [1, 2] has stimulated several analytical studies (see, for example, [3-6]) on the subject matter. From their independent analyses of the vortex instability of free convection flow adjacent to an inclined, upward-facing heated plate, both Hwang and Cheng [3] and Haaland and Sparrow [4] found that the susceptibility of the flow to the vortex mode of instability increases with increasing angle of inclination from the vertical. Subsequently, Kahawita and Meroney [5] re-examined the same problem and predicted that for a Prandtl number of 0.72 the vortex mode of instability crosses over into the wave mode of instability at an inclination angle of about 17 deg from the vertical. Their prediction thus agrees well with the experimental observation of Lloyd and Sparrow in water [2]. This inclined plate problem was also analyzed by Iyer and Kelly [6] who found that for a Prandtl number of 6.7 the crossover from the vortex to the wave mode of instability occurs at an inclination angle of 4 deg from the vertical. However, their calculations of the total amplification of each disturbance from its predicted point of onset of instability to the point of observed instability showed that good correltaions with the experimental observations were achieved. In addition, they found that for the upward-facing heated plate the susceptibility of the flow to the wave mode of disturbances increases with increasing angle of inclination from the vertical. This finding is in qualitative agreement with another analysis [7] and available experimental data [2, 8].

In all the analytical studies on both the vortex and wave modes of instability of flow over inclined, heated plates that have been conducted to date, the main flow and thermal fields employed in the analyses were approximated by the similarity solution for a vertical plate, with the gravity component parallel to the inclined plate, $g \cos\gamma$, incorporated in the Grashof number. That is, in these analyses, the normal component of the buoyancy force that induces the streamwise pressure gradient in the main flow is neglected. Thus, the instability results from these analyses are not valid for angles of inclination from the vertical that are not small (say, for γ larger than 45 deg). Furthermore, it is precisely this normal buoyancy force component that is responsible for the occurence of the longitudinal vortex rolls; the neglect of this component in the main flow in the stability calculations will lead to serious errors in the results when the angles of inclination from the vertical are large. In view of this and the fact that the first onset of the instability of the flow is of the vortex mode for inclination angles γ larger than about 17 deg, an accurate analysis of the vortex instability of the flow for inclination angles 0 deg $< \gamma \leq$ 90 deg from the vertical or 0 deg $\leq \phi <$ 90 deg from the horizontal, without approximation in the main flow, is warranted. This has motivated the present study.

In the present investigation, attention is focused on the analysis of vortex instability of free convection flow over inclined, upward-facing heated plates for angles of inclination from the horizontal, ϕ, that range from 0 to close to 90 deg. This is in constrast to the previous analyses [3-6] that are generally valid only for $\phi \geq 45$ deg. Thus, the present study covers the range of angles $0 \leq \phi \leq 45$ deg that are close to the horizontal in which no reliable stability results are available in the literature. In the main flow analysis, both the streamwise and normal components of the buoyancy force are retained in the momentum equations. The governing conservation equations are transformed such that the nonsimilarity parameter $\xi(x)$ varies with the streamwise coordinate x to a positive power and depends also on the angle of inclination from the horizontal, ϕ. The resulting system of equations is then solved by an efficient finite-difference method. This approach is different from other mainflow analyses that are based on either a perturbation solution from the vertical plate

Contributed by the Heat Transfer Division and presented at the 20th ASME/AIChE National Heat Transfer Conference, Milwaukee, Wisconsin, August 2-5, 1981. Manuscript received by the Heat Transfer Division August 31, 1981.

(see, for example, [13]) or a perturbation solution from the horizontal plate [14]. It also differs from the recent analysis of Hasan and Eichhorn [15] for inclination from the vertical. The stability analysis is based on the linear theory. The eigenvalue problem consisting of the coupled differential equations for the velocity and temperature disturbance amplitude functions, along with their boundary conditions, is solved by Runge-Kutta integration scheme in conjunction with Newton-Raphson interation technique.

Numerical results of interest, such as the local wall shear stress, the local Nusselt number, and the critical Grashof number, are presented for fluids having Prandtl numbers of 0.7 (such as air) and 7.0 (such as water) for angle of inclination ϕ ranging from 0 to 80 deg from the horizontal. The present results are also compared with available wave and vortex instability results in the literature.

Analysis

The Main Flow and Thermal Fields. Before proceeding to the vortex instability problem, attention is directed to a new analysis of the main flow and thermal fields. Consider an inclined flat plate which makes an acute angle ϕ from the horizontal, with its heated surface facing upward in a quiescent fluid at temperature, T_∞. The heated surface of the plate is maintained at a uniform temperature, T_w. The physical coordinates are chosen such that x is measured from the leading edge of the plate and y is measured normal to the plate. Under the assumption of constant fluid properties, along with application of the Boussinesq approximation, the governing conservation equations for the laminar boundary layer flow problem under consideration can be written as

$$\frac{\partial U}{\partial x}+\frac{\partial V}{\partial y}=0 \tag{1}$$

$$U\frac{\partial U}{\partial x}+V\frac{\partial U}{\partial y}=-\frac{1}{\rho}\frac{\partial P}{\partial x}+g\beta\sin\phi(T-T_\infty)+\nu\frac{\partial^2 U}{\partial y^2} \tag{2}$$

$$0=-\frac{1}{\rho}\frac{\partial P}{\partial y}+g\beta\cos\phi(T-T_\infty) \tag{3}$$

$$U\frac{\partial T}{\partial x}+V\frac{\partial T}{\partial y}=\kappa\frac{\partial^2 T}{\partial y^2} \tag{4}$$

where P is the difference between the static pressure and the hydrostatic pressure (i.e., $P=0$ outside the boundary layer) and the other conventional notations are defined in the Nomenclature. The streamwise pressure gradient induced by the buoyancy force can be related to the temperature difference through equation (3) as

$$-\frac{1}{\rho}\frac{\partial P}{\partial x}=g\beta\cos\phi\frac{\partial}{\partial x}\int_y^\infty(T-T_\infty)dy \tag{5}$$

The boundary conditions for equations (1–4) are

$$U=V=0, T=T_w \text{ at } y=0$$
$$U\to 0, T\to T_\infty \text{ as } y\to\infty \tag{6}$$

Equations (1), (2) with (5), and (4) can be transformed from the (x,y) coordinates to the dimensionless coordinates $(\xi(x), \eta(x,y))$ by introducing a pseudo-similarity variable η and an x-dependent nonsimilar parameter ξ as

$$\eta=\frac{y}{x}\left(\frac{Gr_x\cos\phi}{5}\right)^{1/5}, \xi=\xi(x) \tag{7}$$

along with a reduced stream function $f(\xi,\eta)$ and a dimensionless temperature $\theta(\xi,\eta)$ defind, respectively, by

$$f(\xi,\eta)=\psi(x,y)\Big/5\nu\left(\frac{Gr_x\cos\phi}{5}\right)^{1/5}, \theta(\xi,\eta)=\frac{T-T_\infty}{T_w-T_\infty} \tag{8}$$

The stream function $\psi(x,y)$ satisfies the continuity equation (1) with $U=\partial\psi/\partial y$, $V=-\partial\psi/\partial x$, and $\mathrm{Gr}_x=g\beta(T_w-T_\infty)x^3/\nu^2$ is the local Grashof number.

By introducing equations (7) and (8) into equations (2) with (5), (4), and (6), one can arrive at the following system of equations:

Nomenclature

D^n = $d^n/d\eta^n$, differential operator
f = $\psi(x,y)/[5\nu(\mathrm{Gr}_x\cos\phi/5)^{1/5}]$, reduced stream function
g = gravitational acceleration
Gr_x = $g\beta(T_w-T_\infty)x^3/\nu^2$, local Grashof number
L = x, characteristic length
Nu_x = local Nusselt number
p' = perturbation pressure
P = mainflow pressure
Pr = Prandtl number
t = dimensionless amplitude function of temperature disturbance
t' = perturbation temperature
T = mainflow temperature
u,v,w = dimensionless amplitude functions of velocity disturbances
u',v',w' = axial, normal, and spanwise components of velocity disturbances
U,V = axial and normal velocity components of mainflow
x,y,z = axial, normal, and spanwise coordinates
$Y=\eta, Z$ = dimensionless normal and spanwise coordinates

Greek Symbols

α = $2\pi/\lambda$, dimensionless wavenumber of disturbances
β = coefficient of thermal expansion
γ = angle of inclination from the vertical
δ = boundary layer thickness
η = $(y/x)(\mathrm{Gr}_x\cos\phi/5)^{1/5}$, pseudo-similarity variable
θ = $(T-T_\infty)/(T_w-T\infty)$, dimensionless temperature
κ = thermal diffusivity of fluid
λ = dimensionless wave length
ν = kinematic viscosity of fluid
ξ = $(\mathrm{Gr}_x\cos\phi/5)^{1/5}\tan\phi$, buoyancy force and inclination parameter
ρ = density of fluid
τ = local shear stress
ϕ = angle of inclination from the horizontal
ψ = stream function

Superscripts

$+$ = dimensionless disturbance quantity
$*$ = critical condition
$\hat{}$ = resultant quantity

Subscripts

w = condition at wall
∞ = condition at free stream

$$f''' + 3ff'' - (f')^2 + \frac{2}{5}\left(\eta\theta + \int_\eta^\infty \theta d\eta + \frac{3}{2}\xi\int_\eta^\infty \frac{\partial\theta}{\partial\xi}d\eta\right) + \xi\theta$$
$$= 3\xi\left(f'\frac{\partial f'}{\partial\xi} - f''\frac{\partial f}{\partial\xi}\right) \quad (9)$$

$$\frac{1}{\mathrm{Pr}}\theta'' + 3f\theta' = 3\xi\left(f'\frac{\partial\theta}{\partial\xi} - \theta'\frac{\partial f}{\partial\xi}\right) \quad (10)$$

with the boundary conditions

$$f(\xi,0) = f'(\xi,0) = 0, \theta(\xi,0) = 1; f'(\xi,\infty) = \theta(\xi,\infty) = 0 \quad (11)$$

In the foregoing equations, the primes denote partial differentiation with respect to η and ξ is found to have the expression

$$\xi = \left(\frac{Gr_x\cos\phi}{5}\right)^{1/5}\tan\phi \quad (12)$$

Equations (9–11) are valid for all angles except $\phi = \pi/2$ (i.e., a vertical flat plate) because $\xi \to \infty$ as $\phi \to \pi/2$. They reduce to those equations for free convection flow over a horizontal flat plate [14] when $\xi = 0$ (i.e., when $\phi = 0$). The problem of a vertical plate can be found in the classical study of Ostrach [16]. The recent analysis of the main flow by Hasan and Eichhorn [15] for inclination from the vertical is good for $\phi = \pi/2$ and smaller, but it is not accurate for small values of ϕ and fails at $\phi = 0$ deg. Their main flow solution is therefore not suitable for use in the flow instability analysis when the angle ϕ is small (say, 0 deg $\leq \phi <$ 45 deg), as is encountered in the present study. The present main flow analysis thus has advantage over all other previous treatments of the inclined plate problem in free convection.

Equations (9–11) were solved by an efficient finite-difference method to provide the main flow quantities that are needed in the stability calculations and to provide other physical quantities, such as the local Nusselt number Nu_x and the local wall shear stress τ_w. The last two quantities are defined by

$$\mathrm{Nu}_x = \frac{-k(\partial T/\partial y)_{y=0}}{T_w - T_\infty}\frac{x}{k}, \tau_w = \mu\frac{\partial U}{\partial y}\bigg|_{y=0} \quad (13)$$

In terms of the dimensionless variables, equation (13) can be reduced to

$$\mathrm{Nu}_x\left(\frac{\mathrm{Gr}_x\cos\phi}{5}\right)^{-1/5} = -\theta'(\xi,0),$$
$$\tau_w\frac{x^2}{5\mu\nu}\left(\frac{\mathrm{Gr}_x\cos\phi}{5}\right)^{-3/5} = f''(\xi,0) \quad (14)$$

Formulation of the Stability Problem. The derivation of the governing equations for the disturbances is based on linear stability theory. By confining attention to neutral stability, the disturbance quantities u', v', w', p', and t' may be assumed to be independent of x because of their weak x-dependence under this condition. In addition, it is known from experiments [1] that the secondary flow vortex rolls are unchanging with time and periodic in the spanwise coordinate. Thus, the disturbances are taken to be functions of (y,z). These disturbance quantities are superimposed on the two-dimensional main flow quantities $U, V, W = 0$, P and T to obtain the resultant quantities $\hat{u}, \hat{v}, \hat{w}, \hat{p}$ and $\hat{t}$ as

$$\begin{aligned} \hat{u} &= U(x,y) + u'(y,z) \\ \hat{v} &= V(x,y) + v'(y,z) \\ \hat{w} &= w'(y,z) \\ \hat{p} &= P(x,y) + p'(y,z) \\ \hat{t} &= T(x,y) + t'(y,z) \end{aligned} \quad (15)$$

It is noted here that the x-dependence of the disturbance amplitude functions needs to be taken into account if the higher-order effects from the boundary layer growth on the disturbances are to be included in the analysis (see, for example, [17–21]).

The resultant quantities given by equation (15) satisfy the continuity equation, the Navier-Stokes equations, and the energy equation for an incompressible, three-dimensional steady fluid flow. Substituting equation (15) into these equations, subtracting the two-dimensional main flow, and linearizing the disturbance quantities, one arrives at the following equations for the disturbances:

$$\frac{\partial v'}{\partial y} + \frac{\partial w'}{\partial z} = 0 \quad (16)$$

$$u'\frac{\partial U}{\partial x} + v'\frac{\partial U}{\partial y} + V\frac{\partial u'}{\partial y} = g\beta\sin\phi t' + \nu\left(\frac{\partial^2 u'}{\partial y^2} + \frac{\partial^2 u'}{\partial z^2}\right) \quad (17)$$

$$u'\frac{\partial V}{\partial x} + v'\frac{\partial V}{\partial y} + V\frac{\partial v'}{\partial y} = -\frac{1}{\rho}\frac{\partial p'}{\partial y} + g\beta\cos\phi t' + \nu\left(\frac{\partial^2 v'}{\partial y^2} + \frac{\partial^2 v'}{\partial z^2}\right) \quad (18)$$

$$V\frac{\partial w'}{\partial y} = -\frac{1}{\rho}\frac{\partial p'}{\partial z} + \nu\left(\frac{\partial^2 w'}{\partial y^2} + \frac{\partial^2 w'}{\partial z^2}\right) \quad (19)$$

$$u'\frac{\partial T}{\partial x} + v'\frac{\partial T}{\partial y} + V\frac{\partial t'}{\partial y} = \kappa\left(\frac{\partial^2 t'}{\partial y^2} + \frac{\partial^2 t'}{\partial z^2}\right) \quad (20)$$

Next, after eliminating the pressure terms between equations (18) and (19) by cross differention, the above system of equations (16–20) is nondimensionalized by introducing the following dimensionless quantities

$$Y = \frac{y}{L}\left(\frac{\mathrm{Gr}_L\cos\phi}{5}\right)^{1/5}, Z = \frac{z}{L}\left(\frac{\mathrm{Gr}_L\cos\phi}{5}\right)^{1/5} \quad (21)$$

$$u^+ = \frac{u'}{\frac{\kappa}{L}\left(\frac{\mathrm{Gr}_L\cos\phi}{5}\right)^{2/5}}, v^+ = \frac{v'}{\frac{\kappa}{L}\left(\frac{\mathrm{Gr}_L\cos\phi}{5}\right)^{1/5}},$$
$$w^+ = \frac{w'}{\frac{\kappa}{L}\left(\frac{\mathrm{Gr}_L\cos\phi}{5}\right)^{1/5}}, t^+ = \frac{t'}{T_w - T_\infty} \quad (22)$$

in which $\mathrm{Gr}_L = g\beta(T_w - T_\infty)L^3/\nu^2$ is the Grashof number based on a characteristic length $L(x)$ defined by $L = x$, such that $Y = \eta$ and $\mathrm{Gr}_L = \mathrm{Gr}_x$. In addition, the main flow quantities, such as $\partial U/\partial x$, $\partial U/\partial y$, V, $\partial V/\partial x$, $\partial v/\partial y$, $\partial T/\partial x$, and $\partial T/\partial y$, are expressed in terms of $f(\xi,\eta)$, $\theta(\xi,\eta)$ and their derivatives. The resulting dimensionless disturbance equations are further simplified by letting

$$u^+ = u(Y)e^{i\alpha Z}, v^+ = v(Y)e^{i\alpha Z},$$
$$w^+ = w(Y)e^{i\alpha Z}, t^+ = t(Y)e^{i\alpha Z} \quad (23)$$

where α is the dimensionless wave number of the disturbances. That is, the stationary longitudinal vortex rolls are taken to be periodic in the spanwise Z-direction, with amplitude functions depending only on Y. The result of the aforementioned operation leads to the following system of equations for the disturbance amplitude functions:

$$[(D^2 - \alpha^2) - B_1 D + B_2]u = B_3 v - 5\mathrm{Pr}(\mathrm{Gr}_x\cos\phi/5)^{1/5}\tan\phi t \quad (24)$$

$$[(D^2 - \alpha^2)^2 - B_1 D(D^2 - \alpha^2) - B_2(D^2 - \alpha^2)]v = B_4\alpha^2 u + 5\alpha^2\mathrm{Pr}(\mathrm{Gr}_x\cos\phi/5)^{2/5}t \quad (25)$$

$$[(D^2 - \alpha^2) - B_1\mathrm{Pr}D]t = B_5 u + B_6 v \quad (26)$$

with the boundary conditions

$$u=v=Dv=t=0 \text{ at } \eta=0 \text{ and } \eta=\infty \tag{27}$$

In equations (24–27), D^n stands for $d^n/d\eta^n$ and the boundary conditions, equation (27), arise from the fact that the disturbances vanish at the wall and in the free stream. The condition $Dv=0$ results from the continuity equation $\partial v^+/\partial Y+\partial w^+/\partial Z=0$ along with $w^+=0$ at $\eta=0$ and $\eta=\infty$. The coefficients $B_1(\xi,\eta)$ through $B_6(\xi,\eta)$ in the equations have the expressions

$$B_1=2\eta f'-3f-3\xi\partial f/\partial\xi \tag{28}$$

$$B_2=2\eta f''-f'-3\xi\partial f'/\partial\xi \tag{29}$$

$$B_3=5f'' \tag{30}$$

$$B_4=\frac{1}{5}(4\eta^2 f''+2\eta f'-6f-12\xi\eta\partial f'/\partial\xi + 12\xi\partial f/\partial\xi+9\xi^2\partial^2 f/\partial\xi^2) \tag{31}$$

$$B_5=-\frac{1}{5}(2\eta\theta'-3\xi\partial\theta/\partial\xi) \tag{32}$$

$$B_6=\theta' \tag{33}$$

The system of equations consisting of the three coupled differential equations, equations (24–26), along with their boundary conditions, equation (27), constitutes an eigenvalue problem of the form

$$E(\mathrm{Gr}_x,\alpha;\mathrm{Pr},\phi)=0 \tag{34}$$

In determining the neutral stability curve for a given Prandtl number, Pr, and a given angle of inclination, ϕ, the value of α satisfying equation (34) is sought as the eigenvalue for a prescribed value of Gr_x.

Numerical Method of Solutions

The system of equations for the main flow and thermal fields, equations (9–11), was solved by a finite-difference scheme similar to, but modified from that described in [22] to provide the main flow quantities $B_1(\xi,\eta)$ to $B_6(\xi,\eta)$ that are needed in the stability computations as well as the local Nusselt number and the wall shear stress. The details of the finite-difference method of solution are omitted here. The stability problem, equations (24–27), was solved by a fourth-order Runge-Kutta numerical integration scheme. The integration of the equations was started from $\eta=\infty$ to $\eta=0$ (at the wall). Thus, to proceed with the numerical integration, the boundary conditions at $\eta=\infty$ needed to be approximated by the asymptotic solutions of equations (24–26) at $\eta=\eta_\infty$ (i.e., at the edge of the boundary layer). The asymptotic solutions for u,v, and t at $\eta=\eta_\infty$ and the procedure for the numerical solution of the eigenvalue problem parallel those described in [23] and are therefore not repeated here. It suffices to mention the highlights of the eigenvalue problem. With a preassigned value of $\xi=(\mathrm{Gr}_x\cos\phi/5)^{1/5}\tan\phi$, the main flow solution is first obtained for a fixed Prandtl number, Pr. Next, with the inclination angle ϕ specified, the parameter $\mathrm{Gr}_x\cos\phi/5=(\xi/\tan\phi)^5$ is known and equations (24–26) are numerically integrated from $\eta=\eta_\infty$ to $\eta=0$, starting with the asymptotic solutions for u, v, and t at η_∞. The remaining eigenvalue α is then determined by the Newton-Raphson differential-correction iterative scheme until the boundary conditions at the wall ($\eta=0$) are satisfied within a certain specified tolerance [23]. This yields a converged value of α for given values of Pr, ϕ, and Gr_x.

In the main flow solutions by the finite-difference method, variable step sizes were used in the ξ-direction. The step size was increased gradually with increasing ξ and ranged from $\Delta\xi=0.05$ for $0\le\xi\le0.5$ to $\Delta\xi=2.0$ for $\xi\ge40$. The use of the varying step sizes in $\Delta\xi$ cut down computation time considerably without sacrifice in the accuracy of the numerical results. A step size of $\Delta\eta=0.02$ was used in the main flow calculations, whereas in the stability calculations, $\Delta\eta$ was taken to be 0.04. In addition, values of $\eta_\infty=10$ and 6, respectively, for Pr = 0.7 and 7 were found to be sufficient in both the main flow and stability calculations.

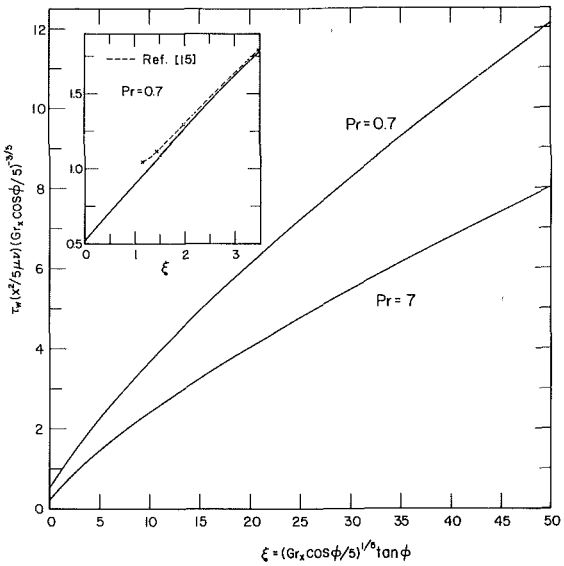

Fig. 1 Local wall shear stress results, Pr = 0.7 and 7

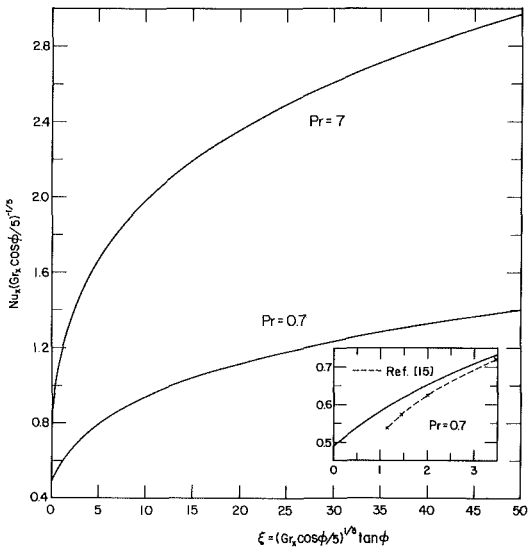

Fig. 2 Local Nusselt number results, Pr = 0.7 and 7

Results and Discussion

The local wall shear stress in terms of $\tau_w(x^2/5\mu\nu)/(Gr_x\cos\phi/5)^{3/5}$ and the local Nusselt number in terms of $\mathrm{Nu}_x/(\mathrm{Gr}_x\cos\phi/5)^{1/5}$ as a function of $\xi=(\mathrm{Gr}_x\cos\phi/5)^{1/5}\tan\phi$ are shown, respectively, in Figs. 1 and 2 for both Pr = 0.7 and 7. As can be seen from the figures, both the wall shear stress and the local Nusselt number increase with increasing value of ξ; that is, these two quantities increase with increasing inclination angle, ϕ, for a given Grashof number Gr_x or increase with increasing value of Gr_x for a given angle, ϕ. This behavior can be best observed from a log-log plot such as Fig. 3, which shows the variation of Nu_x with Gr_x at various angles of inclination, ϕ. The lines for $\phi=0$ deg (the horizontal plate) in this figure are given by $\mathrm{Nu}_x(\mathrm{Gr}_x/5)^{-1/5}=0.4891$ for

$Pr = 0.7$ and 0.8592 for $Pr = 7$. For the case of vertical plate ($\phi = 90$ deg), separate calculations were performed to obtain $Nu_x(Gr_x/4)^{-1/4} = 0.4995$ for $Pr = 0.7$ and 1.0538 for $Pr = 7$. These latter results provide Nu_x versus Gr_x curves that essentially coincide with those lines for $\phi = 75$ deg and, to keep clarity of the figure, they are not illustrated. The trend exhibited in Fig. 3 is to be expected physically, because as the plate is tilted from the horizontal toward the vertical orientation (i.e., as ϕ increase from 0 deg), the buoyancy force becomes more pronounced, and the stronger the buoyancy force the larger the wall shear stress and hence the surface heat-transfer rate. Figures 1–3 also reveal that while the local shear stress is higher for $Pr = 0.7$ than for $Pr = 7$, the local Nusselt number is higher for $Pr = 7$. This is due to the fact that a smaller Prandtl number gives rise to a larger velocity gradient at the wall and hence a higher wall shear stress, whereas a larger Prandtl number results in a larger wall temperature gradient and hence a larger heat-transfer rate.

The analysis of Hasan and Eichhorn [15] for inclination from the vertical fails at $\phi = 0$ deg (i.e., a horizontal plate), and their results for small values of ϕ (i.e., small values of ξ) are thus not accurate. This is demonstrated in the insets of Figs. 1 and 2 for $Pr = 0.7$, in which their results, shown with a dotted line, are seen to deviate further from the present results as ξ (i.e., ϕ) decreases to zero. The analysis of Pera and Gebhart [14] for slightly inclined plates (i.e., small angles, ϕ), on the other hand, is based on a perturbation solution from the horizontal plate. They presented results only for the values of $0 \leq \xi \leq 1.0$, which were found to be in excellent agreement with the present solution in that ξ range.

The neutral stability curves for $Pr = 0.7$ and 7 are plotted, respectively, in Figs. 4 and 5 for several representative values of the inclination angle ϕ ranging from 0 deg (i.e., a horizontal plate) to 75 deg. It is seen from the figures that as the angle, ϕ, increases from 0 deg, the neutral stability curve shifts right-upward, indicating a stabilization of the main flow to the vortex mode of instability at a larger wave number. Plotted with dotted lines in the figures for comparisons are the neutral stability curves that were obtained by using the approximate main flow solution without the streamwise pressure gradient term, as was done by Hwang and Cheng [3] and by Haaland and Sparrow [4]. As is expected, use of the approximate main flow solution provides stability results that deviate considerably from those in which the streamwise pressure gradient term was taken into account in the main flow. The deviation in the two sets of results is larger for $Pr = 0.7$ than for $Pr = 7$ and is seen to become more pronounced as ϕ decreases.

The critical Grashof number Gr_x^* and the critical wave number α^* can be found from the minima of the neutral stability curves. These critical values are listed in Table 1 for the various angles of inclination that were investigated and are also plotted with solid lines in Fig. 6 for both $Pr = 0.7$ and 7. These results cover the values of ξ from 0 to 80 for $Pr = 0.7$

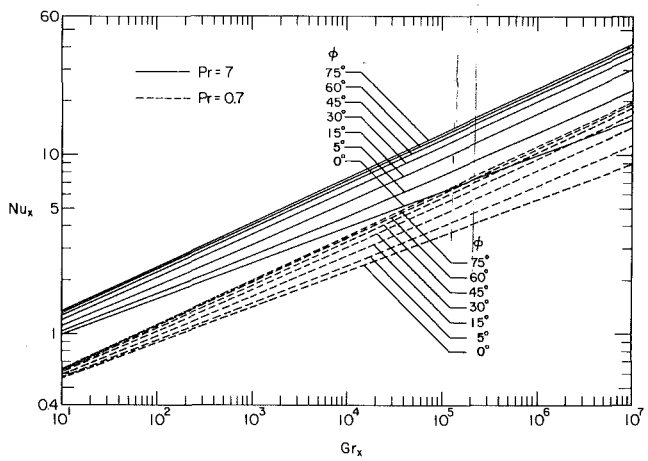

Fig. 3 Local Nusselt number versus local Grashof number for various angles of inclination, Pr = 0.7 and 7

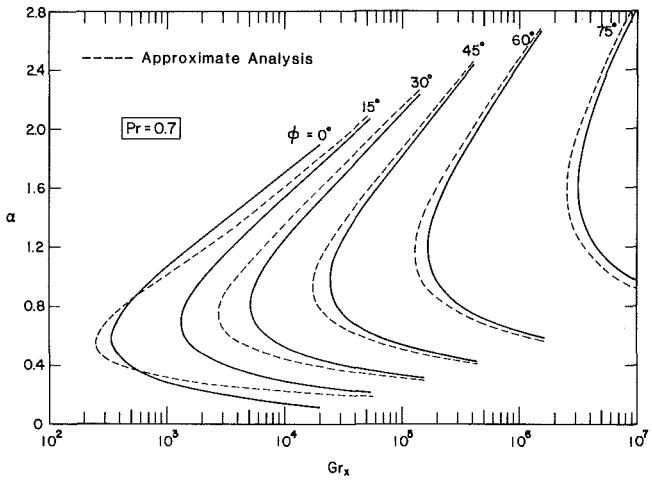

Fig. 4 Representative neutral stability curves, Pr = 0.7

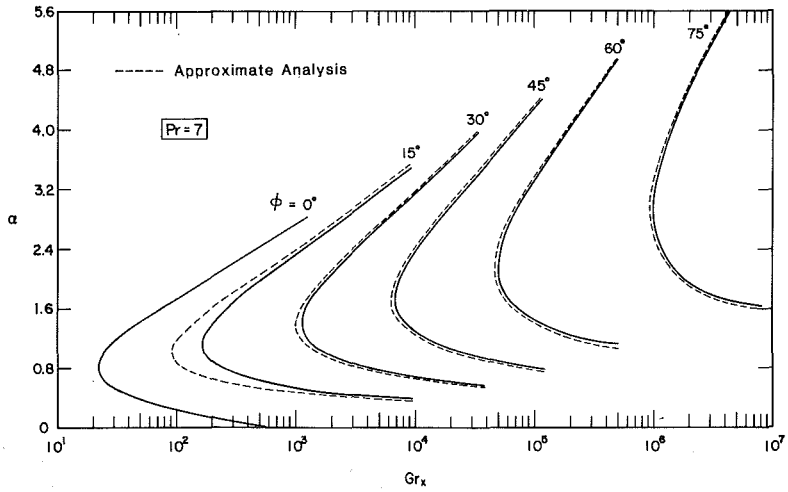

Fig. 5 Representative neutral stability curves, Pr = 7

Table 1 Critical Grashof and wave numbers for Pr = 0.7 and 7

	Pr = 0.7		Pr = 7	
ϕ	Gr_x^*	α^*	Gr_x^*	α^*
0°	340	0.583	22	0.825
10°	893	0.645	89	1.025
15°	1.32×10^3	0.682	168	1.116
30°	5.17×10^3	0.805	1.14×10^3	1.398
45°	2.45×10^4	0.965	6.82×10^3	1.725
60°	1.67×10^5	1.184	4.97×10^4	2.159
70°	9.49×10^5	1.428	2.90×10^5	2.579
75°	3.14×10^6	1.610	9.83×10^5	2.930
80°	1.63×10^7	1.900	5.03×10^6	3.458

and from 0 to 64 for Pr = 7 in the main flow solutions as ϕ was varied from 0 to 80 deg. Included in the figure for comparisons are two dotted lines from the present results that are based on the approximate main flow solution and the experimental results of Lloyd and Sparrow for water [2]. The approximate analysis yields the Gr_x^* versus ϕ relationship $[Gr_x \cos(\pi/2-\phi)/4]^{1/4} \tan(\pi/2-\phi) = 7.48$ for Pr = 0.7 and 5.83 for Pr = 7, which are in excellent agreement with the results of Haaland and Sparrow [4] for Pr = 0.733 and 6.7. As can be seen from Table 1 or Fig. 6, the critical Grashof number increases (with a corresponding increase in the critical wave number) as the angle of inclination increases. This implies that inclined free convection flow becomes more stable to the vortex mode of instability as the plate is tilted toward the vertical orientation. For a vertical plate, the critical Grashof number from the vortex mode of instability becomes infinity. This is because at the vertical orientation there is no buoyancy force component normal to the plate and hence the vortex instability of the flow does not take place. Inspection of Fig. 6 also reveals that a fluid with Pr = 7 (such as water) is more susceptible to the vortex mode of instability than does a fluid with Pr = 0.7 (such as air). It is also seen from the figure that the critical Grashof numbers for Pr = 7 from the analysis are about two to three orders of magnitude lower than the experimental results for water with Pr = 5.5 [2]. This discrepancy in the results between theory and experiment is attributable to the fact that natural disturbances in boundary layer flow need to amplify before they can be detected, whereas the analysis is based on the linear theory in which the disturbances are considered to be infinitesimally small.

The stability results based on the approximate main flow solution show considerably good agreement with those without the approximation for $\phi \geq 50$ deg when Pr = 0.7 and $\phi \geq 30$ deg when Pr = 7. However, for smaller angles, a rapid deviation between the two sets of results is seen to take place as ϕ approaches 0 deg. When ϕ is small, the streamwise pressure gradient term in the main flow, which results from the normal component of the buoyancy force, becomes significant and can no longer be neglected. As a result, the use of an approximate main flow solution without the streamwise pressure gradient term leads to considerable errors in the stability results. From a comparison between the two sets of results, it can be deduced that the streamwise pressure gradient term has a stabilizing effect of the flow. This is due to an increase in the flow velocity near the wall as a result of the existence of a favorable pressire gradient in the flow. In contrast to previous studies on the vortex instability of free convection flow over inclined plates, which have provided critical stability results for inclination angles close to the vertical, the present study has predicted critical stability results that cover the inclination angles form the horizontal to essentially the vertical.

It is interesting to compare the present vortex instability results with available wave instability results in the literature [7, 11]. Such a comparison is also made in Fig. 6. The analytical wave instability results of Haaland and Sparrow [7]

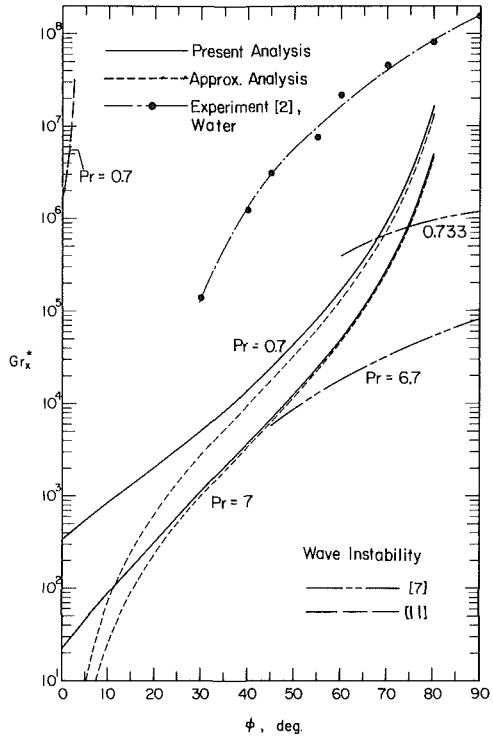

Fig. 6 Critical Grashof number versus angle of inclination, Pr = 0.7 and 7

for 45 deg $\leq \phi \leq$ 90 deg, with the heated surface facing upward, show that inclined free convection flow becomes more stable to the wave mode of disturbances as the angle of inclination from the horizontal, ϕ, increases, attaining the maximum critical Grashof numbers of 1.2×10^6 and 8.3×10^4, respectively, for Pr = 0.733 and 6.7 when the plate is vertical (i.e., when $\phi = 90$ deg). In addition, a comparison between the vortex and wave instability results from the linear theory indicates that as the angle, ϕ, increases a crossover in the onset of the flow instability from the vortex mode to the wave mode takes place at an angle ϕ of about 68 deg for Pr = 0.7 and about 40 deg for Pr = 7. Thus, the predicted first onset of the instability of the flow is of the vortex mode when $\phi < 68$ deg for Pr = 0.7 and when $\phi < 40$ deg for Pr = 7, whereas the first instability is of the wave mode when $\phi > 68$ deg and $\phi > 40$ deg, respectively, for Pr = 0.7 and 7. The wave instability analysis of Pera and Gebhart [11] for horizontal ($\phi = 0$ deg) and slightly inclined plates, on the other hand, predicts critical Grashof numbers that are much larger than the critical Grashof number for $\phi = 90$ deg. For Pr = 0.7, their results yield, for example, $5\,(Gr_x^* \cos\phi/5)^{1/5}$ of about 64 for $\xi = 0$, 86 for $\xi = 0.5$, and 114 for $\xi = 1.0$, which correspond respectively to Gr_x^* of about 1.7×10^6 for $\phi = 0$ deg, 7.5×10^6 for $\phi = 1.67$ deg, and 3.1×10^7 for $\phi = 2.51$ deg. The existence of a large discrepancy in the Gr_x^* results between the two wave instability analyses [7, 11] for 0 deg $\leq \phi \leq$ 2.5 deg and 45 deg $\leq \phi \leq$ 90 deg is very surprising. The cause for this

discrepancy warrants further investigations. At $\phi = 0$ deg, the vortex mode of instability predicts $Gr_x^* = 340$ for $Pr = 0.7$, which is very low compared to the Gr_x^* value of 1.7×10^6 from the wave mode of instability [11]. Thus, it is evident that for free convection flow over a horizontal plate, the vortex mode of instability will take place long before the wave mode of instability sets in; that is, the first onset of instability for such a flow configuration is due to the vortex mode of disturbances.

Conclusions

In studying the vortex instability of laminar free convection flow over inclined surfaces, a new analysis of the main flow and thermal fields has been undertaken. It has been found that the flow becomes less susceptible to the vortex mode of instability as the angle of inclination, ϕ, increases from the horizontal, with a minimum critical Grashof number occuring at $\phi = 0$ deg and a maximum critical Grashof number of infinity at $\phi = 90$ deg. A comparison with the results from the wave mode of instability has revealed that inclined free convection flow is more susceptible to the vortex mode of instability at small angles of inclination from the horizontal, but becomes more susceptible to the wave mode of instability at inclination angles near the vertical.

Acknowledgment

The present study was supported in part by grants from the National Science Foundation (NSF ENG 75-15033 A01 and NSF CME 79-19459).

References

1 Sparrow, E. M., and Husar, R. B., "Longitudinal Vortices in Natural Convection Flow on Inclined Surfaces," *Journal of Fluid Mechanics*, Vol. 37, 1969, pp. 251–255.

2 Lloyd, J. R., and Sparrow, E. M., "On the Instability of Natural Convection Flow on Inclined Plates," *Journal of Fluid Mechanics*, Vol. 42, 1970, pp. 465–470.

3 Hwang, G. J., and Cheng, K. C., "Thermal Instability of Laminar Natural Convection Flow on Inclined Isothermal Plates," *Canadian Journal of Chemical Engineering*, Vol. 51, 1973, pp. 659–666.

4 Haaland, S. E., and Sparrow, E. M., "Vortex Instability of Natural Convection Flow on Inclined Surfaces," *International Journal of Heat and Mass Transfer*, Vol. 16, 1973, pp. 2355–2367.

5 Kahawita, R. A., and Meroney, R. N., "The Vortex Mode of Instability in Natural Convection Flow Along Inclined Plates," *International Journal of Heat and Mass Transfer*, Vol. 17, 1974, pp. 541–548.

6 Iyer, P. A., and Kelly, R. E., "The Stability of the Laminar Free Convection Flow Induced by a Heated Inclined Plate," *International Journal of Heat and Mass Transfer*, Vol. 17, 1974, pp. 517–525.

7 Haaland, S. E., and Sparrow, E. M., "Wave Instability of Natural Convection on Inclined Surfaces Accounting for Nonparallelism of the Basic Flow," ASME JOURNAL OF HEAT TRANSFER, Series C, Vol. 96, 1973, pp. 405–407.

8 Lock, G. S. H., Gort, C., and Pond, G. R., "A Study of Instability in Free Convection from an Inclined Plate," *Applied Scientific Research*, Vol. 18, 1967, pp. 171–182.

9 Tritton, D. J., "Transition to Turbulence in the Free Convection Boundary Layers on an Inclined Heated Plate," *Journal of Fluid Mechanics*, Vol. 16, 1963, pp. 417–435.

10 Lloyd, J. R., "Vortex Wavelength in the Transition Flow Adjacent to Upward Facing Inclined Isothermal Surfaces," *Proceedings of the 5th International Heat Transfer Conference*, Vol. III, Paper No. NC 1.8, 1974, pp. 34–37.

11 Pera, L., and Gebhart, B., "On the Stability of Natural Convection Boundary Layer Flow over Horizontal and Slightly Inclined Surfaces," *International Journal of Heat and Mass Transfer*, Vol. 16, 1973, pp. 1147–1163.

12 Shaukatullah, H., and Gebhart, B., "An Experimental Investigation of Natural Convection Flow on an Inclined Surface," *International Journal of Heat and Mass Transfer*, Vol. 21, 1978, pp. 1481–1490.

13 Kierkus, W. T., "An Analysis of Laminar Free Convection Flow and Heat Transfer About an Inclined Isothermal Plate," *International Journal of Heat and Mass Transfer*, Vol. 11, 1968, pp. 241–253.

14 Pera, L., and Gebhart, B., "Natural Convection Boundary Layer Flow over Horizontal and Slightly Inclined Surfaces," *International Journal of Heat and Mass Transfer*, Vol. 16, 1973, pp. 1131–1146.

15 Hasan, M. M., and Eichhorn, R., "Local Nonsimilarity Solution of Free Convection Flow and Heat Transfer from an Inclined Isothermal Plate," ASME JOURNAL OF HEAT TRANSFER, Series C, Vol. 101, 1979, pp. 642–647.

16 Ostrach, S., "An Analysis of Laminar Free-Convection Flow and Heat Transfer About a Flat Plate Parallel to the Direction of the Generating Body Force," *NACA*, TN 2635, 1952.

17 Gaster, M., "On the Effects of Boundary-Layer Growth on Flow Stability," *Journal of Fluid Mechanics*, Vol. 66, 1974, pp. 465–480.

18 Eagles, P. M., and Weissman, M. A., "On the Stability of Slowly Varying Flow: The Divergent Channel," *Journal of Fluid Mechanics*, Vol. 69, 1975, pp. 241–262.

19 Saric, W. S., and Nayfeh, A. H., "Nonparallel Stability of Boundary-Layer Flows," *Physics of Fluids*, Vol. 18, 1975, pp. 945–950.

20 Smith, F. T., "On the Non-parallel Flow Stability of the Blasius Boundary Layer," *Proceedings of the Royal Society of London*, Vol. 366 A, 1979, pp. 91–109.

21 Hsu, C. T., and Cheng, P., "Vortex Instability in Buoyancy-Induced Flow over Inclined Heated Surfaces in Porous Media," ASME JOURNAL OF HEAT TRANSFER, Vol. 101, Series C, 1979, pp. 660–665.

22 Cebeci, T., and Bradshaw, P., *Momentum Transfer in Boundary Layers*, ch. 7, Hemisphere Publishing Corp., Washington, D.C., 1977.

23 Moutsoglou, A., Chen, T. S., and Cheng, K. C., "Vortex Instability of Mixed Convection Flow over a Horizontal Flat Plate," ASME JOURNAL OF HEAT TRANSFER, Vol. 103, Series C, 1981, pp. 257–261.

Measurements and Calculations of Transient Natural Convection in Water

B. Sammakia

B. Gebhart
Fellow ASME

Department of Mechanical Engineering and Applied Mechanics, University of Pennsylvania, Philadelphia, Pa. 19104

Z. H. Qureshi

Department of Energy Engineering, University of Illinois, Chicago, Ill. 60680

Transient natural convection adjacent to a flat vertical surface with appreciable thermal capacity is investigated both experimentally and numerically. The surface is immersed in initially quiescent water, and has the same uniform temperature distribution. It is then suddenly loaded with a uniform and constant heat flux thereby generating a buoyancy induced flow adjacent to the surface. Surface temperature response was recorded by means of thermocouples embedded inside the surface, and boundary layer temperature measurements were also taken. An explicit finite difference numerical scheme is used to obtain solutions to the partial differential equations describing the conservation of mass, momentum, and energy in their time dependent form. Good agreement between the calculated and measured results is observed for both the heating and cooling transient processes.

Introduction

Studies of natural convection flows have been more concerned, in the past, with steady-state conditions. Meanwhile recent engineering developments have led to a increasing interest in accurate investigations of the transient process. Both the heating and cooling processes, by natural convection, have many technological applications. These applications include the cooling of the core of a nuclear reactor in the case of power or pump failures, and the warm up and cooling of electronic equipment.

This type of investigation was pioneered by Illingworth [1], who studied the simpler circumstance of transient natural convection adjacent to an infinite isothermal flat vertical surface. For such a geometry no leading edge exists and heat is transferred solely by conduction in a one-dimensional process. The results of this simplified analysis is particulary relevant, because at short times, all such transient processes are one-dimensional, even if a leading edge does exist. The one-dimensional process will last, at any downstream location, until the leading edge effect reaches that location, after which convection effects set in until the eventual steady-state is achieved.

Several other studies of one-dimensional conduction transients followed, dealing with different boundary conditions, such as surfaces where the temperature or heat flux are time varying [2, 3]. In [4], the effect of suction of the surface was considered, while [5] investigated the effect of including mass transfer. Although these one-dimensional studies are useful, they are only valid for a short period at the very start of the transient. Such analysis do not give any indication as to the duration of this one-dimensional process, which ends with the arrival of the leading edge effect.

Sugawara and Michiyoshi [6] presented the results of a numerical analysis for transients adjacent to a semi-infinite vertical flat surface. An estimate of the total time duration of the transient process was obtained. Siegel [7] used an integral method analysis to investigate a similar flow circumstance. He used the Karman-Polhausen method to solve the time dependant integral momentum and energy boundary layer equations. The time duration of the one-dimensional conduction regime, as well as the total transeint time were predicted. The boundary layer thickness was found to reach a maximum during the transient, and a minimum in the heat-transfer coefficient was reported. Some of these predictions were substantiated by the experimental observations of Klei [8] and Goldstein and Eckert [9].

Gebhart [10] presented the results of an integral method analysis, taking into account the effect of the surface thermal capacity. Measurements by Gebhart and Adams [11] showed close agreement with the analytical results. Goldstein and Briggs [12] presented the results of an analysis to predict the duration of the one-dimensional regime, for various heating boundary conditions. In [13] and [14], Gebhart and coworkers observed the propagation of the leading edge effect and related their measurements to the predictions of [12]. Brown and Riley [15] presented an analysis for the three stages of the transient process for an isothermal surface.

To obtain more detailed solutions the full boundary layer equations were solved by Hellums and Churchill [16] in their time-dependent, partial-differential form. Finite difference calculations were carried out for a semi-infinite isothermal surface. As in [7], [8], and [9], a minimum in the heat-transfer coefficient was found during the transient. Sammakia and Gebhart [17] and [18] report the results similar calculations for a surface of finite thermal capacity, suddenly heated by loading it with a uniform and constant heat flux. The effect of the magnitude of the surface thermal capacity was found to play a major role in determining the nature of the resulting transient. As predicted in [7], all the transients were found to start as a one-dimensional conduction process, to be terminated by the arrival of the leading edge effect. However the duration of the one-dimensional process was found to depend on the thermal capacity parameter $Q^* = c''(\nu^2 g\beta q''/k^5)^{1/4}$.

In the present study the results of an experimental investigation of transients in water are reported. The surface was heated by suddenly loading it with a uniform and constant flux. The surface thermal capacity was relatively small, resulting in a transient dominated by the one-dimensional conduction process. Surface and boundary layer temperature measurements show good agreement with the results of the numerical analysis. The analysis is extended to include the cooling transients, when the energy input suddenly ceases.

Apparatus

A vertical surface dissipating a uniform and constant heat flux was used to generate a buoyancy induced flow in water. The surface assembly consists of two 0.00127-cm thick, 130.5-cm long, and 46.6-cm wide inconel-600 foils, separated by teflon layers. Embedded in the teflon layers were several 127-micron, copper-constantan thermocouples, placed at different locations along the vertical center line of the surface. The

Contributed by the Heat Transfer Division for publication in the JOURNAL OF HEAT TRANSFER. Manuscript received by the Heat Transfer Division November 2, 1981.

teflon and foil had been previously fused together by heating them under high pressure. The surface was then stretched vertically between two stainless steel knife edges. The whole assembly was supported by a stainless steel frame, placed in a 1.83 m × 0.622 m × 1.83 m high tank made of stainless steel. The surface was positioned vertically using a plumb line, and it's leading edge was kept at a distance of 20 cm from the bottom of the tank. The tank was insulated by surrounding it with layers of polyurethane and fiberglass insulation, while a polyurethane raft, coated with teflon sheets, floated on the surface of the water. The tank was filled with highly purified water, of approximately 1.5 MΩ-cm resistivity, to reduce electrical leakage to the water. After the water was filtered and demineralized it was deaerated by passing it through a vacuum chamber at 63-cm Hg vacuum, before putting it into the tank. To avoid contamination of the water, only stainless steel and teflon were allowed to come in contact with it.

The plate resistance was measured by connecting it in series to a precise resistor and passing a trickle current through it. The voltage thus measured gave the plate resistance. A Hewlett Packard 6475C-d.c. power supply was used as an energy source to heat up the surface. The surface heat flux was calculated from the measurements of the voltage drop across the foil and the current flowing through an accurate resistor connected in series to the surface.

Temperature measurements in the boundary layer were made by a 0.0127-mm dia chromel-alumel thermocouple, attached to a manual sliding traverse mechanism. Due to the importance of the accurate positioning of the probe from the surface, the location of the surface was determined by the completion of a resistance circuit composed of the surface itself, and two stainless steel capillary tubes adjacent to and parallel to the probe.

Before starting any experimental run, the tank water was thoroughly stirred to insure temperature uniformity. After stirring, about 90 min would be allowed for any circulation to dampen out before the experimental run was performed. Before loading the current onto the surface, the current was initially loaded on a dummy load of approximately the same resistance as the actual surface, and connected in parallel to the surface. To start the experimental runs, the current was suddenly switched from the dummy load to the surface. This insured that no surges would occur due to suddenly switching on the power supply.

Analysis

The equations governing the conservation of mass, momentum, and energy for natural convection flows adjacent to a flat, vertical surface are given below. The surface is of finite thickness and possesses an appreciable thermal capacity. It is initially immersed in a quiescent fluid at uniform temperature, and then suddenly subjected to a sudden constant energy input uniformly distributed over the entire surface element. The equations are given in non-dimensional form, and the boundary-layer type and Boussinesq approximations have been made, see [17].

$$\frac{\partial U}{\partial X}+\frac{\partial V}{\partial Y}=0 \tag{1}$$

$$\frac{\partial U}{\partial \tau}+U\frac{\partial U}{\partial X}+V\frac{\partial U}{\partial Y}=T+\frac{\partial^2 U}{\partial Y^2} \tag{2}$$

$$\frac{\partial T}{\partial \tau}+U\frac{\partial T}{\partial X}+V\frac{\partial T}{\partial Y}=\frac{1}{\mathrm{Pr}}\frac{\partial^2 T}{\partial Y^2} \tag{3}$$

where the nondimensional quantities are

$$T=\frac{t-t_\infty}{(\nu^2 q''^3/g\beta k^3)^{1/4}}=\frac{t-t_\infty}{\frac{q''x}{k}}(\mathrm{Gr}_x^*)^{1/4};$$

$$\tau=\frac{\bar{\tau}}{(k/g\beta q'')^{1/2}}=\frac{\alpha\bar{\tau}}{x^2}\,\mathrm{Pr}\,(\mathrm{Gr}_x^*)^{1/2}$$

Nomenclature

c_p = specific heat of the fluid
c'' = thermal capacity of element per unit surface area
g = acceleration of gravity
Gr* = modified Grashof number, $\frac{g\beta q'' x^4}{k\nu^2}$, dimensionless
G^* = $5\left[\frac{g\beta q'' x^4}{5K\nu^2}\right]^{1/5}$, dimensionless
k = thermal conductivity
L = height of plate
Pr = Prandtl number
q'' = instantaneous energy generation rate per unit of element surface area
Q^* = thermal capacity parameter related to the element storage capacity, $c''\left[\frac{g\beta q''\nu^2}{k^5}\right]^{1/4}$, dimensionless
t = static temperature
t_0 = instantaneous local plate temperature
t_∞ = temperature of the undisturbed fluid
T = nondimensional temperature, $\frac{(t-t_\infty)}{\left(\frac{\nu^2 q''^3}{g\beta k^3}\right)^{1/4}}$
u = component of velocity in vertical direction
U = nondimensional velocity, $\frac{u}{\left(\frac{\nu^2 g\beta q''}{k}\right)^{1/4}}$
v = component of velocity in horizontal direction
V = nondimensional velocity, $\frac{v}{\left(\frac{\nu^2 g\beta q''}{k}\right)^{1/4}}$
x = vertical distance above bottom of plate
X = nondimensional vertical distance $\frac{x}{\left(\frac{\nu^2 k}{g\beta q''}\right)^{1/4}}$
y = horizontal distance from plate
Y = nondimensional horizontal distance $\frac{y}{\left(\frac{\nu^2 k}{g\beta q''}\right)^{1/4}}$

Greek

α = thermal diffusivity of fluid
β = coefficient of thermal expansion of fluid
ν = kinematic viscosity
ρ = density of fluid
$\bar{\tau}$ = time
τ = non-dimensional time, $\frac{\bar{\tau}}{\left(\frac{k}{g\beta q''}\right)^{1/2}}$ = tau

Subscripts

0 = at solid-fluid interface
ss = steady state
∞ = free stream conditions

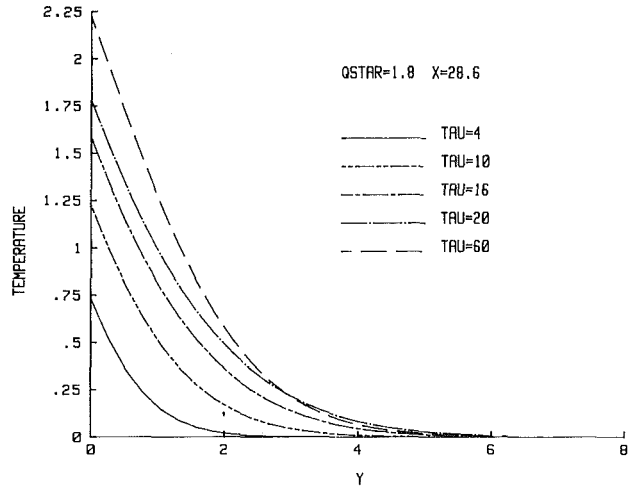

Fig. 1 Transient temperature profiles during heating for $X = 28.6$, $Q^* = 1.8$

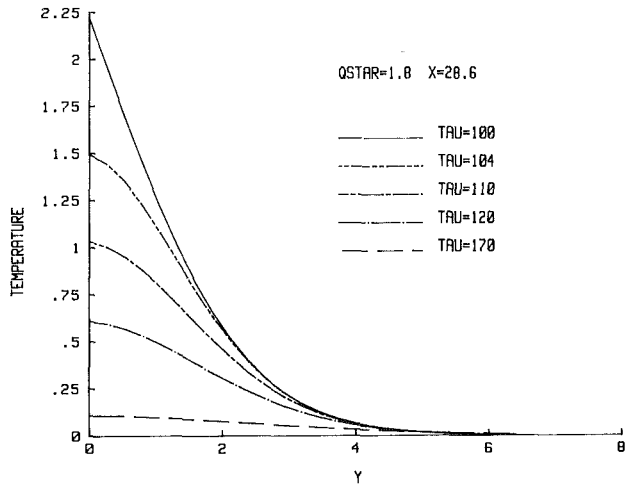

Fig. 3 Transient temperature profiles during cooling for $X = 28.6$, $Q^* = 1.8$

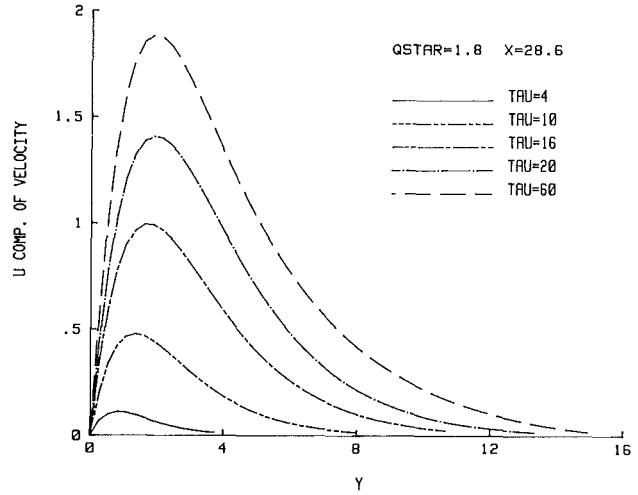

Fig. 2 Transient velocity profiles during heating for $X = 28.6$, $Q^* = 1.8$

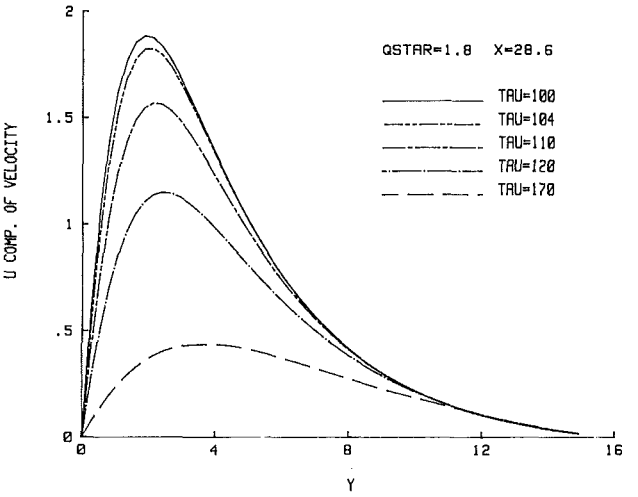

Fig. 4 Transient velocity profiles during heating for $X = 28.6$, $Q^* = 1.8$

$$U = \frac{u}{(\nu^2 g\beta q''/k)^{1/4}} = \frac{ux/\nu}{(\mathrm{Gr}_x^*)^{1/4}}$$

$$V = \frac{v}{(\nu^2 g\beta q''/k)^{1/4}} = \frac{vx/\nu}{(\mathrm{Gr}_x^*)^{1/4}}$$

$$X = \frac{x}{(\nu^2 k/g\beta q'')^{1/4}} = (\mathrm{Gr}_x^*)^{1/4}$$

$$Y = \frac{y}{(\nu^2 k/g\beta q'')^{1/4}} = \frac{y}{x}(\mathrm{Gr}_x^*)^{1/4}$$

Equations (1) to (3) are subject to the following boundary and initial conditions:

$$\tau = 0 \qquad U = V = T = 0 \tag{4}$$

$$X = 0 \qquad U = T = 0 \tag{5}$$

$$Y = 0 \qquad U = V = 0 \tag{6}$$

$$Y \to \infty \qquad U, T \to 0 \tag{7}$$

For $\tau_s > \tau > 0$ and $Y = 0$

$$1 = Q^* \left.\frac{\partial T}{\partial \tau}\right|_0 - \left.\frac{\partial T}{\partial Y}\right|_0 \tag{8}$$

For $\tau \geq \tau_s$ and $Y = 0$

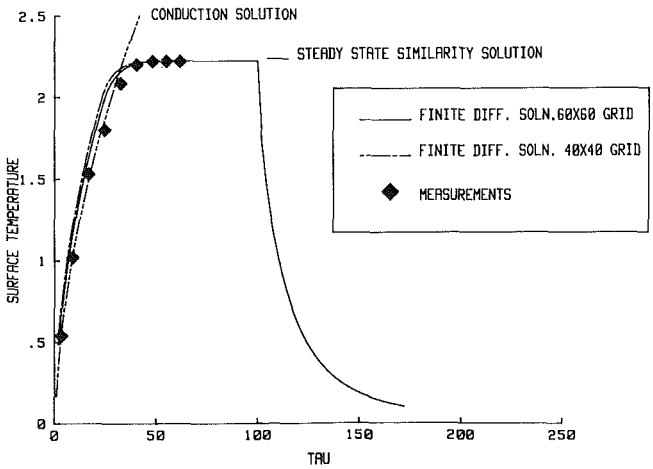

Fig. 5 Surface temperature history for $X = 28.6$, $Q^* = 1.8$

$$Q^* \left.\frac{\partial T}{\partial \tau}\right|_0 = \left.\frac{\partial T}{\partial Y}\right|_0 \tag{9}$$

The nondimensional thermal capacity parameter, Q^*, is given by

$$Q^* = c''\left(\frac{\nu^2 g\beta q''}{k^5}\right)^{1/4} = \frac{c''}{\rho c_p x}\,\mathrm{Pr}\,(\mathrm{Gr}_x^*)^{1/4}$$

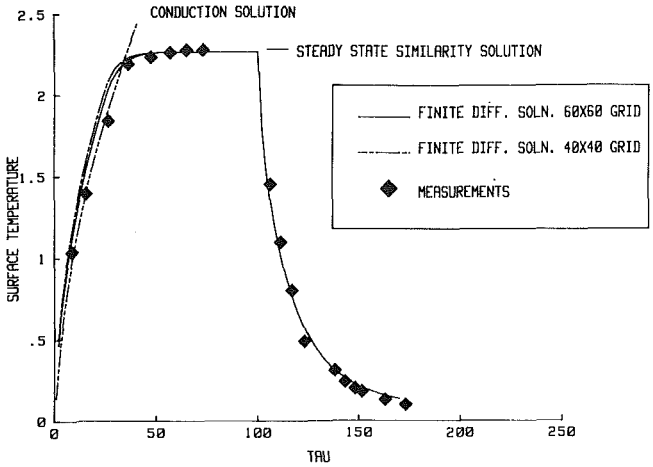

Fig. 6 Surface temperature history for $X = 31.3$, $Q^* = 2$

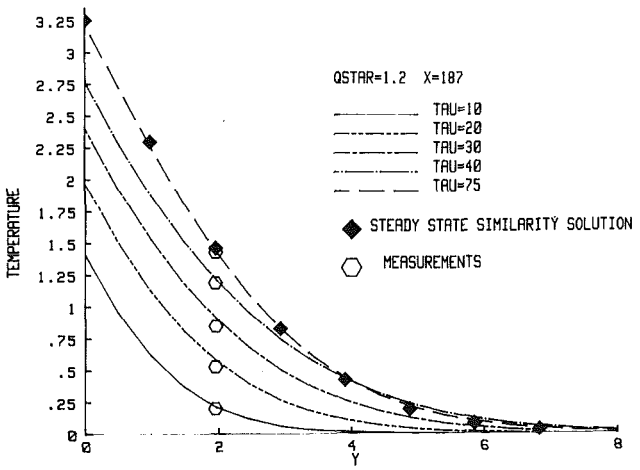

Fig. 7 Transient temperature profiles during heating for $X = 187$, $Q^* = 1.2$

Equation (4) represents an initially quescient ambient medium with a uniform temperature distribution, (5) specifies no transport upstream of the leading edge, and (6) represents a non-slip, impervious boundary condition at the surface. Equation (8) results from an energy balance at the solid-fluid interface, during the heating process. Here τ_s represents the time at which the energy supply to the surface is switched off, thereby starting the cooling process. The two terms on the right hand side represent energy storage in the element of the surface, and energy convected away by the fluid, respectively. The energy storage rate within the surface has a maximum value at the beginning of the transient process. This decreases during the whole transient period and is zero as steady state is achieved. Meanwhile energy transfer to the fluid increases from zero at the beginning of the transient until it reaches its final steady-state value. Equation (9) results from an energy balance at the solid fluid interface during the cooling process, and simply states that energy convected by the fluid comes from the energy previously stored in the surface. The cooling process continues until the temperature field reaches a uniform distribution at t_∞. The medium becomes quiescent once more.

Numerical Procedure and Results

An explicit finite difference scheme, similar to that discussed in [16], is used to solve equations (1-3), subject to the appropriate boundary and initial conditions. The space under investigation is divided into a grid of dimension MxN in the x and y directions, respectively. Then the appropriate set of finite-difference equations are solved at each grid point,

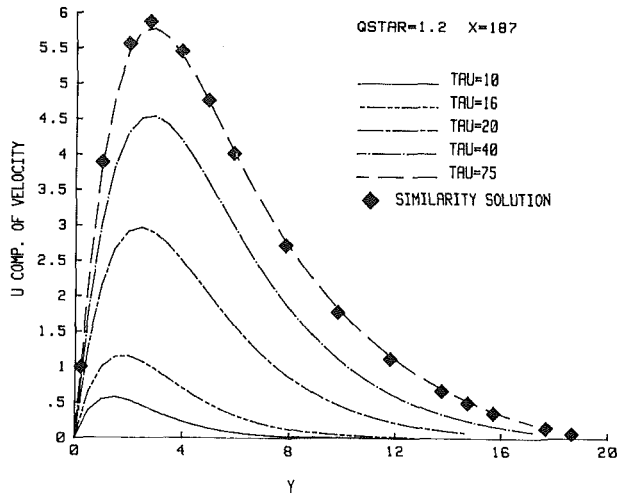

Fig. 8 Transient velocity profiles during heating for $X = 187$, $Q^* = 1.2$

starting at the time $\tau = 0$. The solution is then marched in time, using a sufficiently small time step, until the values of U, V, and T converge to their steady-state values. During the cooling process calculations are carried out till the surface temperature reaches a level of about 5 percent of its steady-state value. The accuracy of the calculated steady-state results from the numerical scheme is ascertained by comparing them to those obtained by solving the steady-state similarity equations, using a conventional Runge Kutta integrating technique.

The relevant parameters in the above equations and boundary conditions are the Prandtl number, Pr, a modified form of the Grashof number, Gr_x^*, and the nondimensional thermal capacity of the plate, Q^*. The properties of the fluid used to nondimensionalize the above parameters were computed at an average film temperature, averaged between the values at the start and end of the transient. Since the temperature variation during the whole process is of the order of a few degrees centigrade no significant error is anticipated due to using single average values.

When a thin vertical surface of appreciable thermal capacity, is suddenly loaded with a uniform and constant energy flux heat flows by conduction inside the surface element. This simple one-dimensional thermal transport also extends into the quiescent fluid during the early stages of the transient process. During the one-dimensional process in the fluid the only component of velocity is the one parallel to the surface. Thus, a one-dimensional layer of fluid near the surface moves upwards, and grows in thickness with time. As the flow field develops an entrainment velocity, v, this process ends in what is known as "the leading edge effect." This is discussed in detail in [18], and different flow regimes are shown to occur depending upon the nondimensional thermal capacity parameter, Q^*. For small values of Q^* the transient process is found to be close to a one-dimensional conduction regime during most of the total transient time. Large deviations from the conduction regime occur only near the end of the transient, as the leading edge effect arrives and convection sets in.

The present calculations apply to three different circumstances, each corresponding to a particular experimental run. Figures 1 and 2 are the transient temperature and velocity profiles in the water, during the heating process, for $X = 28.6$ and $Q^* = 1.8$. This value of X corresponds to a modified Grashof number $Gr_x^* = 6.69 \times 10^5$ which is predicted by [19] to fall well within the laminar flow regime, while the Q^* value shows it to be a one-dimensional conduction transient during most of the transient response. The transient process is seen to virtually end at around $\tau = 60$, with very little development

between $\tau = 60$ and 100. Both the temperature and velocity boundary layer thicknesses increase until they attain their eventual steady-state values. The ratio of the final steady-state thermal to viscous boundary layer thicknesses (δ_t/δ) is approximately equal to ($1/\sqrt{\text{Pr}}$, which is predictable, see [20].

The transient profiles during the cooling process for the same circumstances are shown in Figs. 3 and 4 for the temperature and velocity profiles, respectively. The energy input into the surface is terminated at Tau = 100. Five different subsequent profiles are presented here. In Fig. 3, the surface temperature is seen to drop sharply during the early transient, while the temperature profile near the outer edge of the boundary layer remains almost unaffected during that period. In both Figs. 3 and 4, the boundary layer thickness is observed to remain constant as the temperature and velocity levels continue to deteriorate, this is in sharp contrast to the heating process, wherein the boundary layers grow in thickness with increasing time.

Figure 5 shows the calculated surface temperature trace $T \propto (t_0 - t)$, during the heating and cooling processes. Also shown in Fig. 5 is the one-dimensional conduction solution, for a surface of finite thermal capacity, suddenly exposed to a uniform energy generation rate, as presented in [12]. Results of the finite difference solution are shown for two different grid sizes, during the heating process. Agreement between the numerical and exact solutions is found to improve with increasing the number of grid points. The measured surface temperature response is found to closely follow the exact solution during the early transient, until convection effects set in and steady state is approached. Agreement, with the steady-state similarity solution, as shown on Fig. 5 is found to be excellent.

In Fig. 6, the calculated surface temperature trace is compared with measurements, for $Q^* = 2.0$ and $X = 31.3$. Again, the conduction solution is shown, as well as calculations for two different grid sizes. Here also the measured response is observed to follow the conduction solution during the early transient. The steady-state similarity solution is also shown to be in good agreement with the finite difference calculations.

The calculated transient responses, during the heating process, are shown in Figs. 7 and 8 for $X = 187$ and $Q^* = 1.2$. Also shown on Fig. 7 are the measured temperatures in the thermal boundary layer, and shown in Figs. 7 and 8 are the steady-state temperature and velocity profiles, calculated from the similarity solution. Good agreement is found for both the temperature and velocity profiles.

An interesting aspect of steady-state temperatures is always the x variation of the surface temperature t_0. It is shown in [20], that, for a uniform surface flux condition, $t_0 - t_\infty$ varies as $x^{1/5}$. A comparison of our calculated surface temperatures at $X = 187$ and $X = 28.6$ indicates that $(t_0 - t_\infty)$ does indeed vary as $x^{1/5}$. Also, the similarity formulation indicates that the thermal boundary region thickness grows downstream as $x^{1/5}$. Again, by comparing Figs. 7 and 1, this result is also seen to arise, $\delta_t \propto x^{1/5}$. Figure 8 shows the corresponding transient velocity profiles. The ratio of the thermal to velocity boundary region thicknesses is again $1/\sqrt{\text{Pr}}$.

Concluding Remarks

The computed results for transient laminar natural convection flow adjacent to a vertical surface subject to a uniform flux boundary condition show good agreement with the experimental measurements. Calculations and measurements are presented for several different conditions and for both heating and cooling transient processes. Both the steady-state values and the early transient values are found to be consistent with previous analytical and numerical results. These responses are in close agreement with earlier predictions from an integral analysis. During the cooling process the temperature parameter approaches zero asymptotically. Calculations were terminated at about 5 percent of its final steady-state value.

During the early cooling regime, the computed temperature at and near the surface is observed to drop considerably, while the velocity field remains almost unchanged from its steady-state value. This is seen in Figs. 3 and 4 at $\tau = 104$. This arises because the entire thermal boundary layer occurs deep within the viscous boundary layer. During the heating regime both the thermal and viscous boundary layers increase in thickness with increasing time. However, during cooling the temperature and velocity levels drop off across boundary layers of almost constant thickness.

The steady-state surface temperature excess, $t_0 - t_\infty$, is found to increase with increasing downstream location, x, as $x^{1/5}$, in agreement with the similarity formulation. The thermal region thickness, δ_t, is also found to grow as $x^{1/5}$ with increasing x, while maintaining the ratio $\delta_t/\delta \simeq 1/\sqrt{\text{Pr}}$ for the different downstream locations.

Acknowledgments

The authors with to thank Mr. Y. Joshi for his helpful suggestions. Financial support for this study was provided by the National Science Foundation under Grant MEA-8200613.

References

1 Illingworth, C. R., "Unsteady Laminar Flow of Gas Near an Infinite Plate," *Proceedings of the Cambridge Philosophical Society*, Vol. 46, part 4, 1950, pp. 603–613.

2 Schetz, J. A., and Eichhorn, R., "Unsteady Natural Convection in the Vicinity of a Doubly Infinite Vertical Plate," ASME JOURNAL OF HEAT TRANSFER, Vol. 84, Series C, 1952, pp. 334–338.

3 Menold, E. R., and Yang, K., "Asymptotic Solutions for Unsteady Laminar Free Convection on a Vertical Plate," ASME *Journal of Applied Mechanics*, Vol. 84, Series E, 1962, pp. 124–126.

4 Rao, A. K., "Laminar Natural Convection Flow with Suction or Injection," *Applied Sci. Res.*, 1962, p. 1.

5 Soundalgekar, V. M., and Wavre, P. D., "Unsteady Free Convection Flow Past an Infinite Vertical Plate with Constant Suction and Mass Transfer," *International Journal of Heat and Mass Transfer*, Vol. 20, 1977, pp. 1363–1373.

6 Sugawara, S., and Michiyoshi, I., "The Heat Transfer by Natural Convection in the Unsteady State on a Vertical Flat Wall," *Proc. Ist Japan Nat. Congress Appl. Mechanics*, 1951, pp. 501–506.

7 Siegel, R., "Transient Free Convection from a Vertical Flat Plate," Trans. ASME, Vol. 80, 1958, pp. 347–359.

8 Klei, H. E., "A Study of Unsteady State Natural Convection for a Vertical Flat Plate," B.S. thesis, MIT, Cambridge, Mass., 1957.

9 Goldstein, R. J., and Eckert, E. R. G., "The Steady and Transient Free Convection Boundary Layer on a Uniformly Heated Vertical Plate," *International Journal of Heat and Mass Transfer*, Vol. 1, 1960, pp. 208–218.

10 Gebhart, B., "Transient Natural Convection from Vertical Elements," ASME JOURNAL OF HEAT TRANSFER, 1961, pp. 61–70.

11 Gebhart, B., and Adams, D. E., "Measurements of Transient Natural Convection in Flat Vertical Surfaces," ASME JOURNAL OF HEAT TRANSFER, Vol. 83, 1962, pp. 1–4.

12 Goldstein, R. J., and Briggs, D. G., "Transient Free Convection about Vertical Plates and Cylinders," ASME JOURNAL OF HEAT TRANSFER, Vol. 86C, 1964, p. 490.

13 Gebhart, B., and Dring, R. P., "The Leading Edge Effect in Transient Natural Convection Flow from a Vertical Plate," ASME JOURNAL OF HEAT TRANFER, Vol. 89C, 1967, p. 24.

14 Mahajan, R. L., and Gebhart, B., "Leading Edge Effects in Transient Natural Convection Flow Adjacent to a Vertical Surface," ASME JOURNAL OF HEAT TRANSFER, Vol. 100, 1978, pp. 731–733.

15 Brown, N., and Riley, N., "'Flow Past a Suddenly Heated Vertical Plate," *Journal of Fluid Mechanics*, Vol. 59, 1973, pp. 225–237.

16 Hellums, J. D., and Churchill, S. W., "Transient and Steady State, Free and Natural Convection Numerical Solutions—I: The Isothermal Vertical Plate," *AIChE Journal*, 1962, pp. 690–692.

17 Sammakia, B., and Gebhart, B., "Transient and Steady State Numerical Solutions in Natural Convection," *Numer. Heat Transfer*, Vol. 1, 1978, pp. 529–542.

18 Sammakia, B., and Gebhart, B., "Transient Natural Convection Adjacent to a Vertical Flat Surface: The Thermal Capacity Effect," *Numer. Heat Transfer*, Vol. 4, 1981, pp. 331–344.

19 Qureshi, Z. H., and Gebhart, B., "Transient and Transport in a Buoyancy Driven Flow in Water Adjacent to a Vertical Uniform Flux Surface," *IHJMT*, Vol. 21, 1978, pp. 1467–1479.

20 Gebhart, B., *Heat Transfer*, 2nd ed., McGraw-Hill, New York, 1971.

Numerical Study of the Onset of Double-Diffusive Cellular Convection due to a Uniform Lateral Heat Flux

S. Takao
M. Tsuchiya
U. Narusawa[1]
Technical Research Center,
Nippon Kokan K.K.,
Kawasaki, Japan

When a fluid with a vertical solute gradient of $(-dS/dy)_0$ is heated laterally, roll cells start to form at the boundary, developing into a series of convective layers. Numerical experiments were performed to investigate the onset of the abovementioned double-diffusive convection under the application of a uniform lateral heat flux. The paper reports the results and discussion of the following aspects of the stability of double-diffusive convection; (i) the relationship between the critical value, $(Ra/Rs)_c$, above which convection cells form along the vertical wall and the nondimensional slot width, (d/L), (ii) the effect of the Lewis number on $(Ra/Rs)_c$. It was also confirmed that values of $(Ra/Rs)_c$ as well as H/L (the nondimensional vertical size of incipient cells) obtained in this numerical experiment for wide slot widths $(d/L > \sim 30)$, agreed well with those obtained previously by physical experiments.

1 Introduction

When a fluid with a stable, vertical solute gradient is heated laterally, one of the following two phenomena occurs: (*a*) the fluid will be lifted upward slightly to offset a positive buoyancy force created by the heating while heat is conducted through the fluid; (*b*) the distortion of the stable gradient due to heating will produce roll cells, which will develop into a series of layers growing laterally from the heated boundary (see Fig. 1).

In general, the behavior of a fluid under the presence of gradients of two properties with different molecular diffusivities is called "double-diffusive convection." The stability problem described above is only one of many interesting features of double-diffusive convection [1], the study of which is essential to the understanding of the layered structures observed in the ocean as well as in large energy-storing reservoirs.

Thorpe, Hutt, and Soulsby [2] (henceforth to be referred to as THS) were the first to analyze the stability of a fluid with a linear salt gradient in a narrow vertical slot heated at one wall and cooled at the other. Their analysis, which was approximate in the sense that it only satisfied no normal flow conditions at the walls, indicated the condition of marginal stability as follows,

$$R_x \left(= \left(\frac{D_T}{D_S} - 1\right) \frac{gD^4 \alpha (\partial T/\partial x)_0}{\pi^4 \nu D_T}\right) = -96a\,(1+a^2)^2 \qquad (1a)$$

$$R_z \left(= \frac{gD^4 \beta (\partial S/\partial y)_0}{\pi^4 \nu D_s}\right) = -16\,(5a^2-1)(1+a^2)^2 \qquad (1b)$$

The parametric forms of equations (1) show that for a given value of Rz (i.e., for given values of slot width, d, and the initial vertical solute gradient, $(\partial S/\partial y)_0$,), instability sets in at the value of Rx given in equation (1*a*). Later, Hart [3] and Wirtz and Liu [4] obtained more accurate solutions, satisfying all the boundary conditions. However, it should be noted here that the approximate solution by THS agrees reasonably well with their own experimental results as well as with other more accurate solutions. Chen, Briggs and Wirtz have studied the onset of cellular convection in a semiinfinite body of fluid, both experimentally [5] and numerically [6], showing that for an aqueous solution of salt the motion of fluid is determined by the Rayleigh number, defined as

$$R = \frac{g\alpha\Delta T}{\nu D_T}\left(-\frac{\alpha\Delta T}{\beta(\partial S/\partial y)_0}\right)^3,$$

and that if $R > 15000 \pm 2500$, cellular convection develops. Later, Chen [7] confirmed through a numerical experiment that the criteria of the onset of cellular convection for a semiinfinite body of fluid is valid if the slot width is larger than ~ 1 cm.

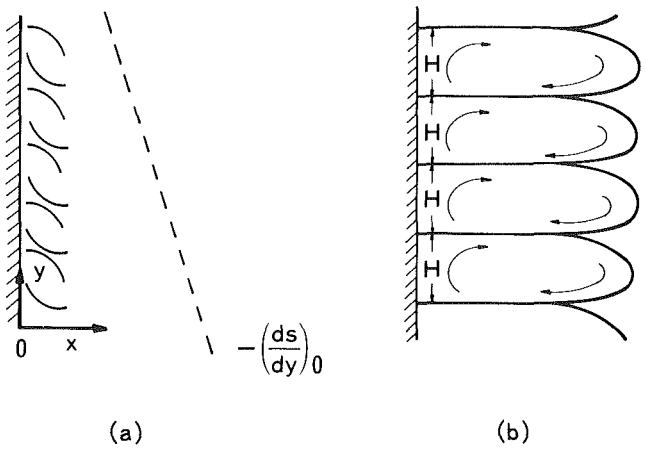

Fig. 1 (*a*) Roll cell formation in a fluid with a vertical solute gradient, $-(dS/dy)_0$, due to lateral heating, (*b*) development of a series of convective layers.

All the abovementioned studies of cellular convection due to lateral heating are concerned with the case of a constant wall temperature. Recently, an experimental investigation of double-diffusion cellular convection due to a uniform lateral heat flux has been performed by Narusawa and Suzukawa [8]. (Details of the experimental results will be discussed later in Section 4.) This paper deals with the numerical experiment of the same problem with the following objectives in mind:

(*i*) The effect of the gap width on stability criteria will be examined.

(*ii*) The numerical results for wide gap conditions, simulating a semi-infinite body of fluid, will be compared with those of the physical experiments, reported previously.

[1] Present address: Department of Mechanical Engineering, Northeastern University, Boston, Mass.

Contributed by the Heat Transfer Division for publication in the JOURNAL OF HEAT TRANSFER. Manuscript received by the Heat Transfer Division September 2, 1981.

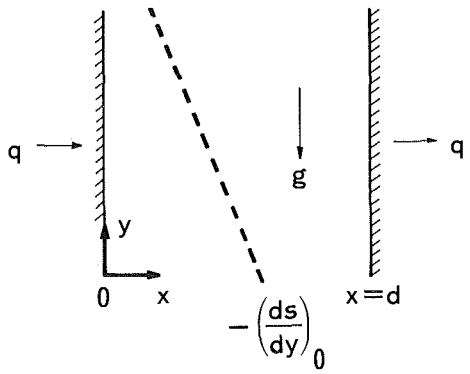

Fig. 2 A sketch of the present problem

2 Formulation

Consider the case in which a fluid with an initial, vertical solute gradient of $(ds/dy)_0$ is contained in a slot of width, d (Fig. 2). A uniform heat flux, q, is applied to $x = 0$ and extracted at $x = d$. Assuming two-dimensional motion, the governing equations, based on the Boussinesq approximation and a linear equation of state, become as follows,

$$\frac{\partial u}{\partial x} + \frac{\partial v}{\partial y} = 0 \tag{2}$$

$$\frac{Du}{Dt} = -\frac{1}{\rho_0}\frac{\partial P}{\partial x} + \nu\nabla^2 u \tag{3a}$$

$$\frac{Dv}{Dt} = -\frac{1}{\rho_0}\frac{\partial P}{\partial y} + \nu\nabla^2 v - \frac{\rho'}{\rho_0} g \tag{3b}$$

$$\frac{DT}{Dt} = D_T \nabla^2 T \tag{4}$$

$$\frac{DS}{Dt} = D_s \nabla^2 S \tag{5}$$

$$\rho = \rho_0[1 - \alpha(T - T_0) + \beta(S - S_0)] \tag{6}$$

where

$$\frac{D}{Dt} = \frac{\partial}{\partial t} + u\frac{\partial}{\partial x} + v\frac{\partial}{\partial y}, \quad \nabla^2 = \frac{\partial^2}{\partial x^2} + \frac{\partial^2}{\partial y^2}$$

and $\rho' = \rho - \rho_0$ with ρ_0 indicating the reference density.

After some manipulations of the above equations, such as (*a*) the cancellation of pressure terms from equations (3*a*) and (3*b*), (*b*) the introduction of a stream function, ψ, where

$$u = -\frac{\partial \psi}{\partial y} \quad \text{and} \quad v = \frac{\partial \psi}{\partial x},$$

and vorticity,

$$\omega\left(= \frac{\partial u}{\partial y} - \frac{\partial v}{\partial x}\right)$$

and (*c*) the introduction of nondimensional quantities defined as

$$\begin{Bmatrix} x \\ y \end{Bmatrix} = L\begin{Bmatrix} \bar{x} \\ \bar{y} \end{Bmatrix}, \quad \begin{Bmatrix} u \\ v \end{Bmatrix} = \frac{D_T}{L}\begin{Bmatrix} \bar{u} \\ \bar{v} \end{Bmatrix}, \quad t = \frac{L^2}{D_T}\bar{t}, \quad \omega = \frac{D_T}{L^2}\bar{\omega}$$

$$\psi = D_T\bar{\psi}, \quad S - S_0 = -L\left(\frac{dS}{dy}\right)_0 \bar{S}, \quad T - T_0 = (q/k)L\bar{T} \tag{7}$$

where

$$L = \left[\frac{D_T}{g\alpha(q/k)}\right]^{1/4} \tag{8}$$

the following set of governing equations in nondimensional form can be obtained,

$$\frac{\partial \bar{\omega}}{\partial \bar{t}} = J_{\bar{x}\bar{y}}(\bar{\omega}, \bar{\psi}) + Pr\left(\nabla^2\bar{\omega} - \frac{\partial \bar{T}}{\partial \bar{x}} + \frac{\mathrm{Rs}}{\mathrm{Ra}}\frac{\partial \bar{S}}{\partial \bar{x}}\right) \tag{9}$$

$$\frac{\partial \bar{T}}{\partial \bar{t}} = J_{\bar{x}\bar{y}}(\bar{T}, \bar{\psi}) + \nabla^2\bar{T} \tag{10}$$

$$\frac{\partial \bar{S}}{\partial \bar{t}} = J_{\bar{x}\bar{y}}(\bar{S}, \bar{\psi}) + \frac{1}{\mathrm{Le}}\nabla^2\bar{S} \tag{11}$$

$$\nabla^2\bar{\psi} + \bar{\omega} = 0 \tag{12}$$

where

$$J_{Xy}(X, Y) = \frac{\partial X}{\partial x}\frac{\partial Y}{\partial y} - \frac{\partial X}{\partial x}\frac{\partial Y}{\partial y}$$

It should be noted that the reference length scale, L, defined in equation (8) can be interpreted as a measure of thermal boundary layer thickness along a vertical wall in the absence of an initial solute gradient [9]. As can be seen from equations (9–12), the behavior of fluid depends on three nondimensional parameters of Pr, Le and Rs/Ra = $\beta(dS/dy)_0/\alpha(q/k)$. Since we are mainly interested in an aqueous solution, Pr is ~5 – 10 whereas Le is of the order of 100, regardless of solute substance. And once substances of both solute and solvent are fixed, Rs/Ra becomes the primary nondimensional parameter to describe the stability of the fluid.

In the absence of convective cells, the lateral heating in-

Nomenclature

a = parameter used in equations (1) and (28)
b = slot width
D_s = mass diffusivity
D_t = thermal diffusivity
E_b = base flow kinetic energy per wavelength
E_p = perturbed flow kinetic energy per wavelength
g = gravitational acceleration
h = vertical cell height
k = thermal conductivity
K = wave number
L = reference length scale defined as $\left[\frac{\nu D_T}{g\alpha(q/k)}\right]^{1/4}$
Le = Lewis number ($= D_T/D_S$)
p = pressure
Pr = Prandtl number ($= \nu/D_T$)
q = applied heat flux
R = Rayleigh number defined as $\frac{g\alpha\Delta T}{\nu D_T}\left[-\frac{\alpha\Delta T}{\beta(ds/dy)_0}\right]^3$
Ra = Rayleigh number defined as $\frac{g\alpha(q/k)L^4}{\nu D_T}$
Rs = solute Rayleigh number defined as $\frac{g\beta[-(ds/dy)_0]L^4}{\nu D_T}$
Rx = $\left(\frac{D_T}{D_S} - 1\right)\frac{gd^4\alpha(\partial T/\partial x)_0}{\pi^{4\nu}D_T}$ (See equation (1*a*))
Rz = $\frac{gd^4\beta(\partial S/\partial Y)_0}{\pi^4\nu D_T}$ (See equation (1*b*))
S = solute concentration
$\bar{S}$ = $-\frac{S - S_0}{L(dS/dy)_0}$

duces a vertical motion. Taking this time-dependent motion as a basic flow, the governing equations can be linearized. Although, for the case of a narrow slot, the base flow equations could take steady-state forms as was assumed by Hart [3], Wirtz and Liu [4] and Paliwal and Chen [10], it is more natural to assign a time-dependent form for the present investigation, in which the width of the slot will be varied widely. Letting the subscripts b and p denote the base and perturbed states, respectively, the unknown quantities can be written as follows,

$$X = X_b(\bar{t},\bar{x}) + X_p(\bar{t},\bar{x},\bar{y}) \quad \text{for} \quad X = \bar{\omega}, \bar{u}, \bar{v}, \bar{T} \text{ and } \bar{S} \tag{13}$$

It should be noted that consideration of a vertically infinite space allows the base flow to be independent of y. (From here on, the bar indicating the nondimensional quantities will be dropped, unless noted otherwise.)

Substitution of equation (13) into equations (9–12) yields the following sets of equations:

Base flow equations:

$$\frac{1}{\mathrm{Pr}}\frac{\partial \omega_b}{\partial t} = \frac{\partial^2 \omega_b}{\partial x^2} - \frac{\partial T_b}{\partial x} + \frac{\mathrm{Rs}}{\mathrm{Ra}}\frac{\partial S_b}{\partial x} \tag{14}$$

$$\frac{\partial T_b}{\partial t} = \frac{\partial^2 T_b}{\partial x^2} \tag{15}$$

$$\frac{\partial S_b}{\partial t} = \frac{1}{\mathrm{Le}}\frac{\partial^2 S_b}{\partial x^2} + v_b \tag{16}$$

$$\frac{\partial v_b}{\partial x} = -\omega_b \tag{17}$$

Perturbed flow equations:

$$\frac{1}{\mathrm{Pr}}\left(\frac{\partial \omega_p}{\partial t} + u_p\frac{\partial \omega_b}{\partial x} + v_b\frac{\partial \omega_p}{\partial y}\right) = \nabla^2\omega_p - \frac{\partial T_p}{\partial x} + \frac{\mathrm{Rs}}{\mathrm{Ra}}\frac{\partial S_p}{\partial x} \tag{18}$$

$$\frac{\partial T_p}{\partial t} + u_p\frac{\partial T_b}{\partial x} + v_b\frac{\partial T_p}{\partial y} = \nabla^2 T_p \tag{19}$$

$$\frac{\partial S_p}{\partial t} + u_p\frac{\partial S_b}{\partial x} + v_b\frac{\partial S_p}{\partial y} = \frac{1}{\mathrm{Le}}\nabla^2 S_p + v_p \tag{20}$$

$$\nabla^2\psi_p = -\omega_p \tag{21}$$

where $u_p = -\dfrac{\partial \psi_p}{\partial y}$ and $v_p = \dfrac{\partial \psi_p}{\partial x}$.

Initial conditions are those consistent with a quiescent body of fluid, whereas at the side boundaries, conditions of a uniform heat flux, and of no solute flux together with the no-slip conditions have to be satisfied. Also, we set the stream function $\psi_p = 0$ along the side boundaries. Then, the initial and boundary conditions in nondimensional form can be written as shown below.

Boundary conditions for the base flow:

$$\frac{\partial T_b}{\partial x}(t,0) = \frac{\partial T_b}{\partial x}(t,d/L) = -1$$
$$\frac{\partial S_b}{\partial x} = v_b = 0 \text{ at } x = 0 \text{ and } d/L \tag{22}$$

Initial conditions for the base flow:

$$T_b(0,x) = v_b(0,x) = \omega_b(0,x) = 0 \tag{23}$$

Boundary conditions for the perturbed flow:

$$\frac{\partial T_p}{\partial x} = \frac{\partial S_p}{\partial x} = u_p = v_p = \psi_p = 0 \quad \text{at} \quad x = 0 \quad \text{and} \quad d/L \tag{24}$$

Initial conditions for the perturbed flow:

$$T_p(0,x,y) = S_p(0,x,y) = 0 \tag{25}$$

3 Numerical Method and Procedure

Since the numerical scheme to be described in this section is quite similar to those employed by the previous investigators [4–7], only an outline will be presented here.

As is depicted in Fig. 1, it is expected that the perturbed state is periodic in the y direction. We therefore assume the following form for the perturbed quantities,

$$A = [A_R(t,x) + i \cdot A_I(t,x)] \cdot e^{iKy}, \text{ for } A = \omega_p, \psi_p, T_p \text{ and } S_p \tag{26}$$

where $2\pi/K$ is some integer multiple of the expected vertical height of the roll cells. Substitution of equation (26) into equations (18–21) and into equations (24) and (25) yields eight simultaneous equations (four each from real and imaginary parts) with corresponding initial and boundary conditions. Of these eight equations, six equations derived from equations (18–20) give the unsteady evolution of ω_p, T_p and S_p, while the other two derived from equation (21) give the relationship between ψ_p and ω_p. Finite difference forms of both basic and perturbed flow equations were written, using the forward difference scheme for time derivatives and the central dif-

Nomenclature (cont.)

t = elapsed time
$\bar{t} = \dfrac{D_T}{L^2}t$
Δt = time increment
T = temperature
$\bar{T} = \dfrac{T - T_0}{L(q/k)}$
u = horizontal velocity component
$\bar{u} = \dfrac{L}{D_T}u$
v = vertical velocity component
$\bar{v} = \dfrac{L}{D_T}v$
x = horizontal coordinate
$\bar{x} = x/L$
Δx = spacial increment
y = vertical coordinate
$\bar{y} = y/L$

Greek letter

$\alpha = -\dfrac{1}{\rho}\left(\dfrac{\partial \rho}{\partial T}\right)$
$\beta = \dfrac{1}{\rho}\left(\dfrac{\partial \rho}{\partial S}\right)$
ν = kinematic viscosity
ρ = density
$\rho' = \rho - \rho_0$
ψ = stream function
$\bar{\psi} = \psi/D_T$
ω = vorticity
$\bar{\omega} = \dfrac{L^2}{D_T}\omega$

Subscript

c = critical condition
I = imaginary part
0 = reference quantity
R = real part
b = base flow quantity
p = perturbed flow quantity

Table 1 Summary of physical experiments

Solute/Solvent	HCl/H_2O	$NaCl/H_2O$	$CuSO_4/H_2O$
Range of $(-dS/dy)_0$ [wt%/cm]	0.01–0.17	0.05–0.42	0.05–0.52
Range of applied heat flux [cal/cm^2 s]	$0.5 \times 10^{-3} - 4 \times 10^{-3}$		
Pr	5–8	5–10	6–8
1/Le	$(24 \pm 2) \times 10^{-3}$	$(9 \pm 2) \times 10^{-3}$	$(3.5 \pm 1) \times 10^{-3}$
L [cm]	0.3×10^{-1}–1.1×10^{-1}	0.3×10^{-1}–1.1×10^{-1}	0.3×10^{-1}–1.1×10^{-1}
Critical value of (Ra/Rs)	0.74–0.78	0.27–0.30	0.12–0.14
Nondimensional cell size, H/L, near the critical condition	9–11	8–10	7–8

ference scheme for space derivatives, respectively. (For boundary points, Aziz-Hellums formulae [11] were utilized.)

To determine the stability of the fluid layer, random disturbances were initially applied to the perturbation vorticity, and the behavior of the temporal kinetic energy change of the perturbed flow was observed; i.e., if the kinetic energy decays (grows) with time, the fluid system can be regarded as stable (unstable). Since this method of stability analysis has been discussed in detail and utilized successfully by many previous investigators [4, 6, 7, 12, 13], it will not be elaborated upon here. The kinetic energy per wavelength, E, can be expressed as,

$$E_b = \int_0^{2\pi/K} \int_0^{d/L} \frac{1}{2} \rho_0 D_T^2 v_b^2 \, dx \cdot dy$$

$$= \rho_0 D_T^2 \frac{\pi}{K} \int_0^{d/L} v_b{}^2 \, dx \, dy, \quad \text{for the base flow} \qquad (27a)$$

and

$$E_p = \frac{1}{2} \rho_0 D_T^2 \frac{\pi}{K} \int_0^{d/L} \left[K^2 (\psi_R^2 + \psi_I^2) \left(\frac{\partial \psi_R}{\partial_x} \right)^2 + \left(\frac{\partial \psi_I}{\partial_x} \right)^2 \right] dx \qquad (27b)$$

for the perturbed flow.

The outline of the computational procedure is as follows:

(*i*) assign small random perturbations in vorticity (in the order of magnitude of $10^{-6} - 10^{-7}$), generated from the Poisson random number generator [14], at all grid points;

(*ii*) solve the base flow equations;

(*iii*) obtain the stream function corresponding to the perturbed vorticity from the relationship between the vorticity and the stream function ($\sim$ equation (21)), using the Gaussian elimination method [15];

(*iv*) compute ω_p ($\sim$ equation (18)), T_p ($\sim$ equation (19)) and S_p ($\sim$ equation (20)) for a new time level; and

(*v*) compute the kinetic energy from the Simpson's rule for integration and return to step (*ii*).

In order to perform a computation, the value of the wavenumber, K, in addition to the nondimensional parameters of Rs/Ra, Le, Pr, and d/L, have to be given a priori. Therefore, by systematically varying the value of K, the fastest-growing wave mode, which would dominate the flow pattern, was sought. The condition of computational stability, derived from equations (14), (15) and (16), is

$$\Delta t < a_1 \frac{(\Delta x)^2}{2\mathrm{Pr}}, \quad (a_1 < 1)$$

A series of preliminary runs was performed to determine a_1 and Δx with $\Delta t = a_1 (\Delta x)^2/2$ Pr and Pr = 6.25 (corresponding to an aqueous solution,) with results that when a_1 and Δx are varied from 0.1 to 0.5 and 0.03 to 0.3, respectively, the predicted velocity distributions of the base flow were nearly identical. Therefore the values of $a_1 = 0.5$ and $\Delta x = 0.3$ were used throughout this study. (Our value of $\Delta \bar{x} = \Delta x/L = 0.3$ is comparable in magnitude to $\Delta \bar{x}$ (defined as $\Delta x/d$) of 0.02 $\sim$ 0.05 used by Chen [7].) It should also be mentioned here that the accurate spatial resolution of the boundary layer is not so significant a requirement because instability first occurs in the region away from the boundary layer [3], [7]. All computations were performed using an IBM-370/158 digital computer.

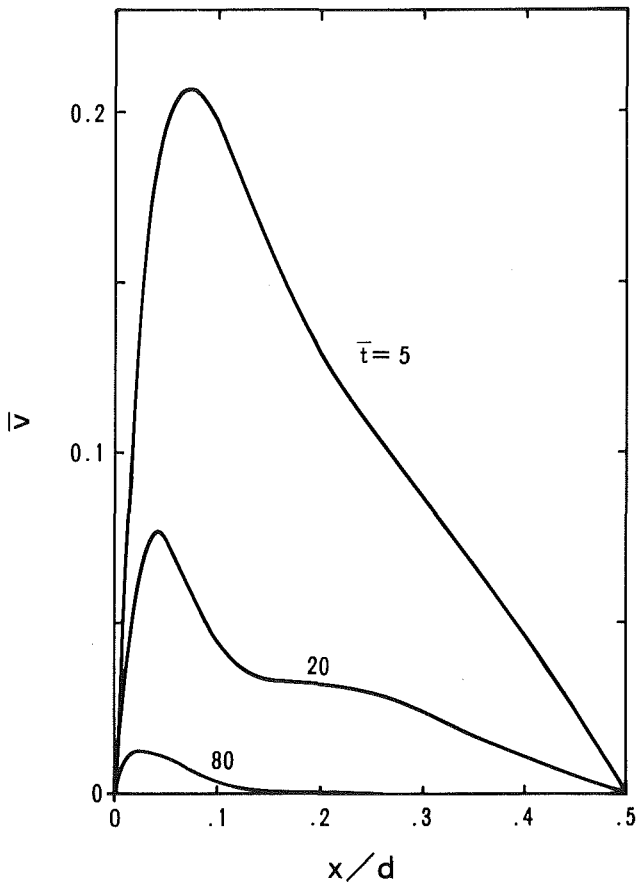

Fig. 3 Base flow velocity profile for solute/solvent = $NaCl/H_2O$, Ra/Rs = 0.65 and d/L = 10 ($\bar{t}$ = elapsed time)

4 Discussion

The analytical results of THS, equations (1*a*) and (1*b*), can be rewritten in terms of the nondimensional parameters in this investigation. The equations then become,

$$(1 - \mathrm{Le}) \left(\frac{d}{L} \right)^4 = -96\pi^4 a (1 + a^2)^2 \qquad (28a)$$

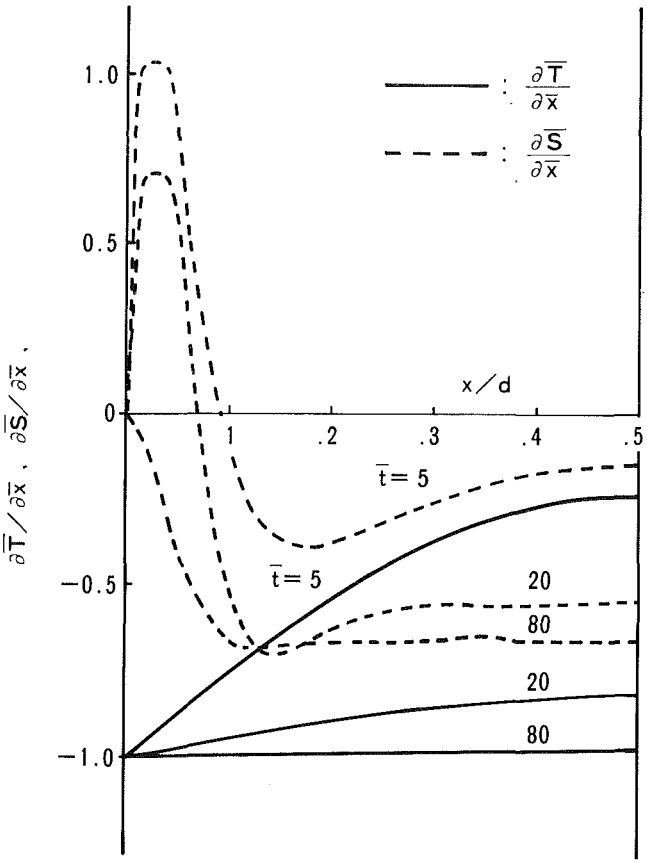

Fig. 4 Base flow profile of horizontal temperature and solute concentration gradients for solute/solvent = NaCl/H_2O, Ra/Rs = 0.65 and d/L = 10

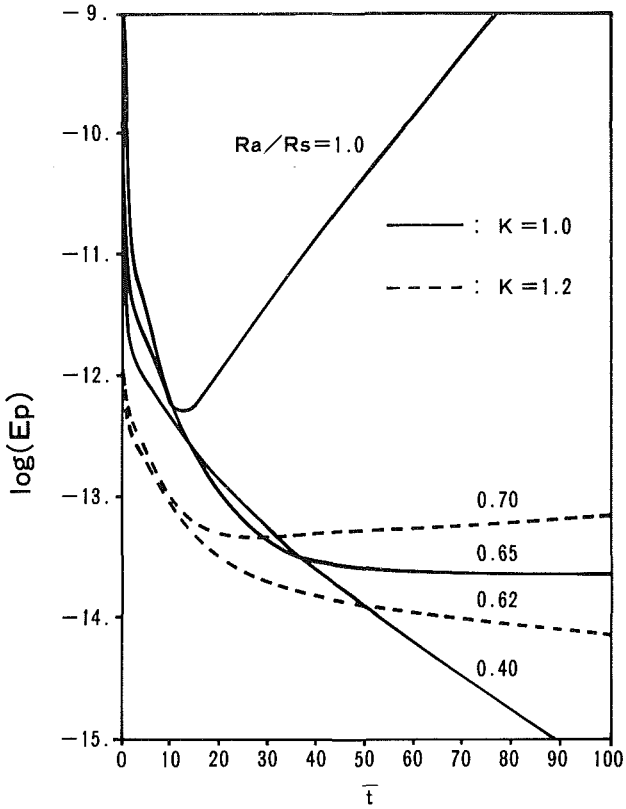

Fig. 5 Temporal changes of perturbation kinetic energy for NaCl/H_2O and d/L = 10

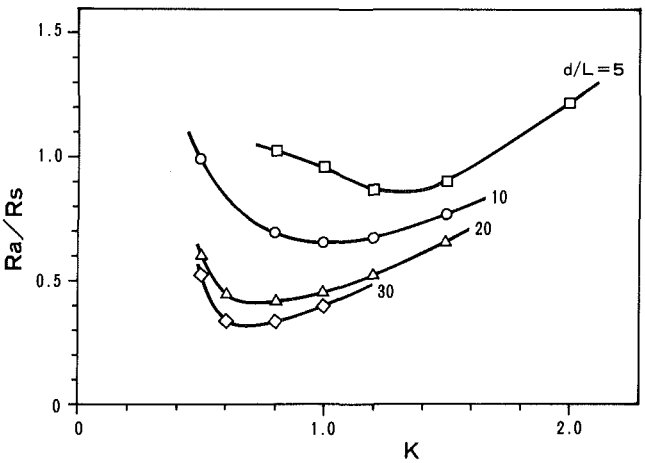

Fig. 6 Ra/Rs versus K for d/L = 5, 10, 20, and 30

$$(-\mathrm{Le})\left(\frac{d}{L}\right)^4 \frac{\mathrm{Rs}}{\mathrm{Ra}} - = 16\pi^4(5a^2-1)(1+a^2)^2 \quad (28b)$$

In deriving the above equations, $(\partial T/\partial x)$ was set to $(-q/k)$ (equal to the steady-state temperature gradient). Rewriting the THS results in this way is appropriate since their solution satisfies only the no normal flow conditions at the vertical boundaries. Equations (28) have been used to estimate starting values for our computations. For the case of a semi-infinite body of fluid, the results and experimental ranges of the aforementioned series of experiments conducted by Narusawa and Suzukawa [8], using a wide tank (10-cm wide × 16-cm deep × 23.5-cm high) are tabulated in Table 1. It should be noted that the critical value of Ra/Rs in this table was defined as the value above which roll cells covered the entire heated wall of the test tank.

Typical base flow profiles are plotted in Figs. 3 and 4. Figure 3 shows time changes of the vertical velocity profile. It can be seen that, as a heat flux is applied at the wall, vertical flow develops and then decays slowly. Figure 4 depicts the corresponding lateral temperature and solute concentration gradients, indicating that negative horizontal gradients of both temperature and solute concentration develop and finally reach steady-state values. Sharp changes in both the vertical velocity as well as the solute gradient near the wall indicate the presence of the boundary layer. Since both $(\partial T/\partial x)$ and $(\partial S/\partial x)$ are negative except for the region near the wall, it is seen from equation (9) that $(\partial T/\partial x)$ and $(\partial S/\partial x)$ act as a vorticity source and sink, respectively.

Figure 5 shows some computed results of the temporal change of perturbation kinetic energy; its growth or decay after a sharp initial drop due to viscous damping, indicates the stability of the fluid. The solid lines (for K = 1.0, d/L = 10) clearly illustrate a subcritical (Ra/Rs = 0.40), a neutral (Ra/Rs = 0.65) and a supercritical (Ra/Rs = 1.00) condition. However, locating an exact value of Ra/Rs for which the neutral state of $dE_p/dt = 0$ is achieved, can be difficult. Thus the value of Ra/Rs corresponding to this neutral stability was interpolated from two data points; one with a positive and the other with a negative value of dE_p/dt (see the two dotted lines, Fig. 5) with the $|d(\log E_p)/dt|$ of these two points being less than 1/200. In Fig. 6, each data point corresponds to the value of Ra/Rs for which the growth rate of perturbation kinetic energy is zero, with the minimum point of a curve for a given slot width being the critical condition above which cellular convection occurs. This method of systematic search for the critical condition was performed for d/L = 5, 10, 20, and 30. For $d/L > 30$, this approach has to be abandoned because of the prohibitively large amount of computing time entailed.

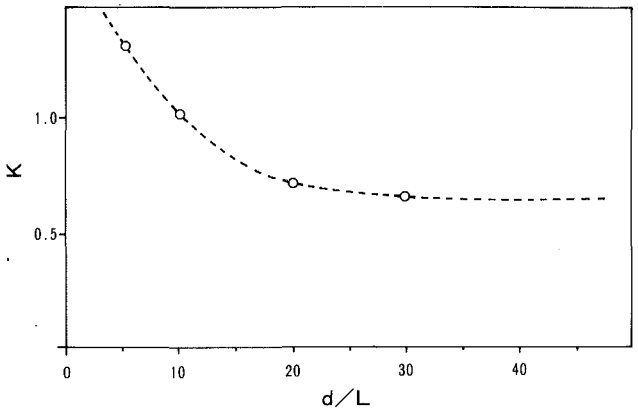

Fig. 7 Critical wavelength, K_c, versus slot width, d/L

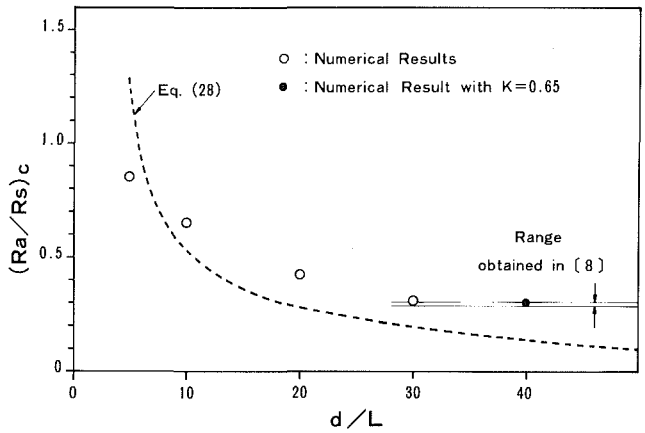

Fig. 8 $(Ra/Rs)_c$ versus d/L

Figure 7 shows the relationship, obtained from Fig. 6, between the wave number, K_c, corresponding to the critical value of Ra/Rs (= $(Ra/Rs)_c$) and the slot width, d/L. It can be seen that the change of K_c with d/L becomes very small as d/L increases beyond 20. Here, the asymptotic value of K_c for $d/L > 30$ was estimated to be ~ 0.65, and it should be noted that the wavelength $2\pi/K$, for $K = 0.65$ is 9.67, which agrees reasonably well with the experimental value of the vertical size of cells listed in Table 1. Using this asymptotic value of K_c, the critical value of Ra/Rs for $d/L = 40$ was obtained from two runs, one with Ra/Rs = 0.25 and the other with Ra/Rs = 0.32. The former resulted in $d(\log E_p)/dt = -2.5 \times 10^{-3}$ (decay in perturbation kinetic energy), while for the latter $d(\log E_p/dt = 0.8 \times 10^{-3}$ (growth in perturbation kinetic energy) with an interpolated critical value of Ra/Rs = 0.30.

Figure 8 is the summary of $(Ra/Rs)_c$ plotted against d/L. The circles at d/L = 5, 10, 20, and 30 indicate values of $(Ra/Rs)_c$ obtained from Fig. 6, while the solid circle at d/L = 40 is the numerical result for $K = 0.65$. Solid lines indicate the range of $(Ra/Rs)_c$ obtained in the physical experiment (see Table 1), whereas the dotted line is the plot of equation (28) of the THS analysis. Since there is very little change in $(Ra/Rs)_c$ when d/L is changed from 30 to 40, and since $(Ra/Ra)_c$ at $d/L = 40$ is very close to the experimentally obtained value of 0.28 −0.30, it was concluded that the effect of the slot width is negligible if $d/L \geq \sim 30$. For the range of $d/L < 30$, Fig. 8 shows the increase in $(Ra/Rs)_c$ with a decrease in d/L. This numerical results, in turn, confirm the validity of the experimental results of Narusawa and Suzukawa [8] in that their tank width of 10 cm was indeed large enough to simulate a semi-infinite body of fluid. (In terms of the experimental range shown in Table 1, the slot width corresponding to d/L = 40 is 1.2 − 4.4 cm, depending on the applied heat flux.)

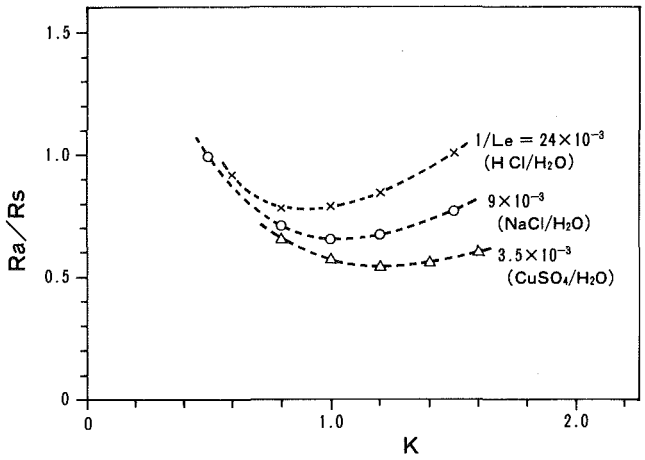

Fig. 9 Effect of the Lewis number on the critical condition for a fixed value of $d/L = 10$

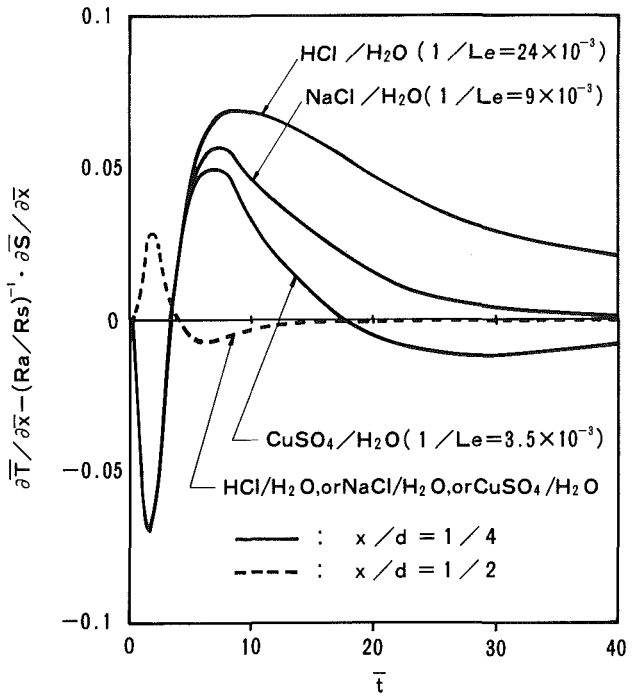

Fig. 10 Temporal changes of $\partial\bar{T}/\partial\bar{x} - (Ra/Rs)^{-1} \cdot \partial\bar{S}/\partial\bar{x}(\alpha - \partial\bar{p}/\partial\bar{x})$ for $(Ra/Rs) = 0.65$ and $d/L = 10$

The discrepancy between the numerical experiments and the THS analysis (dotted line) is quite significant, although the THS analysis supports the general tendency in the $(Ra/Rs)_c - (d/L)$ relationship for $d/L < \sim 20$. It is interesting to note that Ra/Rs is the common unifying parameter in the present case of a uniform heat flux, compared with the case of a constant wall temperature, in which the stability criterion for a narrow slot is quite different from that for a semi-infinite body of fluid (see section 1).

To see the effect of the Lewis number on the onset of instability, additional numerical computations for 1/Le = 24 $\times 10^{-3}$ (HCl/H_2O) and 3.5 $\times 10^{-3}$ ($CuSO_4/H_2O$) with a particular slot width of $d/L = 10$ were performed, and the results are plotted in Fig 9. As can be seen, $(Ra/Rs)_c$ and the corresponding wavelength ($=2\pi/K$) are $(Ra/Rs)_c = 0.78$ at $2\pi/K = 7.39$ for HCl/H_2O, 0.65 at 6.10 for $NaCl/H_2O$ and 0.53 at 5.24 for $CuSO_4/H_2O$, respectively. This tendency for both $(Ra/Rs)_c$ and the corresponding wavelength to decrease with a decrease in the diffusivity ratio (= 1/Le) is quite

consistent with the results of the physical experiments, although the values themselves are different from those in Table 1 because of the effect of the slot width.

Both Hart [3] and Chen [5] showed from observation of the base flow characteristics that instability sets in when the horizontal temperature gradient is large while at the same time the horizontal density gradient is nearly zero. Figure 10 was plotted to illustrate the temporal change of the value $(\partial \bar{T}/\partial \bar{x} - (\mathrm{Ra/Rs})^{-1} \cdot \partial \bar{S}/\partial \bar{x})$ for the three cases of HCl/H_2O (subcritical), $NaCl/H_2O$ (critical) and $CuSo_4/H_2O$ (supercritical). A negative value of the ordinate indicates a positive horizontal density gradient and vice versa. A larger value of 1/Le means either enhanced solute diffusion or lessened thermal diffusion in the horizontal direction; which, in turn, results in a smaller (or a negative) horizontal density gradient since both the solute and the temperature gradients are negative. The consequences of this effect are indicated in Fig. 10 as marked differences in temporal changes of the horizontal density gradient among the three solutes at $x/d = 1/4$. At $x/d = 1/4$, for both the HCl/H_2O (subcritical condition) and the $NaCl/H_2O$ (critical condition) cases the horizontal density gradient is negative and slowly decays to zero, while for the $CuSO_4/H_2O$ (supercritical condition) case the density gradient approaches zero from the positive direction. (Growth of perturbation kinetic energy occurred for the $CuSO_4/H_2O$ case at $\bar{t} = 25 - 30$). For all three cases, temporal changes of the density gradients at $x/d = 1/2$ are nearly the same as shown by a single dotted line in Fig. 10. The above description suggests that a positive density gradient in a major portion of the flow is likely to cause instability.

5 Conclusions

(*i*) The time needed to establish a steady-state decreases with d/L, and narrow slot cases can be treated as steady-state problems, validating the approximate study the THS. However, the steady-state solution fails to predict the critical condition for large values of d/L, since a breakdown of the conduction-dominated state occurs before the steady-state is reached, resulting in a value of $(\mathrm{Ra/Rs})_c$ much higher than that predicted by the THS analysis. (This conclusion is the same as the one reached by previous investigators for the case of a constant temperature wall.)

(*ii*) In our case the constant heat flux, the principal nondimensional parameter, governing the stability of double-diffusive convection is the same, i.e., Ra/Rs, for both the narrow slot problem and the semi-infinite body of fluid.

(*iii*) The value of $(\mathrm{Ra/Rs})_c$ decreases with the increase of d/L up to $d/L \sim 30$; however for larger values of d/L, the problem can essentially be regarded as the case of a semi-infinite body of fluid, and $(\mathrm{Ra/Rs})_c$ was found to take a constant value of ~ 0.30, which agrees well with the results obtained previously by a set of physical experiments.

(*iv*) The effect of Le has been investigated numerically, and it was found that the temporal change of the horizontal density gradient in the fluid depends heavily on Le, indicating that, given Pr and d/L, $(\mathrm{Ra/Rs})_c$ increases with a decrease in Le.

References

1 Turner, J. S., *Buoyancy Effects in Fluids*, Cambridge University Press, 1979, pp. 251–287.

2 Thorpe, S. A., Hutt, P. K., and Soulsby, R., "The Effect of Horizontal Gradients on Thermohaline Convection," *Journal of Fluid Mechanics*, Vol. 38, 1969, pp. 375–400.

3 Hart, J. E., "On Sideways Diffusive Instability," *Journal of Fluid Mechanics*, Vol. 49, 1971, pp. 279–288.

4 Wirtz, R. A., and Liu, L. H., "Numerical Experiments on the Onset of Layered Convection in a Narrow Slot Containing a Stably Stratified Fluid," *International Journal of Heat and Mass Transfer*, Vol. 18, 1975, pp. 1299–1305.

5 Chen, C. F., Briggs, D. G., and Wirtz, R. A., "Stability of Thermal Convection in a Salinity Gradient due to Lateral Heating," *International Journal of Heat and Mass Transfer*, Vol. 14, 1971, pp. 57–66.

6 Wirtz, R. A., Briggs, D. G., and Chen, C. F., "Physical and Numerical Experiments on Layered Convection in a Density-Stratified Fluid," *Geohpys. Fluid Dyn.*, Vol. 3, 1972, pp. 265–288.

7 Chen, C. F., "Onset of Cellular Convection in a Salinity Gradient due to a Lateral Temperature Gradient," *Journal of Fluid Mechanics*, Vol. 63, 1974, pp. 563–576.

8 Narusawa, U., and Suzukawa, Y., "Experimental Study of Double-Diffusive Cellular Convection due to a Uniform Lateral Heat Flux," *Journal of Fluid Mechanics*, Vol. 113, 1981, pp. 387–405.

9 Gill, A. E., "The Boundary Layer Regime for Convection in a Rectangular Cavity," *Journal of Fluid Mechanics*, Vol. 26, 1966, pp. 515–536.

10 Paliwal, R. C., and Chen, C. F., "Double-Diffusive Instality in an Inclined Fluid Layer: Part 2—Stability Analysis," *Journal of Fluid Mechanics*, Vol. 98, 1980, pp. 769–785.

11 Aziz, K., and Hellums, J. D., "Numerical Solution of the Three-Dimensional Equations of Motion for Laminar Natural Convection," *Physics Fluids*, Vol. 10, 1970, pp. 315–324.

12 Gresho, P. M., and Sani, R. L., "The Stability of Fluid Layer Subjected to a Step Change in Temperature: Transient versus Frozen Time Analysis," *International Journal of Heat and Mass Transfer*, Vol. 14, 1971, pp. 207–222.

13 Chen, C. F., Liu, D. C. S., and Skok, M. A., "Stability of Circular Couette Flow With Constant Finite Acceleration," ASME *Journal of Applied Mechanics*, Vol. 95, 1973, pp. 347–354.

14 Carnahan, B., Luther, H. A., and Wilkes, J. O., *Applied Numerical Methods*, John Wiley and Sons, 1969, pp. 545–549.

15 Richtmyer, R. D., and Morton, K. W., *Difference Methods for Initial-Value Problems*, Interscience Publishing, 1967, pp. 198–201.

Natural Convection in Evaporating Minute Drops[1]

Nengli Zhang[2]

Wen-Jei Yang
Mem. ASME

Department of Mechanical Engineering
and Applied Mechanics,
The University of Michigan,
Ann Arbor, Mich. 48109

Interfacial flow structures in small liquid drops evaporating on flat plates are cinematographically investigated using the methods of direct photography and laser shadowgraphy. Various liquids of relatively low boiling point were evaporated on glass and copper plates at room temperature. The laser shadowgraph records the flow patterns simultaneously at both the liquid-air interface and the liquid-solid interface, from which the evaporation rate is determined. It reveals the existence of three distinct flow structures at the liquid air interface: stable, substable, and unstable. An interfacial flow map is constructed. The direct photography is employed to study the morphology during the entire process of the unstable-interface type evaporation. The mechanism of ripple formation which enhances the evaporation rate is found to be caused by hydrophilicity of the liquid.

Introduction

It has been known that interfacial turbulence produced by surface tension gradients causes significant enhancements in both heat and mass transfer (e.g., references [1-3]). Most studies on interfacial turbulence are focused on pools of liquids. A review of the literature pertinent to the problems of interfacial turbulence is presented in [3] and will not be repeated here. Reference [4] reported a preliminary finding of surface tension/temperature driven mechanism in minute drops evaporating on a flat plate by means of the laser shadowgraphy. Three fundamental structural forms of interfacial flow, radial stripes, polygonal cells and ripples are revealed and related to three stages of drop evaporation. The mechanism of ripple formation is caused by the liquid-air interface tension changes in the negative direction.

The present study is a continuation of the work of [4] using both the direct photography and laser shadowgraphy to observe the interfacial flow patterns of evaporating drops on glass and copper plates. The latter method leads to the classification of three distinct interfacial forms and the construction of an interfacial flow map for drop evaporation. The direct photography is used to investigate the morphology during the entire process of the unstable-interface type evaporation. The drop lifetime history is determined and correlated. Traditionally, interfacial instability has been considered due to ever present, small, random fluctuations at the interface through the Marangoni effect. The present study sheds light on the mechanism of interfacial turbulence which will be related to some aspects of physical chemistry on the surface of the evaporating drop, namely through the absorption of water vapor in the ambient resulting in the formation of a binary-component mixture in the evaporating drop.

Experimental Apparatus and Procedure

Two different methods of observation were adopted: direct photography and laser shadowgraphy. The apparatus for direct photography consisted of a white light source, a glass plate coated with developed emulsion on one side, and a movie camera, as shown in Fig. 1. The developed emulsion had a specific density such that the photography density was approximately 1.7. When the light source and the camera were situated at proper positions, the process of drop evaporation could be recorded clearly in photos with sharp contrast.

The laser shadowgraphy used the apparatus, consisting of a laser light, a test plate, and two aluminized mirrors, a screen and a camera, as illustrated in Fig. 2. A minute drop was placed on an optically flat glass plate of 102 mm × 127 mm and 1.5-mm thickness for evaporation in open air. A C.W. Radiation Model SP2, 2.5-mW cylindrical helium-neon laser was used as the light source. The two mirrors were aluminized on the surface nearest to the objects that were viewed so that light could be reflected with no refraction. They were mounted in parallel on a specially-designed frame set at 45 deg. The test plate was inserted into the vertical light beam between the two mirrors. The mirror arrangement was used to obtain a horizontal view of the evaporating drop. The optical path from the lower mirror was horizontal and intercepted by a vertical screen. The image on the screen was recorded by a 16-mm Bolex H16 EBM movie camera having a Nikon Nikkor 300-mm 1:4.5 lens. A Kalt 72-mm Close-Up Dioptor lens was mounted on top of the Nikon lens to photograph the air-liquid and liquid-glass interfaces of an evaporating drop. A drop was carefully placed on the test plate by means of a 50 μl Monoject micro syringe. The needle tip was touching the plate

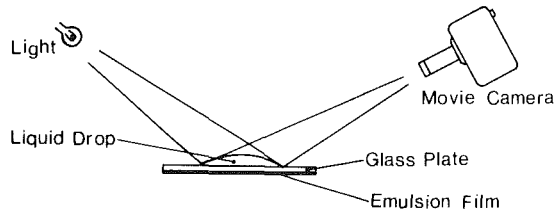

Fig. 1 A schematic of direct photography

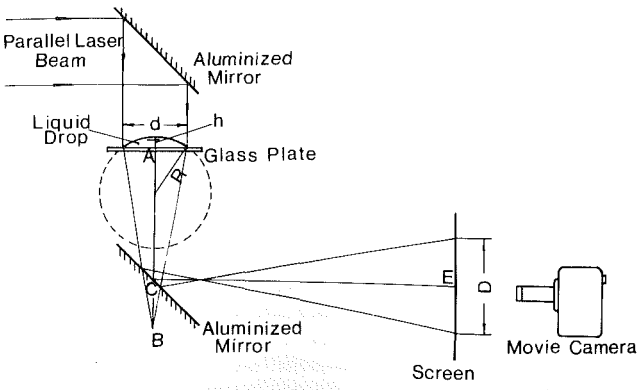

Fig. 2 A schematic of laser shadowgraphic system

[1] The research work was supported by the National Science Foundation under Grant No. ENG-7816972.

[2] Visiting Scholar on leave from the Department of Thermal Engineering, Tsinghua University, Beijing, China

Contributed by the Heat Transfer Division for publication in the JOURNAL OF HEAT TRANSFER. Manuscript received by the Heat Transfer Division December 14, 1981.

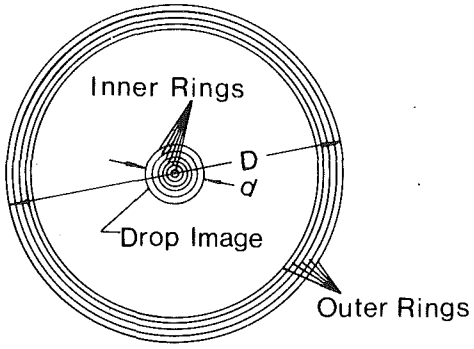

Fig. 3 Two sets of rings in a drop image on screen

surface before and during the injection to permit the formation of a calm, unsplashing drop.

A freshly polished (wiped with dry clean cotton balls) glass plate would not hold unstable-type liquid drops which would spread over it as a thin film. To maintain consistency and for reproduction of the test results, each experiment was conducted at least 24 hrs after wiping both the glass and copper test plates with dry clean cotton balls. The test surface was covered by a very soft tissue paper over the waiting period during which the surface became free of residual liquid molecules while remaining intact from impurity in the ambient air. From the macroscopical point of view, then, the effects of wetting is considered solely related to the balance of three surface tension forces; namely liquid-solid, solid-air and air-liquid as indicated by the magnitude of the surface tension coefficient of the testing liquid. The microscopical observation of wetting phenomena is beyond the scope of the present study.

Photographic Observations

Various liquids at low boiling point labelled with "reagent" were studied, including acetone, methanol, ethanol, ethyl acetate, benzene, chloroform, methylene chloride, cyclohexane, carbon tetrachloride, and ethyl ether. Each minute drop evaporated on an unheated plate in open air.

The photographs by the laser shadowgraphy exhibited two sets of rings: one appearing inside the drop image and the other outside the drop image, as schematically illustrated in Fig. 3. The inner set of rings depicted the flow pattern at the liquid-solid interface, i.e., drop periphery. They correspond to the Fresnel diffraction of circular aperture. This set of rings propagated outward as drop evaporation proceeded, i.e., as the drop periphery moved inward. Therefore, the speed of the moving rings reflected the contracting velocity of the drop periphery. The outerset of rings, however, portrayed the flow

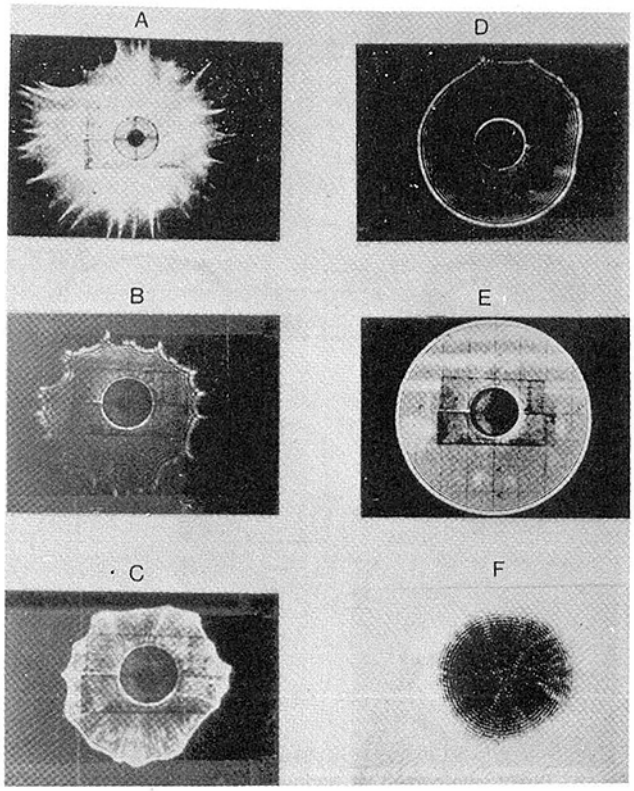

Fig. 4 Instant laser shadowgraph of various drops evaporating on a glass plate (*a*) methanol, (*b*) acetone, (*c*) ethyl acetate, (*d*) methylene chloride, (*e*) cyclohexane, and (*f*) image of drop periphery

structure at the air-liquid and liquid-solid interfaces of the drop.

In Figs. 4(*a*) through 4(*e*), the circle at the center of each photo represented the image of each drop. The rectangle outside the circle was a piece of transparent Scotch tape attached to the center of the screen. This was done to balance the illumination of the other portion of the screen and to enhance the contrast of the inner rings which was printed separately in Fig. 4(*f*). The inner rings in Fig. 4(*f*) were similar in appearance for all three types of evaporation since the inner rings showed the drop periphery which remained circular in shape during the evaporation of tiny minute drops.

When a drop formed a spherical segment, with a very smooth surface, the outer rings exhibited perfect concentric circles; Fig. 4(*e*) for cyclohexane. This type of phase change, classified as "stable-interface type evaporation," occurs in the drops of cyclohexane, carbon tetrachloride, and ethyl ether. On the other hand, should a drop surface be rippled,

Nomenclature

D = diameter of outermost ring on screen (Figs. 2 and 3), m
d = diameter of drop (Fig. 2) and its image on screen (Fig. 3), m; d_0, initial value.
d_e = equivalent diameter of drop on test plate at zero time, m
E = $(\sigma d_0/\mu\alpha)(T_w/T_b)/\epsilon^{1/4}$
e = electronic charge ($=1.5924 \times 10^{-19}$ °C)
f = focal length of spherical-segmented drop, m
h = height of spherical segment (Fig. 2), m
k = Boltzmann constant ($=1.38 \times 10^{-23}$ J/K)
Ma = Marangoni number $= (T_w - T_b)\, d_e\, (d\sigma/dT)\,/\,(\mu\alpha)$
Ma* = modified Marangoni number $= (\sigma d_0/\mu\alpha)\,(T_w/T_b)$
n = refractive index
R = radius of spherical segment (Fig. 2), m
T_∞ = ambient temperature, K
T_w = temperature of test plate, K
T_b = boiling temperature of liquid, K
t = time, s
V = instantaneous volume of drop, m^3; V_0, initial value
α = thermal diffusivity of liquid, m^2/s
ϵ = dielectric constant
ζ = electrokinetic potential of interface, V
μ = absolute viscosity, Pa • S
π = repulsive pressure of thin layer of polar organic liquid over water, N/cm
σ = surface tension at air-liquid interface of contaminated drop, N/cm; σ_0, of pure liquid
τ = drop lifetime, s
ψ = electrostatic potential of interface, V

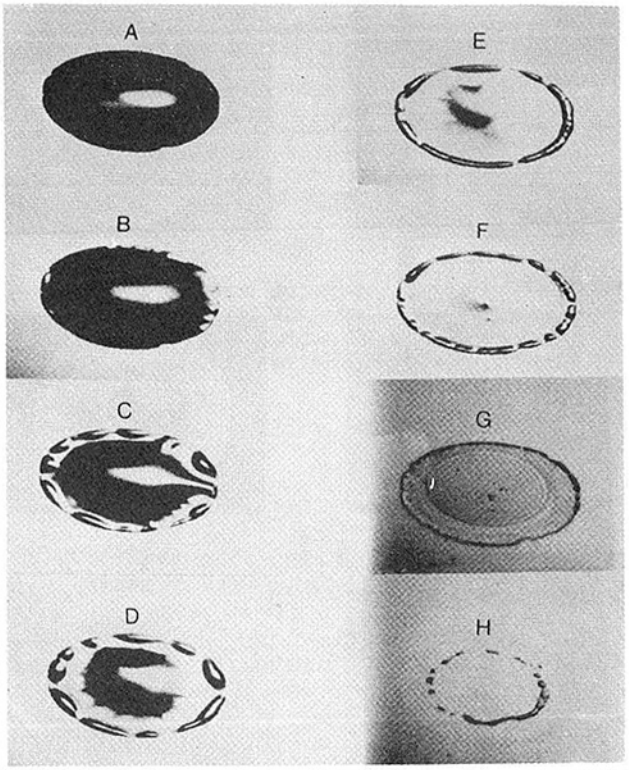

Fig. 5 Direct photograph at various instants during evaporation process of an acetone drop on a glass plate (*a*)

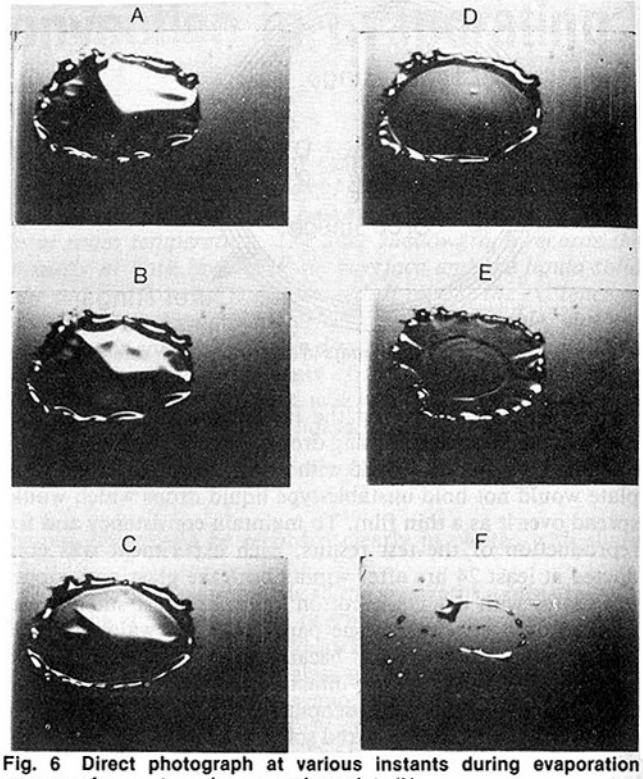

Fig. 6 Direct photograph at various instants during evaporation process of an acetone drop on a glass plate (*b*)

the outer rings were dissolved to form irregular radiant stripes within a sawtooth-like circle, Figs. 4(*a*) and 4(*b*) for methanol and acetone, respectively. The drops of acetone, ethyl alcohol, and methanol exhibited the behavior, which is called "unstable-interface type evaporation." There is a group of liquids such as ethyl acetate, benzene, chloroform, and methylene chloride whose interfacial flow patterns are in between the two limits, Figs. 4(*c*) and 4(*d*), for ethyl acetate and methylene chloride, respectively. The outer rings were retained but their shape was distorted from a circular shape and spiked. This group is categorized into "substable-interface type evaporation." In reference [4], these three basic flow structures were referred to as "radial stripes," "polygonal cells," and "ripples," named after their respective appearances. It was thought that the three flow patterns would appear in sequence during the entire process of evaporation for all liquids. However, the present study revealed that each structure is characteristic of a group of liquids and describes the nature of air-liquid and liquid-solid interfacial activities.

The direct photography was utilized to observe the morphology of drops undergoing the unstable-interface type evaporation. Two series of photos, Figs. 5 and 6, were taken on an acetone drop with the camera at two different angles. The evaporation process can be divided into three stages: quiescent, vigorous, and residual stages. The duration of these three stages varies with liquids. In the quiescent stage, the drop formed a spherical segment with a very smooth surface, as shown in Fig. 5(*a*). Then, tiny liquid blisters began to appear at the drop periphery. The location and order of the blister formation were randomly formed until the entire periphery was filled with the blisters, Figs. 5(*b*) through 5(*e*) and Figs. 6(*a*) through 6(*c*). Meanwhile, the spherical segment gradually deformed into a radial ridge but the air-liquid interface continued to sink in. In Figs. 5(*f*) and 6(*d*), the ridge disappeared completely because the liquid had either evaporated or moved toward the drop periphery until it formed a very thin film surrounded by a circular torous-shaped periphery. Evaporation proceeded rapidly during this stage, particularly at the drop center but slow at the torous surface because of high boiling point of the absorbed water. Due to a change in the surface tension/temperature gradient, the film then retracted and pulled the liquid in the torous toward the drop center, thus creating concentric ripples, Figs. 5(*g*) and 6(*e*). Finally, the torous retracted, attracting the remaining liquid to form a tiny hemisphere. Evaporation continued but at a very low rate in the residual stage. However, when the ambient temperature was raised by approximately 4°C, for example, due to heating by an illuminating lamp, the torous was not able to retract into a single tiny drop due to insufficient surface tension force. The torous then broke up into numerous tiny drops on a circle, as seen in Figs. 5(*h*) and 6(*f*).

Results and Discussion

In experimental investigation, it is important to determine the nondimensional parameters which govern the interfacial turbulence in minute drops evaporating on an unheated horizontal plate. Since the liquid volume is so tiny and thin, flow patterns are induced mainly by a surface tension driven instability. In other words, buoyancy-driven convection is very small and can be neglected. Hence, the Marangoni number $\mathrm{Ma} = (T_w - T_b)\, d_e\, (d\sigma/dT)/(\mu\alpha)$ could be an important parameter. Electrostatic and Electrokinetic potentials of interface, ψ and ζ, respectively, are also origins of the interfacial phenomena. They can be expressed in dimensionless form as $\psi e/(kT)$ and $\zeta e/(kT)$ where e expressed the electronic charge; k, Boltzmann constant; and T, interfacial temperature in the absolute scale. The polar group, because of van der Waals bonds to the water, may absorb water vapor from the ambient air during the evaporation process. Water molecules, absorbed from the air-liquid interface into the drop, induce the repulsive pressure in the liquid, which leads to lower values of surface tension. In general, the larger is the dielectric constant, ϵ, the higher is hydrophilicity of the liquid.

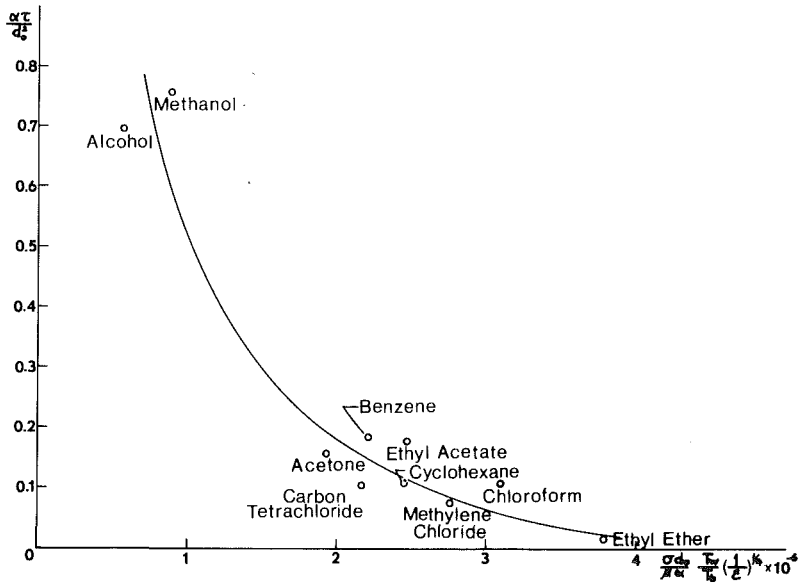

Fig. 7 Correlation of drop lifetime of various liquids

Hence, ϵ could be another parameter controlling the interfacial flow patterns. The dimensionless quantities associated with heat transfer such as the Prandtl and Jakob numbers are considered unimportant in the present study since evaporation takes place at room temperature. Also neglected are the influence of the Reynolds, Weber, and Froude numbers. However, a modified Marangoni number defined as $Ma^* = \sigma d_0 (Tw/Tb)/(\mu\alpha)$ is proposed which will be combined with $\epsilon^{1/4}$ for correlating test data for the drop lifetime.

Experimental evidence indicated that drop lifetime was strongly dependent on the magnitude of the dielectric constant of liquids ϵ. Test data on the lifetime τ in dimensionless form $\alpha\tau/d_0^2$ was correlated with the dimensionless parameter E, defined as $Ma^*/\epsilon^{1/4}$. Here, α denotes thermal diffusivity; d_0, initial diameter of drop image on the screen (i.e., initial diameter of the drop on the test plate); σ, air-liquid surface tension; μ, liquid viscosity; and T_w and T_b, temperature at plate surface and saturated state of the liquid, respectively. The physical properties in [6–10] were employed. Figure 7 shows that the dimensionless drop lifetime decreases with an increase in E. Among those liquids being tested, ethyl ether drops shared the shortest lifetime, whereas the two alcohols enjoyed the longest lifespan.

A method is developed to determine the drop volume-time history from the shadowgraph: First, the diameter of liquid-solid interface on the test plate, d, and that of the outermost ring on the screen, D, were measured. The distances AC and CE are known where A denotes the drop center on the test plate, while C and E are its images on the plate front mirror and the screen, respectively (see Fig. 2). Then, by a simple geometric relationship, the focal length of the drop, f, which is equal to AB, can be expressed as

$$f = \mathrm{AB} = \frac{d(\mathrm{AC}+\mathrm{CE})}{D+d} \tag{1}$$

This equation also applies when B falls between A and C. Now, one can evaluate the radius of the spherical segment using the relationship

$$\frac{1}{f} = (n-1)\frac{1}{R} \tag{2}$$

where n is the refractive index. For the liquids tested here, n varies from 1.3 to 1.5. Then, the volume of the drop can be determined as

$$V = \pi h^2\left(R - \frac{h}{3}\right) \tag{3}$$

wherein the height of the spherical segment is

$$h = R - \sqrt{R^2 - d^2/4} \tag{4}$$

Typical test results were listed in Table 1. The volume-time history is presented in Fig. 8 for the stable-type and Fig. 9 for both substable- and unstable-interface type evaporations. V_0 denotes the initial drop volume and τ indicates the drop lifetime. In both the stable- and sub-stable-evaporation cases, test results fall close to a single curve. In the unstable evaporation case, each liquid is represented by a specific curve. However, one thing in common among the three liquids is that the time history can be distinctly divided into three stages: In stage 1, evaporation is controlled by the pure component (methanol or ethanol or acetone); in stage 2, water is absorbed from the ambient and is transported to the edges (polarity); and in stage 3, evaporation is controlled by pure component—water. The broken lines show the vigorous evaporation stage in which determination of V were very difficult due to the irregularity in drop shapes. Why is this particular stage of unstable-interface type evaporation so different in the evaporation rate from the other stages or the other types of evaporation? The answer must be related to the formation of a torous during that stage.

A liquid with a larger dielectric constant ϵ is generally characterized by high hydrophilicity, as shown in Table 2. It is theorized that during evaporation, water molecules in the air are absorbed by the surface of the liquid drop, as shown in Fig. 10(*a*). The absorbed water molecules migrate down along the drop surface toward the periphery (Fig. 10(*b*)). When the water concentration reaches a certain level, liquid blisters begin to appear in random order at the drop periphery (Fig. 10(*c*)). This is because the repulsive pressure π (5 may also be referred to as "repulsive force") causes a reduction in surface tension from a value σ_0 for pure liquid:

$$\sigma = \sigma_0 - \pi$$

in which σ is the surface tension of the liquid with absorbed water molecules. When π exceeds σ_0, σ becomes negative. The net effect of a negative σ is a tendency for the drop surface to expand, leading to the formation of a torous at the periphery accompanied by a significant enhancement in the evaporation rate, Fig. 10(*d*). The drop surface recedes very rapidly until the central portion of the drop forms a very thin film, Fig.

Table 1 Typical test results

Methanol			Ethanol			Acetone		
t	*D*	*d*	*t*	*D*	*d*	*t*	*D*	*d*
s	cm	cm	s	cm	cm	s	cm	cm
0	25	0.65	0	20	0.67	0	15	0.7
1	20	0.65	4	18	0.67	3.5	13	0.7
6	12	0.65	6	16	0.67	6.5	11	0.7
13.5	11	0.65	14.5	14.5	0.67	9.5	9	0.7
25.5	10	0.65	24	13	0.65	12	8	0.7
33	9	0.65	50	12	0.65	15	7	0.7
40	8	0.65	62	11	0.65	19	6	0.7
47	7.5	0.65	67	10	0.65	23	5	0.7
52	6	0.65	80	9	0.65	27	4	0.7
120	-	-	140	-	-	30	-	-
.	.	.	.	.	.	.	.	.
.	.	.	.	.	.	.	.	.
.	.	.	.	.	.	.	.	.
150	-	-	210	12	0.25	40	2	0.3
160	10	0.25	260	12	0.2	56	2	0.2
190	10	0.2	305	4	0.2	70	0	0
240	4	0.2	363	0	0			
320	0	0						

Benzene			Methylene chloride			Ethyl acetate			Chloroform		
t	*D*	*d*	*t*	*D*	*d*	*t*	*D*	*d*	*t*	*D*	*d*
s	cm	cm	s	cm	cm	s	cm	cm	s	cm	cm
0	24	0.8	0	18	0.65	0	18	0.75	0	16	0.8
1.5	22	0.75	2.5	17	0.65	6.5	16	0.75	6	15	0.8
7.5	20	0.75	4	16	0.6	9.5	15	0.75	8.5	14	0.8
12	18	0.75	6	14	0.6	13	14	0.75	11	13	0.8
17.5	16	0.75	8	13	0.6	16	13	0.75	14	12	0.8
23.5	14	0.75	10	13	0.55	19.5	12	0.75	19	12	0.75
29.5	13	0.7	14.5	13	0.5	28.5	11	0.75	24	12	0.7
34	12	0.7	21	13	0.45	36.5	10	0.75	33	12	0.65
41	11	0.7	25	12	0.4	39.5	9	0.75	39.5	12.2	0.6
47.5	10	0.7	29	11	0.4	44.5	9	0.7	47	12.2	0.55
54.5	9	0.7	30.5	10	0.4	49.5	8	0.7	54.5	12.2	0.5
70	9	0.65	32.5	9	0.4	55	7	0.7	59	12.2	0.45
73.5	9	0.6	34	8	0.35	58	6	0.7	65.5	12.2	0.4
79.5	8.5	0.55	35.5	6	0.35	69	5	0.7	69.5	13	0.35
86	8	0.5	37	5	0.3	87.5	5	0.65	78	12.6	0.3
92.5	8	0.4	38.5	4	0.3	96	5	0.6	80.5	12	0.3
100	8	0.3	40.5	4	0.25	107	4	0.5	85.5	13	0.25
110	7	0.25	42.5	0	0	114.5	3.6	0.4	89.5	14	0.2
115	0	0				120	0	0	92	14	0.15
									97	0	0.

Cyclohexane			Ethyl ether			Carbon tetrachloride		
t	*D*	*d*	*t*	*D*	*d*	*t*	*D*	*d*
s	cm	cm	s	cm	cm	s	cm	cm
0	14	0.8	0	12	0.65	0	14	0.85
2.5	13	0.75	1.5	10	0.65	2	12	0.85
5	12	0.7	2.5	9	0.6	4.5	10	0.85
7.5	11	0.7	6.5	9	0.55	6.5	10	0.8
11	10	0.7	7.5	9	0.5	10.5	10	0.75
15	9	0.65	10	8	0.5	15.5	10	0.7
19	9	0.6	11.5	8	0.45	23	10	0.65
22.5	8.5	0.6	12.5	8	0.4	34	10	0.6
31	6.6	0.6	15	8	0.35	39	9.6	0.55
37.5	6.6	0.55	16.5	7	0.35	45.5	9	0.55
39	6.4	0.55	17	7	0.3	51.5	9	0.5
42.5	6.0	0.55	18.5	6	0.25	57.5	9	0.45
45	6.0	0.5	19	5	0.2	69	8	0.4
49	5.6	0.5	22.5	0		72.5	8	0.35
55	5.0	0.5				78	7	0.35
61	5.0	0.45				80.5	6	0.35
62.5	4.4	0.45				83	6	0.3
64.5	4.0	0.4				87.5	6	0.25
66.5	3.0	0.35				100	0	0
69.5	2.4	0.35						
71	2.4	0.3						
75	2	0.2						
80	0	0						

AC = 6.3 cm
CE = 95.25 cm

10(*e*). The surface tension of the liquid film acts to pull the liquid from the torous toward the center to form a new, tiny hemispherical drop, Fig. 10(*f*). The new drop evaporates at a low rate as it contains a substantial fraction of water in it. Figure 10(*g*) is the alternate of Fig. 10(*f*) when the ambient temperature is raised.

In order to verify that the repulsive pressure contributes to a reduction in surface tension at the air-liquid interface, a drop of ethyl ether mixed with 1 percent by volume of carbon tetrachloride was placed on the glass plate. Two photos in Fig. 11, obtained by direct photography, show the formation of liquid blisters at the drop periphery which eventually

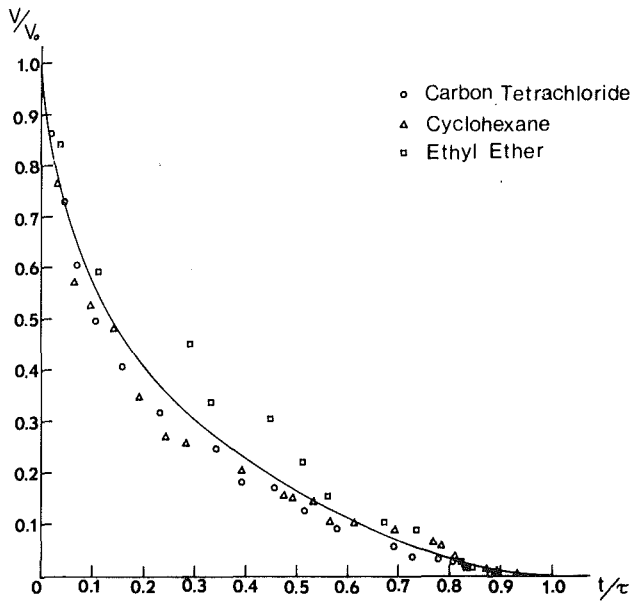

Fig. 8 Stable-type drop evaporation

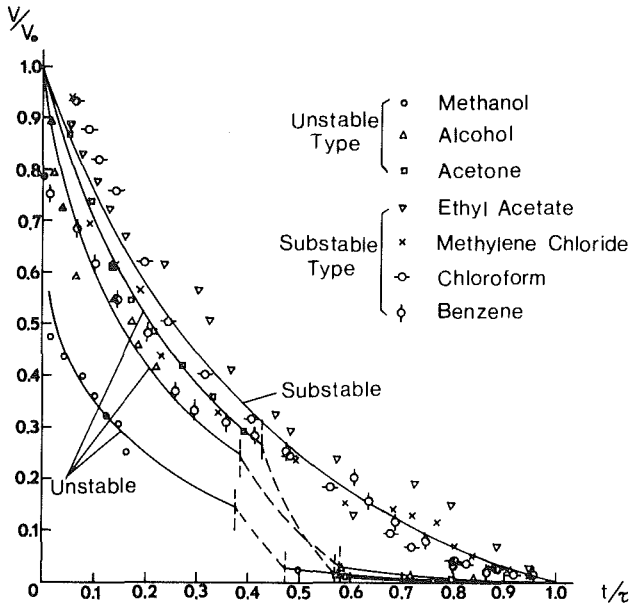

Fig. 9 Unstable- and substable-type drop evaporation

Table 2 Some properties of the liquids tested

Fluid	Boiling point T_b,K	Dielectric strength ϵ	Surface tension σ,N/m	Solubility water	alcohol	ether	acetone	benzene
Stable-type								
carbon tetrachloride	349.7	2.238	0.0269	i	s	inf	s	inf
cyclohexane	353.9	2.023	0.0257	i	inf	inf	inf	inf
ethyl ether	307.7	4.335	0.0172	del	inf	inf	v	inf
Substable-type								
ethyl acetone	350.3	6.02	0.024	s	inf	inf	v	v
benzene	353.3	2.284	0.0292	del	inf	inf	inf	-
chloroform	334.3	4.806	0.0273	del	inf	inf	s	inf
methylene chloride	313.	9.08	-	del	inf	inf	-	-
Unstable-type								
methanol	337.8	33.62	0.0224	inf	inf	inf	inf	inf
ethanol	351.5	24.3	0.0024	inf	inf	inf	inf	inf
acetone	329.4	20.7	0.024	inf	inf	inf	inf	inf

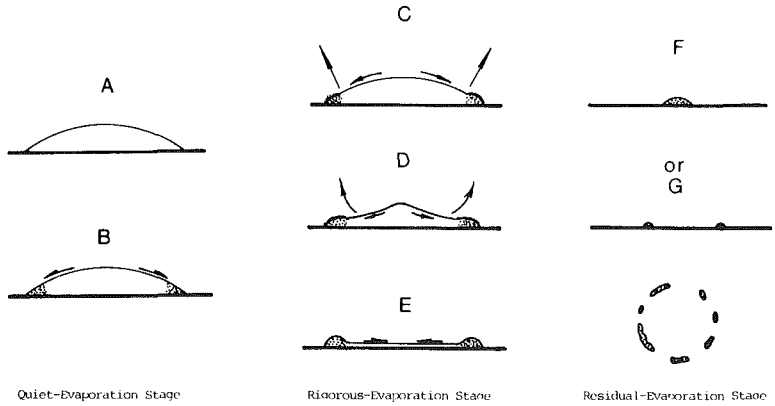

Fig. 10 Mechanics of unstable-type drop evaporation

developed into a torous. Another test method involved an addition of 1 percent by volume of carbon tetrachloride to a drop of a pure ethyl ether after the latter was placed on the test plate. A torous was seen at the drop periphery during the process of evaporation. This is in contrast to the pure component evaporation where no liquid blisters or torous were observed when drops of either pure ethyl ether or pure carbon tetrachloride were evaporated. The pure component drops remained in the shape of a spherical segment with a placid surface throughout the entire evaporation process.

In order to prove no influence of physico-chemical characteristics of test surface on the nature of interfacial turbulence, tests on the evaporation of various liquids were repeated on a polished copper plate under the identical situation as using the glass plate. A series of photos, by direct photography in Fig. 12, showed the evaporation process of an acetone drop. The variation of drop morphology is identical with that which had occurred on the glass plate. For example, the formation of liquid blisters followed by a very thin film in the central portion of the drop appeared in Fig. 12(*b*) to 12(*f*).

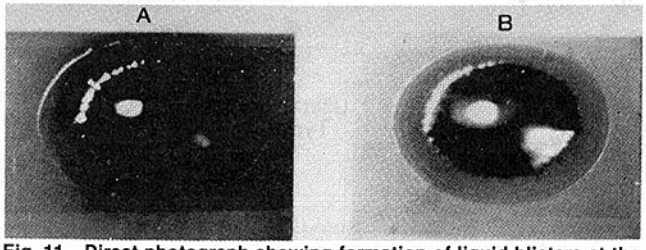

Fig. 11 Direct photograph showing formation of liquid blisters at the periphery of an ethyl ether drop mixed with 1 percent by volume of carbon tetrachloride during evaporation process on a glass plate

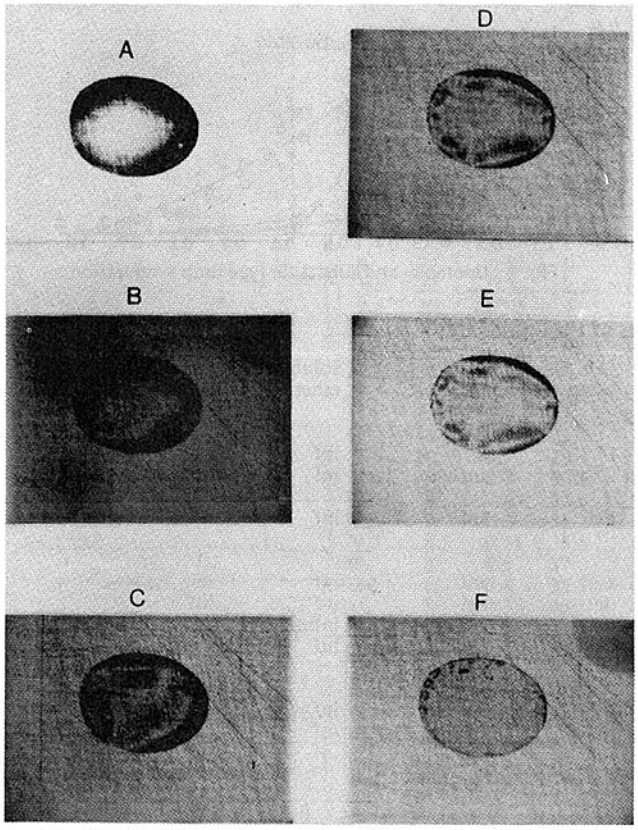

Fig. 12 Direct photograph at various instants during evaporation process of an acetone drop on a copper plate

We have thus proved that the liquid blisters and the torous were not produced as a result of surface characteristics of the test plates.

An interfacial flow map was constructed in Fig. 13 to define the domains of the three basic interfacial flow structures. The figure is a plot of the Marangoni number versus the dielectric constant. It is seen that unstable interfacial type liquids are characterized by high Ma and ϵ, whereas the liquids with low Ma and ϵ have stable interface during their evaporation. However, the addition of a small amount of stable-interfacial type liquid can induce an interfacial turbulence in another stable-interfacial type liquid, as previously discussed. For example, both carbon tetrachloride and ethyl ether take the form of a spherical segment with a perfectly smooth surface during evaporation. However, in presence of 1 percent by volume of carbon tetrachloride, interfacial turbulence appears in the drop evaporation of ethyl ether.

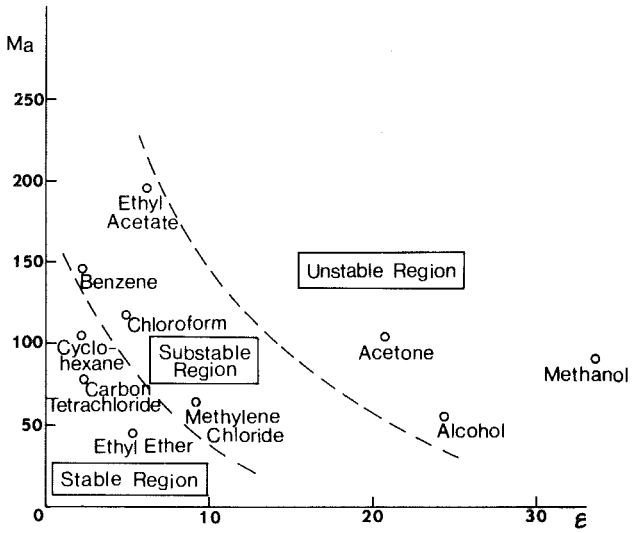

Fig. 13 Interfacial flow map

Conclusions

Interfacial stability in liquid drops evaporation on flat plates at room temperature was studied by both the direct photography and laser shadowgraphy. A method was developed to determine the volume-time history of evaporation drops from shadowgraphic photos. It is concluded from both flow visualization and volume-time history that liquids can be classified into three types: unstable, substable, and stable evaporation. The interface of stable-type drops remains smooth and takes the shape of a spherical segment. The unstable-interface type drop undergoes three stages of the evaporation process: quiet, rigorous, and residual evaporation. A theory is proposed and confirmed that the vigorous stage of an unstable interfacial type drop is caused by the action of surface tension on the drop interface mixed with the water molecules that are absorbed from the ambient during the process of evaporation. An interfacial flow map is constructed which defines the domains.

References

1 Brian, P. L. T., Vivian, J. E., and Matiatos, D. C., "Interfacial Turbulence During the Absorption of Carbon Dioxide into Monoethanolamine," *AIChE Journal*, Vol. 31, 1967, pp. 28–36.

2 Berg, J. C., Boudart, M., and Acrivos, A., "Natural Convection in Pools of Evaporating Liquids," *Journal of Fluids Mechanics*, Vol. 24, 1966, pp. 721–735.

3 Kenning, D. B. R., "Two-Phase Flow with Nonuniform Surface Tension," *Applied Mechanics Review*, Vol. 21, 1968, pp. 1101–1111.

4 Yang, Wei-Jei, and Nouri, A., "Interfacial Turbulence in Minute Drops Evaporating on a Flat Plate," *Letters Journal Heat Mass Transfer*, Vol. 8, 1981, pp. 115–125.

5 Davies, J. T., and Rideal, E. K., *Interfacial Phenomena*, 2nd ed., Academic Press, New York, 1963.

6 Dean, J. A., ed., *Lange's Handbook of Chemistry*, 12th ed., McGraw-Hill, New York, 1979.

7 Weast, R. C., ed.-in-chief, *CRC Handbook of Chemistry and Physics*, 59th ed., CRC Press, Inc., West Palm Beach, Florida, 1978–79.

8 Raznjevic, K., *Handboook of Thermodynamics Tables and Charts*, translated by M. Boskovic and R. Podhorsky, Hemisphere Publishing Corp., Washington, D.C., 1976.

9 Gray, D. E., coordinat. ed., *American Institute of Physics Handbook*, 3rd ed., McGraw-Hill, New York, 1972.

10 National Research Council, U.S.A., *International Critical Tables of Numerical Data, Physics, Chemistry and Technology*, McGraw-Hill, New York, 1933.

Comparison of the Rhine River and the Öresund Sea Water Fouling and Its Removal by Chlorination

L. Novak
Alfa-Laval,
Lund, Sweden

Microbiological fouling is usually the main fouling mechanism occurring on heat transferring surfaces immersed in natural water of temperature between 5–50°C. The fouling rate of two natural waters – the Rhine river and the sea water of Öresund – has been studied. The dependence of fouling on flow rate and temperature is given. Chlorination is one of the most common biofouling control methods and it may be used for removal of already formed microbiological deposits. Tests performed on the Rhine water deposit are described and a mathematic description of the chlorination kinetics is presented. The dependence of biofilm destruction on flow rate, temperature, concentration, and operation conditions was examined.

Introduction

A substantial number of heat exchangers, particularly plate heat exchangers, are designed for heat transfer duties in which all kinds of natural water sources (sea, river, and lake water) are used as a cooling medium. Water of this type with all its impurities causes more or less heavy fouling of these units. Although different types of fouling deposit may be formed, microbiological fouling is usually predominant up to temperature of 50°C.

The aim of this study was therefore to extend the existing information about the effect of process variables on biofilm formation and its destruction by chlorine.

The tests were carried out with the Rhine river water in Ludwigshafen, West Germany, which is a typical highly polluted river with very high fouling potential and with sea water of Öresund in Landskrona, Sweden, which is not at all typical of sea water, since its salinity is roughly 1/3 of the typical standard sea water.

Experimental Method

The tests have been carried out on two identical Alfa-Laval portable fouling units (PFU). The PFU is designed for testing the fouling rate, and testing fouling preventive methods, as well as for testing fouling removal methods. The schematic diagram of the PFU is shown in Fig. 1.

Test water enters the test plate heat exchanger (PHE) and is heated up by circulating heating medium (demineralized water). After having passed the test PHE, the hot test water enters the recovery PHE and is cooled down by the cool circulation medium. In this manner roughly 80 percent of the heat transferred in the test PHE is recovered. The flow rate of test water as well as the flow rate and the temperature of circulating heating medium are maintained constant during the test by flow and temperature controllers.

The test heat exchangers were of a plate type (Alfa-Laval P-01) with the heat transfer area of 0.032 m^2 per plate and plate spacing of 2.4 mm. The plate groupings used in this study are schematically shown in Fig. 2. All plates were made of commercially pure Titanium (ASTM Grade 1). The passes were thermally insulated from each other by an "insulation"

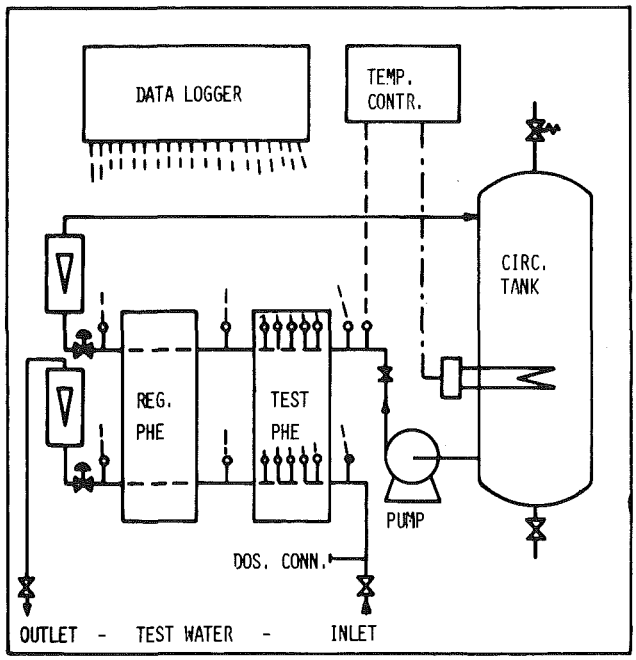

Fig. 1 Schematic diagram of the portable fouling unit

plate [1] which was fitted with a pair of thermocouples for measuring liquid temperature between passes. This arrangement allowed to evaluate the fouling history simultaneously at six or four temperatures and three different flow rates.

The formation of fouling deposit was evaluated in terms of fouling resistance R_f, calculated for the specific passes (Fig. 2) from the initial (or clean) overall heat-transfer coefficient calculated from the temperature record at the beginning of each test series and the actual heat-transfer coefficient calculated from the temperature record during the test. If necessary, the heat-transfer coefficients were corrected with respect to the actual temperature and flow rate.

Test conditions in specific passes are shown in Table 1. Nevertheless, due to fouling and fluctuations of the Rhine water and the Seawater temperatures, the temperatures shown in Table 1 changed slightly during the test. The temperature difference between heating medium and test water was as low as 6–10°C, and the mean slime mass temperature was only

Contributed by the Heat Transfer Division and presented at the 20th ASME/AIChE National Heat Transfer Conference, Milwaukee, Wisconsin, August 2–5, 1981. Manuscript received by the Heat Transfer Division October 7, 1981.

2–4°C higher than the water bulk temperature. Before starting a new series of tests, the test heat exchanger was dismantled and cleaned manually with diluted sodium hydroxide solution.

For the last series of tests with the Rhine water (Test Series D) one spiral heat exchanger (SHE) was connected in series to the plate heat exchanger. The spiral heat exchanger had a heat transfer area of 0.31 m^2, channel spacing of 5 mm, and channel width of 75 mm. All parts of the exchanger were made of Titanium.

The chlorination tests were performed simply by continuous injection of sodium hypochlorite solution into the inlet pipe of the test rig. The residence time of the hypochlorite before reaching the test heat exchanger was less than 10s.

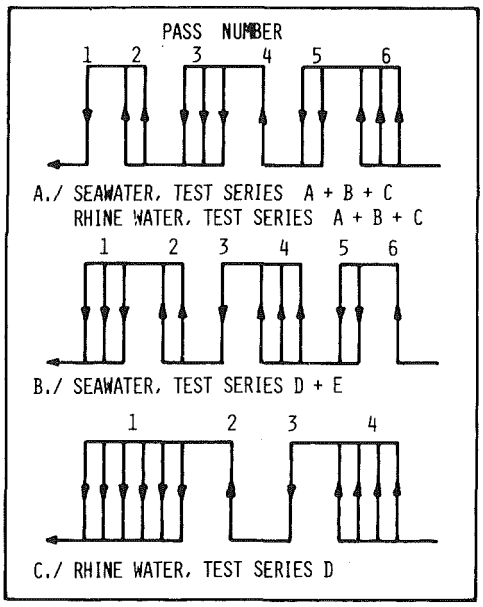

Fig. 2 Plate grouping of the test plate heat exchanger, test water side

Test Results

Chemical Composition of Test Waters.

The Rhine Water. The chemical composition of the Rhine water on the test site is shown in Table 2. Microbiological examination has not been made.

Sea Water of Öresund. The Öresund sea water is a mixture of a regular sea water coming from the North Sea with a low salinity water of Baltic Sea. The composition of this water is not quite stable and depends on weather and tide. Table 3 shows the composition of this water on the test site. Microbiological examination has not been made.

Properties of Slime Deposit. At the end of the first test with the Rhine water, a chemical analysis of the slime deposit has been made. The results of this analysis are summarized in Table 4. As seen, the content of silica was highest in the fastest passages, the content of iron was highest in the slowest passages while the contents of calcium, aluminium and kalium were highest in the middle of the temperature interval and without any obvious influence of flow velocity.

Besides this, several determinations of dry solids (105°C) of sea water slime have been made. All value has ranged from 8.2 to 12.5 percent of wet deposit.

No microbiological analysis of the deposits has been made. No scaling has been observed.

Appearance and strength of the slime deposit was a function of flow velocity. Slime deposit formed under high shear stresses was more uniform, homogeneous, and even had better adhesion to the metal surface as slime formed under low shear stresses.

The Fouling Rate. The fouling process is obviously a

Table 1 Summary of test conditions

Test water	Temperature of heating medium °C	Water bulk temperature °C	Mean water velocity m/s	Initial shear stress Pa	Initial heat flux kW/m^2
Sea water Test Series A+B+C	50	18–45	0.12–0.14 0.17–0.23 0.35–0.43	5.5–9.0 13–20 50–68	11–16 18–21 24–27
Sea water Test Series D+E	40	8–36	0.17–0.18 0.34–0.36 0.51–0.53	13–14 28–30 100–108	12–15 17–19 22–27
Rhine water Test Series A+B+C	40	11–38	0.15–0.16 0.22–0.23 0.43–0.45	8.5–10 17–22 65–80	9–11 17–20 25–28
Rhine water Test Series D PHE	40	17–35	0.13 0.19 0.77	6.7 14.5 190	10.0 14.2 22.5
Rhine water Test Series D SHE	31	19–27	0.43	7.5	9.1

Nomenclature

C = concentration of hypochlorous acid, kg/m^3
G = weight of polymers or slime deposit, kg
K = deposition/removal rate constant
N = number of microorganisms
R_f = fouling resistance, m^2K/W
R_f' = fouling resistance of residual deposit which cannot be removed by chlorination, m^2K/W
T_b = water bulk temperature, °C
T_s = wall temperature, °C
T_m = mean slime temperature, $(T_b + T_s)/2$, °C
k = constant in equation (6)
m = exponent in equation (3)
n = exponent in equation (1)
p = exponent in equation (3)
t = time, s
t_1 = chlorination time, s
t_2 = time between subsequent chlorinations, s
v = flow velocity, m/s
τ = shear stress at the wall-fluid interface calculated from the pressure drop, channel crossectional area and surface area of the channel, Pa

function of time. Nevertheless, due to incessant changes of environmental conditions such as water quality and temperature, the real fouling seldom proceeds during long periods of time along a specific and mathematically well-defined curve such as sigmoidal growth [2]. Although short periods of exponential growth do exist, the extended periods of exponential growth in nature are rare. Growth more often occurs in spurts followed by stationary or decreasing phases [3].

Also in this study, the observed fouling rate was as a rule not exponential. An outline of exponential growth was observed only during relatively short periods of time and mainly during the first days of some tests. In fact, the nonlinear fouling curves had usually a good linear approach in logarithmic diagram and could be approached by expression:

$$\frac{dR_f}{dt} = K\,t^n \tag{1}$$

where the exponent n had a value ranging from zero (linear growth) to about 0.8. Figure 3 shows typical fouling curves obtained in this study, as well as curves obtained by others in laboratory [4] and field [6] studies. While in laboratory studies [4, 5], asymptotic fouling has been obtained during 5–15 days; in field studies [6, 7, 8], asymptotic fouling has not even been reached during 50–70 days. Likewise in this study, test periods of up to 90 days were not sufficiently long for estimation of asymptotic value of fouling resistance. In fact the asymptotic value has never been reached in these tests. Therefore the following discussion gives information solely about the development of microbiological fouling during the growth period and not about the asymptotic value.

Table 2 Composition of the Rhine water

pH	–	7.6–7.9
Suspended matter	mg/l	10–100
Conductivity	μS/l	350–800
Tot. hardness as $CaCO_3$	mg/l	160–170
Calcium	mg/l	55–60
Chloride	mg/l	40–120
Sulphate	mg/l	29–42
Iron	mg/l	0.15–0.90
Manganese	mg/l	0.20–0.80
HCO_3^-	mg/l	140–170
Ammonia	mg/l	0.05–0.40
Nitrate NO_3^-	mg/l	4.5–6.5
Phosphate	mg/l	1.0–1.5
Oxygen	mg/l	8–12

Table 3 Composition of the seawater in Landskrona

pH	–	7.4–8.3
Salinity	mg/l	$7.5\text{–}15\cdot10^3$
Chloride	mg/l	$4.1\text{–}8.3\cdot10^3$
Sodium	mg/l	$2.3\text{–}4.6\cdot10^3$
Sulphate	mg/l	$0.42\text{–}0.86\cdot10^3$
Calcium	mg/l	88–176
Total alkalinity as $CaCO_3$	mg/l	25–75
Phosphor as PO_4^-	mg/l	0.003–0.13
Nitrate NO_3^-	mg/l	0.005–0.06

Since both linear and nonlinear fouling curves were observed, for simpler evaluation of test results, all the fouling curves obtained were linearized prior to further evaluation.

The Effect of Temperature on Fouling Rate. Since the fouling rate at each flow velocity has been evaluated at two different temperatures, the effect of temperature on fouling rate was simply evaluated by comparison of mean values of fouling rate for each series. The evaluation was done by linear extrapolation between each pair of temperatures and was expressed in terms of the fouling rate at 25°C in the case of the Rhine water (Fig. 4) and at 30°C in case of sea water (Fig. 5). In the Rhine water, the fouling rate reached a maximum at a mean slime temperature of approximately 32°C and in sea water at approximately 35–37°C.

The Effect of Flow Rate on Fouling Rate. To eliminate the effect of temperature on the fouling rate, linearized rate values, obtained with the Rhine water were recalculated according to Fig. 4 from the actual temperatures to temperature of 25°C. Recalculated data are shown in Fig. 6 as a function of water shear stresses. It may be discussed whether shear stresses or the linear flow velocity should be used as a correlating parameter of biological fouling. However, comparison of the fouling rate obtained during Test Series D with the Rhine water (see Table 5) indicates clearly that the comparison of microbiological fouling on velocity basis is not adequate.

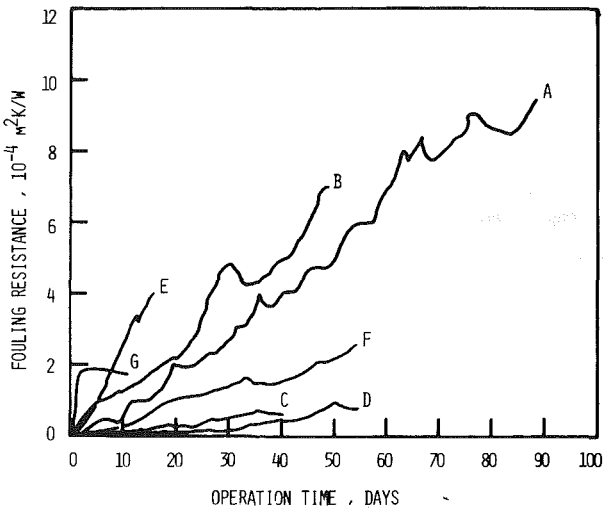

Fig. 3 Development of fouling resistance at various conditions:

(A) Rhine water, v = 0.2 m/s, τ = 18 Pa, T_b = 22°C
(B) sea water, v = 0.14 m/s, τ = 9 Pa, T_b = 35°C
(C) sea water, v = 0.53 m/s, τ = 108 Pa, T_b = 22°C
(D) Rhine water, v = 0.77 m/s, τ = 190 Pa, T_b = 23°C
(E) reference [6], sea water, v = 0.6 m/s, τ = 2 Pa, T_b = 25°C
(F) reference [6], sea water, v = 1.8 m/s, τ = 14 Pa, T_b = 25°C
(G) reference [4], lab. study, v = 0.6 m/s, τ = 2.3 Pa, T_b = 28°C

Table 4 Chemical composition of slime deposit from the Rhine water at the end of Test Series A

Pass number	1	2	3	4	5	6
Residue at 105°C, %	9.0	10.1	10.5	10.1	10.8	10.9
Residue at 850°C, %	6.2	6.9	7.0	7.3	7.7	7.2
Silica	1.10	1.19	1.04	1.40	1.38	1.05
Iron	0.77	0.95	1.17	0.77	0.98	1.27
Calcium	0.49	0.54	0.52	0.64	0.63	0.57
Aluminium	0.38	0.43	0.47	0.50	0.47	0.42
Kalium	0.14	0.17	0.21	0.21	0.19	0.17
Sodium	0.04	0.04	0.25	0.09	0.05	0.12
Other elements found by spectral analysis:	Mg, Mn, P, Zn, S, Ag, Cu, Cl B, Co, Cr, Mo, Ni, Pb, Sb, Sn, V, Ti, Ba					

All values are in % of the wet slime.

Similarly, linearized values of the fouling rate obtained with sea water were recalculated according to Fig. 5 but in this case to temperature of 30°C (see Fig. 7).

As seen in both cases, the fouling rate decreased considerably with increasing shear stresses, but the sensitivity was somewhat lower than the one previously observed [1].

Comparison of Fouling Rate in the Rhine River and in the Öresund Sea Water. Figure 8 shows the average values of the linearized fouling rate observed during tests with the Rhine water and the Öresund sea water. As seen, the fouling rate of the Rhine water was between 20 and 40 percent higher than the fouling rate of the Öresund sea water. The low fouling rate of sea water Test Series E was a result of intermittent chlorination performed daily during half-hour at a dosing level of 2 ppm. As seen, no drastic reduction of the fouling rate has been observed during the winter months. Therefore, the drastic reduction of fouling rate which is frequently observed during winter months is probably caused, to the greatest extent, by lower temperature of cooling water.

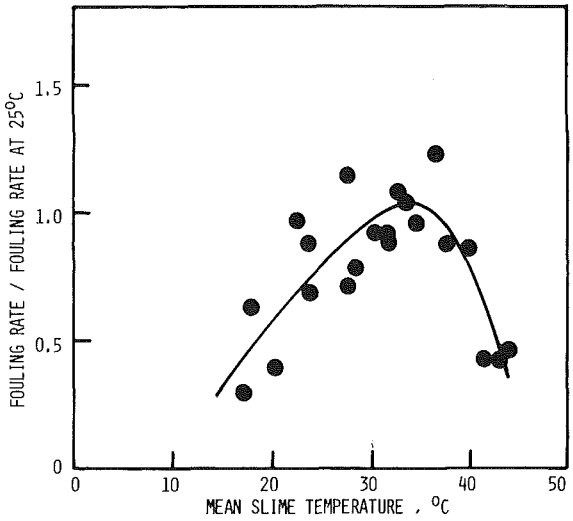

Fig. 4 Dependence of the Rhine water fouling on temperature

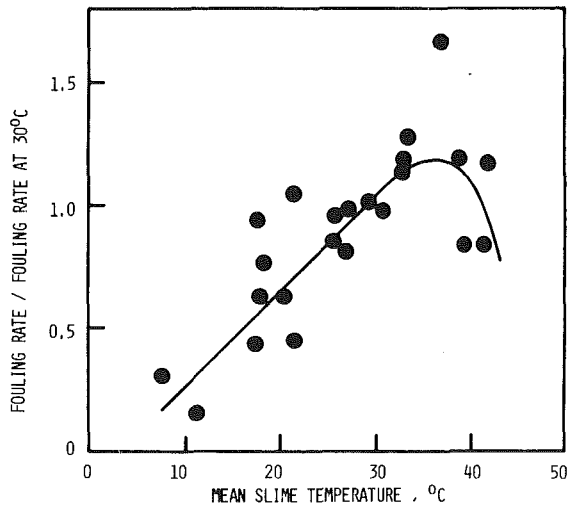

Fig. 5 Dependence of the Öresund Sea water fouling on temperature

Removal of Biological Fouling by Chlorination.

The Action of Chlorine. Hypochlorous acid is an extremely powerful oxidizing agent which easily diffuses through the cell walls of microorganisms. It is considered that hypochlorous acid oxidizes the active sites on certain enzyme sulfhydryl groups, which constitute intermediate steps in the production of adenosine triphosphate (ATP) essential for respiration, since ATP serves as the prime energy carrier in living organisms [9, 10, 11].

Beside this, it is considered that hypochlorous acid also attacks the extracellular polymers of microbiological slime. These polymers maintain the integrity of the biofilm matrix. Oxidative action of chlorine causes depolymerization and results in removal of the weakened biofilm matrix by fluid shear stress [2].

This destructive action differentiates chlorine from other nonoxidizing biocides and indicates that chlorination would be used not only for disinfection and control of biological fouling, but also for removal of already formed slime deposits as well.

The Kinetics of Slime Removal. The effect of chlorination upon unicellular organisms may be described by the following expression, which sometimes is called Chick's law [3]:

$$\frac{dN}{dt} = -KN \tag{2}$$

where dN/dt is the death rate.

Since slime deposits consist of living organisms as well as of extracellular polysaccharides and polypeptides, the death of the unicellular organisms does not necessarily result in immediate destruction and release of the slime deposit. The immediate effect of such disinfection of living organisms may

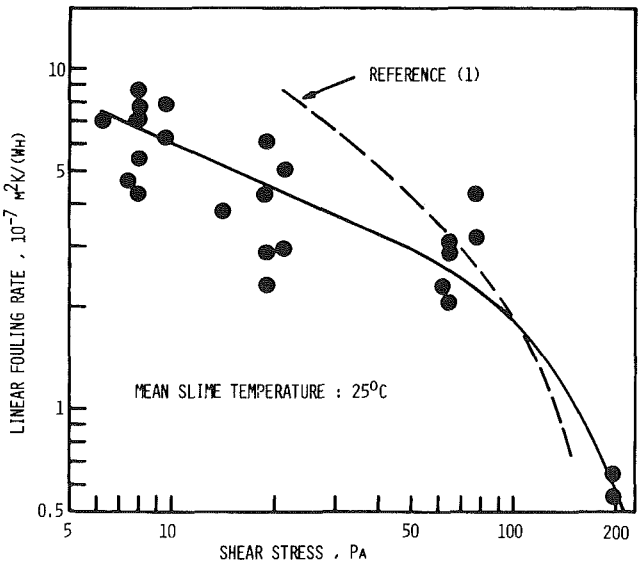

Fig. 6 Dependence of the Rhine water fouling on shear stress

Table 5 Comparison of fouling rate at 25°C in different heat exchangers, the Rhine water of Test Series D

Exchanger type	Flow velocity m/s	Shear stress Pa	Fouling rate 10^{-7}•m²K/W•h
PHE	0.13	6.7	7.4
	0.19	14.5	4.3
	0.77	190	0.6
SHE	0.43	7.5	5.0

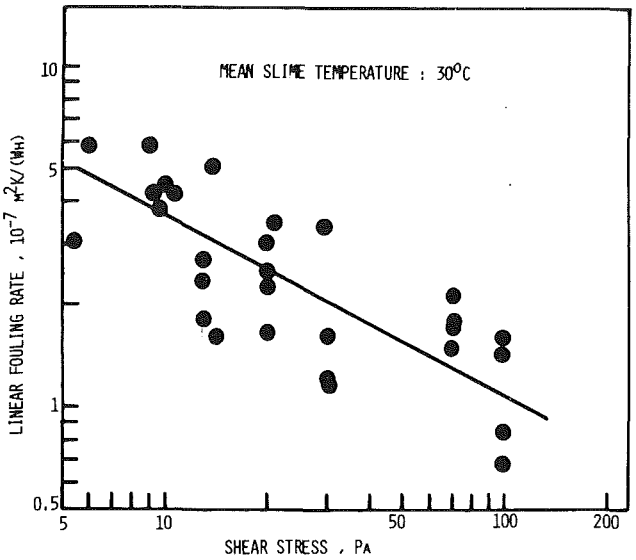

Fig. 7 Dependence of the Oresund Sea water fouling on shear stress

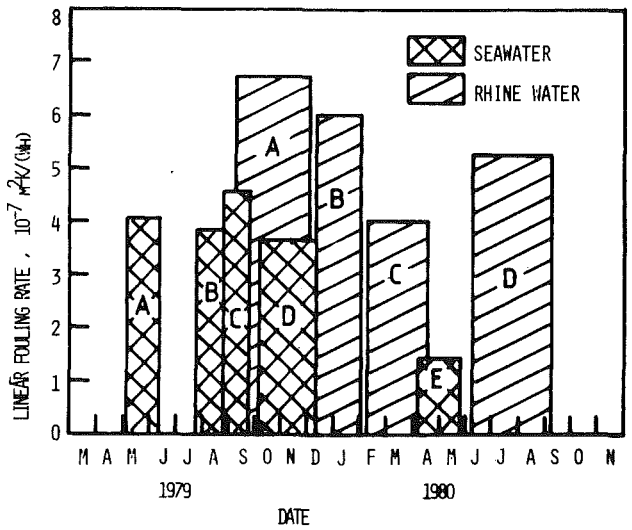

Fig. 8 Fouling rate of the Rhine water and the Oresund Sea water at water temperature of 30°C and shear stress of 15 Pa

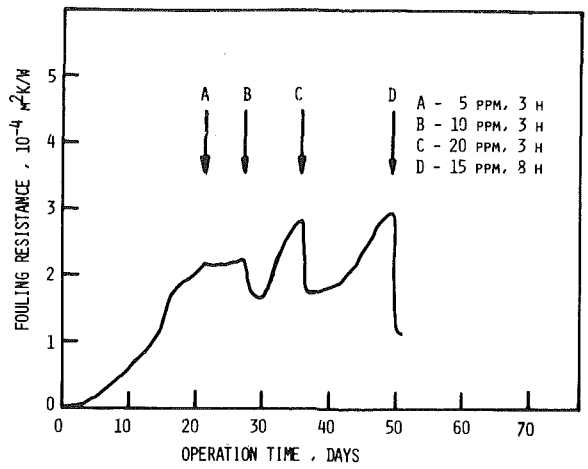

Fig. 9 Reduction of fouling resistance by chlorination (Rhine water, Test Series B)

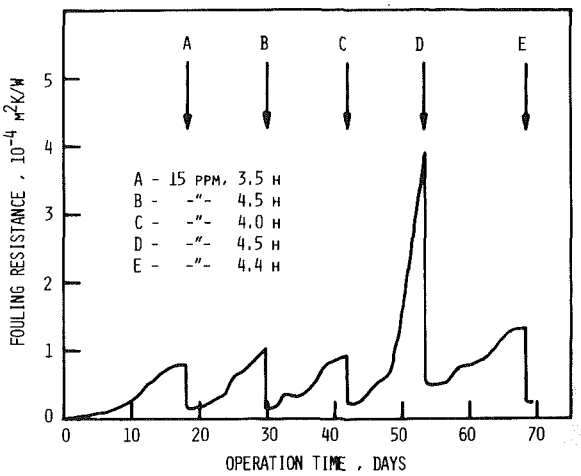

Fig. 10 Reduction of fouling resistance by chlorination (Rhine water, Test Series C)

be limited only to reduction or inhibition of slime production. Therefore, the above equation (2) does not necessarily describe the removal of slime deposit.

As mentioned above, chlorine (hypochlorous acid) not only kills the living organisms, but also attacks the extracellular polymers. This attack (destruction and release) may be perhaps explained – like a disinfection of unicellular organisms [3] – by analogy with chemical reactions.

Assuming that diffusion rate of hypochlorous acid into the slime is sufficient, i.e., concentration of hypochlorous acid in slime is approximately constant and equal to the concentration in water phase, the destruction rate of polysaccharides can be, in analogy with chemical reactions described by expression:

$$\frac{dG}{dt} = -K\,C^m\,G^p \tag{3}$$

If the destructed slime is continuously removed by water shear stresses, equation (3) would also describe the removal rate of the slime deposit.

Nevertheless, the assumption of a high diffusion rate of hypochlorous acid in a slime deposit is not correct, as may be easily shown by calculation of concentration profile of hypochlorous acid in a hypothetical slime deposit being in contact with chlorinated water and having for the sake of simplicity diffusional properties of water.

Since hypochlorous acid is a very strong oxidant and reacts quickly with a number of organics [11], we have all reasons to believe that for low concentrations of hypochlorous acid, as applied in this study, the slime destruction is mass transfer controlled, and therefore exponents m and p in equation (3) are equal to 1.

Further, fouling resistance is proportional to the amount of the deposit. Assuming that heat conductivity of the deposit is constant, equation (3) may be rewritten as

$$\frac{dR_f}{dt} = -KCR_f \tag{4}$$

If the deposit contains a part which can not be removed by action of hypochlorous acid, for example, scale or accumulated sediment, equation (4) is modified as follows:

$$\frac{dR_f}{dt} = -KC(R_f - R_f') \tag{5}$$

The rate constant, K, is a function of temperature, water quality, slime properties, and flow conditions. It should be pointed out that equations (4) and (5) are valid for constant

Table 6 The rate of slime removal KC in different passes

Pass number	3	4
Shear stress, Pa	9	72
Temperature, °C	25.4	21.5
KC, 10^{-7} m²K/Ws	4.2	5.1

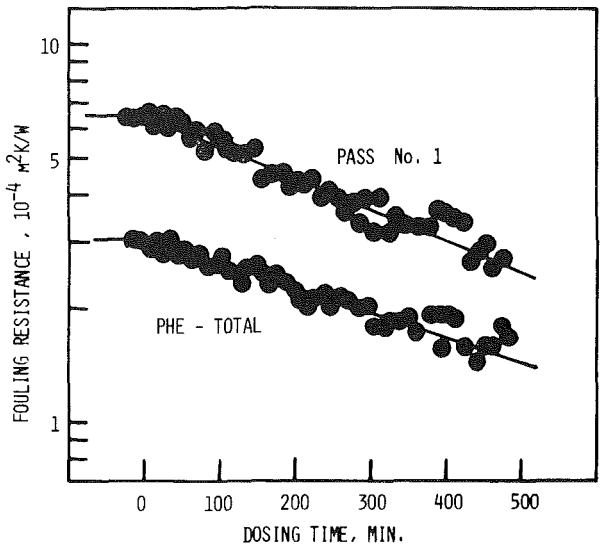

Fig. 11 Reduction of fouling resistance by dosage of 20 ppm sodium hypochlorite (Rhine water, Test Series D, test no. 11)

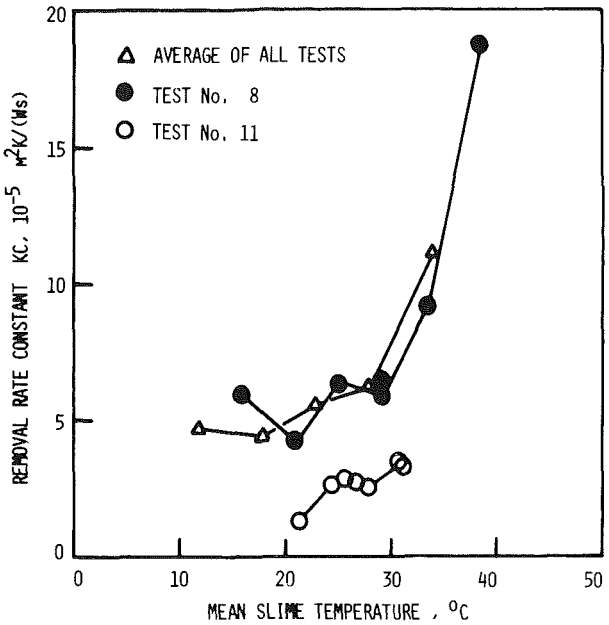

Fig. 12 Dependence of removal rate constant *KC* on temperature

concentration, C, of hypochlorous acid in water, and that this concentration, due to chlorine demand of water itself, is not necessarily equal to the nominal concentration calculated from the dosage rate.

Upon integration, equations (4) and (5) give the first-order relationships; and when the logarithm of R_f or $(R_f - R_f')$ is plotted against time, a straight line with slope of KC will be obtained.

From January to September 1980, a total of eleven chlorination tests on slime deposits carried out in Ludwigshafen formed in the Rhine water.

The effect of chlorination on slime deposit was very strong. As seen in Figs. 9 and 10, the dosage of only 10–15 ppm may considerably reduce the fouling resistance within only a few hours.

Figure 10 clearly demonstrates that periodic chlorination performed every 10–15th day at a level of 10–20 ppm would be able to keep the fouling resistance of a heat exchanger at a reasonable level for a long time. On the other hand, Fig. 9 indicates that periodic chlorination may be insufficient if performed too late after cleaning of the heat exchanger, or in too long intervals.

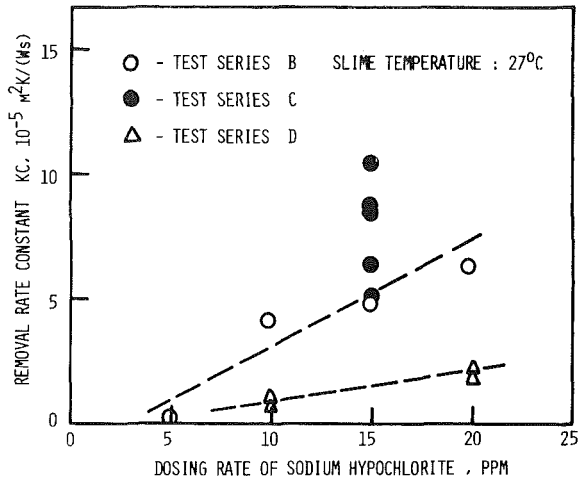

Fig. 13 Dependence of removal rate constant *KC* on dosing rate of sodium hypochlorite

For the purpose of examination, whether or not equations (4) and (5) describe the kinetics of chlorination, the fouling resistance of the whole test heat exchanger, as well as that of the specific passages, has been measured several times during the chlorination tests No. 7, 8, 10 and 11. Figure 11 shows the reduction of fouling resistance of the test heat exchanger during the test No. 11. As seen, the reduction of the logarithm of fouling resistance with time was roughly linear, which indicates that equations (4) and (5) describe the kinetics of chlorination at low concentrations of hypochlorous acid. This conclusion agrees well with the work of Bryers et al. [2], in which the authors suggest that chlorination would be a reaction of the first order or mass transport controlled.

Obtained data are unfortunately not sufficient for determination, whether the chlorination is reaction of the first order or is controlled by mass transport.

The Effect of Operational Variables. When applying the results of this study to other systems, it should be always kept in mind that the slime deposit has been formed at the same conditions – temperature and flow velocity – as the chlorination procedure has been carried out and that therefore the properties of the slime deposit were not identical in the specific passages.

The Effect of Temperature. The experimental method allowed for simultaneous evaluation of destruction rate constant at six different temperatures and three different flow rates. The effect of temperature and flow rate on the rate of biofilm destruction could therefore be evaluated simply by comparison of the particular destruction rate constants. Figure 12 shows the average values of KC obtained in this study.

As seen, temperature had a promoting effect. The increase in temperature from 15 to 35°C increased the rate of biofilm removal roughly by a factor of 2. Interestingly the diffusion rate of hypochlorous acid in pure water increases from 15 to 35°C roughly by a factor of 1.7.

The Effect of Flow Rate. The rate of biofilm removal was independent of flow rate in this experimental arrangement. This is clearly demonstrated by comparison of the mean values of the destruction rate constant for passages 3 and 4 (see Table 6).

It should be again pointed out that due to different shear stresses, the properties of the slime deposit in specific passages were not identical. Slime formed under higher shear stresses was more compact and strong and not at all as voluminous as slime formed under low shear stresses. Therefore, to avoid missunderstanding, the results of this study should be in-

terpreted as follows: It has been shown that within the range of shear stresses 5–200 Pa, (i.e., highly turbulent flow), and under conditions that chlorination is performed in the same flow conditions as the slime deposit has been formed, the rate constant of slime removal was independent of flow rate.

The Effect of Concentration. Figure 13 shows the values of the rate constant KC calculated for the whole test exchanger and recalculated from the actual average temperature to temperature of 27°C. The figure gives an indication that the chlorine demand of the Rhine water was less than 5 ppm and that the rate of biofilm destruction was proportional to the net concentration of hypochlorous acid.

The difference between Test Series D and Test Series B and C is very interesting. These differences and especially the difference between Test Series D and Test Series B and C can not be explained by the chlorine demand of the Rhine water. However, a look at the history of the tests presents a credible explanation: While chlorination tests of Test Series C were performed in 12–17 day intervals and always had good performance, chlorination tests of Test Series D were performed after the 51st and the 91st day and the first tests of Test Series B were performed with too low dosage of hypochlorite. Therefore, slime deposits in Test Series C were always "fresh," contained less foreign debris, and had probably higher sensitivity to chlorine.

Chlorination Procedure. Since the quality of removed slime is proportional to the applied amount of hypochlorous acid (chlorine), and since the quantity of formed slime is proportional to the growth time, there is obviously also a rough proportionality between the chlorine (hypochlorous acid) dose and the time during which the fouling resistance again reaches the original value. This proportionality may be expressed as:

$$t_2 = kCt_1 \tag{6}$$

where t_1 is chlorination time and t_2 is time between chlorinations during which fouling resistance (amount of slime deposit) reaches the value prior to chlorination and C is net concentration in ppm (not the dosing rate). The value of the constant k depends naturally on the fouling rate and on the rate of fouling removal. The value of the constant k ranged in this study (all performed tests) from 3.9 to 8.0 ppm^{-1} with the average value of 5.8 ppm^{-1}. The fouling rate of the Rhine water belongs certainly to the highest of all. Since the test conditions used in this study cover most of the operating conditions used in plate heat exchangers, the value of k = 4.0 ppm^{-1} would be sufficient for good control of microbiological fouling in plate heat exchangers (i.e., temperature = max. 40°C, shear stress = min. 10 Pa).

Generally, the optimal chlorination procedure can be determined for a specific exchanger designed with specific fouling margins by equations (1) and (4) or (5) and using figures similar to Figs. 4–7 and 12 but determined for that specific water source. However, in order to obtain a high efficiency of the chlorination procedure, fouling margins exceeding a value of $2\times10^{-4}m^2K/W$ should not be considered. It should be pointed out that in waters with pH- value above 8.0, the above values are not sufficient due to reduced efficiency of hypochlorous acid.

Conclusions

The results of the tests may be summarized as follows:

- Microbiological fouling reached its maximum at a temperature of approximately 30–37°C.
- The rate of microbiological fouling is dependent on water shear stresses and decreases with increasing shear stresses.
- The slime deposit is rapidly destroyed by hypochlorous acid at relatively low concentrations of 10–15 ppm and can be removed by water shear stresses.

References

1 Novak, L., "Control of the Rhine Water Fouling," *Fouling of Heat Transfer Equipment*, edited by E. F. C. Somerscales and J. G. Knudsen, Hemisphere Publishing Co., 1981, pp. 397–408.

2 Bryers, J. D., Characklis, W. G., Zelver, N., and Nimmons, M. J., "Microbial Film Development and Associated Energy Losses," *Proceedings of the 6th OTEC Conference*, Washington D.C., Vol. 4, 1979, pp. 4c4/1–4c4/8.

3 Brock, T. D., *Biology of Microorganisms*, 3d ed., Prentice Hall, 1977, pp. 409 and 746.

4 Characklis, W. G., Zelver, N., Turakhia, M., and Nimmons, M. J., "Fouling and Heat Transfer," *Fouling in Heat Exchange Equipment*, ASME, HTD-Vol. 17, 1981, pp. 1–15.

5 Harthy, D. W. S., and Bott, T. R., "Deposition and Growth of Microorganisms on Simulated Heat Exchanger Equipment," *Fouling of Heat Transfer Equipment*, edited by E. F. C. Somerscales and J. G. Knudsen, Hemisphere Publishing Co., 1981, pp. 335–344.

6 Ritter, R. B., and Suitor, J. W., "Fouling Research on Copper and its Alloys — Seawater Studies," Progress report to INCRA, Project No. 214a, Heat Transfer Research, Inc., Alhambra, Calif., Apr. 1976.

7 Little, B., Morse, J., Loeb, G., and Spiehler, F., "Biofouling and Corrosion Study of OTEC Heat Exchanger, Candidate Metals," presented at Corrosion 80, Chicago, Mar. 3–7, 1980, Paper No. 43.

8 Fetkovich, J. G., Granneman, G. N., Mahaligham, L. M., and Meier, D. L., "Measurements of Biofouling in OTEC Heat Exchangers," *Proceedings of The 5th OTEC Conference*, Miami Beach, Vol. 4, 1978, pp. VIII.7–VIII.40.

9 Betz Laboratories, Inc., *Handbook of Industrial Water Conditioning*, 7th ed., Trevose, Pa., 1976, pp. 24–29.

10 Drew Chemical Corporation, *Principles of Industrial Water Treatment*, 1st ed., Boonton, N. J., 1977, pp. 99–103.

11 Jolley, R. G., Gorchev, H., and Hamilton, D. H., *Water Chlorination — Environmental Impact and Health Effect*, Vols. 1 and 2, Ann Arbour Science, 1978.

Forced-Convection Heat Transfer in a Spherical Annulus Heat Exchanger[1]

D. B. Tuft
Engineer,
University of California,
Lawrence Livermore National Laboratory,
Livermore, Calif. 94550
Mem. ASME

H. Brandt
Professor of Mechanical Engineering,
University of California at Davis,
Davis, Calif. 95616
Mem. ASME

Results are presented of a combined numerical and experimental study of steady, forced-convection heat tranfer in a spherical annulus heat exchanger with 53°C water flowing in an annulus formed by an insulated outer sphere and a 0°C inner sphere. The inner sphere radius is 139.7 mm, the outer sphere radius is 168.3 mm. The transient laminar incompressible axisymmetric Navier-Stokes equations and energy equation in spherical coordinates are solved by an explicit finite-difference solution technique. Turbulence and buoyancy are neglected in the numerical analysis. Steady solutions are obtained by allowing the transient solution to achieve steady state. Numerically obtained temperature and heat-flux rate distributions are presented for gap Reynolds numbers from 41 to 465. Measurements of inner sphere heat-flux rate distribution, flow separation angle, annulus fluid temperatures, and total heat transfer are made for Reynolds numbers from 41 to 1086. The angle of separation along the inner sphere is found to vary as a function of Reynolds number. Measured total Nusselt numbers agree with results reported in the literature to within 2.0 percent at a Reynolds number of 974, and 26.0 percent at a Reynolds number of 66.

1 Introduction

In a spherical annulus heat exchanger (see Fig. 1), fluid enters and exits the annulus through diametrically opposed openings in the outer sphere, and temperature control is achieved on a material inside the inner sphere. The spherical annulus heat exchanger is suited to situations requiring maximum volume of inner sphere material per unit surface area. Applications exist wherever the temperature of a large volume of material must be controlled by a relatively low volume of working fluid [1]. Applications include cryogenic storage systems and guard heating systems. In addition, certain gyroscopic gymbols are cooled by spherical annulus flow [2], and the heat exchanger has been proposed for cooling spherical fuel elements in homogeneous nuclear reactors [3].

This paper presents a numerical and experimental study of steady, forced-convection heat transfer in a spherical annulus with a 0°C cooled inner sphere and an insulated outer sphere. Water at 53°C enters the annulus at the bottom and exits at the top.

In the numerical analysis, the transient finite difference equations of mass, momentum, and energy conservation are solved in spherical coordinates for laminar, incompressible, axially symmetric flow. Computed temperature and heat-flux rate distributions are compared to measurements. The spherical coordinate system is shown in Fig. 1.

It is believed that this is the first combined analytical and experimental investigation of heat transfer in a spherical annulus. In addition, this numerical analysis is the first-two-dimensional analysis using the full Navier-Stokes equations for steady spherical annulus forced-convective heat transfer, and these experiments are the first in which local variations of inner sphere heat flux and separation angle have been measured.

One of the first analytical treatments of fluid flow in a spherical annulus was by Cobble [4] who assumed a simplified

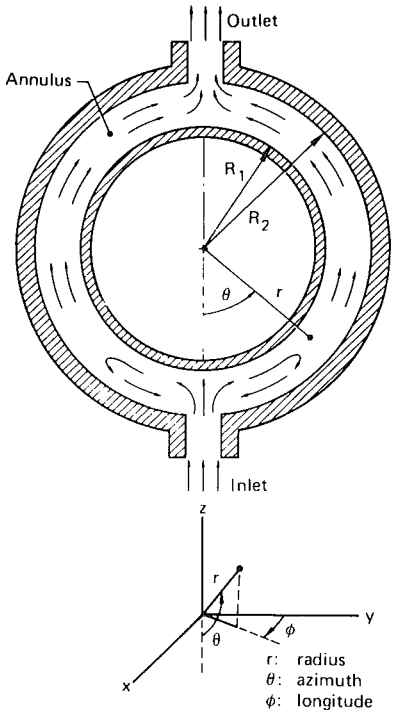

Fig. 1 Spherical annulus heat exchanger and coordinate system

tangential velocity distribution and then calculated heat transfer based on the energy equation. Ward [5] provided a flow visualization study of isothermal flow in a spherical annulus between 60 and 120 deg downstream of the entrance. Rundell, Ward, and Cox [1] measured the fluid temperature profiles and the total inner sphere heat-transfer coefficient for steady flow. They obtained a heat-transfer correlation for two sets of sphere sizes. Bozeman and Dalton [6] added to the isothermal flow visualization work by focusing on the entrance region.

Rundell observed a flow rate independent separation point located at approximately 45 deg downstream of the inlet. Bozeman showed that upstream of the separation point the

[1]Work performed under the auspices of the U.S. Department of Energy by the Lawrence Livermore Laboratory under contract number W-7405-Eng-48.

Contributed by the Heat Transfer Division and presented at the ASME Winter Annual Meeting, Washington, D.C., November 20, 1981. Manuscript received by the Heat Transfer Division July 27, 1981. Paper No. 81-WA/HT-8.

flow is characterized by a high-velocity jet of fluid near the inner sphere with a relatively low-velocity return flow near the outer sphere.

The problem of laminar natural convection flow is a closed spherical annulus was solved numerically by Brown [7] by an explicit finite difference technique coupled to an iterative solution of the vorticity stream function relation. Astill [2] applied a boundary layer order of magnitude analysis to the steady laminar incompressible Navier-Stokes equations in spherical coordinates to reduce them to a set of parabolic differential equations. Astill used boundary layer assumptions that were valid in regions of nearly parallel flow, and thus separated and recirculating flows could not be handled. The present numerical analysis extends the work of Astill by including all the terms in the Navier-Stokes equations, thus allowing treatment of separation and recirculating flows in the inlet and outlet regions.

Newton [8] investigated spherical annulus convective heat transfer experimentally. Local velocity and temperature profiles and total heat-transfer coefficients were measured with air as the working fluid.

A numerical analysis of the transient filling of a spherical annulus was presented by Tuft [9]. A modified form of the Marker-and-Cell method was used to handle the free surface aspects of the problem. The full Navier-Stokes equations were solved, and recirculation and separation were considered. Transient temperature contours and inner sphere heat flux at various times were presented.

2 Numerical Solution Technique

The governing equations are the conservation equations of mass, radial momentum, azimuthal momentum, and energy. The variables of pressure, velocity, and temperature are used, and the equations are solved in the spherical $r-\theta$ plane shown in Fig. 1. For all equations, transient laminar incompressible axially-symmetric flow of a fluid with constant properties is assumed. The assumption of flow symmetry has been checked by dye injection and has been studied experimentally by others [1, 3, 5]. In the energy equation, viscous dissipation is neglected, and, in the momentum equations, buoyancy forces are neglected. It is recognized that buoyancy forces may be important at low Reynolds numbers.

The governing equations for this problem are:

Radial Momentum

$$\frac{\partial u}{\partial t}+\frac{1}{r^2}\frac{\partial}{\partial r}(r^2u^2)+\frac{1}{r\sin\theta}\frac{\partial}{\partial\theta}(uv\sin\theta)-\frac{v^2}{r}=-\frac{1}{\rho}\frac{\partial P}{\partial r}$$
$$+\frac{1}{r^2\sin\theta}\left\{\frac{\partial}{\partial\theta}\left(\nu\sin\theta\frac{\partial u}{\partial\theta}\right)-\frac{\partial}{\partial\theta}\left(\nu\sin\theta\frac{\partial}{\partial r}(rv)\right)\right\} \quad (1)$$

Azimuthal Momentum

$$\frac{\partial v}{\partial t}+\frac{1}{r^2}\frac{\partial}{\partial r}(r^2uv)+\frac{1}{r\sin\theta}\frac{\partial}{\partial\theta}(v^2\sin\theta)+\frac{uv}{r}=-\frac{1}{\rho r}\frac{\partial P}{\partial\theta}+$$
$$+\frac{1}{r}\left\{\frac{\partial}{\partial r}\left(\nu\frac{\partial}{\partial r}(rv)\right)-\frac{\partial}{\partial r}\left(\nu\frac{\partial u}{\partial\theta}\right)\right\} \quad (2)$$

Continuity

$$\frac{1}{r^2}\frac{\partial}{\partial r}(r^2u)+\frac{1}{r\sin\theta}\frac{\partial}{\partial\theta}(\sin\theta v)=0 \quad (3)$$

Energy

$$\frac{\partial T}{\partial t}+\frac{1}{r^2}\frac{\partial}{\partial r}(r^2uT)+\frac{1}{r\sin\theta}\frac{\partial}{\partial\theta}(vT\sin\theta)=$$
$$\left[\frac{1}{r^2}\frac{\partial}{\partial r}\left(ar^2\frac{\partial T}{\partial r}\right)+\frac{1}{r^2\sin\theta}\frac{\partial}{\partial\theta}((a\sin\theta))\frac{\partial T}{\partial\theta}\right] \quad (4)$$

The differential equations are written in terms of the radial velocity, u, azimuthal velocity, v, pressure, P, and temperature, T. The momentum and energy equations are nonlinear parabolic partial-differential equations. The energy equation is coupled to the momentum equations by velocity, and the momentum equations are uncoupled from the energy equation.

Equations (1–4) are approximated by variable-mesh finite differences. The full spherical axisymmetric geometry is modeled by a variable mesh containing sixteen radial cells and 84 azimuthal cells. A geometrically stretched mesh is used to improve resolution near the inner sphere and in the inlet region. The radial stretching factor is 1.07, and the azimuthal stretching factor is 1.007. Variable donor-cell differencing [10] is applied to the convective terms, and forward-time centered-space finite differences to all other terms [11]. The finite-difference equations are given in [12].

Nomenclature

A = inner sphere area, m^2
a = thermal diffusivity, m^2/s
c = specific heat, J/kg°C
H = total system heat-transfer coefficient, $H=Q/A\ (T_1-T_B)$, W/m²°C
h = local heat-transfer coefficient, W/m²°C
k = thermal conductivity, W/m°C
$\dot{m}$ = mass flow rate, kg/s
Nu = Nusselt number, dimensionless
P = pressure, Pa
Q = total system heat-transfer rate, $Q=\dot{m}c\ (T_{out}-T_{in})$, W
q = local heat-transfer rate, equation (5), W/m²
Re = Reynolds number, equation (7), dimensionless
r = radial coordinate, m
R = sphere radius, m
t = time, s
T = temperature, °C
$\bar{T}$ = average temperature, °C
u = radial velocity, m/s
v = azimuthal velocity, m/s
$\bar{V}$ = average velocity across annulus, m/s
∂ = partial derivative
Δ = increment
θ = azimuthal coordinate, degrees
ν = kinematic viscosity, m²/s
ρ = density, kg/m³
ϕ = longitudinal coordinate, degrees

Subscripts

a = conditions across annulus
B = bulk, average of inlet and outlet conditions
D = inner sphere diameter
e = conditions at equator ($\theta=90$ deg)
f = annulus flow
g = gap, (R_2-R_1)
in = average conditions at the inlet
i = radial index
j = azimuthal index
out = average conditions at the outlet
r = radial direction
θ = azimuthal direction, azimuthal location
s = separation
t = total
w = conditions across inner sphere wall
1 = inner sphere
2 = outer sphere

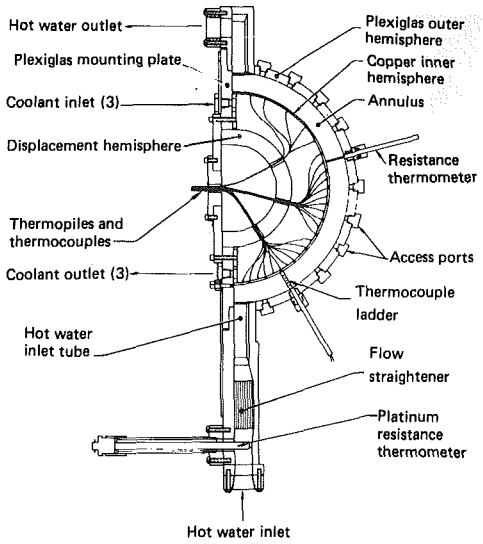

Fig. 2 Cross-sectional drawing of the spherical annulus apparatus

No-slip boundary conditions are imposed at both the inner and outer sphere walls. The temperature of the inner sphere wall either is held constant at a temperature of $T=0°C$, or is maintained at the experimentally measured temperature distribution. At the outer sphere wall, zero heat flux is specified. Application of explicit boundary conditions on pressure at the walls is not required because a slope boundary condition is implicitly applied by the solution technique. In addition, singularities in the equations at $\theta=0$ and $\theta=\pi$ are avoided by placement of velocities in the finite-difference mesh.

The numerical solution of the finite-difference equations proceeds in three steps. The first step is the explicit solution of velocity from the finite-difference momentum equations. In the second step, the continuity equation is satisfied by simultaneously iterating pressures and velocities until mass conservation is achieved. The pressure-velocity iteration begins by calculating the divergence in a cell and adjusting the cell pressure and velocities to force the divergence to zero. In so doing, the neighboring cells are affected, and the mesh must be swept iteratively to relax the solution. Iterations are continued until the maximum cell divergence in the mesh drops below a specified limit. When all cells have converged, the velocity solution with correct vorticity and vanishing divergence is achieved [12]. An equivalent technique was introduced by Chorin [13] and has been applied by others [10, 14].

In the third step, the finite-difference energy equation is solved explicitly for temperature using the velocity solution from step two.

3 Experimental Apparatus

Spherical Annulus Apparatus. The experimental apparatus consists of a spherical annulus approximated by hemispheres (see Fig. 2). Hemispheres are used to permit circulation of cooling water inside the inner hemisphere. The effect of using hemispheres is discussed later.

The inner hemisphere is made of 3.175-mm thick copper with an outer radius of 139.7 mm, and the outer hemisphere is made of 12.7-mm thick Plexiglas with an inner radius of 168.3 mm. Both inner and outer hemispheres are supported by a 12.7-mm thick Plexiglas mounting plate that provides a thermally insulated plane. Access ports located every 15 deg around the outer hemisphere allow temperature probes to be inserted into the annulus. The access ports are located in a plane perpendicular ($\phi=90$ deg) to the Plexiglas mounting plate. The 38.1-mm diameter inlet and outlet tubes are also Plexiglas. A bundle of glass tubes straightens the flow before it enters the annulus.

Water Flow System. The water flow system consists of separate tanks and flow loops to provide cold and hot water to the spherical annulus apparatus. Cooling water obtained from a reservoir containing a fifty-fifty mixture by volume of ice cubes and water is pumped through the inside of the inner hemisphere. Three centrifugal pumps on parallel insulated lines provide cooling water flow at 0.14 kg/s.

Annulus water temperature is controlled to 53.0 $\pm 1°C$ by a proportional temperature controller and electric heaters. The annulus water is pumped with a centrifugal pump through insulated lines. Immediately downstream of the pump, a flow rate controller provides flow rate regulation to within ± 1.5 percent of set point.

A pair of direct acting solenoid valves with an opening time of less than 50.0 ms is used to divert the annulus water flow into a weighting tank for flow rate measurement. A digital timer is used to actuate simultaneously the valves for a timed period. The collected water is then weighed on a balance scale.

Instrumentation. Instrumentation consists of sixteen spot-welded, cooper-constantan thermocouples and thirteen heat-flux thermopiles (see Fig. 2) around the inner hemisphere, six resistance thermometers for measuring average water temperature in the annulus, and three thermocouple ladders for measuring water temperature distribution in the annulus. All instrumentation is located in a plane perpendicular to the Plexiglas mounting plate ($\phi=90$ deg), with the exception of two thermocouples located at longitudes of $\phi=\pm 15$ deg and at an azimuth of $\phi=85$ deg to check the symmetry of the temperature field. An integrating digital voltmeter, a digital delay generator, a crossbar scanner, and a digital printer are used to collect voltage data.

The inner hemisphere thermocouples and thermopiles are constructed from 0.076-mm constantan wire spot welded to the inner hemisphere. The copper of the inner hemisphere acts as a common leg for all thermocouples. To achieve enough resistance to produce welds, both sides of the copper hemisphere are plated with 0.0051-mm thick nickel.

Each thermocouple ladder has five thermocouples positioned across the annulus gap. The ladder thermocouple junctions are chromel-constantan constructed from 0.076-mm wire with a bead size of approximately 0.254 mm.

Each heat-flux thermopile consists of ten copper constantan thermocouples placed on alternating sides of 6.4-mm dia and 3.17-mm thick copper plugs that were installed in the inner hemisphere. The plugs were insulated from the hemisphere by a 1.27-mm thick film of epoxy [12].

A 40-channel crossbar scanner is used to scan thermocouple and thermopile channels, and voltage is measured with an integrating digital voltmeter. The integration period is controlled by a digital delay generator, and a digital printer is used to print channel number and voltage. The digital voltmeter, when calibrated against a precision voltage standard, varied by no more than ± 1.0 μv over a range from 0 μv to 500 μv.

4 Experimental Procedure

Calibration. All thermocouples and resistance thermometers were individually calibrated against a platinum resistance thermometer which has an accuracy of $\pm 0.01°C$. The accuracy of the calibrated thermocouples was $\pm 0.1°C$. A linear curve was fitted to the resistance thermometer calibration data between 20 and 55°C by the least squares

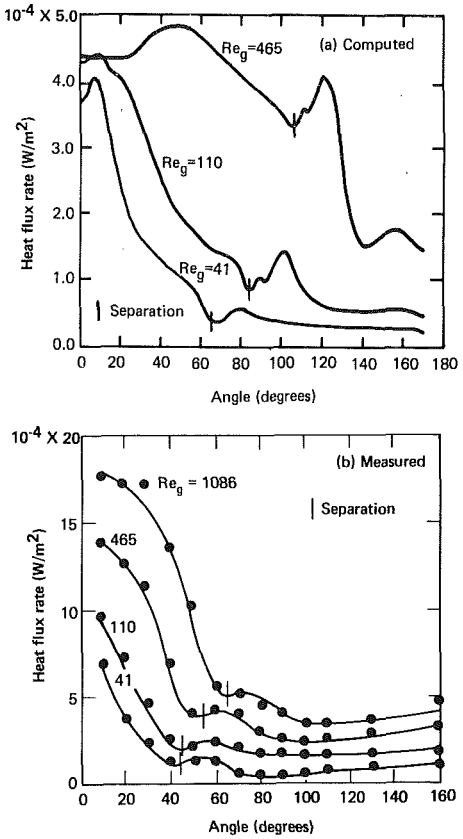

Fig. 3 (*a*) Computed inner sphere heat-flux rate profile with measured temperatures as boundary conditions (see Fig. 5); (*b*) Measured inner sphere heat-flux rate profiles

method. The linear curves fit the calibration data to within $\pm 0.15°C$ for the worst case.

Annulus flow rate measurement was achieved by collecting and weighing a timed flow sample. The standard deviation of collected water weight was less than 2.0 percent of the average weight. The overall accuracy of the flow rate measurement was ± 0.45 g/s which represents an accuracy of ± 3.2 percent.

Data Acquisition. In all experiments, temperature fluctuations were observed due to eddies and turbulence in the flow. To obtain an average temperature reading, a 30.0 s or longer integration period was used for ladder thermocouples and a 10.0 s or longer period for spot-welded thermocouples.

The accuracy of the thermopile heat-flux gages was determined in a separately designed experiment in which the temperature rise in a calorimeter was compared with the heat flux measured by the gages. The ten thermocouples of the heat flux gages produced a multiplication of the output voltage and, as a result, temperature differences across the inner hemisphere wall as low as $\pm 0.008°C$ could be measured. Thus, the accuracy of the heat-flux measurements ranged from $\pm$ 0.93 to $\pm$ 11.1 percent at a flow of $Re_g = 41$ and $\pm$ 0.46 to $\pm$ 2.8 percent at a flow of $Re_g = 465$. The maximum accuracy occurred at the inlet and the minimum accuracies were observed in the region between $\theta = 80$ and 100 deg.

Data Reduction. Voltages were converted into temperature and heat flux by a computer code written specifically for that purpose. Calibration data for individual thermocouples, material property tables, thermocouple sensitivity data, and resistance thermometer equations were built into the data reduction code.

The local heat transfer per unit area at the inner wall was calculated from the expression

$$q_w = -k_w \frac{\Delta T_w}{\Delta r_w} \tag{5}$$

where k_w is the thermal conductivity of the copper wall and ΔT_w is the measured temperature difference across the wall. The thermal diffusivity of the copper was measured by a laser flash method. The density and specific heat also were measured, and thermal conductivity was calculated from the measured values.

It is of interest to compute the total Nusselt number based on the total amount of heat transferred. The expression used to calculate the total Nusselt number is

$$\mathrm{Nu}_g = \frac{\dot{m}c(T_{\mathrm{out}} - T_{\mathrm{in}})}{A(\bar{T}_1 - T_B)} \left(\frac{R_2 - R_1}{k_f}\right) \tag{6}$$

where T_B is the bulk fluid temperature calculated as the arithmetic average of the measured inlet and outlet temperatures, and $\bar{T}_1$ is the area weighted average temperature of the inner wall.

The average velocity varies with angle in the spherical annulus. The velocity used to calculate the Reynolds number is the average velocity at $\theta = 90$ deg. Material properties used to calculate the Reynolds number are evaluated at the bulk fluid temperature. The expression used for the gap Reynolds number is

$$\mathrm{Re}_g = \frac{\bar{V}_e(R_2 - R_1)}{\nu} \tag{7}$$

The Reynolds number is based on the gap width because of historic precedent. Astill [2] based his results on the gap Reynolds number, and Rundell [3] discussed the disadvantage of using a Reynolds number based on hydraulic diameter.

As a part of the data reduction for each experiment, a numerical integration of local heat-flux measurement was performed, and the integrated heat flux rate was compared to the total heat-flux rate calculated from the expression

$$Q = \dot{m}c(T_{\mathrm{out}} - T_{\mathrm{in}}) \tag{8}$$

5 Discussion of Results

Experimental results reported in the literature [1, 3, 5, 6] indicate that turbulence and vortex shedding are present in spherical annulus flow at Reynolds numbers as low as 200. In this study, turbulence in the flow was visually observed at a Reynolds number of 41. This paper presents a laminar computational analysis of spherical annulus flow to extend the numerical work of Astill [2]. It is recognized that the laminar computational results are compared with experimental results over a range of Reynolds numbers for annulus flow that contains turbulence.

Figure 3 shows computed and measured inner sphere heat-flux rates. The numerical computation results shown in Fig. 3(*a*) are for laminar flow at gap Reynolds numbers ranging from 41 to 465. All computations are made with measured inner sphere temperature distribution as a boundary condition and with an insulated outer sphere. No-slip velocity conditions are applied at sphere walls, and the inlet fluid temperature is specified at the measured value. Constant material properties of water at the measured bulk temperature are used. In each calculation the transient solution is carried out in time until the maximum time rate of change of temperature at any point is less than $0.05°C/s$.

The computed inner sphere heat-flux rate shown in Fig. 3(*a*) is based on the hot water temperature gradient at the wall. Heat transfer at all Reynolds numbers decreases from a maximum value near the inlet to a well-defined local minimum downstream. This local minimum was found always to coincide with flow separation. Separation in the calculations is identified by a zero velocity gradient normal to

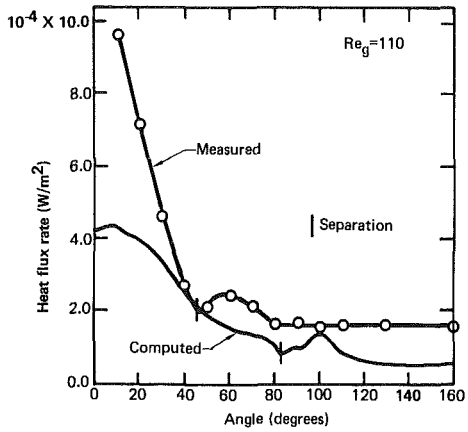

Fig. 4 Measured and computed heat-flux rate distributions for $Re_g = 110$

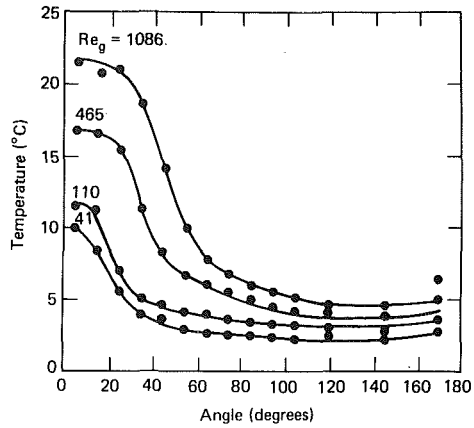

Fig. 5 Measured distributions of inner hemisphere temperature

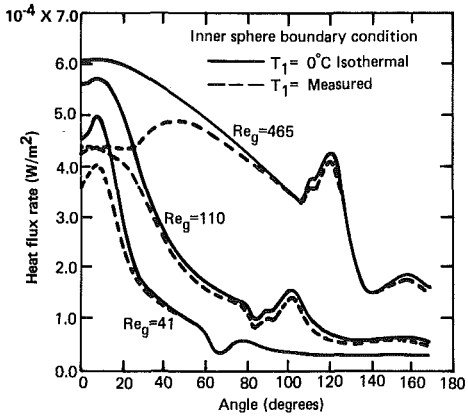

Fig. 6 Computed heat-flux rate profiles for different inner sphere boundary conditions

the wall. The increase in heat-flux rate just beyond separation is due to a recirculation eddy formed near the inner sphere just downstream of separation.

Measured inner hemisphere heat-flux rate as a function of azimuthal angle is shown in Fig. 3(*b*) for selected Reynolds numbers from 41 to 1086. The location of separation in the experiments is determined from the shape of the heat-flux rate distribution. Laminar computations indicate that separation coincides with a local minimum in the heat-flux rate profile. Therefore, the separation angle in the experiment was determined from the location of the local minimum.

The large heat-flux rates near the inlet resulting from the jetting action of the flow make the inlet region an important part of the spherical annulus heat exchanger. For example, in the experiments, at $Re_g = 110$, the flow separates at 45 ± 5 deg, and the region between inlet and separation accounts for 32 percent of the total heat transfer with 15 percent of the total area.

Measured and computed heat-flux rate distributions are shown in Fig. 4 for $Re_g = 110$. The profiles shown are typical of computed and measured profiles at all Reynolds numbers considered in this study. In the computations, measured inner wall temperature distribution and hot water inlet temperatures are specified as boundary conditions, and material properties at the measured bulk temperature are used.

Measured distributions of heat-flux rate show the same general trends as computed distributions. Both profiles begin at a maximum near the inlet and drop to a local minimum at separation, followed by a small increase and a relatively level portion. The maximum heat-flux rate occurs near the inlet where maximum wall jet velocities and fluid temperatures exist. The decrease in heat-flux rate with increasing angle is created by deceleration of the wall jet in the adverse pressure gradient and the increasing thickness of the thermal boundary layer. At the point of separation, the velocity gradient at the wall is zero and a local minimum in the heat-flux rate occurs due to stagnant fluid near the wall. Just downstream of separation, a reverse flow eddy is created. The heat-flux rate increases in the area of the eddy. The flow reattaches downstream of the eddy and the heat-flux rate decreases to a minimum. The relatively flat region downstream of reattachment occurs in a region of low flow velocity.

Two major differences are observed between measured and computed heat-flux rates. The first difference is the magnitude of the heat-flux rate. In this example, the measured heat-flux rate is more than twice the computed rate in some areas. Turbulence is not accounted for in the computations, and is responsible for experimental heat-flux rates that are higher than computed. Experiments with turbulent flow over spheres have shown that heat flux increases with turbulence [15, 16]. Vortex shedding and irregular flow patterns beginning near the inlet are reported in the majority of the spherical annulus experimental flow studies in the literature [1, 3, 5, 6]. Newton [8] reports fluctuations in temperature near the inlet region exceeding 50 percent of the average values. Temperature fluctuations near the inner hemisphere are also observed at all Reynolds numbers considered in this study. These results suggest that the spherical annulus is an unstable flow geometry with turbulence and vortex motion present even at low flow rates.

The second major difference between measured and computed results is the location of separation. Separation creates a local minimum in the heat-flux rate profile and causes a distinct change in the shape of the profile. In Fig. 4, the measured separation angle is 45 ±5 deg, and the computed separation angle is 82 deg. The omission of turbulence and buoyancy in the computation may account for the differences in the computed and measured separation angles. Buoyancy would have the effect of opposing the wall jet momentum, thereby causing earlier separation.

A numerical integration of the measured local heat-flux rates agreed in the worst case within ±10.2 percent of the total heat transferred from the annulus fluid. The total heat transfer from the annulus was calculated using equation (8) and measured temperatures. On the average, the results agreed within ±5.9 percent. This comparison demonstrated the accuracy of the thermopile heat-flux rate measurement technique. A similar integration of computed heat-flux rates agreed within ±2 percent of total heat transfer computed from equation (8).

Measured distributions of inner hemisphere temperature

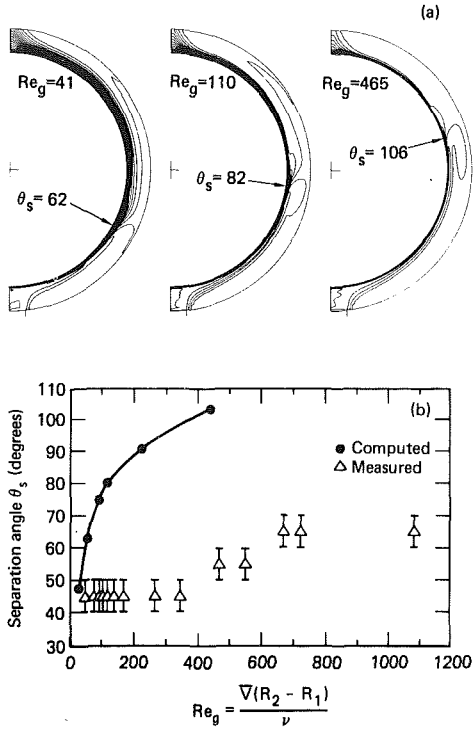

Fig. 7 (*a*) Computed temperature contours at 2.0°C increments with separation angles indicated; (*b*) computed and measured separation angles

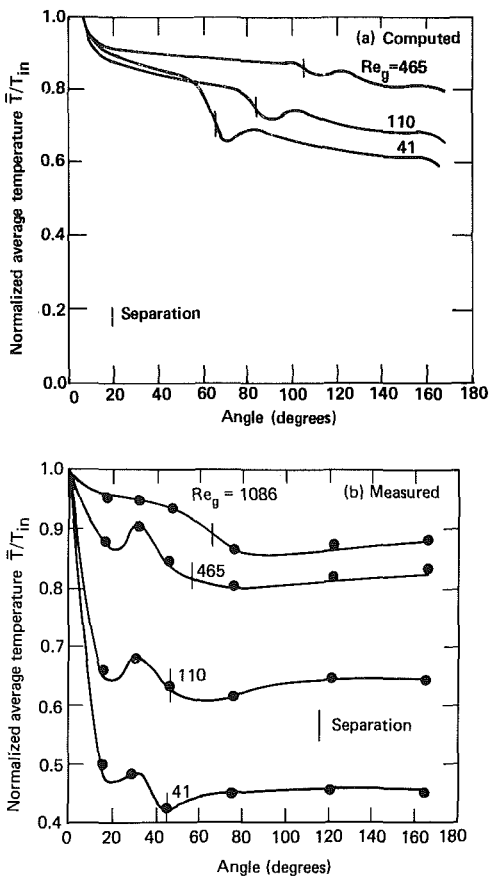

Fig. 8 (*a*) Computed normalized average azimuthal fluid temperature profiles with measured temperature boundary conditions (see Fig. 5); (*b*) Measured normalized average azimuthal fluid temperature profiles

are shown in Fig. 5 for various Reynolds numbers. These temperature distributions were specified as boundary conditions for all calculations presented in this paper unless otherwise specified. The average temperature of the inner sphere for use in equation (6) is computed based on area weighting. Thus, higher temperatures near the inlet have a reduced effect on the computed average because of the smaller amount of area involved. The increase in temperature at 170 deg is due to recirculation of the cooling water above the coolant inlet (see Fig. 2), as well as stagnation flow of the hot water in the annulus near 180 deg.

To check the use of hemispheres to approximate spheres, and to check the symmetry of the inner hemisphere temperature field, thermocouples are placed at three longitudes at an azimuth of $\theta = 85$ deg. The temperature spread at these longitudes was found to range from 12 to 26 percent of the average temperature. For example, at $Re_g = 110$ the temperature spread was 0.89°C and the average inner sphere temperature was 3.60°C. Similar longitudinal asymmetries in temperature were reported by Rundell [3]. In addition, the symmetry of flow in the annulus was checked qualitatively by dye injection, and a symmetrical flow pattern was observed.

Figure 6 shows computed heat-flux rate profiles using 0°C isothermal and measured temperatures as inner sphere boundary conditions (see Fig. 5). As expected, the 0°C isothermal inner sphere creates higher heat-flux rates, especially near the inlet where measured inner sphere temperatures are highest. The largest difference occurs at $Re_g = 465$ near the inlet. At this Reynolds number the annulus flow rate approximately equals the coolant flow rate.

Computed temperature contours for various Reynolds numbers over the range studied are shown in Fig. 7(*a*). Contours are plotted at 2.0°C increments and are computed with measured temperatures as boundary conditions. The location of separation is indicated in each case. The effect of separation and thermal boundary-layer growth on temperature contours can be seen.

Plots of computed and measured separation angles as a function of gap Reynolds number are shown in Fig. 7(*b*). Both computed and measured separation angles vary with Reynolds number. For all experiments up to $Re_g = 360$, separation occurs at 45 ± 5 deg. At $Re_g = 465$, separation shifts to 55 ± 5 deg, and, for Reynolds numbers above 690, separation occurs at 65 ± 5 deg. Previous investigations [1, 3, 5] have reported a fixed separation angle at approximately 45–50 deg based on flow visualization. The laminar computations predict larger separation angles that increase more rapidly with Reynolds number than measured angles.

Fluid viscosity plays an important role in the computed location of separation. Both viscosity and buoyancy oppose the momentum of the wall jet and help create separation. Computations with constant geometry and flow rate show that the separation angle decreases as the fluid viscosity increases in the absence of buoyancy. Several calculations were performed in which flow rates and fluid viscosities were varied independently by factors as high as 10. In all cases, the separation angle was found to depend on the Reynolds number, as shown in Fig. 7. These computations demonstrate that the location of laminar separation is dependent only on the balance between viscous and inertia forces in the absence of buoyancy forces. The computed minimum angle at which separation occurs (48.7 deg) agrees with experiments and with the observation of Rundell [1, 3] who observed by flow visualization a fixed separation angle at approximately 45 deg.

Figure 8 shows plots of computed and measured average temperature for various Reynolds numbers. The computed temperatures shown in Fig. 8(*a*) are arithmetic averages of cell temperatures at each azimuthal angle normalized by the inlet

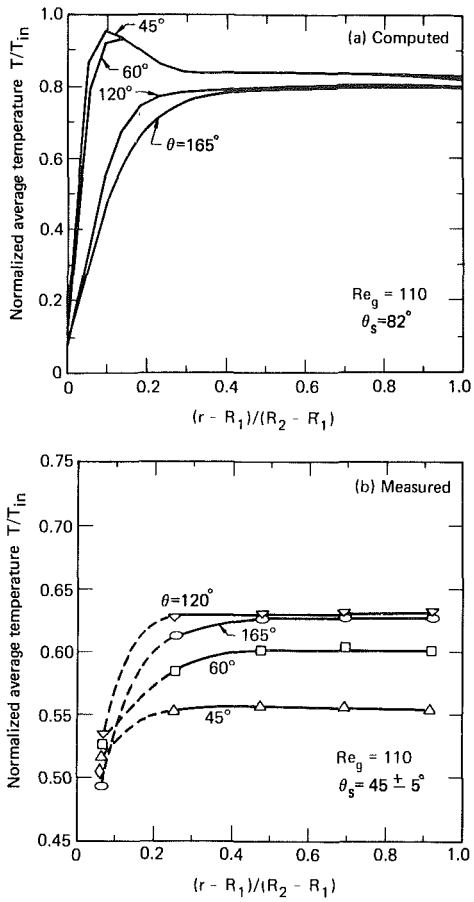

Fig. 9 (*a*) Computed normalized radial temperature profiles with measured temperature boundary conditions (see Fig. 5), (*b*) Measured normalized radial fluid temperature profiles

temperature. The location of separation is indicated on each curve as determined by the presence of a zero velocity gradient at the inner sphere. Separation causes dips in the computed temperature curves which become less and less pronounced as the Reynolds number increases.

Figure 8(*b*) shows the distribution of normalized average annulus water temperature measured for various Reynolds numbers. Average water temperature in the annulus was measured with resistance thermometers that measure average temperature across the annulus. In each case, the measured minimum temperature exists just downstream of separation. The separation angle indicated on each curve was deduced from the shape of the measured heat-flux rate profile (see Fig. 3(*b*)). At $Re_g = 465$ and above, the average temperature downstream of separation increases continuously. The increase is less than 2.0°C and is attributed to asymmetric cooling of the inner hemisphere.

Computed and measured radial temperature profiles are shown in Fig. 9 for $Re_g = 110$. Temperatures are normalized by the inlet temperature. In the computation of Fig. 9(*a*), the separation angle is 82 deg, whereas the measured separation angle corresponding to Fig. 9(*b*) is 45 ±5 deg. The computed profiles at 45 and 60 deg are upstream of separation and show the effect of the wall jet. Downstream of separation the computed temperatures are lower and show the same general shape as the measured profiles.

Measurements of local temperature at various radial and azimuthal locations were made with thermocouple ladders. The integrating digital voltmeter with a 30-s integration period and thermocouple ladders were used to obtain the temperature profiles shown in Fig. 9(*b*). All the measured

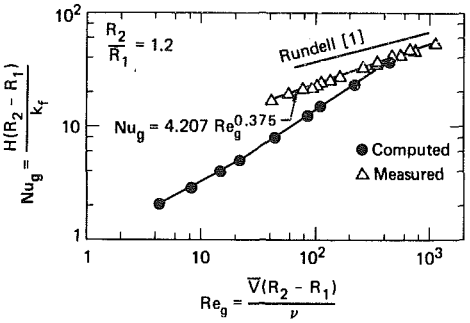

Fig. 10 Computed and measured total system Nusselt numbers

profiles are downstream of separation. After separation, measured temperatures outside the inner wall boundary layer increase as hot fluid from the separated wall jet begins to mix with colder fluid in the annulus. Temperatures near the inner hemisphere are lower at 165 deg than at 120 deg in both computations and measurements, and reach approximately the same temperature in the region from the annulus center to the outer hemisphere.

Figure 10 shows the computed and measured total system Nusselt numbers as a function of gap Reynolds number. The total Nusselt number is calculated from average inner sphere temperature, average hot water inlet and outlet temperatures, and annulus mass flow rate using equation (6). A correlation based on a nonlinear least squares curve fit to the experimental data is given. The experimental correlation by Rundell [1] is also plotted for comparison. In Rundell's experiments, the inner sphere was heated with steam, and room-temperature water was pumped through the annulus. A full spherical annulus was used which included a concentric pipe inlet and outlet for heating and cooling fluids. Thus, the inlet and outlet areas were considerably different from these experiments.

In general, for heat exchangers, Nusselt numbers for heating situations are higher than cooling situations. The difference is attributed to differences in fluid viscosity near the wall where the heat transfer is taking place. For heating, the fluid near the wall is less viscous than the fluid in the center and, consequently, the velocity of the heated fluid near the wall is greater for heating than for cooling. Seider and Tate [17] have suggested the empirical correction factor $(\mu_1/\mu_B)^{0.14}$ to account for the effect of temperature variation of physical properties. When measured Nusselt numbers from Rundell's experiments and from these experiments are multipled by this factor, they agree within 2 percent at $Re_g = 974$ and within 26 percent at $Re_g = 66$. Differences in the inlet and outlet regions and methods of inner sphere temperature control may account for the different slopes.

The slope of the computed data is larger than the measured data because computed separation angles increase with Reynolds number faster than in the experiments. The wall jet acts over a larger area in the computations due to the increased separation angle. Since the wall jet is the region of highest heat flux rates, the computed heat transfer increases more rapidly than measured heat transfer. Experimental Nusselt numbers, like the local heat flux rates, are higher than computed due to turbulence.

6 Summary and Conclusions

A combined experimental and analytical study of steady, forced-convection heat transfer in a spherical annulus has been performed. It is believed that this is the first experimental study of spherical annulus convective heat transfer where local variations of inner sphere heat transfer have been measured. In addition, this study presents the first actual

measurement of separation angle by other than flow visualization means.

The experimental data indicate that the stagnation and wall jet regions are important to the total heat-transfer process. For example, at $Re_g = 41$, the wall jet separated at 45 ± 5 deg, and the region between inlet and separation accounted for 38 percent of the total heat transfer with only 15 percent of the total area. Similarly, at $Re_g = 465$, the wall jet separated at 55 ±5 deg, and the corresponding values for heat transfer and area are 44 and 22 percent, respectively.

The location of separation as indicated by measured heat-flux distributions was found to be a function of Reynolds number. Below $Re_g = 350$, separation occurred at 45 ± 5 deg in agreement with the fixed separation angle observed by Rundell [1]. For larger Reynolds numbers, the separation angle increased. Fluctuations in temperature were observed at all flow rates, especially in the inlet region and near the inner sphere. Measured total Nusselt numbers agreed well with results reported in the literature after being adjusted to account for the effects of heating versus cooling.

Experimental heat-flux rates are over two times larger than computed laminar heat-flux rates, and the measured separation angles are considerably less than computed separation angles. These major differences between experiment and computations are attributed to the presence of vortex shedding and turbulence in the experiments which were not modeled in the computations. In addition, neglecting buoyancy in the computation may affect the computed separation angle. Temperature fluctuations are present in the experiments near the inner sphere at all angles, and fluctuations of over 50 percent of the average value are observed near the inlet.

The numerical analysis is the first one in which the full laminar axisymmetric Navier-Stokes equations (excluding buoyancy) have been applied to steady spherical annulus convective heat transfer. Astill [2] previously performed a similar analysis in which simplified equations, also neglecting buoyancy, were solved numerically. In the present study the computed angle of wall jet separation was found to be a function of Reynolds number. Computations at constant flow rate showed that the separation angle decreased with increasing viscosity. It was also found by varying viscosity and flow rate independently that the separation angle depends only on the Reynolds number in the absence of buoyancy.

Calculations at higher Reynolds numbers may require a different solution technique than used here. The code used for these calculations was originally written for transient solutions involving a free surface [9]. The code was modified to exclude the free surface treatment for this study. The transient solution technique was expensive to use for steady-state results. Long thermal time constants required the solution to be carried on for a long time requiring as much as one hour on a CDC 7600 computer. In addition, a finer mesh would be required to resolve the boundary layer at high Reynolds number. For these reasons, different radius combinations and Reynolds number above 465 were not considered in this numerical study.

The results of this study indicate that a computational turbulence model is required even at relatively low Reynolds numbers. The most critical areas for turbulence modeling are the stagnation and wall jet regions. Turbulence in these types of flows has been studied by others, and the results could be applied to develop a model for spherical annulus flow [18–20]. However, the general qualitative features and trends of spherical annulus flow are predicted by the laminar model.

7 References

1 Rundell, H. A., Ward, E. G., and Cox, J. E., "Forced Convection in Concentric-Sphere Heat Exchangers," ASME JOURNAL OF HEAT TRANSFER, Vol. 90, 1968, pp. 125–129.

2 Astill, K. N., "An Analysis of Laminar Forced Convection Between Concentric Spheres," ASME JOURNAL OF HEAT TRANSFER, Vol. 98, 1976, pp. 601–608.

3 Rundell, H. A., "Forced Convection in Concentric Sphere Heat Exchangers," Ph.D. dissertation, Department of Mechanical Engineering, University of Houston, Houston, Texas, 1966.

4 Cobble, M. H., "Spherical Shell Heat Exchanger—Dirichlet Problem," *Journal of the Franklin Institute*, Sept. 1963, pp. 197–206.

5 Ward, E. G., "Flow Through the Annulus Formed Between Concentric Spheres," Master's thesis, Department of Mechanical Engineering, University of Houston, Houston, Texas, 1966.

6 Bozeman, J. D., Dalton, C., "Flow in the Entrance Region of a Concentric Sphere Heat Exchanger," ASME JOURNAL OF HEAT TRANSFER, Vol. 92, 1970, pp. 184–185.

7 Brown, J. R., "Natural Convection Heat Transfer Between Concentric Spheres," Ph.D dissertation, Department of Mechanical Engineering, University of Texas, Austin, Texas, 1967.

8 Newton, R. L., "An Experimental Investigation of Forced Convection Between Concentric Spheres," Master's thesis, Department of Mechanical Engineering, Tufts University, Medford, Mass., 1977.

9 Tuft, D. B., "Calculation of Laminar Incompressible Fluid Flow and Heat Transfer During Spherical Annulus Filling," Lawrence Livermore Laboratory Report UCID-18168, 1979.

10 Hirt, C. W., Nichols, B. D., and Romero, N. C., "SOLA—A Numerical Solution Algorithm for Transient Fluid Flows," Los Alamos Scientific Laboratory Report LA-5852, 1975.

11 Roache, P. J., *Computational Fluid Dynamics*, Hermosa Publishers, Albuquerque, New Mexico, 1972.

12 Tuft, D. B., "An Experimental and Numerical Study of Steady Forced-Convection Heat Transfer in a Spherical Annulus," Lawrence Livermore National Laboratory Report UCRL-53081, 1980.

13 Chorin, A. J., "Numerical Solution of the Navier-Stokes Equations," *Math. Comp.*, Vol. 22, 1968, p. 745.

14 Amsden, A. A., and Harlow, F. H., "The SMAC Method: A Numerical Technique for Calculating Incompressible Fluid Flows," Los Alamos Scientific Laboratory Report LA-4370, 1970.

15 Gostkowski, V. J., and Costello, F. A., "The Effect of Free Stream Turbulence on the Heat Transfer from the Stagnation Point of a Sphere," *International Journal of Heat and Mass Transfer*, Vol. 13, 1970, pp. 1382–1386.

16 Newman, L. B., Sparrow, E. M., and Eckert, E. R. G., "Free-Stream Turbulence Effects on Local Heat Transfer From a Sphere," ASME JOURNAL OF HEAT TRANSFER, Vol. 94, 1972, pp. 7–15.

17 Sieder, E. N., and Tate, C. E., "Heat Transfer and Pressure Drop of Liquids in Tubes," *Ind. Eng. Chem.*, Vol. 28, 1936, p. 1429.

18 Gardon, R., and Akfirat, J. C., "The Role of Turbulence in Determining the Heat-Transfer Characteristics of Impinging Jets," *International Journal of Heat and Mass Transfer*, Vol. 8, 1965, pp. 1261–1272.

19 Poreh, M., Tsuei, R. G., and Cermak, J. E., "Investigation of Turbulent Radial Wall Jet," ASME *Journal of Applied Mechanics*, Vol. 34, 1967, pp. 457–463.

20 Wolfshtein, M., "Convection Processes in Turbulent Impinging Jets," Ph.D. dissertation, Department of Mechanical Engineering, University of London, London, England, 1967.

Heat Transfer in Laminar Flow With a Phase Change Boundary

S. Asgarpour

Y. Bayazitoglu
Assoc. Mem.

Mechanical Engineering and Materials Science Department,
Rice University,
Houston, Texas 77001

Thermal analysis of a shell-and-tube heat exchanger with a phase change material (PCM) on the shell side and a heat transfer fluid flowing through the tube is presented. The phase change material was initially liquid at its solidification temperature. The heat transfer fluid originates from an isothermal reservoir at a temperature which is lower than the temperature of the phase change material. Numerical results of finite difference method are obtained with a ratio of the thermal properties of the phase change material to the fluid to represent n-octadecane, wax-water system. Variations of the temperature distribution for the fluid, and the PCM, and the interface position of the phase change material in the radial and axial directions are presented. The bulk temperature of the fluid is shown to be a function of the Stefan number, the Fourier number and the velocity profile. It is also shown that the Biot number varies in the axial direction and the heat capacity effects of the phase change material, even at low Stefan numbers are significant.

1 Introduction

Phase change materials are ideally suited to situations where a large amount of energy must be stored but only a small temperature difference between the phase change material and the heat-transfer fluid is possible. One class of storage unit which has recently received attention is the shell-and-tube heat exchanger with the phase change material on the shell side and the fluid on the tube side. As the energy recovery cycle begins, the phase change material is largely liquid. Initially, sensible heat is recovered until the phase change material temperature approaches its freezing point, after which latent heat is removed and the phase change material begins to solidify adjacent to the tube. As energy recovery proceeds, the boundary between the solid and liquid phase of the phase change material moves with time. Since the heat transfer between the working fluid and the phase change material depends on the axial position along the tube, this boundary also varies with the axial direction.

The present work investigates the transient problem of heat recovery from a phase change material around a tube as shown in Fig. 1. The problem consists of four regions. The phase change material fills the shell side in Region 4 between $0 \le x \le L_2$ and it is initially at a liquid state. A laminar flow of a fluid flows from an isothermal reservoir into the tube passing through Regions 1, 2, and 3. While Region 2 is surrounded by the phase change material, Regions 1 and 3 are insulated. The isothermal reservoir is at a temperature which is lower than the phase change material solidification temperature.

Since the analytical solutions of Stefan type problems are difficult to obtain except for certain idealized cases, the numerical methods of finite differences or of finite elements are probably the most convenient for solving complicated problems and the method of finite differences [1-7] is probably the most popular one. The most recent studies of the shell-and-tube heat storage restrict themself to one-dimensional phase change heat transfer. Balhet, Vanburen, and Viskanta [8] studied the problem assuming a constant fluid temperature. Shamsundar [9] neglected the heat capacity of the phase change material and assumed a constant heat-transfer coefficient and a uniform fluid bulk temperature along the axis of the tube. Shamsundar and Srinivasan [10] incorporated the fluid bulk temperature variation but kept their constant heat-transfer coefficient assumption at the tube wall. Here, we present the interaction of the heat-transfer fluid with the phase change material at the wall, through solving an unsteady, two-dimensional, nonlinear energy equations.

2 Analysis

The thermal and the geometric symmetry of the problem indicate that the temperature field in both fluid and phase change material vary with the axial (x-direction) and the radial (r-direction) as shown in Fig. 1. The mathematical formulation of the problem, including the axial conduction effects is given in nondimensional form as follows.

The energy equation for the fluid inside the tube:

$$\frac{\partial^2\theta_i}{\partial\xi^2}+\frac{1}{\eta}\frac{\partial\theta_i}{\partial\eta}+\frac{\partial^2\theta_i}{\partial\eta^2}=\frac{\mathrm{RePr}}{2}\left[\bar{u}\frac{\partial\theta_i}{\partial\xi}+\bar{v}\frac{\partial\theta_i}{\partial\eta}\right]+\frac{\alpha_s}{\alpha}\frac{\partial\theta_i}{\partial\mathrm{Fo}} \quad (1)$$

where $i = 1, 2, 3$ indicates Regions 1, 2, and 3.

The energy equation for the phase change material is

$$\frac{\partial^2\theta_4}{\partial\xi^2}+\frac{1}{\eta}\frac{\partial^2\theta_4}{\partial\eta^2}+\frac{\partial^2\theta_4}{\partial\eta^2}=\frac{\partial\theta_4}{\partial\mathrm{Fo}} \quad (2)$$

The equation (1) and (2) are subjected to the following boundary conditions:

$$\theta_1\left(-\frac{L_1}{R},\ \eta,\ \mathrm{Fo}\right)=0 \quad (3a)$$

$$\frac{\partial\theta_i(\xi,\ 0,\ \mathrm{Fo})}{\partial\eta}=0 \text{ where } i=1,2,3 \quad (3b)$$

$$\frac{\partial\theta_i}{\partial\eta}(\xi,\ 1,\ \mathrm{Fo})=0 \text{ where } i=1,3 \quad (3c)$$

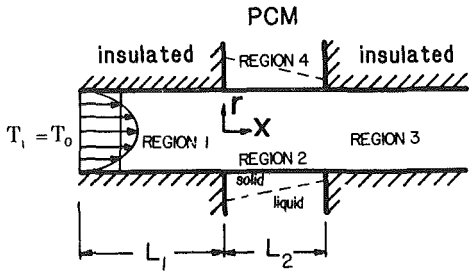

Fig. 1 Schematic description showing different regions in mathematical model

Contributed by the Heat Transfer Division for publication in the JOURNAL OF HEAT TRANSFER. Manuscript received by the Heat Transfer Division April 30, 1982.

$$\theta_1(0,\ \eta,\ \mathrm{Fo}) = \theta_2(0,\ \eta,\ \mathrm{Fo}), \frac{\partial\theta_1}{\partial\xi}(0,\ \eta,\ \mathrm{Fo}) = \frac{\partial\theta_2(0,\ \eta,\ \mathrm{Fo})}{\partial\xi} \tag{3d}$$

$$\theta_2\left(\frac{L_2}{R},\ \eta,\ \mathrm{Fo}\right) = \theta_3\left(\frac{L_2}{R},\ \eta,\ \mathrm{Fo}\right), \frac{\partial\theta_2}{\partial\xi}\left(\frac{L_2}{R},\ \eta,\ \mathrm{Fo}\right) = \frac{\partial\theta_3}{\partial\xi}\left(\frac{L_2}{R},\ \eta,\ \mathrm{Fo}\right) \tag{3e}$$

$$\theta_2(\xi,\ 1,\ \mathrm{Fo}) = \theta_4(\xi,\ 1,\ \mathrm{Fo}), \frac{\partial\theta_2}{\partial\eta}(\xi,\ 1,\ \mathrm{Fo}) = \frac{k_s}{k}\frac{\partial\theta_4}{\partial\eta}(\xi,\ 1,\ \mathrm{Fo}) \tag{3f}$$

$$\frac{\partial\theta_3(\infty,\ \eta,\ \mathrm{Fo})}{\partial\xi} = 0 \tag{3g}$$

$$\theta_4(\xi,\ \eta^*,\ \mathrm{Fo}) = 1 \tag{3h}$$

$$\frac{\partial\theta_4}{\partial\eta}\left[1+\left(\frac{\partial\eta^*}{\partial\xi}\right)^2\right] = \frac{1}{\mathrm{Ste}}\frac{\partial\eta^*}{\partial\mathrm{Fo}} \tag{3i}$$

$$\left.\frac{\partial\theta_4}{\partial\xi}\right|_{\xi=0} = 0,\quad \left.\frac{\partial\theta_4}{\partial\xi}\right|_{\xi=\frac{L_2}{R}} = 0 \tag{3j}$$

Various dimensionless quantities are defined as

$$\xi = \frac{x}{R},\ \eta = \frac{r}{R},\ \eta^* = \frac{r^*}{R},\ \bar{v} = \frac{v}{\mathrm{U}},\ \bar{u} = \frac{u}{\mathrm{U}},$$

$$\theta_i = \frac{T_i - T_\mathrm{o}}{T_m - T_\mathrm{o}},\ \theta_b = \frac{T_b - T_\mathrm{o}}{T_m - T_\mathrm{o}},$$

$$\mathrm{Re} = \frac{2\rho\ \mathrm{U}\ R}{\mu},\ \mathrm{Pr} = \frac{C_P\mu}{k},\ \mathrm{Ste} = \frac{C_{ps}(T_m - T_\mathrm{o})}{h_{sl}},\ F_\mathrm{o} = \frac{\alpha_s t}{R^2}$$

In the foregoing analysis, the densities of the solid and liquid phases of the phase change material are equal. The solidification temperature of phase change material, the physical properties of the phase change material and the fluid are constant. The viscous dissipation effect is neglected. A steady flow of a Newtonian fluid in the tube is considered. Since the velocity fluid is independent of the temperature fluid, if desired, the velocity field can be obtained by solving the Navier-Stokes equations. Knowing that the heat-transfer characteristics of the present problem will be a function of the velocity profile of the fluid, we will consider the two limiting velocity profiles. That is, the fluid will have a uniform velocity profile along the axial direction of the tube or it will reach its fully developed velocity profile very near the inlet of Region 1 and will have a parabolic velocity profile along the axial direction of the tube.

2.1 Transformation. A transformation of the equations associated with the PCM (Region 4) is required to remove the difficulty of tracking the interface. Following the procedure of Landau [11] the radial coordinate η is replaced by η' defined by the following transformation

$$\eta \rightarrow \eta' = \frac{\eta^* - \eta}{\eta^* - 1} \tag{4}$$

This change of variable fixes the interface at $\eta' = 0$, which applies only to Region 4, and equation (2) becomes

$$\frac{\partial^2\theta_4}{\partial\xi^2} + 2\left[\frac{1-\eta'}{\eta^*-1}\frac{\partial\eta^*}{\partial\xi}\right]\frac{\partial^2\theta_4}{\partial\xi\partial\eta'} + \left\{\frac{(\eta'-1)^2}{(\eta^*-1)^2}\left(\frac{\partial\eta^*}{\partial\xi}\right)^2 + \frac{1}{(\eta^*-1)^2}\right\}\frac{\partial^2\theta_4}{\partial\eta'^2} + \left\{\frac{1-\eta'}{\eta^*-1}\frac{\partial^2\eta^*}{\partial\xi^2} + \frac{2(\eta'-1)}{(\eta^*-1)^2}\left(\frac{\partial\eta^*}{\partial\xi}\right)^2 - \frac{1}{\eta^*+\eta'-\eta^*\eta'}\frac{1}{(\eta^*-1)} + \frac{(1-\eta')}{(\eta^*-1)}\frac{\partial\eta^*}{\partial\mathrm{Fo}}\right\}\frac{\partial\theta_4}{\partial\eta'} = \frac{\partial\theta_4}{\partial\mathrm{Fo}} \tag{5}$$

The transformation makes it necessary to alter the boundary conditions of Regions 2 and 4 as follows,

$$\theta_2(\xi,\ 1,\ \mathrm{Fo}) = \theta_4(\xi,\ 1,\ \mathrm{Fo}) \tag{6a}$$

$$\frac{\partial\theta_2}{\partial\eta^*}(\xi,\ 1,\ \mathrm{Fo}) = -\frac{k_s}{k\ (\eta^*-1)}\frac{\partial\theta_4}{\partial\eta'}(\xi,\ 1,\ \mathrm{Fo}) \tag{6b}$$

$$\theta_4(\xi,\ 0,\ \mathrm{Fo}) = 1 \tag{6c}$$

Nomenclature

C_p = specific heat of fluid
C_{ps} = specific heat of phase change material
k = thermal conductivity of fluid
k_s = thermal conductivity of phase change material
h = convective heat-transfer coefficient
h_{sl} = latent heat of fusion of phase change material
r = radial coordinate
r^* = location of phase change interface in radial direction
R = radius of tube
t = time
T = temperature
u = axial velocity
U = mean velocity, $2/R^2 \int_\mathrm{o}^R ur\,dr$
$\bar{u}$ = dimensionless axial velocity, u/U
v = radial velocity
$\bar{v}$ = dimensionless radial velocity, v/U
x = axial coordinate
Bi = Biot number, $-\partial T_4(x,R,t)/\partial r \cdot R/[T_2(x,R,t) - T_b(x,t)] = h\,R/k_s$
Fo = Fourier number, $\alpha_s t/R^2$
PCM = phase change material
Pr = Prandtl number, $C_p\mu/k$
Pe = Péclét number, Re Pr
Re = Reynolds number, $2\,\rho\,U\,R/\mu$
Ste = Stefan number, $C_{ps}(T_m - T_\mathrm{o})/h_{s1}$

Greek Letters

α = thermal diffusivity of fluid, $k/\rho C_p$
α_s = thermal diffusivity of phase change material, $k_s/\rho_s C_{ps}$
η = dimensionless radial coordinate, r/R
η' = dimensionless transformed coordinate, $(\eta^* - \eta)/(\eta^* - 1)$
η^* = dimensionless location of phase change interface in radial direction
θ_i = dimensionless temperature variable, $(T_i - T_\mathrm{o})/(T_m - T_\mathrm{o})$
θ_b = dimensionless bulk temperature of fluid, $(T_b - T_\mathrm{o})/(T_m - T_\mathrm{o})$
ξ = dimensionless axial coordinate, x/R
ρ = density of fluid
ρ_s = density of phase change material
μ = viscosity of fluid

Subscripts

b = bulk
m = melting
o = inlet to Region 1
i = Regions 1, 2, 3, and 4

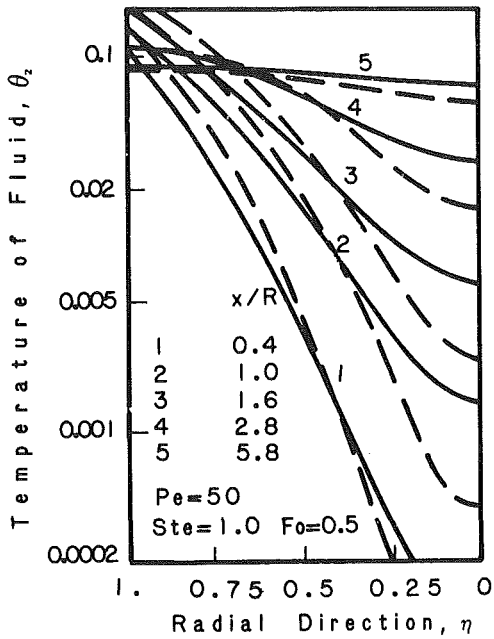

Fig. 2 Temperature distributions in the fluid (– uniform velocity, ··· parabolic velocity)

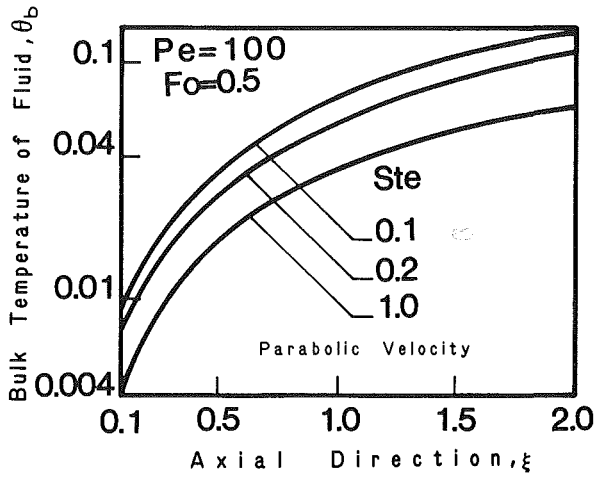

Fig. 3 Comparison of bulk temperature for different Stefan numbers

$$-\frac{\mathrm{Ste}}{\eta^*-1}\frac{\partial\theta_4}{\partial\eta'}\left(1+\left(\frac{\partial\eta^*}{\partial\xi}\right)^2\right)=\frac{\partial\eta^*}{\partial\mathrm{Fo}} \tag{6d}$$

$$\left.\frac{\partial\theta_4}{\partial\xi}\right|_{\xi=0}=-\left(\left.\frac{\partial\eta^*}{\partial\xi}\right|_{\xi=0}\right)\left(\frac{1-\eta'}{\eta^*-1}\right)\left(\left.\frac{\partial\theta_4}{\partial\eta'}\right|_{\xi=0}\right)=0 \tag{6e}$$

$$\left.\frac{\partial\theta_4}{\partial\xi}\right|_{\xi=\frac{L_2}{R}}=-\left(\left.\frac{\partial\eta^*}{\partial\xi}\right|_{\xi=\frac{L_2}{R}}\right)\left(\frac{1-\eta'}{\eta^*-1}\right)\left(\left.\frac{\partial\theta_4}{\partial\eta'}\right)\right|_{\xi=\frac{L_2}{R}}=0 \tag{6f}$$

2.2 Method of Solution. The nonlinear character of the governing equations precludes an analytical solution. Finite difference techniques are used because of their simplicity and relatively low cost. The existence of possible sharp gradients in the neighborhood of $\xi = 0$, suggests the use of variable mesh spacing. The Crank-Nicholson method is chosen in lieu of forward or backward difference methods because it is a second-order approximation in time, whereas both the forward and backward difference methods are only first-order approximations in time.

The heat balance equation for the phase change interface, equation (6*d*), is nonlinear and requires an iterative

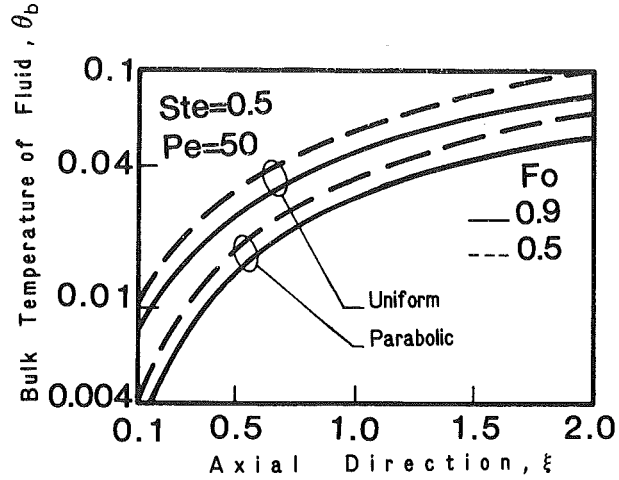

Fig. 4 Effect of velocity profile and Fourier number on bulk temperature

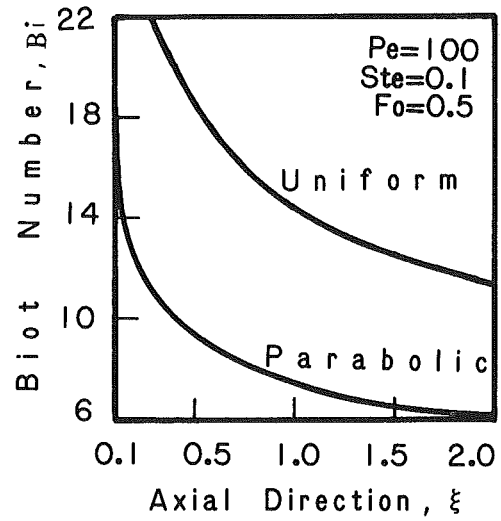

Fig. 5 Effect of velocity profile on Biot number

procedure, therefore the Newton-Raphson method is chosen. The finite difference analogue for the energy equations for the fluid and the phase change material results in five and nine unknows, respectively, per node. If a standard Crank-Nicholson procedure is followed, a difference solution technique other than the simple tridiagonal bond matrix solver would be required. Two possible alternatives could be either an iterative Gauss-Seidel procedure, or a Gaussian elimination procedure, neither of which are attractive from a computing cost stand point.

The standard alternating direction procedure (Douglas [12]) breaks a singie time step increment into two steps, each of which calls for the solution of a simple tridiagonal matrix. The resulting procedure is identical to the Crank-Nicholson with the addition of a term which is second order in time. This method can be applied directly to the energy equations written for the fluid, but must be modified when applied to the phase change material energy equation as follows.

The additional four unknowns in the energy equation for the phase change material come from the mixed derivative term, $\partial^2\theta/\partial\xi\partial\eta$. If this term be treated at time level n instead of half the half time level between {n and $n+1$} errors may be encountered either if a big time step size is chosen, or if the magnitude of the mixed derivative term itself is large compared to the others.

An alternating direction method can be developed for the energy equation written for the phase change material. To do

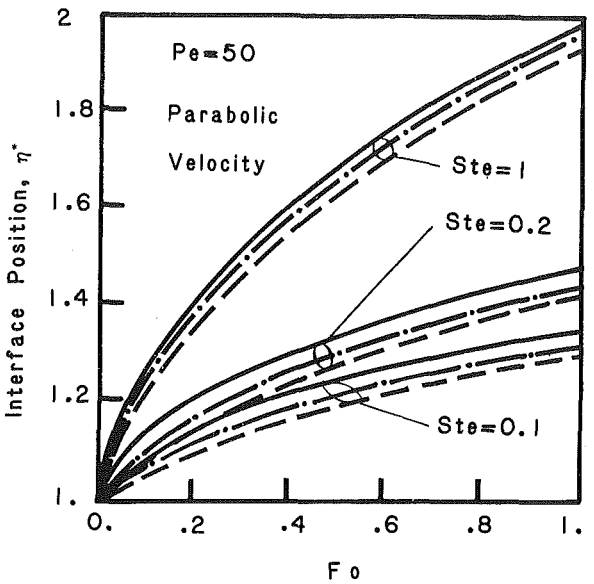

Fig. 6 Effect of Stefan number on the interface position (– x/R = 0.1, – • – x/R = 1, – – – x/R = 2).

this we break down the Crank-Nicholson operator into three separate operators, each calling for the solution of a tridiagonal matrix. The proposed method uses one step to create an intermediate approximation θ^*. The next step is used to predict θ_{n+1} with some simplifying assumptions concerning the mixed derivative terms. The third step is used as a corrector to the results of the second step. Further details of the finite difference equations can be found in reference [13].

3 Results and Discussion[1]

The parameters which one needs for calculation of the temperature distribution and the interface position are the ratio of the thermal conductivity of the phase change material to that of the fluid, the ratio of the thermal diffusivity of PCM to that of the fluid, the Peclet and the Stefan numbers, the mesh size of each region, and the time step size. The results of this work are obtained for a case where the thermal conductivity ratio is 4 and thermal diffusivity ratio is 2.5. This represents a system which consists of wax (n-octadecane) as the PCM and water as the heat-transfer fluid.

The effect of velocity profile on the temperature distribution in the fluid can be studied with Fig. 2. The temperature profile is flatter with the uniform velocity profile, and near the wall it is steeper with the parabolic velocity profile. Hence, the uniform velocity profile leads to a higher heat transfer from the PCM to the fluid, resulting in a higher rate of solidification and a higher temperature gradient at the wall for the phase change material in Region 4. In addition high Stefan numbers (which indicate either a higher differential between the melting and the entrance temperature, or a lower latent heat of fusion) will result in more solidification. Figure 3 shows the effect of Stefan number on the bulk temperature of the fluid and its variation in the axial direction. The bulk temperature decreases as Stefan number increases because a higher Stefan number implies a thicker layer of solid which in turn increases the thermal resistance between the fluid and the liquid PCM. In Fig. 3, we have presented the results for the Fourier number of 0.5. The results at different Fourier numbers indicate that, at a fixed axial location, as the solidification process proceeds, the bulk temperature decreases merely because of the increase in thermal resistance between fluid and the liquid PCM. This is shown in Fig. 4. The same figure also shows the effect of the velocity profile on the bulk temperature.

Figure 5 shows the effect of the velocity profile on Biot number. The Biot number is directly proportional to the gradient of the temperature profile near the wall and inversely proportional to the difference between the wall temperature and bulk temperature. With a fluid having a uniform velocity profile, indicating higher temperature gradient at the wall and higher bulk temperature of the fluid, and lower wall temperature, we have higher Biot numbers than with a fluid having a parabolic velocity profile. It is interesting to observe the significant variation of the Biot number in the axial direction. Recalling the relation of the Biot number to the convective heat-transfer coefficient, h, Fig. 5 indicates the possible errors, that may be introduced, in the applications where the bulk temperature of the fluid is calculated through a heat balance equation in the axial direction using a constant heat-transfer coefficient.

Figure 6 shows the effect of the Stefan number on the phase change interface position. A higher Stefan number results in faster solidification.

Most of the currently available studies of the shell-and-tube heat storage system either assume a one-dimensional axisymmetric model, or solve Laplace's equation (Laplace's equation can be solved if the heat capacity of PCM is negligible, implying a small Stefan number) for PCM, subject to a convective boundary condition at the tube wall.

To study the heat capacity effects of the PCM, the total heat removal from the tube surface and the total heat required for change of phase at the interface at each time level was calculated for Pe = 50 and uniform velocity profile. The difference in these two values indicates the amount of sensible heat removed from the PCM. Table 1 lists these values for various Stefan numbers. For Ste = 1, sensible heat represents 33 percent of the total heat removed and for Ste = 0.1, the sensible heat represents from 1.7 to 6 percent of the total heat

Table 1 Effect of Stefan number on heat capacity for Pe = 50 and uniform velocity

Ste	Fo	*Qa*	*Qp*	*Qs*	% Error
1	0.1	70.52	46.79	33.62	33.48
	0.5	30.375	20.406	9.96	32.8
0.5	0.1	84.26	65.23	9.03	22.5
	0.5	44.74	33.896	10.85	24.2
	0.9	35.96	27.3	8.67	24.1
0.1	0.1	113.7	111.74	1.95	1.7
	0.5	64.07	61.77	2.3	2.6
	0.9	51.8	48.47	3.23	6.4

Qa = dimensionless total heat abstraction
Qp = dimensionless total heat for phase change
Qs = dimensionless total sensible heat

Table 2 Comparison of axial gradient of temperature to the gradient of temperature in radial direction for uniform velocity profile

Fo = 0.5	Maximum temperature gradient in axial direction ∇T_{max}	Minimum temperature gradient in radial direction ∇T_{min}	$\frac{\nabla T_{max}}{\nabla T_{min}}$
Ste = 1., Pe = 50	0.061	1.081	0.0564
Ste = 0.5, Pe = 50	0.0737	0.9615	0.0766
Ste = 0.5, Pe = 100	0.0504	1.0465	0.04816
Ste = 0.1, Pe = 100	0.0775	0.897	0.086

[1] The results and discussion of this work are presented in terms of non-dimensionalized parameters, e.g., temperature, interface position, axial and radial directions.

removed. Even for Ste = 0.1, the heat capacity effects of the phase change material are not negligible.

The temperature gradient in the axial direction in the PCM is found to be negligible. The maximum temperature gradient was calculated and compared to the minimum gradient of the temperature in the radial direction for the case where the length of the shell was twice the radius. Table 2 represents the results for Pe = 50, 100, and Ste = 0.5, and 1.

During the latent heat storage cycle, the phase change material around the tube will liquify, and depending on the orientation of the tube, the free convective heat transfer can significantly enhance the heat-transfer rate in the PCM. Here we have presented the calculations for the energy recovery cycle, that is, PCM will solidify around the tube, and initially it is at its solidification temperature. Therefore the free convection effect in the PCM is not considered.

References

1 Eyres, N. R., Hartree, D. R., Ingham, J., Jackson, R., Sargant, R. J., and Wagstaff, J. B., "The Calculation of Variable Heat Flow in Solids," *Philosophical Transactions of the Royal Society of London*, Vol. 240, series A, 1947, pp. 1-58.

2 Douglas, J., and Gollie, T. M., Jr., "On the Numerical Integration of a Parabolic Differential Equation Subjected to a Moving Boundary Condition," *Duke Math. Journal*, Vol. 22, 1955, pp. 557-571.

3 Murray, W. D., and Landis, F., "Numerical and Machine Solutions of Transient Heat Conduction Problem Involving Melting or Freezing," *Trans.* ASME. Vol. 81, 1959, pp. 106-112.

4 Hettz, W. L., and Westwater, J. W., "Extension of a Numerical Method for Melting and Freezing Problems," *International Journal of Heat and Mass Transfer*, Vol. 13, 1970, pp. 1371-1375.

5 Lazaridis, A., "A Numerical Solution of the Multidimensional Solidification (or Melting) Problem," *International Journal of Heat and Mass Transfer*, Vol. 13, 1970, pp. 1459-1477.

6 Padmanabhan, T. V., and Subbarasu, K., "Numerical Solution for Heat Conduction Problem with Freezing," *Indian Journal of Technology*, Vol. 13, Nov. 1975, pp. 477-479.

7 Kimasta, N., "On the Numerical Solution of Phase Change Problem in Transient Nonlinear Heat Conduction," *International Journal for Numerical Method for Engineering*, Vol. 10, 1976, pp. 833-844.

8 Balhelt, A. G., VanBuren, P. D., and Viskanta, R., "Heat Transfer During Solidification Around a Cooled Horizontal Cylinder," AIChE, No. 189, Vol. 75, 1973, pp. 103-113.

9 Shamsundar, N., "Heat Transfer in Thermal Storage Systems," Prepared by University of Houston, Report No. ERDA EG-77-C-04-3974/EFTts.

10 Shamsundar, N., and Srinivasan, R., "Effectiveness-NTU Charts for Heat Recovery From Latent Storage Units," ASME, J. of Solar Energy Engin., Vol. 102, 1980, pp. 263-271.

11 Landau, H. G., "Heat Conduction in a Melting Solid," *Quart. App. Math*, Vol. 8, No. 1, 1950, pp. 81-94.

12 Douglas, J., "Alternating Direction Methods for Three Space Variables," *Numerische Mathematik*, Vol. 4, 1962, pp. 41-63.

13 Asgarpour, S., Ph.D. dessertation, Rice University, 1981.

C. P. Hedderich
Lieutenant, U.S. Navy.

M. D. Kelleher
Professor.
Mem. ASME

G. N. Vanderplaats
Associate Professor.
Mem. ASME

Department of Mechanical Engineering,
Naval Postgraduate School,
Monterey, Calif. 93940

Design and Optimization of Air-Cooled Heat Exchangers

A computer code has been developed for analysis of air-cooled heat exchangers and was coupled with a numerical optimization program to produce an automated air-cooled, heat-exchanger design and optimization procedure. A general iteration free approximation method was used for the analysis which calculates the mean overall heat-transfer coefficient and the overall pressure drop for many flow arrangements. The analysis takes into account the variation of the heat-transfer coefficients and the pressure drop with temperature and/or length of flow path. The code is not limited to surfaces found in the literature, but will accommodate any triangular pitch bank of finned tubes in multiple-pass configurations. The numerical optimization code is a general purpose program based on the Method of Feasible Directions and the Augmented Lagrange Multiplier Method. The capability is demonstrated by the design of an air-to-water finned-tube heat exchanger and is shown to be a useful tool for heat exchanger design.

Introduction

The design of an air-cooled crossflow heat exchanger is a complex task requiring the examination and optimization of a wide variety of heat transfer surfaces. Smith [1] has listed some typical advantages of direct cooling with air as compared to cooling with water in a shell-and-tube exchanger. Studies have shown that a poor choice of either the heat-transfer surfaces or design parameters can more than double the costs chargeable to a heat exchanger [2].

For the optimized design of heat exchangers with the computer, reliable, but fast, calculation methods for the mean overall heat-transfer coefficient and the overall pressure drops are needed for the following reasons:

(*a*) Conventional simple methods using mean values of temperatures as reference temperatures can lead to undesirable errors [3].

(*b*) Numerical stepwise integrations are prohibitively time consuming.

A number of heat-exchanger design methods have been proposed to determine the optimum heat-exchanger design. Bergles et al. [4] performed an evaluation of different objective functions for compact heat exchangers with different heat-transfer surfaces, but the same specifications. The method did not include any actual optimization techniques, but results did show that a great improvement in heat-exchanger performance can be made by proper selection of design parameters.

The method of Fax and Mills [5] used Lagrange multipliers to optimize a heat-exchanger design under specified constraints. This technique required that the objective function and constraints be expressed explicitly and be differentiable throughout the range of interest. The total number of constraints had to be less than the total number of variables, and all constraints had to be equality constraints.

Mott et al. [2] discuss a computerized procedure for designing a minimum cost heat exchanger. The method minimizes a cost index expressed as a function of fluid pumping power. The algorithm imposed no constraints. The concepts and techniques of nonlinear programming have been applied to optimizing the design of heat exchangers. Palen et al. [6], in 1974, proposed using the Complex Method [7], for the heat-exchanger optimization problem. They found a minimum cost shell-and-tube exchanger by varying six geometrical parameters. The Complex Method requires several feasible starting designs before optimization can be performed.

Johnson et al. [8] coupled an existing shell-and-tube condenser design code with a constrained function minimization code to produce an automated marine condenser design program of vastly different complexity.

The most complete work to date has been accomplished by Afimiwala [9]. He has applied various nonlinear programming methods of optimization to the heat-exchanger design problem, including an experimental interactive graphical approach and exterior penalty function techniques. The gradient-based search methods of Davidon-Fletcher-Powell and conjugate gradient were used for the resulting unconstrained minimizations. The exterior penalty method is extremely useful, since an initial solution satisfying the constraints is not required. The gradient based search methods are efficient when considering computer time.

Finally, Fontein and Wassink [10] utilized the Simplex Method of Nelder and Mead [11], and a steepest decent method for optimizing a shell-and-tube exchanger.

It can be seen that although there are many methods that have been presented for heat-exchanger optimization, each of the methods has its own limitations; none is completely general. Of all the design procedures cited above (those of which are applicable to crossflow, air-cooled heat exchangers), all are limited to the 120 individual surfaces found in the open literature [12] for the calculation of the airside heat-transfer coefficient and friction factor. Therefore, the designer is faced with choosing an optimum surface from a number of individual optimal designs calculated from one of the above methods. In addition, the above methods treat the overall heat-transfer coefficient as a constant, or they become involved with time-consuming numerical stepwise integrations in an attempt to account for the varying heat-transfer coefficients.

This paper tries to bridge this gap by presenting an optimization routine that: (*a*) selects an optimal surface; (*b*) takes into account the varying heat-transfer coefficients and friction factors across the exchanger; (*c*) performs each analysis in an iterative-free manner, and may start with an infeasible design. The emphasis here is on the iterative-free analysis technique. Therefore, only a brief discussion of numerical optimization is presented in the following section. A more detailed discussion of the analysis technique is then

Contributed by the Heat Transfer Division and presented at the ASME Winter Annual Meeting, Washington, D.C., November 15-20, 1981. Manuscript received by the Heat Transfer Division August 10, 1981.

given, followed by a representative design example. Additional details may be found in reference [13].

Numerical Optimization

Almost all design problems require either the maximization or the minimization of some parameter. This parameter is usually called the design objective function. For example, the problem may call for a heat exchanger with a minimum volume. The expression for volume would be the design objective function. For the design to be acceptable, it must satisfy certain constraints. For example, an air heater must be designed so that it will fit into a given space. Therefore, the engineer must set design constraints on the maximum size of the exchanger.

Many numerical optimization techniques have been developed specifically for computer utilization. These techniques usually do not require a specific algebraic equation, but rather any computer algorithm to which design variables can be input and from which the objective function and design constraint values can be determined is aceptable. For this reason, nonlinear programming methods were chosen for the air-cooled, heat-exchanger design. Some of these techniques were summarized by Shah et al. [14].

An optimization program based upon the method of feasible directions and the Augmented Lagrangian Multiplier Method was chosen for this project [15, 16]. This program is called control Program for Engineering Synthesis and Constrained Function Minimization (COPES/CONMIN). It is a well established general purpose nonlinear optimization program that has been used extensively in numerous different optimization applications including thermal engineering. Therefore, for the heat-exchanger design problem, it was necessary to develop a subroutine, ANALIZ, which for a given design, would analyze an air-cooled heat exchanger, and which would be suitable for coupling with the optimizer.

In discussing optimization, the following definitions will be useful:

1 Design Variables – those parameters which the optimization program can change in order to improve the design. COPES/CONMIN can handle in excess of 200 design variables!

2 Design Constraints – those parameters which must not exceed given bounds for the design to be acceptable. COPES/CONMIN can handle thousands of design constraints.

3 Objective Function – the parameter which is going to be minimized or maximized.

To couple the analysis subroutine directly to COPES/CONMIN it is required that the subroutine name ANALIZ be used. The heat-exchanger analysis which forms the content of the subroutine ANALIZ for the present problem is developed later in this paper.

The general nonlinear constrained optimization problem can be written mathematically as follows [17]:

Minimize $F(\bar{X})$ (1)

Subject to:

$$g_j(\bar{X}) \leq 0 \qquad j=1,m \tag{2}$$

$$h_k(\bar{X}) = 0 \qquad k=1,l \tag{3}$$

$$X_i^l \leq X_i \leq X_i^u \qquad i=1,n \tag{4}$$

where the vector, $\bar{X}$, is the vector of n design variables. The objective function, $F(\bar{X})$, given by equation (1), as well as the constraint functions given by equations (2) and (3), may be linear or nonlinear functions of the design variables. They may be explicit or implicit functions of $\bar{X}$, but must have continuous first derivatives. The number of inequality constraints is m, and l is the number of equality constraints. Side constraints, X_i^l and X_i^u, are the lower and upper bounds placed on the design variables. Side constraints could be included in equation (2), but are treated separately for efficiency. References [18–25] provide an extensive discussion of numerical optimization techniques and their application to engineering design.

Although the original version of COPES/CONMIN performs very well with inequality constraints, equality constraints such as

$$h_k(\bar{X}) = 0$$

Nomenclature

A = total heat transfer area, m
A_{ff} = free flow area
c_p = specific heat, kJ/kg C
$\dot{C}$ = heat capacity rate = $\dot{m}c_p$ W/C
D = diameter, mm
f = friction factor, dimensionless
F = LMTD correction factor, dimensionless
g = gravitational acceleration, m/s^2
H = corrected heat transfer coefficient, W/m^{2}C
h = bank height, m
J = Colburn factor, St Pr$^{2/3}$, dimensionless
k = thermal conductivity, W/mC
L = length, m
l = fin height, mm
$\dot{m}$ = mass flow rate, kg/s
N = number of tubes
n = number of . . . (when used with appropriate subscript)
p = pressure, Pa
P = pitch, mm
Pr = Prandtl number, dimensionless
$\dot{Q}$ = heat-transfer rate, W
r = radius, mm
R = heat-transfer resistance, m^2 °C/W
Re = Reynolds number based on tube i.d. or fin root diameter, dimensionless
s = distance between adjacent fins, mm
S = fin spacing center-to-center, mm
t = fin thickness, mm
T = temperature, °C
ΔT = temperature difference, °C
U = overall heat-transfer coefficient, W/m °C
w = bank width, m
η_0 = surface efficiency, dimensionless
η_f = fin efficiency, dimensionless
μ = viscosity, Pa • s
ρ = density, kg/m
θ = pitch angle (see Fig. 2)

Subscripts

a = air
c = cold
f = fin
ff = free face
h = hot
i = inside
j = reference number, I or II
l = limiting
L = longitudinal
m = mean
0 = outside
p = pass
r = rows
t = transverse
T = total
w = water
x = cross-sectional (flow)
1 = entering
2 = leaving
∞ = ambient

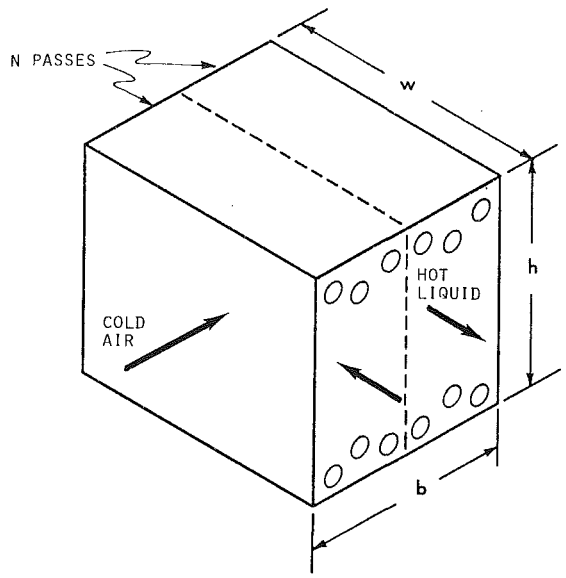

Fig. 1 Heat exchanger geometry

cannot be dealt with directly, but must be treated separately, using a different method.

A recent addition to COPES (still in the development stages), has put the Augmented Lagrangian Multiplier method (ALM) at the disposal of the programmer. Because of its good rate of convergence and its theoretical properties, the ALM is preferred for equality constrained problems [26]. For detailed explanation of the ALM, its background and mathematical derivation, consult reference [26].

Heat Exchanger Analysis

To produce a complete detailed design package, an analysis program for an air-cooled heat exchanger must be coupled with a numerical optimization scheme. The analysis subroutine should:

1 take into account the variation of heat-transfer coefficients and differential pressure drop with temperature and/or length of flow path;

2 be iterative free, if possible;

3 be written in such a manner that the optimizer will play a role in surface selection.

With the number of design variables approaching the practical limit, the importance of an iterative free analysis subroutine cannot be overemphasized. The reason being, that at the beginning of each design iteration in the optimization routine CONMIN, the calculation of all gradients (of the objective and each active constraint) requires a complete pass through the heat-exchange analysis routine, ANALIZ. Therefore, the computational time required by ANALIZ directly affects the time required to reach the optimum.

Problem Formulation. The air-cooled heat exchanger is shown schematically in Fig. 1. A crossflow arrangement with both fluids unmixed was chosen. The energy balances and heat-transfer rate equation for the heat exchanger can be written as:

$$\dot{Q}_3 = \dot{m}_a c_{p,a} (T_{c,2} - T_{c,1}) \tag{5}$$

$$\dot{Q}_4 = \dot{m}_w c_{p,w} (T_{h,1} - T_{h,2}) \tag{6}$$

$$\dot{Q}_5 = U_m A \Delta T_m \tag{7}$$

where $\dot{m}_a$, $T_{c,1}$, $T_{c,2}$ and $\dot{m}_w$, $T_{h,1}$, $T_{h,2}$ are the fluid mass flow rates, entering temperatures, and exit temperatures of air and water, respectively. U_m is the true mean overall heat-transfer coefficient based on the outside root tube area, A is the total heat transfer surface area of the exchanger used to compute U_m, and ΔT_m is the mean temperature difference of the exchanger (MTD).

The optimizer will manipulate the design variables in order to find an optimum, while at the same time, insuring that the energy balance is satisfied, that is:

$$\dot{Q} = \dot{Q}_3 = \dot{Q}_4 = \dot{Q}_5 \tag{8}$$

where $\dot{Q}$ may be some given heat transfer rate.

Performance Calculation Procedure. With the temperatures, mass flow rates, and specific heats all specified in the listing of design parameters (whether they be constant or variable), the only unknown quantities on the right-hand side of equations (5-7) are U_m, A, and ΔT_m.

For many flow arrangements, various approaches for determining MTD, mainly using diagrams, are available [27], which have proven very useful in manual design efforts. For computerized design, however, an explicit, approximate equation is desirable in order to achieve a fast, sufficiently accurate calculation of the mean temperature difference of a given flow arrangement.

Roetzel et al. [28], presented such an approximate equation together with empirical coefficients for nine counter-current crossflow arrangements as they apply to air-cooled heat exchangers.

Roetzel used the familiar equation for the MTD of the given flow arrangement ΔT_m:

$$\Delta T_m = F \cdot \Delta T_{lm} \tag{9}$$

where ΔT_{lm} is the log mean temperature difference in the limiting case of pure countercurrent flow, and F is a log-mean temperature difference correction factor determined by a different set of coefficients for each flow arrangement. Roetzel reported the following function suitable for F:

$$F = 1 - \sum_{i=1}^{m} \sum_{k=1}^{n} a_{ik} (1 - \nu_{1,m})^k \sin(2\, i \arctan R) \tag{10}$$

where $\nu_{1,m}$ is the dimensionless LMTD,

$$\nu_{1,m} = \frac{\Delta T_{l,m}}{T_{h,1} - T_{c,1}} \tag{11}$$

$$R = \frac{T_{h,1} - T_{h,2}}{T_{c,2} - T_{c,1}} \tag{12}$$

and the coefficients $a_{i,k}$ of the approximating equation (10), were calculated using a standard least squares estimation program [29], and are reported in reference [28]. The assumption that both streams were unmixed was used in their calculation.

When more than four tubeside passes are used, it is assumed that the heat exchanger has approached the limiting case of pure counterflow, and F is set equal to one [2].

Having determined the MTD, the remainder of the analysis procedure follows Roetzel's [30] general approximation method for determining the mean overall heat-transfer coefficient, U_m, for any flow arrangement while taking into account the variation of the heat-transfer coefficients and the pressure drop with temperature and/or length of path.

Before continuing with specific analysis procedures, a brief summary of Roetzel's general approximation method is in order.

The local overall heat-transfer coefficient based on the outside root tube area can be written as follows:

$$U = \frac{1}{\frac{A_0}{A_i}\frac{1}{H_i} + \frac{A_0 \ln(r_0/r_i)}{2\pi k L} + \frac{1}{H_0 \eta_0}} \tag{13}$$

where η_0 is the efficiency of the extended surface.

In order to determine the individual convection heat-transfer (film) coefficients, H_i and H_0, according to the conventional methods, the coefficients would be considered constant, and the necessary fluid properties for their calculation would be evaluated at some mean bulk temperatures, $T_{h,b}$ and $T_{c,b}$.

However, the film coefficients are not constant, but vary with temperature and/or length of flow path. Roetzel has taken these variations into account with the use of corrected reference temperatures. Two sets of corrected reference temperatures are determined: $T_{h,I}$, $T_{c,I}$ and $T_{h,II}$, $T_{c,II}$. Details of the determination of these reference temperatures can be found in references [31] and [32]. Therefore, for each set of corrected reference temperatures, the film coefficients are determined in the conventional manner using the reference temperatures in place of the bulk temperatures.

With the film coefficients $H_{i,I}$, $H_{0,I}$, $H_{i,II}$ and $H_{0,II}$, two local overall heat-transfer coefficients, U_I and U_{II} can be calculated from equation (13).

Finally, the true mean overall heat-transfer coefficient is calculated as:

$$\frac{1}{U_m} = \frac{1}{2}\left[\frac{1}{U_I} + \frac{1}{U_{II}}\right] \tag{14}$$

The corrected reference temperatures are now used to determine the thermal conductivities and absolute viscosities of fluids for later use in the calculation of the film coefficients. Water and air were chosen as two fluids that were likely to be involved in air-cooled, heat-exchanger design. The thermal conductivities of air and water and the viscosity of air can be approximated by a second-order polynomial.

Calculations for the tubeside heat-transfer coefficient in the laminar, transition, and turbulent regions all involve a correction, such as $(\mu/\mu_{\text{wall}})^{0.14}$. In the past, an iterative procedure was required to determine the inside tube wall temperature in order to evaluate μ_{wall}. Roetzel [34] has developed an iteration-free method for determining this correction. Roetzel's method assumes that the tubeside fluid viscosity follows the Andrade equation, that is:

$$\mu = \alpha e^{\beta/T} \tag{15}$$

The tubeside heat-transfer coefficient is calculated from one of three Nusselt-type empirical equations, as follows [33]:

For laminar flow, Reynolds Number < 2,100

$$\frac{HD_i}{k} = 1.86\left(\text{Re Pr}\frac{D_i}{L}\right)^{1/3}\left(\frac{\mu}{\mu_{\text{wall}}}\right)^{0.14} \tag{16}$$

For transition regions, 2,100 < Re < 10,000

$$\frac{HD_i}{k} = 0.116[\text{Re}^{2/3} - 125]\left[1 + \left(\frac{D_i}{L}\right)^{2/3}\right]\text{Pr}^{1/3}\left(\frac{\mu}{\mu_{\text{wall}}}\right)^{0.14} \tag{17}$$

For turbulent flow, Re > 10,000

$$\frac{HD_i}{k} = 0.027\,\text{Re}^{0.8}\text{Pr}^{1/3}\left(\frac{\mu}{\mu_{\text{wall}}}\right)^{0.25} \tag{18}$$

Therefore, before any calculations can even begin, the Reynolds number, Re, must be computed to determine the type of flow.

The Reynolds number will be calculated as

$$\text{Re}_j = \frac{D_i m_h}{A_x \mu_{h,j}}$$

D_i, m_h are supplied in the initial list of parameters and μ_h is calculated from equation (15). This leaves only the cross-sectional flow area, A_x, to be determined, where:

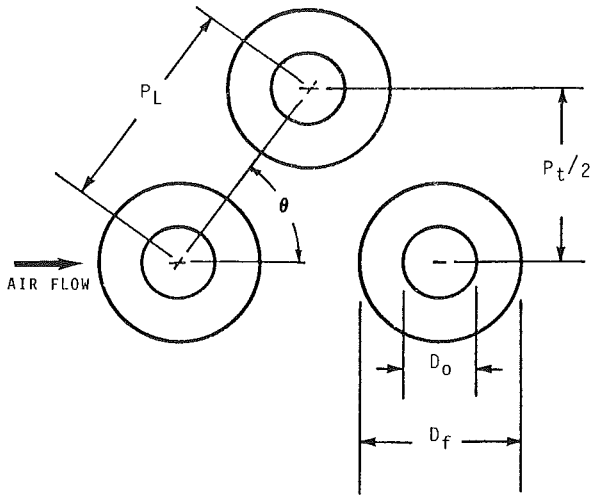

Fig. 2 Tube field layout

$$A_x = N_p \frac{\pi D_i^2}{4}$$

and N_p is the number of tubes per pass. With Re calculated, the Prandtl number is computed from given and previously determined thermophysical properties.

The uncorrected tubeside heat-transfer coefficients, $H_{i,j}$, that is $H_{i,j}$ without the viscosity correction factor, can be calculated from the proper choice of equations (16-18). Before the viscosity correction factor can be determined using Roetzel's method, the outside heat-transfer resistance, R, must be computed.

Equation (13) can be written in a more gener form as

$$U = \frac{1}{R_i + R_{\text{wall}} + R_0} \tag{19}$$

where R_i, R_w, R_0 are the inside, wall, and outside heat-transfer resistances, respectively. Additional resistances, such as contact or fouling, can also be added here.

In order to have the optimization program play a significant role in the selection of an optimized surface for a finned tube heat exchanger, an explicit equation for H_0 involving the tube and bank design parameters as independent variables is a necessity.

In the past, comparison methods, as described by Shah [35], were used to choose the best surface from a list of surfaces for which experimental heat-transfer and friction data existed. The data is presented in graphical form, where friction and Colburn factors are plotted as a function of Reynolds Number. With J, $\dot{m}_a$, c_p and Pr known, the film coefficient can be computed.

Therefore, in previous heat-exchanger optimization programs, a given surface (described by its pitch, outside fin diameter, fin thickness, fin spacing, and outside tube diameter) had to be chosen beforehand. After the surface configuration had been selected, expressions for f and J were obtained by fitting polynomials to the experimental data described earlier.

Briggs and Young [36] provide a means of getting past this obstacle with an improved convection heat-transfer correlation for air flowing across triangular pitch banks of high finned tubes, as shown in Fig. 2.

Briggs and Young expanded the work of Ward and Young [37] to cover a total of eighteen differently configured finned tube banks in order to determine the effect of fin thickness and tube pitch on the airside heat-transfer coefficient. The heat-transfer data for the high-fin banks were correlated to give

$$N_u = \frac{H_{0,j} D_0}{k_j} = 0.1378\,\mathrm{Re}^{0.718}\mathrm{Pr}^{1/3}\left(\frac{S}{l}\right)^{0.296} \tag{20}$$

where s is the distance between adjacent fins and l is the fin height. Equation (20) is based on tubes having a wide range of fins heights, fin thicknesses, fin spacing, and outside tube diameter, and can be used to predict $H_{0,j}$ for a bank of tubes six rows deep. Figure 11 of reference [37] is used to correct $H_{0,j}$ for banks of other than six rows.

In order to calculate the outside heat-transfer resistance, which will be used to calculate the correction for the tubeside heat-transfer coefficient, and finally, the local overall heat-transfer coefficients, the extended surface efficiency, η_0, must be computed.

The surface efficiency can be expressed as [33]

$$\eta_0 = 1 - \frac{A_f}{A}(1-\eta_f)$$

where η_f, the fin efficiency for a radial fin, can be found from the analytical form involving modified Bessel functions [33].

The finned area, A_f, and the total heat-transfer area, A, are computed as follows:

$$A_f = N_T w n_f \frac{\pi}{2}(D_f^2 - D_0^2)$$

$$A = N_T W\left[n_f \frac{\pi}{2}(D_f^2 - D_0^2) + (1 - n_f t)\pi D_0\right]$$

With R calculated from equation (19), the correction to the tubeside film coefficient can be made.

In the past, with the tubeside heat-transfer coefficient dependent on the wall temperature, the dependence has either been neglected, or the wall temperature has been calculated with an iterative technique. Roetzel [34] has proposed an improved iterative-free method for finding the "Sieder-Tate" correction, $(\mu/\mu_{\text{wall}})^{0.14}$, when the tubeside fluid obeys Andrade's viscosity equation.

All the parameters on the right-hand side of equation (19) are now available. Therefore, the two reference overall heat-transfer coefficients, U_{I} and U_{II}, can be calculated. The mean overall heat-transfer coefficient follows easily from equation (14). With U_m, $\dot{Q}_5$ can be calculated, with the heat balance to be performed by the optimizer.

The final calculations before computing objective and constraint functions for the optimization problem involve the pressure drops in the heat exchanger.

The basic equations that will be used for the calculation of the pressure losses are as follows:

(*a*) Tubeside [33]

$$\Delta p_i = \frac{f_i \dot{m}_h^2 w n_p}{2 g_c A_{x,t}^2 \rho D_i \left(\frac{\mu}{\mu_{\text{wall}}}\right)^z} + \frac{(n_p - 1)\dot{m}_h^2}{2 g_c A_{x,T}^2 \rho} \tag{21}$$

where $z = 0.14$ below Re = 2100 and $z = 1.25$ for Re greater than 2100.

(*b*) Airside [38]

$$\Delta p_0 = \frac{f_0 n_r \dot{m}_c^2}{{}_{ff} g_c \rho} \tag{22}$$

where A_{ff} is the minimum flow area.

The friction factor for the tubeside flow, f_i, is taken from Fig. 9.5 of reference [33], assuming fully developed flow. For use on the computer, an explicit expression for f was obtained by fitting a line and an exponential to the experimental data of Fig. 9.5. This follows

$$f_i = 64/R_e \qquad R_e < 1000$$

$$f_i = 0.46\,R_e^{-0.27} \qquad R_e \geq 1000$$

Just as in the case of the airside film coefficient, for surface optimization on the computer, an explicit equation for the airside friction factor, f_0, is desirable. Robinson and Briggs [38], presented such an expression for f_0 for air flowing across triangular pitch banks of finned tubes. Robinson and Briggs's work closely parallels that of Briggs and Young [36]. The Robinson-Briggs Correlation

$$f_0 = 18.93\,R_e^{-0.316}(P_t/D_0)^{-0.927}(P_t/P_L)^{0.515} \tag{23}$$

covers the range of tube sizes and pitches used in air-cooled heat exchangers [38].

Therefore, with $\mathrm{Re_I}$ and $\mathrm{Re_{II}}$, the four reference pressure drops, $\Delta p_{i,j}$ and $\Delta p_{0,j}$, may be computed from equations (21) and (22). Following Roetzel's general approximation method:

$$\Delta p_i = \frac{U_m}{2}\left[\frac{\Delta p_{i,\text{I}}}{U_{\text{I}}} + \frac{\Delta p_{i,\text{II}}}{U_{\text{II}}}\right]$$

For a gas, an additional correction is needed because the density in equation (23) is strongly dependent on pressure, which is changing through the exchanger. Using the inlet pressure as reference

$$\Delta p_0' = \frac{U_m}{2}\left[\frac{\Delta p_{0,\text{I}}}{U_{\text{I}}} + \frac{\Delta p_{0,\text{II}}}{U_{\text{II}}}\right]$$

$$\Delta p_0 = \left[1 - \left(1 - 2\frac{\Delta p_0'}{p_1}\right)^{1/2}\right] \tag{24}$$

All the necessary information from an analysis viewpoint has now been calculated. Functions needed for the numerical optimization process follow.

The choice of objective functions for minimization are defined as follows:

(*a*) Volume $= w\,h\,[D_f + (n_r - 1)\,P_L \cos\theta]$ (25)

where

$$\theta = \arcsin(P_t/2P_L)$$

(*b*) Heat-transfer area

$$= N_T w\left[\frac{\pi}{2s}(D_f^2 - D_0^2) + \left(1 - \frac{t}{s}\right)\pi D_0\right]$$

(*c*) Air horsepower $= \dfrac{\Delta p_a \cdot \dot{m}_a}{\rho}$

(*d*) Airside pressure drop

(*e*) Tubeside pressure drop

Results

Case studies were chosen as the best way to test the capabilities of the program for Heat Exchanger Design using Numerical Optimization (HEDSUP). The design problems posed were made as realistic as possible.

HEDSUP currently has the capability to design for nine different configurations of triangular pitch banks of finned tubes:

TYPE 1 – 1 Row, 1 PASS
TYPE 2 – 2 Row, 1 PASS
TYPE 3 – 3 Row, 1 PASS
TYPE 4 – 4 Row, 1 PASS
TYPE 5 – 2 Row, 2 PASS
TYPE 6 – 3 Row, 3 PASS
TYPE 7 – 4 Row, 2 PASS
TYPE 8 – 4 Row, 4 PASS
TYPE 10 – PURE COUNTERFLOW

Type 10 will include exchangers with a configuration of n rows, n passes, where n can go from five to twenty.

The banks must be constructed of high-finned tubes ($l >$ 1.59 mm [33]) with the fins having rectangular profile of constant thickness.

At present, HEDSUP can provide the design parameters for an air-cooled heat exchanger optimized for any one of the following design objectives:

(*a*) Minimum volume
(*b*) Minimum heat-transfer surface area
(*c*) Minimum air horsepower
(*d*) Minimum airside pressure drop
(*e*) Minimum tubeside pressure drop

Additional design objectives can be used, provided that they can be expressed as a function of the design variables. It should also be pointed out that any design variable may simultaneously be a design objective as long as it conforms to the restrictions of both. For example, an exchanger may be designed for minimum bank height.

The airside fluid is restricted to dry air. The tubeside fluid is presently limited to water in single phase. Other tubeside fluids can be used by HEDSUP, provided that their viscosities obey Andrade's Law and the fluid thermal conductivities can be expressed as a function of temperature. The fluid specific gravity would also have to be placed in the denominator of equation (21).

Case Study. An air-cooled heat exchanger is to be designed for minimum volume with a heat-transfer rate 2.93×10^6 W (10^7 Btu/hr). Water is to be cooled from 93.4°C (200°F) to 51.7°C (125°F). Dry air will enter the exchanger at 35°C (95°F) and leave at 54.4°C (130°F). Specifications call for a fan that can produce a pressure difference of 498 Pa (2 in. H_2O). Although air outlet temperature and air mass flow rate are design variables in an air-cooled heat exchanger, these are fixed in this specific problem used to illustrate the procedure. They could have been considered as design variables.

The design variables must be singled out and given side constraints. All parameters must be given an initial value and only the values of the design variables will change.

Assuming constant specific heats, the mass flow rates of both fluids can be determined because the heat-transfer rate and temperature differences are given

$$\dot{m}_w = \frac{\dot{Q}}{C_{p,h}\Delta T_h} = 16.8 \text{ kg/s}$$

$$\dot{m}_a = \frac{\dot{Q}}{C_{p,c}\Delta T_c} = 150 \text{ kg/s}$$

A crossflow arrangement, fin profile, and tube material must be chosen.

The design variables for this example are

$5.89 \le D_i \le 59.06$ mm	$0.0 \le P_t \le 102.0$ mm	$t^i = 0.58$ mm
$6.1 \le D_0 \le 63.5$ mm	$0.0 \le w \le 12.6$ mm	$S^i = 2.82$ mm
$1.59 \le l$	$0.0 \le h \le 12.7$ mm	$P_L{}^i = 54.0$ mm
$0.25 \le t \le 0.597$ mm	$D_i{}^i = 50.8$ mm	$P_t = 102.0$ mm
$2.0 \le S \le 3.18$ mm	$D_0{}^i = 50.8$ mm	$w^i = 12.34$ mm
$0.0 \le P_L \le 102.0$ mm	$l^i = 11.7$ mm	$h^i = 8.9$ mm

The side constraints on the design variables are of a practical nature with the exception of the lower bounds on fin height. Recall that the use of equation (20) is restricted to high fins. High fins will also tend to keep the fluid unmixed, which was an assumption used when defining the coefficients $a_{i,k}$, used in equation (16).

From the problem statement, the airside pressure drop must be less than 498 Pa.

$$0 \le \Delta p_a \le 498 \text{ Pa}$$

From a practical standpoint:

$$0.0 \le \theta \le 1.3,\ 1.0 \le D_f/D_0 \le 2.5$$

$$0.46 \le \left(\frac{D_0 - D_i}{2}\right) \le 4.6 \text{ mm},\ p_w < 956\, p_a$$

The equality constraint

$$\dot{Q}_5/\dot{Q} = 1.0$$

Table 1 Case study results

$\dot{m}_h = 16.8$ kg/s
$T_{h_1} = 93.3$°C
$T_{h_2} = 51.7$°C

$\dot{m}_a = 150$ kg/s
$T_{c_1} = 35$°C
$T_{c_2} = 54.4$°C

Rectangular fin profile
Aluminum fins
Copper tubes
$\dot{Q} = 2.93 \times 10^6$W

	Initial design TYPE 1	3 ROW 3 PASS	2 ROW 1 PASS	3 ROW 1 PASS	4 ROW 1 PASS	2 ROW 2 PASS	4 ROW 2 PASS	4 ROW 4 PASS	5 ROW 5 PASS
D_i, mm	50.8	12.19	27.84	18.62	11.28	17.17	13.69	13.59	14.55
D_0, mm	63.5	13.28	28.8	19.61	12.22	18.29	14.63	14.61	15.47
l, mm	11.7	2.09	9.98	7.39	7.01	4.11	3.25	2.17	1.86
t, mm	0.58	0.40	0.60	0.60	0.55	0.55	0.53	0.44	0.42
S, mm	2.82	2.03	2.03	2.03	2.03	2.03	2.03	2.03	2.03
P_t, mm	102	18.8	48.8	34.6	29.5	26.5	25.9	23.4	26.5
P_L, mm	54	18.0	48.9	35.9	26.4	26.4	26.5	19.9	20.3
h, m	8.9	12.69	5.69	4.42	3.95	8.69	6.06	12.70	12.68
w, m	12.45	3.07	9.49	5.82	4.97	7.25	4.73	2.70	2.52
$\dot{Q}$, W	6052021	2929416	2930457	2930867	2928756	2930157	2930689	2930702	2930499
Volume, m^3	15.66	1.87	4.93	2.50	1.81	3.12	2.06	2.30	2.58

Optimum design

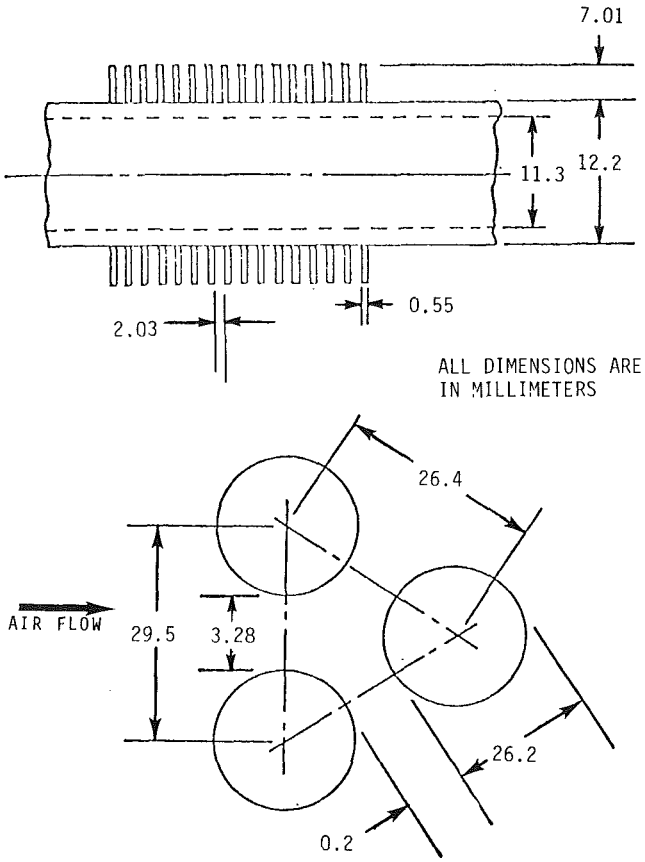

Fig. 3 Case study optimum design

where

$$\dot{Q}_5 = U_m A\, \Delta T_m$$

$$= 2.93 \times 10^6 \text{W}$$

will satisfy the heat balance.

A three-dimensional design matrix can now be constructed of optimum exchanger designs with minimum volumes. The matrix would be constructed by first holding the tube and fin materials constant and varying the configuration, i.e., Type 1, Type 2, Type 3, etc. Next the tube material would be varied with the fin material and exchanger configuration held constant and so forth. However, for this case study, the tube material will be chosen as copper, k = 346 W/m C and the fin material will be aluminum, k = 204 W/m C. Also, in order to simulate an actual trade-off study, the constraint framework will be fixed throughout the individual case studies.

The design matrix is presented in Table 1. The optimum design is a Type 4 configuration and shown in Fig. 3. Typically, for this case study, when starting far from the final design, COPES/CONMIN would require approximately 1700 calls to ANALIZ to reach an optimum. However, when beginning from a reasonable starting point only 600 calls were needed. Note that each call to ANALIZ required approximately 0.06 s of CPU time on an IBM 360/67.

Conclusions

The intent of this investigation was to couple an analysis program with a numerical optimization scheme, COPES/CONMIN, to produce a complete, detailed design program (HEDSUP) for an air-cooled heat exchanger. In addition, the analysis program was to be written such that: (*i*) the variation in the film coefficients with temperature/length of flow path would be taken into account; (*ii*) the surface would be optimized; and (*iii*) it would be iterative free and thus minimize the computer time required during an actual trade-off study.

Although COPES/CONMIN could optimize the objective function satisfying the inequality constraints, a reliable heat balance could not be obtained. The solution to this problem was the addition of the ALM option to COPES. In this way, the method of feasible directions, which works best with inequality constraints, was used to satisfy this type of constraint. The multiplier method, which works best with equality constraints, was used to perform the heat balance.

The results of the case studies show that HEDSUP will yield reliable designs for various design objectives and problems with only minor man-machine interaction.

The value of numerical optimization in a design problem of this size cannot be overemphasized. For example, in the case study, the problem is taking place in a nine-dimensional design space and intuition on how an optimized design "should" turn out is quickly lost. This capability of surface optimization is dependent upon the use of the Briggs-Young and Robinson-Briggs Correlations, equations (20) and (22), respectively. The reliability of the correlations as compared to the "conventional" method, using charts and graphs, is questionable. Actual experimental data for a particular tube and pitch will always be the most useful in predicting pressure drop and film coefficients across banks of finned tubes. However, the correlations mentioned above cover the ranges and pitches used in air-cooled heat exchangers and should therefore be sufficiently accurate in predicting H_0 and Δp_a.

References

1 Smith, E. C., "Air-Cooled Heat Exchangers," *Chemical Engineering*, Nov. 17, 1958, pp. 145–150.

2 Mott, J. E., Person, J. T., and Brock, W. R., "Computerized Design of a Minimum Cost Heat Exchanger," ASME Paper 72-HT-26, 1972.

3 Nakayama, E. U., "Find the Best Air Fin Cooler Design," *Petroleum Refiner*, Vol. 38, No. 4, Apr. 1959, pp. 109–114.

4 Bergles, A. E., Blumenkrantz, A. R., and Taborek, J., *Proceedings of the Fifth International Heat Transfer Conference*, Vol. II, 1974, pp. 239–243.

5 Fax, D. H., and Mills, R. R., Jr., "Generalized Optimal Heat Exchanger Design," *ASME Trans.*, Vol. 79, 1957, pp. 653–661.

6 Palen, J. W., Cham, T. P., and Taborek, J., "Optimization of Shell-and-Tube Heat Exchangers by Case Study Method," *Chemical Engineering Progress Symposium Series*, Vol. 70, No. 138, 1974, pp. 205–214.

7 Box, M. J., "A New Method of Constrained Optimization and Comparisons with Other Methods," *The Computer Journal*, Vol. 8, 1965, pp. 42–52.

8 Johnson, C. M., Vanderplaats, G. N., and Marto, P. J., "Marine Condenser Design Using Numerical Optimization," *Journal of Mechanical Design*, Vol. 102, 1980, pp. 469–475.

9 Afimiwala, K. A., Interactive Computer Methods for Design Optimization, Ph.D. thesis, Mechanical Engineering Department, State University of New York at Buffalo, 1976.

10 Fontein, H. J., and Wassink, J. G., "The Economically Optimal Design of Heat Exchangers," *Engineering and Process Economics*, Vol. 3, 1978, pp. 141–149.

11 Nelder, J. A., and Mead, R., "A Simplex Method for Function Minimization," *Computer Journal*, Vol. 7, 1965, pp. 308–313.

12 Kays, W. M., and London, A. L., *Compact Heat Exchangers*, 2nd ed., McGraw-Hill, 1964.

13 Hedderich, C. P., "Heat Exchanger Optimization," M.S. thesis, Mechanical Engineering Department, Naval Postgraduate School, Monterey, Calif., Sept. 1980.

14 Shah, R. K., Afimiwala, K. A., and Mayne, R. W., "Heat Exchanger Optimization," *Proceedings of the Sixth International Heat Transfer Conference*, Vol. 4, 1978, pp. 185–191.

15 Vanderplaats, G. N., "CONMIN—A FORTRAN Program for Constrained Function Minimization, User's Manual," NASA Ames Research Center Technical Memorandum, NASA TM X-62, 282, Aug. 1973.

16 Madsen, L., and Vanderplaats, G. N., "COPES—A Control Program for Engineering Synthesis Users Manual," Naval Post-graduate School Technical Report NPS-69-81-003 VN, Monterey, Calif., July 1981.

17 Vanderplaats, G. N., "The Computer Design and Optimization," in *Computing in Applied Mechanics*, ASME Symposium, AMD—Vol. 18, ASME, New York, Dec. 1976.

18 Himmelblau, D. M., *Applied Nonlinear Programming*, McGraw-Hill, 1972.

19 Fox, R. L., *Optimization Methods for Engineering Design*, Addison-Wesley, 1971.

20 Pierre, D. A., and Lowe, M. J., *Mathematical Programming Via Augmented Lagrangians*, Addison-Wesley, Reading, Mass., 1975.

21 Johnson, C. M., "Marine Steam Condenser Design Using Numerical Optimization," M.S. thesis, Mechanical Engineering Department, Naval Postgraduate School, Dec. 1977.

22 Fletcher, R., and Reeves, C. M., "Function Minimization by Conjugate Directions," *British Computer Journal*, Vol. 7, No. 2, 1964, pp. 149–154.

23 Zoutendijk, G. G., *Methods of Feasible Directions*, Elsevier, Amsterdam, 1960.

24 Vanderplaats, G. N., and Moses, F., "Structural Optimization by Methods of Feasible Directions," *Journal of Computers and Structures*, Vol. 3, 1973, pp. 739–755.

25 Vanderplaats, G. N., Hicks, R. N., and Murman, E. M., "Aerodynamic Analysis Requiring Advanced Computers NASA SP-347: Part II—Appplication of Numerical Optimization Techniques to Airfoil Design," Mar. 1975, pp. 749–748.

26 Imai, K., "Configuration Optimization of Trusses by the Multiplier Method," Ph.D. thesis, University of California at Los Angeles, June 1978.

27 Bowman, R. A., Mueller, A. C., and Nagle, W. M., "Mean Temperature Difference in Design," *Trans. ASME*, Vol. 62, May 1940, pp. 283–294.

28 Roetzel, W., and Nicole, F. J. L., "Mean Temperature Difference for Heat Exchanger Design—A General Approximation Explicit Equation," JOURNAL OF HEAT TRANSFER, Vol. 97, 1975, pp. 5–8.

29 Middleton, J. A., "Least-Squares Estimation of Nonlinear Parameters—NLIN," Share Program Library Agency, Program Order No. 360D-13.2.003.

30 Roetzel, W., "Heat Exchanger Design With Variable Transfer Coefficients for Crossflow and Mixed Flow Arrangements," *International Journal of Heat Transfer*, Vol. 17, 1947, pp. 1037–1049.

31 Roetzel, W., "Berucksichtigung veranderlicher Warmeubergangskowffizienten und Warmekapazitaten bei der Bemessung von Warmeastaushern," *Warme-und Stoffubertragung*, Vol. 2, 1969, pp. 163–170.

32 Roetzel, W., "Calculation of Single Phase Pressure Drop in Heat Exchangers Considering the Change of Fluid Properties Along the Flow Path," *Warme-und Stoffubertragung*, Vol. 6, 1973, pp. 3–13.

33 Kern, D. Q., and Kraus, A. D., *Extended Surface Heat Transfer*, McGraw-Hill, 1972.

34 Roetzel, W., "Iteration-Free Calculation of Heat Transfer Coefficients in Heat Exchangers," *Chemical Engineering Journal*, Vol. 13, 1977, pp. 223–237.

35 Shah, R. K., "Compact Heat Exchanger Surface Selection Method," *Proceedings of the Sixth International Heat Transfer Conference*, Vol. 4, 1978, pp. 193–199.

36 Briggs, D. E., and Young, E. H., "Convection Heat Transfer and Pressure Drop of Air Flowing Across Triangular Pitch Banks of Finned Tubes," *Chemical Engineering Progress Symposium Series*, Vol. 59, No. 41, 1963, pp. 1–10.

37 Ward, D. J., and Young, E. H., "Heat Transfer and Pressure Drop of Air in Forced Convection Across Triangular Pitch Banks of Finned Tubes," *Chemical Engineering Progress Symposium Series*, Vol. 55, No. 29, 1959, pp. 37–44.

38 Robinson, K. E., and Briggs, D. E., "Pressure Drop of Air Flowing Across Triangular Pitch Banks of Finned Tubes," *Chemical Engineering Progress Symposium Series*, Vol. 62, No. 64, 1966, pp. 177–184.

Effect of Blockage-Induced Flow Maldistribution on the Heat Transfer and Pressure Drop in a Tube Bank

E. M. Sparrow
Fellow ASME

R. Ruiz
Department of Mechanical Engineering,
University of Minnesota,
Minneapolis, Minn. 55455

Detailed experiments, encompassing per-tube heat-transfer measurements and row-by-row pressure measurements, were performed to investigate the response of a tube bank to maldistribution of the flow at the inlet cross section. The maldistribution was created by a partial blockage of the inlet section. Baseline experiments for uniformly distributed inlet flow were also carried out. The experiments spanned an order of magnitude range in the Reynolds number. On the whole, the inlet-section flow maldistribution tends to enhance the heat transfer at a given Reynolds number, with an accompanying additional pressure drop of about 2½ velocity heads. Enhancements in the 30–40 percent range are encountered in the first several rows in the corridor downstream of the unblocked portion of the inlet section. Reductions (up to 50 percent) are confined to a narrow alley behind the blockage. Ten-percent maldistribution-related effects persist to the seventh row, while effects at the 5 percent level occur at least as far downstream as the twelfth row.

Introduction

Flow maldistribution is a widely encountered operational problem in heat-exchanger practice. In general, maldistribution may be classified in two categories, depending on whether the fluid flow which enters the heat exchanger is maldistributed or whether the maldistribution is induced within the heat exchanger itself. The focus of the present paper is on maldistributed entering flows, illustrations of which will be described shortly. Internally induced maldistributions are caused by geometrical irregularities and imperfections, which give rise, for example, to leakage and bypass in shell and tube heat exchangers, and by differential heating, which is of particular relevance in laminar heat exchangers employing viscous liquids.

There are numerous causes of possible maldistributions in the flow that is delivered to the inlet cross section of a heat exchanger. If the inlet were situated downstream of a bend or an elbow, the nonuniform packing of the flow in the bend would be reflected in a nonuniform distribution across the inlet. Furthermore, secondary motions (i.e., corkscrewlike motions) are generated in bends and turns, and such motions further complicate the flow entering the heat exchanger. Overly rapid enlargements of the ductwork which feeds a heat exchanger will give rise to zones of flow separation and recirculation which are carried into the exchanger inlet. Partially open valves and misaligned baffles are sources of nonuniform flow, and the eddies shed from these devices constitute a further degree of complexity. In applications where a heat exchanger is fed from the exhaust of a rotating device such as a gas turbine, there will be a strong swirl superposed on the inlet flow.

The foregoing slate of physical situations which favor maldistributed inlet flows is illustrative rather than exhaustive. Furthermore, the agents causing maldistribution are often compounded, as seen, for example, in a swirling flow delivered to a heat exchanger via a bend and an overly rapid enlargement.

Waste heat recovery systems, which have become an essential factor in effective energy management, are especially vulnerable to pathological ducting arrangements for delivery of hot gases to the heat-exchanger inlet. This is because such systems are often retrofitted in an existing plant site and, as a consequence, both the ductwork and the heat exchanger have to be adaptive to the available space. Even in new installations, the size of waste heat systems and the cost of physical space often leads to nonideal ducting arrangements.

The importance of maldistributed inlet flows is widely recognized among heat-exchanger practitioners (e.g., [1, 2]), but the complexity of the problem appears to have been a deterrent to research at a fundamental level. The work reported in the published literature is mainly focused on estimating the effects of the maldistribution by employing analytical models in which the heat-transfer coefficients, needed as input, are based strictly on assumption (e.g., [3–6]). For example, heat-transfer coefficients for uniformly distributed flows have been employed, while in others, a simple power-law relation between the transfer coefficient and the mass velocity is assumed to hold. It does not appear that detailed measurements have heretofore been made of the transfer coefficients in heat exchangers subject to a maldistributed inlet flow.

In the research to be reported here, experiments are performed in which, seemingly for the first time, heat-transfer coefficients are measured internal to a heat exchanger with a maldistributed inlet flow. In planning the research program, it appeared most appropriate to model a generic type of maldistribution rather than to reproduce one of the myriad of specific maldistribution arrangements that occur in practice. The heat-exchanger configuration to be studied here is, itself, generic – a tube bank through which air passes in crossflow. Attention will be focused on the heat-transfer characteristics of the flow external to the tubes (in contrast to the internal flow).

The special feature of the research is that heat-transfer coefficients were measured at each of the individual tubes of the array. These detailed measurements were performed for both the maldistributed flow and for the case of a uniformly distributed flow, both at the same Reynolds numbers. The

Contributed by the Heat Transfer Division for publication in the JOURNAL OF HEAT TRANSFER. Manuscript received by the Heat Transfer Division October 27, 1981.

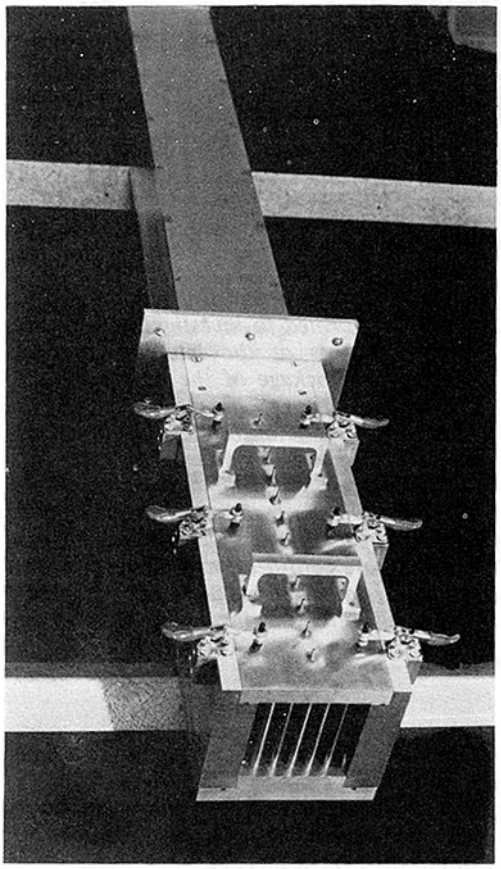

Fig. 1 Photograph of the test section and the afterduct

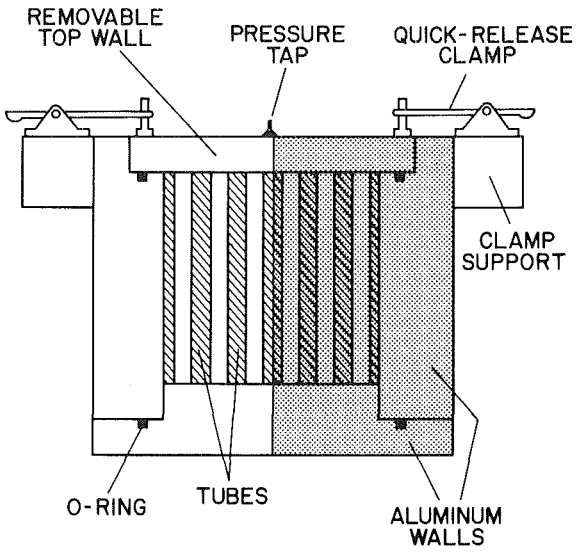

Fig. 2 Schematic diagram of the front face of the test section

per-tube heat-transfer coefficients in the presence of the maldistribution were ratioed with the corresponding coefficients for the uniform flow. The deviation of each ratio from unity provides an immediate index of the effect of the maldistributed inlet flow in either degrading or enhancing the per-tube heat-transfer coefficient.

The aforementioned ratios are presented on a plan view of the tube bank, with each tube being inscribed with its individual ratio. In this presentation, zones of enhancement and degradation are readily identified. In addition, the propagation of the inlet section maldistribution through the heat exchanger can be observed, as can the homogenization of the flow as the maldistribution wanes.

In the experiments, the maldistribution was created by a partial blockage of the inlet cross section of the heat exchanger. Owing to the inability of the entering flow to turn sharply and fill the space downstream of the blockage, a low-velocity recirculation zone is set up. On the other hand, the flow passing through the unconstricted portion of the inlet section creates an alley of relatively high velocity fluid that penetrates the heat exchanger. To create a severe case of maldistribution, the experiments were performed with an inlet-section blockage of 50 percent. The Reynolds number was varied over an order of magnitude during the course of the experiments.

In order to obtain the detailed information described in the foregoing, it was found advantageous to perform mass-transfer experiments rather than direct heat-transfer experiments. The naphthalene sublimation technique was used in the mass-transfer experiments, and the mass-transfer coefficients were converted to heat-transfer coefficients by employing the analogy between the two processes. As the first order of business in the experimental program, the validity of the analogy was examined by comparisons of the present results for uniform inflow with well established results in the heat-transfer literature. The remarkable level of agreement that emerged from these comparisons provides unassailable support for the use of the analogy in heat-exchanger work.

In addition to the heat and mass-transfer studies, the pressure drop was measured as a function of position along the length of the heat exchanger, both for the maldistributed and uniform flow cases. The comparison of the results enables identification of the incremental pressure drop due to the flow maldistribution. These multi-station internal pressure measurements represent a departure from con-

Nomenclature

A_{min} = minimum free flow area between tubes
A_{naph} = per-tube mass-transfer area
D = tube outside diameter
$\mathfrak{D}$ = naphthalene-air diffusion coefficient
f = friction factor, equation (11)
K = per-tube mass-transfer coefficient, $\dot{m}/(\rho_{nw} - \rho_{nb})$
ΔM = per-tube change of mass
$\dot{m}$ = per-tube rate of mass transfer per unit area
N = row number
Nu = Nusselt number
Pr = Prandtl number
p = pressure
p_∞ = pressure upstream of array
Δp = pressure drop, $(p_\infty - p(x))$
Re = Reynolds number, $\rho VD/\mu$
Sc = Schmidt number
Sh = per-tube Sherwood number, $KD/\mathfrak{D}$
S_L = longitudinal pitch
S_T = transverse pitch
V = characteristic velocity, $\dot{w}/\rho A_{min}$
$\dot{w}$ = rate of fluid flow through array
x = axial coordinate
μ = viscosity
ν = kinematic viscosity
ρ = air density
ρ_{nb} = naphthalene vapor density in bulk flow
ρ_{nw} = naphthalene vapor density at tube surface
τ = duration of data run

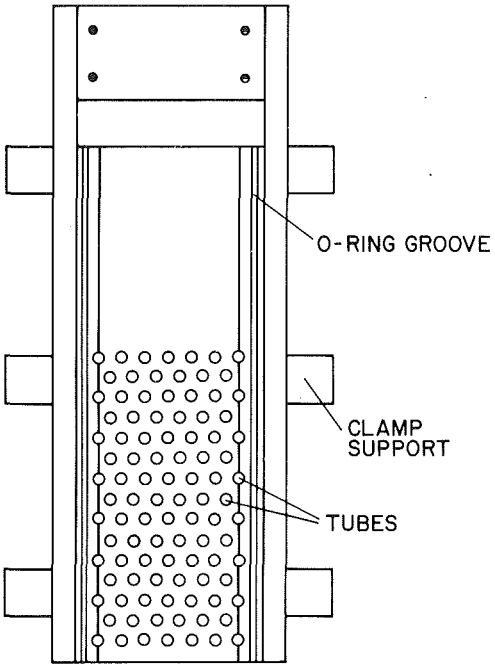

Fig. 3 Plan view of the test section with the top wall removed

ventional heat-exchanger practice where pressure measurements are made only before and after the exchanger.

The Experiments

Experimental apparatus. The description of the experimental apparatus is facilitated by reference to Figs. 1-3. The first of these is a photograph of the test section and related downstream ductwork (hereafter designated as the afterduct). Figures 2 and 3 are schematic diagrams showing various details of the test section.

In Fig. 1, the test section is the portion of the apparatus that is forward of the flange. The photograph was taken with the inlet cross section unblocked, and the first row of tubes can be seen through the open inlet. Another feature of the test section that is evident in Fig. 1 is that the top wall is removable. In connection with the removable top, there are three quick-release clamps affixed to the upper edge of the respective side walls. When the clamps are closed, they bear down on the top wall, causing it to seal against O-rings. With the opening of the clamps, the top wall can be removed in a matter of seconds with the aid of the specially machined handles that are attached to the wall. A row of static pressure taps, deployed along the spanwise centerline of the top wall, can also be seen in Fig. 1.

Figure 2 is a schematic diagram of the front face of the test section, with the blockage in place (but shown as semitransparent in order to reveal the parts that are situated behind the blockage). As seen in the figure, the test section is a square duct whose lower and side walls were fabricated from thick aluminum plates (2.54 cm, 1 in.) to enable laps to be cut for interleaving the walls and ensuring precise positioning. Laps at the outer edges of the bottom wall provided seating for the side walls and, in turn, laps at the upper edges of the side walls seated the top wall. These laps also served as flats into which the O-ring grooves were milled. All surfaces of the duct walls which interface with the airflow were painstakingly polished with 600-grit wet or dry sandpaper (used wet) as the final step of the fabrication process.

The spanwise arrangement of the tubes in the first row can be seen in Fig. 2. This arrangement, which is repeated in the third, fifth, and all other odd rows, includes five regular tubes (away from the side walls) and a half tube adjacent to each of the side walls. The wall-adjacent half tubes were employed to more closely model an infinitely wide array, and the success of this approach will be documented later.

A plan view of the test section with the top wall removed and without the blockage in place is presented in Fig. 3; also, for clarity, the quick-opening clamps are not shown. This figure illustrates the layout of the tube bank. The tubes are seen to be positioned in a staggered array, with six tubes in each row. Precise, positive positioning of the tubes was ensured by seating them in holes that had been drilled into the lower wall of the duct. The aforementioned wall adjacent half tubes situated in the odd numbered rows are seen, in actuality, to be regular tubes that are recessed into the side walls so that only half of each tube is exposed to the airflow.

Further study of the figure shows that the tubes are positioned on equilateral triangular centers. The transverse center-to-center distance, S_T, between the tubes was chosen to be twice the tube diameter, D, (i.e., $S_T/D=2$). The corresponding longitudinal pitch-to-diameter ratio $S_L/D=(\sqrt{3}/2)S_T/\mathrm{D}=0.866(S_T/D)$. The array employed in the experiments contained 15 rows of tubes, as pictured in the figure. The portion of the test section aft of the array served as a downstream plenum chamber.

The experiments will be characterized in dimensionless terms so that the test-section dimensions are relevant only for orientation purposes. The cross section is a 7.62 × 7.62 cm (3 × 3 in.) square. Each tube is 0.635 cm (0.250 in.) in diameter and 7.62 cm (3 in.) in length, and the transverse pitch S_T is 1.27 cm (0.500 in.). The 12:1 aspect ratio of the tube is sufficient to eliminate concern about mass-transfer end effects, especially since there is zero mass transfer at the duct walls (the duct walls are metallic and, therefore, do not participate in the mass-transfer process). It should be noted that in a corresponding heat-transfer experiment, the end effects would, in all likelihood, be greater due to both conductive and convective interactions between the tubes and the duct walls.

As indicated in the Introduction and illustrated in Fig. 2, the selected blockage element constricted half of the inlet cross section. In considering a plate to serve as the blockage element, it was recognized that flow separation would occur at its exposed edge (i.e., the left-hand edge of the element pictured in Fig. 2). To achieve a sharply defined separation, a thin brass plate was used (0.020 cm, 0.008 in.). It was verified that the plate, when in place, did not deform under the action of the forces exerted by the airflow.

For the determination of the pressure distribution along the test section, twelve regularly spaced pressure taps were installed along the spanwise centerline of the top wall, as seen in Fig. 1. The first tap is positioned midway between the second and third rows of tubes, 2.750 cm (1.083 in.) from the leading edge of the duct. All subsequent taps are separated by an axial distance of $2S_L$ (=2.200 cm, 0.866 in.).

In addition to the regular top wall of the test section, a special top wall was fabricated and used during a preparatory stage of each data run. During that stage, it is necessary to pass air through the test section for a preselected time so that thermal equilibrium is achieved between the naphthalene mass transfer element and the flow. During this equilibration period, the mass-transfer element is jacketed by a teflon cover which protrudes above the top of the test section. The special top wall contains an elevated section which accommodates the protruding portion of the jacket. Furthermore, the elevated section can be positioned at any axial station to accommodate a mass transfer element situated in any row of the array.

In the fully assembled experimental apparatus, air was drawn from the temperature-controlled laboratory into the inlet of the test section. The air traversed the test section and exited into the afterduct (Fig. 1), which served as a transition piece between the square test-section geometry and the cir-

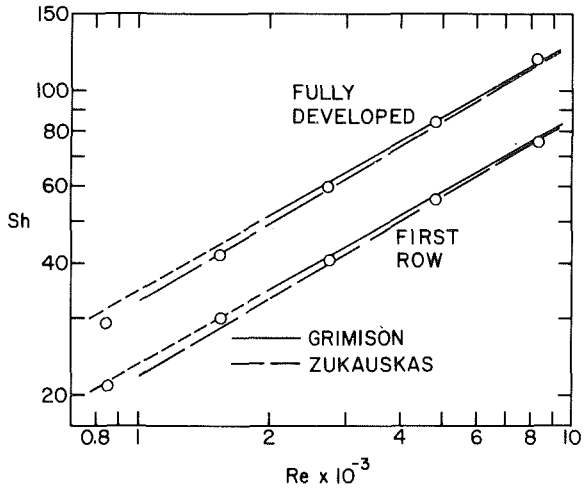

Fig. 4 Comparison of Sherwood numbers for uniform inlet flow with those of the literature

cular downstream piping. The afterduct was designed to be sufficiently long so that the contraction experienced by the flow at the downstream end of the duct (i.e., as the flow entered the downstream circular piping) was not felt in the test section. From the afterduct, the flow passed into a metering section (two calibrated rotameters), through a control valve, and then was ducted to the blowers. The blowers were situated in a service corridor outside the laboratory, and their exhaust was vented to the outdoors. The capacity of the air-handling system was 130 scfm (0.0614 m^3/s). Experiments were performed over the range from 13 to 130 scfm.

The operation of the system in the suction mode and the placement of the blowers outside the laboratory, together with the room temperature control, enabled the attainment of steady, readily measurable operating temperatures in the test section – a necessary prerequisite for the naphthalene sublimation technique. Also, the outside exhaust, coupled with strict handling procedures, ensured that the laboratory was free of naphthalene vapor.

Tubes and naphthalene test element. Each tube is, in actuality, a solid cylinder machined with a shank of smaller diameter at one end to facilitate its seating in the lower wall of the test section. To ensure uniformity of diameter for all the cylinders, they were fabricated from 0.635 cm (0.250 in.) drill rod. The length of each cylinder was machined so that the clearance between the tip of the cylinder and the top wall of the test section was 0.0025–0.005 cm (0.001–0.002 in).

In each data run, only one of the cylinders in the array participated in the mass-transfer process[1]. The participating cylinder was a composite consisting of a naphthalene coating enveloping a metal substrate. The first step in the fabrication of a coated cylinder was to reduce the diameter of the body of one of the aforementioned standard cylinders by about 3/4 mm. Following the undercutting operation, the resulting surface was machined so as to form a 1/4-mm deep screw thread. The purpose of the screw thread was to provide cavities to aid in the adhesion of the naphthalene. The thus-machined cylinder was dipped into a container of molten naphthalene, the dipping process being performed in many stages so that the surface temperature was kept low enough to avoid remelting of the naphthalene that had solidified on it. Once a sufficiently thick coating had been built up, the coated cylinder was machined in a lathe to remove the excess solidified naphthalene. The machining was continued until the diameter of the naphthalene-coated cylinder was equal to the diameter of the uncoated cylinders of the array. The tip was machined to completely remove the solidified naphthalene.

For efficiency in executing the experiments, it was standard practice to coat and machine at least eight to ten cylinders at a time. Upon completion of the coating process, the cylinders were wrapped in impermeable plastic and placed in the laboratory where the experiments were to be conducted. A freshly prepared coated cylinder was employed for each data run (i.e., coated cylinders were never reused). Subsequent to each data run, the remaining naphthalene coating was removed by melting and evaporation in preparation for the next round of coating and machining operations.

Experimental procedure and instrumentation. The key measurements made during a mass-transfer data run included the mass of the naphthalene-coated cylinder, the temperature of the air entering the test section, the airflow rate, and the barometric pressure. The mass measurements were made with a Sartorius analytical balance with a resolution of 0.0001 g and a capacity of 200 g. Air temperature was sensed by an ASTM-certified thermometer with a smallest scale division of 0.1°F. As noted earlier, calibrated rotameters equipped with static pressure taps were employed for the airflow measurements.

In supplementary runs (without mass transfer) made to determine the pressure drop characteristics of the array, the pressure signals from the test-section static taps were conveyed to a specially fabricated selector switch. The output of the switch was fed to the terminals of a Baratron solid-state, capacitance-type pressure meter capable of resolving 10^{-4} mm Hg at levels of 1, 10, and 100 Hg, depending on the sensing head employed.

Certain aspects of the experimental procedure have already been mentioned, and additional relevant details will now be described. To prepare for a data run, the room lighting and the blowers in the air-handling system were turned on at least 30 min before the intended start of the run. A steady temperature was thereby established and subsequently maintained to within 0.05–0.1°C during the data run by the temperature control system of the room.

The next preparatory step involved the attainment of thermal equilibrium between the naphthalene-coated cylinder and the airflow passing through the array. The attainment of temperature equality is a necessary prerequisite for the evaluation of the naphthalene surface temperature from the measured air temperature. To attain the desired equilibrium, the naphthalene-coated cylinder, jacketed in a close-fitting sealed teflon sleeve to minimize extraneous sublimation, was inserted at a preselected position in the array. The cylinder was allowed to remain in the array for about 30 min, during which time it was exposed to the airflow rate that had been set for the data run. After the equilibration period, the cylinder was removed from the array, weighed on the analytical balance (with teflon jacket removed), and then returned (with jacket in place) to the array for an additional 5–10 min equilibration period.

The mass-transfer period was initiated by the removal of the teflon jacket, thereby exposing the naphthalene-coated cylinder to the airflow. During the run, readings of temperature, flow rate, rotameter pressure, and barometric pressure were taken at regular intervals. The duration of the run was chosen so that the average change of thickness of the naphthalene coating due to sublimation would be about 0.0025 cm (0.001 in.), equivalent to about a 0.05 g mass loss. To terminate the run, the naphthalene-coated cylinder was jacketed, removed from the array, and weighed (with jacket removed).

At this point, a supplementary data run was carried out to

[1] The effect of this transfer arrangement on the results will be discussed at the end of the Concluding Remarks section of the paper.

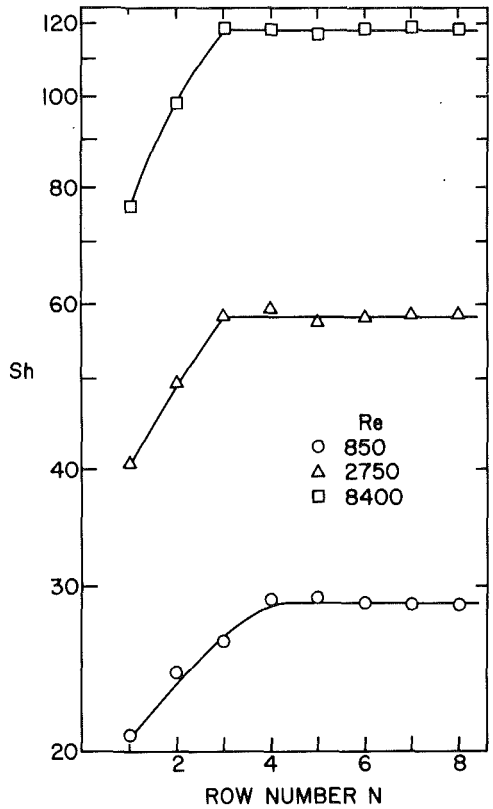

Fig. 5 Row-by-row variation of the Sherwood number for uniform inlet flow

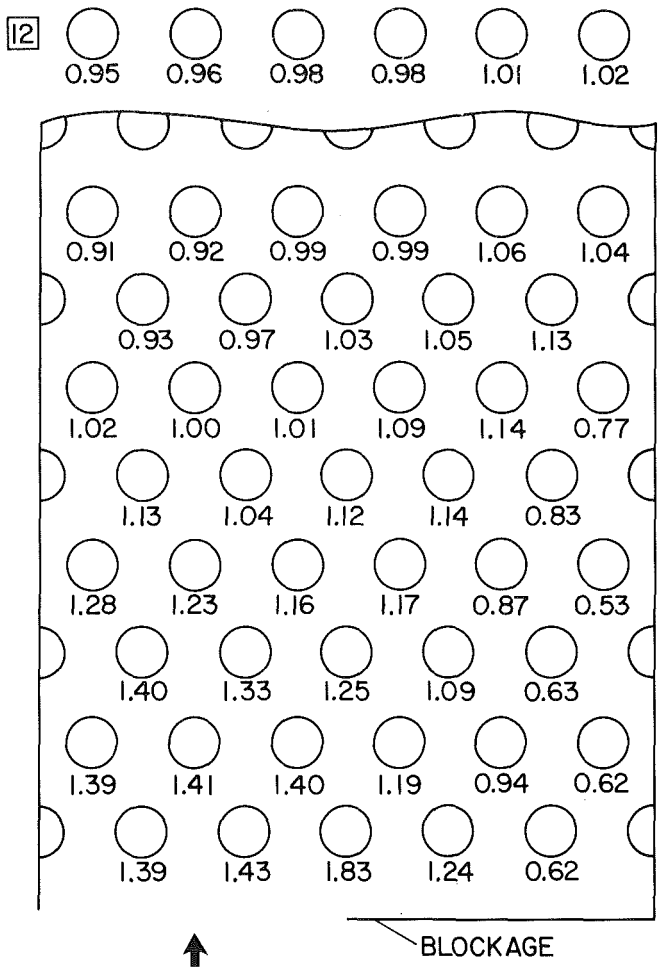

Fig. 6 Per-tube ratio of the maldistribution-affected Sherwood number to that for uniform inlet flow, Re = 850

determine a correction for any extraneous mass transfer that may have occurred in the period between the first and second weighings. All of the steps that had been performed between the first and second weighings were repeated, except for the exposure to the airflow, and following this, a third weighing was made. The thus-determined correction was on the order of 1 percent of the net mass transfer.

Data Reduction

The procedures employed to evaluate the per-tube Sherwood number (i.e., the mass-transfer counterpart of the Nusselt number), the Reynolds number, and the pressure-drop coefficient will now be described. For the Sherwood number determination, the first step is to obtain the per-tube mass-transfer coefficient, K, from its definition

$$K = \dot{m}/(\rho_{nw} - \rho_{nb}) \tag{1}$$

in which $\dot{m}$ is the per-tube mass-transfer per unit time and area, and ρ_{nw} and ρ_{nb} denote the densities of naphthalene vapor at the tube surface and in the bulk airflow. The quantity, $\dot{m}$, was determined from the measured mass loss, ΔM, due to sublimation from the surface of the naphthalene-coated cylinder and from the duration, τ, of the data run and the area, A_{naph}, of the naphthalene surface, so that

$$\dot{m} = \Delta M/\tau A_{\text{naph}} \tag{2}$$

In evaluating A_{naph}, account was taken of the slight change in the cylinder diameter during the data run.

The naphthalene vapor density, ρ_{nw}, was evaluated by a two-step process. In the first step, the naphthalene vapor pressure at the cylinder surface was calculated from the Sogin vapor pressure – temperature relation [7]. Then, the vapor density was determined from the perfect gas law. In these calculations, it was assumed that the surface temperature of the naphthalene coating was equal to the temperature of the air passing through the tube array. The general validity of this assumption was ensured by the equilibration period which preceded each data run.

There are, however, two possible causes of a small temperature difference between the surface and the air. The first is related to the fact that the latent heat of sublimation must be supplied to sustain the mass-transfer process and, if the heat were supplied by the airstream, a temperature difference must exist. The maximum possible difference due to this process was calculated to be 0.09°C. The second possible cause of temperature difference arises from the fact that the airstream thermometer measures the stagnation temperature while the naphthalene surface is at the recovery temperature. For a recovery factor of 0.8, the maximum difference between the stagnation and recovery temperatures was found by calculation to be 0.044°C. The maximum temperature difference due to the aforementioned causes is about 0.13°C, which corresponds to a maximum uncertainty of 1.3 percent in the results. This uncertainty was judged to be tolerable.

Once the mass-transfer coefficient is evaluated from equations (1) and (2), it may be recast in dimensionless form in terms of the Sherwood number, Sh

$$\text{Sh} = KD/\mathfrak{D} \tag{3}$$

where D is the tube diameter and $\mathfrak{D}$ is the naphthalene-air diffusion coefficient. The latter may be eliminated by taking note of the definition of the Schmidt number Sc, which is the mass-transfer counterpart of the Prandtl number. Since $\text{Sc} = \nu/\mathfrak{D}$, equation (3) becomes

$$\text{Sh} = (KD/\nu)\text{Sc} \tag{4}$$

in which ν is the kinematic viscosity of air, and $Sc = 2.5$ for naphthalene diffusion in air.

The Reynolds number definition used to characterize the experiments is that which is standard for tube banks. If $\dot{w}$ is the rate of airflow through the array and A_{min} is the minimum free-flow area between tubes, then $\rho V = \dot{w}/A_{min}$ and

$$Re = \rho VD/\mu = \dot{w}D/\mu A_{min} \quad (5)$$

Attention will be now be turned to the analogy between heat and mass transfer. For heat transfer in a tube bank, it is customary to correlate data in the form

$$Nu = CRe^m Pr^n \quad (6)$$

For mass transfer in a geometrically similar tube bank, the mass-transfer counterpart of equation (6) is

$$Sh = CRe^m Sc^n \quad (7)$$

where the quantities C, m, and n are the same in equations (6) and (7). Thus,

$$Nu = (Pr/Sc)^n Sh \quad (8)$$

which enables the Sherwood number results to be transformed to Nusselt numbers.

The theoretical basis of the analogy is set fourth in [8]. An experimental verification will be presented shortly. In view of the analogy, heat-transfer and mass-transfer terminology will be used interchangeably.

For the presentation of the pressure drop results, the quantity Δp is defined as

$$\Delta p = p_\infty - p(x) \quad (9)$$

where p_∞ is the pressure upstream of the test section and $p(x)$ is the pressure at an axial station x. A dimensionless presentation may be attained by the ratio

$$\Delta p/\tfrac{1}{2}\rho V^2 \quad (10)$$

with $\rho V^2 = \dot{w}^2/\rho A_{min}^2$, and ρ is the average density in the test section. For comparisons with the literature, a friction factor will be defined later.

Results and Discussion

Heat-(mass-)transfer results for uniform inlet flow. The results to be reported first are those corresponding to a uniformly distributed inlet flow. These results will be compared with appropriate heat-transfer results from the literature with a view both to confirming the validity of the heat- and mass-transfer analogy and to demonstrating the propriety of the experimental apparatus and technique. Subsequently, the uniform-inlet-velocity results will be used as a baseline for comparisons with the results for the maldistributed inlet flow.

Figure 4 shows a comparison of the present uniform-inlet-flow results with those of the literature, with the Sherwood number plotted as a function of the Reynolds number. Comparisons are made both for the first-row Sherwood numbers and for the fully developed Sherwood numbers (the fully developed regime will be elaborated upon shortly).

To represent the heat-transfer literature, the widely quoted tube-bank correlations of Grimison [9] and Zukauskas [12] will be used. Grimison's correlation is based on air data ($Pr = 0.7$), and it has become customary to scale his results to other Prandtl (or Schmidt) numbers by a $Pr^{1/3}$ (or $Sc^{1/3}$) factor (e.g., [10]). Thus, using equation (8), Grimison's Nusselt numbers were converted to Sherwood numbers by the relation $Sh = (2.5/0.7)^{1/3} Nu$. Both of the correlations are applicable to the fully developed regime, and for the thermal entrance region it is standard to use the Kays-Lo correction factors [11] (cited in all heat-transfer texts, e.g., [10]), as was done here. In addition, the stated range of the Grimison correlation is $Re > 2000$. Consequently, short dashed lines have been used in the plotting of his correlation for $Re < 2000$.

Examination of Fig.4 indicates that the present mass-transfer data are in excellent agreement with the heat transfer literature. Indeed, the deviations between the data and the correlating lines are much less than the scatter of the heat-transfer data on which the correlations are based. The remarkable agreement evidenced in Fig. 4 confirms both the heat-mass transfer analogy and the present experimental technique.

Attention is now turned to the row-by-row variation of the per-tube Sherwood number. This information is conveyed in Fig. 5 for the three Reynolds numbers for which nonuniform-inlet-flow results will be presented later. These Reynolds numbers are equally spaced logarithmically over an order of magnitude. The figure shows the expected increase of the Sherwood number in the initial rows, as the turbulence spawned by the tubes themselves enhances the mass (heat) transfer in downstream rows. However, a periodic fully developed regime soon sets in wherein the fluid flow about each tube is the same from row to row. As a consequence, the Sherwood number becomes a constant, independent of the row number.

For the higher Reynolds numbers, row-independent Sherwood numbers are in evidence in the third and subsequent rows, while for the lowest Reynolds number thermal development was achieved at the fourth row. These development lengths reflect the rapidity with which the velocity field attains its periodic fully developed regime. The horizontal lines threaded through the fully developed data represent average values, respectively equal to $Sh = 28.8$, 58.3, and 118 for $Re = 850$, 2750, and 8400.

The final matter to be considered with respect to the uniform-inlet-flow experiments is the spanwise uniformity of the Sherwood numbers in any given row, and Table 1 has been prepared in this connection. The table shows the per-tube Sherwood numbers at each of the six tubes that are deployed across the span of the eighth row, respectively for $Re = 850$, 2750, and 8400. Relative to the respective averages, the data scatter by 1–2 percent, which is the estimated accuracy of the results. Furthermore, there is not a consistent pattern in the observed spanwise variations, which suggests that wall effects, if present, are very small. Within the scatter of the data, it is believed that the data can, for practical purposes, be regarded as spanwise uniform.

Heat-(mass-) transfer results for maldistributed inlet flow. As discussed earlier, the flow maldistribution studied here was created by a blockage which closed off half the inlet cross section, as illustrated in Fig. 2. The presence of the maldistribution destroyed the spanwise uniformity that had existed for the unblocked case, necessitating separate mass-transfer measurements for each tube in a given row. Such measurements were made for each tube in the first eight rows and for the tubes of the twelfth row, all for $Re = 850$, 2750, and 8400.

The results will be presented in a format which provides an immediate visual image of the effects of the maldistribution. To this end, the Nusselt (Sherwood) number at a given tube in the presence of the flow maldistribution is ratioed with the uniform-inlet-flow Nusselt (Sherwood) number at the same

Table 1 Spanwise Sherwood number distribution in the eighth row

	Spanwise position					
Re	1	2	3	4	5	6
850	28.7	28.5	29.0	28.8	29.0	28.2
2750	57.8	58.5	58.4	59.4	59.3	56.9
8400	117	119	118	118	119	118

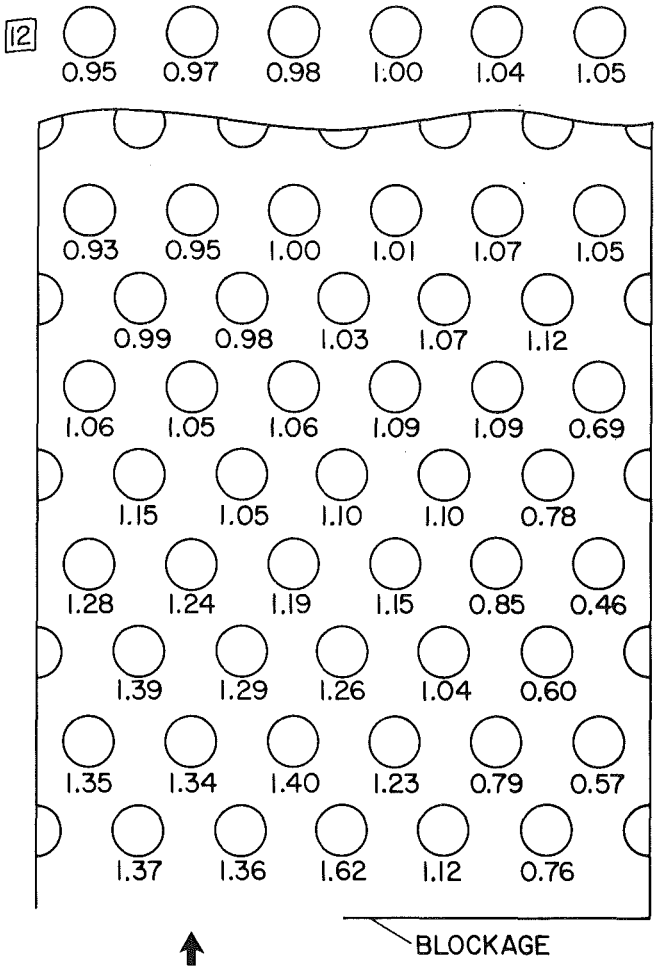

Fig. 7 Per-tube ratio of the maldistribution-affected Sherwood number to that for uniform inlet flow, Re = 2750

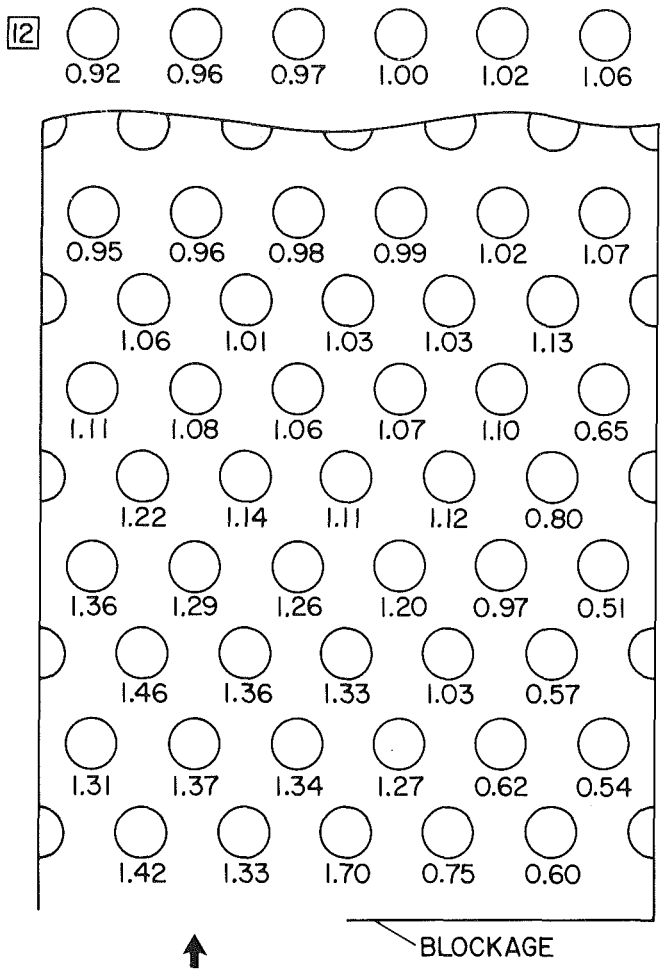

Fig. 8 Per-tube ratio of the maldistribution-affected Sherwood number to that for uniform inlet flow, Re = 8400

tube. These ratios have been recorded adjacent to each tube in a top-view layout of the array. The respective layouts for Re = 850, 2750, and 8400 are presented in Figs. 6–8. The blocked portion of the inlet cross section is also indicated in these diagrams.

In assessing the results of Figs. 6–8, it should be noted that a Nusselt number ratio in excess of one indicates a local enhancement – that is, higher per-tube heat transfer for the maldistributed flow than for the uniform inlet flow. Conversely, a ratio that is less than one indicates a maldistribution-related reduction in heat transfer at the tube in question.

From an overall examination of the figures, a number of common characteristics can be identified. First of all, it appears that ratios in excess of 1 are more in evidence than those below one so that, on the whole, the maldistribution tends to enhance the heat transfer at a given Reynolds number (the ramifications of this finding will be explored in the Concluding Remarks section of the paper). The most significant enhancements occur at tubes situated in the first several rows in the corridor downstream of the open portion of the inlet. However, enhancement also occurs at tubes that are adjacent to this corridor and which, geometrically speaking, are behind the blockage. Heat-transfer degradation (ie., ratios significantly lower than unity) is confined to a narrow alley that is behind the blockage and adjacent to the side wall of the duct. This alley terminates at the sixth row.

The greatest enhancement takes place at the tube situated in the middle of the first row. This tube, which is half shielded by the blockage, is washed by eddies which are generated by the sharp edge of the blockage plate. It is these eddies that are responsible for the high transfer coefficients. Aside form the 60–80 percent enhancement at the first-row middle tube, the highest enhancements, those in the inlet corridor, are in the 30–40 percent range. The greatest reduction, about 50 percent, consistently occurs at the wall-adjacent tube in the fourth row (not in the behind-the-blockage corner region, as might have been expected).

The relatively high heat-transfer coefficients that are in evidence in the inlet corridor are caused by the high velocities which result from the channeling of the flow by the blockage. Owing to the inability of the flow to turn sharply as it passes the blockage plate, there is a separated region behind the blockage which is responsible for the zone of relatively low coefficients.

With increasing downstream distance, the heat-transfer coefficients generally tend toward their values for the uniform-inlet-flow situation, as witnessed by the proliferation of ratios in the neighborhood of unity. However, in the downstream rows (i.e., rows seven and eight), a modest spanwise nonuniformity emerges whose cross-sectional variation is opposite to that of the spanwise nonuniformity which prevails in the upstream rows. Specifically, lower coefficients occur in the unblocked corridor and higher coefficients occur behind the blockage. (This finding, initially unexpected, provided the impetus for the spanwise exploration reported in Table 1 for the case of the uniform inlet flow.)

The aforementioned reversal in the trend of the spanwise variation reflects the tendency of the fluid to move trans-

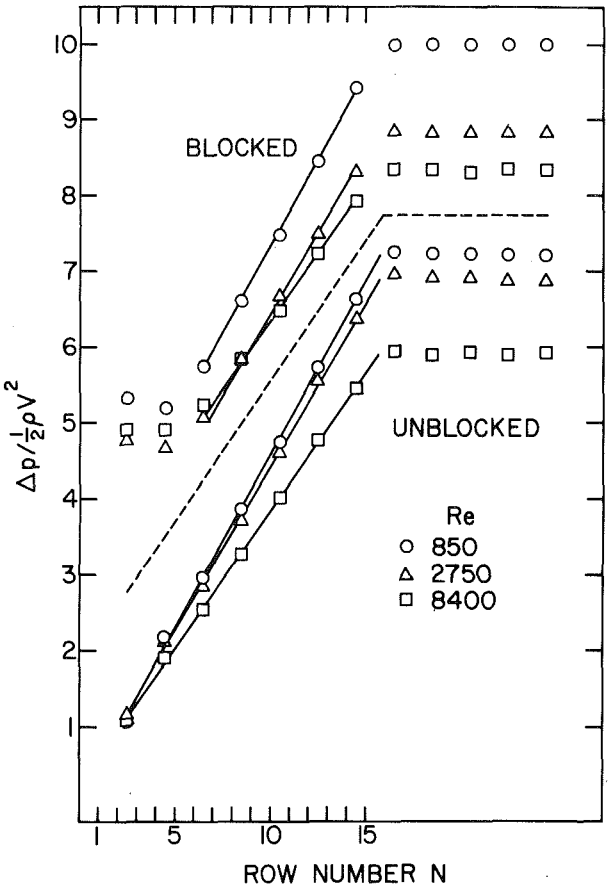

Fig. 9 Distributions of pressure along the tube bank

versely from the inlet corridor into the downstream portion of the region behind the blockage. This transverse flow creates a modest downstream maldistribution which has a high-to-low velocity variation that is opposite to that at the inlet. The data for the twelfth row indicate that this secondary maldistribution is beginning to wane for the lower Reynolds numbers, as evidenced by the approach toward more uniform values of the heat-transfer coefficient. At the highest Reynolds number, the secondary maldistribution has not yet begun to abate.

The foregoing discussion naturally leads to a consideration of the number of rows of the heat exchanger that are affected by the presence of flow maldistribution at the inlet. If the threshold of significant maldistribution-related effects is defined as a ten percent change in the heat-transfer coefficient, then the influence of the maldistribution is seen to extend through the first seven rows of the heat exchanger. Lesser effects, at the 5 percent level, persist at least as far as the twelfth row.

Although the results for the various Reynolds numbers display common trends, there are differences in detail. One of these is the slower development and subsequent slower disappearance of the aforementioned secondary maldistribution at higher Reynolds numbers. In addition, at lower Reynolds numbers, there is an overall trend toward lesser reductions in the heat-transfer coefficient in the wall-adjacent region behind the blockage.

If per-row average values are calculated from the ratios displayed in Figs. 6–8, it is found that for all rows (except for a few 0.98–0.99 values for downstream rows), the row-average coefficient for the maldistributed flow exceeds that for the uniform flow. This finding offers quantitative testimony of the enhancing effect of the maldistribution on heat transfer (at a fixed Reynolds number). The first-row average is the highest among the various row averages for each Reynolds number, respectively equal to 1.30, 1.25, and 1.16 for Re = 850, 2750, and 8400. The percentagewise greater enhancement for the lower Reynolds number is not unexpected.

Pressure drop and friction factor. A knowledge of the pressure drop is a necessary input for heat-exchanger design and is of particular interest when the flow is maldistributed. The present approach to the determination of the pressure drop is much more detailed than that commonly employed for heat exchangers. In the conventional approach, the overall pressure drop is measured by taps situated fore and aft of the exchanger, and entrance and exit losses are calculated and subtracted away in order to obtain the pressure loss in the exchanger proper. In the present experiments, the pressure distribution within the heat exchanger is measured, and no corrections need be made.

The pressure distribution along the tube bank, plotted as $\Delta p/\frac{1}{2}\rho V^2$, is presented in Fig. 9, where $\Delta p = (p_\infty - p(x))$, and the velocity head $\frac{1}{2}\rho V^2$ is evaluated as indicated immediately following equation (10); p_∞ is the pressure upstream of the test section. The data for the unblocked-inlet case are shown in the lower part of the figure, while those for the maldistributed inlet flow are plotted in the upper part of the figure. For each flow configuration, data are presented for Re = 850, 2750, and 8400.

Attention may first be focused on the results for the unblocked inlet. As seen in the figure, the pressure distribution in the array is linear for all of the Reynolds numbers investigated (the flat portion of the distribution which follows the linear portion corresponds to the open duct downstream of the array). The linearity of the pressure distribution shows that fully developed conditions are established very near the inlet of the array. The fact that $\Delta p/\frac{1}{2}\rho V^2$ depends on the Reynolds number indicates that inertial losses, for which $\Delta p \sim \frac{1}{2}\rho V^2$, are not the sole contributor to the pressure drop, so that skin friction must also play a role.

To compare the present results with the literature, friction factors were evaluated from

$$f = (-dp/dN)/\tfrac{1}{2}\rho V^2 \tag{11}$$

where dp/dN, the pressure drop per row, is the slope of the least-squares straight line passed through the data. These friction factors are compared with those of Zukauskas [12] in Table 2 (only two significant figures could be read from the graphical presentation of [12]). The agreement evidenced by Table 2 is remarkable, especially in view of the aforementioned differences in the experimental techniques employed.

Table 2 Comparison of friction factors

	f	
Re	Present	[12]
850	0.456	0.48
2750	0.433	0.42
8400	0.362	0.36

Turning next to the blockage case, Fig. 9 shows that the presence of the maldistribution is felt up to about the sixth row. A modest pressure recovery is experienced by the flow after passing the blockage plate, as reflected by the negative slopes of the initial data points. Beyond the sixth row, a linear pressure variation is established. To examine this linear region, the slopes for the unblocked case have been transposed to the blocked case, and a good fit is found to prevail. This means that the fully developed friction factors for the blocked case are the same as those for the unblocked case listed in Table 2. However, it is evident from Fig. 9 that a

knowledge of the fully developed friction factor is not sufficient to describe the overall pressure drop for the blocked case. Rather, account must be taken of the maldistribution-related incremental pressure drop. This incremental pressure drop is, in effect, an inlet loss. When the fully developed regime is attained (downstream of the sixth row), the incremental pressure drop is about 2½ velocity heads at all three Reynolds numbers investigated.

Concluding Remarks

The work reported here is, seemingly, the first systematic experimental study of the effect of inlet-section flow maldistribution on the heat-transfer and pressure-drop characteristics of a heat exchanger. The maldistribution was created by a partial blockage of the inlet cross section. An inlet-section blockage of 50 percent was used in the experiments, giving rise to severe channeling of the airflow entering the heat exchanger. As noted in the Introduction, a myriad of specific maldistributions are encountered in practice, and it cannot be expected that the results for the type of maldistribution investigated here will be universally applicable. This suggests the need to study the effects of other generic types of maldistributions. The present results do, however, provide insights into effects of maldistribution that were heretofore unknown.

One finding of particular interest is that for a given Reynolds number (i.e., given rate of mass flow through the heat exchanger), maldistribution can lead to an overall enhancement of the heat transfer. On the other hand, as documented in the presentation of results, the maldistributed flow suffers a higher pressure drop at the given Reynolds number. Whether or not these characteristics lead to a *net* enhancement or degradation of heat exchanger performance depends on the conditions under which the system is to be operated. For example, in certain instances, the pressure drop may not be a critical factor or, in other instances, the heat-exchanger-related pressure drop is a small part of the overall system pressure drop. In such cases, it would appear that if the Reynolds number can be maintained despite the higher pressure drop, the overall heat-transfer capability of the exchanger may be greater for a maldistributed flow than for a uniformly entering flow.

If, on the other hand, the higher pressure drop associated with the maldistributed flow requires a reduction in the rate of airflow, the heat-transfer capabilities may be degraded. In general, a definitive judgment about the net effect of maldistribution depends on the conditions under which the two types of flow (i.e., maldistributed and uniform) are compared. Such conditions may include fixed pumping power, fixed pressure drop, fixed heat duty, fixed blower curve, etc. In light of the foregoing, one of the important outcomes of the present research is that a snap judgment should not be made that maldistribution always degrades the performance of a heat exchanger.

One of the features of the present experiments is that only one of the cylinders in the array participated in the heat (mass) transfer process. It is relevant to consider how the heat-transfer coefficients obtained from such a one-at-a-time heating condition compare with those for the case where all cylinders are heated. If there is thorough mixing of the fluid between rows such that the fluid temperature becomes homogenized, the coefficients for the all-cylinders-heated case will be essentially identical to those for the one-at-a-time heating condition. The comparison of the present no-blockage fully developed coefficients with all-cylinders-heated literature information (Fig. 4) affirms this assertion. It is the belief of the authors that the results presented here do not significantly differ from those for the all-cylinders-heated case.

Acknowledgment

This research was performed under the auspices of the Power Program of the Office of Naval Research.

References

1 London, A. L., "Compact Heat Exchangers—Design Methods," in *Low Reynolds Number Flow Heat Exchangers*, Hemisphere Publishing Corporation, Washington, D.C., 1982.

2 Mueller, A. C., "Shell and Tube Exchanger Design," in *Low Reynolds Number Flow Heat Exchangers*, Hemisphere Publishing Corporation, Washington, D.C., 1982.

3 Chiou, J. P., "Thermal Performance Deterioration in Crossflow Heat Exchanger Due to the Flow Nonuniformity," ASME JOURNAL OF HEAT TRANSFER, Vol. 100, 1978, pp. 580–587.

4 Mueller, A. C., "An Inquiry of Selected Topics on Heat Exchanger Design," *Donald Q. Kern Award Lecture, 16th National Heat Transfer* Conference, August, 1976.

5 Dobryakov, B. A., "The Calculation of Heat Exchanger Equipment With Crossflow of the Heat Transfer Agents," *International Chemical Engineering*, Vol. 13, 1973, pp. 81–84.

6 Kutchey, J. A., and Julien, H. L., "The Measured Influence of Flow Distribution on Regenerator Performance," *SAE Transactions*, Vol. 83, Paper No. 740164, 1974.

7 Sogin, H. H., "Sublimation from Disks to Air Streams Flowing Normal to Their Surfaces," Trans. ASME, Vol. 80, 1958, pp. 61–69.

8 Eckert, E. R. G., "Analogies to Heat Transfer Processes," in *Measurements in Heat Transfer*, edited by E. R. G. Eckert and R. J. Goldstein, Hemisphere Publishing Corporation, Washington, D.C., 1976, pp. 397–423.

9 Grimison, E. D., "Correlation and Utilization of New Data on Flow Resistance and Heat Transfer for Cross Flow of Gases Over Tube Banks," *Trans. ASME*, Vol. 59, 1937, pp. 583–594.

10 Incropera, F. P., and Dewitt, D. P., *Fundamentals of Heat Transfer*, Wiley, New York, 1981, p. 355.

11 Kays, W. M., and Lo, R. K., "Basic Heat Transfer and Flow Friction Data for Gas Flow Normal to Banks of Staggered Tubes," Stanford University Technical Report No. 15, 1952.

12 Zukauskas, A. A., "Heat Transfer From Tubes in Crossflow," in *Advances in Heat Transfer*, Vol. 8, Academic Press, New York, 1972, pp. 154–155.

Developing Heat Transfer in Rectangular Ducts With Staggered Arrays of Short Pin Fins

D. E. Metzger
Professor.
Mem. ASME

R. A. Berry
Graduate Student.

J. P. Bronson
Graduate Student.

Mechanical and Aerospace Engineering Department,
Arizona State University,
Tempe, Ariz. 85287

Streamwise heat transfer variation, overall array heat transfer, and overall flow friction behavior are presented for large aspect ratio ducts containing uniformly spaced staggered arrays of circular pin fins which span the entire duct height. The array geometries investigated have short pin heights (length-to-diameter ratio of 1) and moderate spanwise (transverse) and streamwise (longitudinal) pin spacings (pitch-to-diameter ratios of 1.5 and 2.5). Such staggered array geometries are typical of applications found in internally cooled gas turbine engine airfoils. The uncovered duct walls comprise a substantial fraction of the total heat transfer area. Ten pin rows in the streamwise direction are utilized in all the experiments, with a segmented construction allowing determination of spanwise-averaged heat transfer coefficients resolved to a single row spacing in the streamwise direction. Comparisons are made with results of prior studies which are mainly restricted to flow normal to banks of circular cylinders with long length-to-diameter ratios.

Introduction

Heat transfer associated with flow normal to arrays of circular cylinders has been the subject of extensive investigation in the past because of its importance in a wide variety of heat exchanger applications. Much of the prior work is restricted to flow normal to banks of cylindrical tubes where the tube length-to-diameter ratio is very large. In such cases virtually all of the heat transfer area is on the cylindrical surfaces of the tubes themselves. The heat transfer rates on the bounding duct walls (end walls) and the end-wall effects on the tube surface heat transfer adjacent to the walls are unimportant. The very early experimental work for this long tube array case is represented by that of Jacob [1] and Grimison [2]. Much of the work up to 1972 is summarized in a review article by Zukauskas [3]. Heat transfer coefficients in the long tube arrays are observed to increase in the streamwise (longitudinal) direction through the third to fifth row and to remain constant thereafter.

Another extensive group of prior work is concerned with compact heat exchangers of the plate fin type, where flow normal to tube arrays is constrained between closely spaced thin plates attached to the tubes. A recent review of this literature has been given by Webb [4]. The tube lengths exposed between adjacent plates are generally from one-tenth to one-half the tube diameter. As opposed to the unfinned long tube arrays, most of the heat transfer area is on the plates, rather than on the tubes themselves. Rich [5, 6] reported overall average heat transfer and friction characteristics for arrays containing from one to six streamwise tube rows. Overall average heat coefficients were found to be insensitive to plate spacing and lower than those reported for long cylinder arrays. For a four row array with exposed tube length equal to 0.132 D, heat transfer coefficients decreased in the streamwise direction at low Reynolds numbers and increased in the streamwise direction at higher Reynolds numbers. Saboya and Sparrow [7, 8] present more detailed studies of the local heat transfer coefficient variations for exposed tube lengths equal to 0.193 D, but their work is confined to only two streamwise rows of tubes.

In recent years, arrays of intermediate length circular cylinders have been utilized extensively in internally cooled gas turbine engine airfoils. The cooled passage height inside the airfoil is small; manufacturing constraints dictate a pin length of the order of one diameter. In these applications, a significant fraction of the total heat transfer area still is composed of the end-wall area. Theoclitus [9] measured array average heat transfer and flow friction characteristics for pin-fin arrays with length-to-diameter ratios from 12 down to as short as 4. In general the average heat transfer rates reported are all lower than those expected for long cylinder arrays and are slightly lower for short pins ($H/D = 4$) than for long ($H/D = 12$). Damerow et al., [10] covers arrays in the range $2 \leq H/D \leq 4$, but the results are restricted to flow characteristics only. No consistent effect of H/D on flow friction was observed in either [9] or [10].

A recent study by VanFossen [11] presents heat transfer results for several staggered configurations of $H/D = 0.5$ and 2.0 pin arrays similar to those used in the present study. All arrays in [11] consist of four rows of pins in the streamwise direction, and only heat transfer rates averaged over the entire four row array were determined. Brown et al., [12] has presented heat transfer results for array configurations which model quite specifically an application to the trailing edge internal cooling of turbine airfoils. In this study, the cooled channel converges, and each pin row in the streamwise direction has a different length-to-diameter ratio as well as a different mass flux. Even though heat transfer is resolved to individual rows, the large number of parameters involved, coupled with relatively high experimental uncertainties, make the results difficult to generally interpret. Sparrow et al., [13, 14], present performance on a row-by-row basis for short pins, but only the pin surface transfer rates were determined and the pins did not extend across the entire duct height.

The present study was initiated with the objective of investigating the character of the streamwise row-by-row variation of heat transfer in a constant cross sectional area duct with uniform full span short pin arrays. Ten spanwise (transverse) rows of pins in the flow direction were used in all tests with the intent of establishing both the trend and magnitude of the streamwise development of heat transfer.

Experimental Apparatus and Procedures

Figure 1 shows schematically the test section arrangement. Each test geometry consists of individual pin row segments and complementary guard, insulating, and duct segments.

Contributed by the Heat Transfer Division and presented at the ASME Winter Annual Meeting, Washington, D.C., November 15–20, 1981. Manuscript received by the Heat Transfer Division September 29, 1981. Paper No. 81-WA/HT-6.

The segments are stacked together in a support and alignment fixture to form the ten row array as indicated in the figure. Two staggered array geometries were fabricated and tested: $S/D = 2.5$, $X/D = 2.5$, $H/D = 1.0$, and $S/D = 2.5$, $X/D = 1.5$, $H/D = 1.0$. Pin diameters were uniform for each ten row array at 0.508 cm for the $X/D = 2.5$ case and 0.846 cm for the $X/D = 1.5$ case.

Each separate segment consists, as depicted in Fig. 2, of an upper and lower copper bar with one row of pins connected by means of an interference fit. The copper bars are 0.635-cm thick in the pedestal axis direction which provides excellent spanwise temperature uniformity over the test conditions used. Preliminary testing was done early in the apparatus design phase with two sample segments; one fabricated with interference fit, the other with brazed attachment of the pins. In both cases the mating holes were drilled entirely through the bars to maximize the contact area. These preliminary tests indicated that the contact conductance between pin and end-wall was more consistent pin-to-pin with the interference fit fabrication. The relatively poorer performance of the brazed assembly could probably have been improved upon; but since the interference fit contact was adequate and produced a cleaner element, it was selected. Assembly of the pins in the segments was carried out with precision jigs machined for the purpose with heat applied to the end-wall pieces and precooling of the pins to reduce the interference during assembly.

The side walls of the channel are formed by basswood blocks bonded with epoxy to the copper bars to reduce conduction losses through the ends of the bars. Acrylic plastic inserts are used to provide an erosion resistant material in contact with the flow and to provide a means for locating a clean, small diameter (0.16-cm) hole at the side wall for pressure measurements.

The basswood side walls are in turn bonded to aluminum blocks at the outboard ends. The purpose of these outer parts of the segments is to provide an accurately machinable and wear-resistant surface for precisely stacking the individual segments together into a multirow array. The lower, or reference, side of each aluminum piece rests on a rail in the support and alignment fixture when the array is assembled. The reference surfaces were finish-machined after complete segment assembly with their positions carefully controlled ($\pm$ 0.0013 cm for $X/D = 2.5$, $\pm$ 0.0025 cm for $X/D = 1.5$) with respect to the position of the flow sides of the upper and lower bars. The resulting assembled duct has very smooth inside walls regardless of inaccuracies in original machining or bonding.

The upper and lower copper bars of each segment are heated individually through the use of commercially available foil heaters bonded to their outer surfaces. Each of the

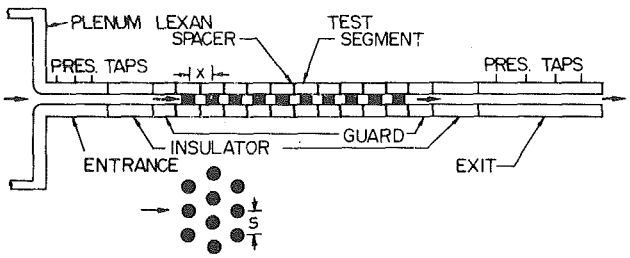

Fig. 1 Test section arrangement

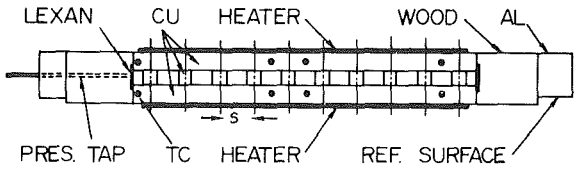

Fig. 2 Individual segment details

twenty-four heaters (including guard segments) are individually controlled with autotransformers. The upstream and downstream guard segments are identical to the pin segments in construction details, except for the absence of pins. Additional basswood segments are installed upstream and downstream of the guard segments to further reduce heat conduction from the test section to the aluminum entrance and exit sections. The entrance and exit sections extend the test section duct height (H) and width (12.7 cm) an additional 12.7 cm upstream and 7.62 cm downstream. Not shown for reasons of clarity in Fig. 1 is the approximately 10-cm thick balsa insulation placed around the segments to reduce heat loss to the laboratory.

Except for duct height and pin diameter, the construction details and dimensions of both the $X/D = 1.5$ assembly and the $X/D = 2.5$ assembly are identical. The necessity of good thermal contact between pin and endwall precluded an adjustable or interchangeable design. All twelve heated segments with associated duct pieces of the $X/D = 1.5$ configuration were duplicated for the $X/D = 2.5$ configuration.

Each of the test segments is separated from adjacent segments by low conductivity 0.079-cm thick plastic spacers. The copper test segments are each 0.079 cm less than 1.27-cm wide in the streamwise direction so that the pin rows have 1.27-cm center-to-center spacing in this direction. This is the case for both the $X/D = 1.5$ and 2.5 configurations. These spacers are fabricated in one piece using special jigs designed for the purpose so that channel height accuracy consistent with the segments themselves is achieved. These plastic spacers are bonded to the downstream side of each segment,

Nomenclature

A = heat transfer area
c_p = fluid constant pressure specific heat
D = pin diameter
f = friction coefficient, $= \Delta P/(2\rho V_{\max}^2 N)$
h = convective heat transfer coefficient, see equation (1)
H = pin height, channel height
$\dot{m}$ = mass flow rate
N = number of pin rows in streamwise direction
Nu = segment Nusselt number, hD/k
$\overline{\text{Nu}}$ = average array Nusselt number over all ten pin rows
$\overline{\text{Nu}}_{1-4}$ = average Nusselt number over first four pin rows
p = pressure
Δp = pressure drop across array
Pr = Prandtl number
$\dot{q}$ = convective heat transfer rate
Re = local Reynolds number, see equation (3)
$\overline{\text{Re}}$ = average of local segment Reynolds numbers
S = pin spacing in spanwise direction
t_b = bulk temperature, see equation (2)
t_{ref} = reference temperature
t_s = heat transfer surface temperature
t_z = zero heat flux surface temperature
$V_{\max}$ = velocity in the minimum free flow area
X = pin spacing in streamwise direction
μ = fluid dynamic viscosity
ρ = fluid density

again using a separate special jig to insure accurate alignment and avoidance of transverse ribs or depressions at the spacer location in the assembled array.

Typical thermocouple placements are also indicated in Fig. 2. Most segments have four thermocouples placed as shown to provide redundancy in the event of failure. Some of the segments have additional thermocouples placed near the outboard edges of the copper pieces to verify the spanwise temperature uniformity. All thermocouples are copper-constantan with insulation left intact down to the welded bead. Beads were located at the center of the copper bar cross section and are held in place with either solder ($X/D = 2.5$) or epoxy ($X/D = 1.5$). Figure 2 also indicates the position of 0-ring grooves which are machined into the upstream face of each assembled segment. After stacking of all segments together on the supporting structure, the 0-rings are compressed in the streamwise direction until the plastic spacers contact the adjacent segments. This seals the flow channel against air leakage in all directions.

A rectangular cross-section plenum chamber containing screens to settle the flow is located upstream of the entrance duct. Pressure taps are located in the plenum, and in the entrance and exit ducts in both the streamwise direction and across the duct span. These pressure lines as well as lines from the side wall taps in the segments are routed through a motor-stepped scanning valve to common water or mercury manometers.

Acquisition of thermocouple and heater power information is accomplished with a digital data logger used in conjunction with a CRT display to assist in setting desired temperature boundary conditions on the test segments. Heating element resistance is a function of heater temperature, and heater power is accurately determined by measuring both the voltage drop across and current through the individual heaters. A rotary stepping switch is used to sequentially switch the individual heater circuits into a measuring configuration where the voltage drop across a calibrated 0.01 percent resistor is used to determine the heater current. Heater current and voltage measurements are conditioned by a solid state a-c/d-c converter.

Air supply is provided by either of two available laboratory supplies, depending on the flow rate required. Both compressor installations are provided with dryers and filters, and flows are measured with orifice installations constructed to ASME standards. Further details of the apparatus construction are available in [15].

All testing is carried out at steady-state conditions and utilizes the segment temperatures and heater power measurements to determine the average convective heat transfer rate for each of the ten pin/end-wall segments. In all cases an isothermal wall boundary condition is used where the individual heaters are adjusted to equalize all the segment temperatures. In a typical test, steady isothermal conditions are achieved on all segments, including the guards, to within $\pm$ 0.1° C.

For a given flow rate and array configuration, two different power levels are used, corresponding to segment temperatures approximately 6° C and 12° C above the duct flow bulk temperature. In a few cases a third power level resulting in temperature differences of approximately 25° C was used as an additional check. For each segment, the heat transfer coefficient is defined in terms of the convected portion of the supplied heater powers and the difference between the segment temperature and an appropriate reference temperature:

$$h = \frac{\dot{q}/A}{(t_s - t_{\text{ref}})} \tag{1}$$

The heat transfer coefficients are determined as the slope of a least-squares linear fit to the data obtained from the two power level runs. For each power level, $\dot{q}$ is the sum of both top and bottom segment heater powers, corrected for conduction losses from the back and ends of the segments and for intersegment conduction across the insulating spacers. Separate auxiliary experiments have been conducted to determine both of these correction terms, and they are both generally small. The close segment-to-segment temperature uniformity maintained in the tests insures a negligible intersegment conduction correction. The backside and end loss ranges from less than 1 percent of the heater power input (at high flow rates) to 6 percent (at the lowest flow rates.) For all of the results reported here the heat transfer area, A, is the actual copper surface area (pin + end wall) exposed to the flow.

The appropriate fluid reference temperature used in all the present results is the streamwise local bulk average temperature which takes into account heat addition to the flow at upstream segments. This deserves special mention here since the relatively small temperature differences used as driving potentials require that care be taken to establish a proper reference temperature.

The local bulk average temperature, t_b, as a function of streamwise position in the array is determined in the present experiments from an energy balance. In the absence of kinetic and dissipative effects, t_b at a given duct location is equal to the duct inlet temperature plus the rise caused by upstream heat addition. However, flow velocities in the present tests, especially at high Reynolds numbers, are high enough to cause variations in t_b in the streamwise direction even in the absence of surface heat transfer. The bulk temperature tends to decrease in the flow direction because of these effects, but this component of the t_b change is independently measurable in the present tests. To measure this component a separate test run was conducted without heater power for each flow condition. Without power applied to the heaters, the individual segments come to thermal equilibrium with the flow at that location and thus the segment temperatures at this condition, $t_{z,i}$, are a measure of the local bulk temperature variation.

The bulk temperature for use with the *ith* segment temperatures for the heated runs is calculated as the sum of this effect and the upstream heat addition:

$$t_{b,i} = t_{z,i} + \sum_{j=i}^{i-1} \frac{\dot{q}_j}{\dot{m} c_p} \tag{2}$$

Over the time period required to obtain the three sets of steady-state temperatures and heater powers there is usually a slight drift in the supply plenum temperature associated with changes in outside air temperature. Compensation is made by adjusting all zero power temperatures to match the plenum temperature present during the heated run.

Fluid properties are evaluated locally at the arithmetic average of the segment and bulk temperatures. For the small temperature differences used, these property variations are small: differences in Reynolds number through the array are typically less than 0.5 percent, and Reynolds number variations between two heated runs are typically less than 2 percent. Reynolds numbers used in the presentation of results are the average of the local values of both heated runs. All Reynolds numbers are based on pin diameter and velocities calculated using the minimum flow area

$$\text{Re} = \rho V_{\max} D/\mu \tag{3}$$

Results

Extraordinary care was exercised during the fabrication of the individual segments to insure attainment of smooth duct walls in the assembled array. Nevertheless, small but inevitable differences between segments imply some

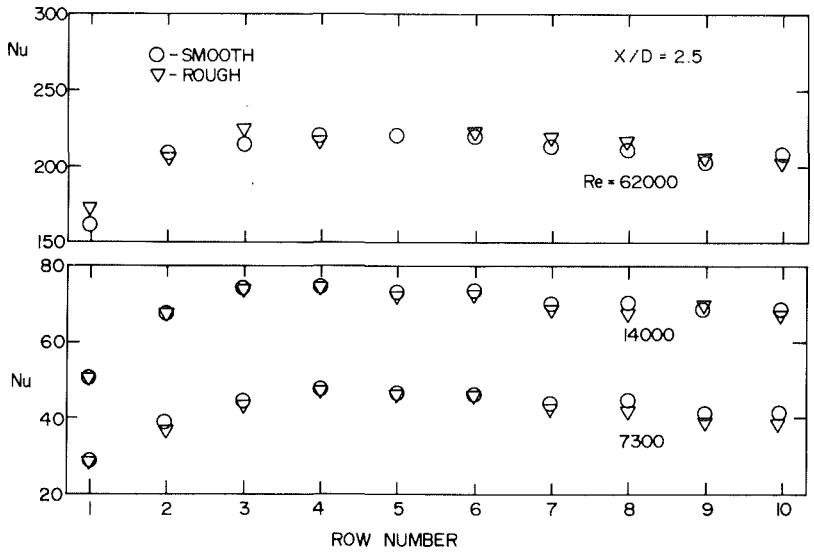

Fig. 3 Comparison of results for two stacking orders

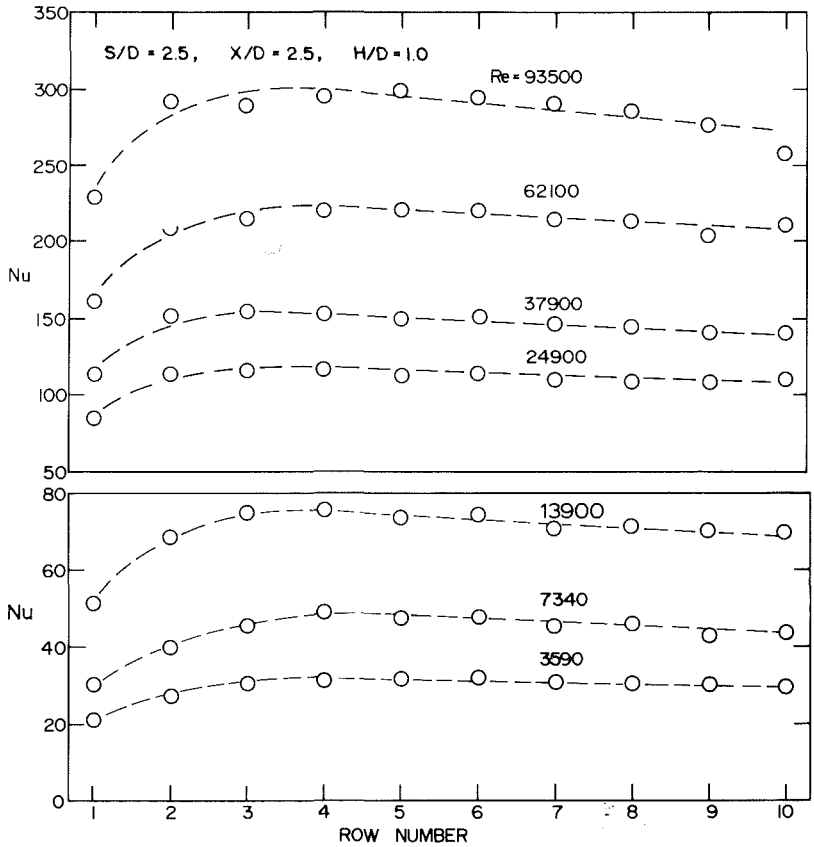

Fig. 4 Nu development for $S/D = 2.5$, $X/D = 2.5$

assembled duct roughness, depending on the order of stacking of the segments. In all cases this roughness is very slight (0.002 cm or less), but careful measurements were made and recorded when the element reference surfaces were machined so that the stacking could be ordered to produce a minimum roughness channel.

It was thought desirable to repeat some tests with different stacking orders as assurance that determination of the streamwise heat transfer variation of interest does not reflect consistent errors coupled to the particular segment order used. For this reason two test series were made with the $X/D = 2.5$ configuration, one where the segments were stacked to give the channel with the minimum possible roughness, and a second series with stacking to give a channel with the maximum possible roughness.

Figure 3 presents a comparison of the minimum and maximum roughness results for three cases which have nearly identical values of Re. The correspondence between the two sets is quite good, and no consistent effect of roughness is apparent. Experimental uncertainties for Nu and Re are estimated to be ± 5 and ± 0.2 percent respectively, based on the methods of Kline and McClintock [12]. The good agreement is expected because both assemblies are actually quite smooth. Aside from the question of roughness, the

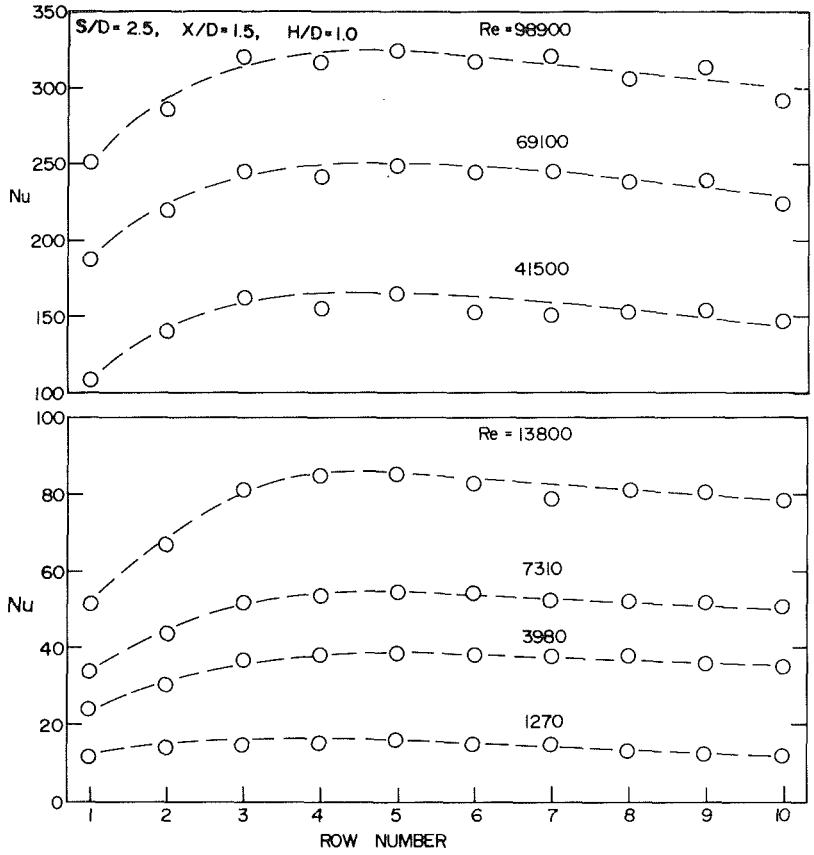

Fig. 5 Nu development for $S/D = 2.5$, $X/D = 1.5$

agreement displayed in Fig. 3 provides confidence in the apparatus.

Figure 4 displays the segment Nusselt number results for the $X/D = 2.5$ array for seven values of $\overline{\text{Re}}$ from 3.59×10^3 to 9.35×10^4. Figure 5 presents similar results for the $X/D = 1.5$ array from $\overline{\text{Re}} = 1.27 \times 10^3$ to 98.9×10^4. In all cases the trend in variation of Nu with position in the array in terms of pin row number is indicated with a dashed line which has been sketched to aid in visualizing the results. The general trend of all these results is an initial rise in Nu encompassing the first three to five rows followed by a subsequent gradual decline in Nu through the remainder of the array.

The first row values from each Reynolds number set for both arrays are shown together on Fig. 6. Agreement is within experimental uncertainty, which lends further credence to the adequacy of the experimental methods and data reduction procedures. The results, which are a combination of both end wall and pin heat transfer, are significantly below the corresponding long cylinder [3] values over most of the Reynolds number range of interest. Like the long cylinder case, the present results exhibit a greater dependence on Reynolds number in the higher Reynolds number range. The results are well represented by two least squares fits

$$\text{Nu} = 0.140\ \text{Re}^{0.611} \quad \text{for } 10^3 \le \text{Re} \le 10^4 \tag{4}$$

and

$$\text{Nu} = 0.022\ \text{Re}^{0.813} \quad \text{for } 10^4 \le \text{Re} \le 10^5 \tag{5}$$

The rise in Nu through subsequent downstream rows is in keeping with trends observed in the previous long cylinder bank cases. No evidence of the contrary trends reported in [6] for $H/D = 0.132$ is seen. Zukauskas [3] reports increases in inner row heat transfer in tube banks of 30 to 70 percent over that of the initial row, with the higher increases associated with smaller X/D. Both of these observations are consistent with the present results.

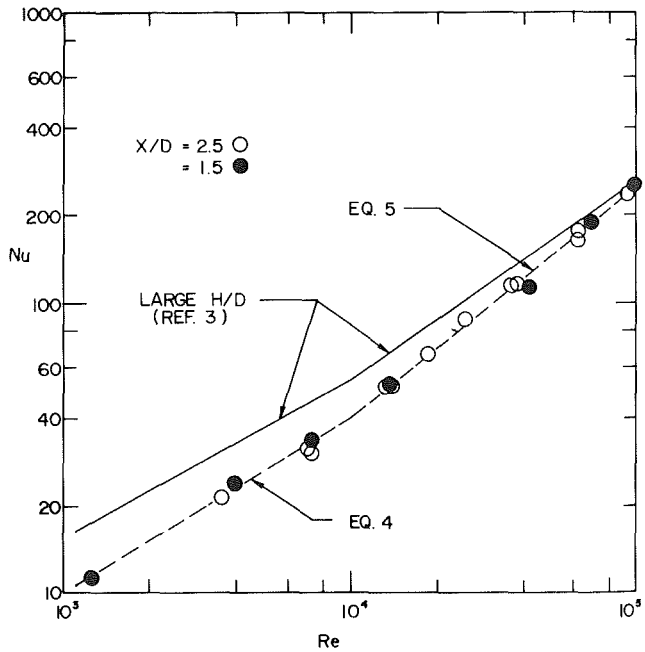

Fig. 6 Nu versus Re, first row

For the long cylinder tube bank case, the array entrance effects associated with the cylinder crossflow alone appear to establish an equilibrium condition at about the third row, and Nu values at subsequent rows remain essentially equal to those at the third row. The decrease in Nu for the downstream segments evident in the present results is different. On the average, the difference between the maximum row heat transfer and the last row heat transfer is approximately 12 percent.

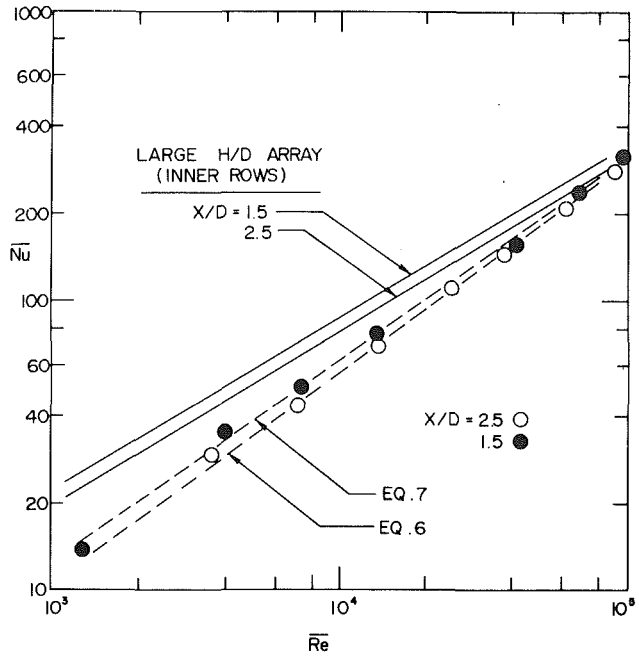

Fig. 7 $\overline{Nu}$ versus $\overline{Re}$

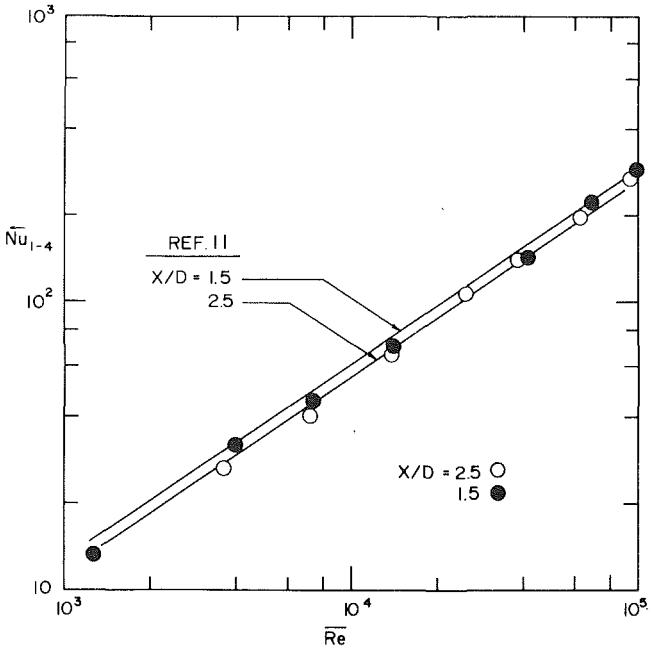

Fig. 8 Comparison of $\overline{Nu}_{1-4}$ with reference [11]

Figure 7 shows mean Nusselt numbers for the entire ten row array as functions of the mean Reynolds numbers. The dashed lines are least squares fits to the present experimental results

$$\overline{Nu} = 0.069\overline{Re}^{0.728} \text{ for } X/D = 2.5 \tag{6}$$

and

$$\overline{Nu} = 0.092\overline{Re}^{0.707} \text{ for } X/D = 1.5 \tag{7}$$

The solid lines are from the recommended correlations for inner rows of long cylinder arrays (evaluated at the present Pr = 0.72) given in [3] for $10^3 \leq \overline{Re} \leq 2 \times 10^5$, and $S/X < 2$

$$\overline{Nu} = 0.35(S/X)^{0.2}\overline{Re}^{0.6}Pr^{0.36} \tag{8}$$

For both the array configurations covered, the present results indicate lower heat transfer than that expected for long cylinders, although the difference is small at the upper end of the $\overline{Re}$ range. This is similar to the comparison for the first row only shown in Fig. 6. On the average, the present mean Nusselt numbers for $X/D = 1.5$ are 5–10 percent higher than those of $X/D = 2.5$. This difference is consistent with the S/X effect embodied in the long cylinder correlation, equation (8).

The $\overline{Re}$ dependence of the present results is somewhat greater than that of long cylinder arrays. This difference seems plausible since the heat transfer through unobstructed channels in turbulent flow is usually characterized by a 0.8 power dependence on the Reynolds numbers, as contrasted with the 0.6 power dependence for the cylinders (equation 8). In this connection it should be noted that the cylindrical heat transfer area on the pedestals comprises only 22 and 35 percent of the total heat transfer area in the $X/D = 2.5$ and $X/D = 1.5$ arrays, respectively.

The recent work of VanFossen [11] is the most appropriate reference for comparison of the present results. The average heat transfer performance over four rows of staggered pins was investigated for two short pin array geometries: half-diameter long pins set in an equilateral triangular array with spacing equal to two diameters, and pins two diameters long set in a similar triangular array at four diameter spacing. The present segment Nusselt numbers for the first four pin rows have been averaged and are presented in Fig. 8. The solid lines represent predictions of the four-row averages of the present

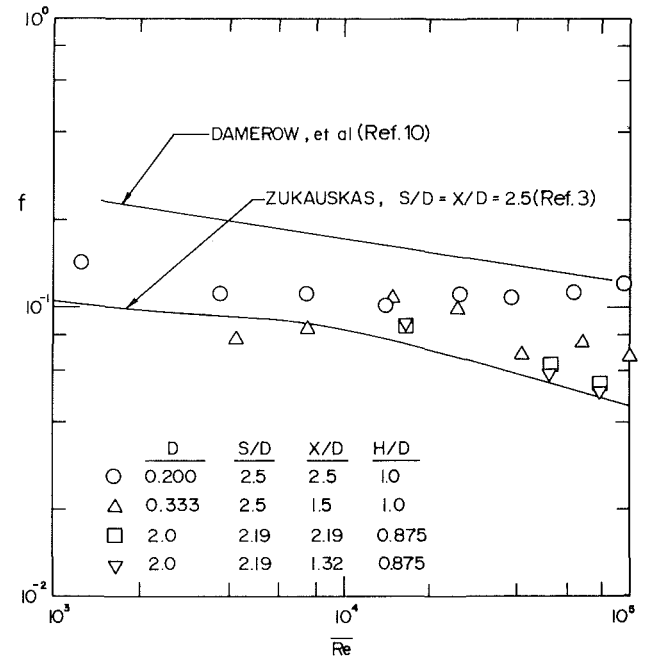

Fig. 9 Friction coefficient results

geometries based on the correlation given in [11]. The differences observed between the two present array configurations is not quite as large as predicted, and the present results generally fall slightly below the predictions. Nevertheless, the overall agreement is excellent.

Finally, Fig. 9 shows the corresponding overall friction coefficient results for the two nominal array geometries of this study. Measurements were made both on the segmented test section used for the heat transfer tests, and on a larger scale plastic test section mounted in a separate wind tunnel. Inadvertently, larger cylinders than desired were fabricated for use in the larger scale rig, so the nondimensional spacings are smaller than the corresponding heat transfer rig values, as listed on the figure. On both rigs, pressure taps in the entrance and exit sections upstream and downstream of the array were used to establish the overall pressure drop across the ten row arrays. The agreement between results from the two rigs is

reasonably good except at high Re; at the present time the latter discrepancy is unexplained. For comparison, Fig. 9 also shows the Zukauskas [3] recommendation for long cylinder arrays as well as that of Damerow et al. [10].

Summary and Conclusions

The streamwise development of heat transfer through regularly spaced staggered arrays of short pin fins has been determined for two ten-row arrangements over Reynolds numbers spanning approximately $10^3 - 10^5$. Nusselt numbers based on pin and end-wall areas taken together and averaged along the pin rows transverse to the mean flow direction are resolved to one pin row spacing. The results were obtained with small temperature differences and essentially constant property conditions. The principal conclusions are the following:

1 The general trend of streamwise development in both configurations at all Reynolds numbers is an initial rise in Nu encompassing the first three to five rows followed by a subsequent gradual decline in Nu through the remainder of the array.

2 The peak row heat transfer tends to occur earlier (third row) in the array with the larger streamwise pin spacing ($X/D = 2.5$) than in the case of smaller streamwise pin spacing (fifth row, $X/D = 1.5$).

3 Heat transfer in the first row of both arrays is found to be identical within experimental uncertainty, but the peak row heat transfer is higher for the arrangement with the smaller streamwise pin spacing. Average heat transfer over any number of pin rows is consequently higher for the smaller streamwise pin spacing.

4 Both first row heat transfer and average heat transfer over the entire array are lower than the corresponding long cylinder (tube bank) case. The differences are greatest at low Reynolds numbers.

5 Average Nusselt numbers encompassing the first four pin rows are in good agreement with the recent four row average measurements of [11].

Acknowledgment

This work was carried out as part of research sponsored by Pratt and Whitney Aircraft, East Hartford, Connecticut.

References

1 Jacob, M., "Heat Transfer and Flow Resistance in Crossflow of Gases Over Tube Banks," *Trans.* ASME, Vol. 60, 1938, pp. 384–386.

2 Grimison, E. D., "Correlation and Utilization of New Data on Flow Resistance and Heat Transfer for Crossflow of Gases over Tube Banks," *Trans.* ASME, Vol. 59, 1937, pp. 583–594.

3 Zukauskas, A., "Heat Transfer From Tubes in Crossflow," in *Advances in Heat Transfer*, Vol. 8, 1972, pp. 93–160.

4 Webb, R. L., "Air-Side Heat Transfer in Finned Tube Heat Exchangers," *Heat Transfer Engineering*, Vol. 1, 1980, pp. 33–49.

5 Rich, D. G., "The Effects of Fin Spacing on the Heat Transfer and Friction Performance of Multirow, Smooth Plate Fin-and-Tube Heat Transfer," *ASHRAE Trans.*, Vol. 79, pt. 2, 1973, pp. 137–145.

6 Rich, D. G., "The Effect of the Number of Tube Rows on Heat Transfer Performance of Smooth Plate-Fin-Tube Heat Exchangers," *ASHRAE Trans.*, Vol. 81, pt. 1, 1975, pp. 307–317.

7 Saboya, F. F. M., and Sparrow, E. M., "Local and Average Heat Transfer Coefficients for One-Row Plate Fin and Tube Heat Exchanger Configurations," ASME JOURNAL OF HEAT TRANSFER, Vol. 96, 1974, pp. 265–272.

8 Saboya, F. F. M., and Sparrow, E. M., "Transfer Characteristics of Two-Row Plate Fin and Tube Heat Exchanger Configurations," *International Journal of Heat and Mass Transfer*, Vol. 19, 1976, pp. 41–49.

9 Theoclitus, G., "Heat Transfer and Flow Friction Characteristics of Nine Pin-Fin Surfaces," ASME JOURNAL OF HEAT TRANSFER, 1966, pp. 385–390.

10 Damerow, W. P., Murtaugh, J. C., and Burggraf, F., "Experimental and Analytical Investigation of the Coolant Flow Characteristics in Cooled Turbine Airfoils," NASA CR-120883, 1972.

11 VanFossen, G. J., "Heat Transfer Coefficients for Staggered Arrays of Short Pin Fins," ASME Paper No. 81-GT-75, Mar. 1981.

12 Brown, A., Mandjikas, B., and Mudyiwa, J. M., "Blade Trailing Edge Heat Transfer," ASME Paper No. 80-GT-45, 1980.

13 Sparrow, E. M., and Ramsey, J. W., "Heat Transfer and Pressure Drop for a Staggered Wall-Attached Array of Cylinders with Tip Clearance," *International Journal of Heat and Mass Transfer*, 1978, pp. 1369–1377.

14 Sparrow, E. M., Ramsey, J. W., and Altemani, C. A. C., "Experiments on In-line Pin Fin Arrays and Performance Comparisons with Staggered Arrays," ASME JOURNAL OF HEAT TRANSFER, 1980, pp. 44–50.

15 Bronson, J. P., MS thesis, Arizona State University, Tempe, Arizona, 1979.

16 Kline, S. J., and McClintock, F. A., "Describing Uncertainties in Single Sample Experiments," *Mechanical Engineering*, Vol. 75, Jan. 1953.

Laminar and Turbulent Boundary Layers on Moving, Nonisothermal Continuous Flat Surfaces

A. Moutsoglou
Assoc. Mem. ASME

A. K. Bhattacharya

Department of Mechanical and Aerospace Engineering, University of Missouri-Rolla, Rolla, Mo. 65401

The heat-transfer characteristics of buoyancy-affected laminar and turbulent boundary layers on nonisothermal continuous flat surfaces that move steadily through a quiescent ambient fluid are studied analytically. Both cooling and heating of the continuous plate which is moving upward or downward in a horizontal, vertical, or inclined direction are considered. A mixing length model for the eddy diffusivities of momentum and heat based on an extension of the Van Driest model is employed in the turbulent boundary layers. Numerical results, such as wall shear stress, surface heat-transfer rate, and surface temperature variation, are presented for various Reynolds and Grashof numbers for fluids with a Prandtl number of 0.7, for both laminar and turbulent boundary layers. A good agreement is found between the analytical and experimental results for friction factor in turbulent boundary layer over an isothermal, continuous moving plate.

Introduction

Quite often there exist certain industrial processes involving continuous surfaces that move steadily through an otherwise quiescent ambient environment for which a correct assessment of the axial temperature variation of the material is of relevant importance. The heat treatment of materials traveling between a feed roll and a wind-up roll or on conveyor belts, the hot extrusion of steel, the lamination and melt-spinning processes in the extrusion of polymers, all possess the characteristics of moving continuous surfaces.

The pioneer work on boundary layers adjacent to moving, continuous surfaces was done by Sakiadis [1]. Of all the works that followed for flat surfaces, all but two were involved with laminar boundary layers. The effects of the buoyancy forces on such flows however were completely neglected with the exception of the relatively recent works of laminar flows over isothermal flat surfaces (see for example [2]). Also, most of the previous studies on boundary layers on such flows have treated the surfaces as either isothermal or having a prescribed uniform heat flux. Only Erickson et al. [3] and Barnett [4] have considered in their analyses the cooling of the surface. Of the two turbulent boundary layer studies, the first one by Sakiadis [1], was an analytical study derived by assuming a one-seventh power velocity profile. The analytical and experimental work of Tsou et al. [5] that followed utilized the law of the wall for the turbulent velocity field. In both studies, however, the effects of the buoyancy force on the momentum balance in the conservation equations were neglected.

In the present study, the effects of the thermal buoyancy force on the flow and heat-transfer characteristics are examined analytically for a cooled or heated continuous nonisothermal flat surface moving in an otherwise quiescent fluid. The plate is moving at a constant velocity in a vertical, inclined or horizontal direction, either upwards or downwards. The simultaneous effects of both components of the buoyancy force are taken into account. An extension of the mixing length model of Van Driest is used to approximate the turbulent eddy diffusivities. The steady, two-dimensional, boundary-layer equations, along with a differential equation for the surface temperature variation, are solved by an efficient finite-difference scheme developed by Keller and Cebeci [6]. Numerical results are obtained for air ($Pr = 0.7$) with Reynolds numbers based on the thickness of the plate, Re, ranging from 0.1 to 50 and buoyancy force parameters, Gr/Re^2, from -10^{-2} to 10^{-2} for angles of inclination γ of 0 (vertical), 45, and 90 deg (horizontal).

Analysis

Consider a continuous flat surface that originates from a slot and is moving upward or downward with a constant velocity, u_0, in an inclined direction through a quiescent ambient fluid. Any stretching of the plate and thus reduction in the thickness of the material is neglected in the analysis. The stationary coordinate frame is attached to the slot with the x-axis extending along the midplane of the plate in the direction of the motion of the plate, while the y-axes are measured from the top and bottom surfaces of the plate normal to each surface (see Fig. 7). The transverse coordinates, y, are taken to be positive in the outward direction toward the fluid for both flows above and below the plate. The sign of the gravitational force then corresponds properly to the assigned direction for y. The temperature of the plate at the slot ($x = 0$) is constant and equal to T_i, whereas the stationary ambient fluid is at a constant temperature, T_∞. The fluid properties are assumed to be constant except that the density variations within the fluid are allowed to induce buoyancy forces according to the Boussinesq approximation. In the analysis with relatively high plate velocities, the radiation from the plate is neglected. Also, any mass transfer in the process is not considered in this analysis. If the width of the plate is large compared to its thickness, the governing steady boundary layer equations are two-dimensional and can be written as

$$\frac{\partial u}{\partial x} + \frac{\partial v}{\partial y} = 0 \tag{1}$$

$$u\frac{\partial u}{\partial x} + v\frac{\partial u}{\partial y} = \pm g\beta\sin\gamma\frac{\partial}{\partial x}\int_y^\infty (T - T_\infty)dy \pm g\beta\cos\gamma(T - T_\infty) + \frac{\partial}{\partial y}\left[(\nu + \epsilon_m)\frac{\partial u}{\partial y}\right] \tag{2}$$

$$u\frac{\partial T}{\partial x} + v\frac{\partial T}{\partial y} = \frac{\partial}{\partial y}\left[(\alpha + \epsilon_h)\frac{\partial T}{\partial y}\right] \tag{3}$$

Contributed by the Heat Transfer Division for publication in the JOURNAL OF HEAT TRANSFER. Manuscript received by the Heat Transfer Division September 16, 1981.

where the conventional symbols are defined in the nomenclature, γ is the acute angle of inclination of the continuous plate measured from the vertical, and the eddy diffusivities ϵ_m and ϵ_h, for the momentum and heat-transfer, respectively, vanish for laminar flow. The first term on the right-hand side of equation (2) represents the streamwise pressure gradient induced by the buoyancy force component perpendicular to the plate, with the plus and minus signs pertaining respectively to fluid above and fluid below the plate. The second term represents the streamwise buoyancy force, and its plus and minus signs refer to the upward and downward motion of the continuous plate, respectively.

The boundary conditions for equations (1-3) are

$$u = u_0, v = 0, T = T_w(x) \text{ at } y = 0$$
$$u = 0, T = T_\infty, \text{ as } y \to \infty \tag{4}$$

in which $T_w(x)$ is the surface temperature of the plate. If the temperature of the continuous plate is uniform across any cross section – a valid assumption as verified from Biot number calculations later in the results – one obtains from the differential heat balance on the plate of thickness, b:

$$-bk_s \frac{d^2 T_w}{dx^2} + b\rho_s C_s u_0 \frac{dT_w}{dx} = k \frac{\partial T}{\partial y}\bigg|_{y=0} \tag{5}$$

where the subscript, s, refers to the plate properties. Equation (5) applies for situations where either the top or the bottom surface of the plate is assumed adiabatic (the cooling of materials while traveling on conveyor belts). For cases where fluid exists simultaneously above and below the plate (the lamination process), equation (5) is still applicable for a vertical or inclined plate, with the modification that b now denotes half the thickness of the plate. With heat transfer from both sides of the plate, the equation is only approximate when the plate is inclined, since the normal components of the buoyancy force act in opposite directions, with respect to the transverse coordinates, y. This approximation however is a good one, as the results indicate that when $\gamma = 45$ deg, the effect of the normal component of the buoyancy force on the flow and heat transfer is not significant when compared to the effect of the streamwise buoyancy force component. For polyvinylchloride (PVC) as the lamination material and air as the ambient fluid at an average film temperature of 123°C, the Peclet number for the plate, $\mathrm{Pe}_s = u_0 b/\alpha_s$, is of the order of 1.7×10^2 Re. For the range of Reynolds number considered in the study $0.1 \le \mathrm{Re} \le 50$, the axial conduction in equation (5) can be neglected, thus reducing the equation to

$$b\rho_s C_s u_0 \frac{dT_w}{dx} = k \frac{\partial T}{\partial y}\bigg|_{y=0} \tag{6}$$

with the boundary condition

$$T_w(x) = T_i \text{ at } x = 0 \tag{7}$$

In the turbulent analysis, a mixing length model proposed by Cebeci and Smith [7] is used to determine the eddy diffusivities appearing in equations (2) and (3). According to that model, the eddy diffusivity for momentum, ϵ_m, for the inner and outer layers is given, respectively, by

$$\epsilon_m = \begin{cases} \epsilon_i = l^2 \left| \dfrac{\partial u}{\partial y} \right| & \text{for } \epsilon_i \le \epsilon_0 \\ \epsilon_0 = (0.075\delta)^2 \left| \dfrac{\partial u}{\partial y} \right| \Gamma & \text{for } \epsilon_0 < \epsilon_i \end{cases} \tag{8}$$

in which the mixing length is approximated by

$$l = 0.4y(1 - e^{-y/A}) \tag{9}$$

and the intermittency factor is given by Klebannof [8]

$$\Gamma = \left[1 + 5.5\left(\frac{y}{\delta}\right)^6\right]^{-1} \tag{10}$$

In an attempt to account for the effects of the buoyancy force on the eddy diffusivities, only the buoyancy force component perpendicular to the plate is considered here in the analysis. Thus, in accounting for the effect of the buoyancy induced streamwise pressure gradient, Cebeci's extension of the Van Driest model [7] is followed. Thus, the Van Driest damping parameter is modified as

$$A = \frac{A^+ \nu}{N(|\tau_w|/\rho)^{1/2}} \tag{11}$$

where

$$N = (1 - 11.8\, p^+)^{1/2} \tag{12}$$

and p^+ for the present study has the form

$$p^+ = \frac{-\frac{\nu}{\rho}\frac{\partial p}{\partial x}}{(|\tau_w|/\rho)^{3/2}} = \frac{\pm \nu g \beta \sin\gamma \frac{\partial}{\partial x}\int_y^\infty (T - T_\infty)\, dy}{(|\tau_w|/\rho)^{3/2}} \tag{13}$$

Nomenclature

A = Van Driest damping factor
A^+ = 26, damping constant
b = thickness or half thickness of plate
B = empirical constant
Bi = $\bar{h}b/k_s$, Biot number
C = specific heat of fluid
C_s = specific heat of plate
C_f = $\tau_w/(\rho u_0^2/2)$, local friction factor
$\bar{C}_f$ = $\tau_w/(\rho u_0^2/2)$, average friction factor
f = $\psi(x,y)/(\nu u_0 x)^{1/2}$, reduced stream function
g = gravitational acceleration
Gr = $g\beta(\Delta T)\, b^3/\nu^2$, Grashof number based on b
Gr_L = $g\beta(\Delta T)\, L^3/\nu^2$, Grashof number based on L
h = $q_w/(T_w - T_\infty)$, local heat-transfer coefficient
$\bar{h}$ = $\frac{1}{L}\int_0^L h(x)\, dx$, average heat-transfer coefficient
k = thermal conductivity of fluid
k_s = thermal conductivity of plate
l = mixing length
L = length of plate
Nu_x = hx/k, local Nusselt number
$\overline{\mathrm{Nu}}$ = $\bar{h}L/k$, average Nusselt number
p^+ = dimensionless streamwise pressure gradient
Pe_s = $u_0 b/\alpha_s$, Peclet number of plate
Pr = Prandtl number
Pr_t = turbulent Prandtl number
q_w = $-k(\partial T/\partial y)_{y=0}$, local surface heat-transfer flux
Re = $u_0 b/\nu$, Reynolds number based on b
Re_L = $u_0 L/\nu$, Reynolds number based on L

The eddy diffusivity for heat, ϵ_h, is evaluated according to Cebeci and Smith [7] from the following

$$\epsilon_h = \frac{\epsilon_m}{\mathrm{Pr}_t} \tag{14}$$

where the turbulent Prandtl number is given by

$$\mathrm{Pr}_t = \frac{0.4[1-\exp(-y/A)]}{0.44[1-\exp(-y/B)]} \tag{15}$$

In equation (15), A is the Van Driest damping factor and B is given by

$$B = \frac{\nu}{(|\tau_w|/\rho)^{1/2}} \mathrm{Pr}^{-1/2} \sum_{n=1}^{5} C_n (\log_{10}\mathrm{Pr})^{n-1} \tag{16}$$

in which

$$C_1 = 34.96, C_2 = 28.79, C_3 = 33.95, C_4 = 6.33, C_5 = -1.186 \tag{17}$$

One of the defects of the mixing-length hypothesis is that when the velocity profile goes through a maximum, as it does in the present problem, the velocity gradient goes through zero inside the boundary layer, thus making ϵ_m and subsequently ϵ_h vanish, which is unrealistic. To avoid this difficulty, the ϵ_m distribution was modified by a "bridging" technique suggested by Launder and Spalding [9].

The governing system of equations was first transformed into a dimensionless form before it was solved numerically. To achieve this, one introduces the following dimensionless parameters:

$$\xi(x) = x/b\ ,\ \eta(x,y) = y\sqrt{u_0/\nu x} \tag{18}$$

$$f(\xi,\eta) = \psi(x,y)/\sqrt{\nu u_0 x}\ ,\ \theta(\xi,\eta) = (T-T_\infty)/(T_i - T_\infty)$$

where b again denotes the thickness of the plate when either the top or bottom surface of the plate is adiabatic or stands for half the thickness of the plate when there is heat transfer from both top and bottom surfaces of the plate, and $\psi(x,y)$ is the stream function satisfying the continuity equation with $u = \partial\psi/\partial y$ and $v = -\partial\psi/\partial x$. By introducing equations (18) into equations (1–4,6,7) one can arrive at the following dimensionless system of equations

$$[(1+\epsilon_m^+)f'']' + \frac{1}{2}ff'' \pm \frac{1}{2}\frac{|\mathrm{Gr}|}{\mathrm{Re}^{2.5}}\xi^{1/2}(\sin\gamma)\left[\eta\theta + \int_\eta^\infty \theta d\eta + 2\xi\int_\eta^\infty \frac{\partial\theta}{\partial\xi}d\eta\right] \tag{19}$$

$$\pm\frac{|\mathrm{Gr}|}{\mathrm{Re}^2}(\cos\gamma)\xi\theta = \xi\left(f'\frac{\partial f'}{\partial\xi} - f''\frac{\partial f}{\partial\xi}\right)$$

$$\left[\left(\frac{1}{\mathrm{Pr}}+\epsilon_h^+\right)\theta'\right]' + \frac{1}{2}f\theta' = \xi\left(f'\frac{\partial\theta}{\partial\xi} - \theta'\frac{\partial f}{\partial\xi}\right) \tag{20}$$

$$\frac{\rho_s C_s}{\rho C}\mathrm{Pr}\ \mathrm{Re}^{1/2}\xi^{1/2}\frac{d\theta_w}{d\xi} = \theta'(\xi,0) \tag{21}$$

$$f(\xi,0) = 0,\ f'(\xi,0) = 1,\ f'(\xi,\infty) = 0$$
$$\theta(\xi,0) = \theta_w(\xi),\ \theta(\xi,\infty) = 0,\ \theta_w(0) = 1 \tag{22}$$

In the foregoing equations, the primes stand for partial differentiation with respect to η, Pr is the Prandtl number, and Gr and Re are the Grashof and Reynolds numbers defined respectively by

$$\mathrm{Gr} = \frac{g\beta(\Delta T)b^3}{\nu^2},\ \mathrm{Re} = \frac{u_0 b}{\nu} \tag{23}$$

where $\Delta T = T_i - T_\infty$ for fluid above the plate and $\Delta T = T_\infty - T_i$ for fluid below the plate. In equations (19–22), $\theta_w(\xi) = [T_w(x) - T_\infty]/(T_i - T_\infty)$ is the dimensionless surface temperature distribution, and the dimensionless property ratio $\rho_s C_s/\rho C$ is an assigned parameter for the problem.

The dimensionless eddy diffusivities for momentum and heat defined, respectively, by $\epsilon_m^+ = \epsilon_m/\nu$ and $\epsilon_h^+ = \epsilon_h/\nu$ are obtained by nondimensionalizing equations (8) and (14). Thus, utilizing equations (18) one can show that

$$\epsilon_m^+ = \begin{cases} \epsilon_i^+ = \{0.4\eta[1-\exp(-y/A)]\}^2\mathrm{Re}^{1/2}\xi^{1/2}|f''(\xi,\eta)| \\ \qquad\qquad \text{for } \epsilon_i^+ \le \epsilon_0^+ \\ \epsilon_0^+ = [0.075\eta_\delta]^2\mathrm{Re}^{1/2}\xi^{1/2}|f''(\xi,\eta)|\dfrac{1}{1+5.5(\eta/\eta_\delta)^6} \\ \qquad\qquad \text{for } \epsilon_0^+ < \epsilon_i^+ \end{cases} \tag{24}$$

where

$$y/A = \xi^{1/4}\mathrm{Re}^{1/4}\eta|f''(\xi,0)|^{1/2}\mathrm{N}/\mathrm{A}^+ \tag{25}$$

$A^+ = 26$, and N is given from equation (12) with

Nomenclature (cont.)

St = $h/\rho C u_0$, local Stanton number
T = fluid temperature
T_i = temperature of plate at point of issuance ($x=0$)
T_w = wall temperature
T_∞ = free-stream temperature
u,v = velocity components in x and y directions
u_0 = velocity of moving plate
x,y = axial and normal components
α = thermal diffusivity of fluid
α_s = thermal diffusivity of plate
β = volumetric coefficient of thermal expansion
γ = angle of inclination from vertical
Γ = intermittency factor
δ = boundary layer thickness
ϵ_m, ϵ_h = eddy diffusivities for momentum and heat
$\epsilon_m^+, \epsilon_h^+$ = dimensionless eddy diffusivities for momentum and heat
η = $y(u_0/\nu x)^{1/2}$, psuedo-similarity variable
η_δ = $\delta(u_0/\nu x)^{1/2}$, dimensionless boundary layer thickness
θ = $(T-T_\infty)/(T_i - T_\infty)$, dimensionless temperature
θ_w = $(T_w - T_\infty)/(T_i - T_\infty)$, dimensionless wall temperature
μ = dynamic viscosity of fluid
ν = kinematic viscosity of fluid
ξ = dimensionless axial parameter
ρ = density of fluid
ρ_s = density of plate
τ_w = $\mu(\partial u/\partial y)_{y=0}$, local wall shear stress
$\bar{\tau}_w$ = $\frac{1}{L}\int_0^L \tau_w(x)dx$, average wall shear stress

$$p^+ = \pm \frac{1}{2} \frac{\mathrm{Gr}}{\mathrm{Re}^{2.5}} \frac{\xi^{1/4} \sin\gamma}{\mathrm{Re}^{1/4} |f''(\xi,0)|^{3/2}}$$

$$\left[\eta\theta + \int_\eta^\infty \theta d\eta + 2\xi \int_\eta^\infty \frac{\partial\theta}{\partial\xi} d\eta\right] \quad (26)$$

For the eddy diffusivity for heat one gets

$$\epsilon_h^+ = \epsilon_m^+ / \mathrm{Pr}_t \quad (27)$$

and Pr_t is given from equation (15) with

$$y/B = \eta\xi^{1/4} \mathrm{Re}^{1/4} |f''(\xi,0)|^{1/2} \mathrm{Pr}^{1/2} / \sum_{n=1}^{5} C_n (\log_{10}\mathrm{Pr})^{n-1} \quad (28)$$

It is noted here that the plus and minus signs that appear in equations (19) and (26) relate to buoyancy assisting and opposing situations, respectively. Furthermore, the plus and minus signs associated with terms that involve "sinγ" (referred to as SIGN1 in the figures) pertain, respectively, to $T_i > T_\infty$ and $T_i < T_\infty$ for fluid above the plate, and to $T_i < T_\infty$ and $T_i > T_\infty$ for fluid below the plate. Likewise, the plus and the minus signs associated with the term that involves "cosγ" (referred to as SIGN2 the in figures), pertain to $T_i > T_\infty$ and $T_i < T_\infty$ for upward moving plate and to $T_i < T_\infty$ and $T_i > T_\infty$ for downward moving plate respectively.

In the turbulent analysis, it was assumed that the flow was turbulent from the start. Equations (19–22) along with $\epsilon_m^+ = \epsilon_h^+ = 0$ for laminar boundary layer or along with equations (24) and (27) for turbulent boundary layer were solved for assigned parameters of Re, $\mathrm{Gr}/\mathrm{Re}^2$, Pr, γ, $\rho_s C_s/\rho C$ for buoyancy assisting and opposing situations, where $\xi = x/b$ varied from 0 to 10^{10}.

Numerical Solution

The solution to the abovementioned system of equations was accomplished by using an efficient and accurate marching finite-difference technique developed by Keller and Cebeci [6]. This method accommodates variable boundary layer thicknesses η_δ, along with variable step sizes for $\Delta\eta$ and $\Delta\xi$. To overcome the deficiency of the mixing length hypothesis concerning the dip of the eddy diffusivity for momentum when the velocity goes through a maximum, the "bridging" technique [9] was utilized. Thus, near the region where the velocity went through a maximum, the points on the ϵ_m curve that dipped were replaced by corresponding points on an interpolated straight line.

Two other expressions for the eddy viscosity for momentum for the outer region, ϵ_m, based on the displacement thickness and momentum thickness were also tested and found to give results which were indistinguishable from the results to be presented. It was also found that the intermittency factor Γ had a minimal effect on the results, as did the above mentioned "bridging" technique.

Results and Discussion

Numerical results for the local and average Nusselt numbers and friction factors, velocity and temperature profiles, and the surface temperature variation were obtained for air with a Prandtl number of 0.7, for both laminar and turbulent regimes. Results are presented for angles of inclination from the vertical of $\gamma = 0$ (vertical), 45, and 90 deg (horizontal) for Reynolds numbers of Re = 0.1, 1, 10, and 50, and various buoyancy force parameters $\mathrm{Gr}/\mathrm{Re}^2$, ranging from -10^{-2} to 10^{-2}. The property parameter $\rho_s C_s/\rho C$ was chosen as 2500, the order of which is characteristic of the extrusion coating process using PVC (polyvinylchloride) as the lamination material, at an average film temperature of 123°C.

The local Nusselt number, Nu_x, and the local friction factor, C_f, as defined in the nomenclature, can be expressed with the aid of equations (18) as

$$\mathrm{Nu}_x = -\theta'(\xi,0)\mathrm{Re}^{1/2}\xi^{1/2}/\theta(\xi,0), \quad C_f = 2f''(\xi,0)/(\mathrm{Re}^{1/2}\xi^{1/2}) \quad (29)$$

The local friction factors versus $\xi = x/b$, the axial distance from the slot, for laminar and turbulent regimes are plotted in Fig. 1 for angles of inclination from the vertical of $\gamma = 0$, 45, and 90 deg, for Reynolds numbers, Re, ranging from 0.1, to 50, and various buoyancy force parameters. In the absence of buoyancy forces, the plate drags the fluid near its surface and accelerates it in the direction of its motion. However, the velocity of the fluid never exceeds the velocity of the plate, and the friction factor as defined in equation (29) remains negative and decreases in magnitude with axial distance from the wall. This trend prevails for both laminar and turbulent regimes, even though the laminar friction factors lie above (i.e., less negative) those of the corresponding turbulent ones. This is in accord with the trends of the velocity profiles in Fig. 4, where the smooth laminar fluid is pulled by the plate with less resistance than the random turbulent fluid, thus resulting in a higher fluid velocity and less negative friction factor for laminar boundary layers. When both buoyancy force components are assisting (both SIGN1 and SIGN2 taken as positive), the fluid near the wall be accelerated further to the point that it may exceed the plate velocity (see Fig. 4), thus reversing the sign of the wall shear stress. It is for the same reasoning that for a given Re as Gr increases, this sign reversal of the friction factor will occur at smaller x/b values for laminar regime than for turbulent regime, resulting in laminar friction factors that are more positive than the corresponding turbulent ones. This difference in the friction factors between laminar and turbulent regimes decreases as Re and Gr decreases. It is also of interest to note from Fig. 1

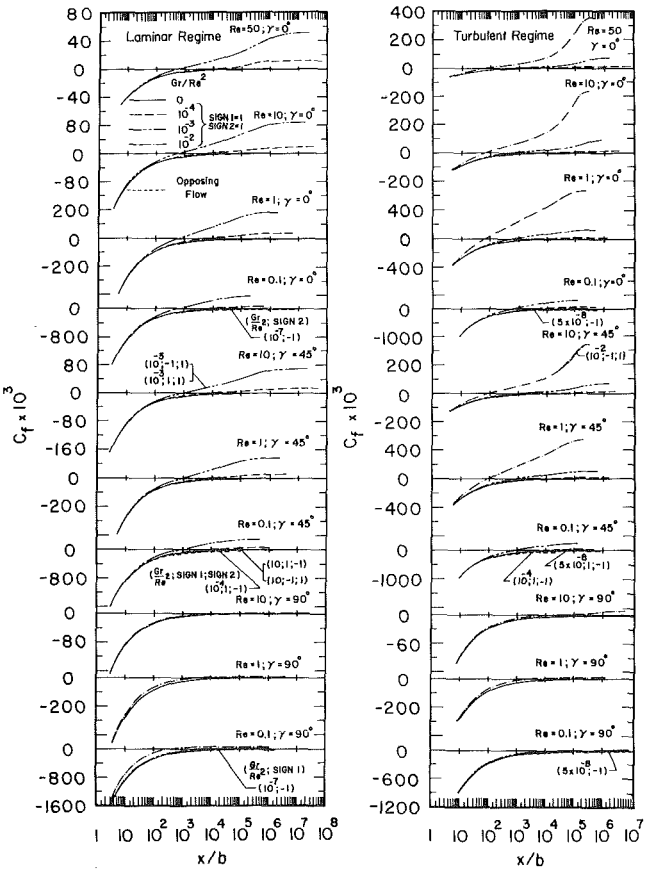

Fig. 1 Local friction factor results, Pr = 0.7

that for $\gamma = 45$ deg, the effect of the buoyancy-induced streamwise pressure gradient (sign of SIGN1) on the friction factor is negligible compared to the effect of the streamwise buoyancy force component (sign of SIGN2). Thus, as shown in Fig. 1, for both laminar and turbulent boundary layers, when $\gamma = 45$ deg, and $\mathrm{Re} = 10$, no distinguishable difference in the local friction factors between the case of SIGN1 = 1 (heating of fluid above the plate or cooling of fluid below the plate) and that of SIGN1 = −1 (cooling of fluid above the plate or heating of fluid below the plate) can be observed when the streamwise buoyancy force is assisting the fluid motion (SIGN2 = 1). However, when the streamwise buoyancy force component acts against the acceleration of the fluid by the motion of the plate (SIGN2 = −1), it results in local friction factors that are more negative than the corresponding ones for no buoyancy force (see Fig. 1 with $\gamma = 45$ deg and Re = 0.1). Finally, as seen from the same figure, the friction factors at a given x/b increase (more negative or less positive) as the plate is tilted from the vertical for a given Re and Gr for both laminar and turbulent boundary layers. Also, the local friction factors for a given x/b and Gr decrease in magnitude (less negative or less positive) as Re increases for both flow regimes.

The corresponding local Nusselt numbers are presented in Fig. 2. As seen from the figure, the local Nusselt numbers increase with axial distance from the slot. It is also found that the buoyancy force affects the turbulent local Nusselt numbers such that for a given Reynolds number, Re, as the Grashof number, Gr, increases from 0, the turbulent local Nusselt number first decreases below its corresponding value for pure forced convection ($\mathrm{Gr}/\mathrm{Re}^2 = 0$), reaches a minimum value, and then increases above the value of zero buoyancy force. This trend is parallel to that observed first experimentally by Hall and Price [10] and analytically by Oosthuizen [11] for turbulent mixed convective flow over stationary isothermal vertical plates. It appears that the present trends are due to the rapid acceleration of the near-the-wall fluid by the assisting buoyancy force which tends to decrease the turbulence intensity and progressively thicken the viscous layer near the wall, thus increasing the thermal resistance of the near-the-wall fluid region. As the buoyancy force is increased further, the increase in convective heat transport due to the larger acceleration of the fluid overtakes the adverse effect of the decrease in turbulence intensity, thus resulting in an overall increase of the turbulent local Nusselt numbers. Since no measurement of the turbulent intensity is possible with the mixing length model used, experiments or more sophisticated closure turbulence models are necessary to verify the present findings. The abovementioned trends are not encountered in laminar boundary layer for which case the local laminar Nusselt numbers increase monotonically as Gr increases from 0. This dipping of the turbulent local Nusselt number below that for $\mathrm{Gr}/\mathrm{Re}^2 = 0$ occurs at lower Grashof number, Gr, as the Reynolds number decreases. Also, the magnitude of the dip decreases as Re decreases. Thus, the initial decrease and subsequent increase in the local Nusselt numbers in turbulent regime can be observed only when Re = 50 for $\gamma = 0$ deg, and when Re = 10 for $\gamma = 90$ deg. The surface temperature gradients as noted from Fig. 5 (see inset) are in accordance with the abovediscussed trends for both turbulent and laminar boundary layers.

As expected, the turbulent local Nusselt numbers are larger than their corresponding laminar ones. As seen also from Fig. 2 for $\gamma = 45$ deg, the effect of the opposing streamwise force component (SIGN2 = −1) is to reduce the local Nusselt numbers below their zero buoyancy force values, while the effect of the streamwise pressure gradient (SIGN1) at $\gamma = 45$ deg is again of little significance. The local Nusselt number values at a fixed location of the plate increase with increasing Re and decrease as the plate is tilted from the vertical, for both laminar and turbulent boundary layers. It is also noted that the local Nusselt number curves level off eventually as x/b increases further, resulting in the crossover of the curves as can be seen in the figure. The leveling off and the crossover of the curves are due to the surface temperature approaching the free stream temperature value at different x/b values (see Fig. 3).

Figure 3 shows the dimensionless surface temperature variation $[T_w(x) - T_\infty]/(T_i - T_\infty) = \theta(\xi, 0)$ with x/b, for both laminar and turbulent regimes. The effect of the buoyancy force on the dimensionless surface temperature is parallel to that on the local Nusselt numbers observed in Fig. 2. Thus, for laminar boundary layers, as the buoyancy force assists the motion of the fluid, it enhances the surface cooling (from an upward moving vertical or inclined plate, or from the top side of a horizontal moving plate) and the surface heating (from a downward moving vertical, or inclined plate, or from the bottom of a horizontal moving plate). These trends are reversed when the buoyancy force opposes the fluid motion. When the plate is inclined with $\gamma = 45$ deg, the streamwise buoyancy force component is the dominant component and the effect of the normal buoyancy force component is of little significance. For turbulent boundary layers, on the other hand, as the assisting buoyancy force is first superimposed on the fluid it decreases the cooling and heating of the moving surface. At larger assisting buoyancy forces, eventually this trend is reversed and further increases in the Grashof number result in the enhancement of the surface cooling and heating. A close inspection of Fig. 3 shows that the cooling or heating of the moving surface is larger for turbulent boundary layers then the corresponding laminar ones. Also, the cooling or heating of the plate is enhanced as Re decreases for both assisting and opposing buoyancy forces.

Representative dimensionless velocity profiles $u/u_0 = f'(\xi, \eta)$ and temperature profiles $(T - T_\infty)/(T_i - T_\infty) = \theta(\xi, \eta)$ are plotted, respectively, in Figs. 4 and 5 for a vertical moving plate ($\gamma = 0$ deg) at $x/b = 5 \times 10^4$, for Reynolds numbers of Re = 0.1, 10, and 50 and buoyancy force parameters $\mathrm{Gr}/\mathrm{Re}^2$, ranging from 0 to 0.01. For the laminar boundary layers, the flow and thermal boundary layer thicknesses are seen to decrease as $\mathrm{Gr}/\mathrm{Re}^2$ increases from zero. No such definite trend can be observed for the turbulent boundary layer. However, it is seen that the flow and thermal boundary layers for turbulent regime are thicker than those for the laminar boundary layer. A close study of the trends of the profiles in the insets of both figures is helpful in describing the variations of the local friction factors and Nusselt numbers with buoyancy force.

In order to present the average friction factors and average Nusselt numbers over the length of the plate, L, one can nondimensionalize equations (1-4), (6-8) and (14) by redefining the axial parameter as $\xi(x) = x/L$ and with η, f, and θ, as defined by equation (18). The resulting dimensionless system of equations was then solved for the dimensionless parameter $(b/L)\ (\rho_s C_s/\rho C) = 0.1$, Reynolds numbers $\mathrm{Re}_L = 10^3,\ 10^4,\ 10^5$, and 10^6 and buoyancy force parameters $\mathrm{Gr}_L/\mathrm{Re}_L^2 = 0,\ 1$, and 10, where the Reynolds number and Grashof number based on the length of the plate are defined by

$$\mathrm{Re}_L = u_0 L/\nu,\ \mathrm{Gr}_L = g\beta(T_i - T_\infty)L^3/\nu^2 \tag{30}$$

The average Nusselt number, $\overline{\mathrm{Nu}}$, and the average friction factor, $\bar{C}_f$, over the length of the plate, L, as defined in the nomenclature, can be expressed using the above mentioned transformation variables as

$$\overline{\mathrm{Nu}} = -2\mathrm{Re}_L^{1/2}\left\{\frac{\theta'(1,0)}{\theta(1,0)} - \int_0^1 \xi^{1/2}\left[\frac{1}{\theta(\xi,0)}\frac{\partial\theta'}{\partial\xi}(\xi,0) - \frac{\theta'(\xi,0)}{\theta^2(\xi,0)}\frac{\partial\theta}{\partial\xi}(\xi,0)\right]d\xi\right\} \tag{31}$$

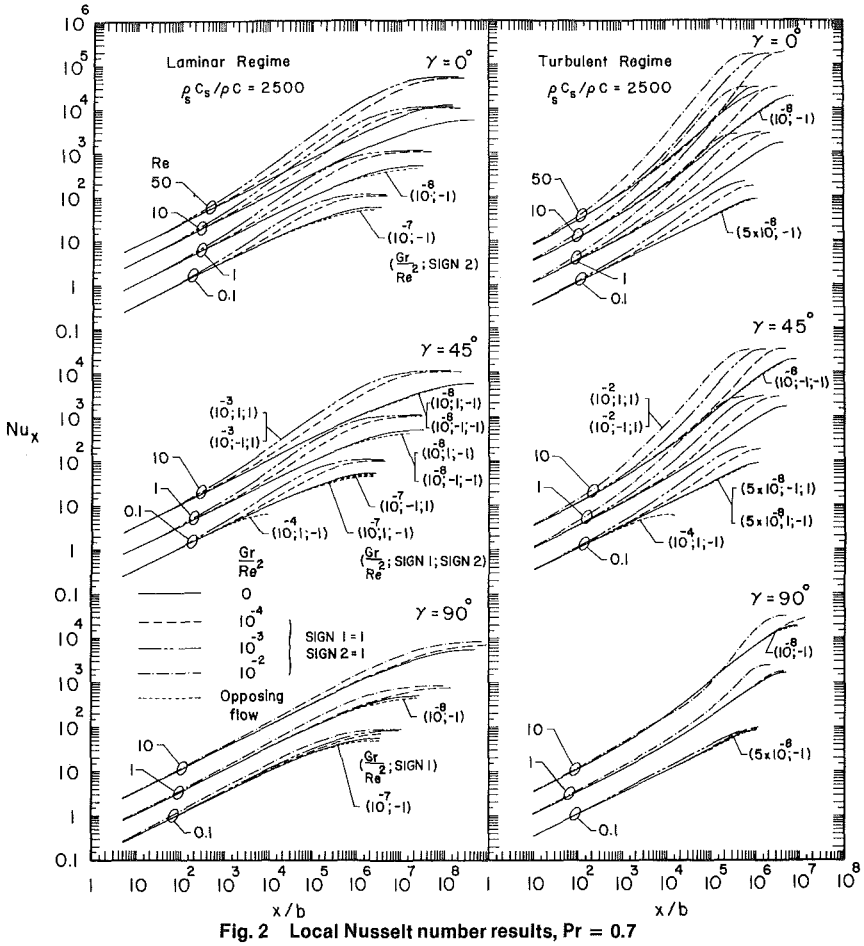

Fig. 2 Local Nusselt number results, Pr = 0.7

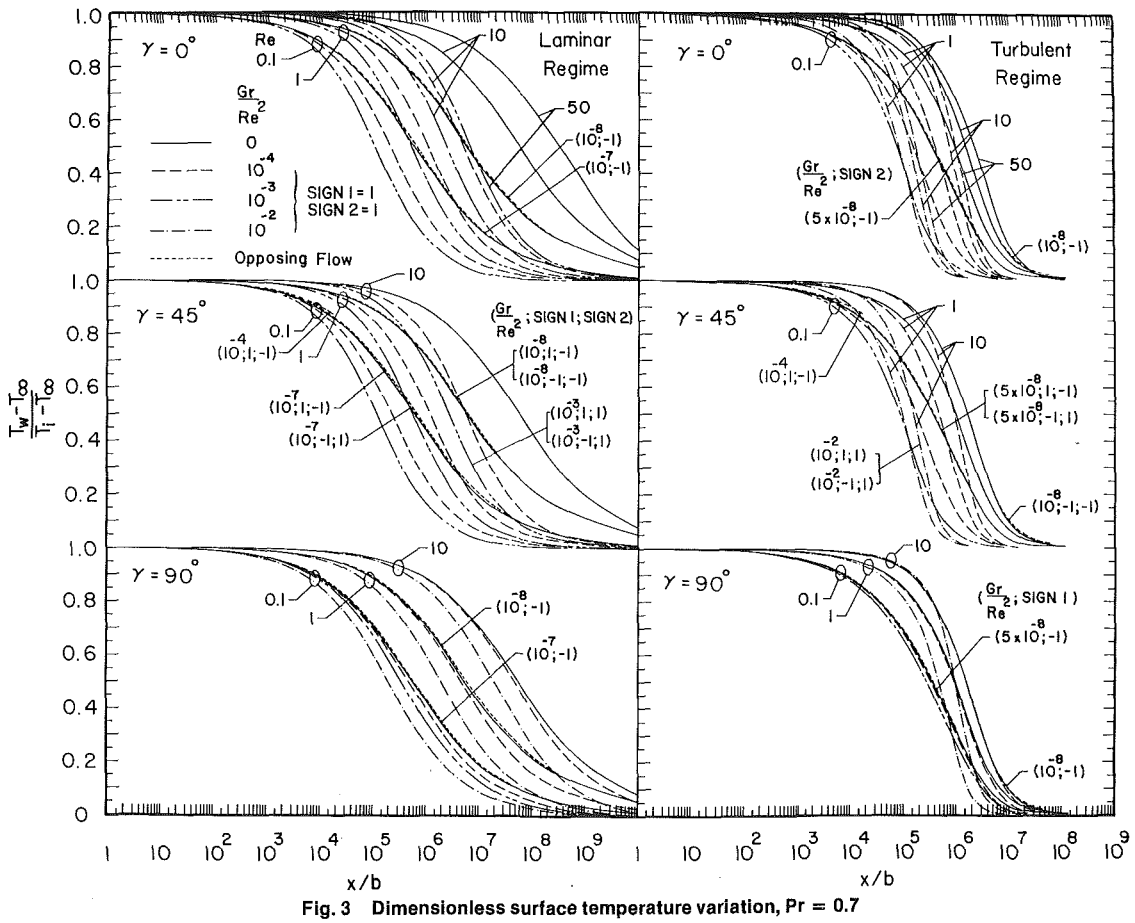

Fig. 3 Dimensionless surface temperature variation, Pr = 0.7

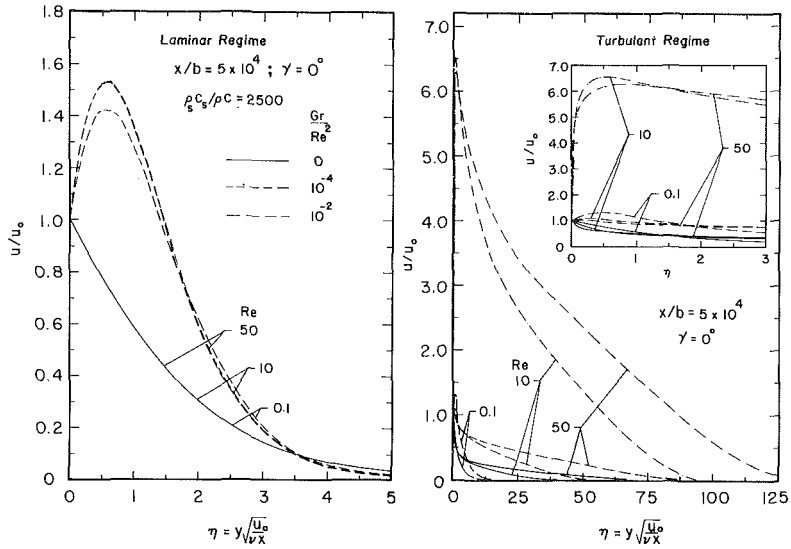

Fig. 4 Dimensionless velocity profiles for $\gamma = 0°$, $x/b = 5 \times 10^4$, Pr = 0.7

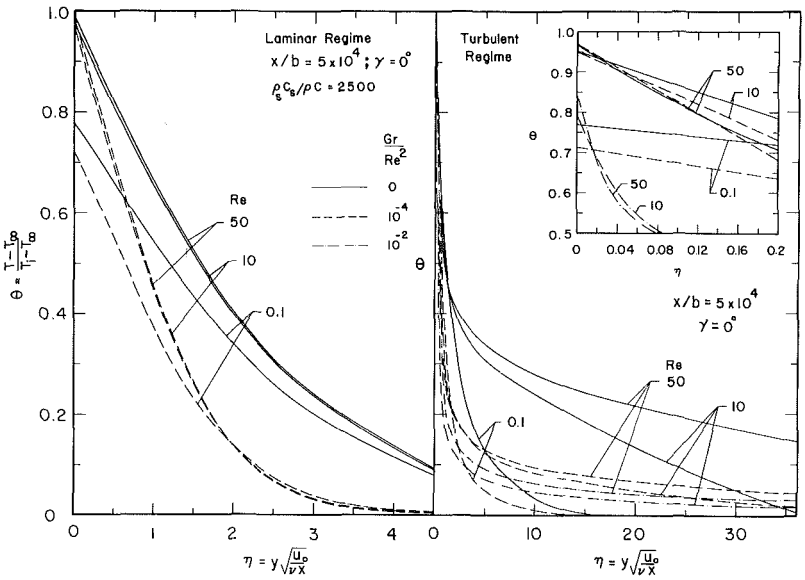

Fig. 5 Dimensionless temperature profiles for $\gamma = 0°$, $x/b = 5 \times 10^4$, Pr = 0.7

$$\bar{C}_f = 4\mathrm{Re}_L^{-1/2}\left[f''(1,0) - \int_0^1 \xi^{1/2}\frac{\partial f''(\xi,0)}{\partial \xi}\,d\xi\right]$$

where again $\xi = x/L$.

The average friction factors and Nusselt numbers for turbulent boundary layers are shown in Figs. 6 and 7 as a function of the Reynolds number based on the length of the plate, Re_L. As observed from Fig. 6, average friction factors may be negative or positive, i.e., the plate may drag the fluid or the fluid may drag the plate, but in either case the friction factor decreases in magnitude as Re_L increases.

As illustrated in Fig. 7, the average Nusselt numbers for turbulent boundary layers are found to increase with increasing value of Re_L. With the aid of Fig. 7, one can show that the Biot number, $\mathrm{Bi} = \bar{h}b/k_s$, ranges from 2.7 (b/L) at $\mathrm{Re}_L = 10^3$ to 145 (b/L) at $\mathrm{Re}_L = 10^6$ when $\gamma = 0$ deg, where the average thermal conductivity of the polymer is taken as $k_s = 8 \times 10^{-4}$ cal/cm-s − °C. This can serve as an indicator for the accuracy of the assumption regarding the uniformity of the plate temperature at any given cross section. For $\mathrm{Bi} < 0.1$, the error involved with this assumption is approximately 5 percent or less.

Finally, the earlier analytical studies of references [1] and [5] along isothermal continuous surfaces without the buoyancy force effect are compared with the present results in Fig. 8 for the case of turbulent boundary layer for $T_w = T_i =$ constant and $\mathrm{Gr}_L/\mathrm{Re}_L^2 = 0$ in the form of local friction factor and Stanton number. In the same figure, the experimental results of reference [5] for friction factor are also shown. The satisfactory agreement with the results of reference [5] supports the validity of the mixing length model that was employed in the present analysis.

Concluding Remarks

The analysis yielded some interesting and unexpected results. In particular, for turbulent boundary layer, for a given Reynolds number, when the buoyancy force assists the motion of the fluid, it was found that as the Grashof number is increased from zero, the local surface heat-transfer rate decreases below its corresponding value for pure forced convection, attains a minimum value, and then increases above the value for zero buoyancy force. The initial dipping of the local heat transfer rate below that for zero buoyancy force was found to occur at lower Grashof numbers as the

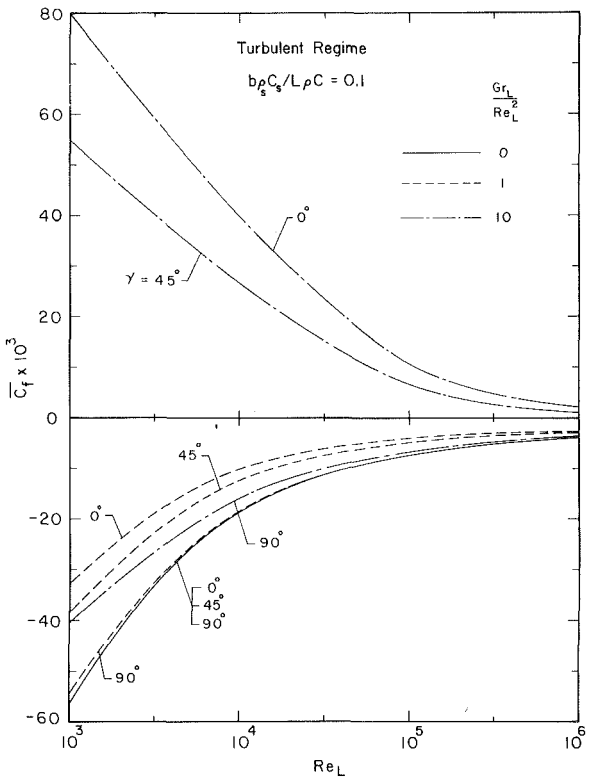

Fig. 6 Average friction factor results for turbulent regime, Pr = 0.7

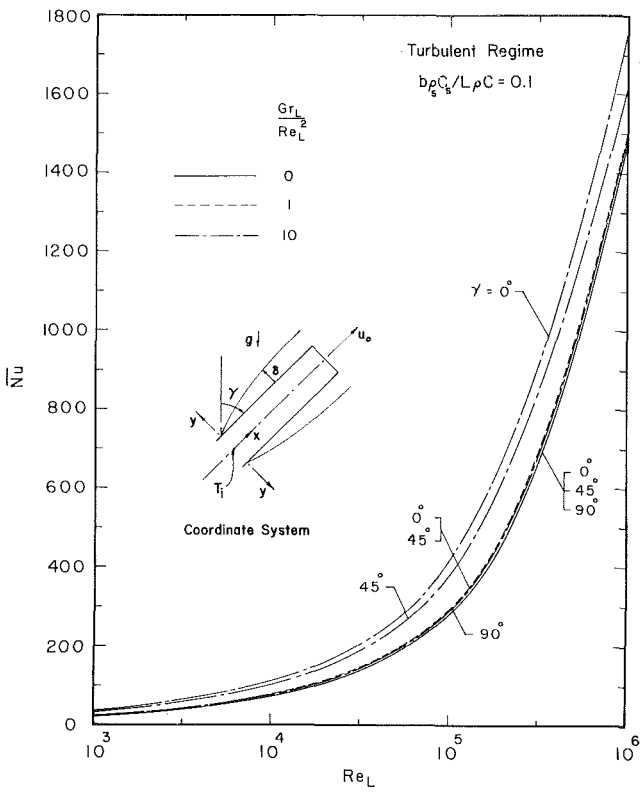

Fig. 7 Average Nusselt number results for turbulent regime, Pr = 0.7

Reynolds number is decreased. For laminar boundary layers, on the other hand, the local surface heat-transfer rate was found, as expected, to increase monotonically with increasing Grashof number, for the buoyancy assisting flow situation.

Acknowledgement

This study was supported in part by the a grant from the National Science Foundation (NSF CME 80-05682).

References

1 Sakiadis, B. C., "Boundary Layer Behavior on Continuous Solid Surfaces: II, The Boundary Layer on a Continuous Flat Surface," *A.I.Ch.E. Journal* Vol. 7, 1961, pp. 221–225.

2 Moutsoglou, A., and Chen, T. S., "Buoyancy Effects in Boundary Layers on Inclined, Continuous, Moving Sheets," ASME JOURNAL OF HEAT TRANSFER, Vol. 102, 1980, pp. 371–373.

3 Erickson, L. E., Fan, L. T., and Cha, L. C., "The Cooling of a Moving Continuous Sheet," *A.I.Ch.E., Chemical Engineering Progress Symposium Series, Heat Transfer*, Los Angeles, Calif. Vol. 62, 1966, pp. 157–165.

4 Barnett, T. R., "Calculation of the Temperature of Filaments in Melt Spinning," *Applied Polymer Symposia*, No. 6, 1967, pp. 51–65.

5 Tsou, F. L., Sparrow, E. M., and Goldstein, R. J., "Flow and Heat Transfer in the Boundary Layer on a Continuous Moving Surface," *International Journal of Heat and Mass Transfer*, Vol. 10, 1967, pp. 219–235.

6 Keller, H. B., and Cebeci, T., "Accurate Numerical Methods for Boundary Layer Flows. II: Two-Dimensional Turbulent Flows," *AIAA Journal*, Vol. 10, 1972, pp. 1193–1199.

7 Cebeci, T., and Smith, A. M. O., *Analysis of Turbulent Boundary Layers*, Academic Press, New York, 1974.

8 Klebannof, P. S., "Characteristics of Turbulence in a Boundary Layer with Zero Pressure Gradient, NACA TN 3178, 1954.

9 Launder, B. E., and Spalding, D. B., *Mathematical Models of Turbulence*, Academic Press, London, 1972.

10 Hall, W. B., and Price, P. H., "Mixed Forced and Free Convection From a Vertical Heated Plate to Air," *4th International Heat Transfer Conference*, Vol. IV, NC 3.3, Paris, 1970, pp. 1–10.

11 Oosthuizen, P. H., "Turbulent Combined Convective Flow Over a Vertical Plane Surface," *5th International Heat Transfer Conference*, Vol. III, NC 4.1, Tokyo, 1974, pp. 129–133.

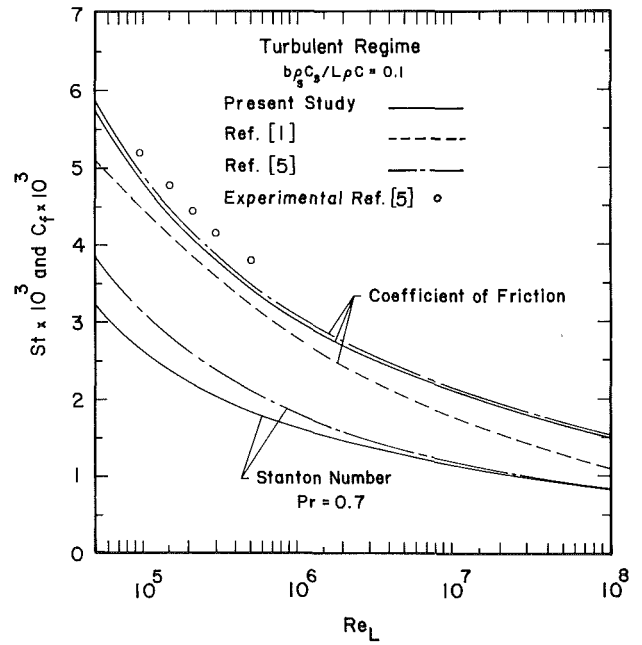

Fig. 8 Comparison between analytical and experimental local friction factor and Stanton number for turbulent boundary layers along isothermal, continuous moving plates, Pr = 0.7

R. J. Goldstein
Department of Mechanical Engineering,
University of Minnesota,
Minneapolis, Minn. 55455
Fellow ASME

J. R. Taylor
The Aerospace Corporation,
Los Angeles, Calif. 90245

Mass Transfer in the Neighborhood of Jets Entering a Crossflow

The mass-transfer coefficient in the neighborhood of a row of jets entering a cross flow is determined by measuring the local sublimation rate from a naphthalene surface. This mass transfer relates directly to the heat transfer that would occur on a film-cooled wall. The experiments indicate that jets significantly increase the transfer coefficient in the neighborhood of the holes through which the jets emanate – in particular, immediately adjacent to the holes and also some distance downstream of the centerlines of the holes.

1 Introduction

Film cooling continues to be a widely used yet not fully understood technique to prevent overheating of surfaces exposed to high-temperature gas streams. The emphasis in terms of applications is towards gas turbine systems – both aircraft and land-based – where higher gas temperatures can lead to significant improvements in economy and output.

In film cooling, a fluid (usually a gas) is injected from and along the surface to be protected from a high-temperature mainstream. The film coolant tends to act as an insulating layer separating the surface from the high-temperature flow. Alternately, one can consider the injected fluid as a dilutant which reduces the temperature in the boundary layer. Early film cooling studies [1] concentrated on two-dimensional flows with the coolant introduced continuously across the span of the surface to be protected. In many applications, however, an injection system with one or more rows of discrete holes along the surface is used. This latter method of injection, producing three-dimensional film cooling, is usually not as effective as two-dimensional film cooling because of the opportunity of the hot mainstream to flow underneath the jets of coolant that emanate from the discrete holes. Recently, two-dimensional arrays of injection holes all along the surface have been studied. This full-coverage film cooling tends to approach transpiration cooling in the limit as the spacing between the injection holes decreases.

In studying either two-dimensional film cooling from a single slot or three-dimensional film cooling from a single row or even several rows of holes, a convenient means of analyzing the problem has been to consider the adiabatic wall temperature and the heat-transfer coefficient as separate quantities to be determined. The adiabatic wall temperature can be put in a convenient dimensionless form as a film cooling effectiveness

$$\eta = \frac{T_{aw} - T_r}{T_2 - T_r} \tag{1}$$

In the idealized limit, the effectiveness would be unity near injection, and far downstream the effectiveness would approach zero as the adiabatic wall temperature approaches the freestream recovery temperature. It should be borne in mind that although the latter is generally true, the effectiveness – particularly with three-dimensional film cooling – is usually well below unity even close to injection.

Use of the adiabatic wall temperature permits the definition of a well-behaved heat-transfer coefficient

$$q = h_H (T_w - T_{aw})$$

or

$$h_H = \frac{q}{T_w - T_{aw}} \tag{2}$$

Note that when the temperature difference $(T_w - T_{aw})$ is zero, q goes to zero without any special requirement on h_H. In addition, some distance downstream from injection, the heat-transfer coefficient should approach the value that would occur on a similar surface with similar mainstream flow and no injected flow.

The present study is concerned with measurements that would lead to prediction of the heat-transfer coefficients in the neighborhood of a single row of injection holes with air as the film coolant and with a mainstream of air. Although a number of different geometries for the injection holes are possible, a system is chosen that approximates one used in many applications. This is a row of circular holes inclined at 35 deg to the surface and spaced apart, center to center, by 3 diameters. Figure 1, which shows part of the test apparatus, gives an indication of this geometry.

Previous Studies

A number of studies have been made on three-dimensional film cooling. Many of these, however, have been concerned primarily with the determination of adiabatic wall effectiveness. Heat transfer is more difficult to determine, particularly close to the injection holes, at least in part due to

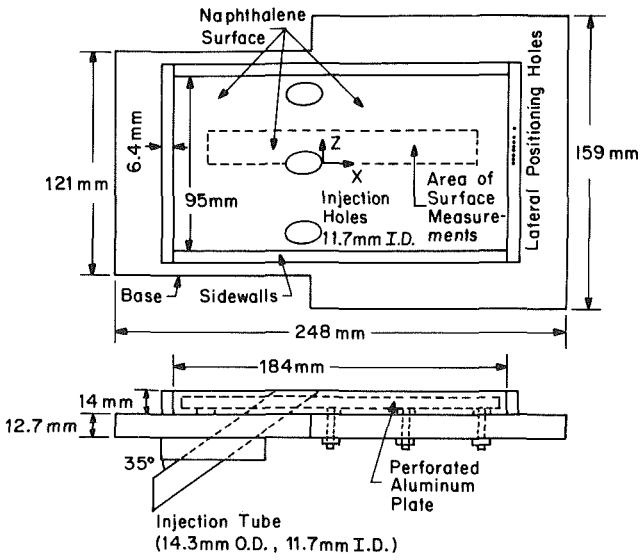

Fig. 1 The naphthalene test plate

Contributed by the Heat Transfer Division and presented at the AIAA-ASME Heat Transfer, Fluids, and Thermophysics Conference, St. Louis, Missouri, June 7–11, 1982. Manuscript received by the Heat Transfer Division January 13, 1982.

thermal conduction through the wall over which the mainstream flows.

Most measurements of heat transfer with film cooling have been done using a system in which averages are taken at least across the span of the tunnel. This includes studies by Metzger and Fletcher [2], Metzger, Kuenstler, and Takeuchi [3], Liess [4], and Mayle and Camarata [5].

Crawford, Kays and Moffat used heat-transfer gauges to study the heat transfer with full-coverage film cooling [6]. Heat transfer has been studied in high-speed tunnels using transient heat flux gauges by Schultz, Oldfield and Jones [7] and Louis [8].

Local measurements of heat transfer on a film-cooled surface with a single row of injection holes have been reported by Eriksen and Goldstein [9] and Jabbari and Goldstein [10]. In these studies, a uniform wall heat flux boundary condition was approximated by having a thin heater stretched across an almost adiabatic surface. Heat-transfer coefficients were determined from local measurements of the wall temperature. The coefficients close to the injection location were larger than those on an equivalent surface without injection. The heat-transfer coefficients increased as the amount of injected gas was increased and tended to decrease some distance downstream of the injection hole, eventually approaching the values observed without injection. For a hole geometry similar to that in the present experiment, the closest to the holes that measurements could be made was approximately 5.57 diameters downstream. The problem with measurements closer to the holes, in these as in other studies, is the error introduced by wall conduction as well as the difficulty in having the heated surface extremely close to the injection region.

The present study was initiated to obtain information on heat and mass transfer very close to injection holes over a range of flow conditions. The geometry chosen was similar to that of reference [9], a single row of holes inclined at 35 deg to the mainstream with 3-diameter center-to-center spacing between the holes. To avoid problems encountered with heat conduction in the wall, a mass-transfer technique was used.

Mass Transfer Systems

A mass-transfer analogy has been used in a number of studies on film cooling. With two-dimensional film cooling, local impermeable wall concentrations following injection of a foreign gas have been used to predict adiabatic film cooling effectiveness for some time [11, 12]. The validity of this mass-transfer analogy for injection through a row of discrete holes was demonstrated in reference [13]. The advantages of the mass-transfer analogy for measuring wall effectiveness are that a large range of densities can be obtained without having large temperature differences and the problems due to wall conduction are avoided.

A different application of the mass-transfer analogy is used in the present work to determine the influence of injection on heat transfer. Naphthalene sublimation has been used to determine average mass-transfer coefficients by determining the mass of naphthalene that is sublimed in either a forced or natural convection system [14]. With this technique a naphthalene surface is cast in the particular geometry desired. With a forced flow across that surface, mass will be continually lost by sublimation due to diffusion and convection in a similar manner to heat transferred from a surface. The analogy between the mass-transfer and heat-transfer processes is direct, taking into account differences in properties and assuming the turbulent transport and boundary conditions are similar for the mass-transfer and heat-transfer systems.

One boundary condition in an isothermal air-naphthalene system would be constant naphthalene vapor pressure and vapor concentration at the surface which is equivalent to a constant wall temperature heat-transfer boundary condition. The only significant difference in boundary conditions appears to be in the velocity at the wall. The finite sublimation of naphthalene gives a normal component of velocity which is absent in most convective heat-transfer studies. In general, this component of velocity is small enough that it does not significantly affect the validity of the analogy to a heat transfer surface with zero velocity normal to the wall.

A mass-transfer coefficient, h_M, is defined by

$$\dot{m} = h_M(\rho_w - \rho_{iw}) \tag{3}$$

This is analogous to equation 2. In the present study, the concentration of naphthalene vapor in both the freestream and in the injected gas is zero, and equation (3) reduces to

$$\dot{m} = h_M \rho_w \tag{4}$$

The analogy indicates that the Sherwood number is equivalent to the Nusselt number if the Schmidt number and the Prandtl numbers are equal. This implies not only equal diffusion coefficients but equal turbulent transport coefficients as well.

The Schmidt number (approximately 2.5 at ambient temperature for naphthalene diffusing in air) has a different value from the Prandtl number of air ($\sim$0.7). The comparison of mass-transfer and heat-transfer results is often put in the form

$$\mathrm{Sh}/\mathrm{Nu} = (\mathrm{Sc}/\mathrm{Pr})^n \tag{5}$$

where n is typically of the order of 0.4.

The validity of the analogy has been demonstrated by Sogin [15]. Local measurements of mass transfer were made by Lee and Barrow [16], Kan, Miwa, Morishita, Munakata and Nomura [17], and Saboya and Sparrow [18].

Experimental Apparatus and Procedure

The experiments were conducted in the University of Minnesota Heat Transfer Laboratory Wind Tunnel. The

Nomenclature

D = injection tube inner diameter, 11.7 mm
h = heat- or mass-transfer coefficient
h_H = heat-transfer coefficient, equation 2
h_M = mass-transfer coefficient, equation 3
h_0 = mass-transfer coefficient in the absence of injection tubes (i.e., from a continuous flat surface)
M = blowing parameter or blowing rate (ratio of mass flux of injected air to mass flux of free stream)
$\dot{m}$ = mass flux of naphthalene from surface
n = a constant
Nu = Nusselt number
Pr = Prandtl number
q = wall heat flux
Sc = Schmidt number
Sh = Sherwood number
T_{aw} = adiabatic wall temperature
T_r = free stream recovery temperature
T_2 = film coolant temperature
X = downstream distance from downstream edge of injection holes
Z = lateral distance across span measured from center of injection holes

Greek Symbols

ρ_w = density of naphthalene at surface
ρ_{iw} = density of naphthalene at an impermeable surface
η = film cooling adiabatic wall effectiveness, equation 1

dimensions of the tunnel test section are 0.355-m high, 0.61-m wide, and 2.5-m long. Sidewalls for the present experiment reduced the width of the channel to about 0.20 m. These walls were set to diverge slightly to maintain a uniform free stream speed of the air in the tunnel. A wire trip followed by sand paper was placed about 0.41 m upstream of the naphthalene plate. The mainstream velocity and the boundary layer profiles were determined using a total pressure probe and static pressure wall taps. With the normal free stream speed of 15 m/s, the boundary layer displacement thickness at the upstream edge of the injection holes was about 2.2 mm. The Reynolds number based on this velocity and D (11.7 mm) was 11×10^3. Extrapolation of the boundary layer thickness upstream indicated that the effective starting point of the boundary layer was 155 mm upstream of the trip wire.

Air was injected through six tubes, spaced three-diameters apart across the span. These tubes are essentially the same as those used in an earlier study [13]. They have an 11.7-mm i.d., a 14.3-mm o.d., and are long enough to assure fully developed turbulent flow at the exit in the absence of a mainstream flow. The flow injected through the tubes could be controlled by needle valves. The overall injected flow was determined by measuring the pressure drop across an orifice plate. Three of the tubes were cut off and the extensions to the plate surface were part of the injection system included in the naphthalene plate shown in Fig. 1. The injection tube Reynolds number was about 2300 at $M = 0.2$ and 23,000 at $M = 2$.

The removable section (Fig. 1) consists of the naphthalene test plate, its support, and three injection tubes, as well as temperature-measuring instrumentation. The main body of the naphthalene test plate is made of aluminum. The opening in the tunnel floor in which the plate sits is 241-mm long by 170-mm wide. The actual naphthalene surface within this plate is 184-mm long by 95-mm wide. Thermocouples are embedded in the test plate to measure the temperature at the naphthalene surface. The tip of the center injection tube near which measurements were made was beveled to reduce the metal exposure so that mass-transfer measurements within 0.1 D of the tube could be made. When the test plate is in the tunnel floor, the three tubes are connected to the lower portion of the injection system through tight plastic sleeves.

In preparing the naphthalene mold, the test plate was placed in an inverted position on a lapped stainless steel plate. The perforated plate within the system (cf. Fig. 1) was heated to about 80°C, somewhat below melting point of naphthalene. After pouring in the molten naphthalene, the system was allowed to cool. When the outer naphthalene surface reached about 40°C, it was freed by a sharp blow to the stainless-steel plate.

Measurements of the naphthalene surface profile were taken before and after exposure in the wind tunnel. For these measurements, the test plate was placed on a lathe bed which can be translated in the X and Z directions. A mechanical depth gauge accurate to approximately 5×10^{-4} mm with a range of 0.2 mm was used to determine surface profiles from measurements at 370 locations in the area shown in the rectangle on Fig. 1. Only differences in naphthalene height or thickness are required. However, after exposure in the wind tunnel, the test plate could not be replaced in exactly the same location on the measuring bed as it had been when the first surface measurements were taken. Therefore, at each Z location, measurements were taken at reference points on the aluminum frame of the test plate. The distance from a point on the naphthalene surface to a line connecting these reference points was determined both before and after exposure in the wind tunnel. The difference between each pair of corresponding measurements is the local change in naphthalene thickness, equivalent to the naphthalene sublimed, and was generally between ~.05 mm to ~.18 mm.

Due to the great sensitivity of the naphthalene vapor pressure to temperature, care was taken to be sure the system was isothermal. Temperatures were measured continuously using thermocouples embedded close to the naphthalene surface, along the injection tubes, and in the mainstream. Usually, the naphthalene surface could be maintained within 0.25°C of the free stream and the injected air within 0.15°C of the free stream.

Measurements of the surface temperature were used to calculate naphthalene vapor pressure and density or concentration. These measurements were taken every five minutes and an average concentration was used to determine the value over the period of the test. At the lowest blowing rate the naphthalene surface was exposed for approximately 90 min. At the highest blowing rate the test runs lasted about 60 min.

Knowing the change of depth and the density of solid naphthalene, the local mass transfer over the period of exposure in the wind tunnel could be obtained. From this and the surface concentration, the mass-transfer rate and the Sherwood number were determined. The measurements were corrected for sublimation during the time profiles were being measured, the time to set up the test plate in the tunnel, and the time for remounting it in the measuring apparatus. The total correction was typically of the order of 6.5 percent of the smallest change in naphthalene thickness.

Mass-Transfer Results

The first measurements of mass transfer were made on a flat uninterrupted surface of naphthalene. From the measurements Sherwood numbers and Stanton numbers for mass transfer were calculated. These results compare favorably to a correlation for heat transfer from a flat surface to a turbulent boundary layer of air taking into account an "unheated" starting length and using equation 5. The experimental points are about 2 percent above the prediction line and have an almost identical slope.

The measurements on the continuous naphthalene surface indicate the validity of the mass-transfer analogy for studying heat transfer. They also give the reference point for mass-transfer coefficients on an undisturbed surface, h_0, to which the results with injection are compared.

The influence of injection through the tubes on mass transfer is presented in terms of the ratio of the mass-transfer coefficient with and without injection, h/h_0. Note that h_0 is determined in the absence of the injection tubes as well. Figure 2 contains plots of the relative mass transfer with distance downstream at different lateral positions, Z. Each part of the figure is for a different blowing rate. The position $X = 0$ corresponds to the downstream edge of the injection holes and $Z = 0$ to the center of a hole.

The results are also plotted in contour form in Fig. 3 for different blowing rates. These contours were obtained from cross plots of the data shown in Fig. 2. The ellipses in Fig. 3 represent the inside surface of the injection hole in the plate of the naphthalene. Contours for h/h_0 less than 1.25 are not drawn as they tend to spread out over large areas.

Several special comparison tests were made. To obtain the test data labelled $M = 0$, the lower portion of each injection tube was plugged. These results essentially show the effect of the tube opening without any net outflow. A test with the top of the injection hole plugged with a nonsubliming material to give a smooth surface yielded results which were very close to those for a continuous surface of naphthalene. The slight difference observed could be explained by the different concentration boundary condition at the plugged hole.

We had postulated that the jets, especially at high blowing rate, might act like solid rods blocking the mainstream flow and produce eddies similar to those around a tube in crossflow. To examine this, a set of mass-transfer data was

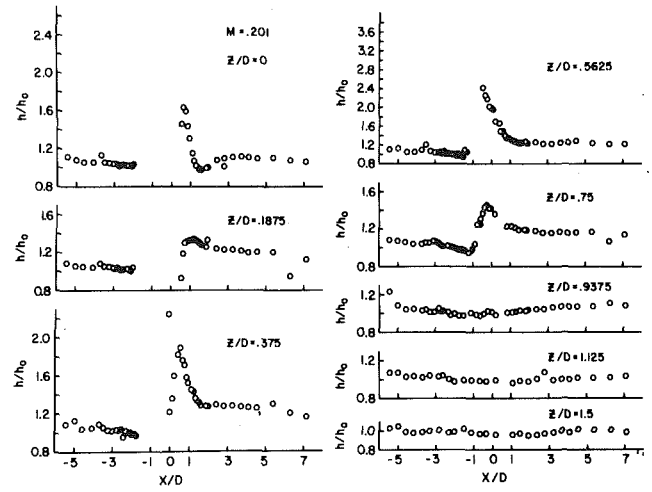

Fig. 2(*a*) Mass-transfer coefficient for $M = .2$

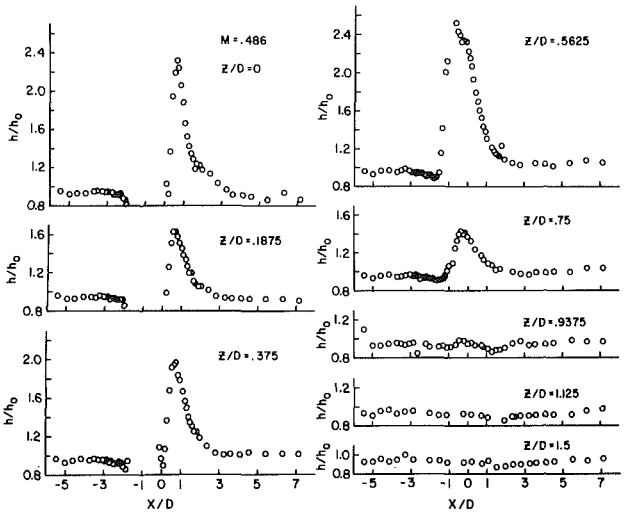

Fig. 2(*b*) Mass-transfer coefficient for $M = .49$

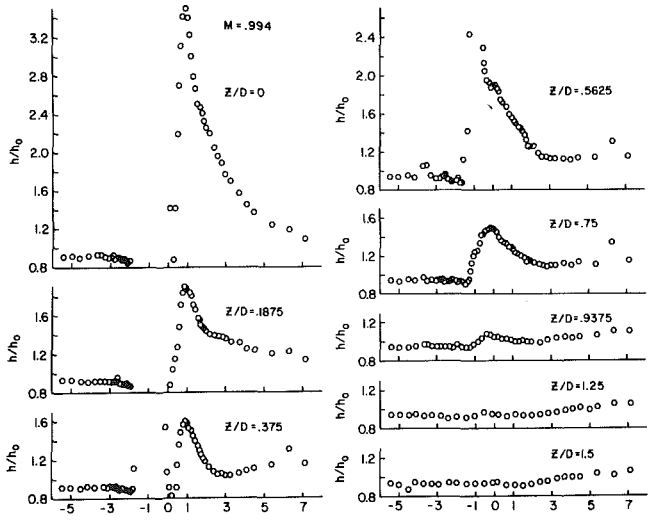

Fig. 2(*c*) Mass-transfer coefficient for $M = 1.0$

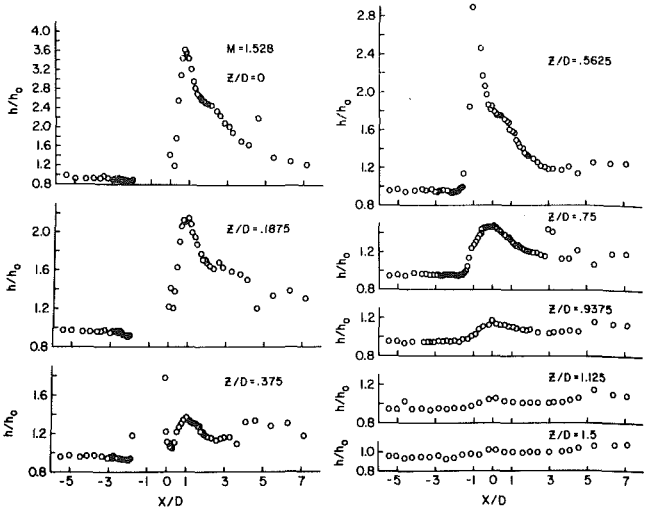

Fig. 2(*d*) Mass-transfer coefficient for $M = 1.53$

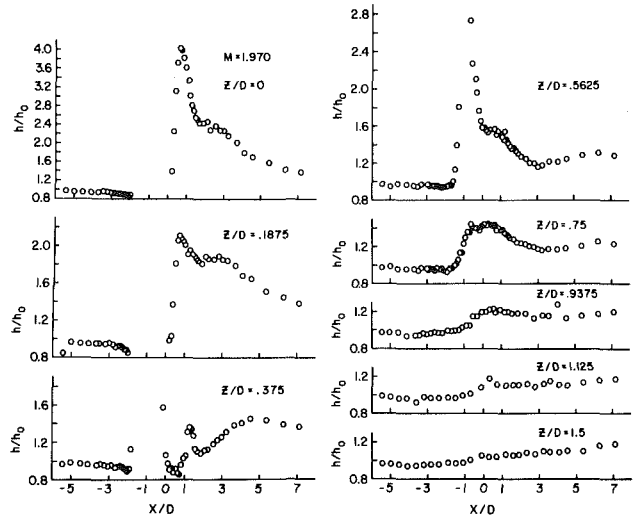

Fig. 2(*e*) Mass-transfer coefficient for $M = 1.97$

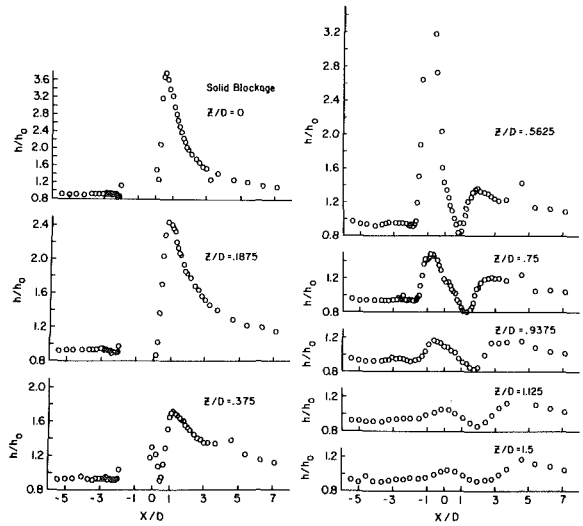

Fig. 2(*f*) Mass-transfer coefficient for solid blockage

obtained with aluminum rods placed into the injection holes to provide some solid blockage of the mainstream crossflow. The rods extended up into the flow a distance of 50 mm past the downstream end of the naphthalene surface.

There are few earlier tests that show the effect of injection on heat and mass transfer close to an injection hole. For a row of inclined holes, heat-transfer data were obtained [9] no closer than $X/D \sim 5.5$. In that study, there was concern for the effect of heat conduction close to injection. The present results are in reasonably good agreement with data from reference [9], although close to the centerline, somewhat higher values of h/h_0 were found with mass transfer. This may be due to the difference in Reynolds number in the two studies, the effect of heat conduction in the tests of reference

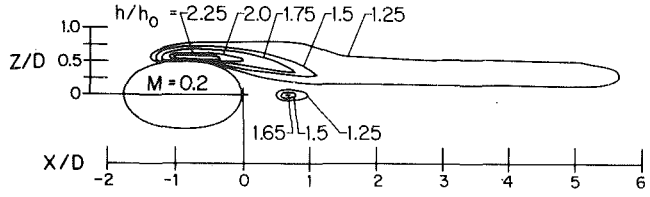

Fig. 3(a) $M = 0.2$

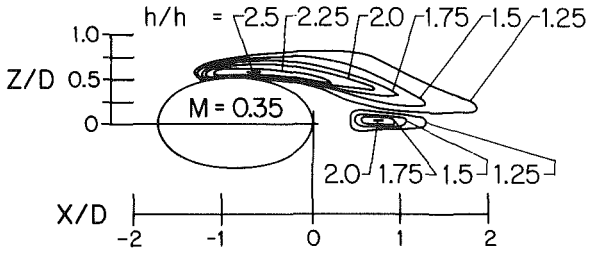

Fig. 3(b) $M = 0.35$

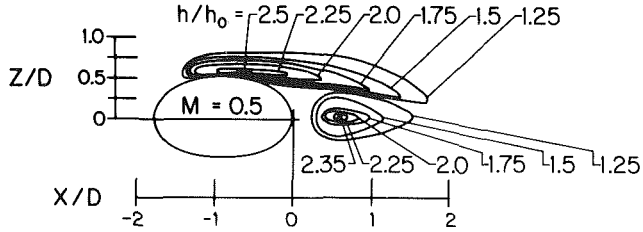

Fig. 3(c) $M = 0.5$

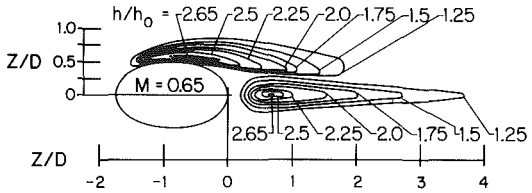

Fig. 3(d) $M = 0.65$

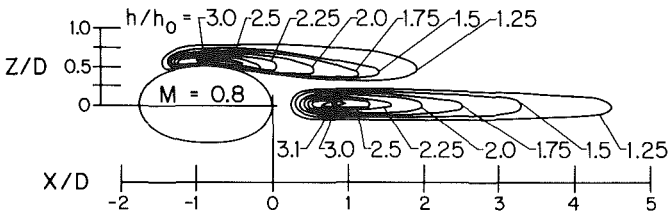

Fig. 3(e) $M = 0.8$

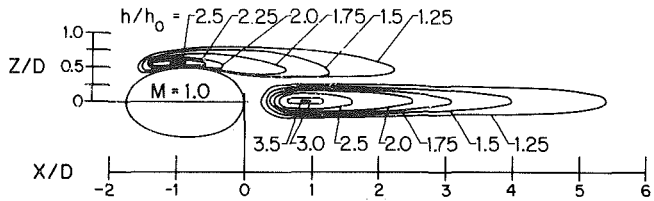

Fig. 3(f) $M = 1.0$

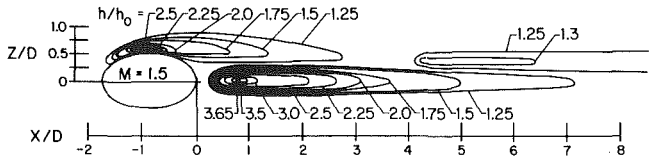

Fig. 3(g) $M = 1.5$

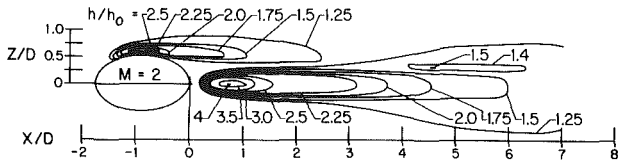

Fig. 3(h) $M = 2.0$

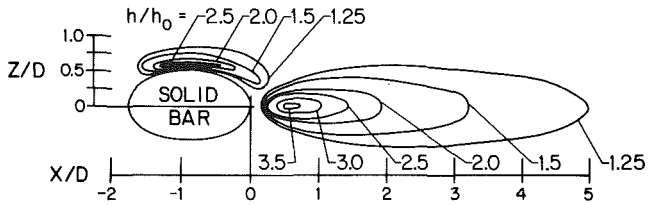

Fig. 3(i) for solid blockage

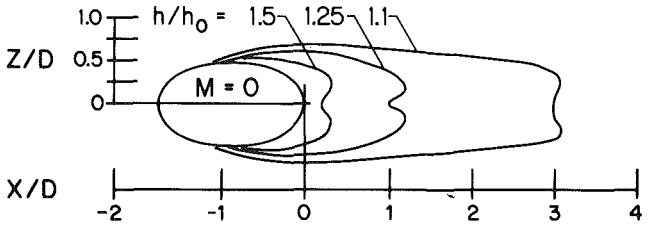

Fig. 3(j) for $M = 0$

Fig. 3 Contours of constant h/h_0

[9], or the lower values of h_0 at a given X/D due to an active surface upstream of the injection holes for this study versus no upstream heating in reference [9].

The results shown in Figs. 2 and 3 can perhaps best be described by considering different regions on the surface around an injection hole. Referring to Fig. 4, (A) corresponds to the region upstream of the injection hole, (B) to a region midway between two holes, (C) to the region immediately downstream of a hole where a low transfer coefficient was observed, (D) to the region of high mass-transfer coefficient immediately adjacent to an injection hole, (E) to the region of high transfer coefficient downstream of the injection hole, and (F) to a region of relatively high transfer coefficient some distance downstream of the injection hole which occurs at the highest blowing rates.

Upstream of the injection hole (region (A)), the mass transfer is little affected by the presence of the jet. At intermediate blowing rates there is a slight decrease of mass transfer, probably due to the slowing down of the mainstream fluid by the jet. At small M there is not enough flow to slow down the mainstream air, while at large M the downstream velocity component of the jets is close to that of the mainstream fluid. With the solid bar (Fig. 2), there is an increase in the mass-transfer coefficient close to the bar. This is probably due to secondary flow similar to that observed near cylinders set normal to a solid surface; the flow induced by the boundary-layer cylinder interaction sweeps out a region upstream of the cylinder. The effect would be smaller with a cylinder inclined downstream.

In the central area between the holes (region (B)), injection

has little effect on the mass-transfer coefficient except at the highest blowing rates. Even then the increase is only of the order of 10 percent, which may be due to mainstream acceleration caused by jet blockage.

Immediately downstream of the injection hole (region (*C*), relatively low mass-transfer rates occur. The minimum occurs at 0.2 to 0.3 diameters downstream for most M. For zero blowing rate, however, there is actually a maximum value at the edge of the injection hole downstream edge. The reduced mass transfer in region C for most M can be explained by the action of the jets creating a stagnation region immediately downstream of injection. The blowing rate has little effect on this region.

For all flow rates other than $M=0$, there is an area (region (*D*)) of very high mass-transfer coefficient along the sides of the injection hole which extends some distance downstream (cf., Fig. 3). This high mass-transfer results from the jet-mainstream interaction creating large shear stresses and eddies at the edges of the jets. A similar region of high mass-transfer rate is present with solid blockage.

Region (*D*) (defined by the $h/h_0=1.25$ contour) extends from $X/D\cong -1.2$ to $X/D\cong 6.$ at $M=0.2$. At $M=0.5$, this length is considerably smaller but gradually increases as M is increased above this point. The minimum, with M, in the extent of region (*D*) may be due to lift-off of the jet from the surface. The maximum value of h/h_0 along the sides of the injection holes is between 2.5 and 3.0 for most M. This maximum usually occurs between X/D of -1 and -0.5. The narrow width of the high mass-transfer coefficient region suggests the scale of the eddies created by the jet-mainstream interaction. This region of high mass-transfer extends considerably further downstream with the jets as contrasted to solid blockage.

Downstream of the injection hole (region (*E*)), the maximum mass transfer occurs at $X/D\cong .75$ for most values of M and at $X/D\cong 0.55$ for solid blockage. The maximum h/h_0 in this region increases from 1.65 at $M=0.2$ to 4.0 at $M=2.0$; it is 3.5 for solid blockage. As M increases from 0.2 to 0.5, the width of the region (defined by the $h/h_0=1.25$ contour) increases and then remains about the same at higher M. The length of the region increases from 1.5 to 3.8 diameters downstream as M increases from 0.5 to 0.65. Further increases in M lengthen the region out to $X/D\cong 7.0$ at $M=1.5$ and past the edge of the naphthalene plate ($X/D=7.16$) at $M=2$. The shape of this region is affected by separation of the jet from the surface which begins to occur at $M\cong 0.5$. With separation, the mainstream flow penetrates beneath the jet and forms large eddies which increase the mass transfer. At small M the jet remains attached to the surface and the increase in mass transfer is quite small. At high M the pattern of mass transfer due to the jets is similar to that with solid blockage except that in the former case the downstream region of high mass transfer is narrower.

At high M, (1.5 and 2.0), two other areas of high transfer coefficient (region (*F*)) are present downstream of injection. This region, symmetrical about the line $Z=0$, apparently results from the partial reattachment of the jet to the surface. A jet entering a cross stream can form a kidney-shaped cross section with two symmetrical lobes that extend close to the surface [19]. When the flow in these lobes touches the surface some distance downstream of injection, increased wall shear and mass transfer can occur.

It is also of interest to see how the mass transfer averaged across the span of the plate varies with position and blowing rate. For Fig. 5, averages were obtained by numerically integrating the local mass-transfer coefficient measurements across the span, considering only the area where there was an active surface and not the open area of the injection hole. A characteristic of these plots is the presence of two maxima. One is due to the high transfer coefficients in region (*D*) and is

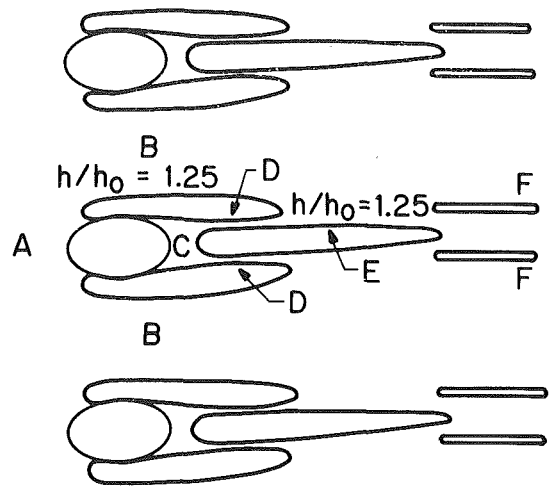

Fig. 4 Regions of high and low mass-transfer coefficient around injection holes

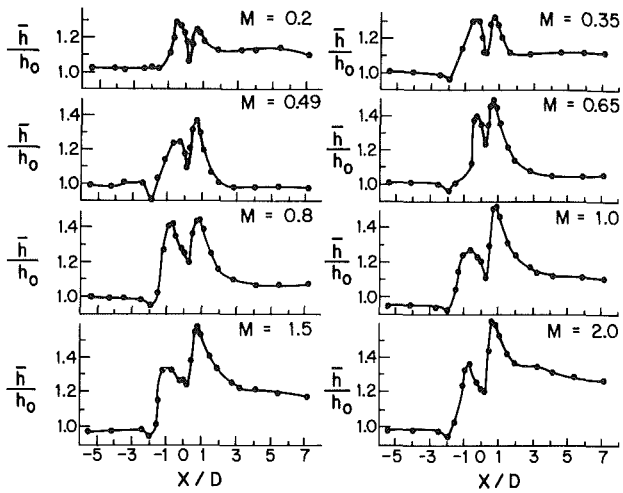

Fig. 5 Average (across span) values of h/h_0 for M = 0.2 to 2.0

at X/D between -1 and -0.5. The second peak at X/D between 0.5 and 0.9 is chiefly due to the high mass-transfer in region (*E*) directly downstream of the hole. As the blowing rate increases, the magnitude of the upstream peak stays approximately constant at about 1.35 while the value of the second maximum increases.

Summary

The mass-transfer coefficient on a surface near a row of holes through which air is injected has been measured. The measurements indicate large increases in the mass transfer close to the sides of the injection holes (region (*D*)) and some distance downstream of the holes (region (*E*)). The results also indicate that the influence of the jets at high blowing rates on the mass transfer is similar in many respects to the effect of solid blockage that occurs if a solid rod is placed into the injection hole and extended far out into the mainstream.

Acknowledgment

Support for the completion of this work from the U.S. Army Research Office under contract number DAAG-29-79-C-0117 is gratefully acknowledged.

References

1 Goldstein, R. J., "Film Cooling," in *Advances in Heat Transfer*, edited by T. Irvine and J. P. Hartnett, Vol. 7, Academic Press, New York, 1971, pp. 321–379.

2 Metzger, D. E., and Fletcher, D. D., "Evaluation of Heat Transfer for Film-Cooled Turbine Components," *J. Aircraft*, Vol. 8, 1971, pp. 33–38.

3 Metzger, D. E., Kuenstler, P. A., and Takeuchi, D. I., "Heat Transfer with Film Cooling Within and Downstream of One to Four Rows of Normal Injection Holes," ASME Paper No. 76-GT-83, 1976.

4 Liess, C., "Experimental Investigation of Film Cooling with Ejection From a Row of Holes for the Application to Gas Turbine Blades," ASME *Journal of Engineering for Power*, Vol. 97, 1975, pp. 21–27.

5 Mayle, R. E., and Camarata, F. J., "Multihole Film Cooling Effectiveness and Heat Transfer," ASME JOURNAL OF HEAT TRANSFER, Vol. 97, 1975, pp. 534–538.

6 Crawford, M. E., Kays, W. M., and Moffat, R. J., "Full-Coverage Film Cooling on Flat Isothermal Surfaces: A Summary Report on Data and Predictions," Report No. HMT-30, Department of Mechanical Engineering, Stanford University, 1979.

7 Schultz, D. L., Oldfield, M. L. G., and Jones, T. V., "Heat Transfer Rate and Film Cooling Effectiveness Measurements in a Transient Cascade," AGARD-CPP-281, 1980.

8 Louis, J. F., "Shock Tunnel Studies of Heat Transfer and Film Cooling Effectiveness," *Proceedings of the 10th Int. Shock Tube Symposium*, Kyoto, Japan, Vol. 5, 1975, pp. 452–471.

9 Erikson, V. L., and Goldstein, R. J., "Heat Transfer and Film Cooling Following Injection through Inclined Circular Tubes," ASME JOURNAL OF HEAT TRANSFER, Vol. 96, 1974, pp. 239–245.

10 Jabbari, M. Y., and Goldstein, R. J., "Adiabatic Wall Temperature and Heat Transfer Downstream of Injection Through Two Rows of Holes," ASME *Journal of Engineering for Power*, Vol. 100, 1978, pp. 303–307.

11 Goldstein, R. J., Rask, R. B., and Eckert, E. R. G., "Film Cooling with Helium Injection into an Incompressible Flow," *International Journal of Heat and Mass Transfer*, Vol. 9, 1966, pp. 1341–1350.

12 Kacker, S. C., and Whitelaw, J. H., "The Dependence of the Impervious Wall Effectiveness of a Two-Dimensional Wall-Jet on the Thickness of the Upper Lip Boundary Layer," *International Journal of Heat and Mass Transfer*, Vol. 10, 1967, pp. 1623–1624.

13 Pedersen, D. R., Eckert, E. R. G., and Goldstein, R. J., "Film Cooling with Large Density Differences Between the Mainstream and the Secondary Fluid Measured by the Heat-Mass Transfer Analogy," ASME JOURNAL OF HEAT TRANSFER, Vol. 99, 1977, pp. 620–627.

14 Christian, W. J., and Kezios, S. P., "Experimental Investigation of Mass Transfer by Sublimation from Sharp-Edged Cylinders in Axisymmetric Flow With Laminar Boundary Layer," *1957 Heat Transfer Fluid Mechanics Institute*, Stanford University Press, Stanford, Calif., 1957, pp. 359–381.

15 H. H. Sogin, "Sublimation from Disks to Air Streams Flowing Normal to Their Surfaces," ASME Transactions, Vol. 80, 1958, pp. 61–69.

16 Lee, K., and H. Barrow, "Transport Processes in Flow Around a Sphere with Particular Reference to the Transfer of Mass," *International Journal of Heat and Mass Transfer*, Vol. 11, 1968, pp. 1013–1026.

17 Kan, S., Miwa, K., Morishita, T., Munakata, Y., and Nomura, M., "Heat Transfer of a Turbine Blade," Tokyo Joint Int. Gas Turbine Conf., Paper *JSME*-30, 1971.

18 Saboya, F. E. M., and Sparrow, E. M., "Local and Average Transfer Coefficient for One-Row Plate Fin and Tube Heat Exchanger Configurations," JOURNAL OF HEAT TRANSFER, Vol. 96, 1974, pp. 265–272.

19 Ramsey, J. W., and Goldstein, R. J., "Interaction of a Heated Jet with a Deflecting Stream," JOURNAL OF HEAT TRANSFER, Vol. 93, 1971, pp. 365–373.

A. Snyder

R. Siegel
Fellow ASME

National Aeronautics and Space Administration, Lewis Research Center, Cleveland, Ohio 44135

Determination of Boundary Shape of Cooled Porous Region

The shape of a cooled porous wall section is found that will provide a uniform surface temperature, as dictated by material limitations, when the surface is subjected to spatially nonuniform heating. In the analysis, local temperatures and pressures in the porous material are expressed in terms of a potential function. From the imposed thermal conditions, this potential function is governed by the dual constraints of both its value and its normal derivative being specified along the heated surface. The unknown shape of this surface is obtained by meeting these dual conditions. The analytical method uses a generalized conformal mapping procedure that includes a curved boundary. The coolant flow can be compressible or incompressible, and its viscosity can depend on temperature.

Introduction

In critical cooling applications where a wall must be protected from a high external heat load, it can be effective to use transpiration cooling. A section of the wall is made of porous material so that coolant can be pumped through it to flow out along the boundary exposed to the heat loading. Since the coolant flow rate depends on the flow resistance of the porous medium, the shape of the region will regulate the distribution of coolant flow exiting along the exposed surface. The shape can thus be tailored to achieve a given amount of cooling along the surface or a given surface temperature distribution.

In this paper the shape of a porous cooled medium will be obtained to maintain the exposed surface at a constant temperature such as would be dictated by temperature limitations of the material. The shape is found for the condition of an imposed heat loading that varies along the surface. As pointed out in [1], the type of inverse heat conduction problem that has been least investigated is where the geometry is partially unknown, as in the present situation.

The present analysis is built on the foundation developed in [2-4]. The flow can be incompressible or compressible, and the fluid viscosity can be a function of temperature. The flow is governed by Darcy's law, and local thermal equilibrium between the fluid and solid are assumed within the porous material. For these conditions the heat-transfer characteristics are related to a potential function found by solving Laplace's equation in the region. However, since the region has an unknown shape, the solution cannot be found in a direct manner.

In [4] a conformal mapping procedure was devised for analyzing a porous insert in a wall with a known curved boundary. A generalized Schwarz-Christoffel transformation was used to map the porous region into a rectangle. Since the region in the present analysis can be shown to occupy a rectangle in the coordinates of a potential plane, the mapping in [4] is used here in an inverse way. To initiate the mapping, the required coolant distribution is used in a locally one-dimensional solution to estimate an initial region shape; the procedure in [4] then provides the actual coolant distribution for this shape. The error between this coolant distribution and the required distribution is used to revise the region shape. Successive corrections done in this way yield the required configuration.

To demonstrate the method and obtain useful results, porous region shapes were obtained for a few different types of heating conditions. One is a heating variation as a power of distance along the surface, and another is a cosine variation. The results show how irregular the surface must be to provide proper coolant distribution for an imposed heating nonuniformity.

Contributed by the Heat Transfer Division for publication in the JOURNAL OF HEAT TRANSFER. Manuscript received by the Heat Transfer Division October 19, 1981.

Analysis

The two-dimensional configuration to be analyzed is shown in cross section in Fig. 1. Two boundaries are porous, and the other two are insulated and are impervious to flow. Coolant from a reservoir at p_∞, t_∞ enters the porous medium through boundary, s_0, and flows out through boundary, s, which is at uniform pressure, p_s. Along s there is a nonuniform heat flux being imposed, and this boundary is to be maintained at uniform temperature. For a given $q_s(z_s)$ variation the shape of s is to be found to yield surface temperature uniformity.

General Equations and Boundary Conditions. The theory accounts for the coolant flow being either compressible or incompressible, and the coolant viscosity can be a function of temperature. The first step in this development is to briefly summarize the relations that can be used between pressure, temperature, coolant exit flow, and imposed heat flux, as derived in [2] and [3]. Then the analysis will be developed to provide a means for obtaining unknown boundary shapes.

The governing equations are conservation of mass,

$$\nabla \cdot \mathbf{u} = 0 \qquad \text{incompressible} \tag{1a}$$

$$\nabla \cdot (\rho \mathbf{u}) = 0 \qquad \text{compressible} \tag{1b}$$

Darcy's law for flow in a porous medium,

$$\mathbf{u} = -\frac{\kappa}{\mu(t)} \nabla p \tag{2}$$

energy conservation for coolant and solid in thermal equilibrium,

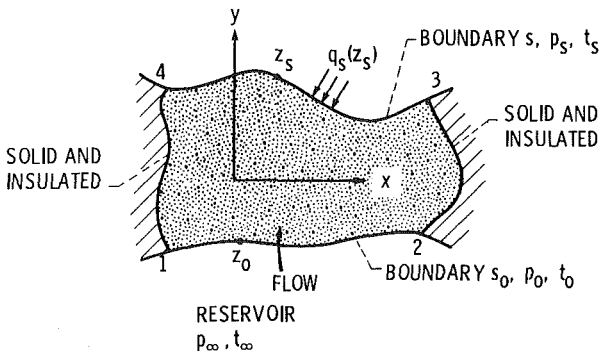

Fig. 1 Geometry and boundary conditions for porous cooled medium

$$\nabla \cdot \mathbf{q} = 0 \qquad \text{where } \mathbf{q} = -k_m \nabla t + \rho \mathbf{u} c_p t \tag{3}$$

and the perfect gas law needed for the compressible case,

$$p = \rho R t \tag{4}$$

The boundary conditions are as follows: Along the coolant exit surface, s,

$$p = p_s = \text{constant} \tag{5}$$

$$t = t_s = \text{constant} \tag{6}$$

$$k_m \mathbf{n}_s \cdot \nabla t = q_s(z_s) \tag{7}$$

Along the surface, s_0, in contact with the reservoir

$$p = p_0 = p_\infty = \text{constant} \tag{8}$$

$$k_m \mathbf{n}_0 \cdot \nabla t = \rho c_p (t - t_\infty) \mathbf{n}_0 \cdot \mathbf{u} \tag{9}$$

At the boundaries that are both solid and insulated, the components of $\mathbf{u}$ and $\mathbf{q}$ normal to the boundaries are both zero.

Relations in Terms of Potential Function. In [2] and [3] it is shown that the temperature distribution, coolant flow, and heat flow can be found in terms of a potential function, ϕ, that satisfies Laplace's equation $\nabla^2 \phi = 0$ in the porous region. Along s_0 the potential function is $\phi = 0$, and along s, $\phi = \phi_s$. The ϕ_s is implicitly related to the pressure ratio p_s/p_∞ by the following two relations, in which $T_0 = t_0/t_\infty$ is an intermediate quantity. The ϕ_s is directly related to T_0 by

$$\phi_s = ln\left(\frac{T_s - 1}{T_0 - 1}\right) \tag{10}$$

For a given ϕ_s value the T_0 is found from (10) and then the following integral can be carried out

$$-\frac{1}{\lambda}\int_{T_0}^{T_s} \frac{MT}{1-T}\, dT = 1 - P_s \tag{11}$$

where P_s is the pressure ratio p_s/p_∞. Thus, ϕ_s is found from the specified pressure ratio by using both equations (10) and (11). Compressibility and viscosity variations with temperature are accounted for by the definitions of M and P in the Nomenclature.

The coolant exit velocity through surface s is given by

$$\frac{wc_p}{k_m} \rho_s \mathbf{u}_s(z_s) \cdot \mathbf{n}_s = |\tilde{\nabla} \phi|_s \tag{12}$$

and the heat flux along s is related to ϕ by

$$\frac{q_s(z_s) w}{k_m (t_s - t_\infty)} = |\tilde{\nabla} \phi|_s \tag{13}$$

The temperature distribution in the medium is related to ϕ by

$$T(x,y) = 1 + (T_s - 1) e^{-[\phi_s - \phi(x,y)]} \tag{14}$$

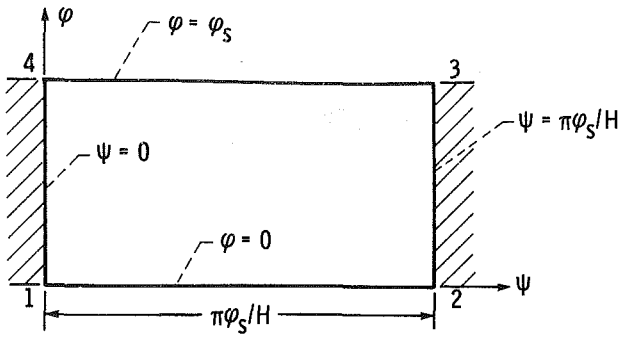

Fig. 2 Porous region mapped into rectangle in *W*-plane

The constraint on ϕ of satisfying equation (13) will lead to the unknown shape of the region.

Potential Plane Geometry for Present Problem. The foregoing relations give the heat transfer and fluid flow quantities in terms of ϕ. If ϕ can be obtained as a function of x and y, then the desired quantities will be known in the physical geometry. The ϕ is defined in [2] as a potential function for energy transfer by the combination of heat conduction and fluid transport. Since conduction and fluid transport are zero at the boundaries that are insulated and solid, the derivative of ϕ is zero normal to these boundaries. The $\phi = 0$ on s_0 and $\phi = \phi_s$ on s, so that in a rectangular coordinate system with ϕ as ordinate, Fig. 2, the s_0 and s surfaces will be mapped into horizontal lines. Since the constant ϕ lines are normal to the other two boundaries, these boundaries are mapped into vertical lines, and the porous region occupies a rectangle. It is convenient for what follows to let the width of the rectangle be $\pi\phi_s/H$, which is general because H can be assigned a range of values when solutions are carried out.

In Fig. 2 the horizontal lines of constant ϕ are known in terms of ϕ_s. If the mapping between Figs. 2 and 1 can be found, then $\phi(x,y)$ can be defined in the physical geometry. Conformal mapping can be used since ϕ is a solution to Laplace's equation. The shape of the boundary s is unknown in the physical plane and will be obtained during the mapping process subject to the dual boundary conditions imposed at that boundary.

The specific geometry of interest here is a porous insert placed in a solid wall to deal with a region that requires enhanced cooling, Fig. 3(*a*). The region is shown in dimensionless form in Fig. 3(*b*). In [4], the heat-transfer characteristics were analyzed for a porous insert having a known curved boundary of arbitrary shape, and a Schwarz-Christoffel method was developed from [5] to transform a

Nomenclature

A = coefficient in equation (31)
c_p = specific heat at constant pressure
F = elliptic integral of the first kind
$F(Z_s)$ = function describing surface heat flux variation
H = height of region mapped into rectangle in V-plane
K = complete elliptic integral of the first kind
k = modulus of elliptic integral: $k' = \sqrt{1-k^2}$
k_m = effective thermal conductivity of porous material
L_s = total length of curved porous surface
M = incompressible flow, $M = \frac{1}{2}\frac{\mu}{\mu_\infty}\frac{t_\infty}{t}$; compressible flow, $M = \mu/\mu_\infty$
n = exponent in power variation of q_s
$\mathbf{n}$ = unit outward normal vector
P = incompressible flow, $P = p/p_\infty$; compressible flow, $P = (p/p_\infty)^2$
p = pressure
q = heat flow rate per unit area
$\mathbf{q}$ = energy flux vector
R = gas constant
S,s = coolant exit surface of porous medium
S_0,s_0 = coolant inlet surface of porous medium
s = distance along exit surface; S dimensionless distance, s/w
T = temperature ratio, t/t_∞
t = absolute temperature
V = intermediate mapping variable, $V = \alpha + i\beta$

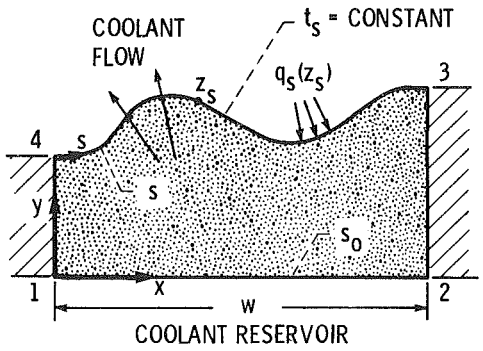

(a) PHYSICAL GEOMETRY.

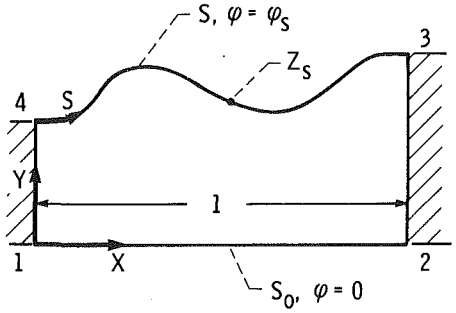

(b) REGION IN DIMENSIONLESS COORDINATES.

Fig. 3 Porous insert in a solid wall

geometry such as Fig. 3(*b*) into a rectangle of width, π, as in Fig. 4. Since between Figs. 2 and 4 there is the simple relation, $dW/dV = \phi_s/H$, this mapping method can be used for the present analysis.

The mapping must be done such that equation (13) is satisfied. In this regard it is helpful to use a reference heat flux, q_r, defined by

$$q_s(Z_s) = q_r(Z_s = 0)F(Z_s) \tag{15}$$

where $F(Z_s) = 1$ at $Z_s = 0$. Then equation (13) gives

$$\frac{q_r w}{k_m(t_s - t_\infty)} F(Z_s) = |\tilde{\nabla}\phi|_s \tag{16}$$

Using the relations $|\tilde{\nabla}\phi|_s = \left[\left(\frac{\partial\phi}{\partial X}\right)^2 + \left(\frac{\partial\phi}{\partial Y}\right)^2\right]^{1/2}\Big|_s$

and $$\frac{dW}{dZ} = \frac{\partial\phi}{\partial X} + i\frac{\partial\psi}{\partial X} = \frac{\partial\phi}{\partial X} - i\frac{\partial\phi}{\partial Y},$$

equation (16) can be written

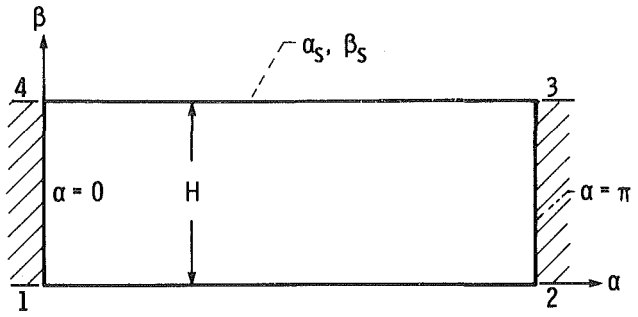

Fig. 4 Region mapped into rectangle in the *V*-plane

$$\frac{q_r w}{k_m(t_s - t_\infty)} F(Z_s) = \left|\frac{dW}{dZ}\right|_s$$

$$= \left|\frac{dW}{dV}\frac{dV}{dZ}\right|_s = \frac{\phi_s}{H}\left|\frac{dV}{dZ}\right|_s \tag{17}$$

Integrating along the entire surface, s, gives

$$\frac{q_r w}{k_m(t_s - t_\infty)} \int_{Z_4}^{Z_3} F(Z_s)\,dZ_s = \frac{\phi_s}{H}\int_{V_4}^{V_3} dV = \frac{\phi_s}{H}\pi \tag{18}$$

Let $\text{INT}\,F(Z_s) \equiv \int_{Z_4}^{Z_3} F(Z_s)\,dZ_s$ so that

$$\frac{q_r w}{k_m(t_s - t_\infty)\phi_s} = \frac{\pi}{H\,\text{INT}\,F(Z_s)} \tag{19}$$

Then, dividing (17) by (18), gives the condition at the boundary as

$$\frac{F(Z_s)}{\text{INT}\,F(Z_s)} = \frac{1}{\pi}\left|\frac{dV}{dZ}\right|_s \tag{20}$$

A convenient quantity for normalizing equation (19) is

$$\int_0^{X_3=1} F(X_s)\,dX_s \equiv \text{INT}\,F(X_s)$$

(this can be calculated analytically if the surface heating is specified by a suitable analytical function; otherwise, numerical integration is used). In most instances the curvature of the interface will not be large so that INT $F(Z_s)$ approximately equals INT $F(X_s)$. It is thus convenient to normalize equation (19) into the form,

$$\frac{k_m(t_s - t_\infty)\phi_s}{q_r w\,\text{INT}\,F(X_s)} = \frac{H}{\pi}\frac{\text{INT}\,F(Z_s)}{\text{INT}\,F(X_s)} \tag{21}$$

In the solution a $F(Z_s)$ function will be specified and the corresponding unknown shape of the porous surface will be found. Then INT $F(Z_s)$ is evaluated. Using (21) this will

Nomenclature (cont.)

$\mathbf{u}$ = velocity vector
W = complex potential function, $\phi + i\psi$
w = width of porous insert
X, Y = dimensionless coordinates x/w, y/w
x, y = rectangular coordinates
z = complex variable $x + iy$; $Z = z/w$

Greek Symbols

α, β = real and imaginary parts of mapping variable V
δ = length in τ-plane corresponding to one side of porous region
κ = permeability of porous material
λ = parameter, $\rho_\infty c_p \kappa p_\infty / 2\mu_\infty k_m$
μ = fluid viscosity
ξ, η = real and imaginary axes of τ-plane
ρ = fluid density
τ = intermediate mapping plane, $\tau = \xi + i\eta$
ϕ = potential function
ψ = coordinate normal to lines of constant ϕ
$\tilde{\nabla}$ = dimensionless gradient, $\mathbf{i}\frac{\partial}{\partial X} + \mathbf{j}\frac{\partial}{\partial Y}$

Subscripts

A = amplitude
n = the n^{th} iteration
r = reference value
s = coolant exit surface exposed to heat load
0 = surface adjacent to reservoir
∞ = in coolant reservoir

Superscripts

$-$ = (overbar) average value

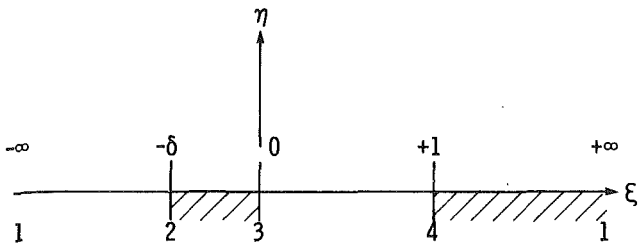

Fig. 5 Intermediate mapping plane, $\tau = \xi + i\eta$

relate $F(Z_s)$ to the parameter $k_m(t_s - t_\infty)\phi_s/q_r w$ INT $F(X_s)$ containing the reference heat flux, the width, w, of the porous insert, and the, ϕ_s, which is obtained from the pressure ratio, p_s/p_∞, by use of equations (10) and (11).

Limiting Case of Locally One Dimensional Solution. This approximation will be an aid in starting the mapping solution. For a one-dimensional case, the boundary 43 in Fig. 3(*a*) is a horizontal line. The region thickness, y_s, is uniform, and the heat flux is uniform and is q_r. The mapping between Fig. 3(*a*) and Fig. 4 gives $H = \pi y_s/w = \pi Y_s$. The $F(Z_s) = 1$ so that from (21), $k_m(t_s - t_\infty)\phi_s/q_r w = H/\pi$. Then $y_s = k_m(t_s - t_\infty)\phi_s/q_r$.

Now consider the approximate thickness variation of the porous region if the fluid and heat flows were all exactly along the y-direction (locally one-dimensional flow) even though nonuniform heating is applied. An average $\bar{Y}_s$ would be $\approx H/\pi$. Since Y_s is inversely proportional to q_s, $Y_s(Z_s)/\bar{Y}_s = \bar{q}_s/q_s(Z_s)$ for this locally one-dimensional solution. Then

$$Y_s(Z_s) \approx \frac{H}{\pi} \frac{\text{INT}\, F(Z_s)/L_s}{F(Z_s)} \tag{22}$$

where

$$L_s = \int_{Z_4}^{Z_3} dZ_s \tag{23}$$

is the total length of the curved porous surface.

Mapping to Determine Unknown Boundary Shape. The characteristics of the porous medium have been shown to be related to the mapping of the physical shape into a rectangle. In this mapping the condition of equation (20) must be satisfied. A porous insert with a known curved boundary was mapped into a rectangle in [4] (Fig. 3(*b*) with a known S into Fig. 4). An intermediate plane shown in Fig. 5 was used wherein the boundary of the porous region was unfolded onto the ξ-axis of an upper half-plane. The curved interface is along the section $0 \le \xi \le 1$, and one side of the region occupies $-\delta \le \xi \le 0$. The mapping between Figs. 4 and 5 is by elliptic functions. The height of the rectangle and the δ are

$$H = \pi K(k')/K(k) \tag{24a}$$

$$\delta = (k'/k)^2 \tag{24b}$$

The variation of α_s as a function of ξ along boundary 43 is

$$\alpha_s(\xi) = \pi\left[1 - \frac{F(\varphi,k)}{K(k)}\right] \text{ where } \varphi = \sin^{-1}\sqrt{\frac{\xi(1+\delta)}{\xi+\delta}} \tag{25}$$

The mapping for a curved surface in [4] contains two relations needed for this analysis. To save space they will not be repeated here (they are equations (28) and (29) in [4]).[1] One relation is for Z_s, and the other is the reciprocal of $dV/dZ|_s$, both as a function of ξ for $0 \le \xi \le 1$ (note that dV here corresponds to dW in [4]).

Throughout the mapping it is convenient to keep the rectangle in Fig. 4 (and hence also in Fig. 2) fixed in size. To begin the calculation a value of H is chosen; this is done by noting that H/π is approximately the average height-to-width ratio of the porous region. From equation (24*a*), the k and k' are found and then $\delta(H)$ is obtained from (24*b*). Then for a given heat flux, $F(Z_s)$ the correct physical surface $Y_s(Z_s)$ is found in an iterative manner as outlined below.

An initial $Y_s(Z_s)$ variation is obtained by using the one-

[1] Note in [4] there is a typographical error in the quantity $g_{3n}(\tau)$. In the exponent, ϕq_n should be ξ_n.

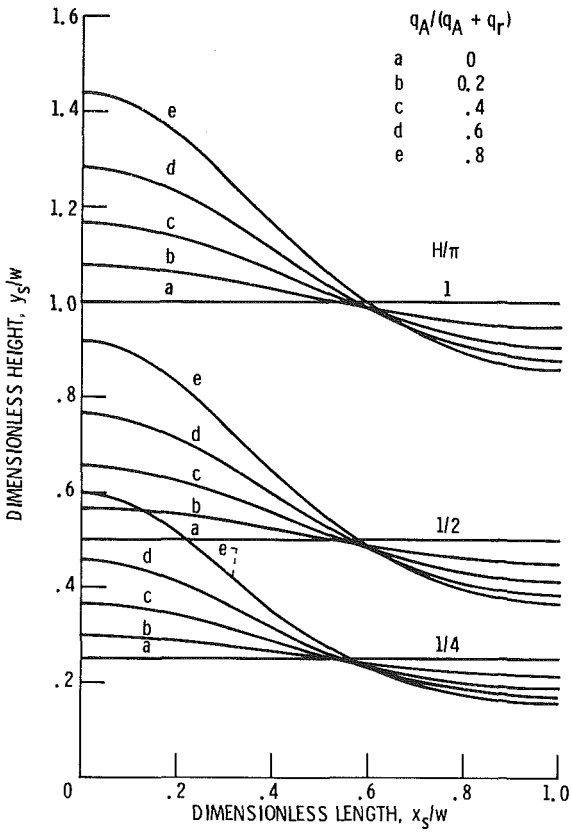

(a) POROUS MEDIA SHAPES.

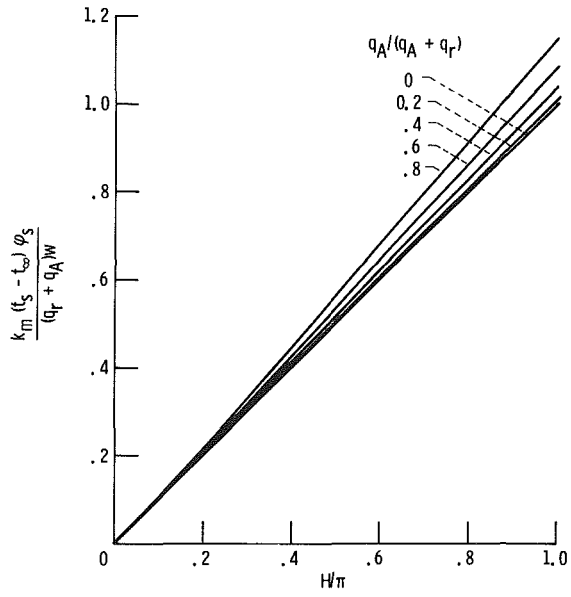

(b) RELATION BETWEEN PHYSICAL PARAMETER AND H.

Fig. 6 Results for cosine heating variation along surface, $q_s = q_r + q_A\left(1 - \cos\frac{\pi x_s}{w}\right)$

dimensional solution in equation (22). To calculate this initial variation, the L_s is found from (23) and INT $F(Z_s)$ is found as defined in relation to equation (19). Starting with $L_s = 1$, the above iterative system quickly converges. The resulting $Y_s(Z_s)$ is modified very near each end of the interface to provide the zero slope required by the constant temperature line intersecting the insulated boundary. In addition, a damping factor between 0 and 1 was used to reduce this initial $Y_s(Z_s)$ variation about the mean value of H/π. The damping decreased the number of iterations in the solution that follows since it was found that the locally one-dimensional solution (22) gives the proper trends in porous surface shape, but usually overestimates the magnitude of the surface shape variations.

With Y_s approximated as a function of X_s, and with $\delta(H)$ calculated from equation (24*b*), all the quantities required for the mapping are known, and as described in [4], the $dV/dZ|_s$ can be found by mapping the porous region into a rectangle. This mapping requires an iteration process and the δ will change somewhat with each mapping iteration. After several iterations are completed the entire $Y_s(X_s)$ curve is shifted to eliminate the difference of δ from the $\delta(H)$ specified initially corresponding to the H/π chosen. This adjustment is accomplished by applying a uniform correction to Y_s given by

$$Y_{s,\text{corrected}} = Y_s + [\delta(H) - \delta]\frac{1}{\pi}\frac{dH}{d\delta} \tag{26}$$

where $dH/d\delta$ is obtained from equation (24). After each of these corrections to Y_s, the mapping process is repeated until the quantity $[\delta(H) - \delta]/\delta(H)$ is less than a specified amount (0.001) and the $Y_s(X_s)$ shape is mapped into a rectangle within a specified tolerance.

From the mapping the $dV/dZ|_s$ is calculated and the error (ER) in satisfying equation (20) is obtained as

$$\text{ER}(X_s) = \frac{F(Z_s)}{\text{INT}\,F(L_s)} - \frac{1}{\pi}\left|\frac{dV}{dZ}\right|_s \tag{27}$$

This $\text{ER}(X_s)$ is used to correct the Y_s at each X_s location. From equations (20) and (22), the local one-dimensional solution indicates that $(1/\pi)\,|dV/dZ|_s = (H/\pi)/L_s Y_s$. Hence to make $|dV/dZ|_s$ larger, the Y_s is decreased. Then to correct the error in equation (27) to zero for the $n+1$ iteration

$$\text{ER}(X_s) = \frac{1}{\pi}\left|\frac{dV}{dZ}\right|_{s,n+1} - \frac{1}{\pi}\left|\frac{dV}{dZ}\right|_{s,n}$$

$$= \frac{H}{\pi}\frac{1}{L_s}\left(\frac{1}{Y_{s,n+1}} - \frac{1}{Y_{s,n}}\right)$$

Solving for $Y_{s,n+1}$ gives

$$Y_{s,n+1}(X_s) = Y_{s,n}(X_s)/\left[\text{ER}(X_s)\frac{\pi}{H}L_s Y_{s,n} + 1\right] \tag{28}$$

To minimize undesirable oscillation, equation (28) is under relaxed and smoothed by using,

$$Y_{s,n+1}(X_s) = (Y_{s,n} + a\bar{Y}_{s,n+1})/(1+a) \tag{29}$$

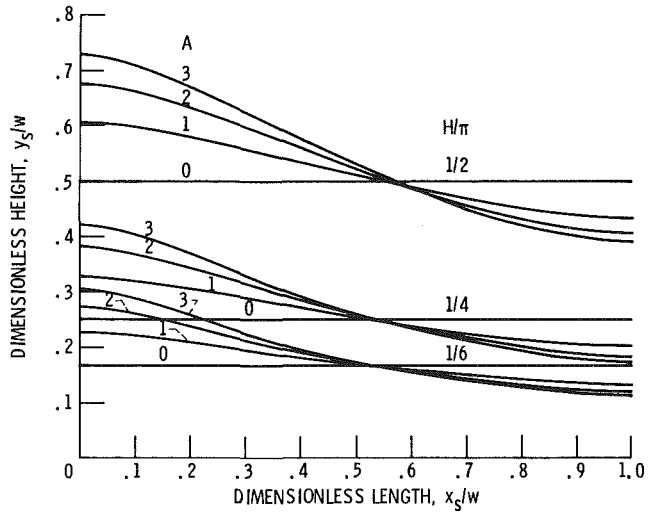

(a) SHAPES OF POROUS MEDIUM FOR LINEAR HEATING, n = 1.

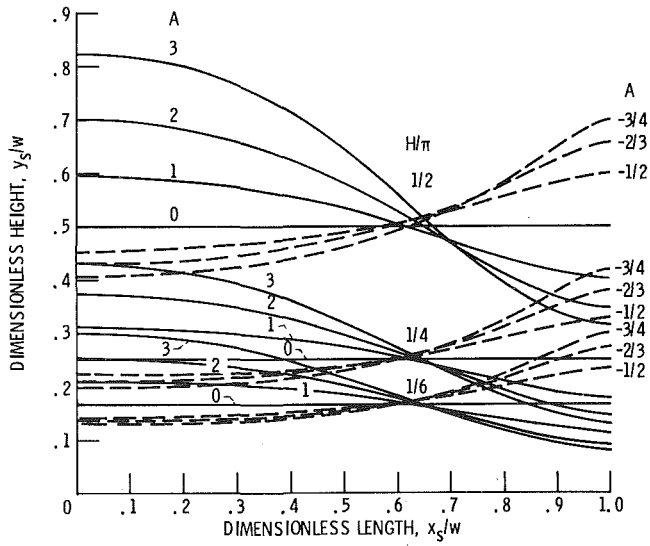

(b) SHAPES OF POROUS MEDIUM FOR CUBIC HEATING, n = 3.

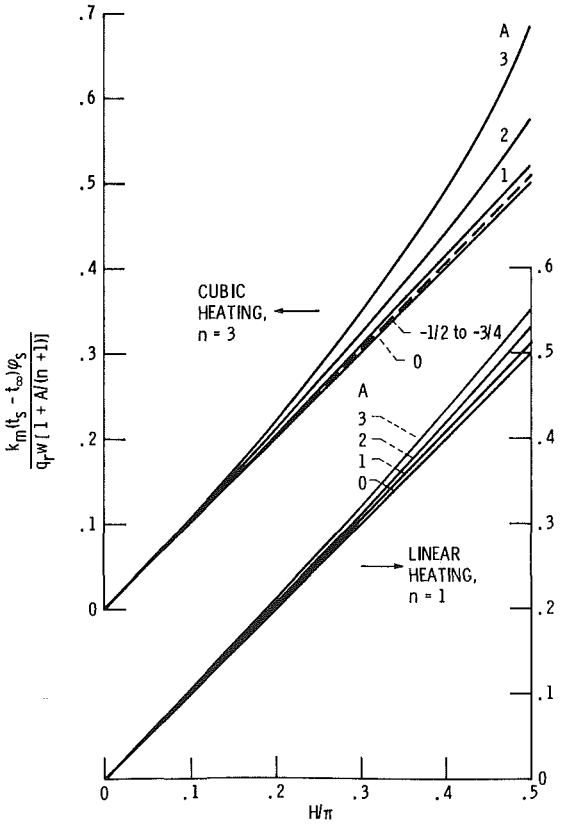

(c) RELATION BETWEEN PHYSICAL PARAMETER AND H.

Fig. 7 Results for power function heating along surface, $q_s = q_r[1 + A(s/w)^n]$

where $\bar{Y}_{s,n+1}$ is obtained from equation (28) using a weighted average error ($\overline{\mathrm{ER}}$) from the adjacent points. The a is positive constant where $a << 1$.

The $Y_s(X_s)$ variation from equation (29) is used to repeat the entire mapping process, and the procedure continued until the solution has converged such that the error $\mathrm{ER}(X_s)$ is reduced to within a small tolerance (0.001 was found adequate) for all X_s.

For each heating function, $F(Z_s)$, the calculation was repeated for several H values. This generated a series of shapes that are a function of a physical parameter as given in the next section.

Results and Discussion

Porous media shapes that provide uniform surface temperature were obtained for a number of different imposed surface heating variations. The results that follow will provide insight, for a variety of conditions, on how irregular the boundary shape must be in relation to the nonuniformity in surface heating. Results were obtained for a cosine heating variation with x_s,

$$q_s = q_r + q_A\left(1 - \cos\frac{\pi x_s}{w}\right) \tag{30}$$

and for linear and cubic variations as a function of distance s along the unknown boundary

$$q_s = q_r[1 + A(s/w)^n] \qquad n = 1,3 \tag{31}$$

Each set of results is presented in two parts. First, the shapes are given for various H values, where H is the height of the rectangle in Fig. 4, and is a convenient quantity to keep fixed for each case during the mapping process. The dimensionless group of physical quantities that governs the solution is on the left side of equation (21). This can be determined in terms of H since INT $F(Z_s)$ is found from the calculations. The dimensionless group is given in the second part of each figure and is used to express the results in the first part in terms of physical variables.

The cosine heating variation in equation (30) has an amplitude q_A and a mean heat flux $q_r + q_A$. Figure 6(a) gives the shapes of the porous medium as a function of H/π and the dimensionless amplitude $q_A/(q_A + q_r)$. When the heating is uniform, $q_A = 0$, the region is of uniform thickness, $y_s/w = H/\pi$. The relation between H and the parameter containing physical quantities is shown in Fig. 6(b). The factor INT $F(X_s)$ in equation (21) is $1 + A/(n+1)$. To use these results, the ordinate of Fig. 6(b) is calculated from the given physical conditions, and the H/π found from the curves. The shape of the porous region can then be interpolated from Fig. 6(a).

For the heating function in equation (31) the shapes of the porous regions are in Fig. 7(a) for a linear variation ($n = 1$), and in Fig. 7(b) for a cubic variation ($n = 3$) as a function of s. For negative A, the linear heating results are not needed, since for the same total heat addition the heating variation has the same straight line shape as for positive A, except with the opposite slope; the resulting shapes are the same as for positive A except that the thickness increases with x_s in an opposite way to those in Fig. 7(a).

From Fig. 7(c), it is evident that the regions having a small average thickness (small H/π) provide good cooling so that they correspond to the combination of a low surface temperature and a large imposed surface heat flux. Since locally thin regions provide large cooling flows, the thickness variation tends to be inverse to the imposed heating variation. The amplitude of the thickness variation relative to the average thickness is generally much less than the corresponding amplitude of the heating variation relative to its mean value. This relative thickness variation increases as the average thickness decreases. For the cubic variation, the surface heating varies most rapidly in the region where $s/w \approx 1$, causing the thickness of the region to change most rapidly toward the right side of the figure.

Figures 6 and 7 provide results for a variety of heating variations. These examples give the designer a good indication of how a porous cooled medium should be shaped to avoid hot spots in an environment that provides nonuniform surface heating. The analytical technique has provided a convenient means for solving the inverse problem to yield the geometry that will provide a uniform surface temperature when a spatial variation of surface heating is imposed.

References

1 Hsieh, C. K., and Su, K. C., "A Methodology of Predicting Cavity Geometry Based on the Scanned Surface Temperature Data—Prescribed Heat Flux at the Cavity Side," ASME JOURNAL OF HEAT TRANSFER, Vol. 103, No. 1, Feb. 1981, pp. 42-46.

2 Siegel, R., and Goldstein, M. E., "Analytical Solution for Heat Transfer in Three-Dimensional Porous Medium Including Variable Fluid Properties," NASA TN D-6941, 1972.

3 Siegel, R., "Shape of Porous Cooled Region for Surface Heat Flux and Temperature Both Specified," *International Journal of Heat and Mass Transfer*, Vol. 16, No. 9, Sep. 1973, pp. 1807-1811.

4 Siegel, R., and Snyder, A., "Heat Transfer in Cooled Porous Region with Curved Boundary," ASME JOURNAL OF HEAT TRANSFER, Vol. 103, No. 4, Nov. 1981, pp. 765-771.

5 Davis, R. T., "Numerical Methods for Coordinate Generation Based on Schwarz-Christoffel Transformations," AIAA Computational Fluid Dynamics Conference, A Collection of Technical Papers, American Institute of Aeronautics and Astronautics, Inc., New York, 1979, pp. 180-194.

Free Convection Diffusion Flames With Inert Additives

M. Sibulkin
Professor of Engineering.
Mem. ASME

C. Y. Wang
Research Assistant.

Division of Engineering,
Brown University,
Providence, R.I. 02912

An analysis of laminar, free-convection, diffusion flames burning on a vertical fuel surface is presented. The study is directed towards determining the effects of inert additives on the boundary layer structure and burning rates. Results are presented for several classes of inert additives using polymethyl methacrylate burning in air as the base system. The use of a fuel-phase additive to release noncombustible gases is modeled by varying the parameter Y_{FT}, the mass fraction of fuel in the gaseous products of pyrolysis. The effects of an additive which promotes char formation is modeled by varying the heat of pyrolysis per unit mass of gaseous pyrolysate released for combustion. The effects of a spray of water droplets on a wall fire is modeled by a combination of the release of a noncombustible gas and a surface heat sink which results from evaporation of water droplets at the fuel surface. The water spray calculations predict an extinction limit which is within a factor of two of experimental results.

Introduction

In this paper an analysis is presented for a free-convection, diffusion flame burning on a vertical, solid fuel surface. This flame system is of particular interest in the area of fire research. Since we assume the flow to be laminar, direct application of the results is limited to the early stages of wall fires and to small scale flammability tests involving vertical fuel surfaces. However, a general problem in the area of fire research has been the difficulty of interpreting experimental results on a theoretical basis. Laminar flow analyses, based on the fundamental equations of fluid mechanics, can lead to greater understanding of the factors affecting heat transfer, burning rates, and extinction limits in solid fuel combustion. In this paper attention is directed to the effects of several types of inert additives on the combustion characteristics of solid fuels.

The first analysis of free convection burning on a vertical fuel surface was presented by Kosdon et al. [1] in connection with experiments on the burning of vertical, cellulose cylinders. Having obtained an analytical relationship between burning rate and heat of pyrolysis, they used their measured burning rate to calculate an effective heat of pyrolysis for cellulose. A more extensive set of numerical calculations for the same problem was made by Kim et al. [2] who plotted the burning rate as a function of mass-transfer parameter, B, and stoichiometric ratio, r. Additional solutions combining forced and free convection have been given by Shih and Pagni [3]. The foregoing analyses included several physical approximations which considerably simplify the mathematical structure of the equations, viz., Lewis number equal to one, infinite chemical reaction rate, and neglect of radiative heat transfer. The effects of radiation were studied by Sibulkin et al. [4] who found that gas phase radiation from the flame to the fuel had a negligible effect on burning rates, but that inclusion of radiation from the hot fuel surface significantly decreased the burning rates. Fuel surface radiation becomes a significant factor for solid fuels (as opposed to liquid fuels) because of their higher surface temperatures during combustion. However, when surface radiation is included in the formulation of the problem, it is no longer possible to obtain a similarity solution of the equations, and in [4] a "local similarity" approximation was made. The effects of using finite rate chemistry (which again increases the mathematical complexity of the problem) were examined by Sibulkin et al. [5] using the local similarity formulation and a one-step global chemical reaction. Using property values for PMMA (polymethyl methacrylate) burning in air, they found that finite rate chemistry had a very small effect on burning rates when combustion occurred but that the specific reaction rate parameters significantly affected the extinction limit. The effect of nonunity Lewis number has recently been investigated by Sibulkin and Malary [13] who find a moderate increase in burning rate as Lewis number increases from 0.5 to 2.0.

The results given in this paper are based on the use of the infinite reaction rate model (which is also known as the flamesheet approximation). The effects of several types of inert additives are examined. In the first set of calculations, additives which transfer mass into the gas phase are considered for two types of pyrolysis behavior: (*i*) zero heat of pyrolysis of the inert material, and (*ii*) heat of pyrolysis of the inert equal to heat of pyrolysis of the fuel. The next set of calculations models a char forming additive which reduces the fraction of the solid fuel which is volatilized. The final set of calculations models the effects of directing a uniform spray of water droplets at the burning surface.

Since these analyses contain a number of simplifying assumptions, the results should be used as a guide to understanding the way in which different types of inert additives modify the burning of solid fuels.

Analysis

The analysis given in this paper applies to laminar, free-convective burning of a vertical, thermally thick fuel surface. A flame sheet model is used, and the unity Lewis number approximation of the previous analyses is retained. Additional assumptions made are: (*i*) the products $\rho\mu$, ρk and $\rho^2 D$ are constant, i.e., independent of temperature and composition; (*ii*) the gases are ideal and the molecular weight and specific heat of the gas mixture are constant (these assumptions are used to relate the buoyancy force to the gas temperature); (*iii*) the gas is optically thin to thermal radiation from the wall and gas phase radiation to the wall may be neglected.

When the binary diffusion coefficients are assumed equal, thermal diffusion is neglected, and the Lewis number is set

Contributed by the Heat Transfer Division and presented at the ASME Winter Annual Meeting, Washington, D.C., November 15-20, 1981. Manuscript received by the Heat Transfer Division December 14, 1981. Paper No. 81-WA/HT-28.

equal to one, the conservation equations are (see, e.g., Williams [6]):

Mass

$$\partial(\rho u)/\partial x + \partial(\rho v)/\partial y = 0 \tag{1}$$

Momentum

$$\rho u(\partial u/\partial x) + \rho v(\partial u/\partial y) = (\partial/\partial y)[\mu(\partial u/\partial y)] + [g(\rho_\infty - \rho)] \tag{2}$$

Energy

$$\rho u(\partial h/\partial x) + \rho v(\partial h/\partial y) = (\partial/\partial y)[(k/c_p)(\partial h/\partial y)] + \dot{q}_C''' \tag{3}$$

Species

$$\rho u(\partial Y_j/\partial x) + \rho v(\partial Y_j/\partial y) = (\partial/\partial y)[\rho D(\partial Y_j/\partial y)] + \dot{m}_j''' \tag{4}$$

where $j = F$(fuel) or O(oxygen) and the notation is defined in the Nomenclature.

A one-step chemical reaction of the form

$$1(\text{kg fuel}) + \nu_s(\text{kg } O_2) \rightarrow \nu_p(\text{kg products}) + h_c(\text{kJ heat})$$

is assumed. The resulting relationship between the mass and energy source terms is

$$\dot{q}_C''' = -\dot{m}_F''' h_c = -\dot{m}_O''' h_c/\nu_s \tag{5}$$

These inhomogeneous source terms can be eliminated by defining the Schvab-Zeldovich variables

$$\beta_{FO} \equiv Y_F - (Y_O - Y_{O,\infty})/\nu_s$$
$$\beta_{FT} \equiv Y_F + (h - h_\infty)/h_c \tag{6}$$

Substituting equations (6) and (5) into equations (4) and (3) gives

$$\rho u(\partial \beta_i/\partial x) + \rho v(\partial \beta_i/\partial y) = (\partial/\partial y)[(k/c_p)(\partial \beta_i/\partial y)] \tag{7}$$

The boundary conditions applying to equations (1 – 4) at $y = \infty$ are

$$u = 0, h = h_\infty, Y_O = Y_{O,\infty} \tag{8}$$

The boundary conditions at $y = 0$, which are more complex, are given by the following:

$$u = 0, h = h_w \tag{9a}$$

The fuel mass balance

$$\dot{m}_T'' Y_{FT} = \dot{m}_T'' Y_{F,w} - (\rho D)_w (\partial Y_F/\partial y)_w \tag{9b}$$

where Y_{FT} is the mass fraction of fuel in the volatile products of pyrolysis. The energy balance

$$(k/c_p)_w (\partial h/\partial y)_w = \dot{m}_T'' h_p + \dot{q}_{Rs}'' \tag{9c}$$

where h_p is the heat of pyrolysis per unit mass of volatile products of pyrolysis and $\dot{q}_{Rs}'' = \epsilon\sigma(T_w^4 - T_\infty^4)$.

Here use has been made of the assumption that the boundary layer is optically thin. The temperature, T, is determined from the enthalpy using the constant specific heat assumption and the flamesheet conditions

$$Y_O = 0 \text{ for } y \le y_{fs}$$
$$Y_F = 0 \text{ for } y \ge y_{fs} \tag{10}$$

The conservation equations and boundary conditions are now transformed from the independent variables (x,y) to independent variables (s,η) using

$$s \equiv 2c_1^{2/3} x^{1/2} \eta \equiv c_1 x^{-1/4} \int_0^y (\rho/\rho_r)\, d\bar{y} \tag{11}$$

where

$$c_1 \equiv (g h_c/4 c_p T_\infty \nu_r^2)^{1/4}$$

The mass conservation equation is satisfied by the use of the stream function, ψ, given by

$$\rho u = \rho_r(\partial\psi/\partial y) \quad \rho v = -\rho_r(\partial\psi/\partial x)$$

Nomenclature

c_p = specific heat at constant pressure
c_1 = constant, equation (11)
D = mass diffusivity
F = fraction of surface covered by water droplets
g = acceleration of gravity
Gr_x = Grashof number, $gh_c x^3/4\nu_r^2 c_p T_\infty$
h = thermal enthalpy
h_c = heat of combustion per unit mass of gaseous fuel
h_p = heat of pyrolysis per unit mass of gaseous pyrolysate
k = thermal conductivity
$\dot{m}$ = mass flux
m^* = nondimensional mass flux, equation (19)
p = (*i*) pressure; (*ii*) nondimensional velocity, equation (13)
Pr = Prandtl number
$\dot{q}$ = heat flux
s = nondimensional streamwise coordinate, equation (11)
T = temperature
u = streamwise velocity
v = normal velocity
W_m = molecular weight of gas phase mixture
x = streamwise coordinate
y = normal coordinate
Y = species mass fraction
Y_{FT} = mass fraction of fuel in gaseous pyrolysate
β_{FO}, β_{FT} = Schvab-Zeldovich variables, equation (6)
ϵ = surface emissivity
η = nondimensional normal coordinate, equation (11)
θ = nondimensional enthalpy (temperature), equation (13)
μ = viscosity
ν = kinematic viscosity
ν_s = stoichiometric oxygen/fuel mass ratio
ξ = nondimensional stream function, equation (12)
ρ = density
σ = Stephan-Boltzmann constant

Subscripts

C = combustion
F = fuel
I = inert
O = oxygen
T = total
W = water
r = reference
Rs = surface radiation
w = surface (wall)
∞ = ambient

Superscripts

$''$ = per unit area
$'''$ = per unit volume

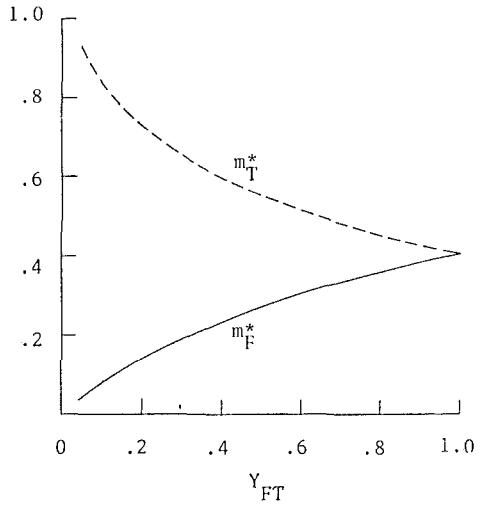

Fig. 1 Effect of inert gas injection on burning rates; $h_{p,l} = 0$

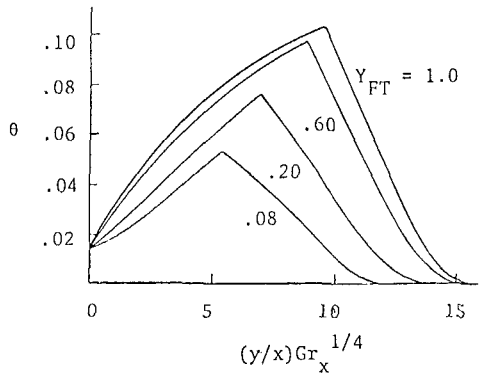

Fig. 2 Boundary layer temperature profiles: $h_{p,l} = 0$

and a nondimensional stream function $\xi(s,\eta)$ is defined by the relation

$$\psi \equiv 4\nu_r c_1 x^{3/4} \xi(s,\eta) \tag{12}$$

Finally a nondimensional streamwise velocity, p, and a nondimensional enthalpy, θ, are defined as

$$p \equiv \partial\xi/\partial\eta \quad \theta \equiv (h-h_\infty)/h_c = (T-T_\infty)/(h_c/c_p) \tag{13}$$

The use of equations (11-13) transforms equations (2) and (7) to partial differential equations in the independent variables s, η. When the radiation term in equation (9c) is absent, the system of equations and boundary conditions is independent of the streamwise variable, s. When the radiation term is included, we use an approximation technique known as "local similarity" in which terms containing $\partial(\ )/\partial s$ (which are small compared to the remaining terms) are neglected. The resulting equations are

$$p'' + 3\xi p' - 2p^2 + \theta = 0 \tag{14}$$

with

$$\xi = \xi(0) + \int_0^\eta p\, d\tilde{\eta} \tag{15}$$

and

$$(1/\mathrm{Pr})\beta_i'' + 3\xi\beta_i' = 0 \tag{16}$$

where $(\ )' \equiv d(\ )/d\eta$. The associated boundary conditions at $\eta = \infty$ are

$$p = \beta_{FO} = \beta_{FT} = 0 \tag{17}$$

Table 1 Properties used in calculations

Gas phase (air)

p	=	1 atm = 1.013×10^5 N/m^2
T_∞	=	298 K
T_r	=	660 K
ρ_r	=	0.5235 kg/m^3
ν_r	=	59.55×10^{-6} m^2/s
c_p	=	1.3 kJ/kg K
W_m	=	28 kg/kg-mole
Pr	=	0.7
$Y_{0,\infty}$	=	0.233

Fuel phase (PMMA)

h_c	=	26560 kJ/kg
$h_{p,F}$	=	1590 kJ/kg
T_w	=	660 K
ϵ	=	0.9

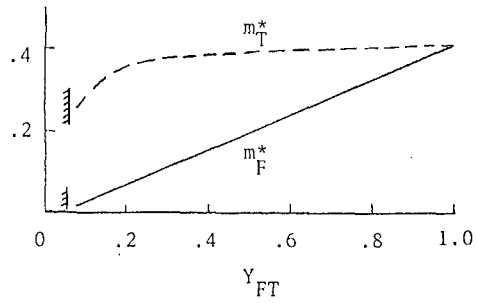

Fig. 3 Effect of inert gas injection on burning rates: $h_{p,l} = h_{p,F}$

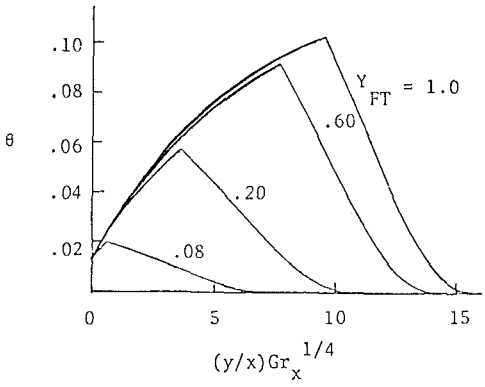

Fig. 4 Boundary layer temperature profiles: $h_{p,l} = h_{p,F}$

The boundary conditions at $\eta = 0$ are

$$p = 0, \quad \theta = \theta_w \tag{18a}$$

$$\beta_{FO}' = 3\mathrm{Pr}\xi[Y_{FT} - \beta_{FO} + (Y_{O,\infty}/\nu_s)] \tag{18b}$$

$$\beta_{FT}' = 3\mathrm{Pr}\xi[Y_{FT} - \beta_{FT} + \theta_w - (h_p/h_c)] + R\mathrm{Pr}(h_p/h_c)s^{1/2} \tag{18c}$$

where

$$R \equiv \frac{\epsilon\sigma(T_w^4 - T_\infty^4)}{\sqrt{2}\rho_r\nu_r h_p c_1^{4/3}}$$

Results for the burning rate, i.e., the total mass flux at the wall, $\dot{m}_T''$, will be presented in terms of the nondimensional parameter, m_T^*, defined by

$$m_T^* = -3\xi(0) = \frac{\dot{m}_T'' x^{1/4}}{\rho_r\nu_r c_1} \tag{19}$$

A nondimensional fuel flux at the wall, m_F^*, is defined in a similar manner. The two parameters are related by $m_F^* = Y_{FT}\, m_T^*$.

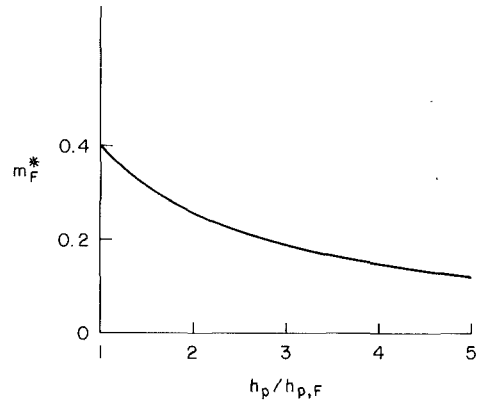

Fig. 5 Change in burning rate due to a char forming additive: $Y_{FT} = 1$

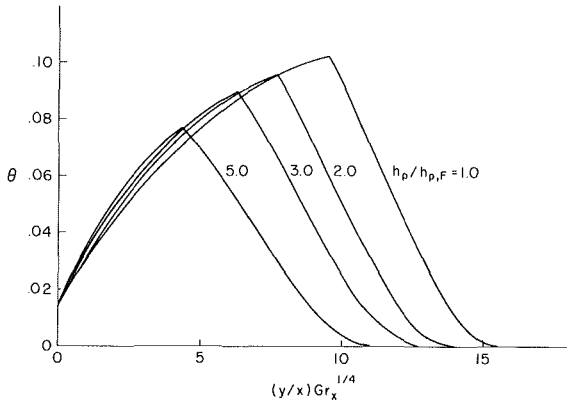

Fig. 6 Boundary layer temperature profiles for the case of a char forming additive: $Y_{FT} = 1$

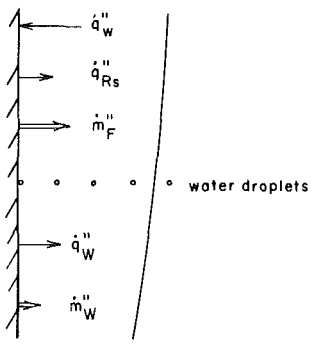

Fig. 7 Heat and mass flux vectors for the case of a uniform water droplet spray impinging on the surface

Method of Solution

The mathematical problem to be solved is the system consisting of equations (14–18), together with equations (6) and (10). The numerical method of solution selected is to replace these equations and boundary conditions by their finite difference equivalents, and to solve the system by iteration. The nonlinear terms are approximated using the technique of quasi-linearization (see [7] and [8]). This approach eliminates the well-known difficulties associated with the use of marching techniques to solve two-point boundary value problems. The method is also well suited to calculations using finite chemical reaction rates. Further discussion of the method of solution is given in [5] and [9].

Results and Discussion

Calculations have been made for inert materials added to PMMA burning in air. The properties used in the calculations are listed in Table 1, and it is implicitly assumed that these properties are not altered by the inert materials. The reference conditions have been chosen at $T_r = 660$ K, which is equal to a value of T_w that is characteristic of PMMA burning in air; the value of ν_r is for nitrogen at that temperature. A value of the boundary condition $\theta_w = 0.0136$ is used which is based upon the enthalpy of nitrogen at T_w. An average value of c_p has been chosen which gives the correct adiabatic flame temperature at the flamesheet for the base case of complete combustion of PMMA. Using these properties, the value of the parameter c_1 is 466.6 $m^{-3/4}$.

Mass Transfer Effects. Inert fuel phase additives may act by reducing the concentration of fuel in the pyrolyzed material injected into the boundary layer. Two cases of this type are considered: an inert heat of pyrolysis $h_{p,I} = 0$; and an inert heat of pyrolysis $h_{p,I} = h_{p,F}$. To illustrate the mass transfer effects most clearly, wall radiation is not included for these cases.

The first case can be interpreted as complete burning of a pure fuel with superimposed blowing. For this system $h_p \equiv \Sigma Y_k h_{p,k} = Y_{FT} h_{p,F}$. The pyrolysis rates[1] for this case are shown in Fig. 1. For values of Y_{FT} decreasing from 1.0, the total burning rate m_T^* increases while the rate of fuel gasification m_F^* decreases. The boundary layer temperature profiles for this case are shown in Fig. 2. As Y_{FT} is decreased, the flamesheet temperature decreases, and its distance from the wall decreases. The net result of these changes is a reduction in the heat flux to the wall. (Since the heat flux is purely convective, it is proportional to the temperature gradient at the wall.) However, even though the heat flux decreases as Y_{FT} decreases, h_p decreases more rapidly which leads to the increase in m_T^* shown in Fig. 1.

The pyrolysis rates for the case $h_{p,I} = h_{p,F}$ are shown in Fig. 3. There is a range of Y_{FT} from 1.0 to 0.4 for which the burning rate m_T^* is nearly constant. It is interesting to note that since h_p is independent of Y_{FT}, the mass-transfer parameter $B \equiv [Y_{O,\infty}(h_c/\nu_s) - c_p (T_w - T_\infty)]/h_p$ is also independent of Y_{FT} for this case; thus $\dot{m}_T \simeq$ constant is not unexpected.[2] For $Y_{FT} < 0.4$, m_T^* decreases substantially and an extinction limit is reached at $Y_{FT} = 0.06$.

These results can be understood more clearly by considering the temperature profiles shown in Fig. 4. As Y_{FT} is decreased, the flamesheet temperature decrease is accompanied by a rapid movement of the flame towards the wall. The result is that the temperature gradient at the wall (and thus the heat flux) remains nearly constant until quite low values of Y_{FT}. Since the rate of heat release at the flame decreases as m_F^* decreases, the fraction of the heat of combustion which is transferred to the wall must be increasing as Y_{FT} decreases. As the extinction limit is approached, the heat flux to the wall is found to approach the heat release rate at the flame. (This extinction limit is primarily of "academic" interest, since the flamesheet approximation, i.e., the assumption of an infinite chemical reaction rate, is not valid at the low flame temperatures corresponding to small values of Y_{FT}.)

Char Formation Effects. A number of fire retardant additives alter the pyrolysis process in such a manner that char formation is enhanced at the expense of volatile products. In this calculation we assume that all the pyrolyzed gas is fuel (i.e., $Y_{FT} = 1$) and that the value of h_c is unchanged. For some types of fire retarded cellulose, the latter has been shown to be a reasonable approximation [10]. Thus the primary effect of char formation for these systems is to in-

[1] It should be noted that for all the cases discussed in this paper, the physical rates $\dot{m}''$ at a fixed position x are proportional to the nondimensional rates, m^*, since $\rho_r \nu_r c_1$ is a constant [cf., equation (19)].

[2] For droplet combustion (see, e.g. [6]), the burning rate is given by $\dot{m}_T = (2\pi kd/c_p)\ln(1+B)$. Thus for constant B, the burning rate is independent of Y_{FT}.

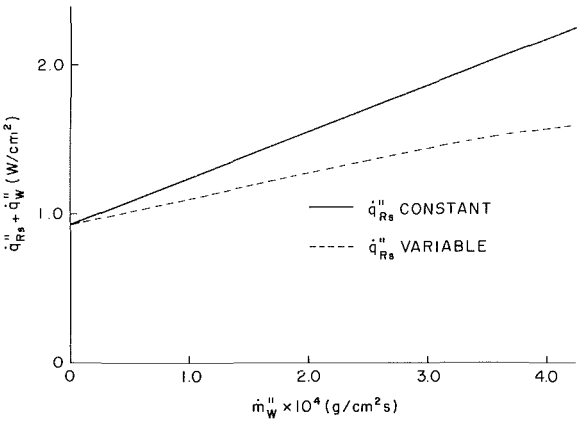

Fig. 8 Surface heat loss rate due to combined effects of radiation and water evaporation (For the variable $\dot{q}''_{Rs}$ curve x = 10 cm)

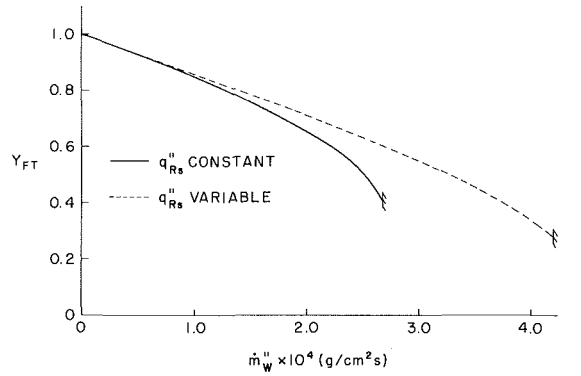

Fig. 9 The variation in fuel fraction Y_{FT} with water application rate: x = 10 cm

crease h_p, the heat of pyrolysis per unit mass of gaseous pyrolysate. The effect of this increase in h_p on the burning rate m_F^* is shown in Fig. 5. Wall radiation is again not included for this case. The results show that

$$\frac{m_F^*}{m_F^*(h_p/h_{p,F}=1)} \simeq \frac{h_{p,F}}{h_p}$$

which implies that the heat flux to the wall is only weakly dependent on h_p. The temperature profiles for this case are shown in Fig. 6. We again find that the decrease in flamesheet temperature is accompanied by a rapid movement of the flame towards the wall which actually results in a small *increase* in heat flux with increasing $h_p/h_{p,F}$.

Water Spray Effects. A review of the literature on the extinction of wood fires by the use of water sprays has recently been given by Heskestad [11]. The effects of an approximately uniform spray of water droplets on the burning rates and extinction limits of vertical plastic fuel panels was investigated by Magee and Reitz [12]. For 36-cm high PMMA panels they found that increasing the water application rate reduced the burning rate and led to extinction at values of $\dot{m}''_W$ of 1.7×10^{-4} and 2.0×10^{-4} g/cm²s for two significantly different spray droplet sizes. Based upon visual observations, they estimated that at least 95 percent of the applied water reached the surface.

A model for this process is shown in Fig. 7. It is postulated that water droplets at $T = T_\infty$ reach the surface without affecting the boundary layer, and that the droplets subsequently vaporize to superheated steam at $T = T_w$. This results in a rate of mass injection $\dot{m}''_W$ into the boundary layer

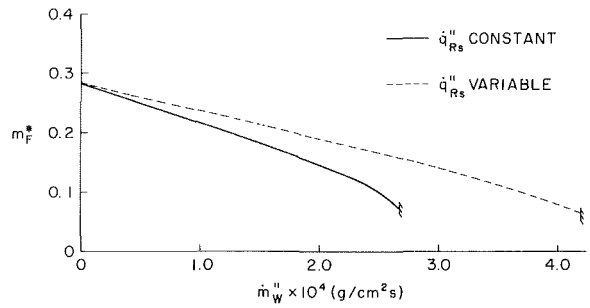

Fig. 10 The effect of water application rate on the burning rate: x = 10 cm

which is equal to the water application rate, and in a surface heat sink $\dot{q}''_W = \dot{m}''_W [h_w(g) - h_\infty(l)]_W$ where $h_{660}(g) - h_{298}(l)] = 3145$kJ/kg. In addition to these fluxes, the heat loss $\dot{q}''_{Rs}$ due to surface radiation is included in the following calculations. Because radiation is included, a specific value of x must be specified in order to determine the value of s in equation (18c). The value selected is x = 10 cm.

Since the precise effect of water droplet deposition on surface radiation is unknown, two limits are considered. As an upper limit, a constant value of $\dot{q}''_{Rs} = \epsilon\sigma(T_w^4 - T_\infty^4)$ is used. To obtain a lower limit, a variable value of $\dot{q}''_{Rs} = (1 - F)\epsilon\sigma(T_w^4 - T_\infty^4)$ is taken where F is the fraction of the surface covered by water droplets. By means of an analysis which considers only the heat flux from the flame to the water droplets on the surface, a simple expression for F as a function of water application rate can be obtained (Appendix A). Since heat transfer from the solid fuel to the water droplets has been neglected, the analysis gives an upper limit for F and thus a lower limit for $\dot{q}''_{Rs}$. The total surface heat loss rate, $\dot{q}''_{Rs} + \dot{q}''_W$, is shown in Fig. 8 for these two limits.

For the water spray problem

$$Y_{FT} = \dot{m}''_F/(\dot{m}''_W + \dot{m}''_F) \tag{20}$$

where the burning rate $\dot{m}''_F$ depends directly on Y_{FT} and indirectly on $\dot{m}''_W$ through the surface heat loss rate (Fig. 8). Thus, a trial-and-error procedure is necessary. At a fixed value of $\dot{m}''_W$, a curve of $\dot{m}''_F$ versus Y_{FT} is generated and the solution satisfying equation (20) is found. This procedure leads to a critical value of $\dot{m}''_W$ above which equation (20) cannot be satisfied. The results of these calculations are shown on Fig. 9 for Y_{FT} and on Fig. 10 for m_F^*. As the water application rate $\dot{m}''_W$ increases, the fuel fraction Y_{FT} decreases and this leads to a reduction in the (nondimensional) burning rate m_F^*. Upper limits for the water application rate are found at $\dot{m}''_W = 2.7 \times 10^{-4}$ g/cm²s for the constant $\dot{q}''_{Rs}$ input and at $\dot{m}''_W = 4.2$ for the variable $\dot{q}''_{Rs}$ input.

The qualitative behavior shown in Fig. 10 is similar to that found in the experiment [12] referred to above. Before comparing the extinction limits a number of cautions must be stated. The present analysis is for a laminar flame at a value of x = 10 cm while the available experimental results are for a 36-cm high plate with turbulent flow over much of the plate. The present analysis uses the thin flame approximation. This approximation has been shown [5] to satisfactorily predict burning rates at conditions away from extinction, but the extinction limit itself is sensitive to the reaction rate parameters used in the calculation. For the present problem, the thin flame results provide an upper bound on the water application rates leading to extinction. These calculated thin flame extinction limits ($\dot{m}''_W \simeq 3 - 4 \times 10^{-4}$ g/cm²s) are roughly twice the values ($\dot{m}''_W \approx 2 \times 10^{-4}$ g/cm²s) found in [12]. It is also interesting to note that for a variety of experimental wood fires tabulated in [11] the water application rates at extinction were in the range $\dot{m}''_W \approx 1 - 3 \times 10^{-4}$

g/cm^2s. We are thus encouraged to believe that the model developed in this paper provides a useful guide for the study of water spray effects on solid fuel fires.

Acknowledgment

This work was supported by the Center for Fire Research of the National Bureau of Standards under Grant NB80NADA1024. The computer program used to make these calculations was developed by K. Annamalai and A. K. Kulkarni.

References

1 Kosdon, F., Williams, F . A., and Buman, C., "Combustion of Vertical Cellulosic Cylinders in Air," *Twelfth International Symposium on Combustion*, The Combustion Institute, 1969, pp. 252–264.

2 Kim, J., deRis, J., and Kroesser, F. W., "Laminar Free Convective Burning of Fuel Surfaces," *Thirteenth International Symposium on Combustion*, The Combustion Institute, 1971, pp. 949–960.

3 Shih, T. M., and Pagni, P. J., "Laminar Mixed-Made, Forced and Free, Diffusion Flames," ASME JOURNAL OF HEAT TRANSFER, Vol. 100, 1978, p. 253.

4 Sibulkin, M., Kulkarni, A. K., and Annamalai, K., "Effects of Radiation on the Burning of Vertical Fuel Surfaces, *"Eighteenth International Symposium on Combustion,"* The Combustion Institute, 1981, pp. 611–617.

5 Sibulkin, M., Kulkarni, A. K., and Annamalai, K., "Burning on a Vertical Fuel Surface With Finite Chemical Reaction Rate," *Combustion and Flame*, Vol. 44, 1982, p. 187.

6 Williams, F. A., *Combustion Theory*, Addison-Wesley, Reading, Mass, 1965.

7 Fay, J. A., and Kaye, H., "A Finite-Difference Solution of Similar Nonequilibrium Boundary Layers," *AIAA J.*, Vol. 5, 1967, p. 1949.

8 Sibulkin, M., and Dennar, E. A., "Radiating Boundary Layers at Planetary Entry Velocities," *International Journal of Heat and Mass Transfer*, Vol. 15, 1972, p. 619.

9 Kulkarni, A. K., "A Study of a Fully Burning Vertical Surface," Ph.D. thesis, Brown University, Providence, R.I., 1980.

10 Shafizadeh, F., Chin, P. S., and DeGroot, W., "Mechanistic Evaluation of Flame Retardants," *Fire Retardant Chemistry*, Vol. 2, 1975, p. 195.

11 Heskestad, G., "The Role of Water in the Suppression of Fire: A Review," *Journal of Fire Flammability*, Vol. 12, 1980, p. 254.

12 Magee, R. S., and Reitz, R. D., "Extinquishment of Radiation Augmented Plastic Fires by Water Sprays," *Fifteenth International Symposium on Combustion*, The Combustion Institute, 1975, p. 337.

13 Sibulkin, M., and Malary, S. F., "Diffusion Flame Calculations for Nonunity Lewis Number," *Combustion Science and Technology*, Vol. 28, 1982, p. 85.

APPENDIX A

Estimate of Fraction of Surface Covered by Water

When a uniform spray of droplets impinges on a surface at a rate, $\dot{n}''$, the steady-state droplet population per unit surface area, n'', is releated to the lifetime, τ, of a droplet by

$$n'' = \dot{n}'' \tau \tag{A1}$$

Assuming that the drops have a diameter, A_d, after impact on the surface and do not overlap, the fraction of the surface covered by water is

$$F = n'' A_d = \dot{n}'' A_d \tau \tag{A2}$$

The lifetime of a droplet is estimated from a simplified energy balance in which heat flux from the flame causes evaporation of water from the surface of the drop so that

$$\dot{q}_w'' A_d \tau = m_d h_{fg} \tag{A3}$$

where m_d is the mass of a drop and h_{fg} is the heat of evaporation. Eliminating τ from equations (A2) and (A3), and using $\dot{m}_W'' = m_d \dot{n}''$ then gives

$$F = \dot{m}_W'' h_{fg} / \dot{q}_w'' \tag{A4}$$

for the fraction of the surface covered by water. As a consequence of the simple nature of the energy balance used, the value of F is independent of A_d.

R. A. Altenkirch
Mem. ASME

M. Rezayat

R. Eichhorn
Fellow ASME

F. J. Rizzo

Department of Mechanical Engineering,
University of Kentucky,
Lexington, Ky. 40506

Boundary Integral Equation Method Calculations of Surface Regression Effects in Flame Spreading

A solid-phase conduction problem that is a modified version of one that has been treated previously in the literature and is applicable to flame spreading over a pyrolyzing fuel is solved using a boundary integral equation (BIE) method. Results are compared to surface temperature measurements that can be found in the literature. In addition, the heat conducted through the solid forward of the flame, the heat transfer responsible for sustaining the flame, is also computed in terms of the Peclet number based on a heated layer depth using the BIE method and approximate methods based on asymptotic expansions. Agreement between computed and experimental results is quite good as is agreement between the BIE and the approximate results.

Introduction

Theoretical determination of the rate at which a flame spreads over the surface of a solid fuel slab of finite thickness is known to be difficult. The discussion that follows here is restricted to the case where a wind, either forced or naturally induced, opposes the spreading flame. For this situation, one obtains a steady spread rate in contrast to the acceleratory character of flame spreading in a following wind, which would occur, for example, in upward flame spread in free convection.

Simultaneous solution for the gas-phase temperature and species distributions and the solid-phase temperature field allows the flame spread rate to be determined as an eigenvalue. The solution to the gas-phase problem provides boundary conditions for use in the solid-phase conduction problem. For example, solution to the gas-phase problem for a specified fuel-bed surface temperature distribution provides the heat flux to the bed. The surface temperature and heat flux then allow the spread rate to be determined from the solid-phase analysis. Iteration is required until the boundary conditions and the associated spread rate allow mass conservation in the solid phase to be satisfied.

That the problem is difficult stems from the facts that it is nonlinear and that the differential equations of interest are elliptic in character. In addition, the shape of the fuel bed is actually an unknown because the surface downstream of the leading edge of the flame regresses as the fuel that persists following passage of the flame is burnt. This feature of the problem has been ignored by most investigators.

Several analytical efforts of merit, which allow the spread rate to be predicted, are the ones by de Ris [1], Frey and T'ien [2], Fernandez-Pello and Williams [3], and Sirignano [4]. The first three consider fuels, as we do here, that gasify prior to combustion so that the flame is in the gas phase, while the last is concerned with a bed that is oxidized on the surface. All introduce approximations that remove some of the nonlinearities or the elliptic nature of part of the problem to facilitate solution. None consider that the shape of the regressing fuel bed is unknown but rather assume that the fuel-bed surface remains in a single plane.

The rate of heat transfer forward of a spreading flame is an important quantity in flame spread theory, for it is this heat transfer that sustains the flame. Under certain conditions, as discussed herein, this forward heat transfer occurs by conduction through the solid fuel. This is the case with which we are concerned exclusively. In addition, there have recently been advanced correlations for flame spreading that employ two dimensionless parameters [5, 6, 7]. One of these parameters is a dimensionless spread rate that compares the actual heat transferred forward of the flame to the maximum that could be transferred, if the flame were adiabatic and if the chemical reactions occurring in the flame proceeded at an infinite rate. The other parameter is a Damköhler number that measures the actual rate at which the reactions take place. The dimensionless spread rate contains a characteristic length that represents the depth of heating normal to the fuel-bed surface. When the bed is heated across its entire thickness (the thermally thin case) there is no ambiguity as to what the heated depth is. But when the heated depth is less than the bed thickness (the thermally thick case), the depth depends on the shape of the regressing surface downstream of the leading edge of the flame, which in turn depends on how fast the gas-phase reaction proceeds. The heated depth usually used in this case [1] is applicable when the rate of the gas-phase reaction is infinitely fast, and the downstream fuel surface regression is negligible.

In the following, we use a boundary integral equation (BIE) method to solve a solid-phase conduction problem pertinent to flame spreading over a solid fuel that gasifies prior to combustion. The problem that we consider is a modified version of the one considered by Fernandez-Pello et al. [8]; the analysis techniques, however, are different. We use the same temperature and heat flux boundary conditions as in [8], but we allow the fuel surface downstream of the leading edge of the flame to regress to a plane that lies at angle ϕ (see Fig. 6) with respect to the unburnt fuel-bed surface. The angle ϕ is allowed to vary from 0–90 deg whereas in [8] only $\phi = 0$ deg and $\phi = 90$ deg were treated. In addition, the Peclet number of the solid, which is based on the flame spread rate and fuel-bed half thickness, takes on finite values. For $\phi = 0$ deg in [8], the Peclet number approaches infinity.

For the computations, the spread rate is specified, not predicted, because, rather than spread rate prediction, our purpose here is to seek (*a*) a solid-phase analysis method that

Contributed by the Heat Transfer Division for publication in the JOURNAL OF HEAT TRANSFER. Manuscript received by the Heat Transfer Division September 23, 1981.

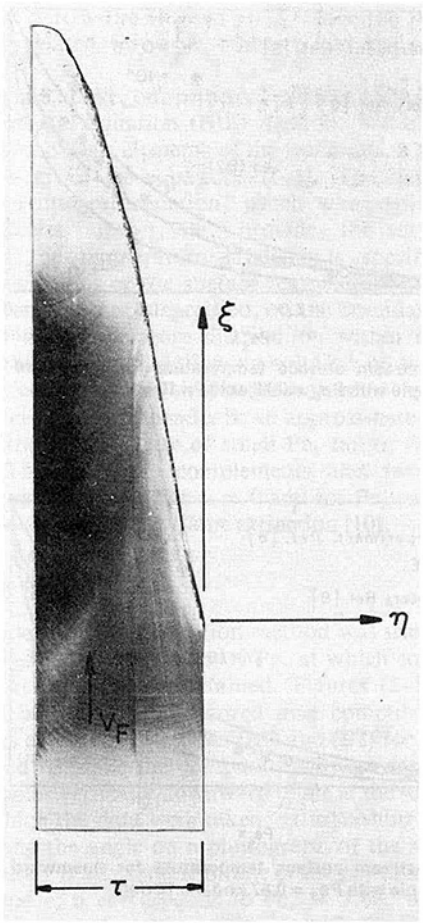

Fig. 1 PMMA sample cross section showing ξ, η coordinate system

could be coupled to a gas-phase analysis to yield the spread rate without being restricted to limiting cases such as infinite bed thickness or particular boundary conditions, (*b*) an estimate of the importance of surface regression, and (*c*) a correction factor, which is equation (10), to be used in the dimensionless flame spread correlations mentioned above. Approximate boundary conditions consisting of a combination of the surface temperature and the surface heat flux are used to solve for the unknown surface temperature and the heat that is conducted through the fuel bed upstream of the spreading flame. The surface temperature results are compared to the measurements and analytical results of Fernandez-Pello et al. [8], and the upstream heat flux computations are compared to approximate methods that we also develop below.

Theoretical Problem

The problem we consider is the following: a rectangular slab of fuel of thickness 2τ is being consumed by a gas-phase flame on both sides of the slab that is spreading at a steady speed, V_F, into a wind moving at speed $(V_g - V_F)$ where V_F/V_g is invariably small. It is apparent that the problem is symmetrical about a center plane located a distance, τ, from each surface of the unburnt slab. Thus, we consider a bed of thickness τ, that is, insulated on one surface with a flame on the other.

The activation temperature, T_a, for fuel gasification or pyrolysis is taken to be large with respect to the temperature, T_v, at which most of the gasification takes place. Two consequences of this assumption are that the gasification is restricted to a thin layer at the fuel-bed surface with the bulk of the bed being an inert solid, and that all the gasification can be considered to take place at T_v [8]. The latter consequence leads to the result that the flux of fuel from the solid to the gas, $\dot{m}''$, is nearly constant in the region in which the fuel vaporizes. Thus, we expect the gasifying surface to form a nearly constant angle, equal to $\sin^{-1}(\dot{m}''/\rho_s V_F)$ with ρ_s the solid density, with respect to the unburnt fuel-bed surface.

Figure 1 shows a photograph of the cross section of one-half of a fuel bed of polymethylmethacrylate, (PMMA), with $2\tau = 2.54$cm, that was burnt vertically downward in air. The flame was extinguished prior to complete consumption of the bed. We consider a coordinate system, (ξ, η), anchored to the flame and located near where the leading edge of the flame would be. The bed then moves in the $+\xi$ direction at speed V_F, and the gas moves in the same direction at speed V_g. Because the flame spreads vertically downward, $V_g \simeq (\nu g \Delta H_c m_{ox,\infty}/T_\infty i c_p)^{1/3}$ [5]. In this expression, ν is the kinematic viscosity, g is the acceleration of gravity, ΔH_c is the heat of combustion of gas-phase fuel, $m_{ox,\infty}$ is the mass fraction of oxygen in the oxidizing environment (air in this case), T_∞ is the ambient temperature, i is the mass of oxygen needed to oxidize fully a unit mass of fuel, and c_p is a gas-phase specific heat.

For a positive axial coordinate, ξ, the fuel-bed surface is at a nearly constant angle with respect to $\eta = 0$ except near the tip of the bed at largest ξ. Near the tip, there is considerable evidence of in-depth gasification, so in this region the model of an inert solid must break down. However, we are principally concerned with a region that is no more than a few characteristic thermal lengths, α_s/V_F, on either side of the

Nomenclature

c_p = specific heat
g = acceleration of gravity
G = Green's function
i = mass of oxygen per unit mass of fuel
K_0 = modified Bessel function
$m_{ox,\infty}$ = ambient oxygen mass fraction
$\dot{m}''$ = surface mass flux of vaporizing fuel
$\hat{n}$ = unit normal
Pe_g = Peclet number, $V_g\alpha_s/V_F\alpha_g$
Pe_p = Peclet number, $V_F\tau_p/\alpha_s$
Pe_s = Peclet number, $V_F\tau/\alpha_s$
r = radial coordinate
s = surface coordinate
T_a = activation temperature for fuel gasification or pyrolysis
T_v = fuel vaporization temperature
T_∞ = ambient temperature
v = arbitrary function
V_F = flame spread rate
V_g = gas velocity
x,y = dimensionless coordinates
α = angle
α_g = thermal diffusivity of gas phase
α_s = thermal diffusivity of solid phase
δ = delta function
ΔH_c = heat of combustion
ϵ = $Pe_s \tan\alpha$
θ = dimensionless temperature
μ = constant
ν = kinematic viscosity
ξ,η = coordinates in physical variables
τ = fuel-bed half thickness
τ_p = thermal penetration depth
ρ_s = solid-phase density
ϕ = angle
ψ = modified dimensionless temperature

flame attachment point, $\xi = 0$. Thus, the tip region should have little influence on the temperature field of interest.

The mathematical statement for the temperature field in the solid consists of the heat conduction equation with appropriate boundary conditions. Because here we deal only with the solid phase, the temperature field and the surface heat flux are determined for a specified (actually experimentally measured) spread rate, if either the temperature or the heat flux is specified at each point on the surface. In the actual flame spread problem, the spread rate would be the unknown and the surface temperature and heat flux known from the solution to the coupled gas-phase problem as mentioned above.

The differential equation, for constant properties, and associated boundary conditions are:

$$\mathrm{Pe}_s \frac{\partial \theta}{\partial x} = \frac{\partial^2 \theta}{\partial x^2} + \frac{\partial^2 \theta}{\partial y^2} \tag{1}$$

$$\frac{\partial \theta}{\partial y} = 0 \text{ for } y = -1, x \le \frac{1}{\tan\phi} \tag{2}$$

$$\theta = 0 \text{ as } x \to -\infty \tag{3}$$

$$\theta = 1 \text{ for } y = -x \tan\phi \tag{4}$$

$$\frac{\partial \theta}{\partial y} = 0 \text{ for } y = 0, x \le 0 \tag{5}$$

In the above formulas, Pe_s is the solid-phase Peclet number, $V_F \tau/\alpha_s$, x and y are ξ and η, respectively, measured in the units of τ, and θ is the temperature above ambient measured in the units $(T_v - T_\infty)$.

The applicability of equations (1-4) is apparent. Equation (5) presumes an adiabatic surface forward of the flame and thus requires comment. The flame spreads over the surface of the fuel bed by transferring heat forward of itself to heat the virgin fuel so that a small amount of gasification takes place upstream of the position where $\theta = 1$. This gas-phase fuel then begins to react with the surrounding oxidizer, and the flame moves forward heating the surface beneath it to $\theta = 1$. For downward spread over slabs of PMMA, the forward heat transfer takes place either by conduction through the solid or through the gas ahead of the flame or by a combination of both. In any of these cases, radiation is unimportant for downward spread because the view factor between the flame and unburnt fuel is small. Thus, we expect equation (5) to apply only when solid-phase heat conduction is the predominant mode of heat transfer forward of the flame.

If, on the contrary, the forward heat transfer is predominantly through the gas phase, equation (5) is inappropriate because then a heat flux from the gas to the solid upstream of $x = 0$ is required to maintain the spreading flame. This situation will not arise if the characteristic length for streamwise conduction in the solid is greater than that in the gas, i.e., if the gas-phase Peclet number, Pe_g, based on the characteristic length for forward heat conduction in the solid, which in this case is α_s/V_F, exceeds unity [3]. Practically speaking, at least for downward spread on PMMA or for spread over PMMA into an opposing flow of oxidizer, Pe_g is large near extinction [6,7]. Far from extinction, Pe_g is small, and gas-phase forward conduction dominates [6,7].

Other approximate boundary conditions than the ones we have imposed here along $y = 0$ for $x \le 0$ and $y = -x \tan\phi$ have been employed by others when Pe_s is specified. As long as the conditions are based on sound physical reasoning, the results obtained using them are apt to be valid. Sibulkin et al. [9], neglecting surface regression, used an exponentially decaying heat flux to the solid along $y = 0$ on either side of $x = 0$. It is easy to show that their results are identical to ours as $\mathrm{Pe}_s \to 0$. This is quite understandable physically because as $\mathrm{Pe}_s \to 0$, θ becomes a function of x alone, and so it is impossible to

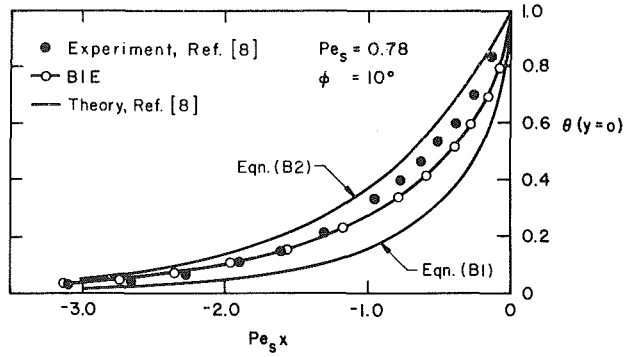

Fig. 2 Upstream surface temperature for downward spread on a PMMA sample with $\mathrm{Pe}_s = 0.78$ and $\phi = 10$ deg

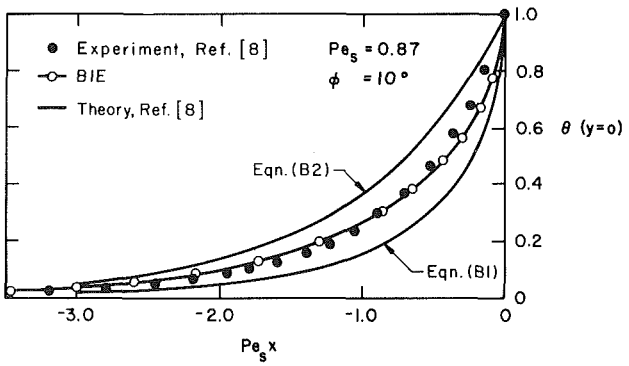

Fig. 3 Upstream surface temperature for downward spread on a PMMA sample with $\mathrm{Pe}_s = 0.87$ and $\phi = 10$ deg

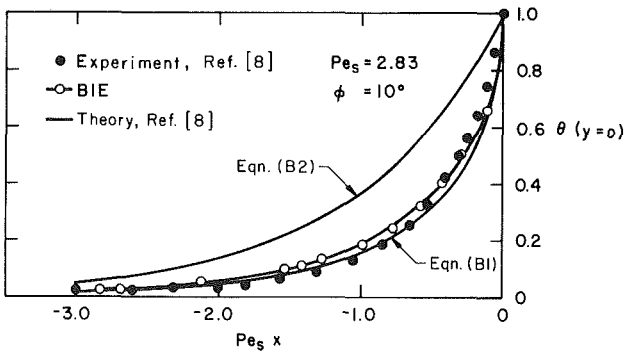

Fig. 4 Upstream surface temperature for downward spread on a PMMA sample with $\mathrm{Pe}_s = 2.83$ and $\phi = 10$ deg

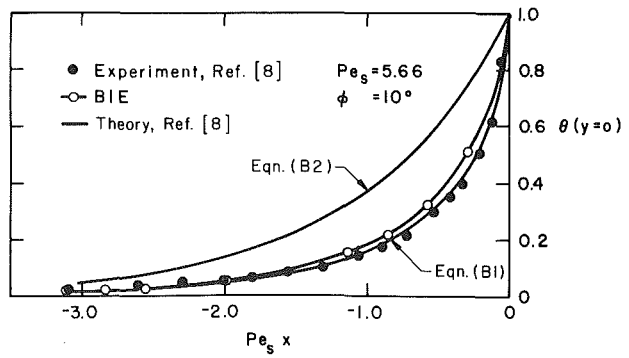

Fig. 5 Upstream surface temperature for downward spread on a PMMA sample with $\mathrm{Pe}_s = 5.66$ and $\phi = 10$ deg

transfer heat across the surface $y=0$; hence the fuel bed is effectively insulated for $x<0$, which is our boundary condition exactly.

As mentioned above, our principal solution technique is the boundary integral equation (BIE) method. We develop, in Appendix A, the basic elements of the technique as applied to the problem given by equations (1-5). The development results in an integral equation, which when solved for a particular Peclet number, Pe_s, provides the surface temperature, if the temperature gradient is specified as a boundary condition, or the surface temperature gradient, if the surface temperature is specified, on the boundaries of the fuel bed. If the temperature distribution within the bed is desired, it can be found, following solution of the integral equation, by comparatively simple quadrature.

We also develop, in Appendix B, an approximate analytical solution to the limiting case of small $Pe_s \tan\alpha$, where $\alpha = (\pi/2-\phi)$. This solution complements the two limiting solutions developed in [8] for $\alpha = 0$ and for $Pe_s \to \infty$ with $\phi = 0$, and should apply near flame extinction [10].

Results and Discussion

The boundary integral equation method was used to solve equations (1-5) for four values of Pe_s at which some of the data in reference [8] were obtained. Figures (2-5) show a comparison between the measured and computed surface temperatures as well as equations (B1) and (B2) for $x<0$. The angles needed to make the computations were measured by burning samples vertically downward in air at the same values of Pe_s at which the data were taken, extinguishing the flame and measuring the angle on a photograph of the same cross section. Figure 1 is an example of one of the photographs used for this purpose; it corresponds to $Pe_s = 5.66$. We did not burn a sample corresponding to $Pe_s = 0.87$ [8], but because the other three values of Pe_s yielded $\phi = 10$ deg, we used 10 deg for a Pe_s of 0.87 also.

It may at first glance seem odd that ϕ is 10 deg for the Pe_s for which we measured ϕ because ϕ is approximately $\sin^{-1}(\dot{m}''/\rho_s V_F)$. If $\dot{m}''$ is fixed, which would be the case here for a unique T_v, then $\sin\phi$ is inversely proportional to V_F. The two largest Pe_s samples have the same V_F, so we expect them to have the same ϕ. For $Pe_s = 0.78$, V_F is larger than for the larger Pe_s values, and it would appear that ϕ ought to be less than 10 deg. But, experimental and theoretical results ([8] and [3]) indicate that as the surface temperature rises from ambient at large negative x to the vaporization temperature, there is an overshoot in temperature such that near $x = 0$ the surface temperature exceeds the constant value eventually reached for positive x. Typically, the overshoot is about 30 K above the downstream value of T_v [8]. For $Pe_s = 0.78$, the overshoot occupies a substantial portion of the length of the regressing surface, causing $\dot{m}''$ for this Peclet number to exceed $\dot{m}''$ for the larger ones [8]. Hence, the tendency for ϕ to decrease as V_F increases as Pe_s decreases is balanced by the increase in $\dot{m}''$, and ϕ remains equal to 10 deg.

As can be seen from the figures, the computed results match the experimental results quite well. For the two larger values of Pe_s, the BIE results are very similar to equation (B1), and it appears that for $Pe_s x > -1$, equation (B1) represents the experimental data slightly better than the BIE method does. For the two smaller values of Pe_s, there is a tendency for the experimental temperatures to be above the computed values for $Pe_s x > -1$. Small values of Pe_s also imply small values of Pe_g so that fuel-bed heating by the gas near $x=0$ for these smaller Peclet numbers may be important. This mode of heating is not considered in the theoretical results and may cause them to underestimate the actual temperature near $x=0$[8].

We estimate for these results, using V_g as noted earlier, that the gas-phase Peclet number varies from 2 to about 4.4. Thus, we expect solid-phase conduction to be the dominant process causing upstream solid heating. For a portion of the length over which the solid is heated upstream of $x=0$, it will be heated by the gas near $x=0$ and cooled by the gas for a portion of the length further upstream. The heating near $x=0$ extends over a longer length for the smaller values of Pe_g so the net effect is that for these values of Pe_g our computed temperatures are too low near $x=0$. As the Peclet number increases, the results near $x=0$ should improve. The cooling effect of the gas phase is less important than the heating effect because the gas-phase thermal conductivity is small compared to that of the solid, and the characteristic temperature difference for cooling, $T_v - T_\infty$, is much less than that for heating, i.e., the difference between the flame and vaporization temperatures [3].

The heat conducted upstream of $x=0$ is used to raise the temperature of the bed to $\theta = 1$ at $x = 0$ when $y = 0$. If we allow the heat conducted upstream of the flame to heat a dimensional depth, τ_p, to $\theta = 1$ at $x = 0$, then τ_p, the penetration depth, is related to the heat conducted, in dimensionless form, by

$$\frac{V_F \tau_p}{\alpha_s} = \int_{-1}^{0} \left.\frac{\partial\theta}{\partial x}\right|_{x=0} dy \tag{6}$$

where the left hand side of equation (6) is obviously the Peclet number based on the heated layer depth, Pe_p, and the right hand side is the dimensionless rate of heat conduction. When α is zero, $Pe_p = Pe_s$ because the penetration depth is then τ. When ϕ is zero, Pe_p is unity because the characteristic length for heat conduction in the x and y direction is the same, i.e., α_s/V_F.

It is usual to classify a fuel bed as thermally thick when $\alpha_s/V_F << \tau$. But this classification is only useful when ϕ is near zero and τ_p is about α_s/V_F. As $\phi \to \pi/2$, which it will near extinction, the solid is heated across its entire thickness, the definition of a thermally thin bed, even though α_s/V_F may be much less than τ. For situations then where $V_F\tau/\alpha_s$ is large, whether or not the fuel bed is thermally thick or thin depends on τ_p/τ, which in turn depends on ϕ. We develop below approximate expressions that can be used to calculate τ_p/τ when the fuel bed is in a transition between being thermally thick and thermally thin as ϕ varies.

Using equations (B3-B6), we can find an expression for Pe_p in equation (6) that is valid for small $Pe_s \tan\alpha$. The result is

$$Pe_p = Pe_s - (\tan\alpha)\frac{Pe_s^2}{2} + (\tan^2\alpha)\frac{Pe_s^3}{12}$$

$$+ (\tan^2\alpha)Pe_s^2 \sum_{n=1}^{\infty} 2\frac{\beta(n)}{n^4\pi^4}(1-\cos n\pi)^2 + \cdots \tag{7}$$

where $\beta(n)$ is given in equation (B5). The first two terms on the right hand side of equation (7), which uses the solution for small $Pe_s \tan\alpha$ to $0[Pe_s\tan\alpha]$, have an interesting physical interpretation. Multiplying equation (7) by $(\alpha_s/V_F)^2$ and retaining two terms on the right hand side we get

$$\frac{\alpha_s}{V_F}\tau_p = \frac{\alpha_s}{V_F}\tau - \frac{\tau^2\tan\alpha}{2} \tag{8}$$

The left hand side represents approximately the volume per unit width near $x = 0$ that is heated to nearly $\theta = 1$ because τ_p is the y-direction conduction length, and α_s/V_F is the x-direction conduction length. The first term on the right hand side is the maximum volume per unit width that could be heated to nearly $\theta = 1$ when the entire thickness at $x = 0$ is at $\theta = 1$. The remaining term accounts for the fact that the triangular cross section downstream of $x = 0$, of volume per unit width $\tau^2\tan\alpha/2$, must be elevated to nearly $\theta = 1$ when α is other than zero.

The physical interpretation of equation (8) can be used to

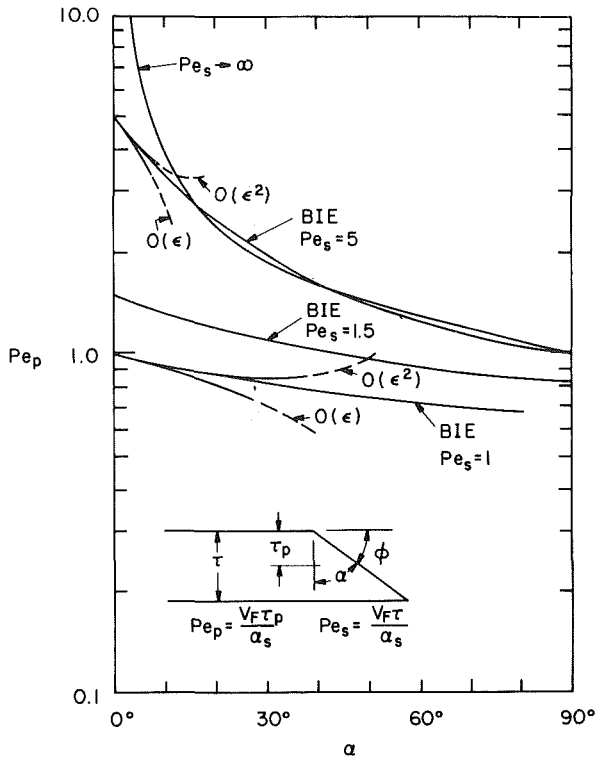

Fig. 6 Upstream heat transfer, Pe_p, as a function of α with Pe_s as a parameter

find an approximate expression for the penetration depth when $\phi \to 0$ and $Pe_s \to \infty$. As a result of the second requirement, the temperature field in the vicinity of $x = 0$ will be affected only slightly by conditions more than a few characteristic lengths, α_s/V_F, downstream of $x = 0$. Thus we estimate that a volume, $\simeq (\alpha_s/V_F)^2 \tan\phi/2$, downstream of $x = 0$, does not need to be heated and that the penetration depth will be correspondingly increased. Because the volume heated when $\phi = 0$ and $Pe_s \to \infty$ is $(\alpha_s/V_F)^2$, this reasoning leads to the result that

$$\frac{\alpha_s \tau_p}{V_F} = \left(\frac{\alpha_s}{V_F}\right)^2 + \left(\frac{\alpha_s}{V_F}\right)^2 \frac{\tan\phi}{2} \tag{9}$$

or in dimensionless form we have

$$Pe_p = 1 + \frac{\tan\phi}{2} \tag{10}$$

The boundary integral equation method can also be used to calculate the forward heat conduction as a function of ϕ with Pe_s as a parameter. Once the unknown boundary data are determined, equation (A5) may be applied to find the temperature field so that Pe_p may be calculated from equation (6). The computation is described in Appendix A.

Figure 6 shows Pe_p plotted against α for several values of Pe_s. Curves labeled with the order symbols were obtained from the asymptotic expansion of θ for small ϵ, with $\epsilon = Pe_s \tan\alpha$, and the one labeled $Pe_s \to \infty$ is the approximate expression, equation (10), that should be valid for large ϵ. The labeling of the latter curve may be somewhat confusing. In the real flame spread problem, ϕ (or α) is not independent of Pe_s, but it is so in the conduction problem that we consider here. Because equation (10) is independent of Pe_s, it is applicable for infinite Pe_s as ϕ varies, although realistically this is not possible.

The three curves labelled $Pe_s = 1$, 1.5, and 5 were obtained from the BIE method. To calculate the value of Pe_p for $Pe_s = 1.5$ and 5 and $\alpha = 90$ deg (i.e., $\phi = 0$ deg), a boundary condition was needed that could be applied at some x location downstream of the origin. An approximate condition was obtained from the limit of Eqn. (B1) as $(y/x)^2 \to 0$ to retrieve the similarity solution that should obtain in this limit. The resulting θ profile was applied at $x = 5$.

For $\alpha = 0$, the value of Pe_p must be equal to Pe_s regardless of the calculation technique. Near $\alpha = 0$, the approximate solution to order ϵ^2 for $Pe_s = 1$ and 5 appears to be valid; it matches the BIE method solution there, for values of ϵ of about 0.35 and smaller. For $Pe_s = 5$, the BIE method gives a value of Pe_p of unity for $\alpha = 90$ deg, which is what is obtained from using the temperature field in equation (B1), the exact solution for $\alpha = 90$ deg in the limit as $Pe_s \to \infty$. Thus, it appears that $Pe_s = 5$ is large enough to be considered infinite. What is most remarkable about the results in Fig. 6 is that the approximate relation for Pe_p in equation (10) that we expected to be valid for large ϵ, (i.e., α near 90 deg), based solely on physical reasoning, nearly coincides with the BIE method results for $Pe_s = 5$ up to an α of about 12 deg!

For $\alpha = 12$ deg and $Pe_s = 5$, we have $Pe_s \tan\alpha = 1.06$, and so when ϵ exceeds unity equation (10) appears to apply. As Pe_s increases, Pe_p must become independent of Pe_s, and the approximate expression will hold to smaller and smaller α because there we only need to require that ϵ exceed unity.

Conclusions

The boundary integral equation method is an attractive one for the solid-phase conduction problem of flame spreading. Only surface temperatures and heat fluxes need to be computed if the temperature distribution in the solid is not desired. And, realistic conditions may be imposed for the shape of the regressing fuel bed downstream of the leading edge of the flame. No particular limits such as small or large Peclet numbers must be applied. Computer results from the method agree well with the limited amount of experimental data to which we have compared them.

Computation of forward heat transfer, which allows the depth of the heated layer to be deduced, can be easily carried out with the boundary integral equation method. The BIE method results, for forward heat transfer, are the same as those that would be computed from the analytical results in [8] for $\phi = \pi/2$ and $\phi = 0$, as long as for the latter condition Pe_s is about 5 or greater.

Our results lend credence to approximate methods that were also presented. The utility of the approximate results is that analytical formulas result, e.g., for Pe_p, that are easy to incorporate into dimensionless correlations [7].

Acknowledgment

We gratefully acknowledge the partial support received for this work from NASA under Grant NSG-3114 with T. H. Cochran serving as technical monitor. Thanks are also extended to M. Vedhanayagam for his help in a portion of the asymptotic expansion work, and to D. J. Shippy for some help in computer programming.

References

1 de Ris, J. N., "Spread of a Laminar Diffusion Flame," *Twelfth Symposium (International) on Combustion*, The Combustion Institute, 1969, pp. 241-252.

2 Frey, A. E., and T'ien, J. S., "A Theory of Flame Spread Over a Solid Fuel Including Finite-Rate Chemical Kinetics," *Combustion and Flame*, Vol. 36, 1979, pp. 263-289.

3 Fernandez-Pello, A., and Williams, F. A., "A Theory of Laminar Flame Spread Over Flat Surfaces of Solid Combustibles," *Combustion and Flame*, Vol. 28, 1977, pp. 251-277.

4 Sirignano, W. A., "Theory of Flame Spread Above Solids," *Acta Astronautica*, Vol. 1, 1974, pp. 1285-1299.

5 Altenkirch, R. A., Eichhorn, R., and Shang, P. C., "Buoyancy Effects on Flames Spreading Down Thermally Thin Fuels," *Combustion and Flame*, Vol. 37, 1980, pp. 71-83.

6 Fernandez-Pello, A. C., Ray S. R., and Glassman, I., "Flame Spread in An Opposed Forced Flow: The Effect of Ambient Oxygen Concentration," *Eighteenth Symposium (International) on Combustion*, The Combustion Institute, 1981, pp. 579–589.

7 Altenkirch, R. A., Eichhorn, R., and Rizvi, A. R., "Correlating Downward Flame Spread Rates for Thick Fuel Beds," submitted to *Combustion Science and Technology*.

8 Fernandez-Pello, A., Kindelan, M., and Williams, F. A., "Distribución Superficial de Temperaturas Durante La Propación de Llama en Sentido Descendente Sobre Láminar de PMMA," *Ingenieriá Aeronáutica y Astronáutica*, Vol. 135, 1974, pp. 41–53; see also Paper WSS/CI 73-8, Western States Section of the Combustion Institute, 1973.

9 Sibulkin, M., Kim, J., and Creeden, J. V., "The Dependence of Flame Propagation on Surface Heat Transfer: Part I—Downward Burning," *Combustion Science and Technology*, Vol. 14, 1976, pp. 43–56.

10 Sibulkin, M., and Little, M. W., "Propagation and Extinction of Downward Burning Fires," *Combustion and Flame*, Vol. 31, 1978, pp. 197–208.

11 Fairweather, G., Rizzo, F. J., Shippy, D. J., and Wu, Y., "On the Numerical Solution of Two-Dimensional Potential Problems by an Improved Boundary Integral Equation Method," *Journal of Computational Physics*, Vol. 31, No. 1, 1979, pp. 96–112.

12 Lachat, J. C., and Watson, J. O., "Effective Numerical Treatment of Boundary Integral Equations: A Formulation for Three-Dimensional Electrostatics," *International Journal of Numerical Methods in Engineering*, Vol. 10, No. 5, 1976, p. 991.

13 Rizzo, F. J., and Shippy, D. J., "An Advanced Boundary Integral Equation Method for Three-Dimensional Thermo-Elasticity," *International Journal of Numerical Methods in Engineering*, Vol. 11, 1977, pp. 1753–1768.

14 Rezayat, J., M.S. thesis, University of Kentucky, Department of Engineering Mechanics, 1981.

15 Van Dyke, M., *Perturbation Methods in Fluid Mechanics*, Academic Press, 1964.

APPENDIX A

The BIE method applied to a set of equations, such as equations (1–5), results in an integral equation that requires only information (potential or flux) to be specified on the surface of the boundary to develop a solution for the unknown surface conditions (flux or potential). Following solution of the integral equation, the distribution of field variables can be found by comparatively simple quadrature. A discussion of the numerical techniques that we used to solve the integral equation (see references [11], [12], and [13]) or perform any necessary integration is beyond the scope of this paper. Also, our development, up to and including presentation of the free-space Green's function, is virtually the same as that of Sirignano [4], upon whose work we have relied heavily.

The differential equation of interest here is $M\psi = 0$, where the operator, M, is $(\nabla^2 - [\mathrm{Pe}_s/2]^2)$, and ψ is defined by

$$\theta = \psi e^{\frac{\mathrm{Pe}_s x}{2}} \tag{A1}$$

For ψ, the operator, M, and an unspecified function, v, Green's theorem yields:

$$\iint_A (vM\psi - \psi Mv)\, dA = \oint_C \left(v\frac{\partial \psi}{\partial n} - \psi \frac{\partial v}{\partial n}\right) ds \tag{A2}$$

where dA is a differential area element in region A, the cross section of the fuel bed, C is the boundary of A, ds is a differential element of arc-length on C, $\partial\psi/\partial n = \nabla\psi \cdot \hat{n}$, and $\partial v/\partial n = \nabla v \cdot \hat{n}$, with $\hat{n}$ the unit outward pointing normal on C.

Now let v be the free-space Green's function, G, that satisfies

$$MG = \delta(x - x_0)\delta(y - y_0) \tag{A3}$$

where δ is the Dirac delta function. Due to properties of the delta function and because $M\psi = 0$, equation (A2) becomes

$$\psi(x_0, y_0) = \oint_C \left[\psi(x,y)\frac{\partial G}{\partial n}\bigg|_{(x,y;x_0,y_0)} - G(x,y;\, x_0,y_0)\frac{\partial \psi}{\partial n}\bigg|_{(x,y)}\right] ds \tag{A4}$$

in which (x_0, y_0) is in A and (x,y) is on C.

A solution to the radially symmetric problem for G for $r > 0$, where $r = [(x-x_0)^2 + (y-y_0)^2]^{1/2}$, is a constant μ times $K_0(\mathrm{Pe}_s r/2)$, the zero order modified Bessel function of second kind [4]. To fix μ, let C in equation (A4) be a disk of small radius, ϵ. Because $K_0(\mathrm{Pe}_s r/2) \sim -1n(\mathrm{Pe}_s r/2)$ for sufficiently small $\mathrm{Pe}_s r/2$, the second integral in equation (A4) vanishes in the limit whereas the first requires that μ be $-1/2\pi$. Expression (A4) for $\psi(x_0, y_0)$ thus has the form

$$2\pi\psi(x_0,y_0) = \oint_C \left(K_0\left(\frac{\mathrm{Pe}_s}{2}r\right)\frac{\partial\psi}{\partial n} - \psi\frac{\partial}{\partial n}K_0\left(\frac{\mathrm{Pe}_s}{2}r\right)\right) ds \tag{A5}$$

Equation (A5) may be applied to determine ψ in A if ψ and $\partial\psi/\partial n$ are known on C, and Pe_s is known. All three are in general not specified so that equation (A5) cannot at present be applied. For the problem we consider here, Pe_s and either ψ or $\partial\psi/\partial n$ on C are specified. To determine the unknown boundary condition so that equation (A5) has utility, we compute the limit in (A5) as (x_0, y_0) in A approaches a point (X_0, Y_0) on C. The result of the limit process if C has a unique tangent plane at (X_0, Y_0) is [14]

$$\pi\psi(X_0,Y_0) = \oint_C \left(K_0\left(\frac{\mathrm{Pe}_s}{2}r\right)\frac{\partial\psi}{\partial n} - \psi\frac{\partial}{\partial n}K_0\left(\frac{\mathrm{Pe}_s}{2}r\right)\right) ds \tag{A6}$$

If (X_0, Y_0) occupies a "corner," the multiplier in front of ψ in equation (A6) is no longer π but is the interior angle in A formed by the corner. When the boundary is smooth the interior angle is obviously π, and hence so is the multiplier.

Equation (A6) constitutes an integral equation for the unknown boundary information (either ψ or $\partial\psi/\partial n$). In the complete flame spread problem, ψ and $\partial\psi/\partial n$ on C would be specified from the solution to the gas-phase problem, and equation (A6) then becomes a relation for determining Pe_s. If the Peclet number so determined satisfies mass conservation in the solid phase, then the solution is complete, and the boundary conditions imposed on the solid phase are the correct ones.

The BIE method, through equation (A5), permits calculation of the field variables at interior points. In the case of Pe_p (equation (6)), we need the value of the flux $\partial\theta/\partial x$ along $x = 0$, but the computation can be made simpler by applying Green's second theorem. We use the differential equation to replace $\nabla^2\theta$ in favor of $\mathrm{Pe}_s\, \partial\theta/\partial x$, realizing that $\partial\theta/\partial x = 0$ as $x \to -\infty$ and that $\partial\theta/\partial y = 0$ for $y = 0$ and $y = -1$. Application of the divergence theorem and the condition $\theta = 0$ as $x \to -\infty$ then gives

$$\mathrm{Pe}_p = \mathrm{Pe}_s \int_{-1}^{0} \theta\Big|_{x=0}\, dy \tag{A7}$$

When equation (A7) is used, equation (A5) must be applied to determine θ along the line $x = 0$. Equation (A7) is easier to apply than equation (6) because θ is easier to get than $\partial\theta/\partial x$ using (A5) and it, unlike $\partial\theta/\partial x$, is not singular at the origin. For results presented here, the integral in equation (A7) was evaluated using four point Gaussian quadrature [14].

APPENDIX B

Approximate Analytical Solution

There are some obvious limiting conditions for the problem composed of equations (1–5). It is logical, and as we shall see, quite fruitful, to attempt to get analytical solutions for these limiting cases. Two limiting cases have been solved in reference [8], one for the condition that $\phi = 0$ and $\mathrm{Pe}_s \to \infty$ and the other for $\phi = \pi/2$, which obtains near flame extinction [10]. The result for $\phi = 0$ and large Peclet number

from [8], which was obtained by converting the problem to a Wiener-Hopf one, is

$$\theta = \text{erfc}\left\{\left[\frac{1}{2}\text{Pe}_s((x^2+y^2)^{1/2}-x)\right]^{1/2}\right\} \tag{B1}$$

For $\phi = \pi/2$, the result from [8] is

$$\theta = e^{\text{Pe}_s x} \tag{B2}$$

It is easy to get an approximate solution for small $\text{Pe}_s \tan\alpha$, where $\alpha = (\pi/2 - \phi)$, by constructing an asymptotic expansion of the form

$$\theta \sim \theta_0 + \epsilon\theta_1 + \epsilon^2\theta_2 + \cdots \tag{B3}$$

with $\epsilon = \text{Pe}_s \tan\alpha$. To do so, the boundary condition along $y = -x \tan\phi$ is transferred to the position $x = 0$ (i.e., $\alpha = 0$) as described by Van Dyke [15]. We assume that the θ_i for $i \geq 1$ are analytic in x as is θ_0. The resulting problems for θ_i can be solved by separation of variables giving θ_0 as in equation (B2),

$$\theta_1 = -\frac{1}{2}e^{\text{Pe}_s x} + \sum_{n=1}^{\infty}\frac{2}{n^2\pi^2}[1-\cos(n\pi)]e^{\beta(n)x}\cos(n\pi y) \tag{B4}$$

where

$$\beta(n) = \frac{\text{Pe}_s + (\text{Pe}_s{}^2 + 4n^2\pi^2)^{1/2}}{2} \tag{B5}$$

and

$$\theta_2 = \frac{1}{12}e^{\text{Pe}_s x} + \sum_{n=1}^{\infty}\frac{2}{\text{Pe}_s n^4\pi^4}\beta(n)[1-\cos(n\pi)]^2 e^{\text{Pe}_s x} \tag{B6}$$

$$-\sum_{n=1}^{\infty}\frac{1}{n^2\pi^2}[1+\cos(n\pi)]e^{\beta(n)x}\cos(n\pi y)$$

$$+2\sum_{k=1}^{\infty}\left[\int_{-1}^{0}\sum_{n=1}^{\infty}\frac{2\beta(n)}{\text{Pe}_s n^2\pi^2}[1-\cos(n\pi)]y\cos(n\pi y)\right.$$

$$\left.\cos(k\pi y)\,dy\right]e^{\beta(k)x}\cos(k\pi y)$$

We tried to get an approximate solution for small $\tan\phi$ by seeking an asymptotic expansion for θ as in equation (B3) with $\epsilon = \tan\phi$. The boundary condition along $y = -x \tan\phi$ was transferred to $y = 0$, and the resulting problems for the θ_i were formulated as Wiener-Hopf problems. The problem for θ_0 is the same as the one solved in [8] for $\phi = 0$, except we did not allow $\text{Pe}_s \to \infty$. After failing to split the kernel in the problem for θ_0, our search for the approximate solution ended. We show in the results section, however, that based on physical arguments it is easy to construct an approximate expression for the heat conducted upstream of $x = 0$ for small $\tan\phi$ when Pe_s is large.

An Experimental Study of Upper Hot Layer Stratification in Full-Scale Multiroom Fire Scenarios

L. Y. Cooper
Assoc. Member ASME

M. Harkleroad

J. Quintiere
Mem. ASME

W. Rinkinen

Center for Fire Research,
National Bureau of Standards,
Washington, D.C. 20234

This paper describes an experimental study of the dynamics of smoke filling in realistic, full-scale, multiroom fire scenarios. A major objective of the study was to generate an experimental data base for use in the verification of mathematical fire simulation models. The test space involved 2 or 3 rooms, connected by open doorways. During the course of the study the areas were partitioned to yield four different configurations. One of the rooms was a burn room containing a methane burner which produced either a constant energy release rate of 25, 100, or 225 kW or a time-varying energy release rate which increased linearly with time from zero at ignition to 300 kW in 10 min. An artificial smoke source near the ceiling of the burn room provided a means for visualizing the descent of the hot layer and the dynamics of the smoke filling process in the various spaces. The development of the hot stratified layers in the various spaces was monitored by vertical arrays of thermocouples and photometers. A layer interface was identified and its position as a function of time was determined. An analysis and discussion of these results are presented.

Introduction

In recent years there has been considerable research activity in the dynamic modeling of environmental conditions which develop in enclosed spaces as a result of hazardous fires. Attention was originally focused on single space enclosures with ventilation from single openings [1, 2, 3] (a closed or partially opened window or door). Work has recently been initiated on the development of computer programs which model the spread of combustion products through connected, multiroom configurations with multiple ventilation openings [4, 5, 6]. In order to gain confidence in these analytic tools, and to improve their predictive capability, comparisons between theory and full-scale experiments are required. To some extent such comparisons have already been successfully carried out [7, 8, 3].

A major goal of this mathematical modeling activity is to provide a tool for estimating the development of hazardous conditions in real fire scenarios. In terms of life safety considerations, one is particularly concerned with reasonably accurate modeling of the environmental conditions from the time of fire ignition until the time when life threatening conditions start to prevail. It is during such time intervals that successful fire detection and occupant egress must occur if a basic condition of safety is to prevail in an occupancy of interest [9]. The present experimental study is concerned with these relatively early time intervals which immediately follow the ignition of life threatening fires.

Objective of The Study

Enclosure fire models differ in a variety of ways. An example of where considerable variation exists is in the degree of detail in the physical description of the actual combustion zone located in the room of fire origin. In spite of such differences there is one feature which is common to all single or multiroom zone-type enclosure fire models; namely, a two-layer description of the intraroom environmental conditions. In the two-layer description, the environment in each room of a modeled space is described by a uniform lower layer of relatively cool and unpolluted ambient air, and by a uniform upper layer of elevated temperature and partially diluted products of combustion. The two layers are assumed to be divided by a sharp horizontal material interface. In the room of fire origin, the products of combustion are diluted with entrained lower layer ambient air as they rise in a plume from the combustion zone itself to the developing upper layer. In the vicinity of open connecting doorways or windows, the upper layer and lower layer of the burn room exchange mass with the layer pairs of adjacent spaces. Similar continuous exchanges between all other connected adjacent spaces also takes place as the various upper layers continue to grow in depth, in temperature, and in combustion product concentration.

If the simulations of a specific mathematical model (which incorporates the two layer approach) are to be used with confidence for a given class of threatening fire scenario, then at least two prior conditions must have been met. The first condition is that the two-layer model is shown to represent a reasonable qualitative description of the real fire environments of interest. The second condition is that quantitative predictions of the model compare favorably with actual data acquired during full scale fire tests. Furthermore, these latter prototype fire tests should cover a significant range of the key parameters which are descriptive of the class of threatening fire scenario of interest.

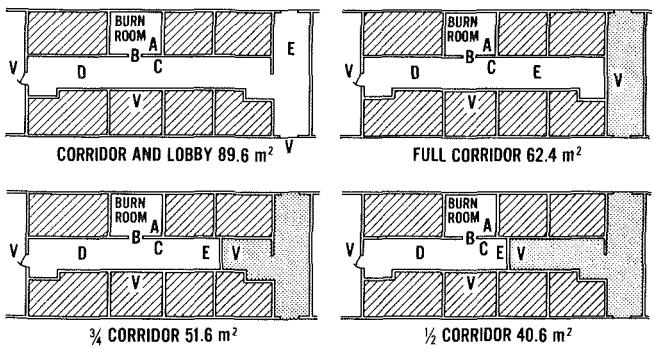

Fig. 1 Sketches of four test configurations with indications of the location of vertical instrument arrays (A, B, C, D, and E) and of video cameras (V)

Contributed by the Heat Transfer Division for publication in the JOURNAL OF HEAT TRANSFER. Manuscript received by the Heat Transfer Division October 7, 1981. Paper No. 81-HT-9.

It was the objective of the present study to generate an experimental data base on the dynamics of smoke filling in realistic, full-scale multiroom fire scenarios so that the data generated by these tests and tabulated here will provide a basis for the previously mentioned comparative checks between theory and experiment.

Description of The Test Program

The test program consisted of a series of separate tests involving a variety of space configurations and fire energy release rates.

For a given test, the test space involved either two or three rooms connected by open doorways, all having a nominal 2.36-m ceiling height. The wall and ceiling surfaces of all rooms were lined with 13-mm thick gypsum board, and the floors were concrete. During the course of the test program the space was partitioned to yield four different configurations ranging in total plan area from 40.6 m^2 to 89.6 m^2. These configurations are sketched in Fig. 1. The doorway between the burn room and its adjacent space (designated here as the corridor) was 2.0-m high and 1.07-m wide. The doorway between the corridor and the next adjacent space (designated as the lobby) was 2.01-m high and 1.32-m wide.

An attempt was made to seal cracks and penetrations in the bounding surfaces of the test space. A 0.15-m × 0.94-m hole with clear opening to the outside (through an unused room and open window of the test facility) was provided next to the floor in a wall surface of the corridor. In concert with the attempts at sealing all surfaces, the hole was to provide the major leakage path for mass exchanges between the test space and the outside environment.

Each test used the same burn room of 14.0 m^2 area. The room contained a 0.30-m × 0.30-m square methane diffusion burner whose burn surface was positioned 0.24 m above the floor and approximately in the center of the room. After ignition from a pilot light, fuel supply to the burner was manually controlled from an outside metering system to produce one of four possible energy release rates: a constant rate, Q, of 25 kW, 100 kW, or 225 kW; or a time varying energy release rate, $Q_{ramp}(t)$, of

$$Q_{ramp}(t) = 30\ t\ \text{kW}, 0 \le t\ (t \text{ in minutes}) \qquad (1)$$

where the time from ignition, t, never exceeded 10 min. These bear a similarity to energy rates that would develop from fires in wastepaper baskets, upholstered chairs, and mattresses.

McCaffrey [10] has studied the free-burn characteristics of the particular burner used in these tests. Using methane for a fuel, and for fire powers between 50 kW and several hundreds of kW he found that, of the total energy release rate of the fire, a fraction, λ_r, of approximately 0.24 is radiated away from the combustion zone. For a 25-kW fire power he found λ_r to be 19 percent.

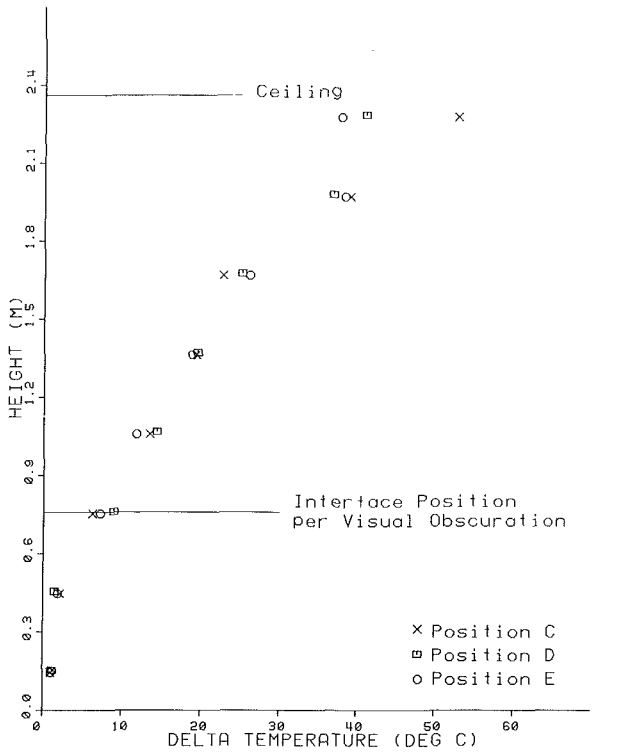

Fig. 2 t = 165 s temperatures at corridor positions, C, D, and E; 100 kW, full corridor

With methane as a fuel the burner produced very little smoke. In order to have a visual tracer of the combustion products as they spread throughout the space, an artificial source of smoke was introduced into the ceiling jet of the burn room. Thus, in every test a highly visible white smoke was generated by a smoke candle and mixed with the fire's products of combustion near their source for up to 5 min. Effective visualization of the upper smoke layers was achieved by deploying fluorescent light fixtures on the floor of the corridor and lobby.

For each of the four spatial configurations of Fig. 1, a separate burn test was run for each of the four energy release rates (16 test runs). For the 100-kW fire power and full corridor configuration of Fig. 1, three additional tests were also run. In these test runs the burn room-to-corridor doorway width was reduced to 1/2, 1/4, and 1/8 of its full value.

Nomenclature

A_B, A_C, A_L = areas of burn room, corridor, and lobby
C_P = specific heat at constant pressure
e = specific internal energy
H = floor-to-ceiling height
h, h_{amb} = specific enthalpy and its ambient value
N = value of N in N percent rule, equation (2)
n = an integer
$\bar{n}$ = unit normal vector
P = absolute pressure
Q = total energy release rate of fire
Q_{ramp} = value of Q for ramp fire, equation (1)
S = internal bounding surface of enclosure
T, T_{amb} = temperature and its ambient value
t, t^* = time after ignition
$\bar{V}$ = velocity vector
z = distance above floor
z_i = z for interface
z_{top} = z for top thermocouple or photometer
Δp = burn room-corridor ceiling pressure difference
$\overline{\Delta T_A}, \overline{\Delta T_D}, \overline{\Delta T_E}$ = $\overline{\Delta T}$ at positions A, D, and E
ΔT_{min} = a minimum value of $N\Delta T_{ref}/100$
ΔT_{ref} = a reference temperature difference, see above equation (2)
$\overline{\Delta T}$ = vertical average of $T - T_{amb}$
Δz_n = vertical distance associated with thermocouple n
λ_r = fraction of Q radiated from fire
λ_c = fraction of Q transferred out of S
ρ, ρ_{amb} = density and its ambient value
τ = volume of enclosure

Instrumentation

The data acquired during the test included temperature measurements from vertical arrays of eight thermocouples each. The arrays were located at positions A, B, C, D, and E which are identified in Fig. 1. Note that the position of E shifts from one configuration to the next, but that positions A, B, C, and D are identical for all configurations. Bare wire, 0.25-mm Chromel-Alumel thermocouples were used. Except for doorway position, B, all arrays used identical 0.30-m spacing of the thermocouples, with the bottom one being 0.15 m from the floor and the top one being approximately 0.07 m from the ceiling. For the B array, the top and bottom thermocouples were 0.30 m, respectively, from the doorway lintel and the floor, and the spacing of all thermocouples was approximately 0.20 m.

Visual evidence of the development and growth of combustion product laden upper layers was obtained by vertical arrays of photometer transmitter-receiver pairs, each transmitter and receiver being separated by a horizontal distance of 1 m. The photometers had been used previously, and are described in [11]. The arrays each had four photometer pairs, and they were located at positions B, D, and E. The photometers at B were positioned 1.04 m, 1.38 m, 1.73 m, and 1.91 m above the floor, while those at D and E were positioned 0.33 m, 0.93 m, 1.56 m, and 2.19 m above the floor. (In the corridor-lobby configuration the 0.33-m photometer was not deployed.)

Visual evidence of layering was also obtained by post-test observations of video tapes which recorded the obscuration of vertical arrays of microminiature incandescent lights. Two arrays of lights were set up at positions D and E. The lights were placed adjacent to and at identical elevations of the D and E thermocouple arrays.

A separate video tape recorder camera with lens approximately 0.5 m from the floor was directed at each of the two arrays of lights. A third video recorder camera was placed directly across the corridor from the burn room with full view of the burner surface, the pilot and the near-ceiling smoke candle. The three cameras were positioned immediately outside of the test space at locations indicated in Fig. 1. Visual access for the first two of these cameras was through plastic inserts in closed doors at the ends of the corridor, or, in the case of the corridor-lobby configuration, at the end of the lobby and at the closed end of the corridor. The third camera viewed the burn room through a plastic insert in the corridor wall.

A single pair of static pressure taps, located at positions A and C and approximately 0.05 m from the ceiling was used to measure the pressure difference between the burn room and the corridor. The measuring system had been used previously, and it is described in [12]. With the A and C thermocouple array data and this reference pressure difference it should be possible to construct the time varying vertical pressure difference field that drives the flow across the burn room-corridor doorway.

During every test a multichannel analog-digital recorder system acquired the data from all the thermocouples and photometers and from the single pressure difference transducer at 5 s intervals.

While some of the data acquired during the tests will be presented and discussed below, for those interested in additional details all of this data is available in unreduced form from the National Bureau of Standards.

Experimental Procedure

The procedure during a given test run was as follows:

All photometer lenses were cleaned and their outputs were nulled. A member of the test team lit the pilot and evacuated the test space. The smoke candle fuse was ignited by means of wooden matches which were themselves ignited with an externally activated electrically controlled hot wire. At the instant that the candle started to smoke, as viewed from the cross-corridor camera, the fuel control system was operated to provide the appropriate rate of fuel supply, and the data acquisition recorder was activated.

The conditions in the test space were observed by television monitors which received the signals from the three video cameras. The test continued for 1–3 min past the time that smoke obscured the entire test space. At this time the fuel supply, the pilot, and all data collection was terminated. The

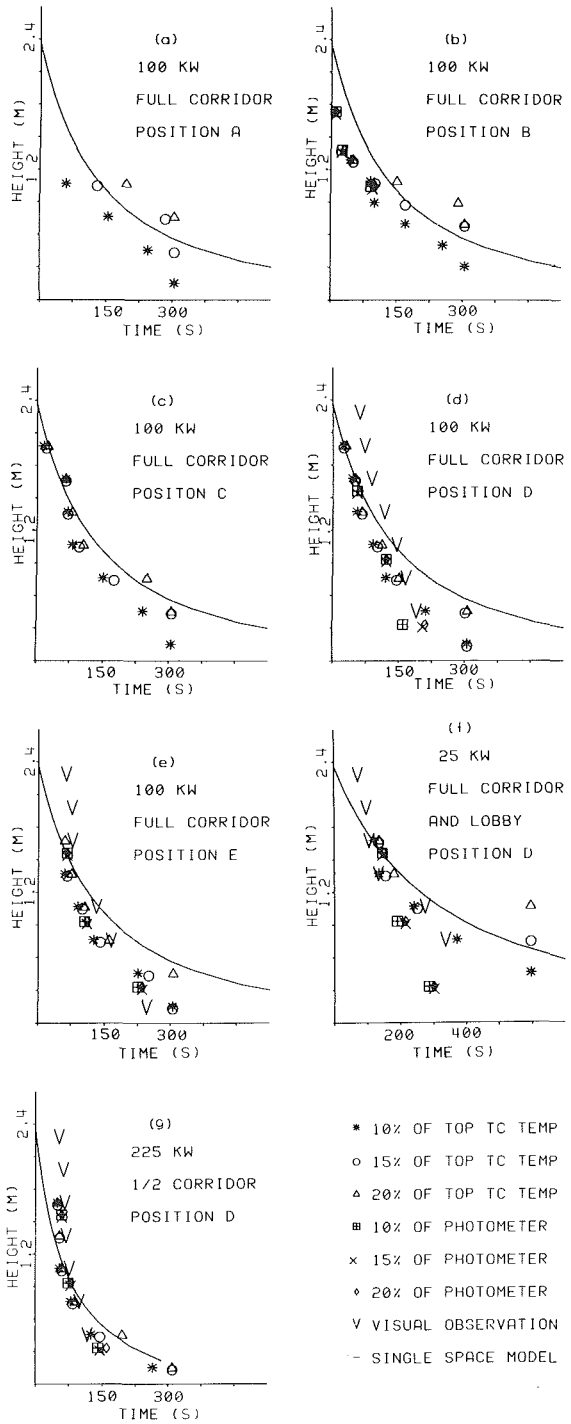

Fig. 3 Elevation of interface according to (*i*) *N* percent rule for *N* = 10, 15, and 20 as applied to thermocouple data and photometer data, (*ii*) obscuration of light array, and (*iii*) single room model

Table 1 Time in seconds after ignition when the layer passes a given z elevation according to: T_D – vertical thermocouple array at position D per 10 percent rule; P_D – vertical photometer array at position D per 10 percent rule; V_D – visual obscuration of vertical light array at position d; etc.

	25 kW 1/2 corridor									25 kW 3/4 corridor								
Z meter	T_A	T_C	T_D	P_D (V_D)	T_E	P_E (V_E)	Z meter	T_B	P_B	Z meter	T_A	T_C	T_D	P_D (V_D)	T_E	P_E (V_E)	Z meter	T_B	P_B
2.29				(81)		(63)				2.29				(68)		(86)			
1.98				(97)		(102)	1.73		5	1.98		25		(86)		(99)	1.73		15
1.68			70	(110)		(115)	1.49			1.68		65	65	(99)		(107)	1.49		
1.56				85			1.38		45	1.56				35		60	1.38		65
1.37		35	75	(117)	105	(173)	1.29	85		1.37		70	70	(106)		(152)	1.29		
1.07	110	120	80	(139)	115	(183)	1.09	115		1.07		120	100	(136)		(183)	1.09	115	
.93				130			1.04		110	.93				115		155	1.04		105
.76	185		140	(186)	130	(195)	.90	145		.76			150	(187)	150	(263)	.90	145	
.46	190	130	280	(200)		(217)	.70	165		.46	290	245	215	(221)	175	(317)	.70	195	
.33				250			.50	255		.33				120		250	.50	270	
.15	425	425	425		425		.30	410		.15	370	370	370		365	(266)	.30	370	
	25 kW full corridor									25 kW full corridor and lobby								
2.29				(81)		(69)				2.29				(72)		(124)			
1.98		55		(101)		(113)	1.73		15	1.98				(97)		(162)	1.73		60
1.68	20	125	100	(105)		(118)	1.49			1.68			120	(105)			1.49		
1.56				105		125	1.38		55	1.56				145		270	1.38		105
1.37		140	110	(144)	120	(131)	1.29	80		1.37			135	(133)		(227)	1.29		
1.07	50	150	165	(215)	155	(185)	1.09	170		1.07	105		240	(274)		(243)	1.09		
.93				210		170	1.04		135	.93				190		275	1.04		145
.76	175	255	220	(241)	165	(211)	.90	205		.76	210		370	(335)		(281)	.90	315	
.46	245	320	310	(278)	175	(264)	.70	295		.46	595	430	595			(265)	.70	595	
.33				230		270	.50	410		.33				285		280	.50		
.15	590	610	595		555	(233)	.30	610		.15		595			590		.30		
	100 kW 1/2 corridor									100 kW 3/4 corridor								
2.29				(47)						2.29				(48)		(60)			
1.98		15		(57)	10		1.73		10	1.98		20		(59)		(65)	1.73		0
1.68	50		40	(62)			1.49			1.68		45	45	(67)		(111)	1.49		
1.56				50			1.38		30	1.56				55		35	1.38		15
1.37		55		(68)	55		1.29			1.37		50	50	(71)	35	(120)	1.29		
1.07		65	50	(77)	65		1.09	60		1.07		85	70	(98)	90	(149)	1.09	75	
.93				75			1.04		65	.93				85		105	1.04		70
.76	95	70	75	(94)	75		.90	80		.76	90	110	100	(126)	105	(209)	.90	80	
.46	140	125	135				.70	90		.46	125	170	180		125	(181)	.70	135	
.33				145	125		.50	125		.33				175		140	.50	210	
.15	280	295	250		295		.30	295		.15	360	360	360		360		.30	360	
	100 kW full corridor									100 kW full corridor and lobby								
2.29				(61)		(63)				2.29				(107)		(64)			
1.98		15	25	(72)		(76)	1.73		10	1.98				(120)		(74)	1.73		
1.68		65	45	(87)		(77)	1.49			1.68		135	115	(160)	155	(88)	1.49		
1.56				55		65	1.38		25	1.56							1.38		
1.37		70	55	(116)	60		1.29	45		1.37		145	120	(175)	170	(119)	1.29		
1.07	60	80	90	(144)	90	(131)	1.09	90		1.07		155	260	(187)	205	(261)	1.09		
.93				120		105	1.04		90	.93							1.04		
.76	155	150	120	(165)	125	(164)	.90	100		.76		435	360	(214)		(311)	.90	410	
.46	245	240	210	(189)	225		.70	170		.46	435		435	435	305		.70	435	
.33				160		225	.50	255		.33							.50		
.15	305	305	305		305	(246)	.30	305		.15					435		.30		
	225 kW 1/2 corridor									225 kW 3/4 corridor								
2.29				(54)						2.29				(52)		(85)			
1.98		20		(64)	20		1.73		20	1.98		20		(60)		(84)	1.73		0
1.68			45	(67)			1.49			1.68		40	40	(66)	30	(115)	1.49		
1.56				60			1.38		25	1.56				50		35	1.38		5
1.37		55		(70)	55		1.29			1.37		55	50	(77)		(144)	1.29	35	
1.07		65	50	(77)	60		1.09			1.07	65	65	55	(88)	70	(152)	1.09	60	
.93				75			1.04		70	.93				70			1.04		65
.76	100	70	75	(99)	70		.90	75		.76	75	90	85	(112)	90	(177)	.90	75	
.46	120	120	120	(117)	130		.70	85		.46	155	155	155	(152)	120	(179)	.70	105	
.33				140			.50	110		.33				150			.50	155	
.15	235	305	260		305		.30	245		.15	295	335	340		330		.30	310	
	225 kW full corridor									225 kW full corridor and lobby								
2.29				(55)		(60)				2.29						(82)			
1.98		15		(70)		(66)	1.73		10	1.98		15		(121)		(93)	1.73		15
1.68		50	35	(79)	45	(70)	1.49			1.68		50	35	(123)	70	(114)	1.49		
1.56				45		65	1.38		35	1.56				190		60	1.38		40
1.37		55	45	(99)		(85)	1.29	45		1.37		60	45	(137)	100	(161)	1.29		
1.07		65	85	(110)	70	(107)	1.09	80		1.07		160	150	(149)		(224)	1.09		
.93				95		100	1.04		70	.93				195		95	1.04		120
.76	135	130	105	(127)	100	(135)	.90	100		.76	230	340	235	(177)	140	(242)	.90	205	
.46	190	190	200	(138)	185	(158)	.70	160		.46	295	365	365	(234)	215	(283)	.70	365	
.33				175		195	.50	205		.33				200		100	.50		
.15	305	305	305		305		.30	305		.15	365			(257)	365		.30		
	ramp fire 1/2 corridor									ramp fire 3/4 corridor								
2.29				(88)		(78)				2.29				(92)					
1.98				(100)		(87)	1.73		25	1.98				(113)			1.73		120
1.68	85		90	(103)		(109)	1.49			1.68		105	110	(123)			1.49		
1.56				95			1.38		60	1.56				120		100	1.38		65
1.37		105		(109)	110	(147)	1.29	80		1.37		145	115	(129)			1.29	70	
1.07		120		(126)	125	(164)	1.09	110		1.07	125	180	145	(141)			1.09	165	
.93				115			1.04		120	.93				150		155	1.04		130
.76	150	130		(145)	130	(168)	.90	120		.76	225	190	170	(178)	195		.90		
.46	165	135	210	(166)	140		.70	160		.46	315	265	245		225		.70	250	
.33				195			.50			.33				225		225	.50	265	
.15	305	305	305		305		.30	305		.15	360	360		360			.30	345	

Table 1 (cont.)

Z meter	T_A	T_C	T_D	P_D (V_D)	T_E	P_E (V_E)	Z meter	T_B	P_B
ramp fire full corridor									
2.29				(70)		(80)			
1.98		30		(85)		(89)	1.73		5
1.68		100	70	(109)		(96)	1.49		
1.56				75		95	1.38		75
1.37		110		(129)	90	(129)	1.29		
1.07	30	140	130	(167)	125	(155)	1.09	145	
.93				165		150	1.04		115
.76	210	185	185	(192)	185	(200)	.90	155	
.46	300	300	280	(222)	295	(243)	.70	275	
.33				190		230	.50	305	
.15	305	305	305		305	(243)	.30		
100 kW full corridor 1/2 door									
2.29				(75)		(77)			
1.98		25	40	(97)		(94)	1.73		10
1.68		75	60	(118)	65	(96)	1.49		
1.56				75			1.38		15
1.37		85	90	(136)	90	(126)	1.29		
1.07		120	125	(176)	115	(151)	1.09		
.93				145			1.04		90
.76	85	200	170	(200)	160	(209)	.90	165	
.46	225	295	265	(225)	275	(243)	.70	295	
.33				245			.50	365	
.15	365	365	365		365	(262)	.30		
100 kW full corridor 1/8 door									
2.29				(92)		(76)			
1.98		60		(123)		(116)	1.73		0
1.68		105	55	(156)	50	(155)	1.49		
1.56				95		215	1.38		5
1.37		120	115	(193)	145	(214)	1.29		
1.07		240	185	(240)	230	(284)	1.09		
.93		220					1.04		135
.76	5	415	290	(290)	345	(334)	.90	465	
.46	15	465	465	(338)	465	(374)	.70		
.33				225			.50		
.15	470						.30		

Z meter	T_A	T_C	T_D	P_D (V_D)	T_E	P_E (V_E)	Z meter	T_B	P_B
ramp fire full corridor and lobby									
2.29				(96)		(130)			
1.98				(108)		(184)	1.73		120
1.68		250	190	(120)	280	(210)	1.49		
1.56				220		335	1.38		170
1.37	130	280		(171)	310	(221)	1.29		
1.07	145	335	315	(298)	325	(227)	1.09	335	
.93				340		340	1.04		260
.76	475	690	595	(360)	340	(261)	.90	510	
.46	590	720	720		475		.70	720	
.33				350		345	.50		
.15	720				720	(281)	.30		
100 kW full corridor 1/4 door									
2.29				(100)		(104)			
1.98		70		(116)		(129)	1.73		30
1.68		95	65	(126)	65	(156)	1.49		
1.56				35		150	1.38		35
1.37		120	120	(169)	125	(212)	1.29		
1.07		205	175	(239)		(251)	1.09		
.93				170	195	220	1.04		180
.76	60	340	265	(299)	270	(264)	.90	430	
.46	190	440	410	(342)	410	(324)	.70	440	
.33				175		325	.50		
.15	430		440	(310)	440		.30		

doors to the test space were opened, and a forced ventilation system was used to clear the smoke.

The tests were run during the daytime in the summer. Tests were separated by a time interval of at least 2 hrs so that at the beginning of a run the test space would be smoke-free and with ambient temperature surfaces.

Results and Discussion

General Observations. In terms of visual observations, a two-layer description of the environments was well substantiated throughout each room, for all test cases, and at least until the upper smoky layer thickness increased to 1/2-2/3 of the total floor-to-ceiling height. After that, the interface position became significantly more diffuse, and the optical density of the corridor (and lobby) lower layers appeared to steadily increase to a state of total obscuration.

The two-layer visualization remained sharper to greater interface depths for tests with more rapid growth of upper layer thickness, (i.e., for test runs with relatively larger fires and relatively smaller floor areas).

Even at early times, though much more so at later times, the introduction of smoke from the upper layer to the lower layer was observed to be by descending wall jets or (inverted) thermals. It is conjectured that these wall layers were generated in the elevated temperature upper layer as a result of heat transfer from the near-wall gases to the relatively cool wall surfaces. Surface cooling of these gases would result in downward directed low speed wall jets (net buoyant forces near the wall being directed downward toward the floor). These would emerge from the upper layer and continue their descent into the lower layer. Once in the cool lower layer, reverse net buoyant forces of these warm wall jets would retard their descent and promote their mixing with the relatively cool and clear lower layer environment.

Position of the Interface. A major purpose of the test program was to generate a data base that would be generally available for future comparisons with the predictions of analytic models. A useful component of such a data base would be the interface elevation in each separate space for a given test run. It is possible to construct such elevation histories from the thermocouple data, the photometer data, and the light obscuration data. However, to do this, an operational definition of the precise position of the interface is required. Thus, although the previously mentioned qualitative visual observations are consistent with a two (homogeneous) layer sharp interface type of zonal model, this is not necessarily the case of the quantitative data of, say, the vertical thermocouple arrays.

An example of the rather diffuse nature of the interface as viewed from the perspective of the thermocouple data is indicated in Fig. 2. There, the thermocouple data from the corridor arrays C, D, and E are plotted at time $t = 165$ s when the visual observations of light array obscuration at both positions D and E indicated (to within 5 s) an interface position 0.76 m above the floor. It is evident from this plot that a two-homogeneous-layer description of the environment in the corridor is an approximation to the actual state. In order to use such an approximation an interface position must be determined from an unambiguous, albeit subjectively formulated, temperature and photometer data reduction scheme. Toward this end the following N percent rule for defining interface elevation was formulated:

First, the rule to be used with thermocouple arrays: At a specific time into a test run one computes a reference upper layer temperature difference $\Delta T_{ref}(t) = \max [T(z_{top}, t)] - T_{amb}(z_{top})$ where $T(z, t)$ is the temperature at elevation, z, and time, t; z_{top} is the elevation of the top thermocouple, $T_{amb}(z) = T(z, t=0)$; and $\max [T(z, t^*)]$ is the maximum value of $T(z, t)$ in the time interval $0 \le t \le t^*$. Then by the N percent rule the interface is defined as passing the elevation $z_i(t)$ at that time t when z_i first satisfies.

$$T(z_i,t) - T_{amb}(z_i) = N\Delta T_{ref}(t)/100 \qquad (2)$$

Also, z_i is defined as monotonic in t, i.e., as time goes on it is

assumed that the upper layer never decreases in thickness. Finally, to account for experimental error in temperature measurements it is reasonable to apply the rule only at such times when the right-hand side of equation (2) exceeds some minimum value $\Delta T_{\min}$. ($\Delta T_{\min}$ here was taken to be 0.5°C.)

An analogous N percent rule to be used with vertical photometer arrays was also formulated, by interpreting z_{top} as the elevation of the top photometer, and by appropriately substituting optical density for temperature in the above. An interface definition similar to the N percent rule was used in [8].

Results of applying the above rule for $N = 10$, 15, and 20 were obtained for all thermocouple and photometer array data of the 100-kW, full-corridor test run (intermediate fire size, intermediate area). The reduced data points for interface elevation which correspond to the fire array locations A–E are plotted in Figs. 3(*a*)–3(*e*), respectively. The 10, 15, and 20 percent rule was also applied to the D array data acquired during the 25-kW, corridor-lobby test run (smallest fire, largest space) and during the 225-kW, 1/2 corridor test run (largest fire, smallest space). These latter results are plotted in Figs. 3(*f*) and 3(*g*). Also included in Figs. 3(*d*)–3(*g*) are interface elevation data points obtained from the time of obscuration of the vertical light arrays at D and E. These data were generated by one number of the test team who reviewed the appropriate video tape data. Finally, each of the Figs. 3(*a*)–3(*g*) includes an analytic estimate of the history of the interface elevation. These curves, designated as single room estimates, are predictions of the interface histories that would result from point sources of strength $(1 - \lambda_r)Q$ located on the floors of single room enclosures (with leakage from below) whose areas are identical to the total plan areas of the respective multiroom spaces [1, 9]. It has been suggested in [9] that for "freely connected" multiroom enclosures fires such relatively easily obtainable predictions may provide reasonable approximations to actual interface elevation histories. The present experiments appear to provide a degree of support for this contention.

From a study of the data of Fig. 3 it was concluded that application of the 10 percent rule would provide a reasonable basis for an experimentally determined interface elevation history. The rule for $N = 10$ was therefore applied to all data of all test runs. The results are presented in Table 1. Also included in Table 1 are the interface elevation histories determined from observations of vertical light array obscuration.

Vertically Averaged Temperatures. It is beyond the intended scope of the present paper to include all of the thermocouple data acquired during the test program. Nevertheless, results which indicate the actual magnitude of the measured temperature increases (as compared to the relative distribution of temperatures per Table 1) would constitute a valuable addition to the data base presented here. Toward this end and for the neighborhood of any particular thermocouple array the time-varying vertically averaged temperature increase, $\overline{\Delta T}$ is estimated from

$$\overline{\Delta T}(t) = \frac{1}{H}\int_0^H [T(z,t) - T_{\text{amb}}(a)]dz$$

$$\approx \frac{1}{H}\sum_{n=1}^{8} [T(z_n,t) - T_{\text{amb}}(z_n)]\Delta z_n \qquad (3)$$

where z_n corresponds to the elevation of the nth thermocouple in the array, and Δz_n is the vertical zone of influence associated with this thermocouple. Equation (3) was applied to all arrays but B. In doing so, Δz_1 to Δz_7 were taken to be

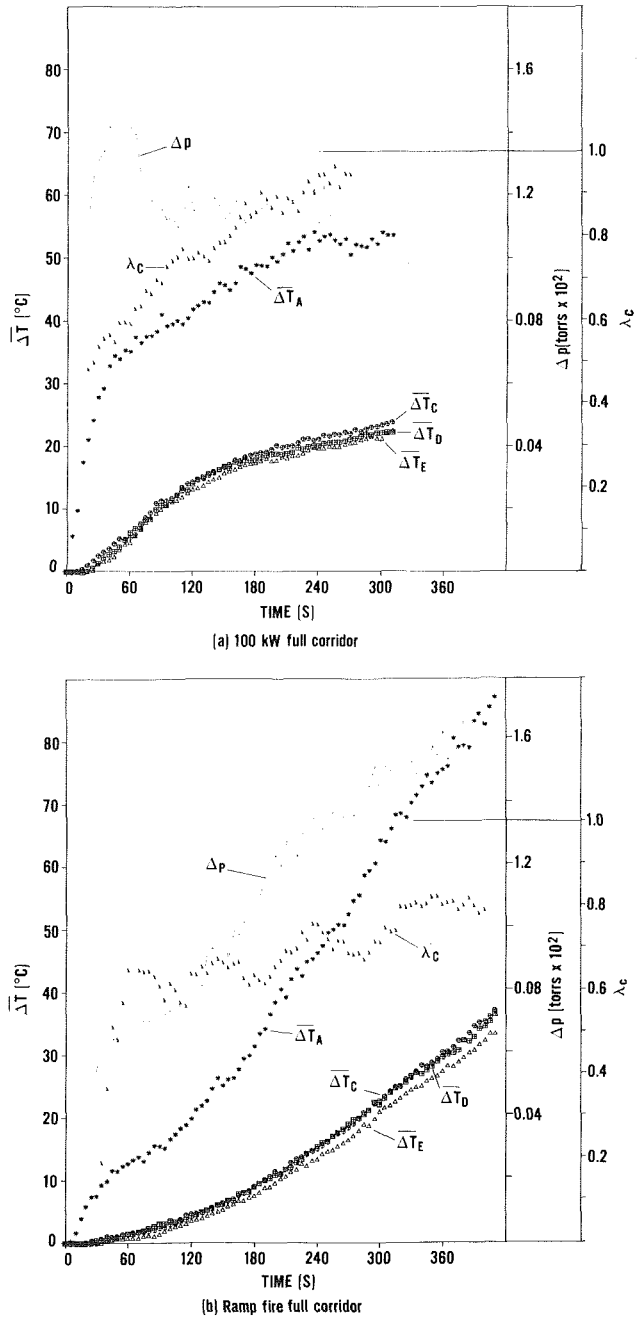

Fig. 4 Vertically averaged temperature changes per equation (3) at burn room and at corridor arrays; λ_c per equation (4); pressure difference, Δp, across doorway

.305 m, and Δz_8 was taken to be between .191 and .241 m, depending on location.

As an illustration of the above data reduction scheme the $\overline{\Delta T}$'s from the thermocouple arrays of the 100-kW, full-corridor test and the full-corridor ramp fire test are plotted in Figs. 4(*a*) and 4(*b*), respectively. The scheme was carried out for all test runs, and smoothed results are presented in Table 2 for arrays A and D, and, in test runs with corridor-lobby configurations, for array E.

In Figs. 4(*a*) and 4(*b*) the similarity between the $\overline{\Delta T}$ histories associated with all corridor thermocouple arrays is noteworthy. A study of all corridor array $\overline{\Delta T}$'s revealed the persistence of this result during all test runs. This is an indication of the relative uniformity in conditions along the length of the corridor. On account of this uniformity, only $\overline{\Delta T}_D$ of the corridor arrays is included in Table 2.

Table 2 Histories of vertically averaged temperatures in burn room, $\overline{\Delta T_A}$, corridor, $\overline{\Delta T_D}$, and lobby, $\overline{\Delta T_E}$; fraction of Q transferred to surfaces, λ_c; near-ceiling pressure drop across doorway, Δp

25 kW	1/2 corridor				3/4 corridor				full corridor				corridor and lobby				
t sec	$\overline{\Delta T_A}$ °C	$\overline{\Delta T_D}$ °C	λ_c	Δp torr X10^2	$\overline{\Delta T_A}$ °C	$\overline{\Delta T_D}$ °C	λ_c	Δp torr X10^2	$\overline{\Delta T_A}$ °C	$\overline{\Delta T_D}$ °C	λ_c	Δp torr X10^2	$\overline{\Delta T_A}$ °C	$\overline{\Delta T_D}$ °C	$\overline{\Delta T_E}$ °C	λ_c	Δp torr X10^2
10	1.7	0.0		.21	5.1	0.0		.36	0.2	0.0		.09					
20	4.7	0.1		.36	7.9	0.0		.51	1.1	0.0		.09	4.3	0.3	0.0		.44
30	7.0	0.0	.27	.44	10.0	0.0	.44	.67	3.5	0.0	.56	.30	6.1	0.1	0.0	.75	.39
40	8.8	0.1	.34	.48	12.1	0.4	.52	.63	5.6	0.0	.45	.35	6.9	0.2	0.0	.75	.49
50	9.8	0.5	.42	.49	11.7	0.8	.63	.62	6.4	0.0	.47	.52	8.0	0.5	0.0	.72	.54
60	10.9	0.9	.53	.53	12.8	0.9	.66	.58	9.7	0.1	.51	.59	9.8	0.8	0.0	.62	.64
70	12.1	1.2	.61	.48	12.2	1.5	.69	.58	11.2	0.6	.52	.63	10.3	1.0	0.0	.62	.68
80	12.8	2.0	.66	.48	12.4	2.3	.78	.54	12.5	0.9	.60	.68	11.5	1.1	0.0	.70	.66
90	12.9	2.7	.68	.48	13.1	2.8	.75	.54	13.1	1.3	.72	.66	13.5	1.8	0.1	.71	.68
100	13.1	3.2	.66	.47	13.5	3.3	.72	.55	14.3	1.5	.71	.67	12.6	2.4	0.2	.72	.67
110	13.8	3.6	.69	.45	13.2	3.6	.72	.56	14.4	2.2	.73	.68	13.4	2.5	0.0	.83	.59
120	13.6	4.0	.70	.41	13.6	3.6	.70	.51	14.4	2.6	.76	.67	13.1	2.8	0.2	.81	.60
140	14.1	5.0	.74	.41	14.6	4.4	.70	.50	14.4	3.1	.71	.60	13.8	3.2	0.3	.81	.63
160	15.2	5.6	.79	.39	13.4	5.1	.77	.55	14.3	3.4	.78	.57	14.5	3.6	0.6	.78	.64
180	15.7	6.2	.82	.43	15.9	5.6	.80	.54	13.5	3.7	.88	.54	14.2	4.1	0.9	.86	.61
200	15.2	6.6	.83	.42	16.0	6.0	.86	.54	13.8	4.2	.82	.54	15.0	4.5	1.1	.90	.57
300	17.4	7.9	.99	.39	17.2	7.2	.93	.54	15.6	5.2	.93	.57	15.9	5.2	1.6	.96	.66
400	18.1	9.0		.40	16.9	7.8		.51	17.2	6.4	.90	.54	16.1	5.6	2.1	.89	.45
500									17.3	7.0	.92	.55	16.8	6.0	2.2	.97	.46
600									18.8	7.7		.57					
100 kW																	
10	10.2	0.2		.97	5.8	0.0		.57	9.8	0.0		.84	5.9	0.0	0.0		
15	14.8	0.0		1.22	10.4	0.0		.92	17.6	0.0		.99	7.8	0.0	0.0		
20	21.1	0.1		1.34	17.3	0.0		1.11	21.0	0.0	.49	1.32	9.5	0.1	0.0	.74	.66
25	25.5	0.7		1.33	21.6	0.1		1.30	24.1	0.5	.50	1.27	11.4	0.0	0.1	.73	.76
30	26.8	1.4	.38	1.36	24.1	0.8	.44	1.30	27.8	1.2	.54	1.32	15.2	0.3	0.1	.72	.84
35	29.3	2.1	.41	1.47	27.3	1.2	.45	1.45	29.2	2.2	.56	1.34	17.2	0.8	0.0	.71	.97
40	33.3	3.4	.47	1.30	31.2	1.9	.52	1.46	32.8	2.7	.57	1.42	20.7	1.3	0.0	.67	.95
45	34.3	5.2	.46	1.34	30.8	2.7	.55	1.39	34.4	3.2	.55	1.39	23.0	1.7	0.0	.66	1.06
50	35.1	7.0	.51	1.32	33.2	3.3	.54	1.37	34.0	3.9	.60	1.39	25.9	2.1	0.0	.67	1.14
55	35.6	8.2	.53	1.34	34.4	4.1	.58	1.34	35.3	5.0	.60	1.42	28.5	2.8	0.0	.68	1.25
60	36.2	9.5	.63	1.28	34.0	5.8	.64	1.32	35.1	6.2	.60	1.41	29.0	3.7	0.1	.70	1.31
70	37.1	12.2	.65	1.16	35.8	8.4	.67	1.27	36.5	7.6	.64	1.24	33.4	5.3	0.2	.74	1.33
80	40.3	14.5	.63	1.12	36.8	10.4	.67	1.23	37.6	8.4	.67	1.18	34.7	6.6	0.3	.77	1.35
90	41.4	16.7	.69	1.15	36.5	12.2	.67	1.17	41.0	10.6	.69	1.15	36.2	7.6	0.7	.78	1.41
100	42.5	18.6	.73	1.15	39.1	13.7	.66	1.12	39.6	11.4	.75	1.13	37.0	8.1	1.0	.81	1.37
150	50.6	24.0	.80	1.11	48.3	19.0	.82	1.15	45.7	16.8	.79	1.12	39.4	12.2	3.0	.89	1.33
200	55.8	26.5	.89	1.17	52.1	21.9	.90	1.16	49.4	18.8	.90	1.15	43.1	13.8	5.1	.95	1.25
250	56.7	29.2	.93	1.10	54.0	23.7	.89	1.19	53.7	20.5	.93	1.13	45.4	15.4	5.8	.94	1.28
300					55.1	25.6	.94	1.11	54.0	22.1		1.13	44.6	16.4	6.9	.94	1.16
350													45.6	17.3	7.9		
225 kW																	
10	7.2	0.0		.79	8.3	0.0		.80	14.8	0.2		1.11	24.1	0.0	0.1		1.40
15	16.4	0.0		1.12	18.4	0.1		1.18	23.9	0.0		1.60	34.4	0.0	0.1		1.78
20	27.2	0.0		1.46	26.2	0.1		1.58	35.5	0.4		1.76	43.3	0.5	0.1	.65	1.91
25	38.0	0.7		1.64	38.8	0.4		1.91	40.4	1.7		2.16	51.0	2.6	0.1	.68	2.03
30	46.5	1.7	.35	1.82	47.3	1.7	.46	2.01	50.9	2.8	.50	2.26	51.0	3.6	0.1	.70	2.11
35	55.6	3.6	.33	1.78	54.0	3.1	.49	2.32	56.6	4.4	.48	2.31	56.8	4.5	0.1	.72	2.03
40	63.1	6.9	.36	1.80	63.8	4.6	.49	2.27	60.2	6.4	.49	2.38	57.6	5.3	0.2	.74	2.20
45	65.4	11.7	.40	1.73	66.6	7.1	.52	2.10	65.4	9.3	.51	2.48	62.2	9.5	0.3	.76	2.22
50	66.7	14.7	.47	1.62	64.4	10.4	.51	2.02	68.6	11.4	.58	2.43	62.0	10.9	0.4	.77	2.18
55	63.6	18.8	.52	1.60	66.3	13.0	.57	2.01	68.8	13.9	.59	2.30	63.8	11.8	0.5	.78	2.09
60	67.0	20.8	.55	1.42	71.7	15.8	.61	2.03	69.0	15.1	.60	2.10	64.8	13.0	0.8	.78	1.98
70	78.6	28.5	.59	1.39	69.4	19.9	.62	1.71	78.7	17.5	.62	2.11	65.5	15.3	1.5	.84	1.91
80	79.9	33.4	.63	1.37	77.8	23.8	.64	1.79	76.0	21.9	.67	1.96	65.9	17.3	2.5	.85	1.83
90	88.3	37.2	.70	1.33	80.3	28.6	.66	1.68	78.0	25.2	.74	1.85	67.5	18.6	3.7	.85	1.74
100	89.4	39.9	.71	1.17	86.2	32.1	.75	1.61	82.4	27.9	.70	1.78	68.3	19.7	4.8	.87	1.65
150	101.8	47.0	.93	1.29	98.5	38.1	.88	1.53	96.2	35.4	.91	1.71	73.1	24.0	9.2	.93	1.60
200	106.4	52.9	.88	1.32	103.0	43.8	.93	1.61	98.4	39.3	.91	1.80	75.0	26.8	11.7	.96	1.61
250	114.0	58.2	.93	1.26	106.3	47.8	.91	1.58	105.2	43.2	.91	1.76	78.1	29.0	13.4	.94	1.58
300	116.9	63.7		1.27	115.4	51.9		1.59	110.7	45.7	.94	1.70	81.2	30.9	14.8	.98	1.57
350									112.8	48.7		1.76	84.6	32.3	16.0		1.59

Table 2 (cont.)

ramp																
10	.1	.1		.16	0.4	0.2		.05	1.7	0.1		.28	1.2	0.1	0.0		.12
20	1.9	.2		.22	0.5	0.2		.07	5.9	0.1		.48	2.2	0.0	0.1	.60	.22
30	3.4	.1	.43	.29	1.6	0.1	.50	.12	7.5	0.2		.56	3.2	1.0	0.0	.63	.24
40	5.0	.1	.53	.38	2.0	0.0	.49	.22	9.9	0.6	.37	.61	4.6	0.0	0.1	.67	.29
50	6.9	.3	.54	.42	4.7	0.1	.57	.33	11.5	0.9	.49	.65	4.7	0.1	0.2	.64	.39
60	8.4	.5	.59	.47	6.5	0.2	.60	.35	12.7	1.5	.66	.67	7.3	0.3	0.2	.67	.45
70	10.2	.8	.64	.54	8.6	0.4	.68	.44	13.8	1.8	.66	.66	9.0	0.4	0.1	.63	.56
80	13.1	1.3	.69	.60	9.4	0.5	.71	.45	14.5	2.4	.65	.71	12.2	0.7	0.2	.67	.62
90	14.9	1.8	.67	.66	10.3	0.7	.70	.50	15.5	3.1	.62	.72	13.8	1.0	0.3	.66	.70
100	17.0	3.0	.70	.67	10.9	1.0	.62	.54	16.6	3.6	.62	.74	16.5	1.5	0.2	.67	.80
150	30.2	9.0	.73	.90	23.8	4.6	.63	.98	25.1	6.2	.67	.96	26.7	4.9	0.6	.74	1.00
200	39.7	16.2	.77	.85	36.1	10.6	.62	1.09	38.4	10.8	.66	1.24	37.5	9.8	1.7	.76	1.29
250	55.1	23.4	.83	1.05	51.9	17.5	.63	1.28	49.4	16.2	.73	1.36	47.2	13.7	3.8	.83	1.36
300									64.3	22.2	.72	1.42	58.7	17.2	6.0	.85	1.54
350									73.4	28.1	.83	1.58	63.1	21.4	8.0	.88	1.57
400									82.6	34.4	.80	1.70	73.5	25.3	10.7	.89	1.62
450													86.2	29.6	13.2	.90	1.73
500													94.8	33.5	15.8	.91	1.72
550													102.6	37.6	18.2	.92	1.80
600													112.8	42.4	20.7		1.88

100 kW	full corridor 1/2 door				full corridor 1/4 door				full corridor 1/8 door			
t sec	$\overline{\Delta T}_A$ °C	$\overline{\Delta T}_D$ °C	λ_c	Δp torr X10^2	$\overline{\Delta T}_A$ °C	$\overline{\Delta T}_D$ °C	λ_c	Δp torr X10^2	$\overline{\Delta T}_A$ °C	$\overline{\Delta T}_D$ °C	λ_c	Δp torr X10^2
10	6.1	0.0		.47	13.8	0.1		1.08	38.3	0.3		2.26
15	6.9	0.0		.73	22.1	0.1		1.49	43.9	0.6		2.34
20	12.1	0.1		.90	29.3	0.2		1.80	48.1	0.7		2.35
25	16.7	0.0	.47	1.18	34.8	0.2	.35	2.03	52.6	0.8		2.45
30	22.7	0.0	.50	1.32	42.1	0.7	.43	2.14	53.7	1.0	.56	2.66
35	26.6	0.6	.50	1.57	45.8	1.0	.49	2.26	59.2	1.1	.61	2.63
40	31.8	1.0	.50	1.70	49.9	1.4	.56	2.30	62.0	1.2	.64	2.77
50	40.3	1.7	.51	1.83	53.4	1.9	.65	2.34	63.7	1.4	.67	2.65
60	43.2	2.5	.58	1.90	57.3	2.1	.66	2.42	70.7	2.2	.74	2.83
70	47.1	3.1	.63	1.98	59.1	3.3	.72	2.47	73.3	2.5	.75	2.76
80	50.2	7.1	.65	1.84	62.4	4.5	.72	2.45	74.4	2.9	.82	2.78
90	49.2	7.0	.67	1.71	68.0	5.1	.72	2.43	76.4	3.6	.84	2.85
100	50.4	8.8	.75	1.75	65.9	5.6	.78	2.39	77.2	3.9	.84	2.94
150	55.7	13.2	.81	1.62	69.0	9.0	.88	2.27	82.6	5.9	.91	2.77
200	57.5	16.5	.88	1.56	72.5	11.2	.90	2.36	87.8	7.0	.90	2.96
250	60.5	18.7	.87	1.67	75.4	12.8	.92	2.29	89.8	8.6	.91	3.08
300	62.7	20.2	.89	1.63	79.6	13.9	.94	2.31	93.9	9.6	.95	2.97
350	64.5	21.7		1.60	79.2	15.1	.90	2.33	96.0	10.4	.95	2.91
400					82.0	15.8	.94	2.40	99.2	11.6	.93	2.87
450									99.6	12.2		3.09

The Heat Transfer to Bounding Surfaces. A necessary prerequisite to the successful modeling of enclosure gas temperatures is an estimate of the total rate of heat transfer to bounding surfaces of the enclosure. As indicated in [9] it is useful to express this heat transfer as a fraction, λ_c, of fire's instantaneous energy release rate. Thus, $\lambda_c Q(t)$ is defined as the instantaneous total rate of heat transfer, radiation plus convection, to the bounding surfaces of the enclosure.

According to a derivation presented in the Appendix, λ_c in the present experiments can be estimated from

$$\lambda_c(t) = 1 - \frac{\rho_{amb} C_p \tau}{Q(t)} \frac{d\overline{\Delta T}(t)}{dt} \tag{4}$$

where ρ_{amb} is the ambient density, C_p is the specific heat at constant pressure, and τ is the total volume of the test space. Here, $\overline{\Delta T}$ is the temperature increase above ambient averaged over the entire test space, and it can be estimated from

$$\overline{\Delta T}(t) = \frac{A_B \overline{\Delta T}_A(t) + A_C \overline{\Delta T}_D(t) + A_L \overline{\Delta T}_E(t)}{A_B + A_C + A_L} \tag{5}$$

where A_B is the area of the burn room, and A_C and A_L are the utilized areas of the corridor and lobby, respectively. With the results of the previous section and using data smoothing techniques $\lambda_c(t)$ has been obtained from equations (4) and (5) for all test runs. These λ_c histories are presented in Table 2. (The values of ρ_{amb} and C_p were taken as 1.18 kg/m^3 and 240 cal/kg°C, respectively.) λ_c is plotted in Figs. 4(*a*) and 4(*b*) for the 100-kW, full-corridor test and for the full-corridor, ramp-fire test, respectively.

It should be noted that the Table 2 estimates of λ_c do not account for the changing enthalpy content of the plume and ceiling jet. This could lead to large errors at early times of a test run when a significant fraction of the $d\overline{\Delta T}/dt$ of equation (4) is associated with the gases in these zones. At $t = 60$ s, when such errors in the λ_c estimates are likely to be less important, the heat-transfer losses for all test runs are in the range of 51–74 percent of Q. At this time heat transfer is still mainly to the upper surfaces of the burn room. Later, when the surfaces of the adjacent spaces become available for cooling, these losses reach a very large fraction of Q, λ_c approaching the general range 0.80–0.95. These results are consistent with observations in [9].

The Pressure Differential Across the Doorway. For each test run, smoothed data for the time-varying, near-ceiling, pressure differential, Δp, between the burn room and the corridor are presented in Table 2. Δp results are also plotted in Figs. 4(*a*) and 4(*b*).

References

1 Zukoski, E. E., "Development of a Stratified Ceiling Layer in the Early Stages of a Closed-Room Fire," *Fire and Materials*, Vol. 2, No. 2, 1978, pp. 54-22.

2 Waterman, T. E., and Pape, R., "A Study of the Development of Room Fires, IIT Research Institute," NBS-GCR-77-110, prepared for U.S. Department of Commerce, NBS, 1976.

3 Emmons, H. W., Mitler, H. E., and Trefethen, L. N., "Computer Fire Code III," Harvard University Division of Applied Sciences, Home Fire Project Technical Report No. 25, 1978.

4 Zukoski, E. E., and Kubota, T., "A Computer Model for Fluid Dynamic Aspects of a Transient Fire in a Two Room Structure," 2nd ed., California Institute of Technology Report, prepared for U.S. Department of Commerce, NBS, 1978.

5 Tanaka, T., "A Model of Fire Spread in Small Scale Buildings," Third Joint Meeting U.S.-Japan Panel on Fire Research and Safety, UJNR, Washington, D.C., 1978.

6 Emmons, H. W., "The Home Fire Project," Harvard University and Factory Mutual Research Corp. Progress Report, NBS Grant 7-9011, 1980.

7 Tanaka, T., "A Model on Fire Spread in Small Scale Buildings—2nd Report," BRI Research Paper No. 84, Ministry of Construction, Japan, 1980.

8 Mulholland, G., et al., "Smoke Filling in an Enclosure," 20th National Heat Transfer Conference, Paper No. 81-HT-8, Milwaukee, 1981.

9 Cooper, L. Y., Estimating Safe Available Egress Time from Fires," National Bureau of Standards NBSIR 80-2172, 1981.

10 McCaffrey, B., "Measurements of the Radiative Power Output of Some Buoyant Diffusion Flames," Western States Section, Combustion Institute, WSS/CI 81-15, Pullman, Wash., 1981.

11 Bukowski, R. W., "Smoke Measurements in Large- and Small-Scale Fire Testing," National Bureau of Standards, NBSIR 78-1502, 1978.

12 Steckler, K., Quintiere, J., and Rinkinen, W., "Fire Induced Flows Through Room Openings—Flow Coefficients," to appear as National Bureau of Standards NBSIR.

APPENDIX

Estimating the Rate of Heat Transfer to the Enclosure Surfaces

The energy and continuity equations for the enclosure can be written as

$$\frac{d}{dt}\int_\tau \rho e d\tau + \int_S \rho e \bar{V}.\bar{n}dS = Q(1-\lambda_c) - P\int_S \bar{V}.\bar{n}dS \quad \text{(A1)}$$

$$\frac{d}{dt}\int_\tau \rho d\tau + \int_S \rho \bar{V}.\bar{n}dS = 0 \quad \text{(A2)}$$

where ρ is the density, e is internal energy, τ and S are the volume and bounding surface of the enclosure space, and where P, the absolute pressure, is approximated as being uniform in τ. Also, $\bar{V}$ is the velocity and $\bar{n}$ is the outward surface normal vector.

e is now expressed as

$$e = h_{\text{amb}} + (h - h_{\text{amb}}) - \frac{P}{\rho} = h_{\text{amb}} + C_p(T - T_{\text{amb}}) - \frac{P}{\rho} \quad \text{(A3)}$$

where h, the enthalpy, is decomposed into its ambient value, h_{amb}, and variations from h_{amb}. Substituting equation (A3) into equation (A1) and using equation (A2) results in

$$\frac{d}{dt}\int_\tau \rho C_p(T - T_{\text{amb}})d\tau - \tau\frac{dP}{dt} + \int_S \rho C_p(T - T_{\text{amb}})\bar{V}.\bar{n}dS = Q(1-\lambda_c) \quad \text{(A4)}$$

The $\tau dP/dt$ term in the above is related to work done as a result of pressure changes within τ, and it will tend to be negligible compared to the energy-transfer term on the right-hand side [1]. The surface integral can also be neglected since, by design, leakage from τ is assumed to occur near the floor of the corridor where $T = T_{\text{amb}}$. Finally, it is reasonable to approximate ρ in the above by ρ_{amb}. Incorporating all of these approximations leads to the equation (4) representation for λ_c.

Effect of Pressure on Bubble Growth Within Liquid Droplets at the Superheat Limit[1]

C. T. Avedisian
Sibley School of Mechanical and Aerospace Engineering, Cornell University, Ithaca, N.Y. 14853
Assoc. Mem. ASME

A study of high-pressure bubble growth within liquid droplets heated to their limits of superheat is reported. Droplets of an organic liquid (n-octane) were heated in an immiscible nonvolatile field liquid (glycerine) until they began to boil. High-speed cine photography was used for recording the qualitative aspects of boiling intensity and for obtaining some basic bubble growth data which have not been previously reported. The intensity of droplet boiling was found to be strongly dependent on ambient pressure. At atmospheric pressure the droplets boiled in a comparatively violent manner. At higher pressures photographic evidence revealed a two-phase droplet configuration consisting of an expanding vapor bubble beneath which was suspended a pool of the vaporizing liquid. A qualitative theory for growth of the two-phase droplet was based on assuming that heat for vaporizing the volatile liquid was transferred across a thin thermal boundary layer surrounding the vapor bubble. Measured droplet radii were found to be in relatively good agreement with predicted radii.

1 Introduction

Intimate contact between a volatile liquid dispersed in another immiscible nonvolatile liquid can be an effective means for transferring heat. Such contact can also suppress nucleate boiling due to a lack of preferred nucleation sites. The volatile liquid may then be heated to temperatures substantially higher than its saturation temperature. There is a practical limit to the temperature a liquid can reach before vaporization must occur. At this temperature an intrinsic phase transition is initiated by the random molecular processes of homogeneous nucleation. If growth of the initial vapor bubbles is sufficiently rapid, explosive boiling can result. The potential for these "vapor explosions" has been recognized in connection with liquid natural gas spills on water, during fuel/coolant interactions in a liquid metal fast breeder reactor [1, 2] and during droplet combustion of high boiling-point fuels which contain a volatile additive [3].

However, evidence indicates that a phase transition is not necessarily explosive when the limit of superheat is reached [4–8]. Homogeneous nucleation theory gives no information concerning the *intensity* of vaporization. This intensity is dependent on the difference in pressure between the gas within the initial vapor bubble and the surrounding liquid. Such a pressure difference exists during the early stages of growth. Indeed, Henry and Fauske [9] and Buchanan and Dullforce [10] theorized that vapor explosions are possible only when bubble growth is inertially controlled. If this excess pressure is reduced sufficiently, vapor explosions could be eliminated. One of the aims of the present work was to demonstrate this experimentally.

The configuration chosen for study was that of droplets of a volatile pure liquid heated in an immiscible nonvolatile liquid. This configuration is relevant to many situations in which vapor explosions are initiated.

To the author's knowledge no work has been reported on bubble growth within liquid droplets heated to their homogeneous nucleation temperatures at pressures above atmospheric. We report here the results of such a study. The present work is distinguished from previous studies [e.g., 11] in that our efforts were concerned with bubbles growing within liquids of finite volumes (i.e., droplets) and not within an infinite sea of superheated liquid, and that the liquids in which the bubbles grew were at reduced temperatures greater than .9.

Our initial efforts were concerned with a study of bubble growth within pure liquid n-octane droplets. High-speed cine photography was used both to record the qualitative aspects of boiling intensity of the test droplets, and to obtain some basic bubble growth data which have not previously been reported. The objectives were to (*i*) study the effect of ambient pressure on the growth rate of bubbles within liquid droplets heated to their limits of superheat, and (*ii*) develop a simple physical model for boiling of the superheated droplets.

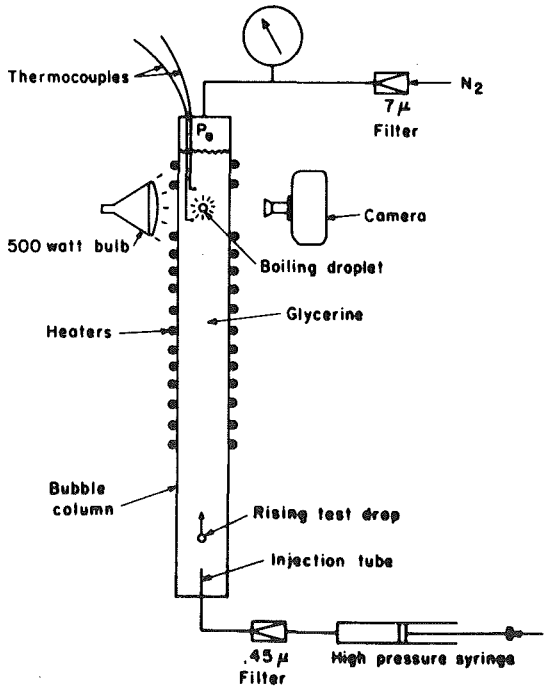

Fig. 1 Schematic diagram of experiment

[1] Part of this paper was presented at the 20th ASME/AIChE National Heat Transfer Conference, Milwaukee, Wisconsin, August 2–5, 1981. Paper No. 81-HT-11.

Contributed by the Heat Transfer Division for publication in the JOURNAL OF HEAT TRANSFER. Manuscript received by the Heat Transfer Division September 7, 1981.

2 Experiment

2.1 Description of the Apparatus. The experiment was a modification of that used by Skripov and Ermakov [4, 5] and Avedisian and Glassman [6] at high pressures. Droplets of a light volatile test liquid were injected into the bottom of a vertical column (Fig. 1) containing a heavier immiscible nonvolatile field liquid. A stable temperature gradient was imposed on the field liquid such that temperature was hotter at the top of the column than the bottom. As the droplets rose, they were progressively heated until they began to boil. The temperature of boiling was obtained by measuring the temperature in the field liquid at the level in the column at which vaporization was observed. Droplet surface temperatures were estimated to be within 1.5°K of the ambient temperature for rise velocities and field liquid temperature gradients typical of the present experiments.

The above method was combined with high-speed cine photography to record the boiling intensity of the droplets. Previous studies by Apfel and Harbison [12] and Mori and Komitori [13] concerned unsupported ethyl ether droplets boiling in glycerine under an effective pressure of .101 MPa.

The bubble column consisted of a heavy walled glass tube 56.8-cm long with nominal dimension of 3.6-cm i.d. and 5.8-cm o.d. The tube was heated by a split aliminum tube clamped to the bubble column and held in place by two band heaters and connecting bolts. The tube was pressurized directly with filtered nitrogen gas. The droplet injection system was similar to that employed by Avedisian and Glassman [6].

The droplets were photographed with a Hycam 16-mm high-speed rotating prism camera equipped with a 75-mm lens and extension tubes. The camera was mounted next to the level of the column at which the droplets were observed with the naked eye to boil. Direct back lighting was used with a GE DXB 500 W bulb, the intensity of which was regulated by a variac. Because the droplets were moving past the field of view of the camera at velocities typically between 20 mm/s and 60 mm/s, some luck was involved in synchronizing the camera start-up with the initiation of boiling. For this reason, maximum camera framing rates of about 1000 frame/s were used. (The framing rate was determined by an electronic timer which put marks on the film in .001 s intervals.) These rates gave us at least 4 s of filming time for a 100 ft. role of film. This was time enough to start the camera before the droplets entered the lens field of view and still have a high probability of photographing their vaporization. A number of successful shots of droplets undergoing what is believed to be homogeneous nucleation at various ambient pressures were obtained and are shown in Figs. 2 to 4.

Droplet vaporization rates were obtained by studying individual frames from the high-speed movies on a motion picture analyzer. Overall droplet diameters (Figs. 2 to 4) were used in our subsequent analysis to avoid possible ambiguities of discerning dimensions of the vapor bubbles within the test droplets due to the backlighting technique employed. Also, only measurements in the undistorted vertical direction were used (distortion due to the curvature of the glass tube).

2.2 Selection of Liquids. The test and field liquids were chosen to satisfy the following requirements: (*i*) $T_{sat2}(P_0) > T_0$, (*ii*) both liquids exhibit low mutual miscibility, (*iii*) availability of physical property data, and (*iv*) $\sigma_2 > \sigma_1 + \sigma_{12}$. The first requirement ensures that the test droplet can be heated to its limit of superheat. The fourth requirement assures that the probability for homogeneous nucleation will be greater in the bulk of liquid 1 than at the liquid 1/liquid 2 interface or within the bulk of liquid 2 [14].

In the present work, droplets of pure n-octane were heated in a field liquid of glycerine. The normal paraffin/glycerine combination satisfies the above requirements and has been found by others [6, 7, 15, 16] to yield reproducible measurements of the limits of superheat of the n-alkanes over a wide range of pressures. The n-octane was obtained from Humphrey Chemical Co. with a stated purity of 99 percent. The glycerine was Eastman "spectrograde." The liquids were used directly as received except for normal filtering.

Nomenclature

A_{cap} = surface area of spherical cap
A_{lv1} = surface area of liquid 1/vapor 1 interface
C_i = constant defined in equation (12)
F = h/R
h = dimension of spherical segment defined in Fig. 9
h_{fg1} = latent heat of vaporization of liquid 1
J = nucleation rate
K = Boltzman constant
k = liquid thermal conductivity
k_f = molecular evaporation rate of species 1
m = molecular mass of species 1
N = number density of molecules within liquid 1
$\bar{P}$ = nondimensional pressure, $P/[\rho_{l2}(C_1\alpha_{l1}/R_0)^2]$
P = pressure
q_1, q_2 = heat-transfer rates over the surface of the vapor bubble at the liquid 2/vapor 1 interface (q_2) and the liquid 1/vapor 1 interface (q_1)
r = radial dimension ($r > R$)
R = radius of two-phase droplet
$\bar{R}$ = gas constant
R_f = final radius of vapor bubble
R_0 = initial liquid droplet radius
t = time
T = temperature
T_0 = limit of superheat of liquid 1, and field liquid temperature
$\bar{T}$ = nondimensional temperature, T/T_0
T_{sati} = saturation temperature of i at P_0
T_t = thermodynamic limit of superheat at P_0 (Fig. 5)
v = molar volume of superheated liquid
V_{l1} = volume of spherical segment of liquid 1 suspended from the vapor bubble
y = nondimensional droplet radius, R/R_0

Greek Symbols

α = liquid thermal diffusivity
Γ = growth probability of a critical size nucleus
ΔA^* = energy of forming a critical size nucleus
ΔP = $P_v - P_0$
ϵ = liquid to vapor density ratio of species 1, $\rho_{l1}(T_0)/\rho_{v1}(T_v)$
ρ = density
σ = surface tension
σ_1 = liquid 1/vapor 1 surface tension
σ_2 = liquid 2/vapor 2 surface tension
σ_{12} = liquid 1/liquid 2 interfacial tension
τ = nondimensional time, $(C_1\alpha_{l1}/R_0^2)t$
ν = kinematic viscosity

Subscripts

0 = ambient (field liquid)
v = vapor bubble
c = critical point property
sat = saturation conditions corresponding to P_0 or T_0
$l1$ = liquid 1
$l2$ = liquid 2
i = species i ($i = 1, 2$)

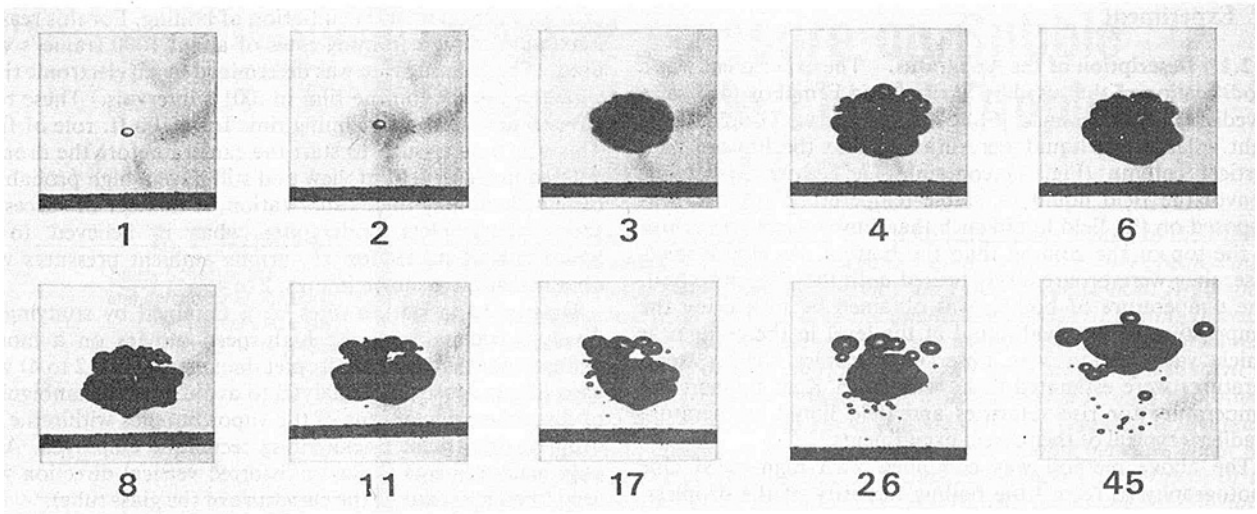

Fig. 2 N-octane droplet boiling in glycerine at $P_0 = .101$ MPa. Number of frame in the motion picture sequence is shown below each photograph. $T_0 \simeq 514°K$, $R_0 \simeq .3$ mm, framing rate = 1033 frames/s.

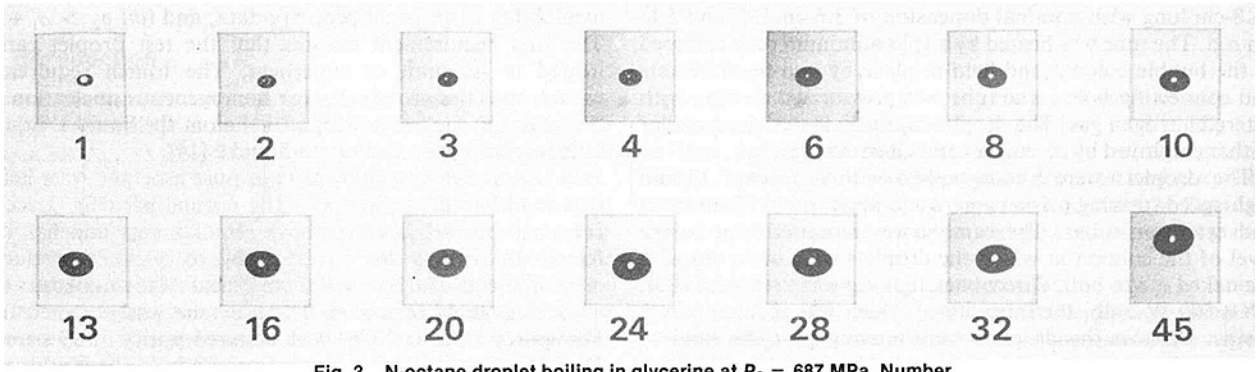

Fig. 3 N-octane droplet boiling in glycerine at $P_0 = .687$ MPa. Number of frame in the motion picture sequence is shown below each photograph. $T_0 \simeq 525°K$, $R_0 \simeq .4$ mm, framing rate = 933 frames/s.

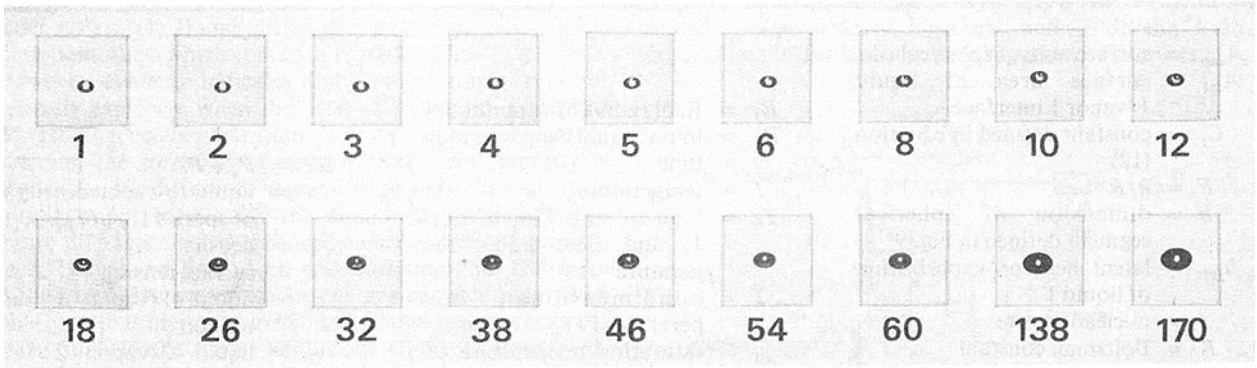

Fig. 4 N-octane droplet boiling in glycerine at $P_0 = 1.22$ MPa. Number of frame in the motion picture sequence is shown below each photograph. $T_0 \simeq 531°K$, $R_0 \simeq .3$ mm, framing rate = 900 frames/s.

2.3 Experimental Observations. High-speed motion pictures of n-octane droplets boiling in glycerine were taken at pressures of .101 MPa, .687 MPa, and 1.22 MPa. The corresponding reduced temperatures ranged from about .9–.94.

At atmospheric pressure the n-octane droplets boiled with a "popping" sound. The droplets appeared to vaporize in an instant with the naked eye. There was little ambiguity about the vertical position in the column at which boiling was observed. As pressure was increased, the audible sound accompanying boiling completely disappeared. For instance, at around .6 MPa the only way to detect boiling was by observing a sudden increase in velocity of the rising droplets.

Figure 2 shows a series of photographs of an octane droplet boiling in glycerine under a pressure of .101 MPa. The photographs were taken from a typical sequence of motion picture frames. A framing rate of 1033 frames was used. The droplet temperature in the first frame was approximately 514°K. Boiling was so intense that complete vaporization occurred in less than 2 ms at a time between the first and third frames in Fig. 2. The stages of growth between these two frames could thus not be recorded by our method because the process was too fast.

The vapor cloud illustrated in frame 3 of Fig. 2 underwent an oscillatory motion, followed by disintegration into a cloud of bubbles (45th frame). The mechanism for this break-up is

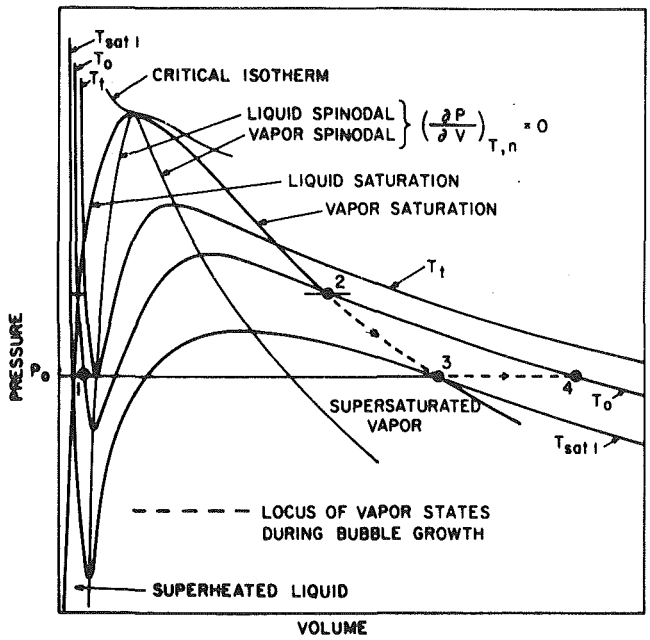

Fig. 5 Pressure-volume phase diagram for a pure substance. "1" represents liquid state; "2" is the initial state in the critical size nucleus; "3" is the vapor state immediately after liquid 1 completely vaporizes; "4" is the state of the final vapor bubble.

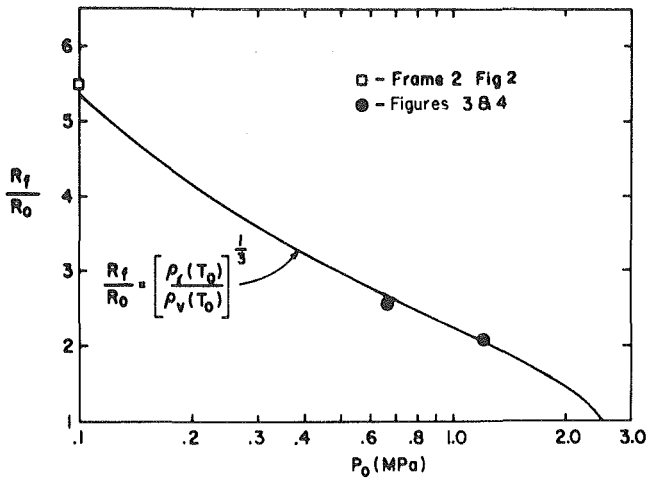

Fig. 6 Variation of final vapor bubble size with ambient pressure

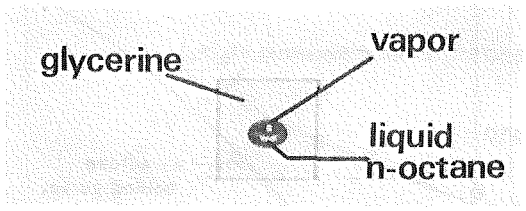

Fig. 7 Photograph of vaporizing two-phase, n-octane droplet in glycerine at 1.22 MPa and $T_0 \simeq 531°K$

probably a Taylor unstable oscillation of the bubble surface. The unstable interface for this effect (liquid over vapor) effectively exists over the upper hemisphere of the bubble; it is here where the deformation of the bubble surface appears most pronounced, as shown in the frames subsequent to frame 6.

The origin of the darkened region or "ring" in the second frame of Fig. 2 is unknown at present. It could have been the remnants of a pressure or shock wave emanating from the droplet surface just prior to the droplet bursting into vapor, but this is just conjecture. The ring was not observed in all the movies which were taken at atmospheric pressure. At pressures above atmospheric, the ring was never observed.

Quite different results were observed at ambient pressures of .687 MPa and 1.22 MPa, as shown in Figs. 3 and 4. The time for complete vaporization, boiling intensity, and size of the final vapor bubble were observed to be strongly affected by changes in ambient pressure. In particular, explosive boiling such as occurred at atmospheric pressure (Fig. 2) was entirely absent at elevated pressures. In addition it took over four times longer for complete vaporization to occur at 1.22 MPa than at .687 MPa. At these pressures, boiling was characterized by growth of apparently only one bubble within the octane droplet (as suggested by Figs. 2 to 4). This single bubble continued to grow until all the liquid octane completely vaporized, after which the bubble size remained constant.

Figure 5 schematically illustrates the initial and final states which are believed to characterize a phase transition via homogeneous nucleation of a liquid droplet in an infinite medium at temperature T_0. ($T_0(P_0)$ is less than the thermodynamic limit of superheat, $T_l(P_0)$, defined by the spinodal curve for a pure liquid $(\partial P/\partial V|_{T,n} = 0)$.) During vaporization the vapor temperature drops from T_0 to close to $T_{satl}(P_0)$ (2→3), after which the vapor becomes superheated as thermal equilibrium is regained (3→4). From mass conservation

$$\frac{R_f}{R_0} \approx \left\{\frac{\rho_{l1}(T_0)}{\rho_{v1}(T_0)}\right\}^{1/3} \tag{1}$$

Using the Peng-Robinson [17] equation of state to estimate superheated liquid and vapor densities, equation (2) is plotted in Fig. 6. As $P_0 \to P_c$, then $T_0 \to T_c$, $\rho_{l1} \to \rho_{v1}$ and therefore $R_f \to R_0$. This fact explains the relative decrease in final bubble size with increasing P_0 as shown in Figs. 3 and 4. At P_0 = .101 MPa by the first accessible time of observation (2nd frame in Fig. 2) the vapor bubble has grown past the size at which excess pressure between vapor and ambient liquid is zero. The subsequent oscillatory motion of the liquid/vapor interface was followed by fragmentation of the bubble. Such explosive vaporization as that illustrated in Fig. 2 did not, therefore, yield a single final bubble.

Figure 7 illustrates the two-phase droplet configuration typically observed at elevated pressures. It consisted of a single vapor bubble beneath which was suspended a puddle of the vaporizing liquid. Such two-phase droplets have been observed by others [e.g., 18–20]. In our present application, the initial bubbles were believed to form by homogeneous nucleation (section 3.2) and not as a result of any pre-existing gas bubbles or dissolved gases in the liquid. Although this two-phase droplet configuration was not observed in the explosive boiling sequence illustrated in Fig. 2, the camera framing rate was too slow to observe the stages of bubble growth in the time between the first three frames.

3 Physical Model

3.1 Introduction. Two steps in the boiling process pertinent to our study are (*i*) an initial or *homogeneous nucleation* phase during which the aforementioned critical size nuclei form within the liquid, and (*ii*) a second or *bubble growth* stage in which the initial microscopic bubble grows as the superheated liquid vaporizes. The first step is absent in most practical boiling situations due to the presence of pre-existing nucleation aids (e.g., dissolved gases, particles, or air bubbles). In the present study, these effects are minimal.

3.2 Homogeneous Nucleation of Bubbles in Liquids. Critical size nuclei form by random density

fluctuations within the liquid. The stochastic nature of the process procludes a precise description of the steps involved in nucleus formation. Only an approximate rate at which the initial vapor bubbles form within a given volume of liquid can be determined. This rate is proportional to the exponential of the energy required to form a critical size nucleus:

$$J \simeq \Gamma\, k_f N \exp\left(-\frac{\Delta A^*}{KT_0}\right) \tag{2}$$

The energy of the critical size nucleus, ΔA^*, is

$$\Delta A^* = \frac{16\pi\,\sigma^3}{3(P-P_0)^2} \tag{3}$$

It is more convenient for our purposes to write equation (2) in terms of temperature:

$$T_0 \simeq \Delta A^* \left[K\, ln\left\{\frac{N\,\Gamma k_f}{J}\right\}\right]^{-1} \tag{4}$$

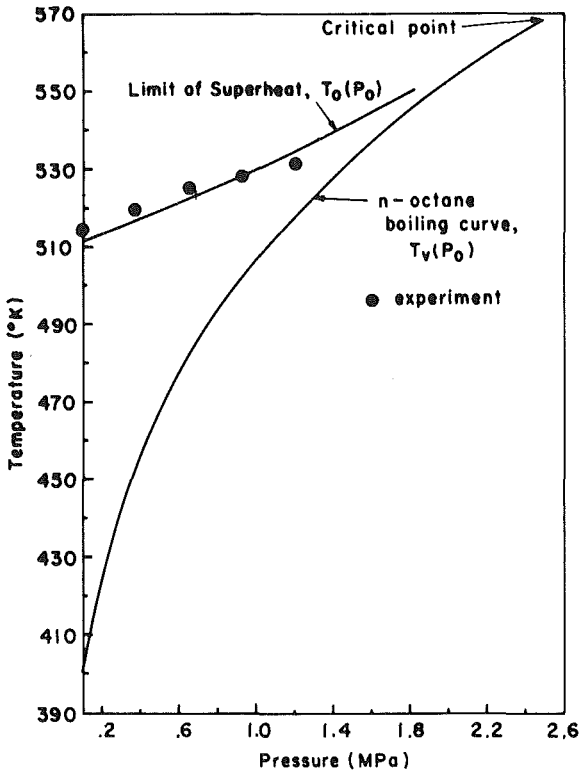

Fig. 8 Variation of limit of superheat with ambient pressure of n-octane

Equation (4) defines the homogeneous nucleation temperature corresponding to the rate J.

In equation (4) the number density of molecules, N (molecules/cm^3), was approximated as

$$N \simeq 6.02 \times 10^{23}/v \tag{5}$$

where v is the molar volume of the superheated liquid (estimated from a correlation for saturated liquids [21]). The nucleus vapor pressure was approximated as

$$P \simeq P_e \exp\left[\frac{v}{\bar{R}T_0}(P_0 - P_e)\right] \tag{6}$$

The equilibrium vapor pressure, P_e, was evaluated from a correlation given by Gomez-Nieto and Thodos [22]. The molecular evaporation rate, k_f, was estimated by the ideal gas collision frequency,

$$k_f \simeq \frac{8P\sigma^2}{(P-P_0)^2}\left(\frac{2\pi}{mKT_0}\right)^{1/2} \tag{7}$$

Finally surface tension was estimated from the generalized relation

$$\sigma = \sigma_0\left(1 - \frac{T_0}{T_c}\right)^{\mu} \tag{8}$$

where for octane, $\sigma_0 \simeq 55.72$, $\mu \simeq 1.3$ [7], and $T_c = 568.8$.

The physical properties appearing in equations (3-8) were estimated by assuming a smooth continuation of the properties at saturation into the region of metastable states. This has been shown to be a reasonably accurate procedure [23].

Γ in equation (2) is the probability of a nucleus of critical size growing by the evaporation of a single molecule. For simplicity, $\Gamma \simeq 1$ was used in this work—every critical size nucleus grows and none decay [14].

An estimate of J commensurate with experiment is required to solve for temperature in equation (4). Experimental conditions were similar to those reported by Avedisian and Glassman [6]. They estimated a nucleation rate of 10^5 nuclei/cm^{3}s. Figure 8 therefore illustrates predicted limits of superheat corresponding to $J = 10^5$. The data shown in the figure represent an average of the vaporization temperatures of approximately ten droplets at the corresponding pressure. The experimentally measured superheat temperatures are in quite good agreement with estimated limits of superheat. This agreement was not unexpected as others have also found similar results for other liquids in bubble column experiments performed at pressures above atmospheric [6, 23-26]. This result substantiates the belief that the type of boiling illustrated in Figs. 2 to 4 was initiated by a homogeneous nucleation mechanism, and not the result of nucleation from

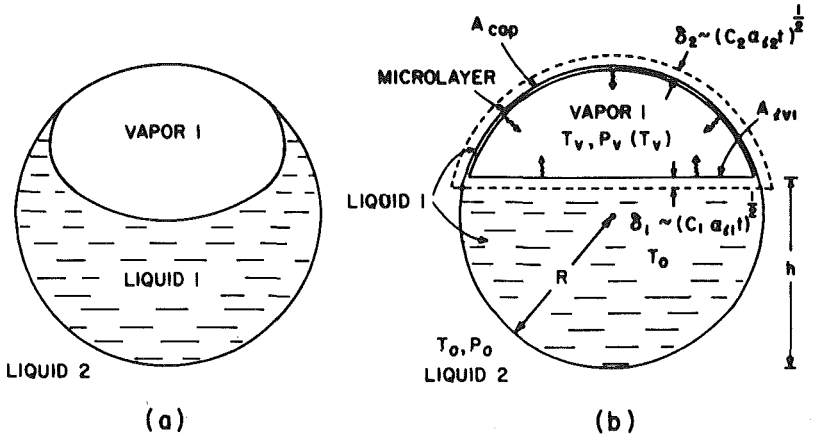

Fig. 9 (a) Schematic illustration of real two-phase droplet; (b) Geometric and heat-transfer model used in the analysis

air bubbles, particles, etc. It also shows that the mere attainment of the limit of superheat is insufficient to ensure a violent boiling process (i.e., a vapor explosion).

3.3 Physical Model for Bubble Growth. A simple model for vaporization of a two-phase droplet was developed in connection with the following assumptions: (*i*) droplet expansion is spherically symmetric, (*ii*) T_0, P_0, and properties are constant, (*iii*) the field liquid is nonvolatile and only supplies heat to the droplet, (*iv*) heat transfer occurs by transient conduction across a thin thermal boundary layer surrounding the vapor bubble, (*v*) the interior of the droplet is at a uniform pressure, and (*vi*) internal liquid motion in the droplet (e.g., acceleration of the liquid at the liquid 1/vapor 1 interface) is neglected. The entire droplet thus uniformly expands as the vapor bubble grows. While not strictly valid, this latter assumption will be useful for estimating the time domain for the various processes controlling vaporization of the two-phase droplets.

To further simplify the development, we modeled the geometry of the two-phase droplet depicted at high pressures in Figs. 3, 4, 7, and 9(*a*) by the representation shown in Fig. 9(*b*). The liquid 1/vapor 1 interface is assumed to be planar. This facilitates a description of the appropriate volume and surface areas required in the analysis.

The model was also used to obtain information on atmospheric pressure vaporization, even though no proof of the assumed droplet geometry at this pressure could be given. This was because significant period for bubble growth at atmospheric pressure was inaccessible by our experimental method. However, the present approach can still be used to obtain an order of magnitude of the time domain over which the various mechanisms controlling bubble growth occurs.

The extended Rayleigh equation [27] relates the vapor pressure within the bubble cap to the temporal variation in radius. In nondimensional form, this equation is

$$y\frac{d^2y}{d\tau^2}+\frac{3}{2}\left(\frac{dy}{d\tau}\right)^2+\left(\frac{4\nu_{l2}}{C_1\alpha_{l1}}\right)\frac{dy}{d\tau}$$

$$\left(\frac{2\sigma_{12}R_0}{\rho_{l2}(C_1\alpha_{l1})^2}\right)\frac{1}{y}=\bar{P}_v-\bar{P}_0 \qquad (9)$$

The viscous term in equation (9) is very small in the present application and was neglected. The surface tension term is initially small, and becomes of increasing importance as growth proceeds. The final vapor bubble (equation (1)) is in static mechanical equilibrium and Laplaces equation applies. Although $\bar{P}_v \neq \bar{P}_0$ due to the finite size of the final vapor bubble, this small final excess pressure is unimportant in the present analysis and was neglected.

The heat-transfer model used to relate $\bar{T}_v$ to y is illustrated in Fig. 9(*b*). Thermal boundary layers exist around the vapor cap in both liquid 2 and at the liquid 1/vapor 1 interface. A thin microlayer of liquid 1 is assumed to be present on the inside surface of the cap. Its existence is justified in terms of the tendency of liquid 1 to spread on liquid 2. Changes in the microlayer volume relative to corresponding changes in the puddle volume were neglected due to the presumed thinness of the microlayer.

An energy balance on the bubble cap yields

$$q_1+q_2=h_{fg1}\rho_{l1}\frac{dV_{l1}}{dt} \qquad (10)$$

For simplicity we treated the phase boundaries as semi-infinite media undergoing transient conduction. Hence.

$$q_i\simeq k_{li}A_{lvi}T_0\frac{(\bar{T}_v-1)}{(C_i\alpha_{li}t)^{1/2}} \qquad (11)$$

where $C_i=\pi$ ($i=1$, 2 and $A_{lv2}=A_{\text{cap}}$). This approximation has been shown to be surprisingly good in describing heat transfer to spherically symmetric expanding vapor bubbles which exist at surfaces and in infinite media (e.g., [28–31]). Equation (11) has also been used in approximating the heat flux to vaporizing bubbles in situations involving heat transfer over part of the surface of the bubbles [29–34]. In

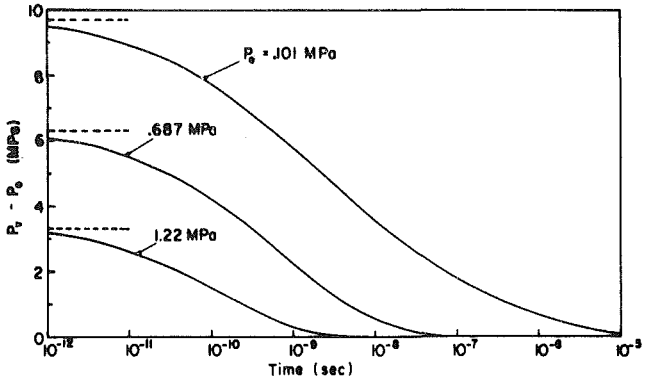

Fig. 10 Calculated variation of ΔP with time at pressures P_0 of .101 MPa, .687 MPa, and 1.22 MPa for an n-octane droplet ($R_0 \simeq .3$mm). Small and large time asymptotes correspond to the nucleation pressure and saturation pressure ($P_v = P_0$), respectively.

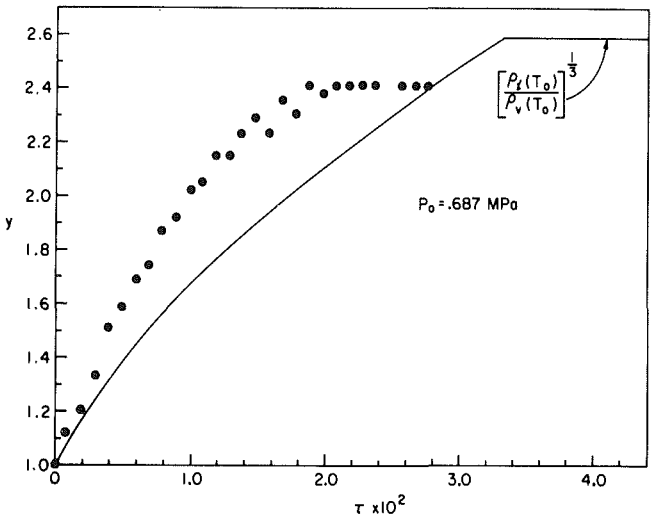

Fig. 11 Comparison between calculated and measured two-phase droplet radii at P_0 = .687 MPa

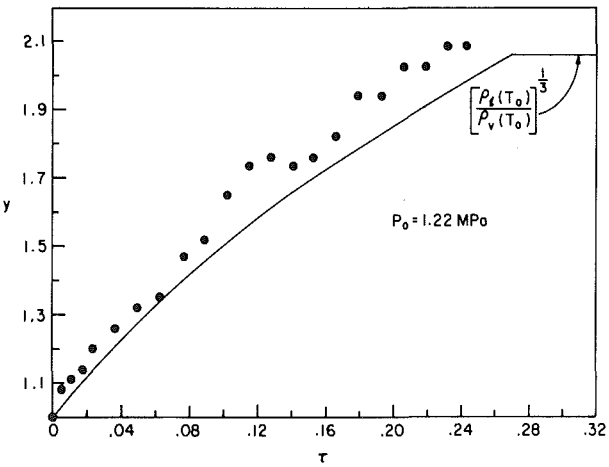

Fig. 12 Comparison between calculated and measured two-phase droplet radii at P_0 = 1.22 MPa

these studies the effects of the thermal boundary layer, radial liquid motion in the field liquid, and sphericity were accounted for by appropriately adjusting the value of C_i. (These studies do not strictly apply to the present problem because of the finite volume of the vaporizing liquid.) C_i is thus more in the vein of an experimentally adjustable parameter, although $C_i = \pi$ gave qualitative agreement with experiment as discussed below.

From geometry we can write that

$$A_{lv1} = \pi R_0^2 F(2-F)y^2 \tag{12}$$

$$A_{\text{cap}} = 2\pi R_0^2 (2-F)y^2 \tag{13}$$

$$V_{l1} = \frac{1}{3}\pi R_0^3 F^2 (3-F)y^3 \tag{14}$$

where $F \equiv h/R$. The total droplet mass (liquid + vapor) at any instant during boiling is equal to the mass of the initial liquid droplet. Hence, we have that

$$F^2(3-F) = \frac{4(\epsilon - y^3)}{y^3(\epsilon - 1)} \tag{15}$$

Solving for F gives

$$F = 2\cos\left[\frac{1}{3}\cos^{-1}\left\{1 - \frac{2(\epsilon - y^3)}{y^3(\epsilon-1)}\right\} + \frac{4\pi}{3}\right] + 1 \tag{16}$$

Combining equations (10–14) and solving for $\tilde{T}_v$ yields

$$\tilde{T}_v = 1 - \frac{4h_{fg1}C_1}{C_{pl1}T_0(\epsilon-1)} \cdot \frac{\tau^{1/2}\dfrac{dy}{d\tau}}{(2-F)\left[F + \dfrac{k_{l2}}{k_{l1}}\left(\dfrac{C_1\alpha_{l1}}{C_2\alpha_{l2}}\right)^{1/2}\right]} \tag{17}$$

The problem as formulated does not explicitly require vapor phase dimensions $(R-h)$ due to equation (16), and thus is at least qualitatively amenable to verification.

Equations (9), (10), (16), and (17), together with the initial condition

$$y(0) = 1, \dot{y}(0) = 0 \tag{18}$$

(i.e., the critical size nucleus is small compared with R_0) are a set of four equations for the unknowns y, $\tilde{T}_v$, $\tilde{P}_v$, and F. They were solved numerically over a range of pressures, P_0. Properties were evaluated at $1/2\,(T_0 + T_v)$. T_0 was estimated by solving equation (4) at each pressure using a nucleation rate of 10^5.

Figure 10 shows the variation of excess pressure within the vapor bubble, $P_v - P_0$, with time corresponding to three different ambient pressures. The initial pressure differences approximately correspond to the limit of superheat of octane. As P_0 increases, $\Delta P \to 0$ earlier in the growth of the bubble. Thus, the driving force for a vapor explosion is diminished earlier as P_0 increases. Growth then becomes controlled by the supply rate of heat to the vapor cap. Since experimentally accessible times are greater than 1 ms, growth is most likely controlled by heat transfer at .687 MPa and 1.22 MPa for the vaporization typical of that illustrated in Figs. 3 and 4. Equation (17) can then be directly integrated to give the variation of y with τ as $\tilde{T}_v$ is constant. Equation (9) is therefore *not* needed in the analysis since $P_v \to P_0$ for the conditions of our high-pressure experiments. Note, too, that vaporization at these two pressures is not explosive.

At .101 MPa a pressure difference, ΔP, exists almost into the experimentally accessible time domain. Vaporization is correspondingly explosive (Fig. 2). While this observation does not conclusively show that inertially controlled growth is capable of producing a vapor explosion, neither does it disprove this contention. Further experimental work is required to elucidate the vaporization process in the time scales which were inaccessible by our method.

A comparison between experimentally measured and predicted droplet radii is shown in Figs. 11 and 12. Similar data could not be obtained for atmospheric pressure boiling by our experimental method. Considering our various approximations and experimental accuracy, there is qualitative agreement between calculated and measured radii. Also, measured radii exhibit evidence of approaching a maximum value given by equation (1). (R_0 is slightly larger due to subsequent superheating of the vapor after the liquid completely vaporizes. This further increase is comparatively small and was neglected.)

4 Conclusions

The boiling of droplets heated to their limits of superheat revealed that ambient pressure strongly affects the bubble growth rate. At .101 MPa droplets of n-octane under 1 mm dia exploded into vapor with an audible "popping" sound when they were heated to within 2°K of the theoretical homogeneous nucleation temperature; the boiling process occurred in less than 2 ms. At pressures above .6 MPa, the intensity of vaporization was considerably reduced, with droplets of the same size requiring over 30 ms to completely vaporize.

Homogeneous nucleation theory was used to provide the initial conditions for a simplified model of droplet boiling which was based on vaporization of a two-phase, liquid-vapor droplet. Predicted droplet radii were shown to be in qualitative agreement with measured radii. The results suggest that vapor explosions are not likely to occur when bubble growth is controlled by heat transfer to the vaporizing liquid. The results also show that while a necessary condition for a vapor explosion is that the liquid be heated to its spontaneous nucleation temperature, sufficient conditions must include consideration of the dynamics of the subsequent growth of the initially formed critical size nuclei.

Acknowledgments

The author wishes to thank Professor S. George Bankoff of Northwestern University for various discussions. Thanks are also due for the services provided by the Cornell University Computer Center. This work was supported by the National Science Foundation under Grant No. CPE-8106348 with Dr. David O. Cooney as project monitor.

References

1 Reid, R. C., "Superheated Liquids: A Laboratory Curiosity and, Possibly, an Industrial Curse, Part II: Industrial Vapor Explosions," *Chemical Engineering Education*, Summer 1978, p. 108.

2 Bankoff, S. G., "Vapor Explosions: A Critical Review," *Proceedings of the 6th International Heat Transfer Conference*, Aug. 7–11, 1978.

3 Lasheras, J. C., Fernandez-Pello, A. C., and Dryer, F. L., "Initial Observations on the Free Droplet Combustion Characteristics of Water-In-Fuel Emulsions," *Combusiton Science and Technology*, Vol. 21, 1979, pp. 1–14.

4 Skripov, V. P., and Ermakov, G. V., "The Limit of Superheating of Liquids," *Russian Journal of Physical Chemistry*, Vol. 37, No. 8, Feb. 1963, pp. 1047–1048.

5 Skripov, V. P., and Ermakov, G. V., "Pressures Dependence of the Limiting Superheating of a Liquid," *Russian Journal of Physical Chemistry*, Vol. 38, No. 2, Feb. 1964, pp. 208–213.

6 Avedisian, C. T., and Glassman, I., "High-Pressure Homogeneous Nucleation of Bubbles Within Superheated Binary Liquid Mixtures," ASME JOURNAL OF HEAT TRANSFER, Vol. 103, No. 2, 1981, pp. 272–280.

7 Eberhart, J. G., Kremsner, W., and Blander, M., "Metastability Limits of Superheated Liquids: Bubble Nucleation Temperatures of Hydrocarbons and Their Mixtures," *Journal of Colloid and Interface Science*, Vol. 50, No. 2, Feb. 1975, pp. 369–378.

8 Blander, M., Hengstenberg, D., and Katz, J. L., "Bubble Nucleation in

n-Pentane, n-Hexane, n-Pentane + Hexadecane Mixtures, and Water," *Journal of Physical Chemistry*, Vol. 75, No. 23, 1971, pp. 3613-3619.

9 Henry, R. E., and Fauske, H. K., "Nucleation Processes in Large Scale Vapor Explosions," ASME JOURNAL OF HEAT TRANSFER, Vol. 101, May 1979, pp. 280-287.

10 Buchanan, D. J., and Dullforce, T. A., "Mechanism for Vapor Explosions, *Nature*, Vol. 245, Sept. 1973, pp. 32-34.

11 Dergarabedian, P., "The Rate of Growth of Vapor Bubbles in Superheated Water," ASME *Journal of Applied Mechanics*, Vol. 20, 1953, pp. 537-545.

12 Apfel, R. E., and Harbison, J. P., "Acoustically Induced Explosions of Superheated Liquids," *Journal of the Acoustical Society of America*, Vol. 57, No. 6, June 1975, pp. 1371-1373.

13 Mori, Y. H., and Komotori, K., "Boiling of Single Superheated Drops in an Immiscible Liquid," *Heat Transfer—Japanese Research*, Vol. 5, No. 3, 1976, pp. 75-95.

14 Avedisian, C. T., "Superheating and Boiling of Water in Hydrocarbons and of Hydrocarbon Mixtures," PhD thesis, Princeton University, 1980.

15 Holden, B. S., and Katz, J. L., "The Homogeneous Nucleation of Bubbles in Superheated Binary Liquid Mixtures," *AIChE Journal*, Vol. 24, No. 2, March 1978, pp. 260-267.

16 Renner, T. A., Kucera, G. H., and Blander, M., "Explosive Boiling of Light Hydrocarbons and Their Mixtures," *Journal of Colloid and Interface Science*, Vol. 52, No. 2, Aug. 1975, pp. 391-396.

17 Peng, D. Y., and Robinson, D. B., "A New Two-Constant Equation of State," *Industrial and Engineering Chemistry Fundamentals*, Vol. 15, No. 1, 1976, pp. 59-64.

18 Sideman, S., and Taitel, Y., "Direct Contact Heat Transfer with Change of Phase: Evaporation of Drops in an Immiscible Liquid Medium," *International Journal of Heat and Mass Transfer*, Vol. 7, 1964, pp. 1273-1289.

19 Selecki, A., and Gradon, L., "Equation of Motion of an Expanding Vapour Drop in an Immiscible Liquid Medium," *International Journal of Heat and Mass Transfer*, Vol. 19, 1976, pp. 925-929.

20 Simpson, H. C., Beggs, G. C., and Sohal, M. S., "Nucleation of Butane Drops in Flowing Water," *Proceedings of the Sixth International Heat Transfer Conf.*, 1978, Paper No. PI-10.

21 Hankinson, R. W., and Thomson, G. H., "A New Correlation for Saturated Densities of Liquids and Their Mixtures," *AIChE Journal*, Vol. 25, No. 4, July 1979, pp. 653-663.

22 Gomez-Nieto, M., and Thodos, G., "Generalized Vapor Pressure Equation for Nonpolar Substances," *Industrial and Engineering Chemistry Fundamentals*, Vol. 17, No. 1, 1978, pp. 45-51.

23 Skripov, V. P., *Metastable Liquids*, Wiley, New York, 1974.

24 Mori, Y., Hijikata, K., and Nagatani, T., "Effect of Dissolved Gas on Bubble Nucleation," *International Journal of Heat and Mass Transfer*, Vol. 19, 1976, pp. 1153-1159.

25 Hijikata, K., Mori, Y., and Nagatini, T., "Experimental Study on Bubble Nucleation in the Oscillating Pressure Field," ASME JOURNAL OF HEAT TRANSFER, Vol. 100, Aug. 1978, pp. 460-465.

26 Forest, T. W., and Ward, C. A., "Homogeneous Nucleation of Bubbles in Solutions at Pressures above the Vapor Pressure of the Pure Liquid," *Journal of Chemical Physics*, Vol. 69, No. 5, Sept. 1978, pp. 2221-2230.

27 Bankoff, S. G., "Diffusion-Controlled Bubble Growth," in *Advances in Chemical Engineering*, Vol. 6, Academic Press, New York, 1966, pp. 1-60.

28 Zuber, N., "The Dynamics of Vapor Bubbles in Nonuniform Temperature Fields," *International Journal of Heat and Mass Transfer*, Vol. 2, 1961, pp. 83-98.

29 Donald, M. B., and Haslam, F., "The Mechanism of the Transition from Nucleate to Film Boiling," *Chemical Engineering Science*, Vol. 8, 1958, pp. 287-294.

30 Jones, O. C., and Zuber, N., "Bubble Growth in Variable Pressure Fields," ASME JOURNAL OF HEAT TRANSFER, Vol. 100, 1978, pp. 453-459.

31 Mikic, B. B., Rohsenow, W. M., and Griffith, P., "On Bubble Growth Rates," *International Journal of Heat and Mass Transfer*, Vol. 13, 1970, pp. 657-666.

32 Jongenelen, F. C. H., Groeneweg, F., and Gouda, J. H., "Effects of Interfacial Forces on the Evaporation of a Superheated Water Droplet in a Hot Immiscible Oil," *Chemical Engineering Science*, Vol. 33, 1978, pp. 777-781.

33 Bankoff, S. G., and Choi, H. K., "Growth of a Bubble at a Heated Surface in a Pool of Liquid Metal," *International Journal of Heat and Mass Transfer*, Vol. 19, 1976, pp. 87-93.

34 Van Stralen, S. J. D., "The Mechanism of Nucleate Boiling in Pure Liquids and in Binary Mixtures—Part 1," *International Journal of Heat and Mass Transfer*, Vol. 9, 1966, pp. 995-1020.

K. N. Agrawal
Lecturer.

H. K. Varma
Professor.

Mechanical and Industrial Engineering,
University of Roorkee,
Roorkee, U.P., India

S. Lal
Director,
Indian Institute of Technology,
Kharagpur, W. Bengal, India

Pressure Drop During Forced Convection Boiling of R-12 Under Swirl Flow

This investigation deals with the pressure drop during forced convection boiling of R-12 under swirl flow inside a horizontal tube. Plain flow and swirl flow pressure drop data are reported for an electrically heated, horizontal, stainless steel, round test-section fitted with twisted tapes having twist ratios from 3.76 to 10.15. A correlation has been presented expressing the swirl flow boiling pressure drop in terms of the twist ratio and the plain flow boiling pressure drop calculated by the Martinelli-Nelson model. The proposed correlation predicts the swirl flow data to within ± 20 percent of the observed values.

Introduction

In recent years, the requirement for more efficient heat-transfer systems has stimulated interest in augmentative heat-transfer methods. In this direction, several investigations have been carried out to determine the effect of swirl motion during forced convection heat transfer. It has been reported that heat-transfer rates and pressure losses increase when swirl generators or spiral flow generators are inserted in the fluid flow. This may result in more compact and perhaps cheaper heat exchanger but with an enhanced pumping power requirement to effect fluid flow. Thus the phenomenon of heat transfer and pressure drop during swirl flow brings in an interesting problem when the advantage of heat-transfer augmentation is accompanied by increased pressure losses.

The pressure drop and heat transfer during swirl flow heating or cooling has been found to depend mainly on the type of swirl generator, its configuration and pitch of the helix [1–5]. Subsequent studies in this field have been mainly devoted towards the analysis and development of correlation for the heat-transfer coefficient and pressure drop [6–9]. However, a large portion of the information available concerns single phase flow with heat transfer. Only very scanty data have been reported for forced convection boiling under swirl flow conditions [10]. The data on fluorinated hydrocarbon refrigerants are still scarce [4,8].

It must be realised that accompanying the growth of data, the phenomenon of swirl flow heat transfer and pressure drop be better understood and satisfactory methods of calculating pressure drops be developed. It is with the aim the present work was taken up and refrigerant 12 was chosen as the working fluid for investigation because of its wide application in the refrigeration industry.

Experimental Program

Figure 1 is a schematic diagram of the experimental set up. It consists of the test section, condensing unit, a preheater, an afterheater, expansion valves, and the necessary measuring instruments and controls. The test section was a 2.1-m long stainless steel tube, with a 10-mm i. d. The heating of the test section was done by passing alternating electric current through it with the help of a step-down transformer. The vapour quality at the entrance to the tube could be regulated by heating the refrigerant in the preheater. The preheater was made up of a 15-m long, 12.5-mm o.d. copper tubing which was heated by a flexible electrical heating tape, 3 kW in capacity. The preheater and test section were housed in two separate wooden boxes and sufficiently insulated. The mass flow rate of the refrigerant was controlled with the help of two valves located before the test section in order to obtain a fine control of flow.

For meauring the pressure drop across the test section, two pressure taps, one each by the side of the copper buss connections were provided. These tappings were made circumferentially approximately at an angle of 90 deg from the tube-tape meeting line. The blurrings of the tap-holes were removed by filing both the inner and outer edges. Pressure was measured with the help of a pressure transducer through thin (1.58-mm dia) copper tubes and hand shut-off valves (Fig. 2). The pressure transducer consisted of 4 strain-gauges in fully compensated bridge. Its pressure range was from 0 to 350 kPa (0–50 psi). The output was adjusted to 0 to 70 mV which was measured with a digital microvoltmeter. The difference of the inlet and outlet pressure readings gave the pressure drop across the test section.

Twisted tapes were made of stainless steel strips, 0.5-mm thick, with the width approximately 5 percent greater than the inside diameter of the tube to allow for contraction in twisting. Steel strips with four different twist ratios were fitted snugly inside the test section. Figure 3 is the photographic view of the four twisted tapes used in the present investigation.

The experimental system was checked for energy balance and the agreement was found generally within ± 5 percent.

Data were collected in the following range of operating parameters:

Mass velocity	194–388 kg/m^{2}s
Heat flux	8000–20,000 W/m^2
Liquid Reynolds number	7000–15000
Inlet vapor quality	20–40 percent
Outlet vapour quality	30–90 percent
Twist ratio	10.15, 7.37, 5.58 and 3.76

Thirty test runs were performed with plain flow and, correspondingly, 120 runs were performed with the four strips. Thus, the results of 150 runs have been included in this paper.

Plain Flow Pressure Drop

All the test data were reduced into desirable parameters by means of a computer program run on a digital computer. Since the pressure taps were located within the swirl section it was not necessary to apply any corrections to the pressure drop data.

The Martinelli-Nelson [13] model was chosen for com-

Contributed by the Solar Energy Division for publication in the JOURNAL OF HEAT TRANSFER. Manuscript received by the Heat Transfer Division April 19, 1982.

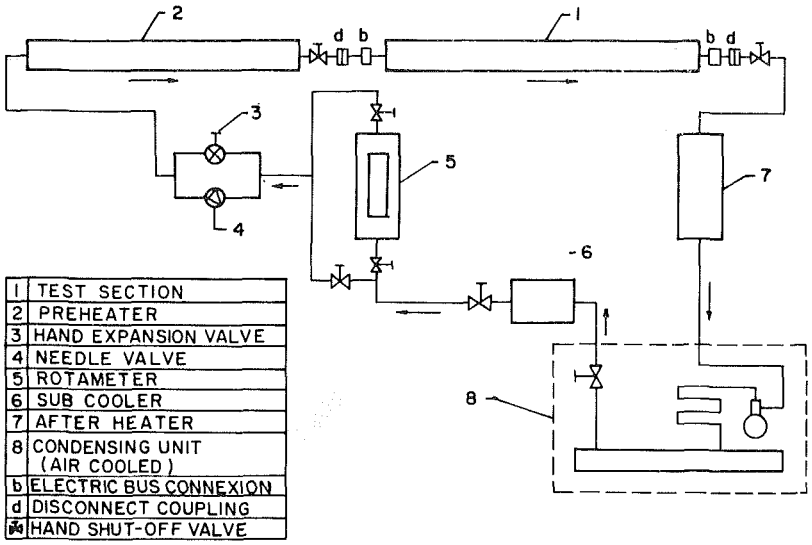

Fig. 1 Schematic diagram of experimental setup

paring the pressure drops observed during forced circulation plain flow boiling of R-12 in the test section. The total pressure drop during plain flow forced circulation boiling of a liquid in a tube is given by equation (1).

$$(\Delta p)_{TP} = (\Delta p)_{TPF} + (\Delta p)_a + (\Delta p)_{gr} \tag{1}$$

The term ΔP_{gr} in equation (1) which accounts for the static pressure drop due to gravity is zero in the present case, since the tube is laid horizontal. Equation (1) then reduces to

$$(\Delta p)_{TP} = (\Delta p)_{TPF} + (\Delta p)_a \tag{2}$$

$(\Delta p)_{TPF}$ is calculated by equation (3) given by

$$\left(\frac{dp}{dL}\right)_{TPF} = \varphi_{Ltt}^2 \left(\frac{dp}{dL}\right)_{LF} \tag{3}$$

In order to determine $(\Delta p)_{TPF}$ by equation (3) the usual procedure of numerical integration was followed. The total tube length was divided in 21 sections, 10-cm long each. For each section mean X_{tt} were calculated. The values of φ_{Ltt} were taken from the curves given in reference [13] at the known values of X_{tt} and at the known test section pressure (reduced into dimensionless form, $p_r = p_m/p_{cr}$). $(dp/dl)_{LF}$ was calculated by equation (4) given by

$$(dp/dL)_{LF} = \frac{4(f)G^2}{2(D)(\rho)} \tag{4}$$

where f is the Blasius friction factor given by equation (5)

$$f = \frac{0.079}{\mathrm{Re}_f^{0.25}} \tag{5}$$

The pressure drop due to acceleration, $(\Delta p)_a$, of the vapour in the tube is given, in general, by equation (6)

$$\left(\frac{dp}{dz}\right)_a = \frac{1}{L}\left[\frac{M.V_{\text{outlet}} - M.V_{\text{inlet}}}{\mathrm{A}}\right]_{\text{general}} \tag{6}$$

Equation (6) may be expanded to find

Nomenclature

A = free flow area of the tube, m^2
C = constant
D = inside diameter of the tube, m
f = Blasius friction factor, defined in equation (5)
G = mass velocity of the total liquid refrigerant, kg/s − m^2
h = heat-transfer coefficient, $W/m^2 - K$
L = test section heated length, m
M = total mass flow rate of refrigerant, kg/s
P = test section pressure, Pa
ΔP = pressure drop across test section heated length, Pa.
q = heat flux, W/m^2
Re = Reynolds number
x = vapour quality
X_{tt} = Martinelli parameter,

$$= \left(\frac{1-x}{x}\right)^{0.9}\left(\frac{\rho_g}{\rho_f}\right)^{0.5}\left(\frac{\mu_f}{\mu_g}\right)^{0.1}$$

V = flow velocity, m/s
v = specific volume m^3/kg
y = twist ratio = $\dfrac{\text{half pitch of the helix}}{D}$
Z = distance along test section heated length from entrance, m.

Greek Letters

ρ = density of refrigerant, kg/m^3
μ = dynamic viscosity, kg/s-m
α = void fraction
φ_{Ltt} = pressure gradient ratio, defined by equation (3)

Subscripts

a = acceleration component
cr = critical value
f = liquid state
g = gaseous state
gr = due to gravitational pull
i = inlet location of the test section
LF = frictional value when total flow is liquid
m = mean value
n = exponent, equation (8)
o = outlet location of the test section
p = plain flow condition
r = reduced
s = swirl flow condition
TP = total value (two phase)
TPF = two phase friction
x = local value

$$(\Delta p)_a = G^2\left[\frac{x^2 v_g}{\alpha} + \frac{(1-x)^2 v_f}{1-\alpha}\right]_{\text{outlet}} - G^2\left[\frac{x^2 v_g}{\alpha} + \frac{(1-x)^2 v_f}{1-\alpha}\right]_{\text{inlet}} \quad (7)$$

The values of α were taken from the charts given in reference [13] at the known values of X_{tt} and the test section pressure. Summing up of the values of $(\Delta p)_{TPF}$ and $(\Delta p)_a$ gave the total pressure drop in the test section.

The comparison of the calculated plain flow pressure drops with the experimentally observed values is done in Fig. 4. It shows that most of the observed pressure drops were within ±20 percent of the prediction by Martinelli-Nelson method.

Swirl Flow Pressure Drop

When twisted tapes were inserted inside the tube to produce swirl flow boiling, the pressure drop increased. It was found that the increase was greater at smaller twist ratio, where twist ratio is defined as the ratio of half of pitch of helix of the twisted tape to the tube diameter. Figure 5 shows a plot of the ratio of observed pressure drop under swirl flow to the observed pressure drop under plain flow versus the twist ratio. It is found that the values of the ratio of pressure drops varied in a range from about 1.1 to 2.2 for $y = 10.15$ and about 1.7 to 3.7 for $y = 3.76$. Blatt [8] has correlated his swirl flow data on the pressure drops of water and R-11 in the following form

$$(\Delta p_s/\Delta p_p)_{obs} = \frac{C}{y^n} \quad (8)$$

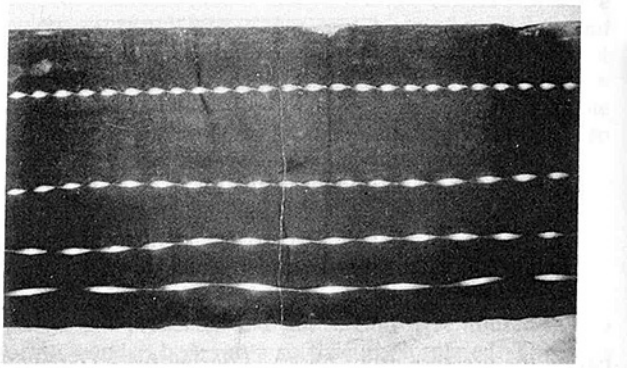

Fig. 3 Photographic view of the twisted tapes used in present investigation

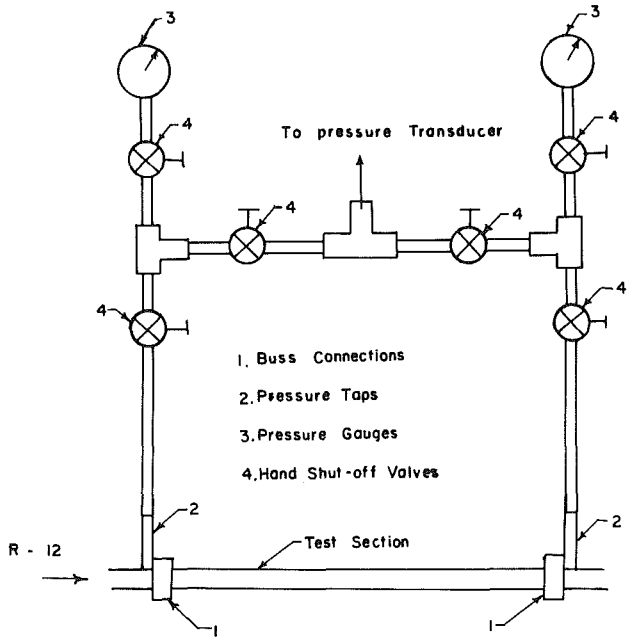

Fig. 2 Attachment used for measuring the pressure drop across the test section

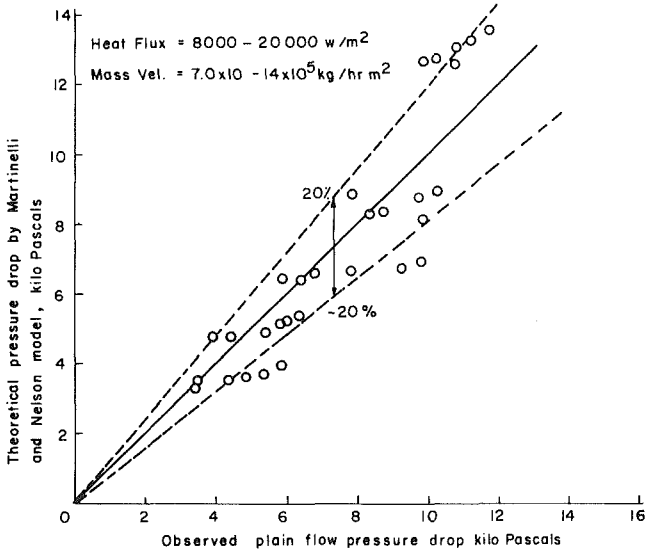

Fig. 4 Comparison of the observed plain flow boiling pressure drops with those predicted by the Martinelli-Nelson model

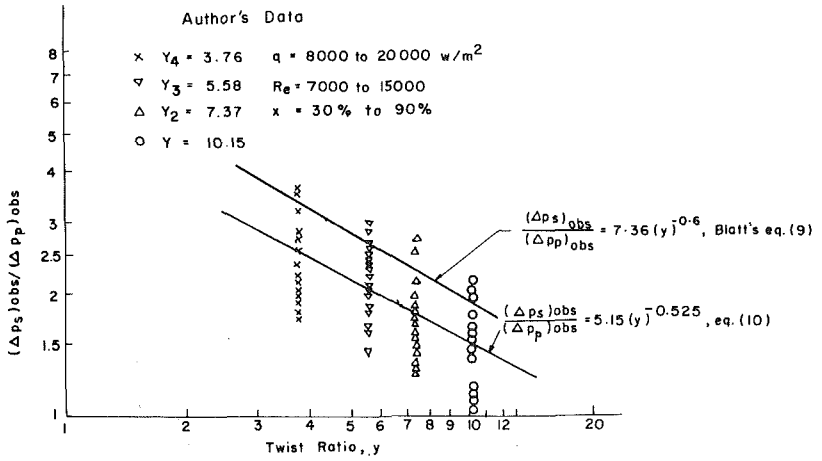

Fig. 5 Variation of $(\Delta p_s/\Delta p_p)_{obs}$ with twist ratio, y

He obtained a best fitting relationship of this type for his data as given by equation (9).

$$(\Delta p_s/\Delta p_p)_{obs} = 7.36/(y)^{0.6} \quad (9)$$

Blatt reported that the experimental values differed from those calculated by equation (9) by ± 25.1 percent.

Authors plotted their experimental data in Fig. 5 in the form of equation (8). The data is best correlated by equation (10) given below:

$$\left(\frac{\Delta p_s}{\Delta p_p}\right)_{obs} = \frac{5.15}{(y)^{0.525}} \quad (10)$$

It may be noticed that the exponent of y in equation (10) does not vary significantly from that of Blatt. Equation (10) is, however, not quite satisfactory since the values of Δp_s calculated with the help of this equation differed from those experimentally determined by ± 50 percent. Blatt's equation (9) has been drawn in Fig. 5 for comparing it with equation (10). It is obvious that equation (9) does not correlate R-12 data well.

Correlation for Pressure Drop in Swirl Flow. The preceding discussion has shown that a satisfactory correlation of the observed pressure drop was not found either with relation proposed by Blatt, i.e., equation (9), or in the form of equation (8), i.e. equation (10). Further, the correlation requires that in order to determine the pressure drop during swirl flow boiling the pressure drop for plain flow boiling be experimentally determined under identical mass flow and heating rates. In order to simplify the procedure to predict the swirl flow boiling pressure drop, the authors tried to correlate it in terms of plain flow boiling pressure drop calculated by using some acceptable method of prediction. The use of such a method to calculate the plain boiling flow pressure drop would eliminate the need of measurement of plain flow boiling pressure drop under identical mass flow rate and heating flux. Since in this investigation the pressure drop for plain boiling flow compared within ± 20 percent with those predicted by the Martinelli and Nelson model [13], and since the method has been found to predict the pressure drop for boiling refrigerants quite well, an attempt was made to study the variation of the ratio of the pressure drop during swirl flow to the Martinelli-Nelson pressure drop during plain flow, Δp_{M-N}.

A graph between $(\Delta p_s/\Delta p_{M-N})$ and the twist ratio, y, has been plotted in Fig. 6. Comparing Figs. 5 and 6, it is seen that the points now tend to bunch together. A straight line is drawn on the same graph to best correlate the data points. The equation of the straight line is

$$\Delta p_s/\Delta P_{M-N} = \frac{5.12}{(y)^{0.509}} \quad (11)$$

A graph between the Δp_s observed and Δp_s calculated by equation (11) is drawn in Fig. 7. It is found that almost all the experimental data is correlated within a deviation of ± 20 percent. Thus, we find that the agreement of experimental swirl flow data on pressure drop is better with equation (11) when Δp_p is calculated by the Martinelli-Nelson method than by equation (10), which uses the experimentally observed plain flow pressure drops. Care should, however, be taken in using equation (11) for fluids other than R-12 because the constant, C, and exponent, n, of equation (8) may be different for different fluids.

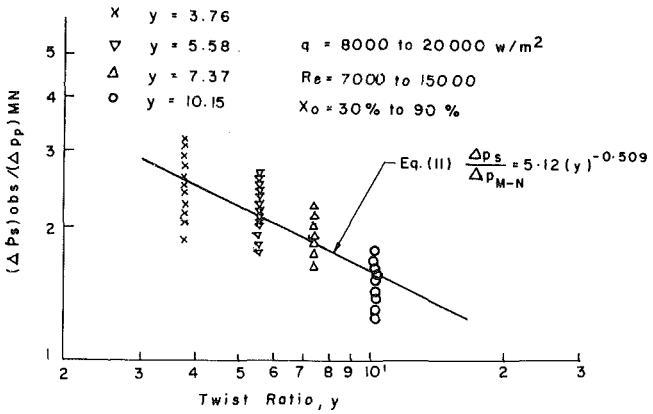

Fig. 6 Variation of Δp_s (obs/Δp_p)$_{M-N}$ with twist ratio, y

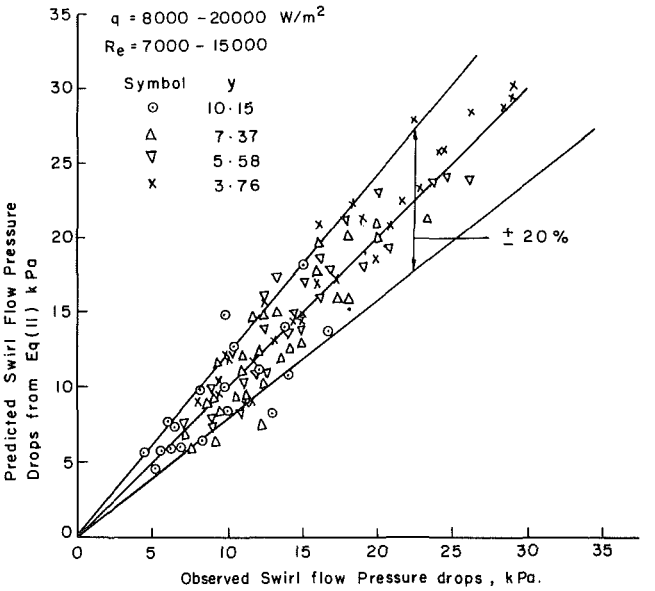

Fig. 7 Comparison of the observed swirl flow boiling pressure drops with those predicted by the proposed equation (11)

Conclusions

1 The pressure drop during plain flow boiling of R-12 compares satisfactorily within ± 20 percent with those predicted by the Martinelli-Nelson model.

2 The swirl flow pressure drop increases when the twist ratio decreases.

3 The authors have been able to develop a successful correlation for the pressure drop during swirl flow boiling of R-12 in the form of the following equation:

$$\frac{\Delta p_s}{\Delta p_{M-N}} = \frac{5.12}{(y)^{0.509}}$$

Acknowledgments

The authors gratefully acknowledge the financial assistance given by the Council of Scientific and Industrial Research, India for this project.

References

1 Royds, R., *Heat Transmission by Radiation, Conduction and Convection*, 1st ed., Constable and Co., London, 1921.

2 Colburn, A. P., and King, W. J., "Heat Transfer and Pressure Drop in Empty, Baffled and Packed Tubes," *Industrioal and Engineering Chemistry*, Vol. 23, 1931, pp. 910-923.

3 Seigel, L. G., "The Effect of Turbulence Promoters on Heat Transfer Coefficients for Water Flowing in Horizontal Tubes," *Trans. ASHVE*, June 1946, p. 197.

4 Bryan, W. L., and Seigel, L. G., "Heat Transfer Coefficients in Horizontal Tube Evaporators," *Refrigerating Engineering*, Vol. 63, May 1955, p. 36.

5 Kreith, F., and Margolis, D., "Heat Transfer and Friction in Turbulent

Vortex Flow," *Applied Scientific Research*, Section A, Vol. 8, 1959, pp. 457–473.

6 Thomas, D. C., and Hayes, P. H., "High Performance Heat Transfer Surfaces," *Industrial and Engineering Chemistry*, Vol. 62, Feb. 1970, p. 4.

7 Hong, S. W., and Bergles, A. E., "Augmentation of Laminar Flow Heat Transfer in Tubes by Means of Twisted Tapes," ASME JOURNAL OF HEAT TRANSFER, Trans. ASME Series C Vol. 98, No. 2, May 1976, p. 251.

8 Blatt, T. A., and Adt., R. R., Jr., "The Effects of Twisted Tape Swirl Generators on the Heat Transfer Rate and Pressure Drop of Boiling Freon 11 and Water," ASME Paper No. 63-WA-42, 1963.

9 Lopina, R. F., and Bergles, A. E., "Heat Transfer and Pressure Drop in Tape Generated Swirl Flow of Single-Phase Water," ASME JOURNAL OF HEAT TRANSFER, Vol. 91, No. 3, Aug. 1969, p. 434.

10 Gambill, W. R., and Bundy, R. D., "An Evaluation of the Present Status of Swirl Flow Heat Transfer," ASME Paper No. 62-HT-42, 1962.

11 Collier, J. G., *Convective Boiling and Condensation*, McGraw Hill, London, 1972, p. 38 and 59.

12 Tatom, F. B., "An Investigation of Heat Transfer and Pressure Drop with Local Boiling and Swirl Flow," MS thesis, Auburn University, Alabama, Dec. 1962.

13 Martinelli, R. C., and Nelson, D. B., "Prediction of Pressure Drop during Forced Circulation Boiling of Water," *Trans. ASME*, Vol. 70, 1948, p. 695.

T. N. Tandon

H. K. Varma

C. P. Gupta

Mechanical and Industrial Engineering Department, University of Roorkee, Roorkee, U. P., India

A New Flow Regimes Map for Condensation Inside Horizontal Tubes

The problem of predicting flow patterns during condensation inside horizontal tubes is discussed. Using the condensation flow pattern data of several investigators, a new flow regimes map with dimensionless gas velocity j_g^* as ordinate and $(1-\alpha)/\alpha$ as abscissa, where α is the void fraction, is generated. Based on these data, a set of new criteria for the transition between different flow regimes is suggested. The proposed flow regimes map gives excellent agreement for annular, semiannular, and wavy flows which exist over a major part of the condensing length during condensation inside horizontal tubes.

Introduction

Condensation inside horizontal tubes is important in a large number of chemical process industries, refrigeration and air-conditioning systems, air-cooled condensers, etc. For economical design and efficient performance of condensers, it is important to select appropriate correlations for the prediction of condensation heat transfer coefficients. Although numerous correlations exist in the literature, no single correlation can be stated to be the best for design purposes.

It is now well established that for the analysis of the condensation (or boiling) process, it is not enough to distinguish the type of flow (viz., laminar or turbulent) only, as contemplated by Martinelli et al. [1, 2, 3], but it is also necessary to ascertain the types of flow pattern that exist at various points along the tube. The performance characteristics of the condenser, namely, heat-transfer coefficient and pressure drop, are governed to a large extent by the mechanism of heat transfer on the inside of the tubes and this in turn depends greatly on two-phase flow patterns. Bell et al. [4] while critically comparing the various heat-transfer correlations for horizontal in-tube condensation, clearly showed that different correlations gave vastly divergent results, differing by a factor of 10 or more for a given set of conditions. This was attributed to the different flow regimes that might be existing during the development of various heat transfer correlations. Bell et al. concluded that (*i*) the designer should determine a priori the flow regime of his case and choose an appropriate correlation, and (*ii*) different heat transfer correlations would be required for different flow patterns.

In this paper the problem of predicting the flow pattern during condensation of pure components inside horizontal tubes is discussed.

Previous Flow Maps

Early flow regime studies of two-phase flow were mainly concerned with adiabatic flows of mixtures of a gas and a liquid. Alves [5] first reported a complete description of two-phase flow patterns of adiabatic mixtures inside horizontal tubes and generated a flow pattern map.

Th earliest generalized flow regime map and perhaps the most widely accepted and used map was proposed by Baker [6]. Baker's flow regime map, in spite of several deficiencies, as pointed out by various investigators, has been used as a thumb rule for comparing experimental results even for diabatic flow cases. This is partly because of the large experimental data base [8] of this map.

Until the last decade, little attention was given to the problem of predicting flow patterns during condensation. Soliman and Azer [7] were the first to develop flow pattern maps based on their condensation data. They observed the flow pattern during condensation of R-12 inside 12.7-mm (0.5-in.) i.d. horizontal copper tube. They identified six major flow patterns, viz., spray, annular, semi-annular, wavy, slug, and plug flows and three transition flow patterns viz. annular-wavy flow, semiannular-wavy flow and spray-annular flow. Out of the four different flow maps generated they found that their experimental data were best represented on a flow regimes map with Froude number, Fr, and gas volumetric ratio, R, as coordinates. Soliman and Azer found their experimental data to be in poor agreement with Baker's map and concluded that Baker's map is inadequate to characterize the different flow regimes during condensation.

Traviss and Rohsenow [8] observed the flow pattern during condensation of Refrigerant-12 in a 8-mm (0.315-in.) i.d. horizontal tube. Their data when plotted on the flow regime map proposed by Soliman and Azer [7] did not give satisfactory correlation. However, this data agreed fairly well with Baker's original map, and they concluded that Baker's map, as modified by Scott [9], agrees better with the flow regime data for small diameter tubes.

Soliman and Azer [10, 11] conducted visual observation of flow patterns in three different tubes of diameters 4.8-mm (0.1875-in.) i.d., 12.7-mm (0.5-in.) i.d., and 15.9-mm (0.625-in.) i.d. with refrigerants R-12 and R-113 as condensing fluids. They found that this time their data were in poor agreement with their earlier [7] map. They again concluded that Baker's map is inadequate to characterize the two-phase flow during condensation. They found their data of this investigation, as well as that of earlier investigation, correlated best on a map using V_l, average liquid velocity, and $(1-\alpha)/\alpha$ as coordinates.

It should be noted that Soliman and Azer [10, 11] did not test their newly proposed map [10, 11] with the experimental data of Traviss and Rohsenow [8]. To test the general applicability of Soliman and Azer's [10, 11] map, the data of Traviss and Rohsenow [8] have been plotted in Fig. 1. It is apparent that nearly the entire semiannular flow data points have occupied the range of wavy flow. For spray and slug flow patterns, the agreement is moderate.

An effort has been made by some investigators [13, 14, 17–19] to select flow map coordinates based on force balance criteria. Jaster and Kosky [17] performed experiments on condensing steam within a horizontal pipe, 12.5-mm i.d. and 2.2-m long. They suggested that the flow transition from the initial annular flow regime to stratified regime is a function of

Contributed by the Heat Transfer Division for publication in the JOURNAL OF HEAT TRANSFER. Manuscript received by the Heat Transfer Division October 26, 1981.

Table 1 Condensation flow pattern data sources

Reference	Refrigerant used	Condenser tube inside diameter, mm	Test section length, m	Number of data points	Number of test runs
7	R- 12	12.7	0.61	93	41
8	R- 12	8.0	4.42	83	83
11	R- 12	4.8	0.61	111	39
		15.9	0.61	138	55
	R-113	4.8	0.61	74	48
		12.7	0.61	79	40
		15.9	0.61	86	43

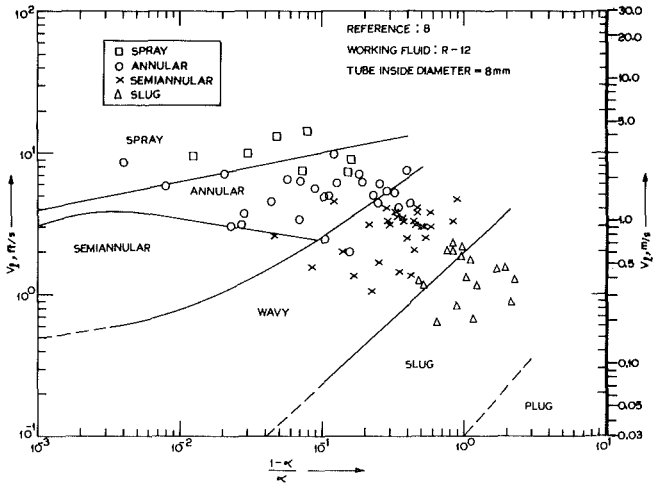

Fig. 1 Comparison of Soliman et al. [10] flow map with condensation data of Traviss and Rohsenow [8]

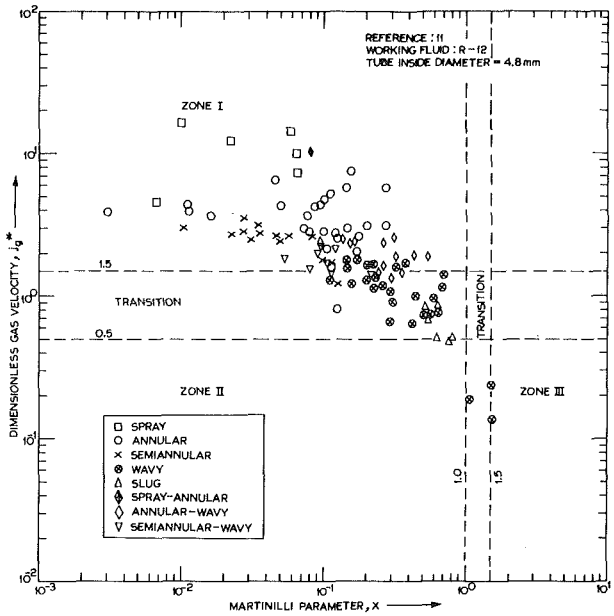

Fig. 2 Comparison of Breber et al. [20] flow map with condensation data of Soliman [11] for 4.8-mm i.d. tube

stress ratio defined as the ratio of axial shear force to gravitational body force.

Palen et al. [18] made visual investigation of condensation in horizontal glass tube 22-mm i.d. and 6.7-m long with water and pentane as condensing fluids. They concluded that Baker's map did not provide a realistic picture of the controlling regimes in condensation. Using their own flow regime data as well as that from other sources [7, 8, 10] they found that shear controlled regimes (annular, mist annular) and gravity controlled regimes (wavy, stratified, slug) are quite well separated by dimensionless gas velocity $j_g^* = 1$. Generally, the transition values were within $j_g^* = 0.5$ and $j_g^* = 1.5$. The mist and mist-annular data were found to fall above $j_g^* = 5$.

The Taitel - Dukler model [14] originally developed for transition between adjacent flow patterns for adiabatic flow without phase change was tested by Breber et al. [19] for condensation data. Using the experimental data of several investigators, they developed a flow regime map with dimensionless gas velocity, j_g^*, as ordinate and Martinelli parameter X as abscissa. While the map was found to give good agreement with moderate and large tube diameters, agreement with the experimental data of Soliman [11] for wavy and slug flows with a small tube diameter of 4.8 mm for fluids R-12 and R-113 was not satisfactory. Figure 2, generated from the data of Soliman [11] for R-12 (4.8-mm dia tube), shows an example of this lack of agreement for small diameter tubes. Referring to Fig. 2, the following observations may be made:

(*i*) Wavy and slug flows were predicted as semiannular [19]. Wavy and slug flow data did not fall in their respective zones.

(*ii*) Semiannular flow data during condensation occupied the spray - annular flow regime.

Keeping the above facts in view, it can be realized that development of a flow regime map which would represent the flow patterns with greater degree of agreement would be of considerable value.

Development of Proposed Flow Regimes Map and Discussion

To achieve the above objective the easily accessible experimental data of references [7, 8, 11] were used; the test conditions for these data are given in Table 1. In all 664 flow

Nomenclature

D = tube diameter, m
Fr = Froude number, reference [7]
g = acceleration due to gravity, m/s^2
G = total mass flux, kg/s m^2
j_g^* = Wallis dimensionless gas velocity, equation (1)
R = gas volumetric ratio, reference [7]
V_l = average liquid velocity, m/s
x = vapour quality
X = Martinelli parameter, reference [3]

Greek Letters

ρ_l = liquid density, kg/m^3
ρ_v = vapour density, kg/m^3
α = void fraction, equation (2)

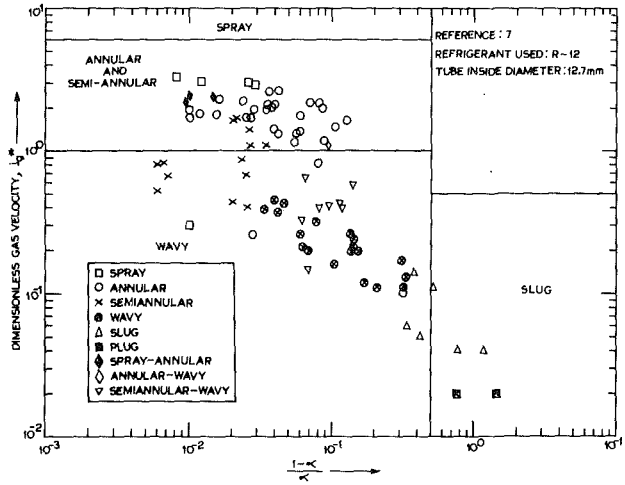

Fig. 3 Comparison of proposed flow map with Spliman et al. [7] data for condensing R-12

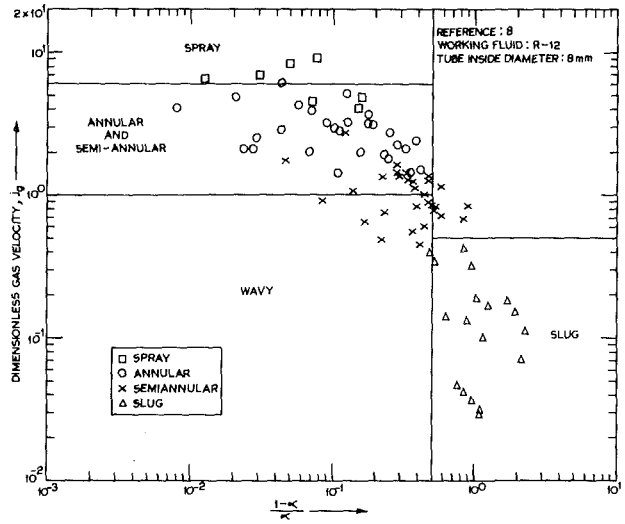

Fig. 4 Comparison of proposed flow map with Traviss and Rohsenow [8] data for condensing R-12

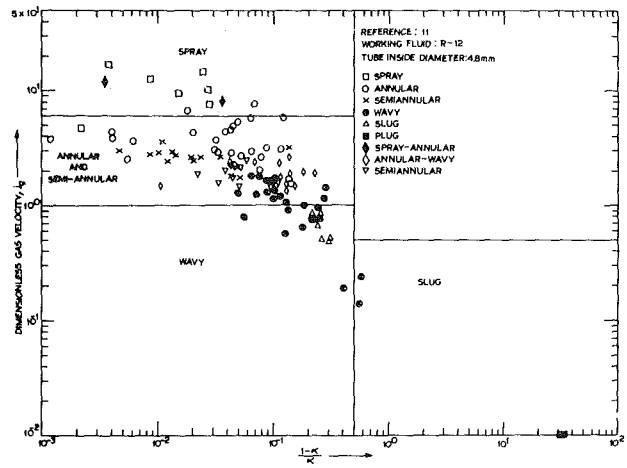

Fig. 5 Comparison of proposed flow map with Soliman [11] data for R-12 with 4.8-mm i.d. tube

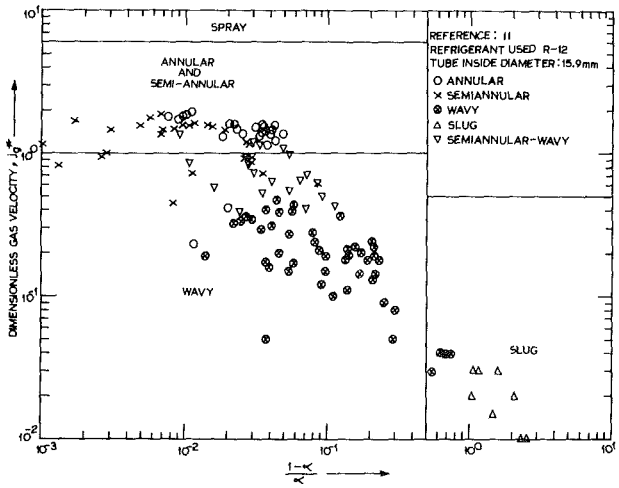

Fig. 6 Comparison of proposed flow map with Soliman [11] data for R-12 with 15.9-mm i.d. tube

pattern observations resulting from 349 runs were used in the development of the flow regime map in the present investigation.

It was considered desirable that the parameters selected for generating flow regime map have theoretical base [18, 19] and significantly characterize the two phase flow pattern.

One such parameter, having a theoretical base is the dimensionless gas velocity j_g^* which was used as a map coordinate by Breber et al. [18, 19]. The force balance approach resulted in a dimensionless group that was termed by Wallis [15] as dimensionless gas velocity, j_g^*, defined as

$$j_g^* = xG/[gD\rho_v(\rho_l - \rho_v)]^{1/2} \tag{1}$$

The void fraction, α, which significantly characterizes the two phase flow pattern was selected as the other parameter; α was calculated from Smith's [12] equation given below

$$\alpha = \left\{1 + (\rho_v/\rho_l)\left(\frac{1-x}{x}\right)\left[0.4 + 0.6\sqrt{\frac{(\rho_l/\rho_v) + 0.4\left(\frac{1-x}{x}\right)}{1 + 0.4\left(\frac{1-x}{x}\right)}}\right]\right\}^{-1} \tag{2}$$

Equation (2) was developed using a large number of experimental data of several investigators. Smith claimed it to be valid for all flow conditions, irrespective of flow patterns, mass velocity, dryness fraction, or pressure.

In the present work, the ratio $(1-\alpha)/\alpha$ was found to be superior to α and was therefore taken as the other correlating parameter. The use of $(1-\alpha)/\alpha$ made the data spread much larger on the abscissa [10, 11].

Selection of $j_g^*$and $(1-\alpha)/\alpha$ as coordinates resulted in the best correlation of the data of Table 1. Figures 3-11 show the data of Table 1 plotted on the proposed flow pattern map. On the map, the transition lines between the major flow patterns drawn are sharp. Despite the wide range of flow conditions and different tube diameters it is seen from Figs. 3 to 10 that there is relatively good agreement for all tube diameters. Figure 10 shows the entire data plotted together on the proposed map. Since annular and semiannular flow data occupied nearly the same region on the proposed map these were grouped together.

It should be noted that the success of a flow map depends on how accurately it predicts the flow pattern under the given operating conditions. Table 2 gives the limits of agreement of the experimental data of Table 1 on the proposed map. It is apparent from Table 2 that the proposed map gives excellent agreement in cases of annular, semiannular, and wavy flows which are predominant during condensation. It may be noted that annular flow exists over a major part of the condensing

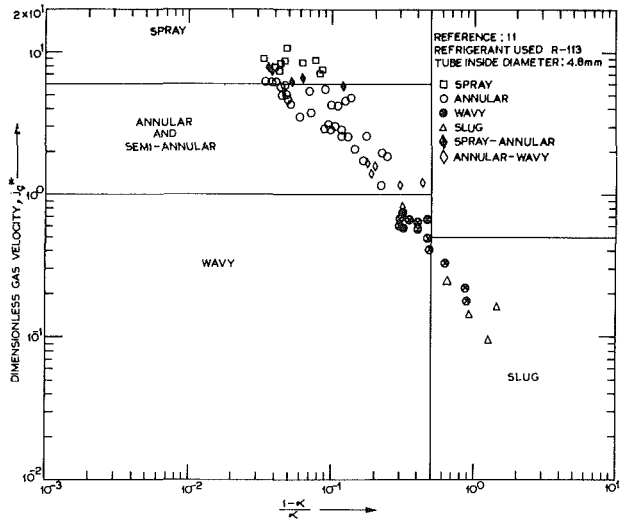

Fig. 7 Comparison of proposed flow map with Soliman [11] data for R-113 with 4.8-mm i.d. tube

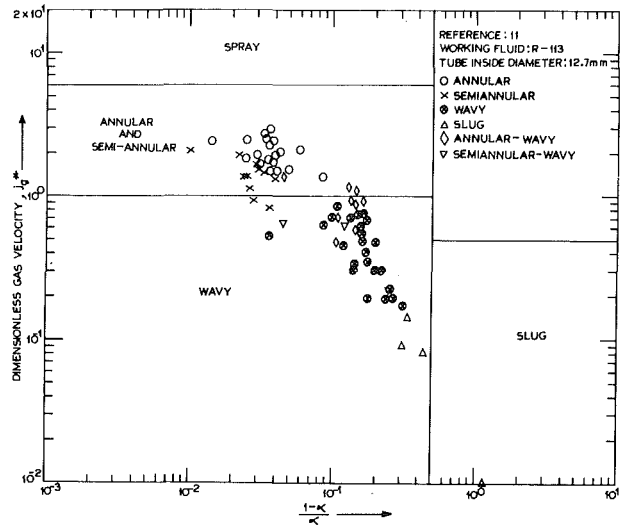

Fig. 8 Comparison of proposed flow map with Soliman [11] data for R-113 with 12.7-mm i.d. tube

length [20] and wavy flow is another significant flow pattern during condensation [10]. For spray, slug and plug flows the agreement is fair.

The results given in Table 2 may be appreciated better if the following facts are kept in view:

(*i*) 95 percent of annular flow data points fall in their specified region, an exceptional agreement.

(*ii*) 47 percent of semiannular data points of Traviss and Rohsenow [8] fall in the wavy region on the proposed map. Traviss and Rohsenow did not observe any wavy flow which is an important flow pattern [10]. They considered semiannular flow to be a transitional flow pattern. It is likely that some of the semiannular data might be belonging to the wavy region. If semiannular data of reference [8] are neglected, the agreement for semiannular data is 75 percent, and that for annular and semiannular data taken together is 90 percent. It is, therefore, believed that prediction for annular and semiannular flows would be even better than that given in Table 2.

(*iii*) It was pointed out earlier that the wavy flow data for the 4.8-mm dia tube did not fall in the appropriate zone on the map suggested by Breber et al. [19]. However, they made the following observation for this discrepancy:

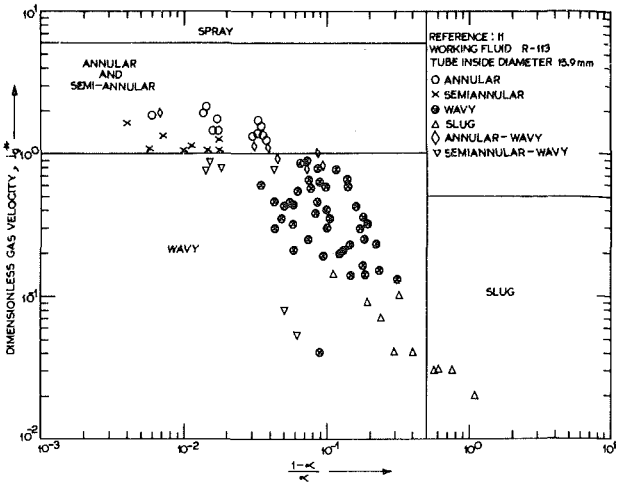

Fig. 9 Comparison of proposed flow map with Soliman [11] data for R-113 with 15.9-mm i.d. tube

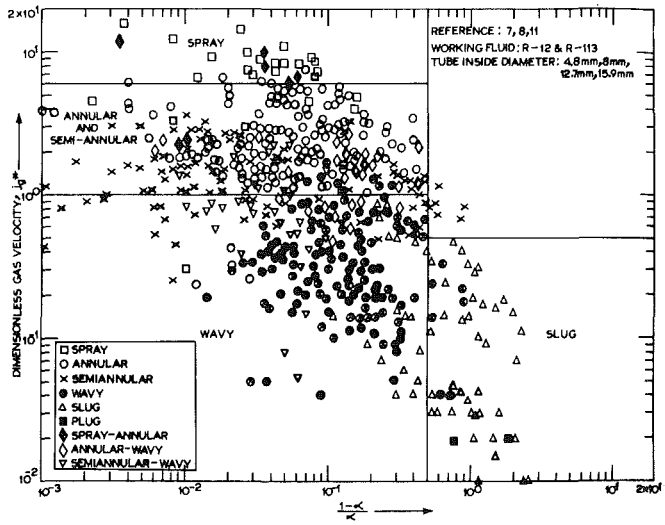

Fig. 10 Proposed flow map showing all data points

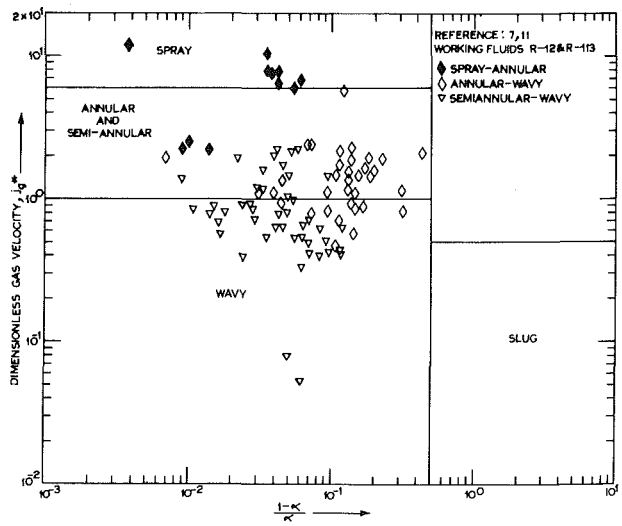

Fig. 11 Comparison of proposed flow map with transition flow pattern data [7, 11]

. . . much of the discrepancy may just be due to the fact that it is extremely difficult to tell the difference between wavy and semiannular flow for such a small tube.

Table 2 Distribution of observed flow patterns expressed as percentage on the proposed flow regimes map

Observed flow pattern \ Flow pattern on map	Spray	Annular and semiannular	Wavy	Slug	Plug	No. of points observed
Spray	69	31				29
Annular and semiannular	2	85	11			284
Wavy		11	88	1		188
Slug			35	65		59
Plug				33	67	9
Spray-annular	64	36				11
Annular-wavy and semiannular-wavy		49	51			84

Table 3 Distribution of observed flow patterns expressed as percentage (major flow patterns grouped as in reference [19])

Observed flow pattern zone \ Flow pattern on proposed map	Annular and spray Zone I	Wavy Zone II	Slug and plug Zone III
Annular and spray Zone I	99 (84)	1 (1)	
Wavy Zone II	11	88 (85)	1 (6)
Slug and plug Zone III		31 (12)	69 (82)

Neglecting the 4.8-mm tube data, Breber et al. [19] found 80 percent of stratified-wavy flow data to fall in the proper region on Taitel - Dukler map. Considering the present map, if we ignore the 4.8-mm tube wavy flow data, the agreement for wavy flow data is 100 percent, a remarkable agreement. It is found that about 52 percent of wavy flow data for 4.8-mm dia tube fall in annular-semiannular region. Therefore, the present authors are inclined to agree with Breber et al. [19] regarding wavy flow data for 4.8-mm dia tube. It is, therefore, believed that prediction for wavy flow regime would also be better than that given in Table 2.

(*iv*) Transition from one flow regime to other is not abrupt. Figure 11 shows the three transitional flow patterns plotted on the proposed map. It is clear from this figure and Table 2 that the data points for the transitional flow patterns show reasonable scatter across their respective boundaries. This should be seen in the light of the fact that there is a transition band between the two adjacent flow regimes.

An approximate comparison of the present map with that of Breber et al. [19] is shown in Table 3 where only major flow patterns have been considered. The values within parenthesis are those given in Table 3 of reference [19]. It is evident that the present map gives a significant improvement in prediction for spray, annular, and wavy flows. For zones I and II the prediction is remarkably good with 99 percent and 88 percent of the data falling in their respective zones.

Proposed Flow Regimes Criteria

On the basis of the data of Table 1, a simplified flow regimes map has been developed and simplified criteria are shown in Fig. 12. The boundaries for different flow patterns are defined below:

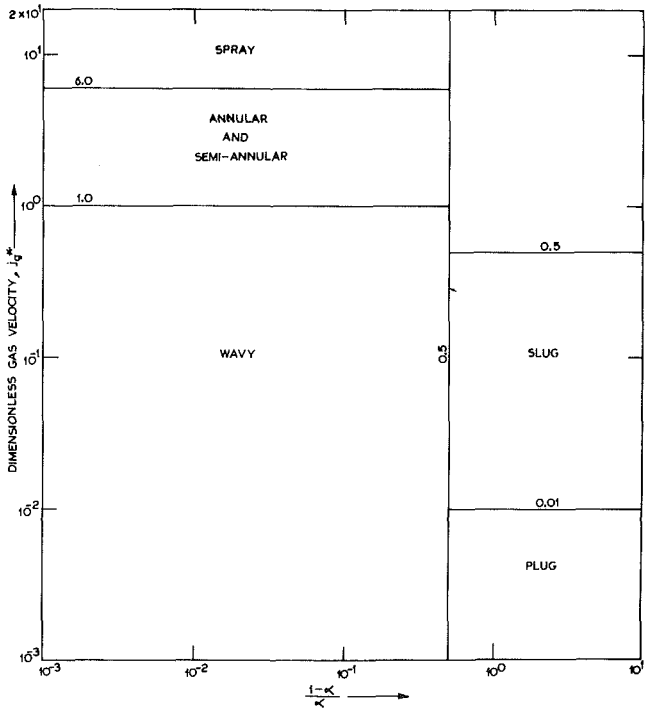

Fig. 12 Proposed simplified criteria for flow patterns during condensation inside horizontal tubes

Spray $\quad j_g^* \geq 6$ and $\dfrac{1-\alpha}{\alpha} \leq 0.5$ (3*a*)

Annular and semiannular $1 \le j_g^* \le 6$ and $\frac{1-\alpha}{\alpha} \le 0.5$ (3*b*)

Wavy $j_g^* \le 1$ and $\frac{1-\alpha}{\alpha} \le 0.5$ (3*c*)

Slug $0.01 \le j_g^* \le 0.5$ and $\frac{1-\alpha}{\alpha} \ge 0.5$ (3*d*)

Plug $j_g^* \le 0.01$ and $\frac{1-\alpha}{\alpha} \ge 0.5$ (3*e*)

Conclusions

Using the flow pattern condensation data of several investigators a new flow regimes map has been generated. It has been found that:

(*a*) The flow pattern data are best correlated on a map using j_g^* and $(1-\alpha)/\alpha$ as coordinates.

(*b*) For annular, semiannular, and wavy flows (which occupy most of the condensing length) the agreement is excellent, and the proposed map gives better prediction than the other existing maps.

(*c*) Annular and semiannular flow data occupy nearly the same region on the proposed map and are therefore grouped together.

A set of new criteria for prediction of different flow patterns is suggested. The degree of simplification achieved and the clearer interpretation of major flow patterns are some of the main advantages of the proposed map.

References

1 Martinelli, R. C., Boelter, L. M. K., Taylor, T. H. M., Thomson, E. G., and Morrin, E. H., "Isothermal Pressure Drop for Two-Phase Two-Component Flow in a Horizontal Pipe," *Trans.* ASME, Vol. 66, 1944, pp. 139–151.

2 Martinelli, R. C., Putnam, J. A., and Lockhart, R. W., "Two-Phase Two-Component Flow in the Viscous Region," *Trans. AIChE*, Vol. 42, 1946, pp. 681.

3 Lockhart, R. W., and Martinelli, R. C., "Proposed Correlation of Data for Isothermal Two-Phase, Two-Component Flow in Pipes, *Chem. Engg. Prog.*, Vol. 45, 1949, pp. 39–48.

4 Bell, K. J., Taborek, J., and Fenoglio, F., "Interpretation of Horizontal Intube Condensation Heat Transfer Correlation with a Two-Phase Flow Map," *CEP Symp. Series*, Vol. 66, No. 102, 1970, pp. 150–163.

5 Alves, G. E., "Co-Current Liquid-Gas Flow in a Pipe Line Contactor," *Chem Engg, Prog.*, Vol. 50, 1954, pp. 449–456.

6 Baker, O., "Simultaneous Flow of Oil and Gas," *The Oil and Gas Journal*, Vol. 53, 1954, pp. 185–195.

7 Soliman, H. M., and Azer, N. Z., "Flow Patterns During Condensation Inside a Horizontal Tube," *ASHRAE Trans.*, Vol. 77, Part 1, 1971, pp. 210–224.

8 Traviss, D. P., and Rohsenow, W. M., "Flow Regimes in Horizontal Two-Phase Flow with Condensation," *ASHRAE Trans.*, Part 2, 1973, pp. 31–39.

9 Scott, D. S., "Properties of Co-current Gas-Liquid Flow", Advances in Chem. Engg., Vol. 4, 1963.

10 Soliman, H. M., and Azer, N. Z., "Visual Studies of Flow Patterns During Condensation Inside Horizontal Tubes," *Heat Transfer Engg.*, Vol. 3, 1974, pp. 241–245.

11 Soliman, H. M., "Experimental and Analytical Studies of Flow Patterns During Condensation Inside Horizontal Tubes," Ph.D. dissertation, Kansas State University, 1973.

12 Smith, S. L., "Void Fraction in Two-Phase Flow: A Correlation Based Upon an Equal Velocity Head Model," *Inst. of Mech. Engg.*, London, Vol. 184, 1969–1970, pp. 647–657.

13 Quant, E., "Analysis of Gas-Liquid Flow Patterns," *CEP Symp. Series*, Vol. 61, No. 57, 1965, pp. 128–135.

14 Taitel, Y., and Dukler, A. E., "A Model for Predicting Flow Regime Transitions in Horizontal and Near Horizontal Gas-Liquid Flow," *AIChE Journal*, Vol. 22, No. 1, 1976, pp. 47–55.

15 Wallis, G. B., "One Dimensional Two-Phase Flow," McGraw-Hill, New York, 1969, p. 113.

16 Mandhane, J. M., Gregory, G. A., and Aziz, K., "A Flow Pattern Map for Gas-Liquid Flow in Horizontal Pipes," *Int. J. of Multiphase Flow*, Vol. 1, 1974, pp. 537–553.

17 Jaster, H., and Kosky, P. G., "Condensation Heat Transfer in a Mixed Flow Regime," *International Journal of Heat and Mass Transfer*, Vol. 19, 1976, pp. 95–99.

18 Palen, J. W., Breber, G., and Taborek, J., "Prediction of Flow Regimes in Horizontal Tube-Side Condensation," *Heat Transfer Engg.* Vol. 1, No. 2, 1979, pp. 47–57.

19 Breber, G., Palen, J. W., and Taborek, J., "Prediction of Horizontal Tubeside Condensation of Pure Components Using Flow Regime Criteria," ASME JOURNAL OF HEAT TRANSFER, Vol. 102, 1980, pp. 471–476.

20 Soliman, M., Schuster, J. R., and Bernson, P. J., "A General Heat Transfer Correlation for Annular Flow Condensation," ASME JOURNAL OF HEAT TRANSFER, 1968, pp. 267–276.

Modes of Circulation in an Inverted U-Tube Array With Condensation

C. Calia
Engineer,
EDS Nuclear, Inc.,
Norcross, Ga. 30092
Assoc. Mem. ASME

P. Griffith
Professor of Mechanical Engineering,
Massachusetts Institute Technology,
Cambridge, Mass. 02139
Mem. ASME

An experiment and analysis was performed on an inverted U-tube steam condenser (similar to a steam generator) to determine the modes of flow that can exist as the rate of steam flow into the condenser is reduced. The condenser consisted of four glass tubes connected to a common inlet plenum and a common exit plenum. Heat-transfer and flow-rate measurements, as well as visual observations were made. Four different modes of operation were identified. Noncondensables were found to substantially alter the plenum to plenum pressure difference and aid flow stability. Satisfactory analytical descriptions of the observations have been developed as well as application of the results to the condensing behavior of nuclear steam generators under abnormal operating conditions.

Introduction

When analyzing an upward condensing flow in a tube bundle, it is not always appropriate to assume approximately uniform flow characteristics for all the tubes. In other words, such a system is not properly modeled by solely considering the characteristics of some "average" tube in the bundle. However, a model for a condensing tube array can be constructed by understanding the various flow modes which can exist for the system, and considering each type of flow (or flow blockage) separately.

In this paper, a method for the construction of the system pressure drop versus flow rate characteristic for a tube bundle in the condensing mode from a model of flow in one tube will be presented. The method for determining system characteristics is based on an experiment performed using a four tube inverted "U-tube" apparatus. The inverted U-tube apparatus is similar in many ways to a steam generator in a pressurized water reactor (PWR). The condensing mode of operation is calculated to occur after certain PWR small break loss of coolant accidents.

To introduce the fundamental concepts important to this problem, the idealized pressure drop characteristic of Fig. 1 for a single inverted U-tube is needed. For a high vapor flow rate or a low cooling rate, vapor will pass through the tube without being fully condensed. In this case, the pressure drop is large and dominated by friction losses. At lower vapor flow rates, much of the vapor is condensed in the tubes, producing an appreciable gravity contribution to the overall pressure drop. When the gravity pressure drop becomes dominant in the tube riser, a flow instability results. The part of the curve with negative slope is the unstable region when the tube is part of a multiple tube array. Some possible modes of operation in this region are transition to reverse flow (siphoning from outlet plenum to inlet), flow blockage in the tube riser, or some type of flow oscillation. The actual flow behavior is governed by the system configuration and the amount and nature of the noncondensables in the system.

Usually not all the tubes are the same length in an inverted U-tube array. The shorter tubes have slightly higher flow rates and less surface area than the longer tubes and thereby become unstable at lower flow rates. Therefore, every tube has a different pressure drop-flow rate characteristic. An average tube model might be used to describe the behavior of the entire tube array, but would be inadequate to depict all possible phenomena when the flow rate is so low that one or more of the tubes fall into the negative slope (unstable) region of the pressure drop versus flow rate curve.

Experiment

A four tube inverted U-tube condenser was constructed from transparent materials to study fluid flow phenomena and determine modes of operation. The apparatus, along with the steam supply system, are shown in Fig. 2.

Laboratory steam was "dried" using a heat exchanger and metered using an ASME standard orifice flow meter. A pressure gauge and thermometer were used to determine the degree of superheating (which was maintained about 2–7°C). The steam was supplied to the four tube condenser via a large quarter-cylinder shaped inlet plenum.

The condensing apparatus consisted of four, 8-mm-i.d. (10-mm-o.d.) Pyrex tubes with average height of about 1.2 m. The "U-bends" were made by using straight pieces of Pyrex tube and brass elbow compression fittings. The four tubes made two passes through a clear plastic shell of height 0.95 m in which 10°C (50°F) cooling water flowed. The tubes exited 0.13 m below the surface of water in the open exit plenum.

Measurements were made of steam mass flow rate, system pressure drop and condensation heat transfer. The flow rate was measured using a U-tube manometer connected to the flange taps of the orfice flow meter. The pressure drop was taken as the difference in pressure between that measured by the manometer attached to the inlet plenum and atmospheric

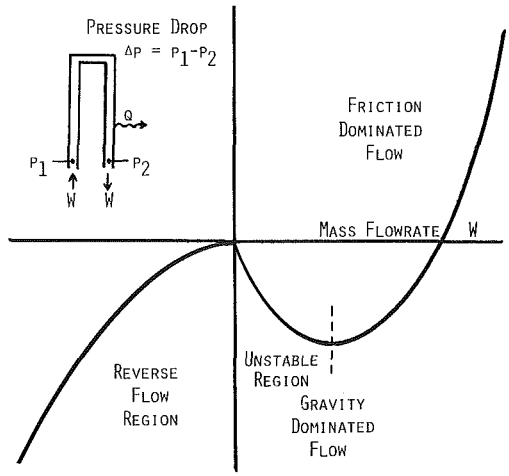

Fig. 1 Idealized pressure drop versus flow rate charactertistic for one tube of an inverted U-tube condenser

Contributed by the Heat Transfer Division for publication in the JOURNAL OF HEAT TRANSFER. Manuscript received by the Heat Transfer Division October 23, 1981.

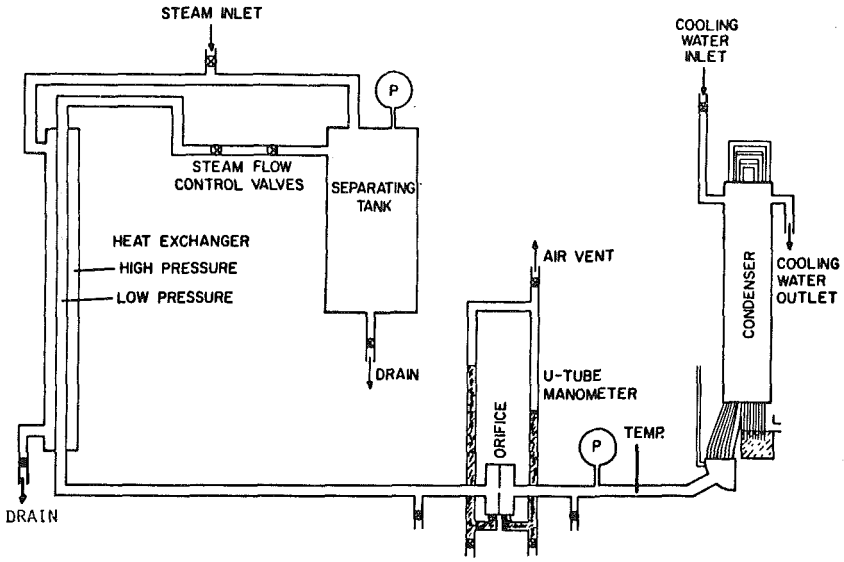

Fig. 2 Experimental apparatus showing steam supply system

pressure which is the condition at the surface of water at the exit.

The steam used in the experiment was measured to contain air in the amount of one part in 16,000 by mass. As the steam condensed, the air coalesced into bubbles representing a fraction of one part in twenty by volume. The presence of noncondensable gas in the system was important in determining some aspects of the condenser operation. Specifically, air would collect in the top of the U-tube thereby preventing reverse flow (siphoning) as an unstable flow mode.

Experimental Results

Four experimental tests were run. In test #1, three tubes were valved-off so that single tube results could be compared to the idealized characteristic of Fig. 1. All four tubes were open but the outlet plenum was emptied to determine the effect of the outlet boundary condition.

Behavior of a One Inverted U-Tube Condenser. In test #1, all tubes but one were shut off in order to establish the flow patterns in a single flow-forced tube. The steam flow rate was started at a high value and then decreased slowly such that the condenser was essentially operating in a steady state at all times. For decreasing values of flow rate, the following flow modes were observed.

(*i*) Steam was not fully condensed and could be seen bubbling into the exit plenum.

(*ii*) An annular condensate film was visible in both sides of the tube with the thickest point near the top of the riser.

(*iii*) Slug flow could be seen at the top of the riser, with the gas forcing the water over the top of the U-bend in an unsteady motion.

(*iii*) A cyclic process occurred whereby a column of water grew in the riser until it reached the top of the tube and quickly siphoned through the downcomer.

Behavior of the Four Tube Array (test #2 and test #3). At high steam flow rates, the four tube condenser behaved similarly to the single tube condenser. That is, each tube demonstrated the same flow pattern as that for the single tube when the flow rate per tube was equal for the two cases. The divergence in the observed flow pattern came about when the pressure drop-flow rate instability occurred. Whereas the single condenser operated in a "fill and dump cycle," the array developed a blockage in one tube. The blocked tube maintained a steady-state water column with length reflecting the pressure drop imposed by the unblocked (active) tubes. As the steam flow rate was decreased, more tubes would block until the pressure drop-flow rate instability was reached for the last active tube.

Since the tube heights varied only slightly, their pressure drop characteristics were similar and consequently, the selection of the first tube to block was random. This was evidenced by the fact that in test #3, the longest tube (tube 1) blocked first, whereas in test #2, the second longest (tube 2) was the first to block.

When the last tube in the array became blocked, a fill and dump cycle ensued whereby all the tubes filled with condensate until one tube siphoned through the downcomer. At still lower steam flow rates, the rate of formation of con-

Nomenclature

A = U-tube cross-sectional area
C = constant in the Wallis flooding correlation
D = U-tube diameter
g = gravitational constant
j_g = superficial gas (steam) velocity
j_g^* = dimensionless superficial gas velocity
j_f = superficial liquid (water velocity)
j_f^* = dimensionless superficial liquid velocity
m = constant in Wallis flooding correlation
N = number of tubes in an array
N_a = number of active tubes
p = pressure
p_1 = minimum pressure drop for the longest tube in an array
p_2 = minimum pressure drop for the shortest tube in an array
Δp = total pressure drop
w = mass flow rate in one tube
W = system mass flow rate
W_1 = system mass flow rate at pressure p_1
W_2 = system mass flow rate at pressure p_2
W_3 = system blocked flow rate
w_b = one tube blocked flow rate
w_c = one tube fully condensed flow rate
w_s = stall flow rate for one tube
w_{sa} = stall flow rate for the average tube
w_{sl} = stall flow rate for the longest tube
w_{ss} = stall flow rate for the shortest tube
ρ_g = gas (steam) density
ρ_f = liquid (water) density

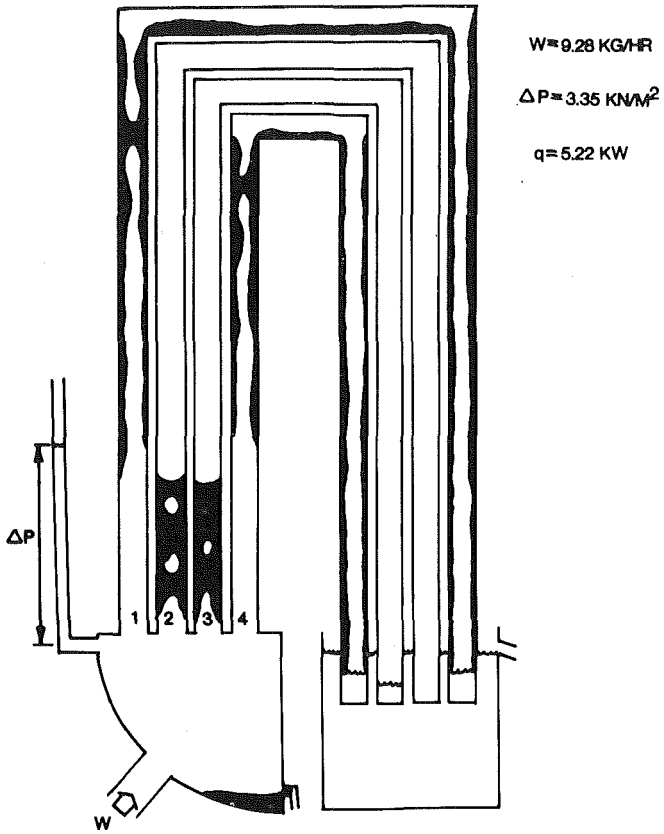

Fig. 3 Example of a steady-state partially active mode from Test #2

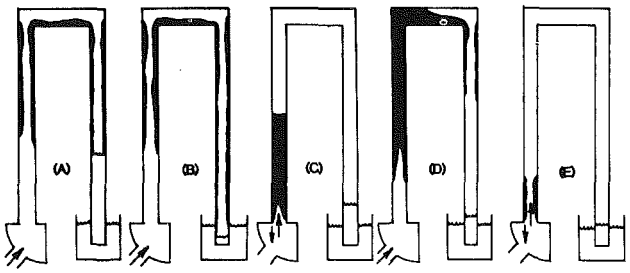

Fig. 4 Five flow modes for a tube in a U-tube array

densate was lower than the limit of counterflow of steam and water at the tube inlets. Refluxing resulted and all the condensate was returned to the inlet plenum where it was drained off to avoid the formation of a two-phase condition at the inlet.

All the above flow phenomena can be summarized by four distinct flow modes:

(*i*) Full Active Mode—Each tube behaves like a single tube condenser

(*ii*) Partially Active Mode—Some tubes are active and some are blocked (see Fig. 3 as an example)

(*iii*) Fill and Dump Mode—The entire array fills and siphons in a cyclic pattern

(*iv*) Reflux Mode—All the condensate is returned to the inlet plenum

Possible Flow Modes for One Tube. From observation of the single tube and the four tube condensers, flow modes for one tube can be summarized into the five categories in Fig. 4. In Fig. 4(*a*), the steam is fully condensed in the downcomer, and the pressure drop characteristic is like the idealized curve of Fig. 1. If noncondensable gas is present, the water column in the downcomer would be replaced by gas, as in Fig. 4(*b*),

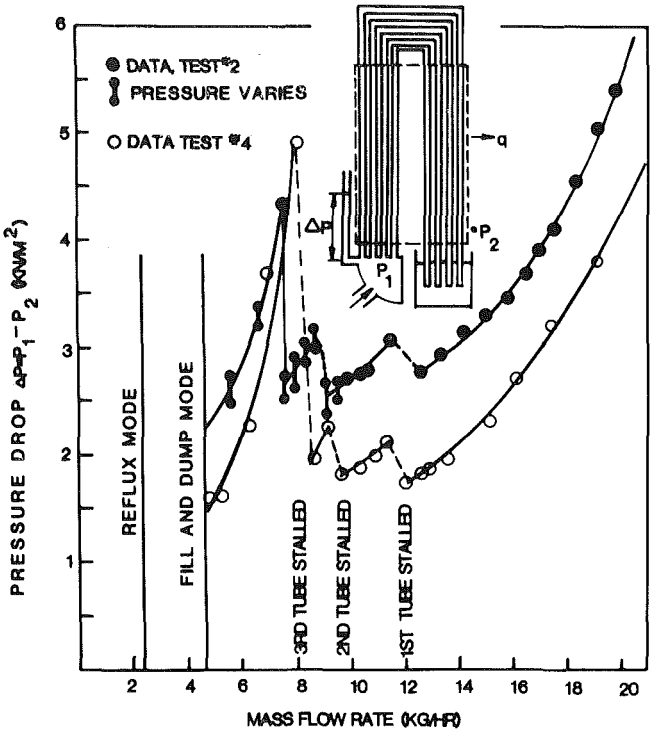

Fig. 5 Pressure drop versus flow rate for the four tube inverted U-tube condenser. The difference in pressure at the same flow rate is the hydrostatic head of 1.25 kN/m^2 at the tube exits in the filled plenum test.

and the pressure drop would be higher. If the tube has an imposed pressure drop as for a blocked tube in an array where other tubes are active, a static water column exists in the riser like that shown in Fig. 4(*c*). Figure 4(*d*) represents a single-tube condenser or the last active tube in an array where the pressure drop-flow rate instability results in a fill and dump cycle. The lowest flow rate regime is the reflux mode of Fig. 4(*e*).

The Pressure Drop Versus Flow Rate Characteristic. Figure 5 is the measured pressure drop curve for the four-tube condenser. The difference between the unfilled exit plenum case (test #4) and the filled exit plenum case (test #2) is the pressure head represented by the 130 mm of water above the tube exits in the filled plenum case. The sharp increases in pressure drop as the flow rate is decreased correspond to the points when tubes become blocked.

Note that four flow modes are represented in Fig. 5. For flow rates $W > 12$ kg/hr, the array is in the fully active mode. For mass flow rates between 4.5 kg/hr and 12 kg/hr, the partially active mode exists. The unstable fill and dump mode is for the flow rates between 2.3 and 4.5 kg/hr. Finally, refluxing occurs for flow rates below 2.3 kg/hr.

The pressure drop $(p_1 - p_2)$ never became negative because noncondensable gas was present. The tube downcomers showed annular condensate films and stagnant gas. Pictures of typical flow configurations are included in reference [5].

The Heat-Transfer Performance. The heat-transfer characteristics of the four inverted U-tube condensing apparatus reveal two distinct phenomena. The active (unblocked) tube heat transfer is defined by a virtually constant temperature difference between the cooling water and the condensing steam, and a constant heat-transfer area. Steam flow to the blocked tubes is controlled by the counter current flow limitation (flooding) phenomenon. The heat transfer in the blocked tubes, then, is a function of the tube geometry and the tube side pressure.

Calculation Method

The analytical approach which aided in understanding the array performance was initiated with a single-tube, pressure drop calculation. A simple, homogeneous, two-phase model was used for the friction and momentum contribution to the pressure drop, and the Thom model was used for the gravity term. (A detailed description of this methodology is given references [1-4].) The calculated single tube pressure drop was modified by subtracting out the pressure drop of the downcomer water column which was replaced by air in the experiment. The result is the calculation line of Fig. 6.

The experimental data plotted in Fig. 6 are the pressure drop versus the average flow rate per active tube. The flow rate, w_b, is the blocked flow rate and represents the maximum mass flow rate of steam and condensate in counterflow. It can be calculated by applying the Wallis flooding criteria [2] such that the gas and liquid mass flow rates are equal (see the Appendix). The stall flow rate, w_s, is the point where the pressure drop-flow rate instability occurs and is the flow rate at the minimum of the pressure drop curve. The flow rate, w_c, is the maximum flow rate at which all the steam can be condensed by one tube and is found from the heat-transfer calculation.

Since the active tubes are the ones that determine the system pressure drop, the flow rate axis in Fig. 6 is such that the data is plotted versus the actual flow in the active tubes. This was achieved by taking the total flow rate, W, and subtracting off the refluxing flow in the blocked tubes, $(4-N_a)\,w_b$, where N_a equals the number of active tubes. The data falls along a single line with the exception of the case where the shortest tube is the only active tube. This presumably occurs because that tube deviates slightly from the other tubes in its construction and therefore has a slightly different pressure drop characteristic.

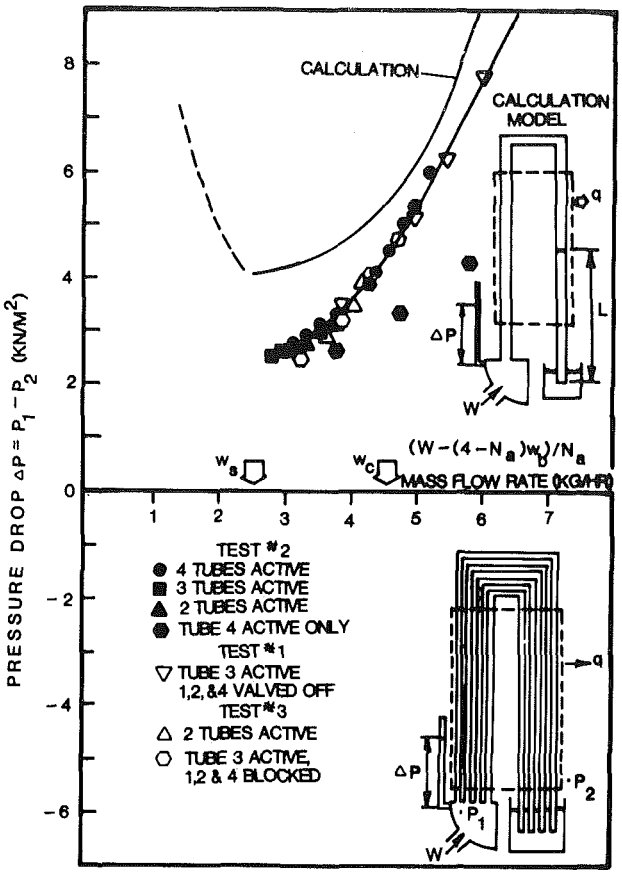

Fig. 6 Pressure drop versus average tube flow rate per active tube with flow rate adjusted to account for blocked tube flow

Recommendations for Predicting the Behavior of an Inverted U-Tube Condensing Array

It is not suggested or implied here that the data from the experiment just discussed can be applied directly to the analysis of a vertical tube condenser. In fact, the purpose of the experiment was to develop and confirm an analytical method for predicting the performance of such a device. This approach will now be presented in a general way.

The tubes in a bundle of U-tubes have different pressure drop characteristics because of their different lengths. Figure 7 shows the pressure drop-flow rate behavior for the longest, shortest, and average tube of an array. The flow rates, w_{ss}, w_{sa}, and w_{sl}, are the stall flow rates for the shortest, average, and longest tubes, respectively.

For an array of N tubes operating at some pressure, p_1, the average length tube has flow rate, w_{sl}, and the system flow rate is $W_1 = w_{sl} N$. Since p_1 is the minimum pressure drop for the longest tube, no tubes are blocked for a pressure drop greater than p_1 and a corresponding system flow rate W_1. Below W_1, flow in the longest tube becomes unstable and transition to the blocked flow mode ensues.

As the system flow rate is decreased from W_1, the stall flow rates for an increasing number of tubes are reached and the average length of the active tubes decreases. The pressure drop variation as each tube stalls is small for a system with a large number of tubes (large N), and the system pressure will decrease steadily. This steady decline continues until the stall point for the last active tube (presumably the shortest), is reached. The system flow rate at that point equals the system stall flow rate $W_2 = w_{ss} + w_b\,(N-1)$, and the pressure drop is p_2. The flow rates W_1 and W_2 and the pressure drops p_1 and p_2 were used to create the system pressure drop—flow rate curve of Fig. 8.

The system blocked flow rate is $W_3 = w_b N$ since w_b is the same for all tubes of the same diameter at the same pressure. Therefore, the array operates in the reflux mode for a flow rate less than W_3 provided the amount of heat transfer necessary to condense all of the steam can occur in the tube risers. For flow rates between W_3 and W_2, the array behaves unstably and operates in the fill and dump mode. The various

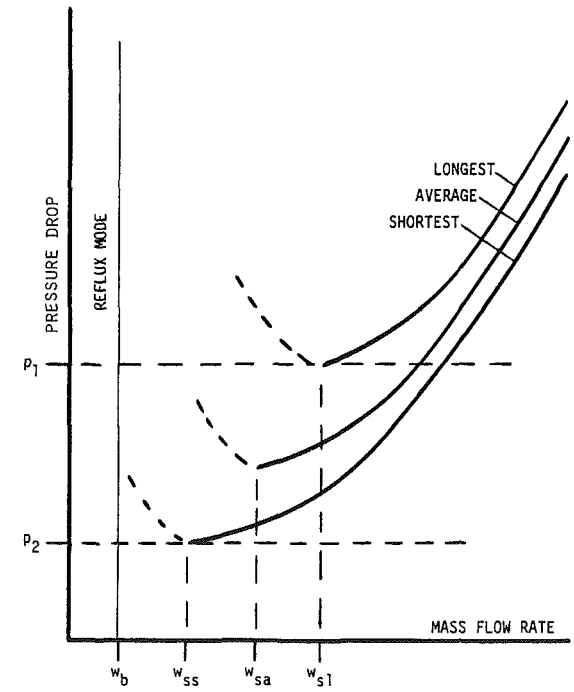

Fig. 7 Pressure drop as a function of flow rate for the longest, shortest, and average length tubes in an inverted U-tube array

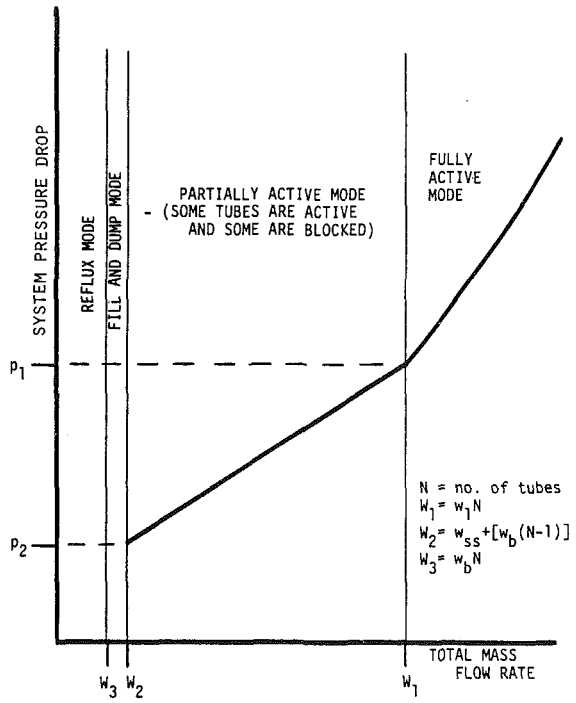

Fig. 8 System pressure drop as a function of flow rate for an array of inverted U-tubes

flow regimes and important transition points are identified in Fig. 8.

Although the above model is complete and consistent, it is perhaps important to identify some possible variations. For instance, if the system was not open at the exit, a build-up of noncondensable gas would occur and the heat-transfer properties of the condenser would change. Another important point is that the analysis assumes that sufficient cold water exists on the outside of the tubes for the necessary heat transfer to take place. Lastly, all the information presented was for the case of decreasing flow rate. For increasing flow rate, it would be necessary to unblock the tubes by filling the risers with water so that siphoning would initiate flow. This would require a high initial pressure drop.

Nuclear Steam Generators

When projecting these results to nuclear steam generators, it appears that at decay heat levels the reflux mode of condensation is probably sufficient to remove all the core energy. From reference [5], the heat removal rate for a typical PWR steam generator is 20–80 MW. The area which is lost to the steam generator when tubes become blocked is insufficient to substantially alter the heat transfer because the steam generator is greatly oversized at decay heat levels.

It is not clear whether there are some additional system effects in multiple steam generator systems caused by the existence of a steam generator to steam generator pressure drop versus flow rate instability .

Conclusion

The experiments run with the four-tube, inverted U-tube condenser demonstrated four clearly defined flow regimes. The flow rates at which the various transitions occurred were determined by the pressure drop-flow rate instability and the flooding criteria. Since the experiment did not directly model an inverted U-tube steam generator, it was necesary to develop a method of prediction based on conventional two-phase theory. This approach is general in that the equations used are valid for a wide range of conditions, thereby lending this method applicable to various thermodynamic and geometric situations.

The analytical approach is based on considering active and blocked tubes separately. The pressure drop for the active tubes is determined from the ideal homogeneous two phase flow model with modifications made to account for effects such as those caused by non-condensable gases. The pressure drop of the active tubes is imposed on the blocked tubes. The blocked tubes do have a effect on the system in that a significant amount of heat transfer occurs in the small refluxing region of the risers. The total performance is then predictable without a complex model and without over-simplifying assumptions.

References

1 Hsu, Y. Y., and Graham, R. W., *Transport Processes in Boiling and Two-Phased Flow*, McGraw-Hill, ch. 5-7, 1976.

2 Wallis, G. B., *One Dimensional Two-Phase Flow*, McGraw-Hill, ch. 1, 2, 4, 1969, pp. 376-343.

3 Thom, J. R. S., "Prediction of Pressure Drop During Forced Circulation Boiling Water," *International Journal of Heat and Mass Transfer*, Vol. 7, 1964, pp. 709-724.

4 Dukler, A. E., and Taitel, Y., "Flow Regime Transitions for Vertical Upward Gas and Liquid Flow: A Preliminary Approach Through Physical Modeling," University of Houston, NUREG-0162, NRC-2, 4, 1977, pp. 21-23.

5 Calia, C., and Griffith, P., "Modes of Circulation in an Inverted U-Tube Array with Condensation," Massachusetts Institute of Technology, NUREG/CR-1699, Oct. 1980.

APPENDIX

When a tube is blocked in an array where at least one tube in the array has flow, the system pressure drop Δp of the active tubes is imposed on this tube and fixes the height of water that can exist in its riser. Since there is no net flow from the inlet to the outlet for the blocked tube, all the steam that enters will be condensed and drain into the inlet plenum. Therefore, the mass flow of steam into the tube must equal the mass flow of water out and is called the blocked flow rate w_b.

$$w_{\text{steam}} = w_{\text{water}} = w_b$$

The limitation of counter current flow of steam and water is determined by the flooding phenomenon. Wallis has correlated flooding data to the equation

$$j_g^{*1/2} + m j_f^{*1/2} = C$$

where constants m and C are empirical coefficients [2].

Substituting expressions for j_g^* and j_f^* and noting that the tube cross-sectional area is $A = \pi/4\, D^4$, the blocked flow rate can be expressed as

$$w_b = \frac{C^2(\pi/4)\,[gD^5(\rho_f - \rho_g)]^{1/2}}{\left[\dfrac{1}{\rho_g^{1/4}} + \dfrac{m}{\rho_f^{1/4}}\right]^2}$$

Condensation of Submerged Vapor Jets in Subcooled Liquids

L-D. Chen

G. M. Faeth
Mem. ASME

Department of Mechanical Engineering and
The Applied Research Laboratory,
The Pennsylvania State University,
University Park, Pa. 16802

A theoretical investigation of turbulent condensing vapor jets submerged in subcooled liquids was conducted. A model of the process was developed employing the locally homogeneous flow approximation of two-phase flow in conjunction with a k-ϵ-g model of turbulence properties. The model was evaluated using existing data for turbulent condensing water, ethylene glycol and iso-octane vapor jets with liquid to vapor density ratios in the range 324–31,200, initial jet Reynolds numbers greater than 15,000 and negligible effects of buoyancy. Good predictions of vapor penetration lengths were obtained using conventional turbulence model constants established for single phase flows.

Introduction

A number of industrial processes involve submerged injection of a condensible vapor into a subcooled liquid, e.g., direct contact feedwater heaters, jet pumps and the containment systems for the primary boiler loop of nuclear power plants. The objective of the present investigation was to develop a model capable of predicting the structure of turbulent submerged condensing jets in order to facilitate the rational design of such systems. The model was evaluated using existing measurements in the literature. The investigation was limited to momentum-dominated flows – where effects of flow stratification and buoyancy are small. Under these conditions, liquid entrainment by the vapor phase, as drops, and vapor entrainment by the liquid phase, as bubbles, is often observed [1–3].

Several models of momentum-dominated submerged condensing jets have already been reported. Weimer, et al. [1] developed an integral model of the process during an earlier investigation in this laboratory. Major assumptions of the analysis were: locally homogeneous flow (LHF), which implies that interphase transport rates are infinitely fast so that both phases have the same velocity and temperature and are in the thermodynamic equilibrium at each point in the flow; similarity of velocity, density and enthalpy profiles; and the use of an empirical entrainment expression. Predictions were compared with measurements of penetration lengths (x_C, the mean distance from the injector where vapor disappears along the axis of the jet) for water [1–3], ethylene glycol [1] and iso-octane [1] vapor jets submerged in subcooled liquids. Upon specifying a single additional empirical constant – related to turbulent unmixedness – the model was capable of correlating the measurements (which involved x_C/d in the range 1.5–35). While this is encouraging, this model provides relatively limited information concerning flow structure; the treatment of turbulence properties is not very sophisticated, with limited generality; and the application of the method in the near-injector region is questionable due to the incorporation of similarity assumptions.

Kudo et al. [4] and Young and co-workers [5, 6] developed models for condensing jets appropriate for short penetration lengths. They assume that there is a smooth, conical-shaped interface between the phases and ignore the presence of dispersed bubbles and drops within the flow. Kudo et al. [4] use a mixing length model to represent turbulent transport in the liquid phase in the region where vapor is present, while an integral model was employed downstream of the two-phase flow region. The combined analysis provided a fair correlation of their measurements of water vapor penetration lengths (x_C/d in the range 0.5–2.5) and the decay of centerline temperature in the flow.

Young and co-workers [5, 6] also assume a smooth conical interface, but seek a phenomenological description of transport rates. This approach provided a satisfactory correlation of their overall interphase heat-transfer rate measurements (x_C/d in the range 1.3–4.3). Cumo et al. [7] and Simpson and Chan [8] report condensing jet properties in the same manner as Young and co-workers [5, 6] – finding interfacial heat-transfer coefficients based on the subcooling of the bulk liquid and estimating the interfacial area from photographs of the flow. For larger penetration lengths, however, the boundary of the region where vapor is observed is not conical [1, 3, 8]; therefore, Simpson and Chan [8] relax the conical interface assumption and directly integrate to find the interfacial area from photographs. An overall correlation of these results, however, has not been found.

Even when curvature of the interface is considered, there are difficulties when a smooth interfacial surface is prescribed. Dispersed bubbles are often observed near the injector exit and clearly dominate the flow when the penetration length is large [1, 3, 4, 7–9]. The absence of a smooth interfacial surface in momentum-dominated condensing jets is particularly evident in short duration flash photographs of the process [5, 6, 9]. It is also probable that liquid is entrained by the high-velocity vapor jet near the injector exit [2]. Therefore, the assumption of a smooth interface, of any shape, provides a questionable framework for the development of a theoretical understanding of high velocity condensing vapor jets.

The objective of the present investigation was to develop a more complete model of submerged condensing vapor jets, capable of treating near-injector phenomena as well as the dispersed flow which is observed for long penetration lengths. The new model was an extension of an analysis developed during earlier work in this laboratory [10–12], which provided reasonably good predictions for a variety of two-phase jet processes, e.g., well-atomized spray evaporation and combustion as well as submerged injection of air into a water bath. The new model employs the LHF approximation in conjunction with a k-ϵ-g turbulence model developed by Lockwood and co-workers [13, 14]. Model predictions were evaluated using existing data for submerged condensing vapor jets.

Data Base

Table 1 is a summary of the test conditions used to evaluate the model. The data base is drawn from measurements in

Contributed by the Heat Transfer Division for publication in the JOURNAL OF HEAT TRANSFER. Manuscript received by the Heat Transfer Division October 7, 1981.

Table 1 Summary of Test Conditions[a]

Substance	Bath pressure (kPa)	d (mm)	B^{-1}	Minimum Re_o	ρ_∞/ρ_o	Maximum $Ri_o \times 10^6$	x_C/d^b	Minimum We_o
Weimer et al. [1], horizontal injection:								
Water	4.3–38	3.17	15–400	22,000	3,980–27,700	0.17	1.7–35	250
Ethylene glycol	1.4–19	3.17	5–114	15,000	3,260–31,200	0.59	1.5–35	100
Iso-octane	15–58	3.17	3–15	150,000	324– 1,180	1.30	3.0–11	2,300
Binford et al. [2], downward vertical injection:								
Water	101.3	10.9–17.2	7–9	280,000	1,600	0.74	1.5–3.0	25,000
Kerney et al. [3], horizontal injection:								
Water	101.3	0.4–9.5	6–31	20,000	1,430–1,635	0.40	2.5–17	930
Kudo et al. [4], downward vertical injection:								
Water	101.3	6.0–17.5	7–9	130,000	1,600	0.75	0.5–2.5	14,000
Young and co-workers [5, 6], horizontal injection:								
Water	101.3–274	6.4	6–8	139,000	660—1,600	0.27	1.3–4.3	15,000
Chan [15], downward vertical injection:								
Water	101.3	3.17–12.7	19–30	53,000	1,600	0.54	5.3–27	15,000

[a]Injection into quiescent liquid baths except Young and co-workers [5, 6] which involved a 3 m/s coaxial flow of water.
[b]Range of $x_C/d<15$ considered in evaluation to avoid effects of injector orientation due to buoyancy.

condensing water, ethylene glycol, and iso-octane vapor jets by Wiemer et al. [1], Binford et al. [2], Kerney et al. [3], Kudo et al. [4], Young and co-workers [5, 6] and Chan [15]. The test conditions generally involved vapor injection into nearly quiescent liquid baths having uniform properties.

Typical of most two-phase flow processes, the topography of condensing jets varies considerably as operating conditions are changed [16]. Therefore, several parameters are provided in Table 1, to help define the conditions considered during the present evaluation of the analysis. A particularly important parameter for condensing jets is the driving potential for condensation, B, defined as follows by Weimer et al. [1]:

$$B=(h_{fs}-h_\infty)/(h_o-h_{fs}) \tag{1}$$

Increasing values of B yield smaller penetration lengths – all other factors being equal. The lowest injector Reynolds number for each data set is indicated in the table; in general, the test conditions represent highly turbulent jets. The density variation of these flows is quite large, with ρ_∞/ρ_o in the range 324–31,200.

In order to minimize the effect of injector orientation, the evaluation only treated cases where effects of buoyancy were small – in spite of the large density variations in condensing jets. Therefore, the data base listed in Table 1 is limited to initial Richardson numbers less than 1.3×10^{-6}, where buoyancy is negligible near the injector exit. Buoyancy still can become important far from the injector; therefore, the present evaluation was also limited to relatively short penetration lengths, $x_C/d<15$. In this range, considering effects of buoyancy in the computations had a negligible effect on the results.

The final parameter listed in Table 1 is the minimum initial Weber number of the flow for each data set. Initial Weber numbers are generally quite large for test conditions in the data base, suggesting a strong tendency for dispersed phases.

A variety of injector configurations, nozzles, and tubes were employed for the tests summarized in Table 1 – original sources should be consulted for details. Specific injector geometry has been shown to have a relatively small influence on flow properties and penetration lengths [3]. The data base has been limited to cases where the flow at the injector exit is choked, but not excessively underexpanded, e.g., the ratio of injector exit mass velocity to sonic exit mass velocity at the bath pressure was limited to the range 1.0–1.7 for the present data base. Unchoked injector flows were avoided since most investigators observe unstable oscillatory injector flow, with the injector passage periodically filling with bath liquid, for these conditions [1–3, 7, 15], and analysis of this behavior was not within the scope of present theoretical considerations. Highly underexpanded flows, on the other hand, yield complex external expansion processes with patches of supersonic flow which would be premature to consider at present.

Theoretical Considerations

The details of the model will be briefly described since there are some differences from the original version [10–12]. The thin shear layer approximations are employed for a steady,

Nomenclature

a = acceleration of gravity
B = driving potential for condensation, equation (1)
C_i = constants in turbulence model
d = injector diameter
f = mixture fraction
g = square of mixture fraction fluctuations
h = enthalpy
k = turbulent kinetic energy
$\dot{m}_o''$ = injector exit mass flux
r = radial distance
Re = Reynolds number, $\rho ud/\mu$
Ri = Richardson number, ad/u^2
Sc = Schmidt number
S_ϕ = source term, Table 2
T = temperature
u = axial velocity
v = radial velocity
v° = weighted radial velocity, equation (5)
We = Weber number $\rho ud/\sigma'$
x = axial distance
x_C = penetration length
α = void fraction
ϵ = dissipation rate of turbulent kinematic energy
μ = molecular viscosity
$\mu_{\text{eff},\phi}$ = effective viscosity
μ_t = effective turbulent viscosity
ρ = density
σ = turbulent Prandtl/Schmidt number
σ' = surface tension
ϕ = generic property

Subscripts

c = centerline value
f = liquid phase
fs = saturated liquid
g = vapor phase
o = injector exit condition
∞ = ambient condition

Superscripts

$(\bar{\ })$ = time averaged quantity
$(\ ')$ = fluctuating quantity

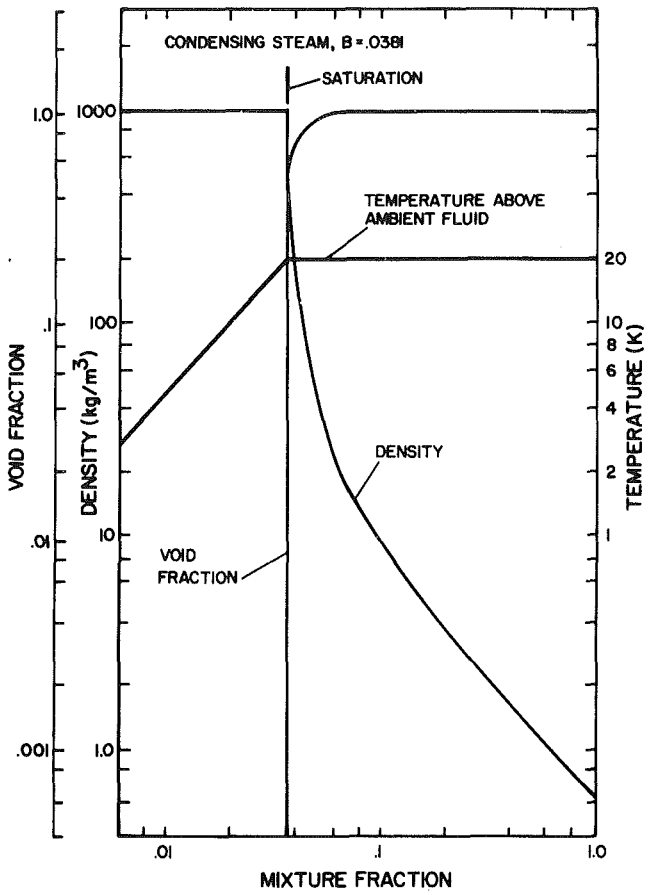

Fig. 1 State relationship for a condensing water vapor jet at atmospheric pressure

axisymmetric turbulent jet in an infinite stagnant environment having uniform properties. While injector exit Mach numbers are approximately unity for the flows to be considered, kinetic energy still represents a small fraction of the enthalpy difference of condensation; therefore, kinetic energy and viscous dissipation were neglected. The LHF approximation was adopted, implying that the velocity and temperature of both phases were the same and that thermodynamic equilibrium was maintained at each point in the flow. Similar to earlier studies of single- and two-phase turbulent jets, the exchange coefficients of mass and heat were assumed to be identical [10–15].

With these assumptions, the instantaneous properties at each point in the flow correspond to the state attained when an amount f (the mixture fraction) of injected fluid and $(1-f)$ of fluid from the surroundings, at their initial states, are adiabatically mixed and brought to thermodynamic equilibrium at the ambient pressure of the flow. Therefore, the scalar thermodynamic properties of the flow are only a function of mixture fraction (termed the state relationship) for prescribed injector and ambient conditions. Given these boundary conditions, the state relationship can be constructed once and for all by simple adiabatic mixing calculations.

A state relationship for a typical condensing jet – providing void fraction, density and temperature defect as a function of mixture fraction – is illustrated in Fig. 1. These conditions involve a saturated water vapor jet injected into subcooled liquid at 80°C and atmospheric pressure. Mixing of ambient liquid with the steam leaving the injector causes the mixture fraction to decrease from unity. In the two-phase region of the flow, mixing occurs at constant temperature. In this case, the addition of ambient liquid causes partial condensation of the vapor when the mixture is equilibrated, which results in increased density and reduced void fraction. As mixing continues, the flow eventually reaches the saturated liquid state at a mixture fraction given by

$$f_{fs} = B/(1+B) \tag{2}$$

The mixture is single-phase liquid for $f<f_{fs}$, tending toward the ambient liquid state as mixing continues and f approaches zero.

Following Lockwood and co-workers [13, 14], as well as earlier two-phase flow analysis in this laboratory [10–12], variable density effects are treated by Reynolds averaging while turbulence properties are found by solving model transport equations for turbulent kinetic energy, rate of dissipation of turbulent kinetic energy, and the square of the concentration fluctuations (k-ϵ-g model). A number of approximations are employed to develop the model transport equations; their usefulness is largely justified by the past success of the method [10–14]. A complete discussion of the development of k-ϵ-g models is provided by Launder and Spalding [17] and Launder [18].

Significant effects of buoyancy are possible for the present flows, due to unusually large density variations. This was evaluated by conducting calculations with and without buoyancy terms present in the governing equations for mean momentum, k and ϵ, employing an approach similar to Rodi and co-workers [19, 20]. In general, the evaluation of the model was limited to conditions where buoyancy had a negligible effect on predictions – as noted earlier. Therefore, since the present results cannot contribute significantly to the evaluation of models of buoyancy in turbulent jets, terms involving buoyancy will be omitted in the following formulation (see Ref. 21 for the complete formulation).

After making these assumptions the governing equations become

$$\frac{\partial \bar{\rho}\bar{u}}{\partial x} + \frac{1}{r}\frac{\partial}{\partial r}(r\bar{\rho}\bar{v}^{\circ}) = 0 \tag{3}$$

$$\bar{\rho}\bar{u}\frac{\partial \phi}{\partial x} + \bar{\rho}\bar{v}^{\circ}\frac{\partial \phi}{\partial r} = \frac{1}{r}\frac{\partial}{\partial r}\left(r\mu_{\mathrm{eff},\phi}\frac{\partial \phi}{\partial r}\right) + S_{\phi} \tag{4}$$

where

$$\bar{\rho}\bar{v}^{\circ} = \bar{\rho}\bar{v} + \overline{\rho' v'} \tag{5}$$

and $\phi = \bar{u}, \bar{f}, k, \epsilon$ or g. The expressions for $\mu_{\mathrm{eff},\phi}$ and S_{ϕ} appear in Table 2.

Empirical constants needed to find turbulence properties are also listed in Table 2. Their values were determined by calibrating the k-ϵ-g model with data from various boundary layer flows [13, 17, 18]. The values appearing in Table 2 were re-evaluated for axisymmetric flows during earlier work in this laboratory [11, 12]. Using these values, good agreement was obtained between predictions and measurements of both mean and turbulent quantities for the following experiments: constant density jets – Hetsroni and Sokolov [22], Wygnanski and Fiedler [23], Becker et al. [24], and Shearer et al. [10]; variable density jets – Corrsin and Uberoi [25] and Shearer et al. [10]; and combusting gas jets have small effects of buoyancy – Mao et al. [11]. Recently, the same constants have demonstrated good agreement with measurements in buoyant combusting gas jets [21]. One undesirable feature of this model is that $C_{\epsilon 2} = C_{g2}$ varies slightly for constant and variable density flows, as noted in Table 2, with the lower value yielding best results for cases where the density varies [10–13]. Due to this uncertainty, both values of these constants were considered during the present calculations.

The flows considered in the calculations were all highly turbulent and the values employed for μ and Sc did not influence the results significantly; therefore, μ was taken as the saturated liquid value at the bath pressure and a constant value of Sc was assumed, as noted in Table 2.

Table 2 Model parameters

ϕ	$\mu_{\text{eff},\phi}$*	S_ϕ
$\bar{u}$	$\mu+\mu_t$	0
$\bar{f}$	$(\mu/\text{Sc})+(\mu_t/\sigma_f)$	0
k	$\mu+(\mu_t/\sigma_k)$	$\mu_t\left(\frac{\partial\bar{u}}{\partial r}\right)^2-\bar{\rho}\epsilon$
ϵ	$\mu+(\mu_t/\sigma_e)$	$\left(C_{\epsilon 1}\mu_t\left(\frac{\partial\bar{u}}{\partial r}\right)^2_4-C_{\epsilon 2}\bar{\rho}\epsilon\right)\frac{\epsilon}{k}$
g	$(\mu/\text{Sc})+(\mu_t/\sigma_g)$	$C_{g1}\mu_t\left(\frac{\partial\bar{f}}{\partial r}\right)^2-C_{g2}\bar{\rho}\frac{\epsilon g}{k}$

C_μ	$C_{\epsilon 1}$	$C_{\epsilon 2}=C_{g2}$	C_{g1}	σ_k	σ_ϵ	σ_f	σ_g	Sc
0.09	1.44	1.84 or 1.92	2.8	1.0	1.3	0.7	0.7	0.7

*$\mu_c=C_\mu\bar{\rho}k^2/\epsilon$

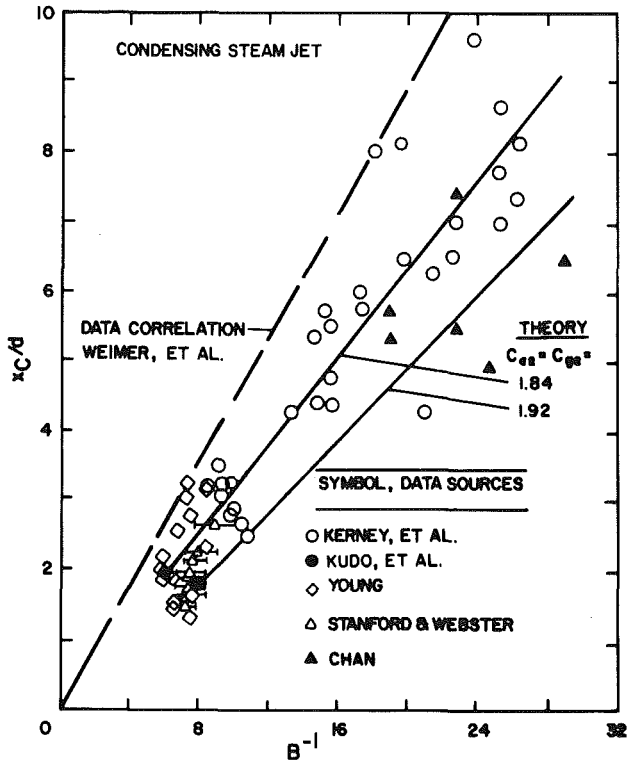

Fig. 2 Predicted and measured penetration lengths for water vapor jets submerged in stagnant subcooled liquid

The mean value of any scalar quantity ϕ (except $\bar{f}$, k, ϵ, g and μ_t which are obtained directly from the solution of equations (3) and (4)) was obtained as follows:

$$\bar{\phi}=\int_0^1\phi(f)P(f)\,df \tag{6}$$

where $\phi(f)$ is known from the state relationship, e.g., Fig. 1, and $P(f)$ is the probability density function (*pdf*) for f. Similar to earlier work [10–14], a clipped Gaussian *pdf* was employed during the computations. This *pdf* is fully defined upon specifying its most probable value and variance – these parameters are obtained from $\bar{f}$ and g at each point in the flow as described by Lockwood and Naguib [13].

Initial conditions were estimated since detailed information was not available for any of the flows considered in the computations. It was assumed that all properties were constant at the injector exit, except for a shear layer having a thickness equal to 0.1 percent of the injector radius. The constant property portion of the flow was specified similar to previous studies [10–12], as follows:

$$x=0,\ 2r/d\le 0.999;\ \bar{u}_o=\dot{m}_o''/\bar{\rho}_o,\ \bar{f}_o=1,$$
$$k_o=(0.02\bar{u}_o)^2,\ \epsilon_o=0.07\bar{u}_o{}^3/d,\ g_o=0 \tag{7}$$

where $\bar{\rho}_o$ was assumed to be the value for saturated vapor, unless the exit quality was known. In the shear layer ($x=0$, $0.999<2r/d\le 1.$), velocity and mixture fraction were assumed to vary linearly, while k_o and ϵ_o were obtained by solving the governing equations assuming that convective and diffusive terms are negligible. The ambient values of $\bar{u}$ (except as noted), $\bar{f}$, k, ϵ, and g were all taken to be zero. The boundary condition along the inner edge of the shear layer was specified by equation (7) until the shear layer reached the jet axis, then all radial gradients at the axis were set equal to zero.

The computations were performed using a modified version of the GENMIX computer program [26]. The large density variations of the present flows created convergence problems, requiring 90 cross-stream grid nodes to obtain acceptable numerical closure. The forward step size was limited to values less than 1.5 percent of the flow width; therefore, up to 1000 axial steps were needed to cover the two-phase flow region for the present data base.

Most of the data base involves measurements of penetration lengths. Since a stochastic computation is used to determine mean properties in the present analysis, the mean void fraction never formally becomes equal to zero; therefore, the boundary of the two-phase region was defined as the point where the mean void fraction is less than 10^{-4} (use of 10^{-5} yields essentially the same results). This value was chosen as a compromise between the greater probability of observing vapor for larger mean void fractions and errors due to the accumulation of round-off errors for smaller void fractions.

Results and Discussion

Condensing Water Vapor Jets. Predicted and measured penetration lengths for condensing water vapor jets at atmospheric pressure are plotted as a function of B in Fig. 2. The data of Binford et al. [2], Kerney et al. [3], Kudo et al. [4], Chan [15] and a portion of Young's data [6] were obtained at atmospheric pressure and are shown directly on the plots. The correlation of Weimer et al. [1], for their entire data base, including results at various bath pressures, is also shown. For injector exit pressures equal to the bath pressure, this correlation takes the form

$$x_C/d=17.8(\rho_o/\rho_\infty)^{1/2}/B \tag{8}$$

and is plotted in Fig. 2 assuming a saturated vapor at the exit of the injector. This correlation tends to overestimate the atmospheric pressure data for water, since it was established over a broader data base involving several condensing substances and a range of bath pressures.

The experimental results illustrated in Fig. 2 are somewhat scattered. This is probably due to difficulties in defining

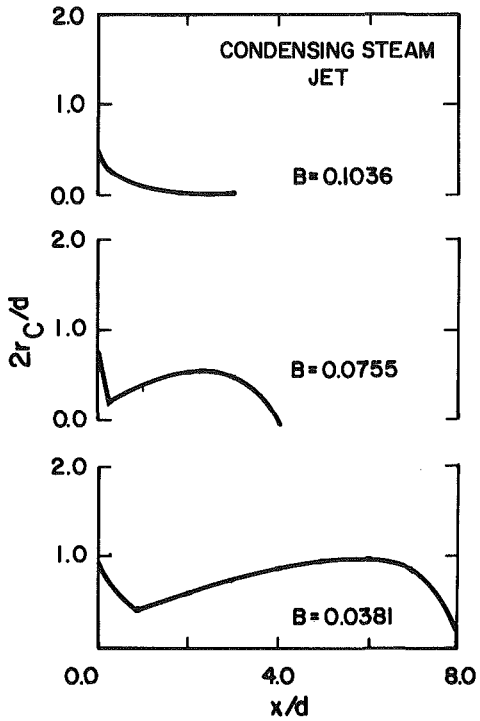

Fig. 3 Predicted boundaries of the two-phase region for water vapor jets submerged in stagnant subcooled liquid: ($C_{\epsilon 2} = C_{g2} = 1.84$)

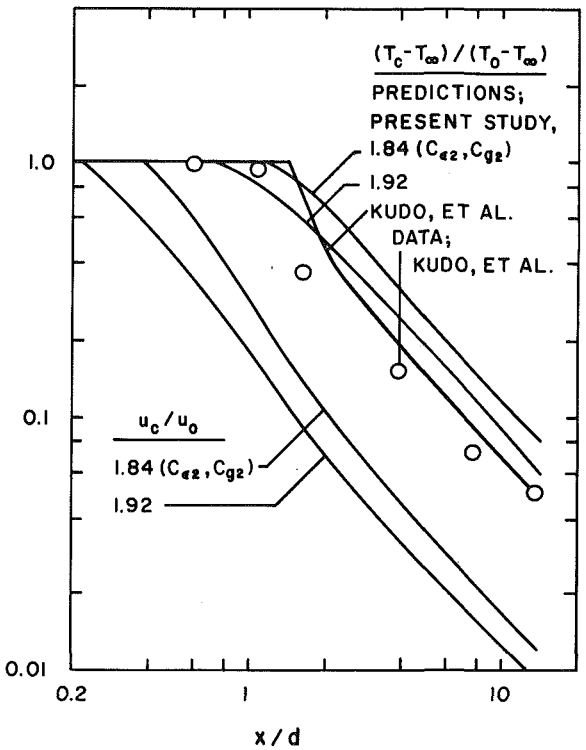

Fig. 4 Predicted and measured variation of mean properties along the axis of condensing water vapor jet at atmospheric pressure with a bath temperature of 20°C

precise boundaries for a turbulent two-phase flow as well as differences in judgment when determining the extent of the vapor region from photographs. Variations in the stability of the injector near the choked flow condition and effects of external expansion for stable underexpanded conditions also contribute to the scatter [1, 3], even though the data base was selected to minimize these effects as much as possible.

Predictions are shown in Fig. 2 for the two values of $C_{\epsilon 2} = C_{g2}$ considered in the calculations. Variables other than B (injector diameter and velocity and the small liquid coflow velocity present during the tests of Young and co-workers [5, 6]) were found to have a small effect on the predicted penetration length for the highly turbulent flows comprising the data base; therefore, only single theoretical curves are shown for each set of turbulence model constants.

In view of the scatter of the data, the predictions illustrated in Fig. 2 are in reasonably good agreement with the measurements – particularly with data obtained directly for water vapor at atmospheric pressure. This is encouraging, since standard turbulence model constants, established for single-phase constant and variable density jets [10–12] have been employed in the computations.

Predicted boundaries for the two-phase region, using $C_{\epsilon 2} = C_{g2} = 1.84$, are illustrated in Fig. 3 for various values of B at atmospheric pressure. For larger values of B, typical of the range examined by Kudo et al. [4] and Young and co-workers [5, 6], the region containing vapor approximates the conical shape used by these investigators in their analysis of the process. As B decreases, however, the vapor containing region expands in the radial direction for a time, as observed by Kerney, et al. [3] and Wiemer et al. [1] for comparable values of B.

The rapid reduction of the radius of the two-phase flow region, near the injector exit and again as the penetration length is approached, seen in Fig. 3, raises questions concerning the adequacy of the shear layer approximations employed in the analysis [5]. It should be recalled, however, that these approximations are actually applied to the governing equations for $\tilde{u}$, $\tilde{f}$, k, ϵ, and g, and these variables do not exhibit excessive axial gradients near the phase boundary. The rapid variation in the phase boundary occurs due to the large sensitivity of void fraction to changes in the mixture fraction near the saturated liquid state (see Fig. 1). This variation is only a factor in the stochastic computation of mean void fraction and is independent of any assumption concerning axial gradients.

Kudo et al. [4] have measured the temperature variation along the centerline of condensing water vapor jet having sonic exit conditions at atmospheric pressure. The measurements and predictions of Kudo et al. [4], along with present predictions, are illustrated in Fig. 4. All the predictions lag the measured rate of temperature defect decay along the axis, with the analysis of Kudo et al. [4] demonstrating the smallest error. This trend suggests that the theories tend to underestimate the width of the flow. Since initial conditions were not measured for this flow, however, uncertainties in prescribing them could contribute to the discrepancy between present predictions and the measurements, e.g., use of an initial velocity profile for fully developed pipe flow would improve present predictions considerably. The present predictions could also be improved by further modification of the constants in the turbulence model; however, this was not felt to be justified on the basis of a single experimental condition. Furthermore, most investigators have observed unstable oscillatory injector flow for sonic exit conditions [1–3], which have tended to increase mixing rates due to flow development effects, and may be a factor in the measurements.

The very short potential core evident in the results illustrated in Fig. 4 was invariably observed throughout the computations. This may explain why the analysis of Weimer et al. [1], which ignores the presence of the potential core, was still reasonably successful in correlating measurements where penetration lengths are short.

Condensing Ethylene Glycol and Iso-Octane Vapor Jets. Predicted and measured penetration lengths for condensing

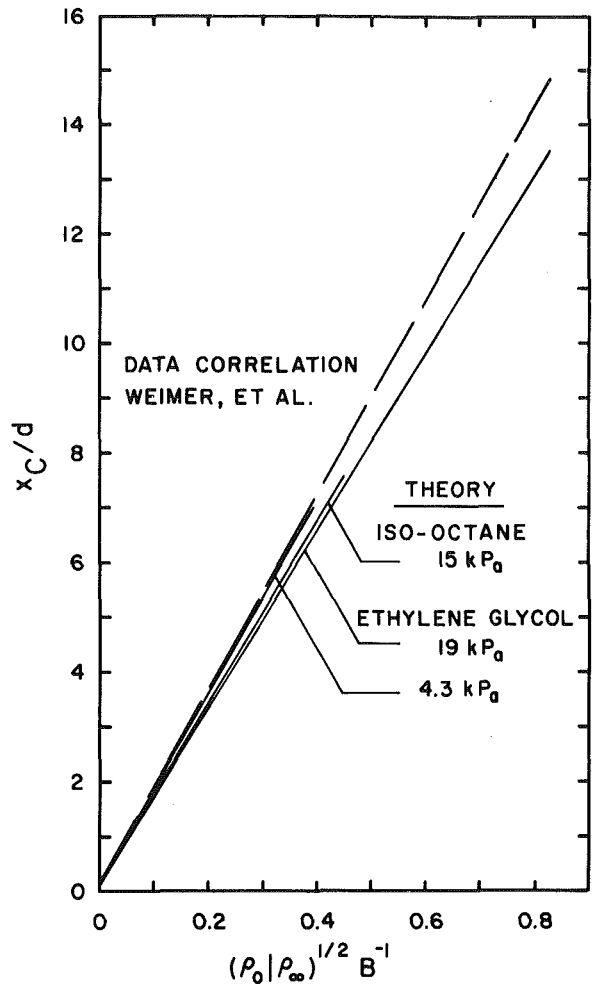

Fig. 5 Predicted and measured penetration lengths for submerged ethylene glycol and iso-octane vapor jets in stagnant subcooled liquid. ($C_{\epsilon 2} = C_{g2} = 1.84$)

ethylene glycol and iso-octane vapor jets are illustrated in Fig. 5. In this case, the data were accumulated at a variety of bath pressures; therefore, the results are plotted according to the empirical expression of Weimer et al. [1], (equation (8)) which was found to correlate results at various bath pressures. The data is represented by equation (8) although individual data points scatter from the correlation similar to the results for water in Fig. 2 [1].

The predictions illustrated in Fig. 5 use $C_{\epsilon 2} = C_{g2} = 1.84$; predictions for the higher value of these constants are about 10 percent lower, similar to the variation for water illustrated in Fig. 2. Three predictions are shown: two predicted curves for ethylene glycol, obtained at bath pressures near the limits of the data base; and one prediction for iso-octane at the lowest pressure in the data base. The predictions support the data correlation of Weimer et al. [1], i.e., the effect of bath pressure and condensing substance is small when the results are plotted as suggested by equation (8). In addition to reproducing these trends, the predicted penetration lengths are in reasonably good quantitative agreement with the measurements.

Conclusions

The present model for condensing jets employs the LHF approximation of two-phase flows in conjunction with a k-ϵ-g model of turbulence. The empirical parameters used in the turbulence model were established earlier by calibration with measurements for a variety of single-phase flows; therefore, the present application for condensing vapor jets did not require additional empiricism. The model provided reasonably good predictions of vapor penetration lengths for momentum-dominated condensing jets with $d = 3.17$-22.2 mm, $B^{-1} = 3$-32, $\rho_\infty/\rho_0 = 324$-$31{,}200$, $x_C/d = 1.3$-15, minimum $Re_0 = 15{,}000$, maximum $Ri_0 = 1.3 \times 10^{-6}$, minimum $We_0 = 100$ and the ratio of injector exit mass flux to sonic mass flux in the range 1.0–1.7. The predictions also supported equation (8) as a reasonable means of correlating the effect of condensation driving potential and bath pressure on vapor penetration lengths.

Comparison of the predicted and measured variation of centerline temperature defect was less satisfactory for the one data set currently available. The present predictions tend to lag the measurements, suggesting that the width of the flow is underestimated by the model; however, more data is needed to fully substantiate this effect. Additional measurements of flow structure would also be desirable in order to adequately evaluate model assumptions – particularly the LHF approximation.

The present model is limited to cases where the injector exit plane pressure is equal to the ambient pressure. Many applications involve underexpanded vapor jets, with the exit plane pressure greater than the ambient pressure, and it would be useful to extend the model to treat such cases. A large portion of the measurements reported in references [1-6, 8, 15] involves underexpanded jets; therefore, a reasonably good data base exists to test such an extension of the model.

The model is also not appropriate for oscillatory subsonic flows, where the injector passage periodically fills with liquid, which are frequently observed for condensing jets having low initial momentum [1, 3, 8, 15, 16].

While effects of buoyancy are often important for condensing submerged jets, due to their large density variation, this was not the case for the existing data base. Additional measurements are needed in order to evaluate whether existing methods for treating buoyant turbulent flows can be applied to condensing vapor jets.

Acknowledgment

This research was supported by the Office of Naval Research, Contract No. N00014-80-C-0517, under the technical management of R. D. Ryan. The authors also wish to acknowledge the help of a reveiwer in pointing out the measurements of Chan and co-workers.

References

1 Weimer, J. C., Faeth, G. M., and Olson, D. R., "Penetration of Vapor Jets Submerged in Subcooled Liquids," *AIChE Journal*, Vol. 19, 1973, pp. 552-558.

2 Binford, F. T., Stanford, L. E., and Webster, C. C., "Nuclear Safety Program Annual Progress Report for Period Ending December 31, 1968," ORNL Report 4374, UC-80-Reactor Technology, 1968, pp. 234-250.

3 Kerney, P. J., Faeth, G. M., and Olson, D. R., "Penetration Characteristics of a Submerged Steam Jet," *AIChE Journal*, Vol. 19, 1972, pp. 548-553.

4 Kudo, A., Egusa, T., and Toda, S., "Basic Study on Vapor Suppression," *Proceedings of the Fifth International Heat Transfer Conference*, Vol. 3, Tokyo, 1974, pp. 221-225.

5 Young, R. J., Yang, K. T., and Novotny, J. L., "Vapor-Liquid Interaction in a High Velocity Vapor Jet Condensing in a Coaxial Water Flow," *Proceedings of the Fifth International Heat Transfer Conference*, Vol. 3, Tokyo, 1974, pp. 226-230.

6 Young, R. J., "Interaction Between a High Velocity Vapor Jet and an External Coaxial Cocurrent Water Flow," Ph.D. thesis, University of Notre Dame, 1973.

7 Cumo, M., Farello, G. E., and Ferrari, G., "Direct Heat Transfer in Pressure-Suppression Systems," *Proceedings of the Sixth International Heat Transfer Conference*, Vol. 5, Toronto, 1978, pp. 101-106.

8 Simpson, M. E., and Chan, C. K., "Hydrodynamics of a Subsonic Vapor Jet in a Subcooled Liquid," ASME JOURNAL OF HEAT TRANSFER, in press.

9 Avery, J. F., and Faeth, G. M., "Combustion of a Submerged Gaseous Oxider Jet in a Liquid Metal," *Fifteenth Symposium (International) on Combustion*, The Combustion Institute, Pittsburgh, 1975, pp. 501-512.

10 Shearer, A. J., Tamura, H., and Faeth, G. M., "Evaluation of a Locally Homogeneous Flow Model of Spray Evaporation," *Journal of Energy*, Vol. 3, 1979, pp. 271-278.

11 Mao, C. P., Szekely, G. A., Jr., and Faeth, G. M., "Evaluation of a Locally Homogeneous Flow Model of Spray Combustion," *Journal of Energy*, Vol. 4, 1980, pp. 78-87.

12 Mao, C. P., Wakamatsu, Y., and Faeth, G. M., "A Simplified Model of High Pressure Spray Combustion," *Eighteenth Symposium (International) on Combustion*, The Combustion Institute, Pittsburgh, 1981, pp. 337-343.

13 Lockwood, F. C., and Naguib, A. S., "The Prediction of the Fluctuations in the Properties of Free, Round-Jet, Turbulent, Diffusion Flames," *Combustion and Flame*, Vol. 24, 1975, pp. 109-124.

14 Gosman, A. D., Lockwood, F. C., and Syed, S. A., "Prediction of a Horizontal Free Turbulent Diffusion Flame," *Sixteenth Symposium (International) on Combustion*, The Combustion Institute, Pittsburgh, 1977, pp. 1543-1555.

15 Chan, C. K., "Dynamical Pressure Pulse in Steam Jet Condensation," *Proceedings of the Sixth International Heat Transfer Conference*, Vol. 5, Toronto, 1978, pp. 395-399.

16 Chan, C. K., and Lee, C. K. B., "A Regime Map for Direct Contact Condensation," *International Journal of Multiphase Flow*, Vol. 8, 1982, pp. 11-20.

17 Launder, B. E., and Spalding, D. B., *Mathematical Models of Turbulence*, Academic Press, New York, 1972, pp. 90-130.

18 Launder, B. E., "Heat and Mass Transport," in *Turbulence*, (edited by P. Bradshaw), *Topics in Applied Physics*, Vol. 12, Springer-Verlag, Berlin, 1978, pp. 232-289.

19 Chen, C. J., and Rodi, W., "A Mathematical Model for Stratified Turbulent Flows and Its Application to Buoyant Jets," *Sixteenth Congress of the International Association for Hydraulic Research*, Sao Paolo, 1975.

20 Hossain, M. S., and Rodi, W., "Influence of Buoyancy on the Turbulence Intensities in Horizontal and Vertical Jets," *Heat Transfer and Turbulent Buoyant Convection*, edited by D. B. Spalding, and N. Afgan, Vol. 1, Hemisphere, Washington, 1977, pp. 39-51.

21 Jeng, S-M., Chen, L-D., and Faeth, G. M., "The Structure of Buoyant Methane and Propane Diffusion Flames," *Nineteenth Symposium (International) on Combustion*, The Combustion Institute, Pittsburgh, in press.

22 Hetsroni, G., and Sokolov, M., "Distribution of Mass, Velocity, and Intensity of Turbulence in a Two-Phase Turbulent Jet," ASME *Journal of Applied Mech.*, Vol. 38, 1971, pp. 314-327.

23 Wygnanski, I., and Fiedler, H. E., "Some Measurements in the Self-Preserving Jet," *Journal of Fluid Mech.*, Vol. 38, 1969, pp. 577-612.

24 Becker, H. A., Hottel, H. C., and Williams, G. C., "The Nozzle-Fluid Concentration Field of the Round, Turbulent, Free Jet," *Journal of Fluid Mech.*, Vol. 30, 1967, pp. 285-303.

25 Corrsin, S., and Uberoi, M. S., "Further Experiments on the Flow and Heat Transfer in a Heated Turbulent Air Jet," NACA Report No. 998, 1950.

26 Spalding, D. B., *GENMIX: A General Computer Program for Two-Dimensional Parabolic Phenomena*, Pergamon Press, Oxford, 1977.

M. D. Mikhailov
Applied Mathematics Center,
Sofia 1000, Bulgaria

M. N. Özisik
Department of Mechanical and Aerospace Engineering,
North Carolina State University,
Raleigh, N. C. 27650
Mem. ASME

B. K. Shishedjiev
Applied Mathematics Center,
Sofia 1000, Bulgaria

Diffusion in Heterogeneous Media

Heat or mass diffusion problems of finite heterogeneous media are characterized by a set of partial differential equations for temperatures or mass concentrations, T_k (x, t), $(k = 1, 2, \ldots, n)$, in every point in space, which are coupled through source-sink terms in the equations. In the present analysis, appropriate integral transform pairs are developed for the solution of the n-coupled partial differential equations subject to general linear boundary conditions. Three-dimensional, time-dependent solutions are presented for the distributions of the potentials (i.e., temperatures or mass concentrations), T_k (x, t), $(k = 1, 2, \ldots, n)$, as a function of time and position for each of the n-components in the medium. The results of the general analysis are utilized to develop solutions for the specific cases of one-dimensional slab, long solid cylinder, and sphere. Numerical results are presented for the dimensionless potentials (i.e., temperature or mass concentration), T_k (x, t), $(k = 1, 2, 3)$, at the center of the slab, long solid cylinder, or sphere for each of the three components of a three-component system.

Introduction

The problems of heat or mass diffusion in heterogeneous media have applications in various branches of science and engineering. Specific examples include, among others, the mass diffusion process involving several chemically reacting components [1] and transient temperature distribution for the components of an heterogeneous medium (i.e., a medium consisting of concrete, soil, water- and/or oil-saturated sand layers) [2]. The mathematical formulation of problems of this type includes a set of diffusion equations in which the potentials (i.e., temperatures or mass concentrations), $T_k(\underline{x}, t)$, $(k = 1, 2, \ldots, n)$ in every point of the space are coupled through source or sink terms. A mathematical model of this type was first proposed by Anzelius [4] by assigning two different temperatures to every point of the space for heat transfer between solid particles and fluid flowing around them. A similar model has been considered in [5] to describe the dynamics of gas absorption by porous adsorbent from an air flow. The physical significance of the potentials defined in this manner is quite apparent for a mass diffusion problem involving multicomponent, chemically reacting n-species. For such a case, there are n different species at every point in the space; hence, one can envision the existance of n different concentration distributions in the medium which are continuous functions of space and time over the region under consideration. In the case of transient heat diffusion in a medium consisting of n different types of materials uniformly dispersed over the region, some clarificaton of the actual physical phenomenon is in order. We shall consider a finite region consisting of uniformly mixed n different types of materials each having different thermal and physical properties. The size of the particles are small compared to the overall dimensions of the region, but the particles are sufficiently large so that the medium cannot be regarded as homogeneous. Therefore, the medium is a heterogeneous one consisting of n different types of materials. Under the steady-state conditions, there is only one temperature profile for the region; for such a case, the effective thermal conductivity, related to the conductivities of the separate components and the detailed structure of the aggregate, can be used [6]. During the transients, however, there will be a different temperature profile for each of the n-components in the medium. The coupling of heat transfer between the components under transient conditions, say, between the components m and p, can be characterized by terms in the form σ_{mp} $(T_m - T_p)$, where $\sigma_{mp} = \sigma_{pm}$ is a heat-exchange coefficient, and T_m and T_p are the temperatures for the components m and p, respectively. Then the mathematical formulation of such a heat-transfer problem leads to a set of n-diffusion equations which are coupled through the source-sink term by relations of the type given above. Similar models have been described in the monograph [2] where methods are also described to derive approximate estimates for the interphase exchange coefficients and the possibilities are discussed for its experimental evaluation. It is interesting to note that identical equations have been proposed in [7] to model filtration in elastic cracking porous media.

The general analysis of heat- and mass-diffusion problems of this type given in [8] is not complete. The objective of this work is to present general solutions belonging to this class, including some applications of the analysis, to the one-dimensional problem and to develop a method for its numerical treatment.

General Analysis

We consider a set of diffusion equations in which the potential T_k $(\underline{x}, t)$, $(k = 1, 2, \ldots, n)$, in every point in space, $\underline{x}$, of a given finite region, V, are coupled through source-sink terms. The mathematical formulation of such a problem consists of n-coupled diffusion equations and given by

$$w_k(\underline{x})\frac{\partial T_k(\underline{x}, t)}{\partial t} + L_k T_k(\underline{x}, t) = P_k(\underline{x}, t)$$

$$+ b(\underline{x}) \sum_{p=1}^{n} \alpha_{kp}[T_p(\underline{x}, t) - T_k(\underline{x}, t)]$$

$$\alpha_{kp} = \alpha_{pk},\ k = 1, 2, \ldots, n,\ \underline{x} \in V \tag{1a}$$

subject to the boundary conditions

$$B_k T_k(\underline{x}, t) = \phi_k(\underline{x}, t),\ k = 1, 2, \ldots, n,\ \underline{x} \in S \tag{1b}$$

and the initial conditions

$$T_k(\underline{x}, 0) = f_k(\underline{x}),\ k = 1, 2, \ldots, n,\ \underline{x} \in V \tag{1c}$$

where the operators L_k and B_k are defined by

$$L_k \equiv -\nabla \cdot [k_k(\underline{x}) \nabla] + d_k(\underline{x}) \tag{1d}$$

$$B_k \equiv \alpha_k(\underline{x}) + \beta_k(\underline{x}) k_k(\underline{x}) \frac{\partial}{\partial n} \tag{1e}$$

Here $\alpha(\underline{x})$, $\beta(\underline{x})$ are prescribed boundary coefficients defined on the boundary surface, S; the functions, $\phi_k(x, t)$, which are the nonhomogeneous part of the boundary conditions (1b) are prescribed functions; $k(\underline{x})$ is associated with the definition of

Contributed by the Heat Transfer Division for publication in the JOURNAL OF HEAT TRANSFER. Manuscript received by the Heat Transfer Division April 24, 1981.

the linear diffusion law; and $\partial/\partial n$ represents the normal derivative at the boundary surface, S, in the outward direction. The term $P_k(\underline{x}, t)$ characterizes a prescribed source term.

This boundary value problem will now be solved by the application of a finite integral transform technique.

Development of the Integral Transform Pair. To develop the desired integral transform pair, we consider the following eigenvalue problem appropriate for the solution of the nonhomogeneous problem defined by equations (1).

$$\mu^2 w_k(\underline{x})\psi_k(\underline{x}) + b(\underline{x}) \sum_{p=1}^{n} \alpha_{kp}[\psi_p(x) - \psi_k(\underline{x})] = L_k\psi_k(\underline{x}),\ \alpha_{kp} = \alpha_{pk}$$

$$k = 1, 2, \ldots, n, \underline{x} \in V \tag{2a}$$

subject to the boundary conditions

$$B_k\psi_k(\underline{x}) = 0,\ k = 1, 2, \ldots, n, \underline{x} \in S \tag{2b}$$

where L_k and B_k are defined by equations (1*d*) and (1*e*), respectively.

We now expand the desired potential, $T_k(\underline{x}, t)$, in terms of the eigenfunctions of the above eigenvalue problem in the form

$$T_k(\underline{x}, t) = \sum_{i=1}^{\infty} A_i(t)\psi_{ki}(\underline{x}),\ k = 1, 2, \ldots, n, \underline{x} \in V \tag{3}$$

where the summation is taken over all discrete eigenvalues, μ_i.

To determine the unknown coefficients, $A_i(t)$, the orthogonality condition for these eigenfunctions is needed, but, the homogeneous problem defined by equations (2) is an eigenvalue problem which does not belong to the conventional Sturm-Liouville system. Therefore, the first step in the analysis is to establish the orthogonality condition as described below.

Equations (2*a*) are written for two different eigenvalues, μ_i and μ_j; the first of these equatons is multiplied by $\psi_{kj}(\underline{x})$, the second by $\psi_{ki}(\underline{x})$, the results are subtracted, integrated over the volume, V, the volume integral is changed to surface integral, the resulting expression is summed up for $k = 1$ to n, and the boundary conditions (2*b*) are utilized. Then, the orthogonality condition for the eigenfunctions $\psi_{ki}(\underline{x})$ is determined as

$$\sum_{k=1}^{n} (\psi_{ki}, \psi_{kj}) = \delta_{ij} N_i \tag{4a}$$

where the normalization integral, N_i, is

$$N_i = \sum_{k=1}^{n} (\psi_{ki}, \psi_{ki}) \tag{4b}$$

and δ_{ij} is the Kronecker delta. In addition, the notation (ψ_{ki}, ψ_{kj}) is used as an abreviation to denote the scalar product of two functions, ψ_{ki} and ψ_{kj}; that is,

$$(\psi_{ki}, \psi_{kj}) \equiv \int_V w_k(\underline{x})\psi_{ki}(\underline{x})\psi_{kj}(\underline{x})\,dv \tag{4c}$$

where $w(\underline{x})$ is the function that appears in equation (2*a*).

Both sides of equation (3) are operated on by the operator

$$\int_V w_k(\underline{x})\psi_{kj}(\underline{x})\,dv$$

the results are summed up for $k = 1, 2, \ldots, n$, and the orthogonality condition (4) is utilized to obtain $A_i(t)$'s. This solution for $A_i(t)$ is then introduced into the expansion (3), and the resulting expression is split up into two parts to define the finite integral transform pair as

Inversion formula:

$$T_k(\underline{x}, t) = \sum_{i=1}^{\infty} \frac{1}{N_i} \psi_{ki}(\underline{x})\,\tilde{T}_i(t) \tag{5}$$

Finite integral transform:

$$\tilde{T}_i(t) = \sum_{k=1}^{n} (\psi_{ki}, T_k) \tag{6}$$

where N_i is defined by equation (4*b*).

Method of Solution. The finite integral transform pair (5) and (6) is now applied to solve the boundary value problem given by equations (1). That is, equations (1*a*) are multiplied by $\psi_{ki}(\underline{x})$, equations (2*a*) by $T_k(\underline{x}, t)$, the results are summed up for $k = 1, 2, \ldots, n$, integrated over the region, V, the definition of the integral transform (6) is utilized and the volume integral is transformed into the surface integral. We obtain

$$\frac{d\tilde{T}_i(t)}{dt} + \mu_i^2 \tilde{T}_i(t) = g_i(t) \tag{7a}$$

where

$$g_i(t) = \sum_{k=1}^{n} \left\{ \int_S k_k(\underline{x}) \begin{bmatrix} \psi_{ki}(\underline{x}) & \dfrac{\partial\psi_{ki}(\underline{x})}{\partial n} \\ T_k(\underline{x}, t) & \dfrac{\partial T_k(\underline{x}, t)}{\partial n} \end{bmatrix} ds + \int_V \psi_{ki}(\underline{x}) P_k(\underline{x}, t)\,dv \right\} \tag{7b}$$

Nomenclature

$b(\underline{x})$ = coefficient in equation (1*a*)
B_k = boundary condition operator defined by equation (1*e*)
$d_k(\underline{x})$ = coefficient in the operator, L_k
$f_k(\underline{x})$ = the initial condition function
$g_i(t)$ = defined by equation (7*c*)
$k_k(\underline{x})$ = coefficient associated with the definition of the linear diffusion law,
L_k = operator defined by equation (1*d*)
N_i = the normalization integral defined by equation (4*b*)
$P_k(\underline{x}, t)$ = the source term in equation (1*a*)
t = time variable
$T_k(\underline{x}, t)$ = the potential (i.e., temperature or mass concentration)
$w(\underline{x})$ = the function in equation (1*a*)
$\underline{x}$ = the space coordinate
$\alpha_k(x), \beta_k(\underline{x})$ = boundary condition coefficients in the operator, B_k
$\alpha_{kp} = \alpha_{Pk}$ = coefficients in equation (1*a*)
$\mu_i, \psi_p(\underline{x})$ = eigenvalues and eigenfunctions of the eigenvalue problem (2)

Superscript

$\sim$ = denotes the integral transform

In equation (7*b*), the integrand of the surface integral is evaluated by utilizing the boundary conditions (1*b*) and (2*b*); then the expression for $g_i(t)$ takes the form

$$g_i(t) = \sum_{k=1}^{n}\left\{\int_S \phi_k(\underline{x}, t)\,\frac{\psi_{ki}(\underline{x}) - k_k(\underline{x})\dfrac{\partial\psi_{ki}(\underline{x})}{\partial n}}{\alpha_k(\underline{x})+\beta_k(\underline{x})}\,ds + \int_V \psi_{ki}(\underline{x})P_k(\underline{x}, t)\,dv\right\} \tag{7c}$$

The initial condition needed to solve equation (7*a*) is determined by taking the finite integral transform of the initial condition (1*c*) according to the transform (6); that is

$$\tilde{T}_i(0) = \sum_{k=1}^{n}(\psi_{ki}, f_k) \equiv \tilde{f}_i \tag{8}$$

The equation (7*a*) is solved subject to the initial condition (8) and the resulting transform inverted by the inversion formula (5). Then general solution of the boundary value problem defined by equations (1) becomes

$$\underline{T}_k(\underline{x}, t) = \sum_{i=1}^{\infty}\frac{1}{N_i}e^{-\mu_i^2 t}\psi_{ki}(\underline{x})\left[\tilde{f}_i + \int_0^t g_i(t')e^{\mu_i^2 t'}\,dt'\right] \tag{9}$$

$$k = 1, 2, \ldots, n, \underline{x} \in V$$

where N_i, $g_i(t')$ and $\tilde{f}_i$ are defined by equations (4*b*), (7*c*), and (8), respectively.

Boundary Conditions All of the Second Kind. In the foregoing problem given by equations (1) if $\alpha_k(\underline{x}) = 0$ for all boundaries and also $d_k(\underline{x}) = 0$, then $\mu_0 = 0$ is also an eigenvalue for the eigenvalue problem (1). For such a case, the corresponding constant eigenfunctions ψ_{k0} and ψ_{p0} must satisfy the equations

$$\sum_{p=1}^{n}\alpha_{kp}(\psi_{p0} - \psi_{k0}) = 0, \quad k = 1, 2, \ldots, n \tag{10}$$

which is apparent from equation (2*a*). Therefore, when the boundary conditions are all of the second kind and $d(\underline{x}) = 0$, $\mu_0 = 0$ is also an eigenvalue. Then the solution (9) includes an additional term corresponding to the zero-eigenvalue and equation (9) takes the form

$$T_k(\underline{x}, t) = \frac{\psi_{k0}}{\sum_{k=1}^{n}(\psi_{k0}, \psi_{k0})}\sum_{k=1}^{n}\psi_{k0}\left\{(1, f_k) + \int_0^t\left[\int_S \phi_k(\underline{x}, t')ds + \int_V P_k(\underline{x}, t')dv\right]dt'\right\} + \sum_{i=1}^{\infty}\frac{1}{N_i}e^{-\mu_i^2 t}\psi_{ki}(\underline{x})\left[\tilde{f}_i + \int_0^t g_i(t')e^{\mu_i^2 t'}\,dt'\right] \tag{11}$$

If the source functions $P_k(\underline{x}, t)$ and $\phi_k(\underline{x}, t)$ are exponentials and q-order polynomials of time, it is desirable to split up the general solution into a set of steady-state problems and a transient homogeneous problem by following a procedure discussed in reference [3] in order to improve the convergence of the series.

One-Dimensional Problem

The one-dimensional form of the problem (1) is given by

$$w_k(x)\frac{\partial T_k(x, t)}{\partial t} = \frac{\partial}{\partial x}\left[k_k(x)\frac{\partial T_k(x, t)}{\partial x}\right] - d_k(x)T_k(x, t) + P_k(x, t) + b(x)\sum_{p=1}^{n}\alpha_{kp}[T_p(x, t) - T_k(x, t)],$$

$$\text{in } x_0 \le x \le x_1, \; t > 0 \tag{12a}$$

$$\alpha_{0k}T_k(x_0, t) - \beta_{0k}k_k(x_0)\frac{\partial T_k(x_0, t)}{\partial x} = \phi_k(x_0, t) \tag{12b}$$

$$\alpha_{1k}T_k(x_1, t) + \beta_{1k}k_k(x_1)\frac{\partial T_k(x_1, t)}{\partial x} = \phi_k(x_1, t) \tag{12c}$$

$$T_k(x, 0) = f_k(x) \tag{12d}$$

where $k = 1, 2, \ldots, n$ and $\alpha_{kp} = \alpha_{pk}$.

The solution of the problem (12) is obtainable from the general solution (9) by restricting it to the one-dimensional case. We find

$$T_k(x, t) = \sum_{i=1}^{\infty}\frac{1}{N_i}e^{-\mu_i^2 t}\psi_{ki}(x)\left[\tilde{f}_i + \int_0^t g_i(t')e^{\mu_i^2 t}dt'\right], \; k = 1, 2, \ldots, n \tag{13a}$$

where N_i, $\tilde{f}_i$ and $g_i(t)$ are obtained respectively from the one-dimensional form of equations (4*b*), (8) and (7*c*) and given by

$$N_i = \sum_{k=1}^{n}\int_{x_0}^{x_1} w_k(x)\,\psi_{ki}^2(x)\,dx \tag{13b}$$

$$\tilde{f}_i = \sum_{k=1}^{n}\int_{x_0}^{x_1} w_k(x)\,\psi_{ki}(x)\,f_k(x)\,dx \tag{13c}$$

$$g_i(t) = \sum_{k=1}^{n}\left[\phi_k(x_0, t)\,\Omega_{ki}(x_0) + \phi_k(x_1, t)\Omega_{ki}(x_1) + \int_{x_0}^{x_1}\psi_{ki}(x')P_k(x', t)\,dx'\right] \tag{13d}$$

here $\Omega_{ki}(x_0)$, $\Omega_{ki}(x_1)$ are defined as

$$\Omega_{ki}(x_0) = \frac{\psi_{ki}(x_0) + k_k(x_0)\psi_{ki}'(x_0)}{\alpha_{0k} + \beta_{0k}} \tag{13e}$$

$$\Omega_{ki}(x_1) = \frac{\psi_{ki}(x_1) - k_k(x_1)\psi_{ki}'(x_1)}{\alpha_{1k} + \beta_{1k}} \tag{13f}$$

The eigenfunctions $\psi_{ki}(x)$ and the eigenvalues μ_i needed in the above solution (13) are the eigenfunctions and eigenvalues of the one-dimensional form of the eigenvalue problem (2) that is

$$\frac{d}{dx}\left[k_k(x)\frac{d\psi_k(\mu, x)}{dx}\right] + [\mu^2 w_k(x) - d_k(x)]\psi_k(\mu, x) + b(x)\sum_{p=1}^{n}\alpha_{kp}[\psi_p(\mu, x) - \psi_k(\mu, x)] = 0, \text{ in } x_0 \le x \le x_1, \; k = 1, 2, \ldots, n \tag{14a}$$

$$\alpha_{0k}\psi_k(\mu, x_0) - \beta_{0k}k_k(x_0)\psi_k'(\mu, x_0) = 0 \tag{14b}$$

$$\alpha_{1k}\psi_k(\mu, x_1) + \beta_{1k}k_k(x_1)\psi_k'(\mu, x_1) = 0 \tag{14c}$$

Boundary Condition of the Second Kind at all Boundaries. If $\alpha_{0k} = \alpha_{1k} = 0$, $\beta_{0k} = \beta_{1k} = 1$, that is the boundary conditions at $x = x_0$ and $x = x_1$ are both of the second kind and $d(x) = 0$, the solution of the problem (12) is obtainable from the one-dimensional form of the general solution (11) as

$$T_k(x,t)=\frac{\psi_{k0}}{\sum_{k=1}^{n}\psi_{k0}^2\int_{x_0}^{x_1}w_k(x)\,dx}\times\sum_{k=1}^{n}\psi_{k0}\left\{\int_{x_0}^{x_1}w_k(x)f_k(x)\,dx+\right.$$

$$\left.+\int_0^t\left[\phi(x_0,t')+\phi(x_1,t')+\int_{x_0}^{x_1}P_k(x,t')\mathrm{dx}\right]dt'\right\}+$$

$$+\sum_{i=1}^{\infty}\frac{1}{N_i}e^{-\mu_i^2 t}\psi_{ki}(x)\left[\tilde{f}_i+\int_0^t g_i(t')e^{\mu_i^2 t'}\,dt'\right],\ k=1,2,\ldots,n \tag{15a}$$

where the constant eigenfunctions ψ_{k0} corresponding to the zero eigenvalue ($\mu = 0$) must satisfy the equations (10), that is

$$\sum_{p=1}^{n}\alpha_{kp}(\psi_{p0}-\psi_{k0})=0,\ k=1,2,\ldots,n \tag{15b}$$

and N_i, $\tilde{f}_i$ and $g_i(t)$ are defined above by the equations (13*b*), (13*c*), and (13*d*), respectively.

To illustrate the application of the general analysis, we consider the following one-dimensional, transient diffusion problem for an heterogeneous medium consisting of n different components. Each component is homogeneous, isotropic, and has constant properties; the coupling coefficients between the components are constant. Initially each component is at the same constant potential (i.e., temperature or mass concentration), T_0. For times $t > 0$, the outer boundary of the region is kept at a constant potential T_w, which is different from T_0. The mathematical formulation of this transient diffusion problem for each of the n components, is given by

$$C_k\rho_k x^{1-2m}\frac{\partial T_k(x,t)}{\partial t}=k_k\frac{\partial}{\partial x}\left\{x^{1-2m}\frac{\partial T_k(x,t)}{\partial x}\right\}$$

$$+x^{1-2m}\sum_{p=1}^{n}\alpha_{kp}\{T_p(x,t)-T_k(x,t)\},$$

$$\text{in } 0\le x\le l,\ \text{for } t>0,\ k=1,2,\ldots,n. \tag{16a}$$

Subject to the boundary conditions

$$\frac{\partial T_k(0,t)}{\partial x}=0,\ k=1,2,\ldots,n \tag{16b}$$

$$T_k(l,t)=T_w,\ k=1,2,\ldots,n \tag{16c}$$

and the initial conditions

$$T_k(x,0)=T_0,\ k=1,2,\ldots,n \tag{16d}$$

where $m = \frac{1}{2}$ for slab, 0 for cylinder, and $-\frac{1}{2}$ for sphere. This problem is now solved as described below.

Analysis

By introducing the following dimensionless variables

$$R=\frac{x}{l},\ \tau=\frac{k^*t}{\rho^*C^*l^2},\ \theta_k(R,\tau)=\frac{T_k(x,t)-T_w}{T_0-T_w},$$

$$\omega_k=\frac{C_k\rho_k}{C^*\rho^*},\ \kappa_k=\frac{k_k}{k^*},\ \sigma_{kp}=\frac{\alpha_{kp}l^2}{k^*} \tag{17}$$

where C^*, ρ^*, and k^* are the reference properties, the problem defined by equations (16) is expressed in the dimensionless form as

$$\omega_k R^{1-2m}\frac{\partial\theta_k(R,\tau)}{\partial\tau}=\kappa_k\frac{\partial}{\partial R}\left\{R^{1-2m}\frac{\partial\theta_k(R,\tau)}{\partial R}\right\}$$

$$+R^{1-2m}\sum_{p=1}^{n}\sigma_{kp}\{\theta_p(R,\tau)-\theta_k(R,\tau)\},$$

$$\text{in } 0\le R\le 1,\ \text{for } \tau>0,\ k=1,2,\ldots,n. \tag{18a}$$

Subject to the boundary conditions

$$\frac{\partial\theta_k(0,\tau)}{\partial R}=0 \tag{18b}$$

$$\theta_k(1,\tau)=0,\ k=1,2,\ldots,n \tag{18c}$$

and the initial conditions

$$\theta_k(R,0)=1,\ k=1,2,\ldots,n \tag{18d}$$

The dimensionless potentials $\theta_k(R,\tau)$ are defined in such a way that the resulting boundary conditions (3*c*) are homogeneous. Therefore, there is no need to split up the problem into the steady-state and the transient parts.

The correspondance between the problem (18) defined above and the more general problem given by equations (12) is as follows.

$$x=R,\ t=\tau,\ T_k(x,t)=\theta_k(R,\tau),\ w_k(x)=\omega_k R^{1-2m},$$

$$k_k(x)=\kappa_k R^{1-2m},\ \alpha_k(x)=0,\ P_k(x,t)=0,\ b(x)=R^{1-2m},$$

$$\alpha_{kp}=\sigma_{kp},\ x_0=0,\ x_1=1,\ \alpha_{0k}=0, \tag{19}$$

$$\beta_{0k}=1,\ \phi_k(x_0,t)=0,\ \alpha_{1k}=1,\ \beta_{1k}=0,$$

$$\phi_k(x,t)=0,\quad f_k(x)=1,$$

Then the solution of the problem (18) is immediately obtained from the solution (13) as

$$\theta_k(R,\tau)=\sum_{i=1}^{\infty}\frac{\sum_{k=1}^{n}\omega_k\int_0^1 R^{1-2m}\psi_k(\mu_i,R)\,dR}{\sum_{k=1}^{n}\omega_k\int_0^1 R^{1-2m}\psi_k^2(\mu_i,R)\,dR}\psi_k(\mu_i,R)e^{-\mu_i^2\tau} \tag{20}$$

The eigenvalue problem for the determination of the eigenfunctions $\psi_k(\mu_i,R)$ and the eigenvalues μ_i is obtained by the simplification of the eigenvalue problem (14). We find

$$\kappa_k\frac{d}{dR}\left\{R^{1-2m}\frac{d\psi_k(\mu,R)}{dR}\right\}+\mu^2\omega_k R^{1-2m}\psi_k(\mu,R)+$$

$$+R^{1-2m}\sum_{p=1}^{n}\sigma_{kp}\{\psi_p(\mu,R)-\psi_k(\mu,R)\}=0$$

$$\text{in } 0\le R\le 1,\ k=1,2,\ldots,n \tag{21a}$$

Subject to the boundary conditions

$$\psi_k'(\mu,0)=0 \tag{21b}$$

$$\psi_k(\mu,1)=0\ (k=1,2,\ldots,n) \tag{21c}$$

In the present problem, the boundary conditions being of the same kind for all components, the solution for the eigenfunctions $\psi_k(\mu_i,R)$ can be assumed in the form

$$\psi_k(\mu_i,R)=E_k\psi(\lambda_i,R) \tag{22}$$

where E_k's are constants which are yet to be determined, and the function $\psi(\lambda_i,R)$ is taken as the solution of the following eigenvalue problem

$$\frac{d}{dR}\left\{R^{1-2m}\frac{d\psi(\lambda,R)}{dR}\right\}+\lambda^2R^{1-2m}\psi(\lambda,R)=0,\ \text{in } 0\le R\le 1 \tag{23a}$$

subject to the boundary conditions

$$\psi'(\lambda, 0) = 0 \tag{23b}$$

$$\psi(\lambda, 1) = 0 \tag{23c}$$

Equations for the determination of the constants E_k are obtained by introducing the solution (22) into equation (21a) and utilizing equation (23a). Then the constants E_k satisfy the following n linear homogeneous equations

$$(\mu^2 \omega_k - \kappa_k \lambda_i^2) E_k + \sum_{p=1}^{n} \sigma_{kp} (E_p - E_k) = 0, \ (k = 1, 2, \ldots, n), \tag{24}$$

Equations (24) can be expressed in the matrix form as

$$[\underline{A}] \{\underline{E}\} = \mu^2 [\underline{\omega}] \{\underline{E}\} \tag{25a}$$

where $[\underline{A}]$ is real, symmetric, square matrix whose elements are all known and given by

$$[\underline{A}] = \begin{bmatrix} \kappa_1 \lambda_i^2 + \sum_{p=1}^{n} \sigma_{1p} - \sigma_{11} & -\sigma_{12} & \cdots & -\sigma_{1n} \\ -\sigma_{21} & \kappa_2 \lambda_i^2 + \sum_{p=1}^{n} \sigma_{2p} - \sigma_{22} & \cdots & -\sigma_{2n} \\ \vdots & \vdots & & \vdots \\ -\sigma_{n1} & -\sigma_{n2} & \cdots & \kappa_n \lambda_i^2 + \sum_{p=1}^{n} \sigma_{np} - \sigma_{nn} \end{bmatrix} \tag{25b}$$

$[\underline{\omega}]$ is a diagonal matrix with known elements, and $\{\underline{E}\}$ is column vector for the unknown constants, E_k, given by

$$[\underline{\omega}] = \begin{bmatrix} \omega_1 & & & \\ & \omega_2 & & 0 \\ & & \ddots & \\ & 0 & & \omega_n \end{bmatrix} \tag{25c}$$

$$\{\underline{E}\} = \begin{bmatrix} E_1 \\ E_2 \\ \vdots \\ E_n \end{bmatrix} \tag{25d}$$

Once the constants E_k, $(k = 1, 2, \ldots, n)$, are determined from the solution of the homogeneous system (25), the general solution $\psi_k(\mu_i, R)$ of the eigenvalue problem (21), which was assumed in the form given by equation (22), is constructed by a linear combination of these E_k's in the form

$$\psi_k(\mu_i, R) = \sum_{j=1}^{n} E_{kij} \psi(\lambda_i, R) \tag{26}$$

Introducing equation (26) into equation (20), the solution for $\theta_k(R, \tau)$ takes the form

$$\theta_k(R, \tau) = \sum_{i=1}^{\infty} \frac{\int_0^1 R^{1-2m} \psi(\lambda_i, R)\, dR}{\int_0^1 R^{1-2m} \psi^2(\lambda_i, R)\, dR} \psi(\lambda_i, R)\, F_k(\lambda_i, \tau) \tag{27a}$$

where

$$F_k(\lambda_i, \tau) = \sum_{j=1}^{n} E_{kij} \frac{\sum_{k=1}^{n} \omega_k E_{kij}}{\sum_{k=1}^{n} \omega_k E_{kij}^2} e^{-\mu_{ij}^2 \tau} \tag{27b}$$

and $\psi(\lambda_i, R)$'s are the eigenfunctions of the eigenvalue problem (23). The solution of the eigenvalue problem (23) is taken as

$$\psi(\lambda_i, R) = (\lambda_i R)^m J_{-m}(\lambda_i R) \tag{28a}$$

which satisfies the equation (23a) and the boundary condition (23b). The boundary condition (23c) is satisfied if λ_i's are taken as the roots of the transcendental equation

$$J_{-m}(\lambda) = 0 \tag{28b}$$

When equation (28a) is introduced into equation (27) and the integrals are evaluated, the solution $\theta_k(R, \tau)$ of the problem (18) becomes

$$\theta_k(R, \tau) = 2 \sum_{i=1}^{\infty} R^m \frac{J_{-m}(\lambda_i R)}{\lambda_i J_{1-m}(\lambda_i)} F_k(\lambda_i, \tau), \quad (k = 1, 2, \ldots, n) \tag{29a}$$

where

$$F_k(\lambda_i, \tau) = \sum_{j=1}^{n} E_{kij} \frac{\sum_{k=1}^{n} \omega_k E_{kij}}{\sum_{k=1}^{n} \omega_k E_{kij}^2} e^{-\mu_{ij}^2 \tau} \tag{29b}$$

and λ_i's are the roots of the transcendental equation (28b).

We recall that if the matrix $[\underline{A}]$ in equation (25b) is real and symmetric, the parameter $\omega_k > 0$, $(k = 1, 2, \ldots, n)$, then the eigenvalues μ_{ij} are real and $\mu_{ij}^2 > 0$. Various methods are available for the computation of all eigenvalue μ_{ij} and the corresponding eigenvectors E_{kij} from equation (25a).

Once μ_{ij} and E_{kij} are determined, the distribution of the potentials $\theta_k(R, \tau)$, $(k = 1, 2, \ldots, n)$, for each of n components in the one-dimensional region $0 \le R \le 1$ is computed from the solution given by equations (29). This solution is valid for a slab, long solid cylinder and solid sphere, depending on the choice of the value of m.

Specific solutions for the distribution of potentials, $\theta_k(R, \tau)$, $(k = 1, 2, \ldots, n)$, for each of the n components in an heterogeneous slab, long solid cylinder and sphere are obtained from equation (29) by setting $m = 1/2$, 0 and $-1/2$, respectively, and by making use of the relations given in Table 1. The results are summarized below.

Slab ($m = 1/2$). By setting $m = 1/2$ in equation (29a) and replacing the Bessel functions by the equivalent trigonometric functions given in Table 1, the solution for a slab becomes

Table 1

m	$x^m J_{-m}(x)$	$x^m J_{1-m}(x)$
$\frac{1}{2}$	$\sqrt{\frac{2}{\pi}}\cos x$	$\sqrt{\frac{2}{\pi}}\sin x$
0	$J_0(x)$	$J_1(x)$
$-\frac{1}{2}$	$\sqrt{\frac{2}{\pi}}j_0(x)$	$\sqrt{\frac{2}{\pi}}j_1(x)$

$$\theta_k(R,\tau)=2\sum_{i=1}^{\infty}(-1)^{i+1}\frac{\cos(\lambda_i R)}{\lambda_i}F_i(\lambda_i,\tau),$$
$$k=1,2,3,\ldots,n \tag{30a}$$

where the function $F_k(\lambda_i, \tau)$ is defined by equation (29*b*) and the eigenvalues λ_i's are the roots of $\cos\lambda_i = 0$, that is

$$\lambda_i=(2i-1)\frac{\pi}{2},\ i=1,2,3,\ldots \tag{30b}$$

Long Solid Cylinder ($m = 0$). By setting $m = 0$ in equation (29*a*), the solution for a long solid cylinder becomes

$$\theta_k(R,\tau)=2\sum_{i=1}^{\infty}\frac{J_0(\lambda_i R)}{\lambda_i J_1(\lambda_i)}F_k(\lambda_i,\tau),\ k=1,2,\ldots,n \tag{31a}$$

where the function $F_k(\lambda_i, \tau)$ is defined by equation (29*b*) and λ_i's are the roots of

$$J_0(\lambda)=0 \tag{31b}$$

Solid Sphere ($m = -1/2$). In the case of a solid sphere, we set $m = -1/2$ in equation (29*a*), and utilize the results in Table 1 together with the definition of spherical Bessel functions. Then the solution for a solid sphere becomes

$$\theta_k(R,\tau)=2\sum_{i=1}^{\infty}(-1)^{i+1}\frac{\sin(\lambda_i R)}{\lambda_i R}F_k(\lambda_i,R),$$
$$k=1,2,\ldots,n \tag{32a}$$

where $F_k(\lambda_i, R)$ is defined by equation (29*b*) and λ_i's are the roots of

$$\frac{\sin\lambda_i}{\lambda_i}=0,$$

that is

$$\lambda_i=i\pi,\ i=1,2,3,\ldots \tag{32b}$$

Numerical Results

To illustrate the application of the foregoing analysis, we calculated the potentials (i.e., dimensionless temperature or mass concentration), $\theta_k(0, \tau)$, in the center of a slab, long solid cylinder and sphere as a function of the dimensionless time, τ, from the solutions given by equations (30), (31) and (32), respectively, for a three component (i.e., n = 3) heterogeneous medium. The system parameters for the components were taken as $\omega_1 = \omega_2 = \omega_3 = 1$, and $\kappa_1 = 0.1$, $\kappa_2 = 1$, $\kappa_3 = 10$, and the calculations were performed for the values of $\sigma_{kp} \equiv \sigma = 0$, 1 and 10.

Figures 1, 2, and 3 show the potentials $\theta_k(0, \tau)$, at $\tau = 0$, for a slab, long solid cylinder and sphere, respectively. The physical significance of the results can be envisioned better by considering the case, say, shown in Fig. 1 for the slab geometry.

All three components initially (i.e., $\tau = 0$) are at the same potential, i.e., $\theta_k(0, \tau) = 1$. During the transients, at any instant, τ, they are at different potentials; but as the steady state (i.e., $\tau \to \infty$) is reached, they all attain the same steady-state potential, $\theta_k(0, \infty) \to 0$.

The parameter σ_k is a measure of the relative magnitude of the coupling between the components; larger is the value of σ_k, stronger is the coupling between the components. For $\sigma = 10$, the curves for the three components are much closer to each other than for $\sigma = 0$. The case $\sigma = 0$ implies that the three components are decoupled. For the case $\sigma \to \infty$, the curves for the components would merge into a single curve.

Figures 2 and 3 are for a long solid cylinder and a solid sphere, respectively. The curves in these figures follow the same general trend as those in Fig. 1 for a slab, except they are slightly shrunk in the time scale. The crossover of the curves for $\sigma = 0$ and $\sigma = 1$ for $\theta_2(0, \tau)$ is apparent in Figs. 2 and 3.

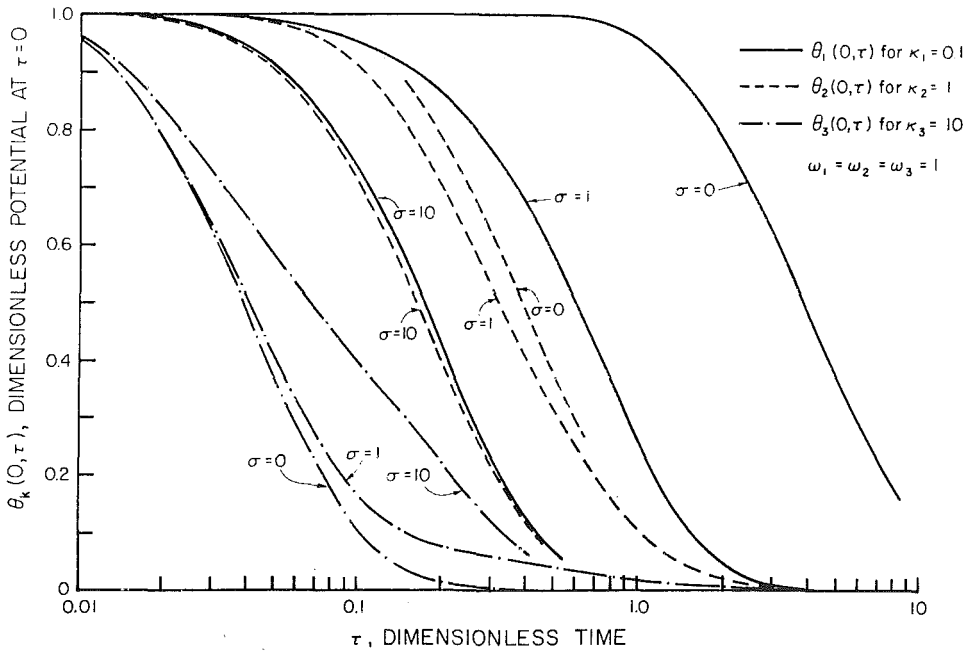

Fig. 1 Dimensionless potentials, $\theta_k(0, \tau)$, at the surface $x = 0$ of a slab as a function of dimensionless time, τ, for each of the three components

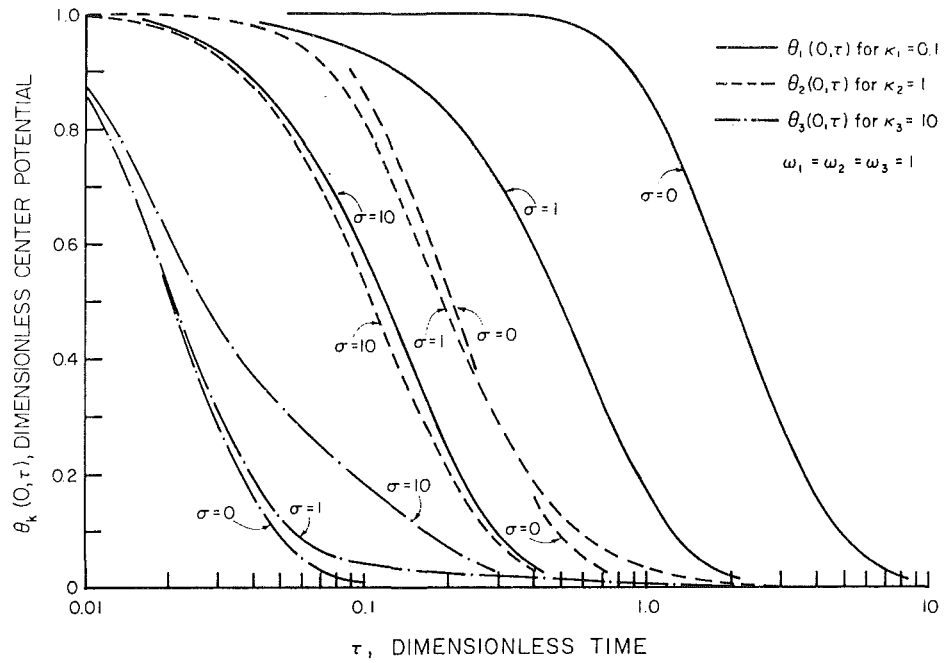

Fig. 2 Dimensionless potentials, θ_k (0, τ), at the center of a long solid cylinder as a function of dimensionless time, τ, for each of the three components

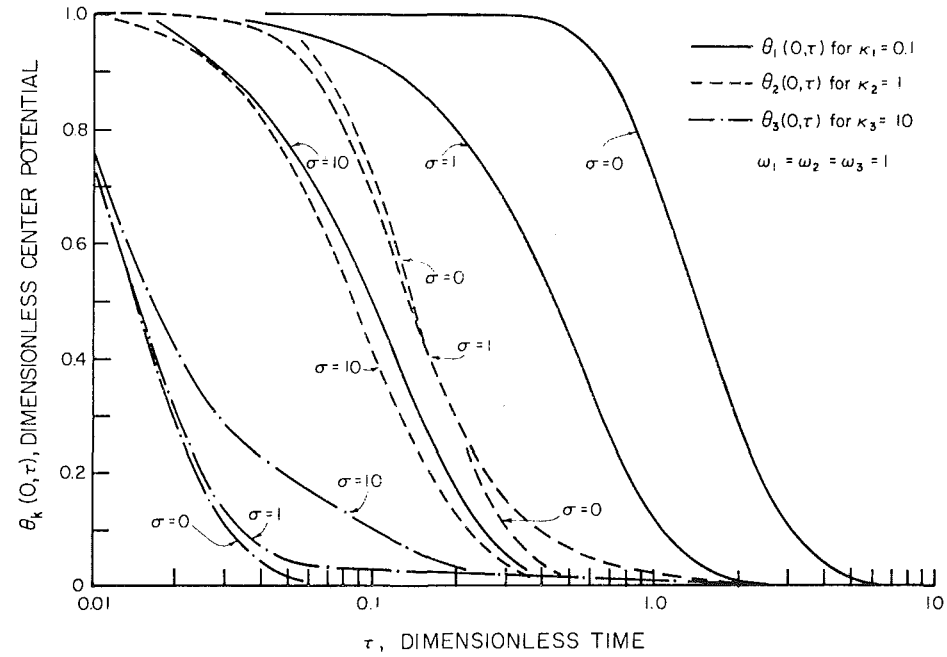

Fig. 3 Dimensionless potentials, θ_k (0, τ), at the center of a solid sphere as a function of dimensionless time, τ, for each of the three components

Conclusion

A methodology is presented for analytical solution of heat or mass diffusion problems of finite heterogeneous media characterized by a set of partial differential equations for the potentials T_k (x, t), (k = 1, 2, . . . , n), coupled through source-sink terms. The application of the above general theory illustrated with numerical examples.

References

1 Nicolis, G., and Prigogine, I., *Self-Organization in Nonequilibrium Systems,* John Wiley and Sons, New York, 1977.

2 Rubinstein, L. I., *Temperature Field in Oil Saturated Layers* (in Russian), Nedra Press, Moscow, 1972.

3 Mikhailov, M. D., "Splitting Up of Heat Conduction Problems," *Letters in Heat and Mass Transfer,* Vol. 4, 1977, pp. 163-166.

4 Anzelius, A., "Uber Erwärmüng durchströmender Medien," *ZAMM,* Aug. 1926.

5 Tikhonov, A. N., Zukhovitskii, A. A., and Zabezinskii, Ja. L., "Gas Absorption From an Air Flow by a Grain Material Layer," *Journal of Physical Chemistry,* Vol. 20, No. 10, 1946 (in Russian).

6 Brailsford, A. D., and Major, K. G., "The Thermal Conductivity of Aggregates of Several Phases, Including Porous Materials," *Brit. J. Appl. Phys.,* Vol. 15, 1964, pp. 313-319.

7 Barrenblatt, G. I., and Zeltov, Ju. P., "On the Basic Equations of Filtration of Homogeneous Liquids in Cracked Media," *Dokl. AN SSSR,* Vol. 132, No. 3, 1960 (in Russian).

8 Mikhailov, M. D., "Mass and Heat Transfer in Capillary Porous Body in Drying Processes," in *Mathematical and Physical Problems of Heat Mass Transfer,* The Institute of Heat and Mass Transfer, AS BSSR, Minsk, USSR, 1973, pp. 166-188.

Journal of Heat Transfer

Technical Notes

This section contains shorter technical papers. These shorter papers will be subjected to the same review process as that for full papers.

The Thermal Response of Heated, Levitated Coal Particles

R. E. Peck[1] and M. A. Pollock[2]

Introduction

A flow reactor employing aerodynamic levitation has recently been developed to study the combustion behavior of single, isolated coal particles. In the past we have used the apparatus to obtain measurements of temperatures and burning rates of levitated coal particles for a variety of experimental conditions. The purpose of this work is to assemble an elementary coal combustion model that will enable us to analyze the thermal response of the heated coal particles. The predicted particle temperature history is compared to the experimental results to indicate the role of heat- and mass-transfer processes during devolatilization, ignition, and combustion of coal particles.

Experimental

The aerodynamic levitation flow reactor (ALFR) system, described fully elsewhere [1], is illustrated in Fig. 1. Spherical coal particles are floated within a vertical free jet on the axis of an electric resistance heating coil and exposed to a prescribed heating rate, reactant composition, temperature, and pressure. The coal samples are 2–6 mm dia pelletized coal spheres having an ASTM proximate analysis of 2.4 percent moisture, 33.5 percent volatile matter, 49.1 percent fixed carbon and 15 percent ash, and a heating value of 26,560 kJ/kg.

Experiments were conducted by releasing a particle on the jet axis, initiating the heater power, and recording the output of a IRCON Model 300T5HC automatic infrared pyrometer that was focused on the levitated coal sphere for the duration of the particle burnout time. The instrument output was calibrated for particle emissivity and transmission losses to provide a real-time indication of the particle temperature.

Theoretical

Here we develop a simplified mathematical model that enables us to calculate the transient temperature response of individual coal particles heated in the ALFR. The time-dependent energy equation of a coal particle of mass, m_p, specific heat, c_p, and temperature, T_P, subject to the present experimental conditions, can be expressed as

$$m_p c_p \frac{dT_p}{dt} = \dot{Q}_{\text{conv}} + \dot{Q}_{\text{rad}} - h_{sg}\frac{dm_v}{dt} + \Delta h_v \frac{dm_v}{dt} + \Delta h_c \frac{dm_c}{dt} \quad (1)$$

The terms on the right-hand side of equation (1) account for heat transfer due to the convection and radiation, the enthalpy of vaporization of the volatiles component, and the internal heat generation due to volatiles and carbon oxidation. Although the complex heat and mass transport and kinetic processes associated with coal combustion are not completely understood quantitatively, we have adopted conventional theory [2–5] to evaluate each contribution to the overall energy balance.

The gas-particle convective heat transfer, $\dot{Q}_{\text{conv}}$, employs a standard Nusselt number correlation for spheres [6] and includes a film theory correction for mass transfer. The average local gas temperature variation is determined from the convective heating by the coil and the particle and by heat release accompanying volatiles combustion and CO oxidation. For $\dot{Q}_{\text{rad}}$ the particle-gas radiation is considered negligible compared to the particle-coil and particle-wall

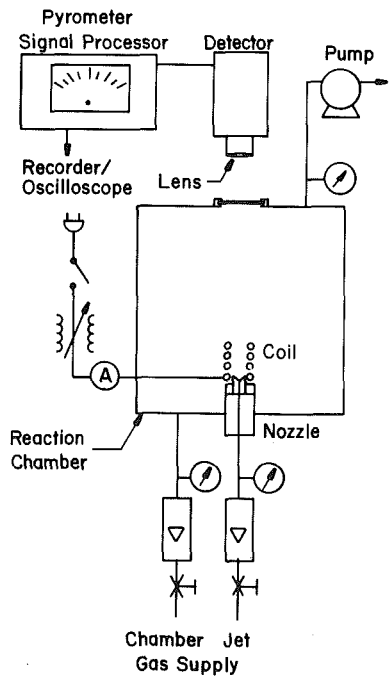

Fig. 1 Schematic diagram of apparatus

[1] Assistant Professor, Department of Mechanical Engineering, University of Kentucky, Lexington, Ky. 40506. Mem. ASME
[2] Graduate Research Assistant, Department of Mechanical Engineering, University of Kentucky, Lexington, Ky. 40506. Mem. ASME
Contributed by the Heat Transfer Division for publication in the JOURNAL OF HEAT TRANSFER. Manuscript received by the Heat Transfer Division April 30, 1982.

radiation. The wall temperature is maintained at 300K and the measured coil temperature history is used for the desired heating rate. Particle emissivity is allowed to vary with burnout as described in [2].

The contribution of the remaining terms in equation (1) all depend on the relative rates of devolatilization and combustion. The rate of volatiles evolution (dm_v/dt) is assumed to be first-order with respect to the remaining volatile matter with a measured [1] rate constant of $k_v = 1 \exp(-15000/RT_p)s^{-1}$ where the activation energy is in kJ/kmol and R is the gas constant. The char burnout is for the most part subject to kinetic control, rather than the usual mass-transfer limitations of large particles, due to the high gas-particle relative velocity. A rudimentary unreacted shrinking core model is used to determine the char reaction rate (dm_c/dt) that is assumed first-order with respect to oxygen concentration with the surface reaction rate taken as $k_c = 100 \exp(-75000/RT_p)$ kg_c/m^2s atm O_2. The latter stages of char burnout are also influenced by the rate of oxidizer diffusion through the porous ash layer on the particle exterior which is estimated by the methods in [5].

The reaction enthalpies needed to complete the evaluation of the chemical source terms in equation (1) are given below. Following [2], about 30 percent of the overall enthalpy of reaction for carbon oxidation ($\Delta h_c = -3.35 \times 10^4 kJ/kg_c$) is released during CO production at the particle surface, and the remaining 70 percent during CO oxidation in the gas phase. The enthalpy of reaction for the volatiles, Δh_v, is assigned a value of $-3 \times 10^4 kJ/kg_v$ so that the overall heat of combustion of the particle is consistent with the experimental value. The enthalpy of sublimation, h_{sg}, is set at 500 kJ/kg_v which is small compared to the combustion term. Most of the volatiles heat release occurs in the gas-phase, but during the final period of char burnout, the volatiles can be assumed to burn at the particle surface.

Equation (1) was numerically integrated using a variable-step, Runge-Kutta method to give the particle temperature history, $T_p(t)$. The particle mass, reactive suface area, and thermal properties were updated at the end of each integration step.

Results and Discussion

The results of the study consist of experimental and theoretical particle temperature histories for systematic variations in heating rate, particle size, and test atmosphere. Temperature profiles for 4.76-mm dia coal spheres heated in air at three different rates ($Q1 < Q2 < Q3$) are presented in Fig. 2. The steady-state radiation heat fluxes $Q1$, $Q2$, and $Q3$ are 48.5, 62.7, and 83 kW/m^2, respectively. The particle temperature initially rises at a rate of about 40°C s^{-1} until the sample reaches about 400°C when a higher heating rate of 100°C s^{-1} accompanies volatiles ignition and combustion. The temperature peaks shortly after carbon oxidation commences and devolatilization subsides and then decays during carbon burnout to a steady-state value of 650–750°C after about 150 s. Also, the peak temperature is higher and occurs earlier for the higher heating rates.

The general correspondence between measured and predicted temperatures confirms that the essential physical and chemical processes have been assimilated in the combustion model. The calculations indicate that the sequential particle heat generation occurs when the volatiles evolve and burn in the wake of the particle, and then the residual carbon is converted heterogeneously to CO and subsequently oxidized to CO_2 in the gas phase. Due to the high gas-particle relative velocity, the carbon burnout appears to be kinetically limited for the duration of the experiment except during the latter stages when diffusion of oxygen through the porous ash layer may become rate controlling.

The same test carried out in an argon atmosphere shows particle temperatures rising to about the same steady-state values indicated in Fig. 2 and well-represented by the model. The effect of increasing particle size, shown in Fig. 3, is to slow the overall heating rate due to the increased thermal mass of the sample and also to lower the peak and final temperature due to altered heat transfer rates.

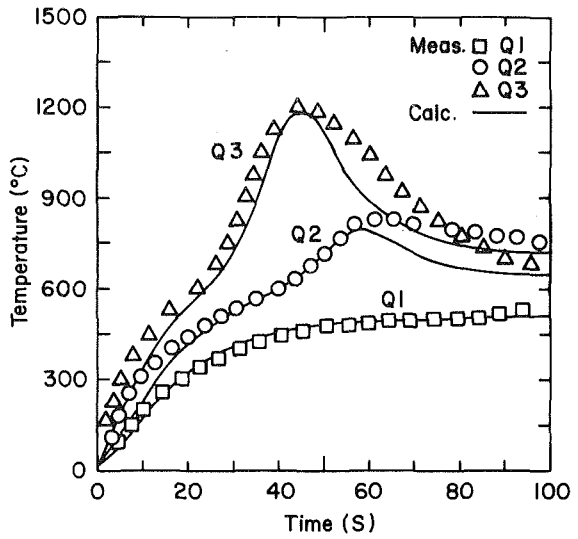

Fig. 2 Time-temperature variation of 4.76-mm coal particles in air (101 kPa) for different heat fluxes ($Q1 < Q2 < Q3$)

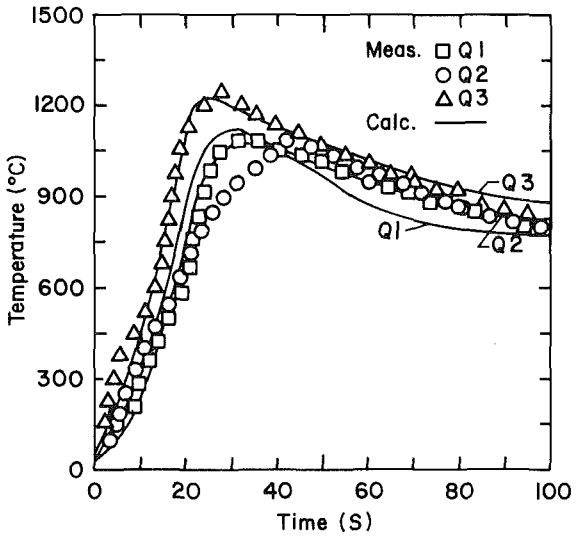

Fig. 3 Time-temperature variation of 6.35-mm coal particles in air (101 kPa) for different heat fluxes ($Q1 < Q2 < Q3$)

In summary, measured temperatures of burning levitated coal particles agree qualitatively with calculated values. This result confirms our ability to model the thermal-environmental conditions in the experimental system. Improved temperature estimates can be accomplished by better defining the gas velocity and temperature distributions and by adopting a more advanced char combustion model. The analysis further substantiates the adequacy of the experimental technique for investigating high-temperature, fluid-particle interactions and for studying heterogeneous reactions under kinetically controlled conditions.

Acknowledgment

We thank the National Science Foundation for supporting this work under Grant ENG 78-05564.

References

1 Peck, R. E., and Pollock, M. A., "Development of an Aerodynamic Levitation Technique to Study Coal Particle Combustion," *Fuel*, Vol. 60, 1981, pp. 727-731.

2 Baum, M. M., and Street, P. J., "Predicting the Combustion Behavior of Coal Particles," *Combustion Science and Technology*, Vol. 3, 1971, pp. 231-243.

3 Mulcahy, M. F. R., and Smith, I. W., "Kinetics of Combustion of Pulverized Fuel: A Review of Theory and Experiment," *Reviews of Pure and Applied Chemistry*, Vol. 19, 1969, pp. 81-108.

4 Field, M. A., Gill, D. W., Morgan, B. B., and Hawksley, P. G. W., *Combustion of Pulverized Coal*, BCURA, Leatherhead, England, 1967.

5 Laurendeau, N. M., "Heterogeneous Kinetics of Coal Char Gasification and Combustion," *Progress in Energy and Combustion Science*, Vol. 4, 1978, pp. 221-270.

6 Rowe, P. N., Claxton, K. T., and Lewis, J. B., "Heat and Mass Transfer from a Single Sphere in an Extensive Flowing Fluid," *Transactions of the Institute of Chemical Engineers*, Vol. 43, 1965, pp. T14-T31.

The Effect of a Concentric Radiating Cylinder on Liquid Spray Cooling in a Hot Gas Discharge

I. S. Habib[1]

Nomenclature

A = cylinder area
D = cylinder diameter
E = emissive power
$\overline{GG}, \overline{GS}$ = directed flux area; volume zone; volume and surface zones
h = convective heat-transfer coefficient
h_g = enthalpy of gas, h_d = enthalpy of droplets
K_i = total absorption coefficient for volume zone, V_i
L = cylinder length
L_e = mean beam length
$\dot{m}_g$ = mass flow rate of gas: $\dot{m}_d$ = mass flow rate of droplets, $\Sigma\ \dot{m}_d$ = total mass flow rate of droplets summed over sizes
P_s = static pressure, P_g = partial pressure of radiating components
$\overline{SS}$ = directed flux area, surface to surface zones
T = temperature, t = time
V_g = gas velocity: V_d = droplet velocity, V_i = zone volume
ϵ = surface emissivity
μ = droplet size in microns
σ = Stefan - Boltzmann constant

Subscripts

d = pertaining to droplet
e = entrance plane
g = gas
i = pertaining to volume and exterior surface zones i, gas region within interior cylinder
ii = pertains to interior surface zones
j, jj = exterior and interior zones, respectively, contributing to the energy exchange
0 = exterior cylinder, gas region between cylinder
s = surface of cylinder
u = exit plane of system
∞ = ambient

[1]Professor of Mechanical Engineering, The University of Michigan—Dearborn, Dearborn, Mich. 48128. Mem. ASME

Contributed by the Heat Transfer Division for publication in the JOURNAL OF HEAT TRANSFER. Manuscript received by the Heat Transfer Division November 13, 1981.

Introduction

The rapid cooling of a hot gas discharge such as a product of combustion in a gas turbine at high temperature and pressure represents a major constraint on the system design requirements. One factor which contributes to the cooling in such situations is the radiative gas emission to the interior walls of the surrounding enclosure. Gas emittance is generally low and, accordingly, the radiative cooling rate is also low. The methods by which gas emittance can be increased are quite limited. At times, radiation plates [1] have been inserted in a hot flowing medium to improve its heat-transfer capability, and seeding a gas with particles having high emissivity can have some but limited effects in augmenting the emission from the gas. Liquid sprays injected in a flowing hot gas stream is a well-known and effective way [2, 3] for cooling the gas in a very short distance. It is generally used where the available heat-transfer surfaces are inadequate in size. In the present work, an analysis is presented to simulate the effects of inserting a concentric tube in a circular duct in which a hot gas discharge is flowing and is cooled by the injection of liquid sprays and by heat exchange to the surrounding walls. The external tube wall is considered to lose heat to the ambient by convection and radiation. The zonal method used in the analysis is one in which two surface zones (exterior and interior) are identified, along with one volume zone. A single volume zone implies that the gas flowing in the interior tube and in the annulus undergoes enough mixing so that at every section the gas is considered to be at one temperature, a situation that can result by the insertion of a porous cylinder. It is felt that a single volume zone can adequately reveal the significance of the interior cylinder while maintaining the complexity of the problem at a reasonable level.

Analysis

The model chosen in this analysis is represented in Fig. 1. A hot product of combustion is discharged into the concentric cylinders system and at the same time cold water sprays are introduced at the entrance at a continuous rate. The coupled interaction of heat and mass transfer between the gaseous medium and the liquid sprays induces continuous changes in the direction of the flow for the gas and the droplets. The droplets are considered spherical and the flow is treated as a quasi-steady transport of heat and mass with no shattering or coalescence of the droplets. The droplet distribution is represented by a log normal relation [2] where five sizes were conveniently chosen such that the percent of drops smaller than a given radius is equal to 10, 30, 50, 70, and 90 percent. The number of drops were chosen so that each size contained 20 percent of the total liquid mass. The use of the zonal

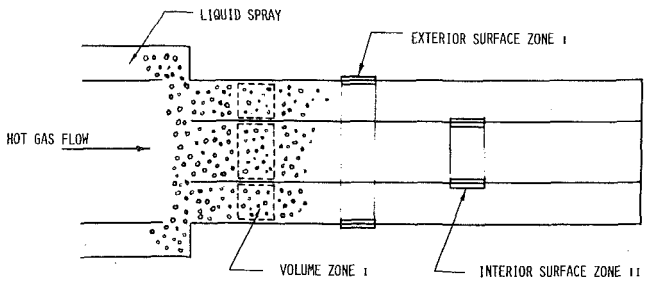

Fig. 1 The model chosen for the study

References

1 Peck, R. E., and Pollock, M. A., "Development of an Aerodynamic Levitation Technique to Study Coal Particle Combustion," *Fuel*, Vol. 60, 1981, pp. 727-731.

2 Baum, M. M., and Street, P. J., "Predicting the Combustion Behavior of Coal Particles," *Combustion Science and Technology*, Vol. 3, 1971, pp. 231-243.

3 Mulcahy, M. F. R., and Smith, I. W., "Kinetics of Combustion of Pulverized Fuel: A Review of Theory and Experiment," *Reviews of Pure and Applied Chemistry*, Vol. 19, 1969, pp. 81-108.

4 Field, M. A., Gill, D. W., Morgan, B. B., and Hawksley, P. G. W., *Combustion of Pulverized Coal*, BCURA, Leatherhead, England, 1967.

5 Laurendeau, N. M., "Heterogeneous Kinetics of Coal Char Gasification and Combustion," *Progress in Energy and Combustion Science*, Vol. 4, 1978, pp. 221-270.

6 Rowe, P. N., Claxton, K. T., and Lewis, J. B., "Heat and Mass Transfer from a Single Sphere in an Extensive Flowing Fluid," *Transactions of the Institute of Chemical Engineers*, Vol. 43, 1965, pp. T14-T31.

The Effect of a Concentric Radiating Cylinder on Liquid Spray Cooling in a Hot Gas Discharge

I. S. Habib[1]

Nomenclature

A = cylinder area
D = cylinder diameter
E = emissive power
$\overline{GG}, \overline{GS}$ = directed flux area; volume zone; volume and surface zones
h = convective heat-transfer coefficient
h_g = enthalpy of gas, h_d = enthalpy of droplets
K_i = total absorption coefficient for volume zone, V_i
L = cylinder length
L_e = mean beam length
$\dot{m}_g$ = mass flow rate of gas: $\dot{m}_d$ = mass flow rate of droplets, $\Sigma\ \dot{m}_d$ = total mass flow rate of droplets summed over sizes
P_s = static pressure, P_g = partial pressure of radiating components
$\overline{SS}$ = directed flux area, surface to surface zones
T = temperature, t = time
V_g = gas velocity: V_d = droplet velocity, V_i = zone volume
ϵ = surface emissivity
μ = droplet size in microns
σ = Stefan - Boltzmann constant

Subscripts

d = pertaining to droplet
e = entrance plane
g = gas
i = pertaining to volume and exterior surface zones i, gas region within interior cylinder
ii = pertains to interior surface zones
j, jj = exterior and interior zones, respectively, contributing to the energy exchange
0 = exterior cylinder, gas region between cylinder
s = surface of cylinder
u = exit plane of system
∞ = ambient

[1]Professor of Mechanical Engineering, The University of Michigan—Dearborn, Dearborn, Mich. 48128. Mem. ASME

Contributed by the Heat Transfer Division for publication in the JOURNAL OF HEAT TRANSFER. Manuscript received by the Heat Transfer Division November 13, 1981.

Introduction

The rapid cooling of a hot gas discharge such as a product of combustion in a gas turbine at high temperature and pressure represents a major constraint on the system design requirements. One factor which contributes to the cooling in such situations is the radiative gas emission to the interior walls of the surrounding enclosure. Gas emittance is generally low and, accordingly, the radiative cooling rate is also low. The methods by which gas emittance can be increased are quite limited. At times, radiation plates [1] have been inserted in a hot flowing medium to improve its heat-transfer capability, and seeding a gas with particles having high emissivity can have some but limited effects in augmenting the emission from the gas. Liquid sprays injected in a flowing hot gas stream is a well-known and effective way [2, 3] for cooling the gas in a very short distance. It is generally used where the available heat-transfer surfaces are inadequate in size. In the present work, an analysis is presented to simulate the effects of inserting a concentric tube in a circular duct in which a hot gas discharge is flowing and is cooled by the injection of liquid sprays and by heat exchange to the surrounding walls. The external tube wall is considered to lose heat to the ambient by convection and radiation. The zonal method used in the analysis is one in which two surface zones (exterior and interior) are identified, along with one volume zone. A single volume zone implies that the gas flowing in the interior tube and in the annulus undergoes enough mixing so that at every section the gas is considered to be at one temperature, a situation that can result by the insertion of a porous cylinder. It is felt that a single volume zone can adequately reveal the significance of the interior cylinder while maintaining the complexity of the problem at a reasonable level.

Analysis

The model chosen in this analysis is represented in Fig. 1. A hot product of combustion is discharged into the concentric cylinders system and at the same time cold water sprays are introduced at the entrance at a continuous rate. The coupled interaction of heat and mass transfer between the gaseous medium and the liquid sprays induces continuous changes in the direction of the flow for the gas and the droplets. The droplets are considered spherical and the flow is treated as a quasi-steady transport of heat and mass with no shattering or coalescence of the droplets. The droplet distribution is represented by a log normal relation [2] where five sizes were conveniently chosen such that the percent of drops smaller than a given radius is equal to 10, 30, 50, 70, and 90 percent. The number of drops were chosen so that each size contained 20 percent of the total liquid mass. The use of the zonal

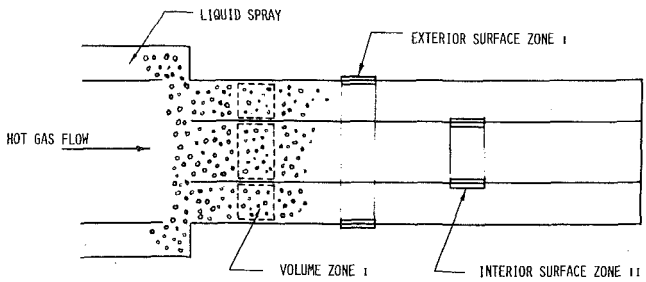

Fig. 1 The model chosen for the study

method proved successful [4-6] in accomodating real gas effects including luminous radiation; accordingly, it is also used in the present analysis. The direction of flow is subdivided into a number of increments. Each increment involves two surface zones and one volume zone. The inner surface zone is examined separately in order to assess the role of such an internal cylinder as a heat sink. Should the interior cylinder be at a temperature below the gas temperature due to radiative interchange directly to the exterior cylinder, such a cylindrical surface, then, induces an additional heat loss from the gas and, hence, the overall gas cooling is augmented. It is important to realize also that the inner cylinder plays the role of a radiation shield for the gas flowing within it, and, in that respect, it has a tendency to reduce the heat transfer from the gas.

An energy balance on an exterior surface zone, i, yields

$$Q_{s,i} = \sum_j \overline{S_j S_i} E_{s,j} + \sum_{jj} \overline{S_{jj} S_i} E_{s,jj} + \overline{S_e S_i} E_e + \overline{S_u S_i} E_u$$

$$+ \sum_j \overline{G_{j,0} S_i} E_{g,j} - A_0 E_{s,i} + h_i A_0 (T_{g,i} - T_{s,i}) \quad (1)$$

$Q_{s,i}$ represents the exterior wall heat-transfer rate leaving the exterior surface by convection and radiation, i.e.

$$Q_{s,i} = h_0 A_0 (T_{s,i} - T_\infty) + \epsilon A_0 \sigma (T^4{}_{s,i} - T^4{}_\infty) \quad (2)$$

The rest of terms in equation (1), respectively, are: exterior tube wall emission from surface zones, j, interior tube wall emission from surface zones, jj, inlet surface emission, exit surface emission, volume zones emission from exterior gas region, emission of exterior wall zone, i, and the convection from the exterior gas region to the exterior surface zone, i. An energy balance on an interior surface zone, ii, gives

$$\sum_j \overline{S_j S_{ii}} E_{s,j} + \sum_{jj} \overline{S_{jj} S_{ii}} E_{s,jj} + \overline{S_{e,i} S_{ii}} E_e + \overline{S_{u,i} S_{ii}} E_u$$

$$+ \sum_j \overline{G_{j,0} S_{ii}} E_{g,i} + \sum_j \overline{G_{j,i} S_{ii}} E_{g,j} - A_i E_{s,ii}$$

$$+ 2 h_i A_i [T_{g,i} - T_{s,ii}] = 0 \quad (3)$$

The terms in equation (3) respectively are: exterior tube wall emission from surface zones, j, the interior tube wall emission from surface zones, jj, inlet surface emission, exit surface emission, volume zones emission from exterior gas region, volume zones emission from interior gas region, emission from interior wall zone, ii, and the convection from the exterior and the interior gas regions to the interior wall surface zone, ii. An energy balance on a volume zone yields

$$[\dot{m}_g (h_g + V_g^2/2)]_1 + [\Sigma \dot{m}_d (h_d + V_d^2/2)]_1 + \sum_j \overline{G_j G_i} E_{g,i}$$

$$+ \Sigma_j \overline{S_j G_i} E_{s,j} + \sum_{jj} \overline{S_{jj} G_i} E_{s,jj} + \overline{S_e G_i} E_e$$

$$+ \overline{S_u G_0} E_u - 4 K_i V_i E_{g,i} - 2 h_i A_i (T_{g,i} - T_{s,ii}) - h_i A_0 [T_{g,i} - T_{s,i}]$$

$$= [\dot{m}_g (h_g + V_g^2/2)]_2 + [\Sigma \dot{m}_d (h_d + V_d^2/2]_2$$

$$+ d/dt [\Sigma m_d (h_d + V_d^2/2)]_i \quad (4)$$

The terms in equation (4) represent, respectively: gas stream energy at inlet, droplets energy at inlet, emission of volume zones, j, emission of exterior surface zones, j, emission of interior surface zones, jj, inlet surface emission, outlet surface emission, emission of volume zone, i, and the convection terms between the gas and the interior and the exterior surfaces. The terms on the right hand side are: the gas stream energy at outlet, droplets energy at outlet, and the time rate of change of droplets energy within the zone, i.

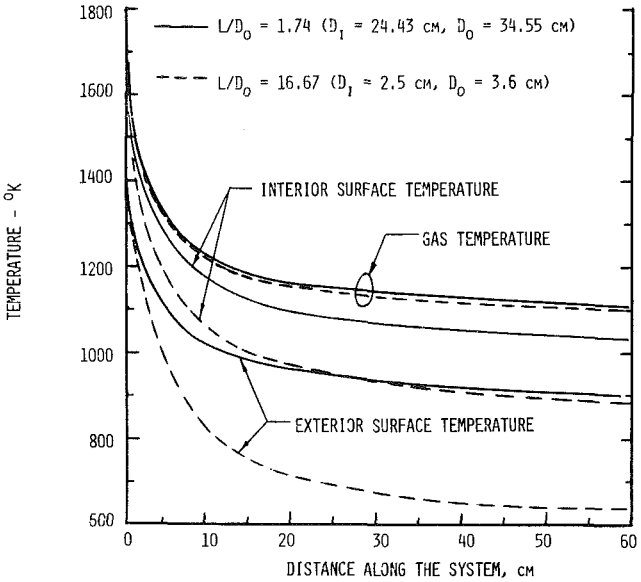

Fig. 2 Temperature of system along the flow: initial conditions, $L/G = 0.2$, $T_g = T_{ii} = 1667°K$, $V_G = 222.5$ M/S, $P_s = 19$ ATM., $T_{s,i} = 1400°K$

The radiative properties and other pertinent conservation equations such as the continuity, momentum and equation of state for the gas stream and the heat, momentum, and mass transfer relations for the droplets have been presented before in reference [2, 3]. The gaseous properties are those recommended originally in reference [4, 5].

Results and Conclusions

The coupled conservation equations for the gas, the concentric cylinders, and the droplets were solved by iteration for each zone as discussed in [2, 3]. However, in the present problem, there is one additional equation representing the energy balance on the interior surface zones. The zone width varied in size in the direction of flow but did not exceed 0.2 cm for a system 60-cm long. For the first zone, changes in the gas and the spray conditions were arbitrarily assumed; however, for the other zones, initial assumptions of such changes were the changes of the previous step. Using the assumed values, the actual changes were then calculated and compared with the assumed changes. If the calculated and the assumed values did not differ more than 2 percent, the calculated values were considered to be correct. Certain surface to surface fluxes, specifically the ones into the exterior surface of the inner cylinder, were evaluated utilizing some of the shape factor relations presented in [7]. A high and a low convection heat-transfer coefficient over the exterior cylinder were used along with two exterior cylinder diameters, 3.6 cm and 34.55 cm, while maintaining the length at 60 cm. The cylinder emissivities were assumed to be unity. The interior convection heat-transfer coefficient was calculated locally for each zone using the turbulent flow relations in tubes [8]. The initial conditions chosen are representative of a product of combustion discharged from a high-pressure gas turbine where surface and gas radiation can be expected to play an important role in the heat exchange. A liquid to gas ratio of

Table 1 Gas mass flow rate and gas temperature along the duct

	$L/D_0 = 1.74$				$L/D_0 = 16.67$			
	Gas flow rate Kg/s		Gas temperature °K		Gas flow rate Kg/s		Gas temperature °K	
X_{cm}	With inner cyliner	No inner cylinder	With inner cylinder	No inner cylinder	With inner cylinder	No inner cylinder	With inner cylinder	No inner cylinder
0	84.345	84.345	1667	1667	0.911	0.911	1667	1667
30	97.869	97.872	1145	1146	1.057	1.061	1139	1142
60	99.177	99.189	1108	1111	1.071	1.079	1098	1103

0.2 was chosen although frequently a higher ratio has been employed in practice. This choice was made in order to maintain a temperature level high enough so radiation terms could be significant. The liquid spray injected at 278 K is considered to have a mass mean radius of 50 microns with a standard deviation of 2.3. This yields the following sizes in microns from the log-normal distribution curve: 17.19, 32.32, 50.00, 77.36, and 145.45μ.

Figure 2 shows the temperature of the gas, the interior cylinder, and the exterior cylinder in the direction of flow for a high exterior convection coefficient (900 W/m^2 – °C) and for two L/D ratios. As depicted, the interior cylinder did exhibit a radiative cooling effect as a result of the cooler exterior cylinder and of the exit plane temperature taken to be 278°K. The cooling effect is more pronounced for the high L/D ratio (small exterior diameter). This can be interpreted as a consequence of two factors, namely (*a*) a lower exterior surface temperature which is due mostly to a lower interior convection coefficient, and (*b*) a lower gas emittance attributed to a lower value of $P_g L_e$. This second factor tends to reduce the gas shielding effect between the two cylinders. Although there appears to be a marked difference between the temperatures of the two cylinders for a high exterior convection coefficient, the exit gas temperature was only 5 degrees below that obtained when the inner cylinder was not present. This may appear to be unexpected. However, when the cooling rate imparted to the gas by the cold liquid spray is examined along with the duration of the gas in the cylinders, it is found that radiative contribution to gas cooling by the inner cylinder is esssentially insignificant relative to the spray cooling effect. The results for the lower exterior convective coefficient (60 W/m^2 – °C) reflected even a lesser significane to the effect of the inner cylinder. Accordingly, with liquid spray cooling for such systems, the use of a concentric cylinder to augment the heat-transfer rates from the gas is unjustified. It is important to emphasize, however, that for systems operating at a similar temperature level but with a much lower gas flow rate, the present results do show that the interior radiating cylinder can be of significance in augmenting the heat-transfer rate from the flowing hot gas. In order to further show the order of magnitude of other changes induced by the presence of the inner cylinder, tabulated results are shown below for the two L/D ratios considered. The gas flow rate indicated represents the initial value at duct entrance plus the amount vaporized from the liquid spray along the flow direction.

Of importance is the level of the gas mass flow rate which can experience a higher cooling effect in the presence of the inner cylinder. Although arriving at an optimum value requires an analysis in which the location of the inner cylinder (and thus its radius) is a variable parameter, calculations were conducted for the present work with $l/D = 16.67$. It is found that for the gas to experience an augmented drop of 20 percent in its temperature (from an overall drop of 556°C to 667°C) between the duct entrance and duct exit, the gas mass flow rate should be at 3.33×10^{-3}kg/s. For this flow rate, the Reynolds number will be in the laminar flow region.

References

1 Mori, Y., Taira, T., and Watanabe, K., "Heat Exchanger Augmentation by Radiation Plates," ASME paper 76-HT-3, 1976.

2 Habib, I. S., "The Interaction of a Hot Gas Flow and a Cold Liquid Spray in Channels," ASME JOURNAL OF HEAT TRANSFER, Vol. 98, 1976, pp. 421-426.

3 Habib, I. S., "Spray Quenching in a Ventilated Duct Fire," ASME JOURNAL OF HEAT TRANSFER, Vol. 102, 1980, pp. 110-114.

4 Johnson, R. R., and Beer, J. M., "The Zone Method Analysis of Radiant Heat Transfer: A Model for Luminous Radiation," *Journal of the Institute of Fuel*, Sept. 1973.

5 Taylor, P. D., and Foster, P. J., "The Total Emissivities of Luminous and Non-Luminous Flames," *International Journal of Heat and Mass Transfer*, Vol. 17, 1974, pp. 1591-1605.

6 Taylor, P. D., and Foster, P. J., "Some Gray Gas Weighting Coefficient for CO_2 - H_2O Soot Mixtures," *International Journal of Heat and Mass Transfer*, Vol. 18, 1975, pp. 1331-1332.

7 Naraghi, M. H. N., and Chung, B. T. F., "Radiation Configuration Factors Between Disks and a Class of Axisymmetric Bodies," ASME Paper 81-HT-56, 1981.

8 Kays, W. M., and Crawford, M. E., *Convective Heat and Mass Transfer*, McGraw-Hill, New York, 1980.

Radiation View Factors by Finite Elements

T. J. Chung[1] and J. Y. Kim[2]

1 Introduction

Calculations of view factors in radiative heat transfer are well documented in standard texts [1, 2]. Typically, various analytical methods and contour integral techniques are used to calculate view factors. For extremely irregular geometries, however, these methods are not well suited and it is shown here that finite elements are quite versatile in this respect. Gaussian quadrature integration is utilized together with finite element geometries [3].

2 Basic Geometric Data

The view factors between various surfaces are given as follows (Fig. 1(*a*))

$$F_{A-B} = \frac{1}{A_A} \int_{A_A} \int_{A_B} \frac{\cos\theta_A \cos\theta_B}{\pi L^2} \, dA_A \, dA_B \qquad (1)$$

To evaluate the integral we establish the coordinate system as shown in Fig. 1(*b*). Let us first consider the unit vector $\mathbf{e}_{A12}$ in the direction from node 1 to node 2,

$$\mathbf{e}_{A12} = \lambda_{Ai} \, \mathbf{i}_i \qquad (2)$$

where

$$\lambda_{A1} = \frac{X_{A21}}{L_{A12}}, \quad \lambda_{A2} = \frac{Y_{A21}}{L_{A12}}, \quad \lambda_{A3} = \frac{Z_{A21}}{L_{A12}}$$

$$L_{A12} = [(X_{A2} - X_{A1})^2 + (Y_{A2} - Y_{A1})^2 + Z_{A2} - Z_{A1})^2]^{\frac{1}{2}}$$

[1] Professor and Chairman, Department of Mechanical Engineering, The University of Alabama in Huntsville, Huntsville, Ala. 35899. Mem. ASME.

[2] Graduate Assistant, Department of Mechanical Engineering, The University of Alabama in Huntsville.

Contributed by the Heat Transfer Division for publication in the JOURNAL OF HEAT TRANSFER. Manuscript received by the Heat Transfer Division February 11, 1982.

Table 1 Gas mass flow rate and gas temperature along the duct

	$L/D_0 = 1.74$				$L/D_0 = 16.67$			
	Gas flow rate Kg/s		Gas temperature °K		Gas flow rate Kg/s		Gas temperature °K	
X_{cm}	With inner cyliner	No inner cylinder	With inner cylinder	No inner cylinder	With inner cylinder	No inner cylinder	With inner cylinder	No inner cylinder
0	84.345	84.345	1667	1667	0.911	0.911	1667	1667
30	97.869	97.872	1145	1146	1.057	1.061	1139	1142
60	99.177	99.189	1108	1111	1.071	1.079	1098	1103

0.2 was chosen although frequently a higher ratio has been employed in practice. This choice was made in order to maintain a temperature level high enough so radiation terms could be significant. The liquid spray injected at 278 K is considered to have a mass mean radius of 50 microns with a standard deviation of 2.3. This yields the following sizes in microns from the log-normal distribution curve: 17.19, 32.32, 50.00, 77.36, and 145.45μ.

Figure 2 shows the temperature of the gas, the interior cylinder, and the exterior cylinder in the direction of flow for a high exterior convection coefficient (900 W/m^2 – °C) and for two L/D ratios. As depicted, the interior cylinder did exhibit a radiative cooling effect as a result of the cooler exterior cylinder and of the exit plane temperature taken to be 278°K. The cooling effect is more pronounced for the high L/D ratio (small exterior diameter). This can be interpreted as a consequence of two factors, namely (*a*) a lower exterior surface temperature which is due mostly to a lower interior convection coefficient, and (*b*) a lower gas emittance attributed to a lower value of $P_g L_e$. This second factor tends to reduce the gas shielding effect between the two cylinders. Although there appears to be a marked difference between the temperatures of the two cylinders for a high exterior convection coefficient, the exit gas temperature was only 5 degrees below that obtained when the inner cylinder was not present. This may appear to be unexpected. However, when the cooling rate imparted to the gas by the cold liquid spray is examined along with the duration of the gas in the cylinders, it is found that radiative contribution to gas cooling by the inner cylinder is esssentially insignificant relative to the spray cooling effect. The results for the lower exterior convective coefficient (60 W/m^2 – °C) reflected even a lesser significane to the effect of the inner cylinder. Accordingly, with liquid spray cooling for such systems, the use of a concentric cylinder to augment the heat-transfer rates from the gas is unjustified. It is important to emphasize, however, that for systems operating at a similar temperature level but with a much lower gas flow rate, the present results do show that the interior radiating cylinder can be of significance in augmenting the heat-transfer rate from the flowing hot gas. In order to further show the order of magnitude of other changes induced by the presence of the inner cylinder, tabulated results are shown below for the two L/D ratios considered. The gas flow rate indicated represents the initial value at duct entrance plus the amount vaporized from the liquid spray along the flow direction.

Of importance is the level of the gas mass flow rate which can experience a higher cooling effect in the presence of the inner cylinder. Although arriving at an optimum value requires an analysis in which the location of the inner cylinder (and thus its radius) is a variable parameter, calculations were conducted for the present work with $l/D = 16.67$. It is found that for the gas to experience an augmented drop of 20 percent in its temperature (from an overall drop of 556°C to 667°C) between the duct entrance and duct exit, the gas mass flow rate should be at 3.33×10^{-3}kg/s. For this flow rate, the Reynolds number will be in the laminar flow region.

References

1 Mori, Y., Taira, T., and Watanabe, K., "Heat Exchanger Augmentation by Radiation Plates," ASME paper 76-HT-3, 1976.

2 Habib, I. S., "The Interaction of a Hot Gas Flow and a Cold Liquid Spray in Channels," ASME JOURNAL OF HEAT TRANSFER, Vol. 98, 1976, pp. 421-426.

3 Habib, I. S., "Spray Quenching in a Ventilated Duct Fire," ASME JOURNAL OF HEAT TRANSFER, Vol. 102, 1980, pp. 110-114.

4 Johnson, R. R., and Beer, J. M., "The Zone Method Analysis of Radiant Heat Transfer: A Model for Luminous Radiation," *Journal of the Institute of Fuel*, Sept. 1973.

5 Taylor, P. D., and Foster, P. J., "The Total Emissivities of Luminous and Non-Luminous Flames," *International Journal of Heat and Mass Transfer*, Vol. 17, 1974, pp. 1591-1605.

6 Taylor, P. D., and Foster, P. J., "Some Gray Gas Weighting Coefficient for CO_2 - H_2O Soot Mixtures," *International Journal of Heat and Mass Transfer*, Vol. 18, 1975, pp. 1331-1332.

7 Naraghi, M. H. N., and Chung, B. T. F., "Radiation Configuration Factors Between Disks and a Class of Axisymmetric Bodies," ASME Paper 81-HT-56, 1981.

8 Kays, W. M., and Crawford, M. E., *Convective Heat and Mass Transfer*, McGraw-Hill, New York, 1980.

Radiation View Factors by Finite Elements

T. J. Chung[1] and J. Y. Kim[2]

1 Introduction

Calculations of view factors in radiative heat transfer are well documented in standard texts [1, 2]. Typically, various analytical methods and contour integral techniques are used to calculate view factors. For extremely irregular geometries, however, these methods are not well suited and it is shown here that finite elements are quite versatile in this respect. Gaussian quadrature integration is utilized together with finite element geometries [3].

2 Basic Geometric Data

The view factors between various surfaces are given as follows (Fig. 1(*a*))

$$F_{A-B} = \frac{1}{A_A} \int_{A_A} \int_{A_B} \frac{\cos\theta_A \cos\theta_B}{\pi L^2} \, dA_A \, dA_B \qquad (1)$$

To evaluate the integral we establish the coordinate system as shown in Fig. 1(*b*). Let us first consider the unit vector $\mathbf{e}_{A12}$ in the direction from node 1 to node 2,

$$\mathbf{e}_{A12} = \lambda_{Ai} \, \mathbf{i}_i \qquad (2)$$

where

$$\lambda_{A1} = \frac{X_{A21}}{L_{A12}}, \quad \lambda_{A2} = \frac{Y_{A21}}{L_{A12}}, \quad \lambda_{A3} = \frac{Z_{A21}}{L_{A12}}$$

$$L_{A12} = [(X_{A2} - X_{A1})^2 + (Y_{A2} - Y_{A1})^2 + Z_{A2} - Z_{A1})^2]^{\frac{1}{2}}$$

[1] Professor and Chairman, Department of Mechanical Engineering, The University of Alabama in Huntsville, Huntsville, Ala. 35899. Mem. ASME.

[2] Graduate Assistant, Department of Mechanical Engineering, The University of Alabama in Huntsville.

Contributed by the Heat Transfer Division for publication in the JOURNAL OF HEAT TRANSFER. Manuscript received by the Heat Transfer Division February 11, 1982.

$$X_{A21} = X_{A2} - X_{A1}, \text{ etc.}$$

$$\mathbf{e}_{A14} = \mu_{Ai}\,\mathbf{i}_i \tag{3}$$

where

$$\mu_{A1} = \frac{X_{A41}}{L_{A14}}, \quad \mu_{A2} = \frac{Y_{A41}}{L_{A14}}, \quad \mu_{A3} = \frac{Z_{A41}}{L_{A14}}$$

$$L_{A14} = [(X_{A4} - X_{A1})^2 + (Y_{A4} - Y_{A1})^2 + (Z_{A4} - Z_{A1})^2]^{\frac{1}{2}}$$

$$X_{A4} = X_{A4} - X_{A1}, \text{ etc.}$$

The unit normal vector out of the surface, A, is

$$\mathbf{n}_A = \mathbf{e}_{A12} \times \mathbf{e}_{A14} = \nu_{Ai}\,\mathbf{i}_i \tag{4}$$

where

$$\nu_{A1} = \lambda_{A2}\,\mu_{A3} - \lambda_{A3}\,\mu_{A2}$$

$$\nu_{A2} = \lambda_{A3}\,\mu_{A1} - \lambda_{A1}\,\mu_{A3}$$

$$\nu_{A3} = \lambda_{A1}\,\mu_{A2} - \lambda_{A2}\,\mu_{A1}$$

Likewise, for the surface, B, the unit vectors $\mathbf{e}_{B12}$, $\mathbf{e}_{B14}$, and $\mathbf{n}_B$ can be derived as

$$\mathbf{e}_{B12} = \lambda_{Bi}\,\mathbf{i}_i \tag{5}$$

$$\mathbf{e}_{B14} = \mu_{Bi}\,\mathbf{i}_i \tag{6}$$

$$\mathbf{n}_B = \mathbf{e}_{B12} \times \mathbf{e}_{B14} = \nu_{Bi}\,\mathbf{i}_i \tag{7}$$

Furthermore, the length, L, connecting the two surfaces, A and B, at arbitrary points can be defined along with the angles θ_A and θ_B measured from their normals to the surfaces by calculating the unit vector along this line L,

$$\mathbf{e}_{AB} = \kappa_{ABi}\,\mathbf{i}_i \tag{8}$$

$$\cos\theta_A = \frac{\mathbf{n}_A \cdot \mathbf{e}_{AB}}{|\mathbf{n}_A||\mathbf{e}_{AB}|}, \cos\theta_B = \frac{\mathbf{n}_B \cdot \mathbf{e}_{BA}}{|\mathbf{n}_B||\mathbf{e}_{BA}|} \tag{9}$$

3 Coordinate Transformations Between Local and Global Coordinates

The local and global coordinates for the surface, A, are related by

$$x_i^A = a_{ij}^A\,X_j^A \tag{10}$$

where

$$a_{11}^A = \lambda_{A1},\ a_{12}^A = \lambda_{A2},\ a_{13}^A = \lambda_{A3}$$

The unit vector in the direction of y on the surface, A, is obtained by

$$\mathbf{e}_y^A = \mathbf{n}_A \times \mathbf{e}_{A12} = \gamma_i^A\,\mathbf{i}_i \tag{11}$$

Thus

$$a_{21}^A = \gamma_1^A,\ a_{22}^A = \gamma_2^A,\ a_{23}^A = \gamma_3^A$$

and

$$a_{31}^A = \nu_{A1},\ a_{32}^A = \nu_{A2},\ a_{33}^A = \nu_{A3}$$

We proceed similarly for the surface B.

4 Finite Element Applications

The isoparametric finite-element functions are introduced to relate the variation of the global coordinates with the nodal values

$$X_i^A = \Phi_N^A\,(\xi_A, \eta_A)\,X_{Ni}^A \tag{12a}$$

or

$$X_i^B = \Phi_N^B\,(\xi_B, \eta_B)\,X_{Ni}^B \tag{12b}$$

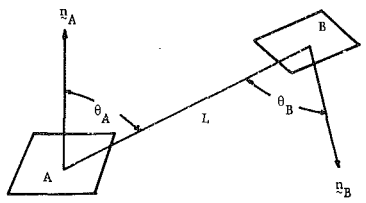

(a) Radiation Between Two Surfaces

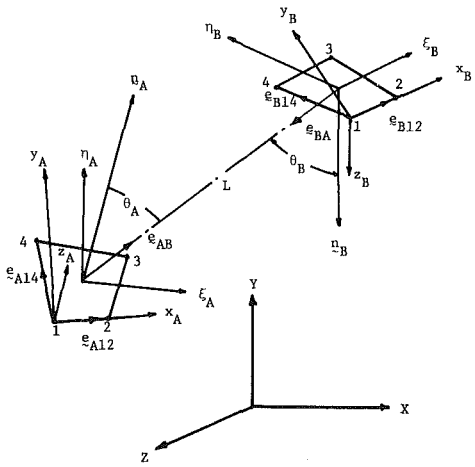

(b) Normals and Coordinate Transformations Between Local and Global Coordinates

Fig. 1 Coordinates for view factors

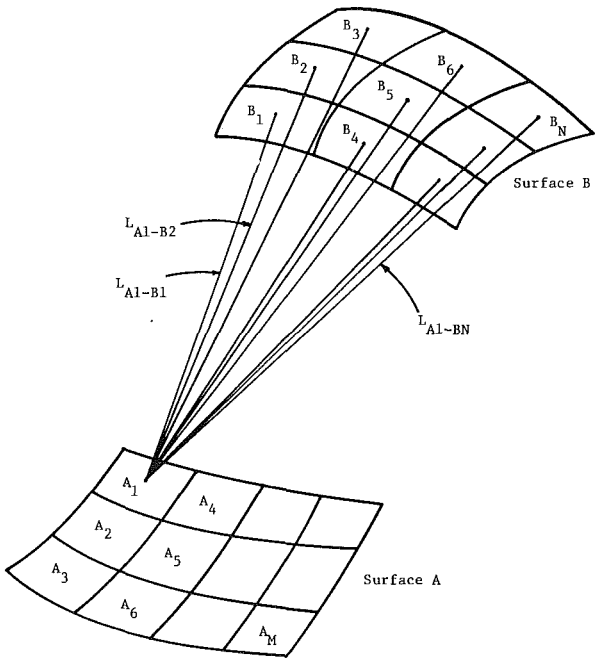

Fig. 2 Global view factor—assembly of local contributions

where Φ_N^A and Φ_N^B may be chosen as linear isoparametric interpolation functions.

The differential area dA_1 or dA_2 in the integral (1) must be transformed into the isoparametric coordinates such that

$$dx\,dy = |J|\,d\xi d\eta \tag{13}$$

where

$$|J| = \begin{vmatrix} \frac{\partial x}{\partial \xi} & \frac{\partial y}{\partial \xi} \\ \frac{\partial x}{\partial \eta} & \frac{\partial y}{\partial \eta} \end{vmatrix} \tag{14}$$

The Jocobian, J, can be evaluated by substituting (12) into (10) for surfaces A and B. Thus,

$$dA_A = dx_A\, dy_A = |J|_A\, d\xi_A\, d\eta_A \tag{15a}$$

$$dA_B = dx_B\, dy_A = |J|_B\, d\xi_B\, d\eta_B \tag{15b}$$

In view of (9) and (15) the view factor F_{A-B} is obtained in the form (Fig. 2),

$$F_{A-B} = \sum_{\alpha=1}^{M} \sum_{\beta=1}^{N} F_{A\alpha-B\beta} = \frac{1}{A_A} \sum_{\alpha=1}^{M} \sum_{\beta=1}^{N} \hat{F}_{A\alpha-B\beta} \tag{16}$$

where

$$A_A = \sum_{\alpha=1}^{M} A_{A\alpha}$$

$$\hat{F}_{A\alpha-B\beta} = \int_{A_{A\alpha}} \int_{A_{B\beta}} \frac{\cos\theta_{A\alpha} \cos\theta_{B\beta}}{\pi L^2_{A\alpha-B\beta}}\, dA_{A\alpha}\, dA_{B\beta} \tag{17}$$

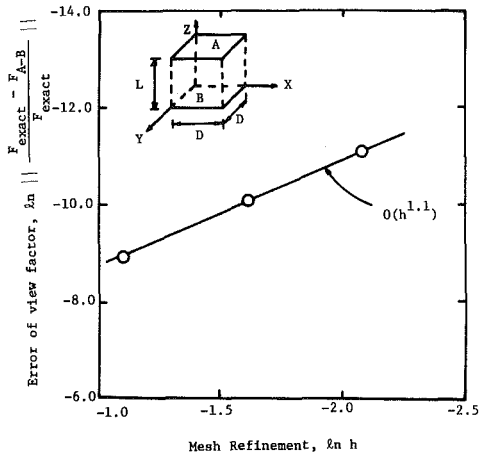

Fig. 3 Convergence curve of view factor error versus mesh size for two parallel 1 × 1 square planes, 1 unit apart

Thus, the Gaussian quadrature intergration can be carried out such that

$$\hat{F}_{A\alpha-B\beta} = \int_{-1}^{1} \int_{-1}^{1} \int_{-1}^{1} \int_{-1}^{1} f(\xi,\eta)\, d\xi_{A\alpha}\, d\eta_{A\alpha}\, d\xi_{B\beta}\, d\eta_{B\beta} \tag{18}$$

where

$$f(\xi,\eta) = \frac{\cos\theta_{A\alpha} \cos\theta_{B\beta}}{\pi L^2_{A\beta-B\beta}} |J|_{A\alpha} |J|_{B\beta}$$

and, thus, in terms of weighting functions and abscissae, we have

$$\hat{F}_{A-B} = \frac{1}{\sum_{\alpha=1}^{M} A_{A\alpha}} \sum_{\alpha=1}^{M} \sum_{\beta=1}^{N} \sum_{i} \sum_{j} \sum_{k} \sum_{l} W_i W_j W_k W_l f(\xi_i^{A\alpha}, \eta_j^{A\alpha}, \xi_k^{B\beta}, \eta_l^{B\beta}) \tag{19}$$

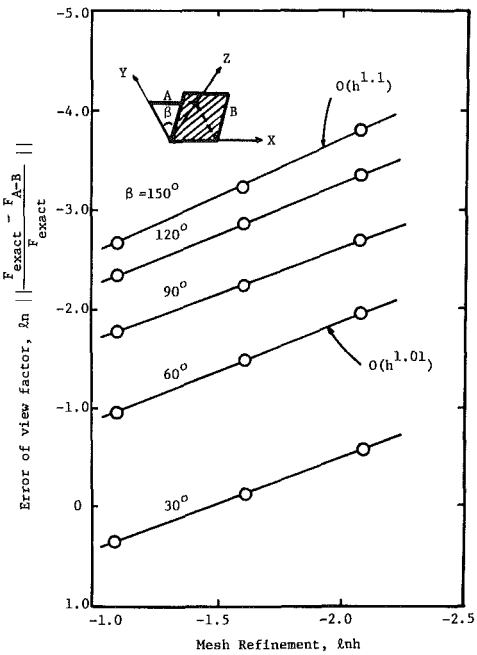

Fig. 4 Convergence curves of view factor error versus mesh size for two intersecting 1 × 1 square planes at angle of 30, 60, 90, 120, and 150 deg

Table 1 View factors F_{A-B} for two square planes, two-point Gaussian quadrature

Solution schemes \ Geometries		Two parallel planes	Two intersection planes				
			30°	60°	90°	120°	150°
Analytic solution		0.19983	0.62020	0.37120	0.20004	0.08700	0.021510
Contour integration [deBastos, 1961]		0.20006	0.62579	0.37255	0.19983	0.08615	0.02112
Finite elements	3 × 3	0.19980	1.53905 1.09247[a]	0.51115 0.45421[a]	0.23359	0.09541	0.02299
	5 × 5	0.19982	1.17043	0.45474	0.22015	0.09196	0.02236
	8 × 8	0.19982	0.96347 0.79660[a]	0.42319 0.40214[a]	0.21261	0.08998	0.02199
	20 × 20	–	0.75673	0.39177	0.20506	0.08797	0.02160
	30 × 30	–	0.71082	0.38481	0.20339	0.08751	0.02152
	40 × 40	–	0.68786	0.38133	0.20255	0.08729	0.02147

[a] Results for six-point Gaussian quadrature

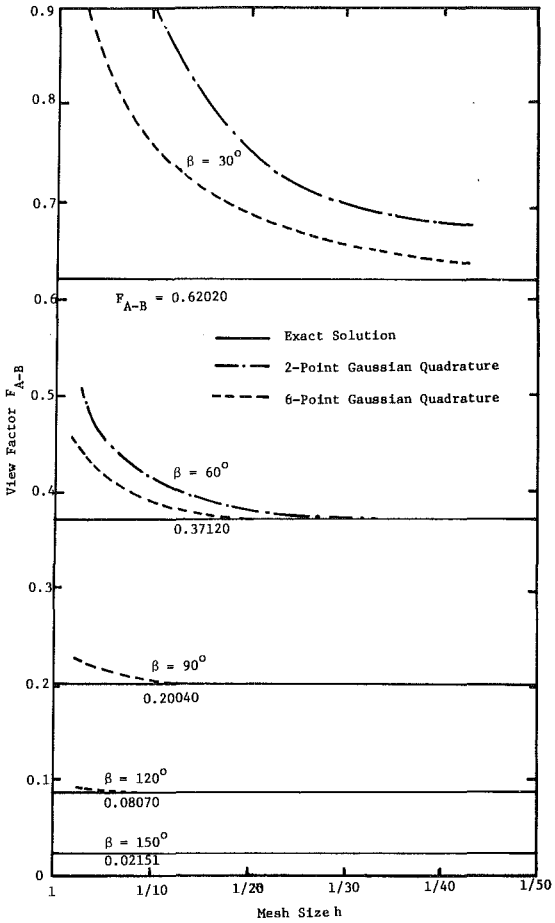

Fig. 5 View factors versus mesh size, intersecting planes

For illustrations, we choose simple geometries shown in Figs. 2-4. The results based on linear isoparametric elements and two-point Guassian quadrature are given in Table 1. It is shown that the most accurate results are obtained for parallel surfaces. In the case of intersecting surfaces with smaller angles, more refined grids and additional number of Guassian points are required for convergence (Figs. 3-5). It is reminded that the power of finite-element method is its capability to handle irregular geometries other than a simple case shown in this example. If convergence is guaranteed from the basic mathematical viewpoint, the accuracy of solution for irregular geometries can be guaranteed. In this note, numerical results shown are based on linear interpolation functions and rather a small number of Gaussian points (two and four points). Although higher-order, finite-element interpolation functions and/or additional number of Gaussian points may be used for further improvement in accuracy, it has been demonstrated that such attempts are scarcely necessary in the example shown in the present study.

5 References

1 Sparrow, E. M., and Cess, R. D., *Radiation Heat Transfer*, Brooks/Cole Publishing Co., 1966.

2 Siegel, R., and Howell, J. R., *Thermal Radiation Heat Transfer*, McGraw-Hill, 1972.

3 Chung, T. J., *Finite Element Analysis in Fluid Dynamics*, McGraw-Hill, 1978.

Comparison of Data With Correlations for Natural Convection Through Rectangular Cells of Arbitrary Aspect Ratio

D. Q. Le,[1] D. W. Hatfield,[2] and D. K. Edwards[3]

Nomenclature

a_m, b_m, c, d_m, e_m = Galerkin coefficients
A = vertical aspect ratio, L/D
A_p = planform (horizontal) aspect ratio, W/D
D = smaller dimension in the plan cross section
k_f, k_w = thermal conductivity of fluid or wall, respectively
L = length between heated and cooled surfaces
m = number of rolls in W-direction
n = number of rolls in L-direction
N_1, N_2 = power integral coefficients
Nu = Nusselt number based upon L
Pr = Prandtl number
Ra = Rayleigh number based on L (Grashof-Prandtl number product)
Ra_n = critical Rayleigh number for linear stability theory mode n
t_w = wall thickness
W = larger dimension in the plan cross section
α = horizontal wave number
β = vertical wave number

Introduction

Natural convection heat transfer through a rectangular box (W by D in cross section and L high) heated from below commences when Rayleigh number Ra (Ra = GrPr) exceeds a critical value. Catton and Edwards [1, 2] proposed a correlation of Nusselt number versus Rayleigh number based upon the approximate integral solution previously used for natural convection between infinite parallel plates [3-5], $W >> L$ and $D >> L$. The integral-theory expression required knowledge of the set of critical Rayleigh numbers indicated by linear stability theory. In the absence of an exact solution to the stability problem, Catton and Edwards [1, 2, 6] advocated using a solution for the infinite height ($L = \infty$) and perfectly conducting walls ($k_w t_w / k_f D >> 1$) but "adjusting" the wave numbers to account for finite end effects and nonconducting sidewalls. An adjustment recipe was offered only for the square planform, $W = D$. Comparison of the recipe to the square-cylinder experimental results of Heitz and Westwater [7] showed reasonable agreement.

Catton [8-10] subsequently applied the internal Galerkin technique and derived the first critical Rayleigh number

[1] University of California, Los Angeles, presently with Rockwell International, Downey, Calif., Student Mem. ASME

[2] University of California, Los Angeles.

[3] University of California, Los Angeles, presently at the University of California, Irvine, Calif., Fellow ASME

Contributed by the Heat Transfer Division for publication in the JOURNAL OF HEAT TRANSFER. Manuscript received by the Heat Transfer Division January 14, 1982.

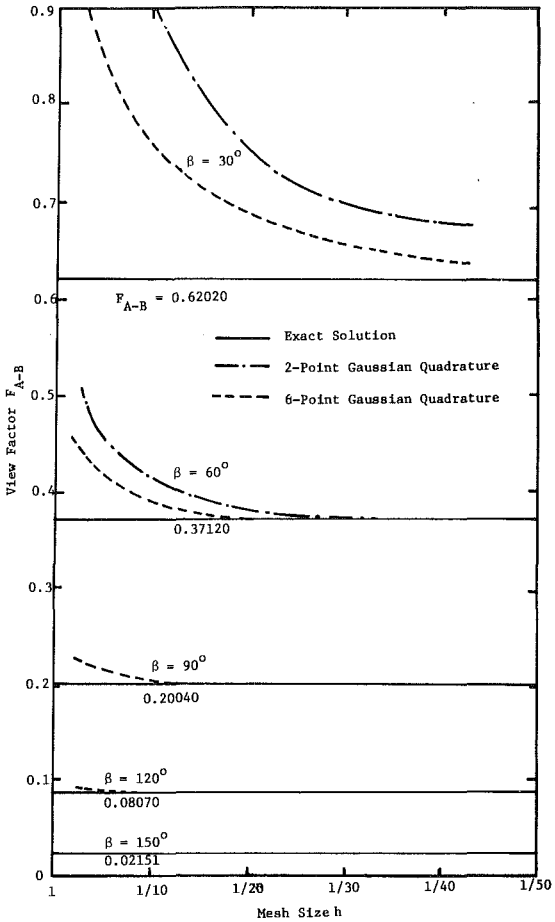

Fig. 5 View factors versus mesh size, intersecting planes

For illustrations, we choose simple geometries shown in Figs. 2–4. The results based on linear isoparametric elements and two-point Guassian quadrature are given in Table 1. It is shown that the most accurate results are obtained for parallel surfaces. In the case of intersecting surfaces with smaller angles, more refined grids and additional number of Guassian points are required for convergence (Figs. 3–5). It is reminded that the power of finite-element method is its capability to handle irregular geometries other than a simple case shown in this example. If convergence is guaranteed from the basic mathematical viewpoint, the accuracy of solution for irregular geometries can be guaranteed. In this note, numerical results shown are based on linear interpolation functions and rather a small number of Gaussian points (two and four points). Although higher-order, finite-element interpolation functions and/or additional number of Gaussian points may be used for further improvement in accuracy, it has been demonstrated that such attempts are scarcely necessary in the example shown in the present study.

5 References

1 Sparrow, E. M., and Cess, R. D., *Radiation Heat Transfer*, Brooks/Cole Publishing Co., 1966.

2 Siegel, R., and Howell, J. R., *Thermal Radiation Heat Transfer*, McGraw-Hill, 1972.

3 Chung, T. J., *Finite Element Analysis in Fluid Dynamics*, McGraw-Hill, 1978.

Comparison of Data With Correlations for Natural Convection Through Rectangular Cells of Arbitrary Aspect Ratio

D. Q. Le,[1] D. W. Hatfield,[2] and D. K. Edwards[3]

Nomenclature

a_m, b_m, c, d_m, e_m = Galerkin coefficients
A = vertical aspect ratio, L/D
A_p = planform (horizontal) aspect ratio, W/D
D = smaller dimension in the plan cross section
k_f, k_w = thermal conductivity of fluid or wall, respectively
L = length between heated and cooled surfaces
m = number of rolls in W-direction
n = number of rolls in L-direction
N_1, N_2 = power integral coefficients
Nu = Nusselt number based upon L
Pr = Prandtl number
Ra = Rayleigh number based on L (Grashof-Prandtl number product)
Ra_n = critical Rayleigh number for linear stability theory mode n
t_w = wall thickness
W = larger dimension in the plan cross section
α = horizontal wave number
β = vertical wave number

Introduction

Natural convection heat transfer through a rectangular box (W by D in cross section and L high) heated from below commences when Rayleigh number Ra (Ra = GrPr) exceeds a critical value. Catton and Edwards [1, 2] proposed a correlation of Nusselt number versus Rayleigh number based upon the approximate integral solution previously used for natural convection between infinite parallel plates [3–5], $W >> L$ and $D >> L$. The integral-theory expression required knowledge of the set of critical Rayleigh numbers indicated by linear stability theory. In the absence of an exact solution to the stability problem, Catton and Edwards [1, 2, 6] advocated using a solution for the infinite height ($L = \infty$) and perfectly conducting walls ($k_w t_w / k_f D >> 1$) but "adjusting" the wave numbers to account for finite end effects and nonconducting sidewalls. An adjustment recipe was offered only for the square planform, $W = D$. Comparison of the recipe to the square-cylinder experimental results of Heitz and Westwater [7] showed reasonable agreement.

Catton [8–10] subsequently applied the internal Galerkin technique and derived the first critical Rayleigh number

[1] University of California, Los Angeles, presently with Rockwell International, Downey, Calif., Student Mem. ASME

[2] University of California, Los Angeles.

[3] University of California, Los Angeles, presently at the University of California, Irvine, Calif., Fellow ASME

Contributed by the Heat Transfer Division for publication in the JOURNAL OF HEAT TRANSFER. Manuscript received by the Heat Transfer Division January 14, 1982.

without recourse to the adjusted wave number approximation. Nevertheless, in view of the simplicity of the adjusted wave number concept and the compact closed-form expressions given by it for the first and higher critical Rayleigh numbers, Edwards, Arnold, and Wu [11] used it as a basis to correlate Nu versus Ra for high-vertical-aspect-ratio ($L/D \geq 4$) rectangular cells. At the time that the correlation was proposed, there were no heat-transfer data for high-L/D, low-W/D rectangles, and none for the intermediate range $1 < L/D < 4$.

It is the purpose of this note to propose a correlation based upon the approximate integral formalism and a one-term Galerkin solution for the first critical Rayleigh number. New data are also presented for $L/D = 2$, $W/D = 1, 2, 4, 8$, and $L/D = 8$, $W/D = 1, 2$, and 16, thus complementing previous data [11] for $L/D = 4$, $W/D = 1, 2, 4, 8$, and 24, and $L/D = 8$, $W/D = 4, 8$. The proposed correlation is shown compared to the new and old data. In particular, it agrees significantly better with the high-L/D, low-W/D results than does the correlation previously proposed [11]. The rectangular enclosures in question are heated from below, cooled from above, filled with an infrared-opaque liquid (silicone oil), and have adiabatic side walls (by virtue of symmetry in the multicellular honeycomb test sections used; see [1, 11-13] for experimental details).

Critical Rayleigh Number

Following Catton [9], the first critical Rayleigh number initiated by linear perturbation theory for thermal stability in the rectangular parallelepiped with adiabatic vertical walls, heated bottom, and cold top was derived. The most unstable perturbations are in the form of rolls with axes parallel to the D-direction. In the internal Galerkin method beam functions that satisfy the boundary conditions are used to approximate the y and z variations of the vertical (z) and W-direction (y) velocity components, while trigonometric profiles are assumed for the x-variations and perturbation temperature profile. In the one-term Galerkin approximation the self-weighted, volume-average error in the approximations is set to zero. The result is a reasonably compact closed-form expression for Ra_1,

$$\mathrm{Ra}_1 = a_m A^4 [m^2 A_p^{-2} + A^{-2}][1 + b_m A_p^{-2} + cA^{-2} + d_m A_p^2 A^{-2} + e_m A_p^2 A^{-4}] \quad (1)$$

where

$$A = L/D, A_p = W/D \geq 1$$

and coefficients a_m, b_m, d_m, and e_m vary with m, the number of rolls in one box side-by-side in the W direction. The exact expressions for the m-dependent coefficients are indicated by the Galerkin solution in terms of hyperbolic and trigonometric functions involving roots to transcendental equations. They are well approximated by

$$a_1 = 158, a_m = 150\, m \geq 2$$
$$b_m = m^2(1 + 3.12m^{-1.4})$$
$$c = 2.49$$
$$d_m = m^{-2}(1.25 - 0.25m^{-0.66})$$
$$e_m = m^{-2}(5.13 - m^{-0.6})$$

Note that these fits are of the one-term equations; they have not been fitted to the data. Note also that the critical Rayleigh number must be minimized with respect to m. The appropriate m is usually the integer closest to $A_p/A = W/L$. At $L/D < 1$, the Galerkin technique requires more than one term to predict adequately Ra_1.

Heat-Transfer Correlation

The power integral formalism indicates that

Table 1 Comparison of equation (1) with experiment for critical Rayleigh number versus vertical and horizontal aspect ratios

L/D	W/D	Ra_1 equation (1)	Ra_1 Exp.	Ref.
1.0	1.0	4.0×10^3	3.7×10^3	[7]
2.3	1.0	3.1×10^4	3.2×10^4	[7]
3.8	1.0	1.9×10^5	3.1×10^5	[7]
6.0	1.0	1.1×10^6	1.1×10^6	[7]
8.0	1.0	3.4×10^6	2.5×10^6	[7]
1.0	6.0	3.2×10^3	2.6×10^3	[12]
1.0	1.0	4.0×10^3	3.8×10^3	[12]
4.1	1.0	2.6×10^5	1.7×10^5	[11]
4.3	2.1	3.6×10^4	2.8×10^4	[11]
3.9	4.3	1.2×10^4	1.2×10^4	[11]
4.0	8.5	1.3×10^4	1.2×10^4	[11]
4.5	26.0	1.5×10^4	1.2×10^4	[11]
7.9	4.5	6.5×10^4	7.1×10^4	[11]
8.0	9.1	4.3×10^4	4.7×10^4	[11]
2.0	1.0	2.1×10^4	2.0×10^4	[13]
2.0	2.0	6.0×10^3	5.5×10^3	[13]
2.0	4.0	5.2×10^3	5.3×10^3	[13]
2.1	8.3	5.4×10^3	4.6×10^3	[13]
8.2	1.0	3.8×10^6	3.7×10^6	[13]
8.5	2.0	4.4×10^5	4.4×10^5	[13]
8.6	17.2	4.9×10^4	5.5×10^4	[13]

$$\mathrm{Nu} = 1 + N_1[1 - \mathrm{Ra}_1/\mathrm{Ra}]^{\cdot} + N_2[1 - \mathrm{Ra}_2/\mathrm{Ra}] + N_3[1 - \mathrm{Ra}_3/\mathrm{Ra}]^{\cdot} + \ldots . \quad (2)$$

where the power integral coefficients are approximately [5]

$$N_1 = 1.4, N_2 = 1.6, N_3 = 1.8, N_n = 2, n > 3$$

The dot notation (following Hollands) indicates that the dotted term is zero when negative; thus until Ra exceeds Ra_n, the nth term and all higher ones are zero. All properties are evaluated at the mean temperature.

Recourse is taken to adjusted wavenumbers for prediction of Ra_n, $n \geq 2$.

$$\mathrm{Ra}_n = (\alpha_n^2 + \beta_n^2)^3 \alpha_n^2 \quad (3)$$
$$\alpha_n^2 = \alpha_0^2 + \alpha_n^2/2$$
$$\beta_n^2 = (n\pi + 0.85)^2$$

and adjusted wavenumber α_0 is found from equating Ra_1 indicated by equation (3) to equation (1). It is necessary to iterate on

$$\alpha_0^2 = \mathrm{Ra}_1^{1/3}[\alpha_0^2 + 8]^{1/3} - 24 \quad (4)$$

where the first iteration begins with $\alpha_0^2 = \mathrm{Ra}_1^{1/2}$.

Comparison with Data

Table 1 compares Ra_1 given by equation (1) with previous data [7, 11, 12] and the new results of Le [13]. The worst discrepancies are with the $L/D = 3.8$, $W/D = 1$ result of [7] and the $L/D = 4.1$, $W/D = 1$ result of [11]; the prediction splits the data, which are in serious disagreement. Higher-term Galerkin approximations were developed for the square cylinder ($W/D = 1$) and the slot (W/D infinite), but they did not agree with experiment any better than the one-term approximation compared in Table 1.

Figures 1-3 show comparisons of the correlation equation (2) with heat-transfer data [11-14]. The data for a given vertical aspect ratio A ($=L/D$) show that when the planform aspect ratio A_p ($=W/D$) is less than A the curve for Nu versus Ra shifts strongly to the right, that is, Ra_1 is strongly increased. When A_p is greater than or equal to A there is little influence of A_p; for a given A curves for $A_p \geq A$ plot almost on top of one another. The integral correlation formula gives a reasonable fit of the data except for the $L/D = 4.1$, $W/D = 1.0$ data previously mentioned, where the experimental value of Ra_1 is in disagreement with that of [7]. When the predicted

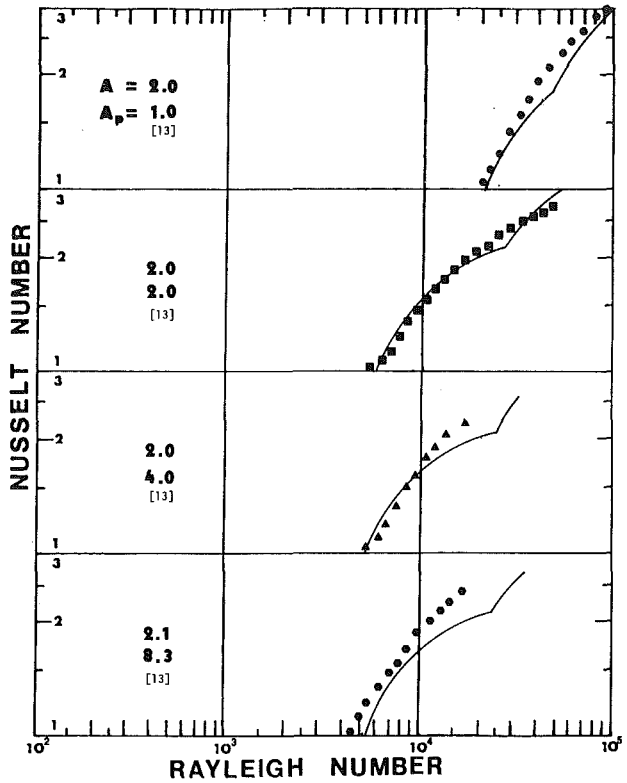

Fig. 1 Comparison of data with integral correlation, equation (2), for $L/D = 2$ and $W/D = 1, 2, 4$, and 8

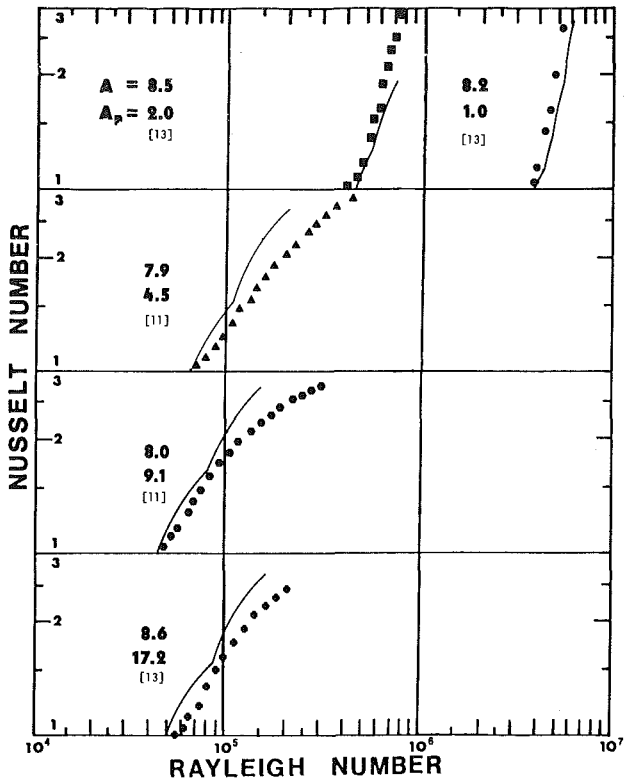

Fig. 3 Comparison of data with integral correlation, equation (2), for $L/D = 8$ and $W/D = 1, 2, 4, 9$, and 17

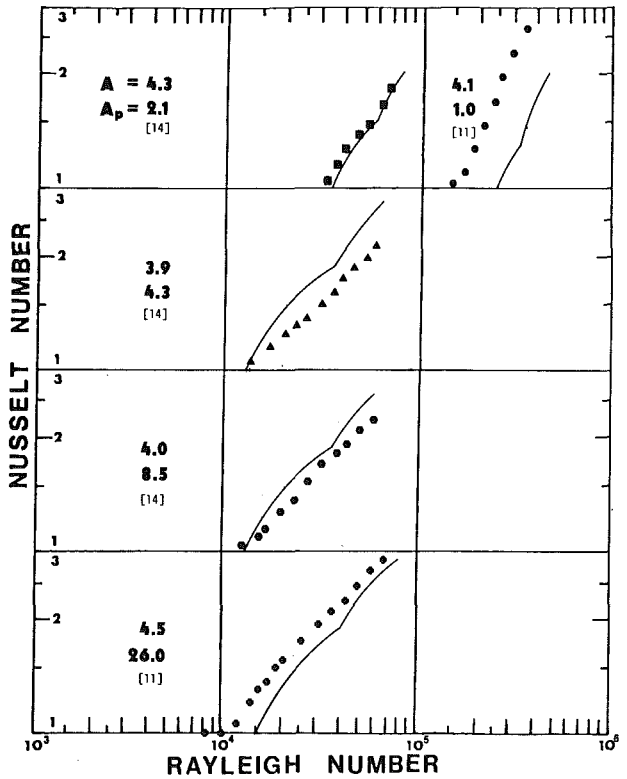

Fig. 2 Comparison of data with integral correlation, equation (2), for $L/D = 4$ and $W/D = 1, 2, 4, 8$, and 26

value of Ra_1 disagrees with that indicated by the data, the entire heat-transfer curve fails to agree with the correlation. A minor failing of the power integral formalism is to show a change of slope in the vicinity of Ra_2, while the data show no abrupt change. Also the power integral indicates no effect of Pr, while one would expect a Pr effect at low Prandtl number. Aside from these points, the one-term Galerkin solution for Ra_1 presented here and the power integral-theory formula for Nu give a useful engineering relation of Nu to Ra.

While comparison in Figs. 1–3 with data is made only in the range $2 \geq L/D \geq 8$ an $1 \geq W/D \geq 2\,L/D$, the agreement in Table 1 for L/D down to 1 and the analytical basis of equation (1) lend confidence to using the correlation for arbitrary $L/D \geq 1$ and arbitrary W/D.

Acknowledgment

This research was conducted through a grant received from the National Science Foundation, ENG 78-25273.

References

1 Catton, I., and Edwards, D. K., "Effect of Side Walls on Natural Convection between Horizontal Plates Heated From Below," ASME JOURNAL OF HEAT TRANSFER, Vol. 89, 1967, p. 295.

2 Edwards, D. K., and Catton, I., "Prediction of Heat Transfer by Natural Convection in Closed Cylinders Heated From Below," *International Journal of Heat and Mass Transfer*, Vol. 12, 1969, p. 23.

3 Malkus, W. V. R., and Veronis, G., "Finite Amplitude Cellular Convection," *Journal of Fluid Mechanics*, Vol. 4, 1958, p. 225.

4 Hollands, K. G. T., "Convectional Heat Transport Between Rigid Horizontal Boundaries After Instability," *Physics of Fluids*, Vol. 8, 1965, p. 389.

5 Catton, I., "Natural Convection in Horizontal Liquid Layers," *Physics of Fluids*, Vol. 9, 1966, p. 2521.

6 Catton, I., and Edwards, D. K., "Initiation of Thermal Convection in Finite Right Circular Cylinders," *AIChE Journal*, Vol. 16, 1970, p. 594.

7 Heitz, W. L., and Westwater, J. W., "Critical Rayleigh Number for Natural Convection of Water Confined in Square Cells with L/D from 0.5 to 8," ASME JOURNAL OF HEAT TRANSFER, Vol. 93, 1971, p. 188.

8 Catton, I., "Convection in a Closed Rectangular Region: The Onset of Motion," ASME JOURNAL OF HEAT TRANSFER, Vol. 92, 1970, p. 186.

9 Catton, I., "The Effect of Insulating Vertical Walls on the Onset of Motion in a Fluid Heated From Below," *International Journal of Heat and Mass Transfer*, Vol. 15, 1972, p. 665.

10 Catton, I., "Effect of Wall Conduction on the Stability of a Fluid in a

Rectangular Region Heated from Below," ASME JOURNAL OF HEAT TRANSFER, Vol. 94, 1972, p. 446.

11 Edwards, D. K., Arnold, J. N., and Wu, P. S., "Correlations for Natural Convection Through High L/D Rectangular Cells," ASME JOURNAL OF HEAT TRANSFER, Vol. 101, 1979, p. 741.

12 Arnold, J. N., "Heat Transfer by Natural Convection in Enclosed Rectangular Cavities," Ph.D. dissertation, University of California, Los Angeles, 1978.

13 Le, D. Q., "Experimental Investigation of Natural Convection Heat Transfer across Multiple Rectangular Cavities at Various Inclinations," M.S. thesis, Univerity of California, Los Angeles, 1981.

14 Arnold, J. N., Edwards, D. K., and Catton, I., "Effect of Tilt and Horizontal Aspect Ratio on Natural Convection in a Rectangular Honeycomb," ASME JOURNAL OF HEAT TRANSFER, Vol. 99, 1977, p. 120.

Natural Convection Fluid Flow Patterns Resulting From the Interaction of a Heated Vertical Plate and an Attached Horizontal Cylinder

E. M. Sparrow[1] and G. M. Chrysler[1]

Introduction

The purpose of this paper is to convey the results of a flow visualization study undertaken as an aftermath of earlier heat-transfer experiments [1] on interactive natural convection between a vertical plate and a short, attached horizontal cylinder. Both the plate and the cylinder were maintained at the same uniform temperature (above the ambient temperature) by separate heating circuits. The plate-to-ambient temperature difference creates an upmoving buoyant boundary layer which washes over the cylinder. In turn, the heated cylinder creates its own field of buoyant fluid which interacts with the plate. The heat-transfer ramifications of these interactions were explored in [1], but the experimental apparatus used there was not conducive to flow visualization studies.

In response to an imperative curiosity about the nature of the pattern of fluid flow, a completely new experimental apparatus was fabricated to facilitate flow visualization. Whereas the heat-transfer experiments of [1] were performed in air, the flow visualization was carried out with water as the working fluid. The dimensions of the new apparatus (i.e., the plate and the cylinder) were properly scaled so that, for practically convenient surface-to-fluid temperature differences, the flow visualization could be performed over the same Rayleigh number range as was employed in the heat-transfer studies.

The actual visualization was performed using the thymol-blue method [2]. This is an electrochemical technique in which a change of color of the fluid occurs in response to an impressed voltage. The color change produces a neutrally buoyant blue fluid which faithfully follows the natural convection motions.

Experimental Apparatus

The vertical plate used in the experiments was fabricated from 0.635-cm thick copper, with finished height and width dimensions of 14.5 cm and 9.67 cm, respectively. At midheight and midway between the lateral edges, a circular aperture was drilled into the plate surface to accommodate the shank of a horizontal cylinder, which was also of copper. The cylinder proper (i.e., the part that participates in the natural convection heat-transfer process) was 1.27 cm in diameter and 1.27-cm long.

The plate-cylinder assembly was heated by electrical resistance wire affixed to the rear face of the plate. The wire layout was chosen so as to promote temperature uniformity, and the measured plate temperature distributions were found to be uniform to within 2 percent of the plate-to-ambient temperature difference. To minimize heat losses which might induce extraneous natural convection motions, the rear face and all edges of the plate were thermally insulated with a water-tolerant closed-pore polystyrene (0.635-cm thick at the edges and 3.81-cm thick at the rear). As an extra precaution, the polystyrene was coated with impermeable, self-adhering plastic.

It was desired that the test chamber in which the apparatus is installed be as large as possible in order to approximate an infinite ambient with respect to natural convection at the plate-cylinder assembly. To this end, a plexiglass tank was fabricated with internal dimensions of 73.7 × 43.2 × 45.7 cm, length × width × height. The plate was installed so that its exposed face was parallel to the width dimension of the tank (the plate was centered in the width). A large clear space (53.3 cm in length) was left between the exposed face and the opposite wall of the tank. The leading edge of the plate (i.e., the lower edge) was positioned 7.6 cm above the floor of the tank, while the water level was maintained at 15.2 cm above the trailing edge of the plate.

The working fluid of the experiments was water, to which minute amounts of certain chemicals were added to facilitate the electrochemical reaction which is the basis of the flow visualization method. The first of the additives is thymol blue, a pH indicator. Next, the solution is titrated to the end point with sodium hydroxide. Then, by the addition of hydrochloric acid, the solution is made acidic and red-yellow in color. When a small d.c. voltage (~6 V) is impressed between two electrodes situated in such a solution, a proton transfer reaction occurs at the negative electrode, which changes the pH from acid to base at that electrode. This change in pH brings about a change of color from red-yellow to blue. The thus-created blue "dye" is neutrally buoyant and faithfully follows the natural convection motions of the fluid.

Since the dye is created at the negative electrode, the configuration and positioning of the electrode affects the type of information that is obtained from the visualization technique. In some of the preliminary data runs, the plate and cylinder surfaces, or certain portions of these surfaces, served as the negative electrode. In other preliminary runs, locally exposed portions of wires were used as the negative electrode in order to provide single or multiple dye filaments. These filaments were found to be highly revealing of the flow field, so that the wire electrodes were used in all the final runs. A bridge-like fixture, mounted on the side walls of the tank, enabled precise positioning of the wire probes. In all cases, a copper plate positioned on the floor of the tank served as the positive electrode.

To obtain a permanent record of the flow pattern, the dye filaments were photographed. Various lighting arrangements were employed in an attempt to obtain high contrast between the blue dye filament(s) and the red-yellow solution. However, owing to the relatively long light path associated with the large dimensions of the tank, there was strong light absorption. Thus, whereas there is no ambiguity in the information conveyed by the photographs, they were not judged to be of publication quality. Instead, the photographs were professionally traced, and it is the tracings that are presented here.

Results and Discussion

From the available collection of photographic results, four

[1]Department of Mechanical Engineering, University of Minnesota, Minneapolis, Minn. 55455

Contributed by the Heat Transfer Division for publication in the JOURNAL OF HEAT TRANSFER. Manuscript received by the Heat Transfer Division January 13, 1982.

Rectangular Region Heated from Below," ASME JOURNAL OF HEAT TRANSFER, Vol. 94, 1972, p. 446.

11 Edwards, D. K., Arnold, J. N., and Wu, P. S., "Correlations for Natural Convection Through High L/D Rectangular Cells," ASME JOURNAL OF HEAT TRANSFER, Vol. 101, 1979, p. 741.

12 Arnold, J. N., "Heat Transfer by Natural Convection in Enclosed Rectangular Cavities," Ph.D. dissertation, University of California, Los Angeles, 1978.

13 Le, D. Q., "Experimental Investigation of Natural Convection Heat Transfer across Multiple Rectangular Cavities at Various Inclinations," M.S. thesis, Univerity of California, Los Angeles, 1981.

14 Arnold, J. N., Edwards, D. K., and Catton, I., "Effect of Tilt and Horizontal Aspect Ratio on Natural Convection in a Rectangular Honeycomb," ASME JOURNAL OF HEAT TRANSFER, Vol. 99, 1977, p. 120.

Natural Convection Fluid Flow Patterns Resulting From the Interaction of a Heated Vertical Plate and an Attached Horizontal Cylinder

E. M. Sparrow[1] and G. M. Chrysler[1]

Introduction

The purpose of this paper is to convey the results of a flow visualization study undertaken as an aftermath of earlier heat-transfer experiments [1] on interactive natural convection between a vertical plate and a short, attached horizontal cylinder. Both the plate and the cylinder were maintained at the same uniform temperature (above the ambient temperature) by separate heating circuits. The plate-to-ambient temperature difference creates an upmoving buoyant boundary layer which washes over the cylinder. In turn, the heated cylinder creates its own field of buoyant fluid which interacts with the plate. The heat-transfer ramifications of these interactions were explored in [1], but the experimental apparatus used there was not conducive to flow visualization studies.

In response to an imperative curiosity about the nature of the pattern of fluid flow, a completely new experimental apparatus was fabricated to facilitate flow visualization. Whereas the heat-transfer experiments of [1] were performed in air, the flow visualization was carried out with water as the working fluid. The dimensions of the new apparatus (i.e., the plate and the cylinder) were properly scaled so that, for practically convenient surface-to-fluid temperature differences, the flow visualization could be performed over the same Rayleigh number range as was employed in the heat-transfer studies.

The actual visualization was performed using the thymol-blue method [2]. This is an electrochemical technique in which a change of color of the fluid occurs in response to an impressed voltage. The color change produces a neutrally buoyant blue fluid which faithfully follows the natural convection motions.

Experimental Apparatus

The vertical plate used in the experiments was fabricated from 0.635-cm thick copper, with finished height and width dimensions of 14.5 cm and 9.67 cm, respectively. At midheight and midway between the lateral edges, a circular aperture was drilled into the plate surface to accommodate the shank of a horizontal cylinder, which was also of copper. The cylinder proper (i.e., the part that participates in the natural convection heat-transfer process) was 1.27 cm in diameter and 1.27-cm long.

The plate-cylinder assembly was heated by electrical resistance wire affixed to the rear face of the plate. The wire layout was chosen so as to promote temperature uniformity, and the measured plate temperature distributions were found to be uniform to within 2 percent of the plate-to-ambient temperature difference. To minimize heat losses which might induce extraneous natural convection motions, the rear face and all edges of the plate were thermally insulated with a water-tolerant closed-pore polystyrene (0.635-cm thick at the edges and 3.81-cm thick at the rear). As an extra precaution, the polystyrene was coated with impermeable, self-adhering plastic.

It was desired that the test chamber in which the apparatus is installed be as large as possible in order to approximate an infinite ambient with respect to natural convection at the plate-cylinder assembly. To this end, a plexiglass tank was fabricated with internal dimensions of 73.7 × 43.2 × 45.7 cm, length × width × height. The plate was installed so that its exposed face was parallel to the width dimension of the tank (the plate was centered in the width). A large clear space (53.3 cm in length) was left between the exposed face and the opposite wall of the tank. The leading edge of the plate (i.e., the lower edge) was positioned 7.6 cm above the floor of the tank, while the water level was maintained at 15.2 cm above the trailing edge of the plate.

The working fluid of the experiments was water, to which minute amounts of certain chemicals were added to facilitate the electrochemical reaction which is the basis of the flow visualization method. The first of the additives is thymol blue, a pH indicator. Next, the solution is titrated to the end point with sodium hydroxide. Then, by the addition of hydrochloric acid, the solution is made acidic and red-yellow in color. When a small d.c. voltage (~6 V) is impressed between two electrodes situated in such a solution, a proton transfer reaction occurs at the negative electrode, which changes the pH from acid to base at that electrode. This change in pH brings about a change of color from red-yellow to blue. The thus-created blue "dye" is neutrally buoyant and faithfully follows the natural convection motions of the fluid.

Since the dye is created at the negative electrode, the configuration and positioning of the electrode affects the type of information that is obtained from the visualization technique. In some of the preliminary data runs, the plate and cylinder surfaces, or certain portions of these surfaces, served as the negative electrode. In other preliminary runs, locally exposed portions of wires were used as the negative electrode in order to provide single or multiple dye filaments. These filaments were found to be highly revealing of the flow field, so that the wire electrodes were used in all the final runs. A bridge-like fixture, mounted on the side walls of the tank, enabled precise positioning of the wire probes. In all cases, a copper plate positioned on the floor of the tank served as the positive electrode.

To obtain a permanent record of the flow pattern, the dye filaments were photographed. Various lighting arrangements were employed in an attempt to obtain high contrast between the blue dye filament(s) and the red-yellow solution. However, owing to the relatively long light path associated with the large dimensions of the tank, there was strong light absorption. Thus, whereas there is no ambiguity in the information conveyed by the photographs, they were not judged to be of publication quality. Instead, the photographs were professionally traced, and it is the tracings that are presented here.

Results and Discussion

From the available collection of photographic results, four

[1]Department of Mechanical Engineering, University of Minnesota, Minneapolis, Minn. 55455

Contributed by the Heat Transfer Division for publication in the JOURNAL OF HEAT TRANSFER. Manuscript received by the Heat Transfer Division January 13, 1982.

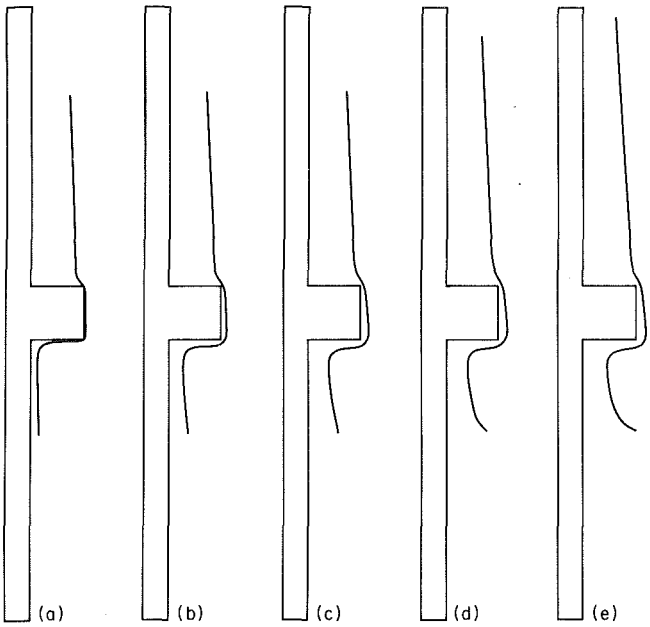

Fig. 1 Streamline patterns in side view. The dye-producing probe is centered between the lateral edges of the cylinder.

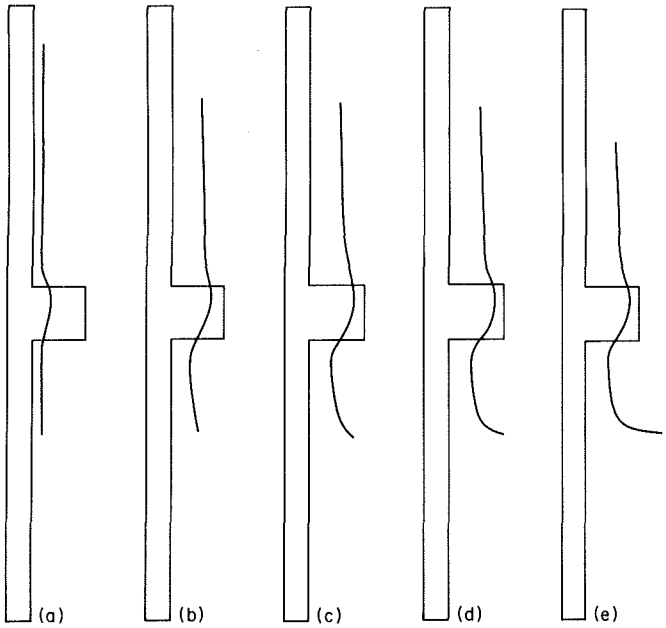

Fig. 2 Streamline patterns in side view. The dye-producing probe is lined up with one of the lateral edges of the cylinder.

figures were assembled for presentation here. Among these, Figs. 1–3 show side views of the cylinder and plate, while Fig. 4 is a head-on view of the cylinder-plate assembly. All of the results correspond to cylinder and plate Rayleigh numbers of 2×10^5 and 3×10^8, respectively.

Attention will now be focused on Fig. 1. This figure is a composite of the tracings of five individual photographs. Each is a side view of the plate and the cylinder and, in each, a streamline corresponding to a thymol-blue dye filament is shown. The lower end of the streamline corresponds to the point at which the blue tracer fluid was created. Thus, proceeding from left to right in Fig. 1., it is seen that the successive cases (*a*) through (*e*) correspond to dye origins that are displaced progressively farther and farther from the surface of the plate.

What cannot be seen in Fig. 1 is that the probe which produces the dye filament is lined up with the vertical diameter of the cylinder, i.e., the probe is centered under the cylinder. As will be seen shortly, there are major differences in the behavior of a centered and a noncentered streamline.

Inspection of Fig. 1 indicates a common overall behavior for all cases, but with important differences in detail depending on the dye origin. From the origin, the fluid not only moves upward but also moves inward toward the plate. Then, as the fluid approaches the cylinder, it turns sharply and flows outward (i.e., away from the plate), moving along the bottom of the cylinder. Another sharp turn is executed at the exposed face of the cylinder, resulting in an upward flow along the vertical diameter of the face. Once the face has been cleared, the upflow continues but is accompanied by an inward motion toward the plate surface.

To assist in identifying the most significant features of the just-described pattern of fluid motion, it is relevant to briefly review the flow pattern that prevails adjacent to a heated vertical plate without a cylinder in place. The buoyancy created by the plate causes an upflow adjacent to the plate surface, and the fluid needed to sustain the upflow is drawn in from the ambient. Thus, as fluid particles move upward, they also move inward. This pattern of fluid flow is, in fact, in evidence in Fig. 1, both below the cylinder and above the cylinder.

The special feature is the flow pattern associated with the

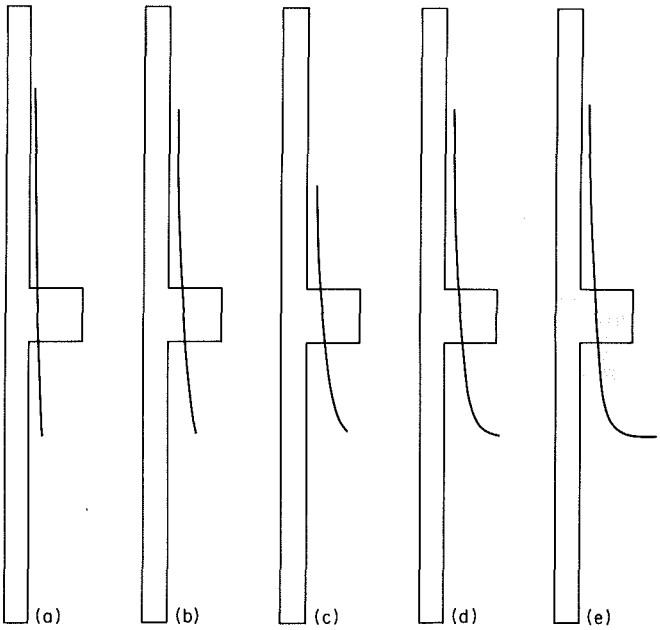

Fig. 3 Streamline patterns in side view. The dye-producing probe is displaced laterally by one-half diameter from one of the lateral edges of the cylinder.

cylinder is the *outward* motion (i.e., away from the plate surface) that is imparted to the fluid as it approaches the cylinder from below. It is interesting to speculate about the cause of the outward motion, especially since it is opposite to the prevailing direction of the flow induced by the plate. It is believed that the outflow is driven by a pressure gradient which is created when the fluid, which approaches from below, stagnates against the cylinder. The stagnation causes a pressure rise, the extent of which depends on the velocity of the approach flow. Available flat plate solutions [3] show that aside from a small region near the plate surface, the magnitude of the approach velocity decreases with increasing distance from the surface. Consequently, there is a decrease in the stagnation pressure along the cylinder, and this gives rise to the observed fluid outflow.

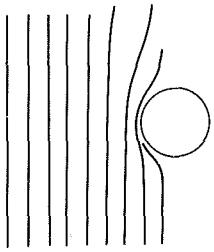

Fig. 4 Streamline pattern in head-on view

Further perspectives about the flow field can be obtained from Fig. 2. The streamlines shown in Fig. 2 were obtained with the dye-producing probe positioned below one of the lateral edges of the cylinder (i.e., the probe was displaced transversely by half a cylinder diameter from that of Fig. 1). Due to this positioning, the visualized streamlines pass around the side of the cylinder. As the upward-moving fluid particles flow around the cylinder, they are propelled outward toward the tip, presumably by the same pressure gradient that was identified earlier. Taken together, Figs. 1 and 2 indicate that the cylinder causes a general outward displacement of the flat-plate induced flow which approaches the cylinder from below.

A final side-view visualization is presented in Fig. 3. For the streamlines of this figure, the probe was positioned to the side of the cylinder – displaced transversely by half a diameter from one of the lateral edges. It is evident from Fig. 3 that the streamlines pictured there are not markedly influenced by the presence of the cylinder. They are essentially the streamlines of the flat plate flow. Thus, it appears that the influence of the cylinder does spread laterally to a significant extent.

The aforementioned finding is amplified in Fig. 4, which is a head-on view of the plate-cylinder assembly. The dye filaments shown in this figure were created by a horizontal wire that was periodically coated with teflon, leaving a periodic array of exposed segments at which the electrochemical reaction could occur. As seen in the figure, the flow approaching the cylinder from below moves laterally outward at first but then swings back as it passes the upper portion of the cylinder. The streamlines which pass near the side of the cylinder also tend to be drawn inward above the cylinder, but those situated farther to the side are unaffected.

In Fig. 4, the two streamlines that are closest to the cylinder appear to be on a collision course, but that is an illusion since, in reality, they do not lie in the same plane (the one closest to the cylinder is forward of its neighbor).

Concluding Remarks

The flow visualization results presented here demonstrate that the flow about a plate-attached horizontal cylinder is strongly three dimensional, with the axial motion of the fluid in the direction away from the plate being especially worthy of note. The observed flow pattern is significantly different from that for the classical long, end-effect-free horizontal cylinder.

In this light, it is quite remarkable that the average heat-transfer coefficients for the two cases are not too different. In [1], it was found that the heat-transfer coefficients for a plate-attached cylinder with a length-diameter ratio of one (i.e., the case studied here) were within 10 percent of those for the classical long horizontal cylinder. For an attached cylinder with a length-diameter ratio of one-half, the deviations were within 20 percent.

The effect of the attached cylinder on the heat-transfer coefficient for the flat plate has not been investigated in the literature. The present flow visualization results indicate that there will be little effect below the cylinder and that the affected region above the cylinder will be confined to a narrow corridor only slightly wider than the cylinder itself.

References

1 Sparrow, E. M., and Chrysler, G. M., "Natural Convection Heat-Transfer Coefficients for a Short Horizontal Cylinder Attached to a Vertical Plate," JOURNAL OF HEAT TRANSFER, Vol. 103, 1981, pp. 630–637.

2 Baker, D. J., "A Technique for the Precise Measurement of Small Fluid Velocities," *Journal of Fluid Mechanics*, Vol. 26, 1966, pp. 573–575.

3 Ostrach, S., "An Analysis of Laminar Free-Convection Flow and Heat Transfer about a Flat Plate Parallel to the Direction of the Generating Body Force," NACA Report 1111, Washington, D.C., 1953.

A Note on Transient Free Convection of Water at 4°C Over a Doubly Infinite Vertical Porous Plate

I. Pop[1] and A. Raptis[2]

Nomenclature

c = parameter of blowing or suction
f = dimensionless function
g = acceleration due to gravity
L = characteristic length of the plate
Pr = Prandtl number, υ/κ
t' = time
t_0 = characteristic time, L^2/υ
T' = fluid temperature
T'_w = constant temperature of the plate
T'_∞ = ambient temperature
$\Delta T'$ = temperature difference in two points of water
u' = velocity along the plate
u_0 = characteristic velocity, $g\vartheta L^2 \times (T'_w - T'_\infty)^2/\upsilon$
v' = velocity normal to the plate
v'_w = velocity of blowing or suction
x' = coordinate along the plate oriented vertically upward
x'_p = penetration distance
$x_{p\max}$ = dimensionless maximum penetration distance
y' = coordinate normal to the plate
ϑ = coefficient of thermal expansion of water at 4°C
η = similarity variable, $y/2\sqrt{t}$
υ = kinematic viscosity
κ = thermal diffusivity
ζ = density
$\Delta\zeta$ = density difference in two points of water

Subscripts

w = wall condition
∞ = ambient fluid condition

Introduction

Considerable work has been done in recent years on the transient free convection flow past a vertical infinite flat plate. Many different mathematical methods and techniques have been used to seek solutions to this class of problems [1–5]. These studies are mainly restricted only to fluids at

[1] University of Cluj, Faculty of Mathematics, Cluj CP 253, Romania
[2] University of Ioannina, Department of Mechanics, Ioannina, Greece

Contributed by the Heat Transfer Division for publication in the JOURNAL OF HEAT TRANSFER. Manuscript received by the Heat Transfer Division October 27, 1981.

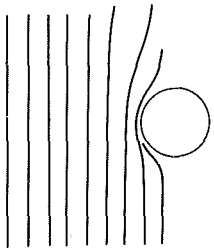

Fig. 4 Streamline pattern in head-on view

Further perspectives about the flow field can be obtained from Fig. 2. The streamlines shown in Fig. 2 were obtained with the dye-producing probe positioned below one of the lateral edges of the cylinder (i.e., the probe was displaced transversely by half a cylinder diameter from that of Fig. 1). Due to this positioning, the visualized streamlines pass around the side of the cylinder. As the upward-moving fluid particles flow around the cylinder, they are propelled outward toward the tip, presumably by the same pressure gradient that was identified earlier. Taken together, Figs. 1 and 2 indicate that the cylinder causes a general outward displacement of the flat-plate induced flow which approaches the cylinder from below.

A final side-view visualization is presented in Fig. 3. For the streamlines of this figure, the probe was positioned to the side of the cylinder – displaced transversely by half a diameter from one of the lateral edges. It is evident from Fig. 3 that the streamlines pictured there are not markedly influenced by the presence of the cylinder. They are essentially the streamlines of the flat plate flow. Thus, it appears that the influence of the cylinder does spread laterally to a significant extent.

The aforementioned finding is amplified in Fig. 4, which is a head-on view of the plate-cylinder assembly. The dye filaments shown in this figure were created by a horizontal wire that was periodically coated with teflon, leaving a periodic array of exposed segments at which the electrochemical reaction could occur. As seen in the figure, the flow approaching the cylinder from below moves laterally outward at first but then swings back as it passes the upper portion of the cylinder. The streamlines which pass near the side of the cylinder also tend to be drawn inward above the cylinder, but those situated farther to the side are unaffected.

In Fig. 4, the two streamlines that are closest to the cylinder appear to be on a collision course, but that is an illusion since, in reality, they do not lie in the same plane (the one closest to the cylinder is forward of its neighbor).

Concluding Remarks

The flow visualization results presented here demonstrate that the flow about a plate-attached horizontal cylinder is strongly three dimensional, with the axial motion of the fluid in the direction away from the plate being especially worthy of note. The observed flow pattern is significantly different from that for the classical long, end-effect-free horizontal cylinder.

In this light, it is quite remarkable that the average heat-transfer coefficients for the two cases are not too different. In [1], it was found that the heat-transfer coefficients for a plate-attached cylinder with a length-diameter ratio of one (i.e., the case studied here) were within 10 percent of those for the classical long horizontal cylinder. For an attached cylinder with a length-diameter ratio of one-half, the deviations were within 20 percent.

The effect of the attached cylinder on the heat-transfer coefficient for the flat plate has not been investigated in the literature. The present flow visualization results indicate that there will be little effect below the cylinder and that the affected region above the cylinder will be confined to a narrow corridor only slightly wider than the cylinder itself.

References

1 Sparrow, E. M., and Chrysler, G. M., "Natural Convection Heat-Transfer Coefficients for a Short Horizontal Cylinder Attached to a Vertical Plate," JOURNAL OF HEAT TRANSFER, Vol. 103, 1981, pp. 630–637.

2 Baker, D. J., "A Technique for the Precise Measurement of Small Fluid Velocities," *Journal of Fluid Mechanics*, Vol. 26, 1966, pp. 573–575.

3 Ostrach, S., "An Analysis of Laminar Free-Convection Flow and Heat Transfer about a Flat Plate Parallel to the Direction of the Generating Body Force," NACA Report 1111, Washington, D.C., 1953.

A Note on Transient Free Convection of Water at 4°C Over a Doubly Infinite Vertical Porous Plate

I. Pop[1] and A. Raptis[2]

Nomenclature

c = parameter of blowing or suction
f = dimensionless function
g = acceleration due to gravity
L = characteristic length of the plate
Pr = Prandtl number, υ/κ
t' = time
t_0 = characteristic time, L^2/υ
T' = fluid temperature
T'_w = constant temperature of the plate
T'_∞ = ambient temperature
$\Delta T'$ = temperature difference in two points of water
u' = velocity along the plate
u_0 = characteristic velocity, $g\vartheta L^2 \times (T'_w - T'_\infty)^2/\upsilon$
v' = velocity normal to the plate
v'_w = velocity of blowing or suction
x' = coordinate along the plate oriented vertically upward
x'_p = penetration distance
$x_{p\max}$ = dimensionless maximum penetration distance
y' = coordinate normal to the plate
ϑ = coefficient of thermal expansion of water at 4°C
η = similarity variable, $y/2\sqrt{t}$
υ = kinematic viscosity
κ = thermal diffusivity
ζ = density
$\Delta\zeta$ = density difference in two points of water

Subscripts

w = wall condition
∞ = ambient fluid condition

Introduction

Considerable work has been done in recent years on the transient free convection flow past a vertical infinite flat plate. Many different mathematical methods and techniques have been used to seek solutions to this class of problems [1–5]. These studies are mainly restricted only to fluids at

[1] University of Cluj, Faculty of Mathematics, Cluj CP 253, Romania
[2] University of Ioannina, Department of Mechanics, Ioannina, Greece

Contributed by the Heat Transfer Division for publication in the JOURNAL OF HEAT TRANSFER. Manuscript received by the Heat Transfer Division October 27, 1981.

normal temperatures and are not applicable to free convective flow of water below 4°C. Water in the temperature range from 0°C to 4°C decreases in volume with increasing temperature contrary to the behaviour of most fluids. That is, the density of water at 4°C is maximum at atmospheric pressure.

Goren [6] showed that for water at 4°C the variations in density are very closely given by

$$\Delta\zeta = \zeta\vartheta(\Delta T')^2 \tag{1}$$

in which $\Delta T'$ is not too large and $\vartheta = 8.0 \times 10^{-6}$ $(°C)^{-2}$. Thus, for small temperature variations free convection in water at 4°C would be much reduced from that at other temperatures and this fact might be an important consideration in certain freezing processes. On the other hand, the analysis of free convection flow of water at 4°C is important in view of several physical problems, such as coolant in many experiments in chemical engineering, atomic energy etc., where one wishes to suppress free convection.

The object of this research note is to apply Goren's idea to the problem of transient free convection flow of water at 4°C over a doubly infinite vertical porous flat plate following a step change of surface temperature. Initially, the plate and the fluid are at the temperature of the surrounding fluid, T'_∞. Then, at time $t' = 0$, the temperature of the plate is suddenly changed to T'_w and maintained at this value for all $t' > 0$, where $T'_w > T'_\infty$. The fluid is subject to a normal velocity of blowing or suction at the plate proportional to $t'^{-1/2}$. As it is well-known, the phenomenon of surface mass transfer has been widely employed for boundary-layer control and to effect of reduction in heat-transfer rates.

The results of the present solution are presented in both graphical and tabular form for a Prandtl number of 11.4 corresponding to water at 4°C and for some values of blowing and suction parameter, c. For comparison we have also included the data from [3] for fluids at normal temperatures and Pr = 1.0. Finally, an estimation is made for the distance of the propagation of the leading edge effect of the plate. These graphs and tables show the direct effect of the mass transfer on the flow characteristics.

Analysis

Consider an unsteady free convection flow of water below 4°C over a doubly infinite vertical flat plate which is initially at the temperature of the surrounding liquid, T'_∞. The axes x' and y' are chosen to be along and normal to the plate. Let u' and v' be the velocity components along x'-and y'-axes, respectively. The vertical homogeneity of the problem demands that the physical variables are functions of y' and t' only. Thus, the motion of fluid in the vicinity of the plate is described by the following set of equations:

$$\frac{\partial v'}{\partial y'} = 0 \tag{2}$$

$$\frac{\partial u'}{\partial t'} + v'\frac{\partial u'}{\partial y'} = g\vartheta(T' - T'_\infty)^2 + \upsilon\frac{\partial^2 u'}{\partial y'^2} \tag{3}$$

$$\frac{\partial T'}{\partial t'} + v'\frac{\partial T'}{\partial y'} = \kappa\frac{\partial^2 T'}{\partial y'^2} \tag{4}$$

An important observation is that the preceding equations are valid for all Grashof numbers, since we use a doubly infinite surface. The initial and boundary conditions pertinent to the physical problem under consideration are

$$\begin{aligned} t' \le 0:&\quad u' = v' = 0, \quad T' = T'_\infty \quad \text{everywhere} \\ t' > 0:&\quad u' = 0, \quad v' = v'_w(t'), \quad T' = T'_w \quad \text{at} \quad y' = 0 \\ &\quad u' \to 0, \quad T' \to T'_\infty \quad \text{as} \quad y' \to \infty \end{aligned} \tag{5}$$

The solution of equation (2) consistent with variable blowing or suction condition at the plate is

$$v' = v'_w(t') = -c(\upsilon/t')^{1/2} \text{ for all } y' \tag{6}$$

where the constant c characterizes the phenomenon of suction or blowing at the plate according to whether it is positive or negative. It should be, however, mentioned that the form of (6) is imposed by the similarity analysis. But this relation is somewhat an unrealistic condition particularly for small times. However, as Schetz and Zeiberg [3] have shown, such a result is not unexpected if it is noted that t' here would play the same role as x'/u_0 in a steady flow problem.

In terms of the following dimensionless variables

$$t = \frac{t'}{t_0}, \quad y = \frac{y'}{L}, \quad u = \frac{u'}{u_0}, \quad T = \frac{T' - T'_\infty}{T'_w - T'_\infty} \tag{7}$$

Equations (3) and (4) can be written as

$$\frac{\partial u}{\partial t} - \frac{c}{t^{1/2}}\frac{\partial u}{\partial y} = T^2 + \frac{\partial^2 u}{\partial y^2} \tag{8}$$

$$\frac{\partial T}{\partial t} - \frac{c}{t^{1/2}}\frac{\partial T}{\partial y} = \frac{1}{\mathrm{Pr}}\frac{\partial^2 T}{\partial y^2} \tag{9}$$

whilst the initial and boundary conditions (5) become

$$\begin{aligned} t \le 0:&\quad u = T = 0 \quad \text{everywhere} \\ t > 0:&\quad u = 0, \quad T = 1 \quad \text{at} \quad y = 0 \\ &\quad u \to 0, \quad T \to 0 \quad \text{as} \quad y \to \infty \end{aligned} \tag{10}$$

Further, if we introduce the new variables η and $f(\eta)$ as

$$\eta = y/2\sqrt{t}, \quad u(t,y) = t\,f(\eta) \tag{11}$$

Equations (8) and (9) then reduce to

$$\frac{d^2 f}{d\eta^2} + 2(\eta + c)\frac{df}{d\eta} - 4f = -4\,T^2 \tag{12}$$

$$\frac{d^2 T}{d\eta^2} + 2(\eta + c)\mathrm{Pr}\frac{dT}{d\eta} = 0 \tag{13}$$

with the appropriate boundary conditions

$$\begin{aligned} &f = 0, \quad T = 1 \quad \text{at} \quad \eta = 0 \\ &f \to 0, \quad T \to 0 \quad \text{as} \quad \eta \to \infty \end{aligned} \tag{14}$$

The solution of equation (13), satisfying (14), can be obtained in a straightforward manner and may be written as

$$T(\eta) = \frac{erfc\{\sqrt{\mathrm{Pr}}(\eta + c)\}}{erfc(\sqrt{\mathrm{Pr}}\,c)} \tag{15}$$

where $erfc$ ( ) is the complementary error function. By substituting the solution (15) into equation (12) the equation becomes linear, and a closed-form solution of this equation subject to the boundary conditions (14) is not feasible for arbitrary c. However, it is easier to integrate the ordinary differential equations (12) and (13) numerically using, for instance, the shooting method or the method of variation of parameter (see Na [7]). We have solved these equations for several values of the parameter, c, with the automatic initial-value technique developed by Nachtsheim and Swigert [8].

From (15) the dimensionless rate of heat transfer is given by

$$-\left(\frac{dT}{d\eta}\right)_{\eta=0} = 2\sqrt{\frac{\mathrm{Pr}}{\pi}}\frac{exp(-\mathrm{Pr}\,c^2)}{erfc(\sqrt{\mathrm{Pr}}\,c)} \tag{16}$$

Another physical quantity of additional interest is the penetration distance of the fluid originally at the leading edge of a semiinfinite flat plate and which is defined as

$$x'_p(y',t') = \int_0^{t'} u'(y',\tau)\,d\tau \tag{17}$$

If we write equation (17) in dimensionless form

$$x_p = \frac{x'_p}{L} \tag{18}$$

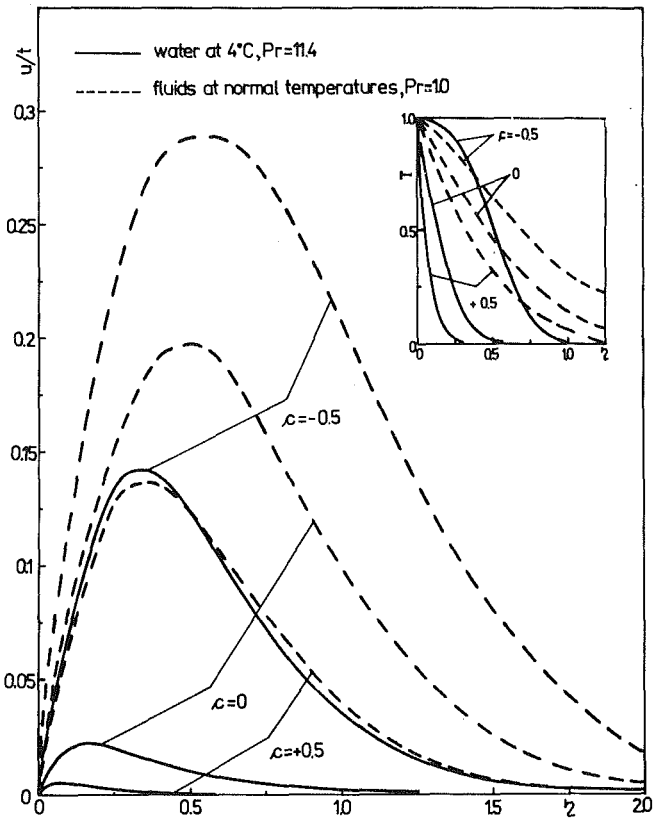

Fig. 1 Transient velocity and temperature profiles in water at 4°C and for fluids at normal temperatures and Pr = 1.0

and taking into account (7) and (11), then we have

$$x_p = 2\,t^2\left\{\eta^4\int_\eta^\infty \frac{f(\eta)}{\eta^5}\,d\,\eta\right\}. \tag{19}$$

Accordingly the maximum penetration distance is obtained by imposing

$$\frac{\partial x_p}{\partial y}=0 \quad \text{or} \quad \int_\eta^\infty \frac{f'(\eta)}{\eta^4}\,d\,\eta=0 \tag{20}$$

Results

Transient velocity and temperature profiles for water at 4°C, along with those for fluids at normal temperatures and Pr = 1.0 obtained in [3], are shown in Fig. 1. We observe from these figures, as one would expect, that the application of suction ($c = +0.5$) reduces the velocity and temperature profiles whereas the blowing ($c = -0.5$) is followed by a considerable increase of these profiles.

In Table 1 some values of the dimensionless skin-friction and the rate of heat transfer at the plate are given. Also included in the table are the results for fluids at normal temperatures and Pr = 1.0. By inspection of this table, it can be noted that the skin-friction decreases with the increase of the surface mass-transfer parameter, c. Contrary to this, the rate of heat transfer increases in magnitude once the parameter c increases. On the other hand, Figs. 1 and Table 1 show that, in general, the phenomenon of reduction of free convection in water at 4°C is more pronounced than for fluids at normal temperatures. However, a rising temperature distribution is seen in Figs. 1 near the plate for water at 4°C in the case of blowing.

Table 2 summarizes results of the penetration distance, $x_p/2t^2$, for several specified values of the blowing or suction parameter, c. For completeness, the roots η_0 of equation (20) and the corresponding maximum penetration distances,

Table 1 The skin friction and the rate of heat transfer at the plate for water at 4°C and for fluids at normal temperatures and Pr = 1.0

c	$(df/d\eta)_{\eta=0}$		$-(dT/d\eta)_{\eta=0}$	
	Pr = 11.4	Pr = 1.0	Pr = 11.4	Pr = 1.0
−0.5	0.92556	1.18613	0.11116	0.57796
0.0	0.33099	1.12838	3.81022	1.12838
+0.5	0.13822	1.02094	12.98162	1.83271

Table 2 The penetration distance, $x_p/2t^2$, for water at 4°C

η	$c=-0.5$	η	$c=0.0$	η	$c=+0.5$
0.03	0.9527×10^{-2}	0.03	0.3067×10^{-2}	0.02	0.9965×10^{-3}
0.06	0.1627×10^{-1}	0.06	0.4368×10^{-2}	0.04	0.1185×10^{-2}
0.12	0.2656×10^{-1}	0.09	0.4995×10^{-2}	0.06	0.1237×10^{-2}
0.18	0.3243×10^{-1}	0.12	0.5169×10^{-2}	0.08	0.1213×10^{-2}
0.21	0.3394×10^{-1}	0.15	0.5070×10^{-2}	0.10	0.1154×10^{-2}
0.24	0.3465×10^{-1}	0.18	0.4819×10^{-2}	0.12	0.1082×10^{-2}
0.27	0.3469×10^{-1}	0.21	0.4494×10^{-2}	0.14	0.1006×10^{-2}
0.30	0.3418×10^{-1}	0.24	0.4140×10^{-2}	0.16	0.9320×10^{-3}
0.60	0.1819×10^{-1}	0.27	0.3785×10^{-2}	0.18	0.8616×10^{-3}
0.90	0.7057×10^{-2}	0.30	0.3443×10^{-2}	0.20	0.7956×10^{-3}
1.20	0.2431×10^{-2}	0.60	0.1204×10^{-2}	0.30	0.5297×10^{-3}
1.50	0.7441×10^{-3}	0.90	0.3747×10^{-3}	0.40	0.3489×10^{-3}
1.80	0.2006×10^{-3}	1.20	0.1033×10^{-3}	0.50	0.2271×10^{-3}
2.10	0.4691×10^{-4}	1.50	0.2483×10^{-4}	0.60	0.1460×10^{-3}
2.40	0.9037×10^{-5}	1.80	0.4942×10^{-5}	0.80	0.5743×10^{-4}
2.70	0.1094×10^{-5}	2.10	0.6215×10^{-6}	1.00	0.2146×10^{-4}

$x_{p\,\max}/2t^2$, are found to be in the intervals

$0.24<\eta_0<0.27$: $0.3465\times10^{-1}<x_{p\ \max}/2t^2<0.3469\times10^{-1}$ for $c=-0.5$

$0.12<\eta_0<0.15$: $0.4819\times10^{-2}<x_{p\,\max}/2t^2<0.5070\times10^{-2}$ for $c=0.0$

$0.06<\eta_0<0.08$: $0.1213\times10^{-2}<x_{p\ \max}/2t^2<0.1237\times10^{-2}$ for $c=+0.5$

It is worth noting here that the penetration distance is greater in the case of blowing than in the case of suction.

Acknowledgments

The authors would like to express their sincere appreciation to Professor T. Y. Na of the University of Michigan-Dearborn for his warm interest in our paper and for supplying us the data in Table 2. We are also deeply indebted to the referees for many helpful comments and suggestions in the writing of this paper.

References

1 Menold, E. R., and Yang, K. T., "Asymptotic Solutions for Unsteady Laminar Free Convection on a Vertical Plate," ASME *Journal of Applied Mechanics*, Vol. 84, 1962, pp. 124–126.

2 Schetz, J. A., and Eichorn, R., "Unsteady Natural Convection in the Vicinity of a Doubly Infinite Vertical Plate," ASME JOURNAL OF HEAT TRANSFER, Vol. 84, 1962, pp. 334–338.

3 Schetz, J. A., and Zeiberg, S. L., "On Unsteady Laminar Flow with Mass Transfer," *Proceedings of the Fourth U.S. National Congress of Applied Mechanics*, Vol. 2, 1962, pp. 1405–1410.

4 Goldstein, R. J., and Briggs, D. G., "Transient Free Convection about Vertical Plates and Cylinders," ASME JOURNAL OF HEAT TRANSFER, Vol. 86, 1964, pp. 490–500.

5 Mizukami, K., "The Leading Edge Effect in Unsteady Natural Convection on a Vertical Plate with Time-dependent Surface Temperature or Heat Flux," *International Journal of Heat and Mass Transfer*, Vol. 20, 1977, pp. 981–989.

6 Goren, L., "On Free Convection in Water at 4°C," *Chemical Engineering Science*, Vol. 21, 1966, pp. 515–518.

7 Na, T. Y., *Computational Methods in Engineering Boundary Value Problems*, Academic Press, New York, 1979.

8 Nachtsheim, P. R., and Swigert, P., "Satisfaction of Asymptotic Boundary Conditions in Numerical Solution of Nonlinear Equations of Boundary-Layer Type," NASA TND - 3004, 1965.

On the Prediction of the Hydrodynamic Flooding Criterion

L. S. Yao[1] and K. H. Sun[2]

Introduction

The countercurrent flow limitation or flooding in two-phase flows has long been a subject of engineering interest in the design of packed columns and two-phase heat-transfer processes [1, 2, 3]. Current concern about the effectiveness of injecting emergency core cooling water into a hot reactor core during a loss-of-coolant accident provides further impetus for flooding research [4–17]. Most recent studies were focused on the flow characteristics of a down-flowing water film with a upward gas flow in a long narrow pipe. A comprehensive review was recently performed by Tien and Liu [1].

Relations between the updrafting gas flow and the downward liquid flow were first correlated by Wallis [2] for his air-water data from round tubes. From his correlation, the critical gas flux above which there is no penetration of downward liquid flow is represented by

$$j_g^* = \left[\frac{\rho_g j_g^2}{gD(\rho_f - \rho_g)}\right]^{1/2} = \text{constant} \tag{1}$$

Equation (1) can be modified by replacing the tube diameter, D, by the characteristic length $[\sigma/gg_c\ (\rho_f - \rho_g)]^{1/2}$ [6, 17] to become

$$\text{Ku} = \frac{\sqrt{\rho_g} j_g}{[gg_c\sigma(\rho_f - \rho_g)]^{1/4}} \equiv \text{constant} \tag{2}$$

where Ku is often called the Kutateladze number. Equation (2) was later derived by Tien et al. [15] by considering inviscid interfacial instability coupled with the kinematic wave theory and the critical wavelength concept.

Sun [6] found that the parameter, Ku, is a constant for flooding at the upper tie plates of the boiling water reactor (BWR) fuel bundles [6, 17]. For the vertical side-entry orifices of the BWR bundles, he found that Ku is a linear function of the Bond number, a dimensionless diameter which is defined as

$$D^* = D\left[\frac{g_c g(\rho_f - \rho_g)}{\sigma}\right]^{1/2} \tag{3}$$

Tien et al. [15] correlated their tube data by setting Ku as a function of $\tanh(D^*)$.

There are generally two types of phenomena corresponding to the threshold of flooding with no liquid penetration. One is the situation in which the liquid pool in the upper plenum is supported by a gas jet injected from below. The other phenomenon is that the liquid film in the tube is held against the tube wall by the upward gas flow. In the former case, the pool is dynamic and the tube is dry. While in the latter case, the liquid film can be considered as stationary and it is referred to as the "hanging film phenomenon" [10, 12].

In cases of flooding with the hanging film phenomenon, Pushkina and Sorokin [7] showed that their wide range of data from different tube sizes and working fluids can be correlated by Ku = 3.2. Wallis and Makkenchery [12] indicated that Ku = 3.2 overpredicted their tube data at small D^*. Analyses of the phenomenon by Wallis and Kuo [11], and Eichhorn [10] pointed out that the contact angle between the fluid and the solid surface can be important. Correlations in the forms of Ku versus D^* with the friction factor as a varying parameter have been proposed by Bharathan [13], Richter [4], and Eichhorn who showed an additional dependence of the contact angle [10].

In cases of dynamic flooding in the liquid pool with no downward liquid penetration, the phenomenon is different from the hanging film situation because the annular flow configuration does not exist and the friction factor associated with the pipe flow is irrelevant. Experimental study of flooding with variation of the depth of the liquid pool in the upper plenum by Wallis [9], Bharathan [13, 14], and Jones [17] showed that the countercurrent liquid and gas flow rates were relatively insensitive to the liquid depth compared to the geometries of the pipe entry and exit. Correlations used for this condition is similar to that for the hanging film condition. However, no fundamental models are available to describe the threshold of flooding with a gas jet in a liquid pool and to predict the critical gas flux above which there is no liquid penetration.

There are similarities between the flooding phenomenon with a gas jet injected into a liquid pool and the hydrodynamic crisis (or the critical heat flux) in a boiled pool [3, 18, 19, 20]. Zuber et al. [18], and Sun and Lienhard [19] suggested that vapor jets and water jets move in opposite direction and compete for the flow passage in a boiling pool. The maximum relative velocity between the countercurrent flows occurs in the limit of Helmholtz instability. Countercurrent flooding limits the amount of water approaching the heating surface and triggers the boiling crisis. Thus, it is reasonable to assume that flooding occurs as Helmholtz instability limits the approach of the liquid to the orifice on the bottom plate where the gas is injected through the orifice.

In the present study, a fundamental model for dynamic flooding with no liquid penetration has been developed by applying the linear instability and the basic inviscid flow theories. The result is compared with available experiments.

Analysis

The idealized model is a gas jet injected upward from a circular hole of diameter, $2a$, into a large liquid pool as shown in Fig. 1. The velocity of the gas jet relative to the liquid jet is

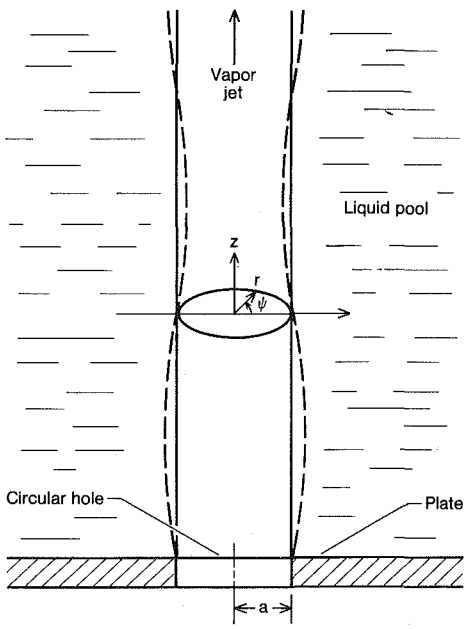

Fig. 1 The physical model—an upward vapor jet from a circular hole of radius a into a large liquid pool

[1]Department of Mechanical and Aerospace Engineering, Arizona State University, Tempe, Ariz. 85281.
[2]Nuclear Power Division, Electric Power Research Institute, Palo Alto, Calif. 94303.

Contributed by the Heat Transfer Division for publication in the JOURNAL OF HEAT TRANSFER. Manuscript received by the Heat Transfer Division April 24, 1982.

assumed constant, designated by W. Since the induced liquid velocity is small compared to the gas velocity, W can be interpreted as the gas inlet velocity.

A straightforward analysis can be performed [21] to show that the onset of the instability of the vapor column occurs when

$$\sqrt{\rho_g}\, W > \frac{k}{k_z}\left[\frac{I_1(ka)}{I_0(ka)}\,\sigma k\left(1-\frac{1}{a^2k^2}\right)\right]^{1/2} \tag{4}$$

Equation (4) shows that the gas jet is unstable when $1 > ak$ where k is the wave number and I's are the Bessel functions. The instability condition, $1 > ak$, represents the physical situation that the vapor jet breaks into vapor bubbles under the influence of surface tension when the wavelength, $\lambda = 2\pi/k$, exceeds the circumference of the jet. This is known as the instability of the Rayleigh jet [22]. Rayleigh also showed that the unsymmetric disturbances are stable, i.e., $k_\psi = 0$. Physically, one can picture that bubbles are formed on the top of a rising gas column when the injection gas speed is low.

The gas jet becomes violent as the injection speed increases. This is known as the Helmholtz instability which causes flooding. Due to the highly irregular motion along the interface, the lowest circumferential mode, $k_\psi = 0$, is not necessary to be most unstable. Determination of critical and fastest-growing modes along the z-direction as well as along the ψ-direction requires a detailed study of nonlinear effects. Since the model does not account for this detail, it is decided to select k_z and k_ψ by matching with the available data.

The well-known Laplace length, $[\sigma/(\rho_f - \rho_g)g]^{1/2}$, used widely in two-phase flow and boiling, is selected as the characteristic length. We set

$$k = \sqrt{k_\psi{}^2 + k_z{}^2} = C_3\left[\frac{(\rho_f-\rho_g)g}{\sigma}\right]^{1/2} \tag{5a}$$

$$\frac{k}{k_\psi} = C_4 \tag{5b}$$

Rearranging equation (4) after substituting equation (5) results in

$$\mathrm{Ku} > C_4C_3{}^{1/2}\left[\frac{I_1\left(\frac{C_3D^*}{2}\right)}{I_0\left(\frac{C_3D^*}{2}\right)}\left(1-\frac{4}{C_3{}^2D^{*2}}\right)\right]^{1/2} \tag{6}$$

Equation (6) provides a criterion for flooding with no liquid penetration. It indicates that the criterion corresponds to a constant Kutateladze number which depends on the Bond number. This is a consequence of competition between the Helmholtz and the Rayleigh-jet instabilities.

Equation (6) shows that the critical Kutateladze number weakly depends on D^* when $D^* >> 2/C_3$. This agrees with the trend of Pushkina and Sorokin's data [7]. In this case, flooding is governed by the Helmholtz instability.

For $D^* < 2/C_3$, Equation (6) indicates that Ku becomes imaginary and the system is unconditionally stable. Physically, it could correspond to the condition in which the surface tension becomes the dominant force, and the jet configuration does not exist. It could also be interpreted that the diameter of the orifice is so small that the Taylor waves can not grow. At zero vapor flow, the potential energy, depending on the depth of the liquid pool, balances statically with the pressure energy of the vapor. Though the current model does not consider this condition, it does show that flooding does not occur when $D^* < 2/C_3$, i.e., when the orifice diameter is smaller than $1/(C_3\pi)$ times the critical Taylor wavelength.

When $D^* > 2/C_3$, the Taylor unstable waves grow to form gas columns. For small D^*, the surface tension breaks up the gas column near the orifice. One can picture that a series of bubbles is formed close to the orifice. This is a consequence of the Rayleigh-jet instability. As D^* increases noticeably larger than $2/C_3$, the height of the gas column increases, and the gas bubbles break away from the top of the gas column. The Rayleigh-jet instability moves upward and interacts with the Helmholtz instability. This results in an increase in the critical Kutateladze number.

The influence of the Rayleigh-jet instability gradually disappears for an even larger D^*, approximately $D^* > 10$. The flooding is then caused solely by the Helmholtz instability and is independent of D^*. Physically, this means that the orifice diameter is no longer a relevant parameter to the flooding phenomenon, if it is far larger than the Taylor unstable wavelength.

Under the condition that D^* is not too small, the Bessel functions can be represented by the governing terms in their asymptotic expansion. Equation (6) becomes

$$\mathrm{Ku} > C_4C_3{}^{1/2}\left[\frac{4C_3D^*-3}{4C_3D^*+1}\left(1-\frac{4}{C_3{}^2D^{*2}}\right)\right]^{1/2} \tag{7}$$

The value of $C_4C_3{}^{1/2}$ is set at 3.2 to match with the experimental data for very large D^*. Due to the similarity of the flooding phenomenon to that of the pool boiling critical heat flux [3, 18, 19], two sets of wave numbers are selected according to [18] to provide the upper and lower bounds of the flooding criterion.

(*i*) Critical wave number

$$\left.\begin{aligned} k_z &= \left[\frac{(\rho_f-\rho_g)g}{\sigma}\right]^{1/2} \\ k_\psi &= 1.93\left[\frac{(\rho_f-\rho_g)g}{\sigma}\right]^{1/2} \end{aligned}\right\} \tag{8}$$

This corresponds to the selection of the Taylor critical wavelength $\lambda_z = 2\pi/k_z = 2\pi\,[\sigma/(\rho_f-\rho_g)g]^{1/2}$. Equation (17) becomes

$$\mathrm{Ku} > 3.2\left[\frac{D^*-0.345}{D^*+0.115}\left(1-\frac{0.848}{D^{*2}}\right)\right]^{1/2} \tag{9}$$

It is obvious that the equation is valid for $D^* > 0.921$. Equation (9) is represented by the dashed line in Fig. 2.

(*ii*) Rapid-growth wave number

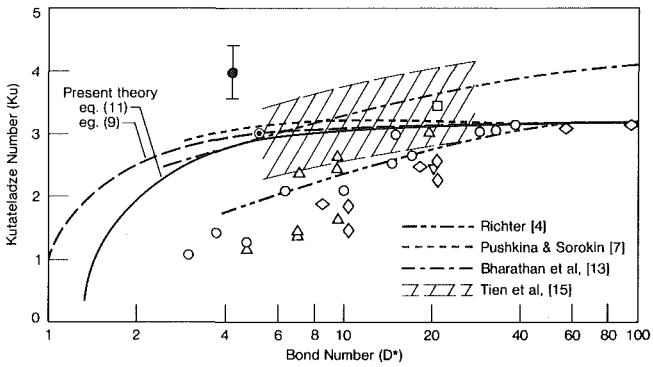

Fig. 2 Comparison of the present theory with data and other analyses: ○ Wallis & Makkenchery [12]; □ Dukler & Smith [5]; ◇ Bharathan [14]; △ Bharathan et al. [13]; ⊙ Jones, 7 × 7 bundle [6]; ● Jones, 8 × 8 bundle [6]; ▽ Wallis et al. [9]; ◇ Richter [4]

$$k_z = \frac{1}{\sqrt{3}}\left[\frac{(\rho_f-\rho_g)g}{\sigma}\right]^{1/2}$$

$$k_\psi = 1.391\left[\frac{(\rho_f-\rho_g)g}{\sigma}\right]^{1/2} \quad (10)$$

This is derived by selecting the rapid-growth Taylor wavelength, $\lambda_z = 2\pi\,[3\sigma/(\rho_f-\rho_g)g]^{1/2}$. Equation (7) becomes

$$\mathrm{Ku} > 3.2\left[\frac{D^*-0.5}{D^*+0.166}\left(1-\frac{1.764}{D^{*2}}\right)\right]^{1/2} \quad (11)$$

Equation (11) indicates there is no flooding limit for $D^* < 1.33$ and is plotted as the solid line in Fig. 2.

Comparison With Experiments and Correlations

The present analysis of the hydrodynamic flooding criterion for the case of a gas jet in a liquid pool without liquid penetration leads to the predictions of the critical Kutateladze number, Ku, as a function of the Bond number, D^*, as shown in Fig. 2. The data that were plotted in Fig. 2 for comparison encompass both steam-water and air-liquid with a wide range of surface tension. The geometry includes single vertical tubes of various sizes and multirod bundles. It should be noted that the data shown in Fig. 2 include both the hanging film type of flooding [4, 5, 7, 9, 12–15] and the flooding in a liquid pool (6, 9, 13, 14, 17]. Since the study by Wallis et al. [9], Bharathan [13, 14], and Jones [17] showed no significant effect of the pool depth on flooding compared to the effect of pipe entry and existing geometries, we shall present all the data here for comparisons.

The data of Pushkina and Sorokin [7] from tests with air and organic liquids are represented by a dotted line in Fig. 2. The data of Tien et al. [15], which has a four-fold variation of the pipe diameter and liquid surface tension, is shown by a band. The upper and lower bounds of the band are the limiting conditions in their correlations, which were obtained from tests with various entry and exit geometries by setting the liquid flow terms equal to zero. There are abundant air-water single tube data with thirtyfold variation of tube diameter from Wallis [9, 12], Richter [4], and Bharathan [13, 14] of Dartmouth College. The scatter of the Dartmouth data is largely attributed to the various tube entry and exit geometries, as was the case of the data of Tien et al. [15]. The single data point of Dukler and Smith [5] was obtained by extrapolating their flooding data on a $j_g^{1/2}$ versus $j_f^{1/2}$ correlation to the coordinate where $j_f = 0$. The steam-water data of Jones [6, 17] for the geometry of 7×7 and 8×8 multihole tieplates were plotted in Fig. 2 by using hydraulic diameters in D^*.

The present theory is also compared with existing correlations for the limiting conditions of flooding without liquid penetration. The correlation developed by Bharathan [13], which reaches the asymptote of $\mathrm{Ku} = 4.2$ for large D^*, is the maximum gas flow at which any liquid film can be present within the tube without being dried out by the gas stream. The correlation is a theoretical envelope not reached by his data and was developed from momentum balance considerations coupled with an empirically determined friction coefficient for air-water flow. Richter [4] used a different approach in his momentum balance consideration by taking into account the effect of waviness in annular flow. In his model he adopted an interfacial friction factor, which was determined empirically for air-water wavy annular flow, and an assumption that the pressure difference between the interface and the bottom of the wave is the dynamic head of the gas flow. He was able to obtain a correlation which matches well with the data of Pushkina and Sorokin [7] at large D^* and agrees reasonably well with the Dartmouth data at lower D^*.

The comparison of data with the present analyses in Fig. 2 shows that the theory, which is fitted to experimental data at $D^* \to \infty$, agrees well with data for $D^* \gtrsim 15$. In the intermediate range of D^*, $5 \lesssim D^* \lesssim 15$, the analyses agree with the data of Tien et al. [15], Pushkina and Sorokin [7], Dukler and Smith [5], but overpredict the Dartmouth College data [4, 9, 12–14] which are consistently lower than the others. At smaller D^*, $D^* \lesssim 5$, the theory agrees with the trend, but overpredicts the few data points of Wallis and Makkenchery [12]. It is noted that the BWR bundle tie-plate data of Jones [6, 17] are above all the tube data. This is probably due to the interactions of the gas jets and their nonuniformities in the liquid pool.

References

1 Tien, C. L., and Liu, C. P., "Survey on Vertical Two-Phase Countercurrent Flooding," EPRI, Report No. NP-984, Feb. 1979.

2 Wallis, G. B., *One-Dimensional Two-Phase Flows*, McGraw-Hill, New York, 1969.

3 Lienhard, J. H., *A Heat Transfer Textbook*, Prentice-Hall, Inc., Englewood, N.J., 1981.

4 Richter, H. J., "Flooding In Tubes and Annuli," presented at the *1980 International Seminar on Nuclear Reactor Safety Heat Transfer*, Dubrovnik, Yugoslavia, Sept. 1–5, 1980.

5 Dukler, A. E., and Smith, L., "Two-Phase Interactions in Countercurrent Flow: Studies of the Flooding Mechanism, "USNRC NUREG/CR-06176, Jan. 1979.

6 Sun, K. H., "Flooding Correlations for BWR Bundle Upper Tie Plates and Bottom Side-Entry Orifices," *Second Multi-Phase Flow and Heat Transfer Symposium-Workshop*, Miami Beach, Fla., Apr. 16–18, 1979, pp. 1615–1635.

7 Pushkina, D. L., and Sorokin, Y. L., "Breakdown of Liquid Film Motion in Vertical Tubes," *Heat-Transfer-Soviet Research*, Vol. 1, No. 5, 1969, pp. 56–64.

8 Zvirin, Y., Duffey, R. B., and Sun, K. H., "On the Derivation of a Countercurrent Flooding Theory," presented at the ASME Winter Annual Meeting, Dec. 3–7, 1979, New York.

9 Wallis, G. B. et al., "Countercurrent Annular Flow Regimes for Steam and Subcooled Water in a Vertical Tube," EPRI Report NP-1336, Jan. 1980.

10 Eichhorn, R., "Dimensionless Correlation of the Hanging Film Phenomenon," presented at the ASME Winter Annual Meeting, Dec. 2–7, 1979, New York, Paper No. 72-WA-FE-16.

11 Wallis, G. B., and Kuo, J. T., "The Behavior of Gas-Liquid Interfaces in Vertical Tubes," *International Journal of Multiphase Flow*, Vol. 2, 1976, pp. 521–536.

12 Wallis, G. B., and Makkenchery, S., "The Hanging Film Phenomenon in Vertical Annular Two-Phase Flow," *Journal of Fluids Engineering*, Vol. 96, Series 1, No. 3, Sept. 1974, pp. 297–298.

13 Bharathan, D., "Air-Water Countercurrent Annular Flows," EPRI Report NP-1165, Sept. 1979.

14 Bharathan, D., "Air-Water Countercurrent Annular Flow in Vertical Tubes," EPRI Report NP-786, May 1978.

15 Tien, C. L., Chung, K. S., and Liu, C. P., "Flooding in Two-Phase Countercurrent Flows," EPRI Report NP-1283, Dec. 1979. (Also, *Physico Chem. Hydrodynam.*, Vol. 1, 1979, pp. 195–220).

16 Liu, J. S. K., Collier, R. P., and Cudnik, R. A., "Flooding of Counter-Current Steam-Water Flow in An Annulus," presented at the ASME Winter Annual Meeting, Dec. 10–15, 1978, San Francisco, Calif.

17 Jones, D. D., "Subcooled Counter-Current Flow Limiting Characteristics of the Upper Region of a BWR Fuel Bundle," General Electric Company, Report NEDG-NUREG-23549, July 1977.

18 Zuber, N., Tribus, M., and Westwater, J. W., "The Hydrodynamic Crisis in Pool Boiling of Saturated and Subcooled Liquids," *Proceedings of the International Heat Transfer Conference*, Boulder, Colorado, August 1961, ASME Publication No. 27.

19 Sun, K. H., and Lienhard, J. H., "The Peak Pool Boiling Heat Flux on Horizontal Cylinders," *International Journal of Heat and Mass Transfer*, Vol. 13, 1970, pp. 1425–1439.

20 Kutateladze, S. S., "Elements of the Hydrodynamics of Gas-Liquid Systems," *Fluid Mechanics—Soviet Research*, Vol. 1, No. 4, 1972, pp. 29–50.

21 Yao, L. S., and Sun, K. H., "On the Prediction of the Hydrodynamic Flooding Criterion," presented at the 20th National Heat Transfer Conference, Aug. 2–5, 1981, Milwaukee, Wis., reprint HTD-Vol. 15, pp. 45–51.

22 Lamb, H., *Hydrodynamics*, 2nd ed., Dover Publications, New York, 1945, pp. 472–473.

A Theory for Prediction of Channel Depth in Boiling Particulate Beds[1]

S. W. Jones,[2] L. Baker, Jr.,[3] S. G. Bankoff,[4] M. Epstein,[5] and D. R. Pedersen[2]

Introduction[6]

In previous investigations of dryout heat fluxes from boiling particulate beds [1, 2], the bed has generally been considered to contain two distinct regions. In the lower region particles remain fixed in place, but the uppermost region is characterized by the presence of channels through the particles. For our purposes, a channel may be considered to be a less restricted vapor pathway through the particulate bed, formed when the frictional force exerted on the particles by vapor rising through the bed is sufficient to physically separate particles. A somewhat idealized channel is depicted in Fig. 1, and will be referred to in the following discussion.

At present, it is not clear what causes limitations in the heat flux from particulate beds having insufficient depth to prevent channels from penetrating completely to their lower boundary. It seems most likely that heat flux limitations in a channeled region result from a hydrodynamic phenomena similar to flooding or from a burnout condition comparable to film boiling. It is well known that the dryout heat flux from a particulate bed which can be completely or almost completely penetrated by channels is much greater than the dryout heat flux from a deeper, but otherwise identical bed.

In particulate beds heated through the base, an abrupt increase in the dryout heat flux is observed at bed depths comparable to, or slightly greater than, the channel penetration depth. In volumetrically heated beds, the measured dryout heat flux increases more gradually as bed height diminishes, partially because of heat generation in the channeled region. In this work, a method is given for predicting the depth of channel penetration from the physical properties of the particulate bed and the coolant in which it is immersed. Thus it is possible to determine the bed height at which the dryout heat flux through a bed may be increased by the presence of channels.

In beds composed of reasonably uniform particles having an average diameter of 1 millimeter or greater, channel formation is negligible, and its effect on dryout is not significant. Consequently, this analysis is limited to particulate beds with an average particle diameter less than 1 millimeter, such as those that have been postulated to form in LMFBR accident scenarios. More details regarding the effect of channels on dryout are available in reference [2].

Theoretical Development

The hydrodynamics of the channeled region would be very difficult to characterize completely. The number of channels per unit area of bed, as well as the channel shape and cross-sectional area, seems to depend on the vapor flux through the bed [2]. However, the depth of the channeled region appears to be somewhat independent of vapor flux, and this, easier to predict. For instance, the channel depth observed in heated beds prior to dryout, with vapor fluxes through the bed of less than 50 percent of the final vapor flux attained at dryout, do not seem to be noticeably different from the channel depths observed at the time of dryout [2].

Thus, the depth to which a channel can penetrate into a boiling particulate bed is found by assuming a one-dimensional flow through the channel and downward liquid flow through the surrounding particles. This separated flow, depicted in Fig. 1, is observed in both particulate beds with heat addition through the base and with induction heating of the particles. Consequently, the effect of vapor generation within the liquid saturated region around a channel is assumed to be negligible.

Due to the complex geometry of the porous bed, a number of approximations are necessary to simplify the analysis. Visual observations suggest that the cross-sectional area of a channel is approximately constant over most of its length, and that, once formed, a channel remains relatively stable. Based on these observations, the momentum equation through a channel is written as if the channel had constant area and was oriented completely vertically. Also, the total cross-sectional area of channels never appears to be more than a few percent of the total cross-sectional area of the bed. The single-phase Blake-Kozeny equation was therefore used to estimate the frictional resistance to the returning liquid flow. These frictional losses were found to be negligible.

In this study, particulate beds were constructed from particles of uniform shape and size, obtained by re-sieving after removal of nonspherical particles [2]. In the vast majority of cases, channels were seen to collapse when the vapor flow was terminated. Thus, it has been assumed that the pressure drop through the channel must be equal to the frictional force exerted on the channel walls, and this frictional force must equal the weight of the bed that has been displaced by the channel.

The pressure drop through the channel is approximated with the pressure drop required for incipient fluidization, and the pressure drop in the liquid region is approximated by the hydrostatic head. The interface between the vapor in the channel and the liquid in the surrounding particles must, consequently, be smooth near the top of the bed where the pressures in the liquid and vapor regions are nearly identical, and become increasingly distorted at greater depths. Also, a force opposing the pressure gradient must be exerted to maintain liquid downflow through the interstitial area around the channels.

The overall vapor fraction in beds at dryout has been estimated by measuring the coolant pool boil-up [2]. Although the data exhibit much scatter, they indicate that about 50 percent of the interstitial volume is occupied by

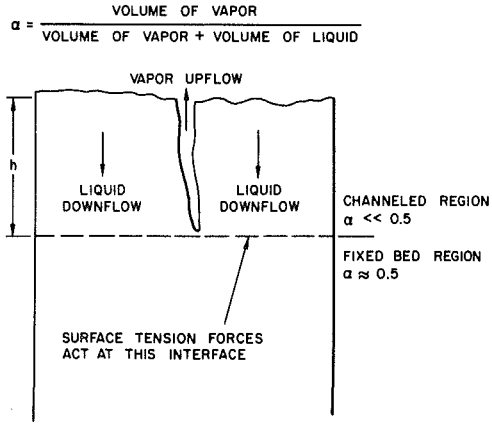

Fig. 1 Schematic of the region around a single channel

[1] Work performed under the auspices of the U.S. Department of Energy.
[2] Reactor Analysis and Safety Division, Argonne National Laboratory, Argonne, Ill. 60439
[3] Technology Management Center, Argonne National Laboratory, Argonne, Ill. 60439
[4] Chemical Engineering Department, Northwestern University, Evanston, Ill. 60201
[5] Fauske and Associates, Inc., Willowbrook, Ill. 60521, Mem. ASME
[6] Request for information should be addressed to D. R. Pedersen.
Contributed by the Heat Transfer Division for publication in the JOURNAL OF HEAT TRANSFER. Manuscript received by the Heat Transfer Division July 20, 1981.

vapor. Observations of channel size and density, however, indicate that vapor occupies no more than 10 percent of the interstitial volume in the channeled region. A noticeable jump in vapor fraction, which can be observed at the test section wall, occurs between the channeled zone, where vapor is predominantly in the channels, and the region below. Thus, it is assumed that surface tension forces provide an additional driving force which acts on the liquid phase.

This surface tension force is approximated by envisioning the bed as a solid penetrated by numerous irregular capillaries, and utilizing equations for capillary rise in a tube, with the tube radius replaced by the mean radius of curvature, which is twice the hydraulic radius of the bed [3]. Effects resulting from the two-phase flow in the region below the channels are ignored, and the surface tension force pulling the liquid down is given as follows:

Capillary force $= \sigma/r_H$, where σ is the interfacial tension and where the hydraulic radius of the bed is given by

$$r_H = S/Z = \frac{D_p \epsilon}{6(1-\epsilon)}$$

Here, D_p is the average particle diameter, ϵ is the porosity, and S and Z are, respectively, the average cross-sectional area and wetted perimeter of the capillaries through the bed.

Under the numerous constraints imposed by the previous discussion, the pressure drop through the channeled region of the bed is given by

$$\Delta P = (\Delta P)_f = \rho_b g h \tag{1}$$

with

$$\rho_b = \epsilon \rho_l + (1-\epsilon)\rho_s$$

where P is pressure, ρ_b is bed density, g is acceleration due to gravity, h is the channel depth, ρ_l is liquid density, ρ_s is solid density, and $(\Delta P)_f$ denotes frictional losses through the channel.

For the liquid phase, the force balance reduces to

$$\Delta P = \rho_l g h + \frac{6\sigma(1-\epsilon)}{\epsilon D_p} \tag{2}$$

Solving equations (1) and (2) for the maximum penetration of the channel yields

$$h = \frac{6\sigma}{(\rho_s - \rho_l) g \epsilon D_p} \tag{3}$$

Comparison with Observations

During a recent investigation of limiting heat fluxes from particulate beds, channel depths were observed and recorded for a variety of experimental systems [2]. A comparison with the channel depths observed in this study is given in Table 1 and shown graphically in Fig. 2. In this table, the observed channel depths are averages over a number of channel depth measurements. The number of measurements, in addition to the maximum observed deviation from the average depth, are included. Equation (3) appears to predict channel depths in metals quite well, but underestimates them by a factor of two for glass. The discrepancy with glass data is largely due to the low density of glass, and the resulting instability of the channels. The lifetime of some channels through glass particulate beds is sometimes little more than the time necessary for a vapor bubble to rise through it, and other channels tend to wander, or sporadically close and reopen.

It should be noted that the experimental values listed in the table are based on observations at the walls of the test section. However, there was no evidence to suggest that channels

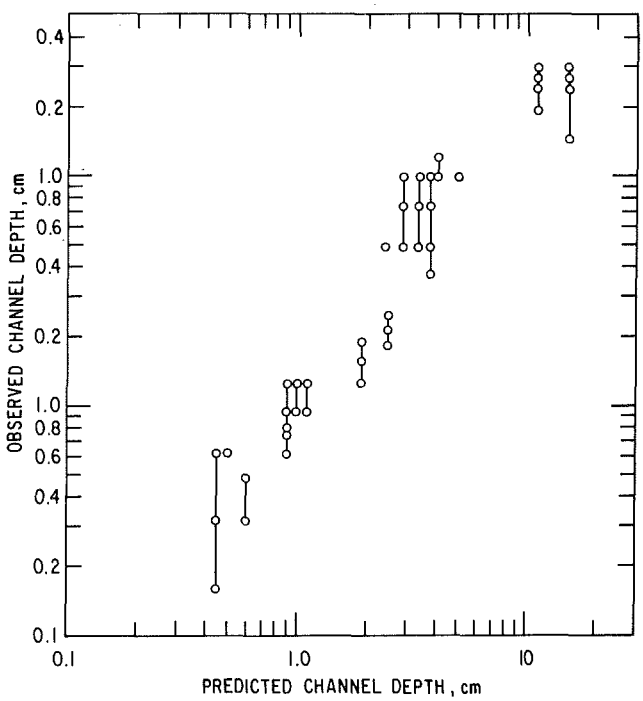

Fig. 2 Comparison of theory with observed channel depths

Table 1 Comparison of predicted channel depths with observed channel depths

System	Average particle diameter (cm)	Observed channel depth (cm)	Number of observations	Maximum deviation from mean (%)	Predicted channel depth (cm)
Lead-Methanol	.046	0.4	3	29	0.6
Lead-H_2O	.093	1.1	6	34	0.9
Lead-H_2O	.078	1.2	13	19	1.1
Lead-H_2O	.046	1.5	9	24	1.9
Copper-H_2O	.11	1.0	11	26	1.0
Copper-H_2O	.046	2.1	16	22	2.5
Glass-Isopropanol	.055	5.0	5	0	2.4
Glass-Isopropanol	.039	7.0	5	46	3.4
Glass-Acetone	.055	7.0	4	40	3.2
Glass-Acetone	.039	10.0	1	-	4.5
Glass-Methanol	.055	7.0	3	42	2.9
Glass-Methanol	.039	11.0	2	18	4.0
Glass-H_2O	.055	27.0	4	25	11.0
Glass-H_2O	.039	27.0	10	44	15.0
Steel-H_2O	.078	1.5	19	28	1.7
Steel-H_2O surfactant ($\sigma \approx 30$ dynes/cm)	.078	0.8	7	21	.9
Steel-Isopropanol	.078	0.4	6	64	0.4
Steel-Methanol	.078	0.6	12	0	0.5

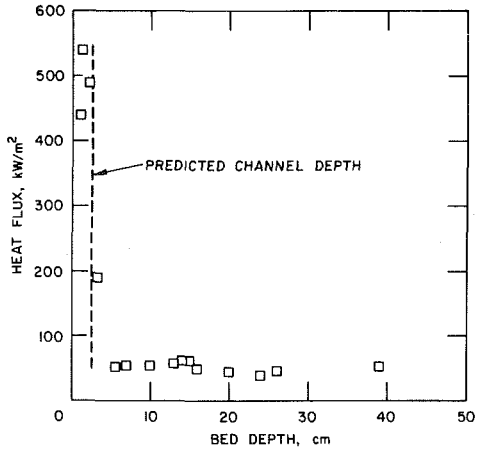

Fig. 3 Dryout heat fluxes from 0.46-mm dia copper particulate beds in water

might extend to different heights in the interior of the bed. In fact, heat flux measurements from shallow beds indicate that channels penetrate completely through the bed at bed depths nearly identical to the observed channel depths listed in Table 1. Figure 3 is a plot of dryout heat flux versus bed depth for copper particulate beds heated through the base. A sharp increase in heat flux is observed at bed depths comparable to the predicted channel penetration depth. This indicates that the predicted channel depth gives a good indication of the bed height at which the mechanism controlling the dryout heat flux changes.

Certainly the most convincing argument for assuming a surface tension force acting at the interface of the channeled region and the fixed bed region is the decrease of channel depth obtained in stainless steel particulate beds immersed in solutions of water with a commercial surfactant. Using a capillary rise technique to measure surface tension, a solution of Kodak Photoflo 200 and water was found to have a surface tension of about 30 dynes/cm, or approximately one-half that of water. Channeling in beds immersed in this solution was found to extend to approximately one-half the depth to which channeling could extend in water without surfactant.

References

1 Dhir, V., and Catton, I., "Dryout Heat Fluxes for Inductively Heated Particles," ASME JOURNAL OF HEAT TRANSFER, Vol. 99, 1977, pp. 250-256.

2 Jones, S. W., "A Study of Dryout Heat Fluxes," Ph.D. dissertation, Northwestern University, Evanston, Ill., 1982.

3 Scheidegger, A. E., "The Physics of Flow Through Porous Media," rev. ed., University of Toronto Press, Toronto, Canada, 1960.

An Exact Solution of the Sublimation Problem in a Porous Medium, Part II – With an Unknown Temperature and Vapor Concentration at the Moving Sublimation Front[1]

Sui Lin[2]

1 Introduction

Processes of heat and mass transfer in a porous medium, such as evaporation, condensation, sublimation and desublimation, have wide applications in separation processes, food technology, heat and moisture migration in soils and grounds, etc. Due to the nonlinearity of the moving boundary problem, solutions usually involve mathematical difficulties. Only a few exact solutions have been found for idealized situations [1-4].

The sublimation problem described in [4] was under the consideration that, during the sublimation process, the vapor pressure acting on the frozen phase is equal to the environmental pressure which remains unchanged. Under this assumption, the sublimation process has a known temperature at the sublimation front, which is equal to the saturation temperature corresponding to the vapor pressure acting on the frozen phase. To generalize the sublimation problem described in [4], the above restriction is eliminated in the present paper. We therefore handle a sublimation problem with an unknown vapor pressure and an unknown temperature at the sublimation front. For a complete description of the problem under such a condition, an additional thermodynamic equation describing the phase change relation is required.

In the following, the sublimation process taking place in a porous half-space with an unknown vapor pressure (or vapor concentration) and an unknown temperature at the sublimation front is investigated. Exact solutions for the temperature and vapor concentration at the sublimation front, the temperature and vapor distributions in the porous body, as well as the location of the moving sublimation front, are obtained.

2 Statement of the Problem

We consider a rigid solid porous half-space initially containing a uniform frozen moisture with a molar concentration, $c_{m,0}$, and having an initially uniform temperature, T_0. The porous body is sublimated by maintaining the surface at $x = 0$ at a constant molar concentration of vapor, $C_{m,s}$ which is lower than the molar vapor concentration at its triple point state, $c_{m,3}$, and at a constant temperature, T_s, which is higher than the initial temperature, T_0. For the purpose of formulation of the sublimation problem, the following assumptions are made:

1 In the frozen region, $s(\tau) < x < \infty$, there is no moisture movement, where $x = s(\tau)$ locates the sublimation front. In the vapor region $0 < x < s(\tau)$, there are heat and moisture flows.

2 The convective terms in the vapor region and the heat transferred by radiation are small and may be neglected.

3 The vapor pressure of the moisture in the sublimation process is low so that the vapor can be considered as an ideal gas.

4 The change of pressure caused by the nonuniformity of the curvature of the frozen-moisture at the sublimation front may be neglected.

5 The thermophysical properties of each phase remain constant but may differ for different phases.

6 The Soret effect, or the thermal diffusion, gives rise to a mass flux which is normally very small relative to the normal Fickian flux, and may be neglected.

For the mathematical formulation of the problem, the system of equations (1-9) in reference [4] can still be used. However, due to an unknown temperature and an unknown vapor concentration at the sublimation front (they are unknown, but remain constant), two additional conditions at the moving phase boundary are required for a complete description of the problem. One condition can be taken as

$$C_m(s,\tau) = C_{m,v} \tag{1}$$

[1] This paper is an extension of the work published in reference [4] which serves as part I of the paper.

[2] Professor, Department of Mechanical Engineering, Concordia University, Montreal, Quebec, Canada H3G 1M8.

Contributed by the Heat Transfer Division for publication in the JOURNAL OF HEAT TRANSFER. Manuscript received by the Heat Transfer Division April 20, 1981.

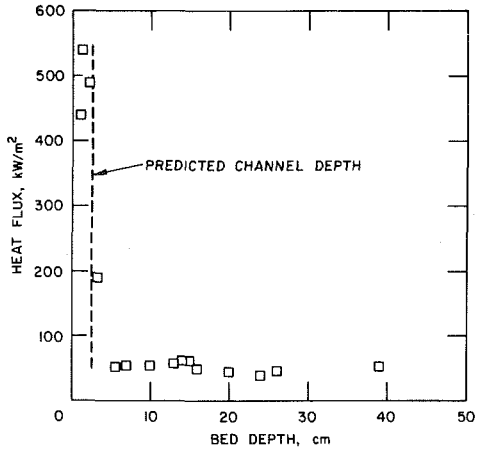

Fig. 3 Dryout heat fluxes from 0.46-mm dia copper particulate beds in water

might extend to different heights in the interior of the bed. In fact, heat flux measurements from shallow beds indicate that channels penetrate completely through the bed at bed depths nearly identical to the observed channel depths listed in Table 1. Figure 3 is a plot of dryout heat flux versus bed depth for copper particulate beds heated through the base. A sharp increase in heat flux is observed at bed depths comparable to the predicted channel penetration depth. This indicates that the predicted channel depth gives a good indication of the bed height at which the mechanism controlling the dryout heat flux changes.

Certainly the most convincing argument for assuming a surface tension force acting at the interface of the channeled region and the fixed bed region is the decrease of channel depth obtained in stainless steel particulate beds immersed in solutions of water with a commercial surfactant. Using a capillary rise technique to measure surface tension, a solution of Kodak Photoflo 200 and water was found to have a surface tension of about 30 dynes/cm, or approximately one-half that of water. Channeling in beds immersed in this solution was found to extend to approximately one-half the depth to which channeling could extend in water without surfactant.

References

1 Dhir, V., and Catton, I., "Dryout Heat Fluxes for Inductively Heated Particles," ASME JOURNAL OF HEAT TRANSFER, Vol. 99, 1977, pp. 250-256.

2 Jones, S. W., "A Study of Dryout Heat Fluxes," Ph.D. dissertation, Northwestern University, Evanston, Ill., 1982.

3 Scheidegger, A. E., "The Physics of Flow Through Porous Media," rev. ed., University of Toronto Press, Toronto, Canada, 1960.

An Exact Solution of the Sublimation Problem in a Porous Medium, Part II – With an Unknown Temperature and Vapor Concentration at the Moving Sublimation Front[1]

Sui Lin[2]

1 Introduction

Processes of heat and mass transfer in a porous medium, such as evaporation, condensation, sublimation and desublimation, have wide applications in separation processes, food technology, heat and moisture migration in soils and grounds, etc. Due to the nonlinearity of the moving boundary problem, solutions usually involve mathematical difficulties. Only a few exact solutions have been found for idealized situations [1-4].

The sublimation problem described in [4] was under the consideration that, during the sublimation process, the vapor pressure acting on the frozen phase is equal to the environmental pressure which remains unchanged. Under this assumption, the sublimation process has a known temperature at the sublimation front, which is equal to the saturation temperature corresponding to the vapor pressure acting on the frozen phase. To generalize the sublimation problem described in [4], the above restriction is eliminated in the present paper. We therefore handle a sublimation problem with an unknown vapor pressure and an unknown temperature at the sublimation front. For a complete description of the problem under such a condition, an additional thermodynamic equation describing the phase change relation is required.

In the following, the sublimation process taking place in a porous half-space with an unknown vapor pressure (or vapor concentration) and an unknown temperature at the sublimation front is investigated. Exact solutions for the temperature and vapor concentration at the sublimation front, the temperature and vapor distributions in the porous body, as well as the location of the moving sublimation front, are obtained.

2 Statement of the Problem

We consider a rigid solid porous half-space initially containing a uniform frozen moisture with a molar concentration, $c_{m,0}$, and having an initially uniform temperature, T_0. The porous body is sublimated by maintaining the surface at $x = 0$ at a constant molar concentration of vapor, $C_{m,s}$ which is lower than the molar vapor concentration at its triple point state, $c_{m,3}$, and at a constant temperature, T_s, which is higher than the initial temperature, T_0. For the purpose of formulation of the sublimation problem, the following assumptions are made:

1 In the frozen region, $s(\tau) < x < \infty$, there is no moisture movement, where $x = s(\tau)$ locates the sublimation front. In the vapor region $0 < x < s(\tau)$, there are heat and moisture flows.

2 The convective terms in the vapor region and the heat transferred by radiation are small and may be neglected.

3 The vapor pressure of the moisture in the sublimation process is low so that the vapor can be considered as an ideal gas.

4 The change of pressure caused by the nonuniformity of the curvature of the frozen-moisture at the sublimation front may be neglected.

5 The thermophysical properties of each phase remain constant but may differ for different phases.

6 The Soret effect, or the thermal diffusion, gives rise to a mass flux which is normally very small relative to the normal Fickian flux, and may be neglected.

For the mathematical formulation of the problem, the system of equations (1-9) in reference [4] can still be used. However, due to an unknown temperature and an unknown vapor concentration at the sublimation front (they are unknown, but remain constant), two additional conditions at the moving phase boundary are required for a complete description of the problem. One condition can be taken as

$$C_m(s,\tau) = C_{m,v} \tag{1}$$

[1] This paper is an extension of the work published in reference [4] which serves as part I of the paper.

[2] Professor, Department of Mechanical Engineering, Concordia University, Montreal, Quebec, Canada H3G 1M8.

Contributed by the Heat Transfer Division for publication in the JOURNAL OF HEAT TRANSFER. Manuscript received by the Heat Transfer Division April 20, 1981.

and the other can be used is the Clausius-Clapeyron equation describing a pure substance undergoing a first-order change of phase [5],

$$\frac{dP_v}{dT_v} = \frac{L}{T_v(V_v''' - V'_v)} \tag{2}$$

where P_v is the vapor pressure, v'_v and v'''_v are the molar volumes of the frozen moisture and vapor at the sublimation front, respectively. In the system of equations, the temperature and vapor concentration at the sublimation front, T_v and $C_{m,v}$, are unknown and have to be determined as a part of the solution.

3 Solution of the Problem

The solutions of the temperature distributions in the frozen and vapor regions remain the same as equations (10) and (12) of [4], respectively, where the dimensionless constant λ is defined by equation (11) of [4]. After the substitution of equations (10–12) into equation (8) in [4], equation (13) of [4] is still valid as an equation for the determination of the three unknowns λ, T_v and $C_{m,v}$.

The solution of the molar vapor concentration, which satisfies equations (3) and (6) in [4] and (1) in this paper, can be presented by

$$C_m(x,\tau) = C_{m,s} + \frac{C_{m,v} - C_{m,s}}{\operatorname{erf}(\sqrt{a_2/a_m}\,\lambda)} \operatorname{erf}\left(\frac{x}{2\sqrt{a_m \tau}}\right) \tag{3}$$

Substitution of equation (11) of [4] and (3) of this paper into equation (9) of [4] yields

$$\frac{\exp[-(a_2/a_m)\lambda^2]}{\operatorname{erf}(\sqrt{a_2/a_m}\,\lambda)} = \left(\frac{C_{m,0} - C_{m,v}}{C_{m,v} - C_{m,s}}\right)\sqrt{\frac{a_2}{a_m}}\sqrt{\pi}\,\lambda \tag{4}$$

For the purpose of determining the three unknowns λ, T_v, and $C_{m,v}$, the Clausius-Clapeyron equation shall now be integrated. Since the vapor pressure, during the sublimation process, is small, v'''_v is much larger than v'_v which may be neglected. Then equation (2) becomes

$$\frac{dP_v}{dT_v} = \frac{L}{T_v v'''_v} \tag{5}$$

We consider the vapor at the sublimation front as an ideal gas so that

$$v'''_v = \frac{R_0 T_v}{P_v} \tag{6}$$

where R_0 is the universal gas constant. Substitution of equation (6) into equation (5) gives

$$\frac{dP_v}{dT_v} = \frac{L P_v}{R_0 T_v^2} \tag{7}$$

Integration of equation (7) yields

$$ln\frac{P_v}{P_3} = \frac{L}{R_0}\left(\frac{1}{T_3} - \frac{1}{T_v}\right)$$

or

$$\frac{C_{m,v} T_v}{C_{m,3} T_3} = \exp\left[\frac{L}{R_0}\left(\frac{1}{T_3} - \frac{1}{T_v}\right)\right] \tag{8}$$

where P_3 and T_3 are the pressure and temperature at the triple point of the moisture, respectively. Equations (13) of [4] and (4), and (8) of this paper are the three equations required for solving λ, T_v and $C_{m,v}$.

4 Dimensionless Representation of Analytical Results

For the purpose of discussion of analytical results, the following dimensionless parameters are introduced:

$$\theta_1 = \frac{T_1 - T_0}{T_v - T_0} \tag{9}$$

$$\theta_2 = \frac{T_2 - T_v}{T_s - T_v} \tag{10}$$

$$\theta_0 = \frac{T_0}{T_3} \tag{11}$$

$$\theta_v = \frac{T_v}{T_3} \tag{12}$$

$$\theta_s = \frac{T_s}{T_3} \tag{13}$$

$$\phi = \frac{C_m - C_{m,s}}{C_{m,v} - C_{m,s}} \tag{14}$$

$$\phi_0 = \frac{C_{m,0}}{C_{m,3}} \tag{15}$$

$$\phi_v = \frac{C_{m,v}}{C_{m,3}} \tag{16}$$

$$\phi_s = \frac{C_{m,s}}{C_{m,3}} \tag{17}$$

$$\eta = \frac{x}{2\sqrt{a_2 \tau}} \tag{18}$$

$$a_{21} = \frac{a_2}{a_1} \tag{19}$$

$$\mathrm{Lu} = \frac{a_m}{a_2} \tag{20}$$

$$k_{21} = \frac{k_2}{k_1} \tag{21}$$

$$L^* = \frac{L}{R_0 T_3} \tag{22}$$

$$\nu = \frac{a_2 C_{m,3} M_m L}{k_1 T_3} \tag{23}$$

where

$$C_{m,3} = \frac{P_3}{R_0 T_3} \tag{24}$$

Then, equations (10), (12), (13) of [4], and (3), (4), and (8) of this paper can be written in dimensionless forms as follows:

$$\theta_1 = \frac{\operatorname{erfc}(\sqrt{a_{21}}\,\eta)}{\operatorname{erfc}(\sqrt{a_{21}}\,\lambda)} \tag{25}$$

$$\theta_2 = 1 - \frac{\operatorname{erf}(\eta)}{\operatorname{erf}(\lambda)} \tag{26}$$

$$\phi = \frac{\operatorname{erf}(\eta/\sqrt{\mathrm{Lu}})}{\operatorname{erf}(\lambda/\sqrt{\mathrm{Lu}})} \tag{27}$$

$$\left(\frac{\theta_s - \theta_v}{\theta_v - \theta_0}\right)\frac{k_{21}\exp(-\lambda^2)}{\operatorname{erf}(\lambda)} - \frac{\sqrt{a_{21}}\exp(-a_{21}\lambda^2)}{\operatorname{erfc}(\sqrt{a_{21}}\,\lambda)} = \frac{\sqrt{\pi}\,\nu\phi_0\lambda}{\theta_v - \theta_0} \tag{28}$$

$$\frac{\exp(-\lambda^2/\mathrm{Lu})}{\operatorname{erf}(\lambda/\sqrt{\mathrm{Lu}})} = \left(\frac{\phi_0 - \phi_v}{\phi_v - \phi_s}\right)\frac{\sqrt{\pi}\,\lambda}{\sqrt{\mathrm{Lu}}} \tag{29}$$

$$\phi_v \theta_v = \exp\left[L^*\left(1 - \frac{1}{\theta_v}\right)\right] \tag{30}$$

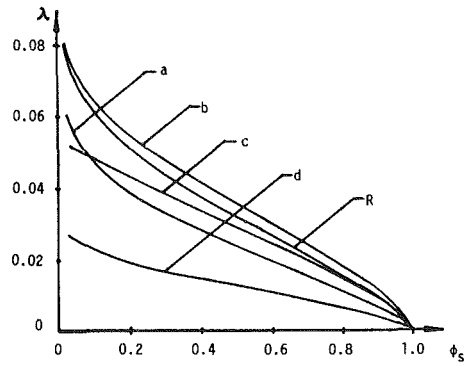

Fig. 1 λ as a function of ϕ_S with k_{21}, a_{21}, Lu, and ν as parameters: R, reference curve with $k_{21} = 1.0$, $a_{21} = 1.0$, Lu = 0.8, $\nu = 2.0$, $L^* = 20.0$, $\theta_s = 1.0$, $\theta_0 = 0.6$, $\phi_0 = 5.0$; a, $k_{21} = 0.6$; b, $a_{21} = 0.4$; c, Lu = 0.1; d, $\nu = 20$

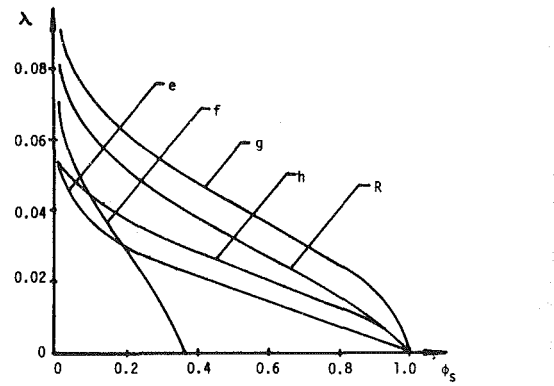

Fig. 2 λ as a function of ϕ_S with L^*, θ_S, θ_0, ϕ_0 as parameters: R, reference curve with $k_{21} = 1.0$, $a_{21} = 1.0$, Lu = 0.8, $\nu = 2.0$, $L^* = 20.0$, $\theta_s = 1.0$, $\theta_0 = 0.6$, $\phi_0 = 5.0$; e, $L^* = 50.0$; f, $\theta_s = 0.95$; $\theta_0 = 1.0$; h, $\phi_0 = 10.0$

Solutions for the three unknowns, λ, θ_v, and ϕ_v, can be obtained by numerical calculation from equations (28–30).

5 Discussion and Conclusions

During the sublimation process, the motion of the sublimation front is proportional to the parameter, λ, which is expressed by equation (11) of [4]. The higher the value of λ, the faster is the movement of the sublimation front. From equations (28–30), it is shown that λ is affected by nine dimensionless parameters: k_{21}, a_{21}, Lu, ν, L^*, θ_s, θ_0, ϕ_0 and ϕ_s. Figures 1 and 2 show that λ is a function of ϕ_s, the dimensionless vapor concentration at $x = 0$, with k_{21}, a_{21}, Lu, ν, L^*, θ_s, θ_0 and ϕ_0 as parameters. An increase of the value of the vapor concentration at $x = 0$, ϕ_s, results in a decrease of the value of the diffusion potential of the vapor between the sublimation front and the surface at $x = 0$, $(\phi_v - \phi_s)$. For such a case, less vapor can be transferred from the sublimation front to the surface at $x = 0$. Therefore the rate of the propagation of the sublimation front decreases. For the limiting case, when the vapor concentration at the surface at $x = 0$ is equal to that of the triple point of the moisture with $\phi_s = 1$, there is no more mass transfer. The sublimation process stops. The relation between λ and ϕ_s is shown in Figs. 1 and 2.

In order to show the effects of the different parameters on the value of λ, curve R in Figs. 1 and 2 is chosen as a reference curve with $k_{21} = 1.0$, $a_{21} = 1.0$, Lu = 0.8, $\nu = 2.0$, $L^* = 20.0$, $\theta_s = 1.0$, $\theta_0 = 0.6$ and $\phi_0 = 5.0$. Curves a, b, c and d in Fig. 1, and e, f, g and h in Fig. 2, represent the effects of the change of the values of k_{21}, a_{21}, Lu, ν, L^*, θ_s, θ_0 and ϕ_0 from the reference data on λ, respectively.

From equations (28–30), it is shown that the dimensionless constant, λ, the dimensionless temperature, θ_v, and the dimensionless vapor concentration, ϕ_v, at the sublimation front are coupled together. As an illustration, the relationship among these three parameters is shown in Fig. 3 for $k_{21} = 1.0$, $a_{21} = 1.0$, Lu = 0.8, $\nu = 2.0$, $L^* = 20.0$, $\theta_s = 1.0$, $\theta_0 = 0.6$, and $\phi_0 = 5.0$. In Fig. 3, λ represents the rate of sublimation, which decreases with an increase of the surface vapor concentration ϕ_s. For sublimation, because the vapor produced at the sublimation front has to be transferred away to the surface at $x = 0$, it requires that the vapor concentration at the sublimation front must be higher than that at the surface at $x = 0$. Therefore, the higher the value of ϕ_s, the higher is the value of ϕ_v, as shown in Fig. 3. An increase of the value of ϕ_v results in an increase of the corresponding saturation temperature, θ_v, at the sublimation front as also shown in Fig. 3.

As an illustration, the distributions of the dimensionless temperatures and the dimensionless vapor concentration are shown in Fig. 4 with $\lambda = 0.05$ and Lu = 1.0. It can be seen that the distributions of the temperature and vapor concentration in the vapor region for this illustration are practically linear.

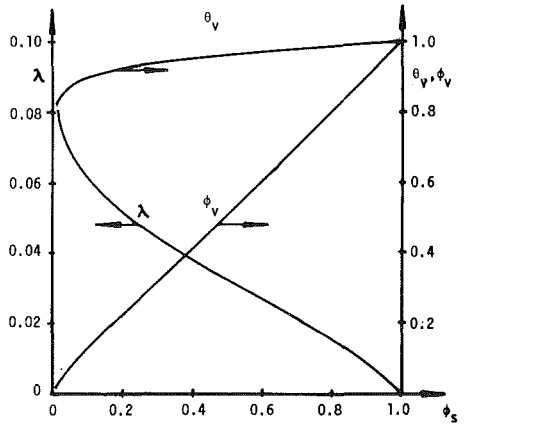

Fig. 3 Relationships among θ_v, ϕ_v, and λ as functions of ϕ_s for $k_{21} = 1.0$, $a_{21} = 1.0$, Lu = 0.8, $\nu = 2.0$, $L^* = 20.0$, $\theta_s = 1.0$, $\theta_0 = 0.6$ and $\phi_0 = 5.0$

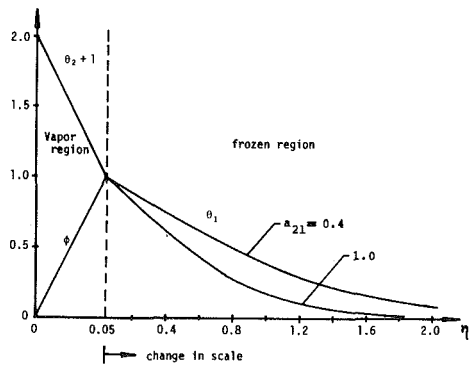

Fig. 4 θ_1, θ_2, and ϕ as functions of η for $\lambda = 0.05$ and Lu = 1.0

For a sublimation process, the maximum allowable molar vapor concentration at the sublimation front is the molar vapor concentration at its triple point state

$$(C_{m,v})_{\max} = C_{m,3} \tag{31}$$

Therefore, the maximum value of the dimensionless molar vapor concentration at the sublimation front can be obtained from equation (16) as follows:

$$(\phi_v)_{\max} = 1 \tag{32}$$

Because ϕ_v has its maximum value of 1, it can be seen from

equation (29) that there is a condition for the limitation of the sublimation process, which can be expressed by

$$C \leqq \frac{1}{\sqrt{\pi}\,\alpha \exp(\alpha^2)\mathrm{erf}(\alpha)} \tag{33}$$

where

$$C = \frac{\phi_0 - 1}{1 - \phi_s} = \frac{C_{m,0} - C_{m,3}}{C_{m,3} - C_{m,s}} \tag{34}$$

and

$$\alpha = \lambda/\sqrt{\mathrm{Lu}} \tag{35}$$

Equation (33) is identical to equation (20) of [4]. Therefore, Fig. 4 in [4] presents also the condition of the limitation of the sublimation process investigated in the present paper. Sublimation can only take place in the region under the sublimation limit curve as shown in Fig. 4 in [4].

From the above discussion, it can be seen that equation (18) in [4], should be corrected as follows

$$C_{m,\max} = \frac{P_3}{R_0 T_3} \tag{36}$$

6 Acknowledgments

The present work is being supported by the Natural Sciences and Engineering Research Council of Canada, under Grant No. A7929.

References

1 Cho, S. H., "An Exact Solution of the Coupled Phase Change Problem in a Porous Medium", *International Journal of Heat and Mass Transfer*, Vol. 18, 1975, pp. 1139–1142.

2 Mikhailov, M. D., "Exact Solution of Temperature and Moisture Distributions in a Porous Half-Space with Moving Evaporation Front", *International Journal of Heat and Mass Transfer*, Vol. 18, 1975, pp. 797–804.

3 Mikhailov, M. D., "Exact Solution for Freezing of Humid Porous Half-Space", *International Journal of Heat and Mass Transfer*, Vol. 19, 1976, pp. 651–655.

4 Lin, S., "An Exact Solution of the Sublimation Problem in a Porous Medium," ASME JOURNAL OF HEAT TRANSFER, Vol. 103, 1981, pp. 165–168.

5 Holman, J. P., *Thermodynamics*, 3rd ed., McGraw-Hill, New York, 1980, section 7-10.

One-Dimensional Phase-Change Problems With Radiation-Convection

R. V. Seeniraj[1] and T. K. Bose[2]

Nomenclature

B_0 = Biot number = hr_0/k
c_p = specific heat, J/kg-K
F = overall radiation shape factor
F_0 = Fourier number, $\alpha t/r_0^2$
k = thermal conductivity, W/m-K
g = solidification rate = $dS/d\tau$, m/s
g_0, g_1 = zero- and first-order solidification rates
H = radiation parameter = $\sigma \epsilon_m Fr_0 T_i^3/k$
h = convective heat-transfer coefficient, W/m^2-K
L = latent heat, J/kg
r = distance from the center of geometry to a point within the solidified layer or space coordinate, m
r_0 = thickness of slab or outer radius of cylinder/sphere, m
S = dimensionless interface distance = r_f/r_0
t = time, s
T = temperature within the solid-layer, K
T_a = ambient temperature, K
T_i = initial temperature, K
U = dimensionless temperature = T/T_i
U_a = dimensionless ambient temperature = T_a/T_i
U_s = dimensionless surface temperature = $U(S, y=0)$
U_{0s}, U_{1s} = zero- and first-order surface temperatures
y = dimensionless space coordinate, r/r_0
α = thermal diffusivity of solid = $k/\rho c_p$, m^2/s
ϵ = Stefan number = $c_p T_i/L$
ϵ_m = emissivity of material
τ = dimensionless time = $kT_i t/\rho r_0^2 L$
τ_t = dimensionless total time for $H = 0$
σ = Stefan-Boltzmann constant
ρ = density, kg/m^3

Introduction

Heat diffusion processes with a change of phase of the material occur in many scientific and engineering problems. They are commonly referred to as Stefan problems or free-boundary problems. In the present Note, asymptotic solutions for one-dimensional heat transfer involving solidification and melting of a planar, cylindrical, and spherical medium with constant thermophysical properties subjected to aerodynamic and radiative cooling or heating are presented and compared with the numerical results. Chung and Yeh [1] have studied this problem using variational and heat balance integral methods for a finite slab and compared their results with the numerical results of Goodling and Khader [2]. No analytical results for cylindrical or spherical phase-change problems are available for radiative boundary condition as to the authors' review. The exact zero-order solutions presented in this analysis are useful in checking the accuracy of approximate analytical and numerical results in the limiting condition of $\epsilon \to 0$. The results of the present analysis were found to be in satisfactory agreement with the numerical results and the earlier results [1, 2]. Effects of different parameters on the phase-change problem are shown in Figs. 1 and 2 and are briefly discussed.

Formulation of the Problem

Initially the entire medium is in liquid or solid state at the fusion or melting temperature, At time $t=0$, radiative and aerodynamic cooling or heating is applied at the outer face and phase change takes place. The one-dimensional heat conduction equation with attendant initial, boundary and interface conditions for the three coordinate system can be written in the following form.

$$\frac{\partial^2 U}{\partial y^2} + \frac{N}{y}\frac{\partial U}{\partial y} = \epsilon \frac{\partial U}{\partial \tau} \tag{1}$$

$N = 0$, 1, and 2 correspond to Cartesian, cylindrical, and spherical systems, respectively.

[1]Research scholar, Indian Institute of Technology, Madras, India
[2]Professor, Department of Aeronautical Engineering, Indian Institute of Technology, Madras, India

Contributed by the Heat Transfer Division for publication in the JOURNAL OF HEAT TRANSFER. Manuscript received by the Heat Transfer Division October 30, 1981.

equation (29) that there is a condition for the limitation of the sublimation process, which can be expressed by

$$C \leqq \frac{1}{\sqrt{\pi}\,\alpha \exp(\alpha^2)\mathrm{erf}(\alpha)} \tag{33}$$

where

$$C = \frac{\phi_0 - 1}{1 - \phi_s} = \frac{C_{m,0} - C_{m,3}}{C_{m,3} - C_{m,s}} \tag{34}$$

and

$$\alpha = \lambda/\sqrt{\mathrm{Lu}} \tag{35}$$

Equation (33) is identical to equation (20) of [4]. Therefore, Fig. 4 in [4] presents also the condition of the limitation of the sublimation process investigated in the present paper. Sublimation can only take place in the region under the sublimation limit curve as shown in Fig. 4 in [4].

From the above discussion, it can be seen that equation (18) in [4], should be corrected as follows

$$C_{m,\max} = \frac{P_3}{R_0 T_3} \tag{36}$$

6 Acknowledgments

The present work is being supported by the Natural Sciences and Engineering Research Council of Canada, under Grant No. A7929.

References

1 Cho, S. H., "An Exact Solution of the Coupled Phase Change Problem in a Porous Medium", *International Journal of Heat and Mass Transfer*, Vol. 18, 1975, pp. 1139–1142.

2 Mikhailov, M. D., "Exact Solution of Temperature and Moisture Distributions in a Porous Half-Space with Moving Evaporation Front", *International Journal of Heat and Mass Transfer*, Vol. 18, 1975, pp. 797–804.

3 Mikhailov, M. D., "Exact Solution for Freezing of Humid Porous Half-Space", *International Journal of Heat and Mass Transfer*, Vol. 19, 1976, pp. 651–655.

4 Lin, S., "An Exact Solution of the Sublimation Problem in a Porous Medium," ASME JOURNAL OF HEAT TRANSFER, Vol. 103, 1981, pp. 165–168.

5 Holman, J. P., *Thermodynamics*, 3rd ed., McGraw-Hill, New York, 1980, section 7-10.

One-Dimensional Phase-Change Problems With Radiation-Convection

R. V. Seeniraj[1] and T. K. Bose[2]

Nomenclature

B_0 = Biot number $= hr_0/k$
c_p = specific heat, J/kg-K
F = overall radiation shape factor
F_0 = Fourier number, $\alpha t/r_0^2$
k = thermal conductivity, W/m-K
g = solidification rate $= dS/d\tau$, m/s
g_0, g_1 = zero- and first-order solidification rates
H = radiation parameter $= \sigma\epsilon_m Fr_0 T_i^3/k$
h = convective heat-transfer coefficient, W/m^2-K
L = latent heat, J/kg
r = distance from the center of geometry to a point within the solidified layer or space coordinate, m
r_0 = thickness of slab or outer radius of cylinder/sphere, m
S = dimensionless interface distance $= r_f/r_0$
t = time,s
T = temperature within the solid-layer, K
T_a = ambient temperature, K
T_i = initial temperature, K
U = dimensionless temperature $= T/T_i$
U_a = dimensionless ambient temperature $= T_a/T_i$
U_s = dimensionless surface temperature $= U(S, y=0)$
U_{0s}, U_{1s} = zero- and first-order surface temperatures
y = dimensionless space coordinate, r/r_0
α = thermal diffusivity of solid $= k/\rho\, c_p$, m^2/s
ϵ = Stefan number $= c_p T_i/L$
ϵ_m = emissivity of material
τ = dimensionless time $= kT_i t/\rho r_0^2 L$
τ_t = dimensionless total time for $H = 0$
σ = Stefan-Boltzmann constant
ρ = density, kg/m^3

Introduction

Heat diffusion processes with a change of phase of the material occur in many scientific and engineering problems. They are commonly referred to as Stefan problems or free-boundary problems. In the present Note, asymptotic solutions for one-dimensional heat transfer involving solidification and melting of a planar, cylindrical, and spherical medium with constant thermophysical properties subjected to aerodynamic and radiative cooling or heating are presented and compared with the numerical results. Chung and Yeh [1] have studied this problem using variational and heat balance integral methods for a finite slab and compared their results with the numerical results of Goodling and Khader [2]. No analytical results for cylindrical or spherical phase-change problems are available for radiative boundary condition as to the authors' review. The exact zero-order solutions presented in this analysis are useful in checking the accuracy of approximate analytical and numerical results in the limiting condition of $\epsilon \to 0$. The results of the present analysis were found to be in satisfactory agreement with the numerical results and the earlier results [1, 2]. Effects of different parameters on the phase-change problem are shown in Figs. 1 and 2 and are briefly discussed.

Formulation of the Problem

Initially the entire medium is in liquid or solid state at the fusion or melting temperature, At time $t=0$, radiative and aerodynamic cooling or heating is applied at the outer face and phase change takes place. The one-dimensional heat conduction equation with attendant initial, boundary and interface conditions for the three coordinate system can be written in the following form.

$$\frac{\partial^2 U}{\partial y^2} + \frac{N}{y}\frac{\partial U}{\partial y} = \epsilon \frac{\partial U}{\partial \tau} \tag{1}$$

$N = 0$, 1, and 2 correspond to Cartesian, cylindrical, and spherical systems, respectively.

[1]Research scholar, Indian Institute of Technology, Madras, India
[2]Professor, Department of Aeronautical Engineering, Indian Institute of Technology, Madras, India

Contributed by the Heat Transfer Division for publication in the JOURNAL OF HEAT TRANSFER. Manuscript received by the Heat Transfer Division October 30, 1981.

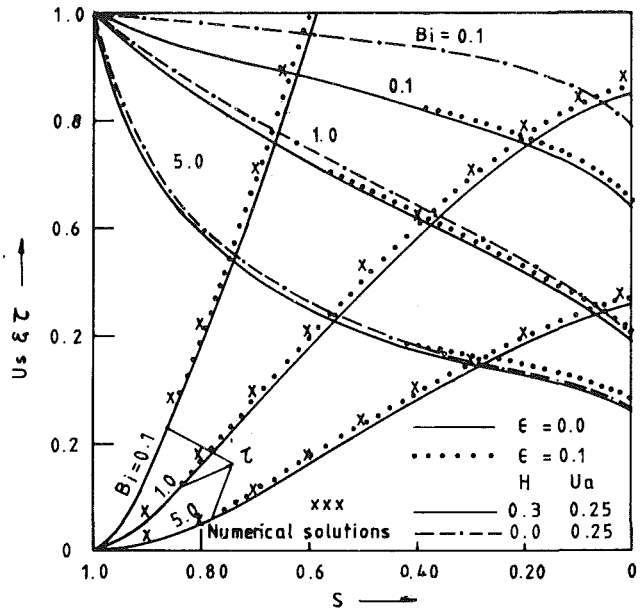

Fig. 1 Solidified layer thickness versus surface temperature and time for cylindrical solidification: (——·——) $H = 0$, $U_a = 0.25$, $\epsilon = 0.0$; (——) $H = 0.3$, $U_a = 0.25$ $\epsilon = 0.0$; (·····) $H = 0.3$, $U_a = 0.25$, $\epsilon = 0.1$; (× × × ×) numerical solutions

$$-\frac{\partial U}{\partial y}(1,\tau) = H[U^4(1,\tau) - U_a^4] + B_0[U(1,\tau) - U_a] \tag{2}$$

$$U(S,\tau) = 1 \tag{3}$$

$$p\frac{ds}{d\tau} = \frac{\partial U}{\partial y}(S,\tau), S(0) = 1 \tag{4}$$

$p = 1$ and -1 represent the solidification and melting, respectively. All the variables and parameters of the problem are defined in the nomenclature.

Perturbation Solutions

Stefan number, ϵ, which is a measure of the heat capacity of the frozen layer to the heat release at the phase change front—normally small for most liquids—is taken as the perturbation parameter. With the following asymptotic expansions,

$$U(S,y) = \sum_{n=0}^{n} \epsilon^n U_n(S,y); g(S) = \sum_{n=0}^{n} \epsilon^n g_n(S)$$

and following the method [3], the solutions are obtained up to the first order for the case of inward solidification and are as follows:

Cylinder

$$U_0 = (1 - U_{0s})\, lny/lnS + U_{0s} \tag{5a}$$

$$U_{0s}^4 + (B_0 lnS - 1)U_{0s}/HlnS = (B_0 U_a lnS - 1)/HlnS + U_a^4 \tag{5b}$$

$$g_0 = (1 - U_{0s})/SlnS \tag{6a}$$

$$\tau_0 = {}_s\int [SlnS/(1 - U_{0s})]dS \tag{6b}$$

$$U_{1s} = F(1 - S^2)(lnS - 1)/4(4H\, U_{0s}^3 lnS + B_0 lnS + 1) \tag{7}$$

$$g_1 = (lnS - 1/2)FS/2 + (4HU_{0s}^2 + B_0)\, U_{1s}/S - F/4S \tag{8a}$$

$$\tau_1 = -{}_s\int (g_1/g_0^2)dS;\ F = (1 - U_{0s})^2/S^2(lnS)^3 \tag{8b}$$

For $H = 0$

$$U_{0s} = (1 - B_0 U_a lnS)/(1 - B_0 lnS) \tag{9}$$

$$\tau_t = (1/4 + 1/2B_0)/(1 - U_a) \tag{10}$$

Sphere

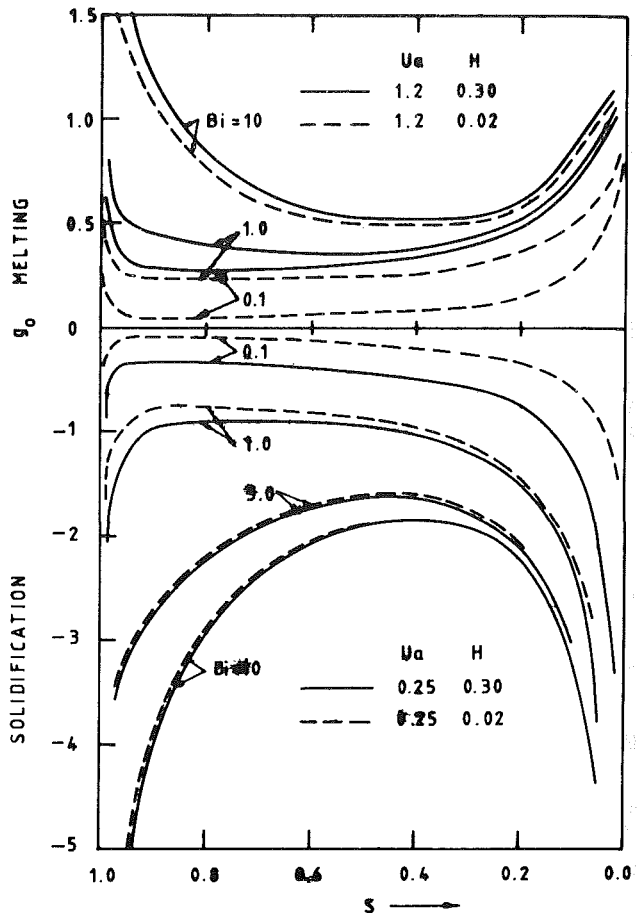

Fig. 2 Rate of interface movement for various Biot numbers and radiation parameters (cylinder)

$$U_0 = 1 + (1 - U_{0s})(1 - S/y)/(S - 1) \tag{11a}$$

$$U_{0s}^4 + [B_0(S-1) - S]U_{0s}/H(S-1) = [B_0 U_a(S-1) - S]/H(S-1) + U_a^4 \tag{11b}$$

$$g_0 = (1 - U_{0s})/S(S-1) \tag{12a}$$

$$\tau_0 = {}_s\int [S(S-1)/(1 - U_{0s})]dS \tag{12b}$$

$$U_{1s} = F(S^3 - 3S^2 + 5S - 1)/6[4H(1-S)\, U_{0s}^3 + (1 - B_0 S) + B_0] \tag{13}$$

$$g_1 = F(1/2 - S/3) + [U_{1s} - F(S^2 - 3S + 4)/6]/S(1-S) \tag{14a}$$

$$\tau_1 = {}_s - \int (g_1/g_0^2)dS;\ F = -(1 - U_{0s})^2/S(S-1)^3 \tag{14b}$$

For $H = 0$

$$U_{0s} = [B_0 U_a(S-1) - S]/[B_0(S-1) - S] \tag{15}$$

$$\tau_t = [1/6 + 1/3B_0]/(1 - U_a) \tag{16}$$

The zero-order surface temperature, U_{0s}, can be obtained from the respective quartic equation in U_{0s} using Cardano's formula [5], and it is provided in reference [4]. For the radiation, $H = \Theta$, the respective expressions for τ_t give the total time for solidification when the heat capacity of the frozen-layer is negligible and these expressions, (9, 10, 15, 16) agree with the solutions of London and Seban [6]. In this note a fourth-order RK-method is employed to evaluate τ_0 and τ_1.

Upon a suggestion from a referee, closed form analytical expressions are given below for inward solidification for the case of small temperature difference between T_i and T_a.

Cylinder

$$\tau = \tau_0 + \epsilon\tau_1 + 0(\epsilon^2) \tag{17}$$

$$\tau_0 = (1/4 + 1/2Br)(1 - S^2) + (S^2/2)lnS \tag{18}$$

$$\tau_1 = -[1/4(1 - BrlnS)][(1 + Br)(1 - BrlnS)$$

$$+(2+2\mathrm{Br}+\mathrm{Br}^2)lnS-(1+\mathrm{Br}-\mathrm{Br}lnS)S^2] \quad (19)$$

Sphere

$$\tau_0=(1-S^2)/2+(1-S^3)/3m \quad (20)$$

$$\tau_1=(m+S)^2/6+[2m-\mathrm{Br}(m+S)]/[6\mathrm{Br}(1-\mathrm{Br})^2(m+S)] \quad (21)$$

where $m = \mathrm{Br}/(1-\mathrm{Br})$. The following are the definitions of the parameters employed in the equations (17-21):

Radiation Biot number, $\mathrm{Br}=\mathrm{B}_0+4\sigma\epsilon_m Fr_i T_i^3/k$

Stefan number, $\epsilon=c_p(T_i-T_a)/L$; $\tau=\epsilon F_0$

Results and Discussion

The number of parameters available to study the thermal characteristics of this problem are B_0, H, U_a, and ϵ. Therefore, only a few sets of representative numerical results are presented graphically. Figure 1 shows the curves of U_s and τ as a function of interface location, S, for various Biot numbers with and without radiation for the case of inward cylindrical solidification. The comparison between the present results and the numerical results based on a modified numerical scheme of Goodrich [9] (shown in Fig. 1 for $\epsilon = 0.1$) shows a satisfactory agreement within 5 percent for $\epsilon \le 0.3$. For small values of $\epsilon = 0(10^{-2})$, the agreement is excellent. Numerical solutions of finite difference scheme are invariably compared with Neumann solutions ($\mathrm{Bi}\to\infty$) or with the quasi-steady-state solutions [10], that is, the limiting case of $\epsilon\to 0$, to check the accuracy. In this aspect, the present zero-order exact solutions are useful in checking the accuracy of different numerical schemes employed in the study of phase change problems.

The effects of Biot and Stefan numbers on thermal characteristics of phase-change process are elaborately discussed by Sparrow and his co-workers [7, 8]. However, in Figs. 1 and 2 the effect of radiation on U_s and g_0 is shown for a cylinder. The effect of radiation for a given U_a on g_0 and U_s is appreciable for $\mathrm{Bi}<1$. It is seen from Fig. 2 that the rate of phase-change process increases rapidly near the end of the process, as at the onset, because the volume of the remaining material yet to participate in the process becomes increasingly smaller. This is in contrast to the planar medium. This may be referred to as the curvature effect of the medium.

Conclusion

One-dimensional heat-transfer problems involving solidification and melting of cylinder and sphere subject to convection-radiation boundary condition are studied using the perturbation method. Though these results are more accurate for $\epsilon \ll 1$, they provide a qualitative heat-transfer information during the process, and it is discussed briefly for the case of cylindrical solidification. The accuracy and the range of the present solutions are sufficient for many engineering applications such as in the design and analysis of experiments in storing solar thermal energy employing phase-change materials (PCM) [7]. The values of Stefan number of PCM's employed in the above application were on the order of 0.05.

Acknowledgment

The authors wish to thank Mr. P. Ramakrishna Rao and Prof. V. M. Krishna Sastri for providing numerical finite difference solutions for comparison of our results shown in Fig. 1.

References

1 Chung, B. T. F., and Yeh, L. T., "Solidification and Melting of Materials Subject to Convection and Radiation," *Journal of Spacecraft and Rockets*, Vol. 12, No. 6, 1975, pp. 329-333.

2 Goodling, J. S., and Khader, M. S., "Inward Solidification With Radiation-Convection Boundary Condition," ASME JOURNAL OF HEAT TRANSFER, Vol. 96, Feb. 1974, pp. 114-115.

3 Yan, M. M., and Huang, P. N. S., "Perturbation Solutions to Phase Change Problem Subject to Convection and Radiation," ASME JOURNAL OF HEAT TRANSFER, Vol. 101, Feb. 1979, pp. 96-100.

4 Seeniraj, R. V., Discussion on "Perturbation Solutions to Phase Change Problem Subject to Convection and Radiation," ASME JOURNAL OF HEAT TRANSFER, Vol. 102, May 1980, pp. 395-396.

5 Richardson, M., *College Algebra*, Prentice-Hall, Englewood Cliffs, 1947, p. 261.

6 London, A. L., and Seban, R. A., "Rate of Ice Formation," Trans. ASME, Vol. 65, 1943, pp. 771-778.

7 Shamsundar, N., and Sparrow, E. H., "Storage of Thermal Energy by Solid-Liquid Phase Change—Temperature Drop and Heat Flux," ASME JOURNAL OF HEAT TRANSFER, Vol. 95, Nov. 1974, pp. 541-543.

8 Shamsundar, N., and Sparrow, E. H., "Analysis of Multidimensional Conduction Phase Change via the Enthalpy Model," ASME JOURNAL OF HEAT TRANSFER, Vol. 96, Aug. 1975, pp. 333-340.

9 Goodrich, L. E., "Efficient Numerical Technique for One Dimensional Thermal Problems With Phase Change," *International Journal of Heat and Mass Transfer*, Vol. 21, 1978, pp. 615-621.

10 Saitoh, T., "Numerical Method for Multidimensional Freezing Problems in Arbitrary Domains," ASME JOURNAL OF HEAT TRANSFER, Vol. 100, May 1978, pp. 294-299.

Transient Response of Fins by Optimal Linearization and Variational Embedding Methods

Y. M. Chang[1], C. K. Chen[1], and J. W. Cleaver[2]

Nomenclature

- b = fin thickness
- E = emissivity
- h = heat-transfer coefficient
- k = thermal conductivity
- L = fin length
- m = exponent of power law
- N = fin parameter
- q = heat-transfer rate
- Q = dimensionless heat-transfer rate $= qL/bk(T_b-T_e)$
- t = time
- T = temperature
- T_b = fin base temperature
- T_e = environment temperature
- x = distance from fin tip
- X = dimensionless distance $= x/L$
- θ = dimensionless temperature
- σ = Stefan-Boltzmann constant
- τ = dimensionless time $= \alpha t/L^2$

Introduction

The study on the transient behavior of the fins is of practical importance. In some fins' applications, the analysis based on the linear cooling law is not applicable because the process is governed by a power law type which is dependent on the temperature, i.e., θ^m. For example, the exponent m may take the values of 0.75, 1.25, 3.0, and 4.0 when the fin is cooled due to the film boiling, natural convection, nucleate boiling, and radiation to the space at the absolute zero temperature, respectively [1]. It seems desirable to develop an analysis for the transient response of a fin with the power cooling law type. Aziz and Na [2] used the coordinate perturbation expansion method to obtain the base heat-transfer rate of the fins. Its solutions hold true only over the early part of the transient period only (τ = 0 to 0.10).

[1]Department of Mechanical Engineering, National Cheng Kung University, Tainan, Taiwan, Republic of China

[2]Department of Mechanical Engineering, University of Liverpool, Liverpool, England

Contributed by the Heat Transfer Division for publication in the JOURNAL OF HEAT TRANSFER. Manuscript received by the Heat Transfer Division September 2, 1981.

$$+(2+2\mathrm{Br}+\mathrm{Br}^2)lnS-(1+\mathrm{Br}-\mathrm{Br}lnS)S^2] \quad (19)$$

Sphere

$$\tau_0=(1-S^2)/2+(1-S^3)/3m \quad (20)$$

$$\tau_1=(m+S)^2/6+[2m-\mathrm{Br}(m+S)]/[6\mathrm{Br}(1-\mathrm{Br})^2(m+S)] \quad (21)$$

where $m = \mathrm{Br}/(1-\mathrm{Br})$. The following are the definitions of the parameters employed in the equations (17-21):

Radiation Biot number, $\mathrm{Br}=\mathrm{B}_0+4\sigma\epsilon_m Fr_i T_i^3/k$

Stefan number, $\epsilon=c_p(T_i-T_a)/L$; $\tau=\epsilon F_0$

Results and Discussion

The number of parameters available to study the thermal characteristics of this problem are B_0, H, U_a, and ϵ. Therefore, only a few sets of representative numerical results are presented graphically. Figure 1 shows the curves of U_s and τ as a function of interface location, S, for various Biot numbers with and without radiation for the case of inward cylindrical solidification. The comparison between the present results and the numerical results based on a modified numerical scheme of Goodrich [9] (shown in Fig. 1 for ϵ = 0.1) shows a satisfactory agreement within 5 percent for $\epsilon \le 0.3$. For small values of $\epsilon = 0(10^{-2})$, the agreement is excellent. Numerical solutions of finite difference scheme are invariably compared with Neumann solutions ($\mathrm{Bi}\to\infty$) or with the quasi-steady-state solutions [10], that is, the limiting case of $\epsilon\to 0$, to check the accuracy. In this aspect, the present zero-order exact solutions are useful in checking the accuracy of different numerical schemes employed in the study of phase change problems.

The effects of Biot and Stefan numbers on thermal characteristics of phase-change process are elaborately discussed by Sparrow and his co-workers [7, 8]. However, in Figs. 1 and 2 the effect of radiation on U_s and g_0 is shown for a cylinder. The effect of radiation for a given U_a on g_0 and U_s is appreciable for $\mathrm{Bi}<1$. It is seen from Fig. 2 that the rate of phase-change process increases rapidly near the end of the process, as at the onset, because the volume of the remaining material yet to participate in the process becomes increasingly smaller. This is in contrast to the planar medium. This may be referred to as the curvature effect of the medium.

Conclusion

One-dimensional heat-transfer problems involving solidification and melting of cylinder and sphere subject to convection-radiation boundary condition are studied using the perturbation method. Though these results are more accurate for $\epsilon \ll 1$, they provide a qualitative heat-transfer information during the process, and it is discussed briefly for the case of cylindrical solidification. The accuracy and the range of the present solutions are sufficient for many engineering applications such as in the design and analysis of experiments in storing solar thermal energy employing phase-change materials (PCM) [7]. The values of Stefan number of PCM's employed in the above application were on the order of 0.05.

Acknowledgment

The authors wish to thank Mr. P. Ramakrishna Rao and Prof. V. M. Krishna Sastri for providing numerical finite difference solutions for comparison of our results shown in Fig. 1.

References

1 Chung, B. T. F., and Yeh, L. T., "Solidification and Melting of Materials Subject to Convection and Radiation," *Journal of Spacecraft and Rockets*, Vol. 12, No. 6, 1975, pp. 329-333.

2 Goodling, J. S., and Khader, M. S., "Inward Solidification With Radiation-Convection Boundary Condition," ASME JOURNAL OF HEAT TRANSFER, Vol. 96, Feb. 1974, pp. 114-115.

3 Yan, M. M., and Huang, P. N. S., "Perturbation Solutions to Phase Change Problem Subject to Convection and Radiation," ASME JOURNAL OF HEAT TRANSFER, Vol. 101, Feb. 1979, pp. 96-100.

4 Seeniraj, R. V., Discussion on "Perturbation Solutions to Phase Change Problem Subject to Convection and Radiation," ASME JOURNAL OF HEAT TRANSFER, Vol. 102, May 1980, pp. 395-396.

5 Richardson, M., *College Algebra*, Prentice-Hall, Englewood Cliffs, 1947, p. 261.

6 London, A. L., and Seban, R. A., "Rate of Ice Formation," Trans. ASME, Vol. 65, 1943, pp. 771-778.

7 Shamsundar, N., and Sparrow, E. H., "Storage of Thermal Energy by Solid-Liquid Phase Change—Temperature Drop and Heat Flux," ASME JOURNAL OF HEAT TRANSFER, Vol. 95, Nov. 1974, pp. 541-543.

8 Shamsundar, N., and Sparrow, E. H., "Analysis of Multidimensional Conduction Phase Change via the Enthalpy Model," ASME JOURNAL OF HEAT TRANSFER, Vol. 96, Aug. 1975, pp. 333-340.

9 Goodrich, L. E., "Efficient Numerical Technique for One Dimensional Thermal Problems With Phase Change," *International Journal of Heat and Mass Transfer*, Vol. 21, 1978, pp. 615-621.

10 Saitoh, T., "Numerical Method for Multidimensional Freezing Problems in Arbitrary Domains," ASME JOURNAL OF HEAT TRANSFER, Vol. 100, May 1978, pp. 294-299.

Transient Response of Fins by Optimal Linearization and Variational Embedding Methods

Y. M. Chang[1], C. K. Chen[1], and J. W. Cleaver[2]

Nomenclature

- b = fin thickness
- E = emissivity
- h = heat-transfer coefficient
- k = thermal conductivity
- L = fin length
- m = exponent of power law
- N = fin parameter
- q = heat-transfer rate
- Q = dimensionless heat-transfer rate $= qL/bk(T_b-T_e)$
- t = time
- T = temperature
- T_b = fin base temperature
- T_e = environment temperature
- x = distance from fin tip
- X = dimensionless distance $= x/L$
- θ = dimensionless temperature
- σ = Stefan-Boltzmann constant
- τ = dimensionless time $= \alpha t/L^2$

Introduction

The study on the transient behavior of the fins is of practical importance. In some fins' applications, the analysis based on the linear cooling law is not applicable because the process is governed by a power law type which is dependent on the temperature, i.e., θ^m. For example, the exponent m may take the values of 0.75, 1.25, 3.0, and 4.0 when the fin is cooled due to the film boiling, natural convection, nucleate boiling, and radiation to the space at the absolute zero temperature, respectively [1]. It seems desirable to develop an analysis for the transient response of a fin with the power cooling law type. Aziz and Na [2] used the coordinate perturbation expansion method to obtain the base heat-transfer rate of the fins. Its solutions hold true only over the early part of the transient period only (τ = 0 to 0.10).

[1]Department of Mechanical Engineering, National Cheng Kung University, Tainan, Taiwan, Republic of China

[2]Department of Mechanical Engineering, University of Liverpool, Liverpool, England

Contributed by the Heat Transfer Division for publication in the JOURNAL OF HEAT TRANSFER. Manuscript received by the Heat Transfer Division September 2, 1981.

In this note, however, the optimal linearization method [3] is imposed on the governing equation for the steady state of the straight fin with a power law cooling process. Then, the variational embedding method [4] is used to solve the linearized partial differential equation instead of the original governing equation for the fin's transient response. Finally, the base heat flux is obtained. It will be seen that the present analysis gives an accurate prediction over the entire transient period ($\tau = 0$ to infinity).

Analysis

Consider the one-dimensional conduction in a straight fin of uniform thickness, b, and length, L. Let the fin be initially at the environment temperature, T_e. At time $t = 0$, the base temperature is suddenly changed to T_b. We assume that the heat dissipated from the fin surfaces follows a power law type dependence on the temperature difference. Referring to the insert in Fig. 1, the energy equation with the aforesaid initial and boundary conditions is

$$\frac{\partial^2\theta}{\partial X^2} - N^2\theta^m = \frac{\partial\theta}{\partial\tau} \tag{1}$$

$$\theta(1,\tau) = 1,\ \theta(X,0) = 0,\ \frac{\partial\theta}{\partial X}\bigg|_{X=0} = 0 \tag{2}$$

where, except for N and θ, the symbols are as defined in the nomenclature. The parameters N and θ are defined appropriately in accordance with the mechanism of the surface heat transfer. For example, with the convecting fin ($m = 1$), $N^2 = 2hL^2/bk$, $\theta = (T-T_e)/(T_b-T_e)$ and for the fin radiating to the zero environment temperature ($m=4$), $N^2 = 2ET_b^3L^2/bk$ and $\theta = T/T_b$.

Steady-State Condition. For the steady-state fin, the governing differential equation (1) simplifies to

$$\frac{d^2\theta}{dX^2} - N^2\theta^m = 0 \tag{3}$$

or

$$\frac{d^2\theta}{dX^2} - N^2\theta^{m-1}\theta = 0 \tag{4}$$

subject to the following boundary conditions

$$\theta(1) = 1, \frac{d\theta}{dX}\bigg|_{X=0} = 0 \tag{5}$$

Together with equation (4), consider the following equation

$$\frac{d^2\theta}{dX^2} - \lambda_m\theta = 0 \tag{6}$$

where λ_m is a constant adjustable parameter which has to be chosen in such a way that the linear equation (6) approximates equation (4) in the optimal sense. To find this parameter, we first form the difference of the equations (4) and (6).

$$\xi(\lambda,\theta) = \lambda_m\theta - N^2\theta^m \quad (m = 1,2,3,4) \tag{7}$$

and consider the integral

$$I(\lambda) = \int_{X_0}^{X_1} \xi^2(\lambda_m,\theta)\,dX \tag{8}$$

where the space interval depends on the problem in consideration.

Suppose that there exists a known function

$$\theta = \psi(X) \tag{9}$$

which satisfies the boundary conditions (5). Substituting equation (9) into equation (8) and performing integration, the expression equation (8) will be the function of λ_m only. A necessary condition for the existence of this minimum is

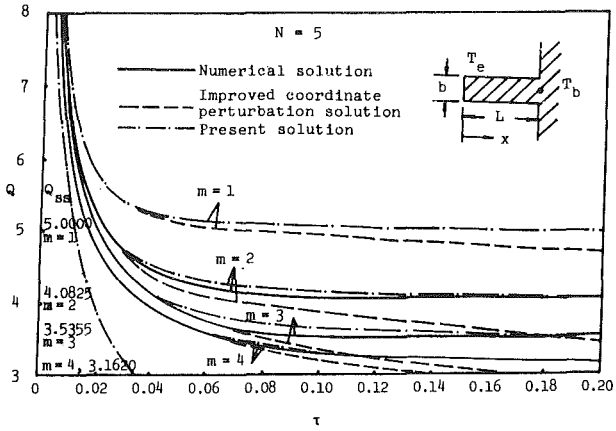

Fig. 1 Transient heat-transfer rate for $N = 5$

$$\int_{X_0}^{X_1} \frac{\partial\xi(\lambda_m,\theta)}{\partial\lambda_m}\,\xi(\lambda_m,\theta)\,dX = 0 \tag{10}$$

Hence, the optimal value of λ_m depends on the form of the chosen function $\psi(X)$ in equation (9), and the linear differential equation (6) with the constant coefficient should be considered "optimal" subject to $\theta = \psi(X)$. To be more specific, suppose the function (9) in the form

$$\theta(X) = \frac{\cosh NX}{\cosh N} \tag{11}$$

The equation (11) represents the solution of the boundary value problem equations (4) and (5) for $m = 1$.

Substituting equation (11) into equation (10), we will get after integrating with respect to X from $X_0 = 0$ to $X_1 = 1$.

$$\lambda_m = \frac{B_m}{A} \tag{12}$$

where

$$\begin{aligned}
A &= \frac{1}{\cosh^2 N}\left(\frac{1}{2} + \frac{\sinh 2N}{4N}\right)\\
m=1 \quad B_1 &= \frac{1}{\cosh^2 N}\left(\frac{1}{2} + \frac{\sinh 2N}{4N}\right)\\
m=2 \quad B_2 &= \frac{N^2}{\cosh^3 N}\left(\frac{\sinh^3 N}{3N} + \frac{\sinh N}{N}\right)\\
m=3 \quad B_3 &= \frac{N^2}{\cosh^4 N}\left(\frac{\sinh 4N}{32N} + \frac{\sinh 2N}{4N} + \frac{3}{8}\right)\\
m=4 \quad B_4 &= \frac{N^2}{\cosh^5 N}\left[\frac{1}{5N}\sinh N\cosh^4 N + \frac{4}{5N}\left(\frac{\sinh^3 N}{3} + \sinh N\right)\right]
\end{aligned} \tag{13}$$

The solution of equation (6) subject to the boundary conditions (5) is

$$\theta = \frac{\cosh\sqrt{\lambda_m}X}{\cosh\sqrt{\lambda_m}} \quad (m = 1,2,3,4) \tag{14}$$

Transient State Condition. As the left-hand side of equation (1) is replaced by the linearized equation (6), equation (1) can be rewritten as

$$\frac{\partial^2\theta}{\partial X^2} - \lambda_m\theta = \frac{\partial\theta}{\partial\tau} \tag{15}$$

and it is to be solved with the boundary conditions and initial condition of (2). The Lagrangian functional which embeds equation (15) is given by

$$J[\theta,\Lambda]=\int_0^{\gamma}\int_0^1 \Lambda(X,\tau)\left[-\frac{\partial\theta}{\partial\tau}+\frac{\partial^2\theta}{\partial X^2}-\lambda_m\theta\right]dXd\tau \qquad (16)$$

where the interval $[0, \gamma]$ is arbitrary.

We shall assume the trial functions of the form

$$\tilde{\theta}(X,\tau)=\frac{\cosh\sqrt{\lambda_m}X}{\cosh\sqrt{\lambda_m}}+\sum_{i=1}^{\infty}X_i(\tau)\cos\left(i-\frac{1}{2}\right)\pi X \quad i=1,2,3.\ldots \qquad (17)$$

$$\tilde{\Lambda}(X,\tau)=\sum_{j=1}^{\infty}\phi_j(\tau)\cos\left(j-\frac{1}{2}\right)\pi X \quad j=1,2,3.\ldots \qquad (18)$$

which satisfy the boundary conditions exactly.

Substituting $\tilde{\theta}(X,\tau)$ and $\tilde{\Lambda}(X,\tau)$ into equation (16) and integrating partially with respect to X, the Euler-Lagrange equation for ϕ_j comes out to be

$$-\dot{X}_j(\tau)+\left[\left(j-\frac{1}{2}\right)^2\pi^2+\lambda_m\right]X_j(\tau)=0 \qquad (19)$$

The solution of equation (19) is

$$X_j(\tau)=C_j\exp\left\{-\left[\left(j-\frac{1}{2}\right)^2\pi^2+\lambda_m\right]\tau\right\} \qquad (20)$$

Therefore, equation (17) is

$$\tilde{\theta}(X,\tau)=\frac{\cosh\sqrt{\lambda_m}X}{\cosh\sqrt{\lambda_m}}+\sum_{i=1}^{\infty}C_i\exp\left\{-\left[\left(i-\frac{1}{2}\int^2\pi^2+\lambda_m\right]\tau\right\}\cos(i-\frac{1}{2})\pi X \qquad (21)$$

Substituting the initial condition (2) into equation (21), multiplying $\cos(i-1/2)\pi X$ and integrating with respect to X, the coefficients C_i come out to be

$$C_i=2(-1)^i\frac{\left(i-\frac{1}{2}\right)\pi}{\left(i-\frac{1}{2}\right)^2\pi^2+\lambda_m} \qquad (22)$$

The base heat-transfer rate in the dimensionless form is given by

$$Q=\sqrt{\lambda_m}\tanh\sqrt{\lambda_m}+2\sum_{i=1}^{\infty}\frac{\left(i-\frac{1}{2}\right)^2\pi^2}{\left(i-\frac{1}{2}\right)^2\pi^2+\lambda_m}\exp\left\{-\left[\left(i-\frac{1}{2}\right)^2\pi^2+\lambda_m\right]\tau\right\} \qquad (23)$$

Discussion

For brevity, we concentrate our discussion on the heat-transfer rate, which is of main interest, rather than the temperature distribution. The solutions of the heat-transfer rate for $N = 5$ and $N = 0$ (no surface heat loss) are shown as follows

$$N=0 \quad Q=2\sum_{i=1}^{\infty}\exp\left[-\left(i-\frac{1}{2}\right)^2\pi^2\tau\right]$$

$$N=5 \quad m=1 \quad Q=5.0000+2\sum_{i=1}^{\infty}\frac{\left(i-\frac{1}{2}\right)^2\pi^2}{\left(i-\frac{1}{2}\right)^2\pi^2+25}\exp\left\{-\left[\left(i-\frac{1}{2}\right)^2\pi^2+25\right]\tau\right\}$$

$$m=2 \quad Q=4.0790+2\sum_{i=1}^{\infty}\frac{\left(i-\frac{1}{2}\right)^2\pi^2}{\left(i-\frac{1}{2}\right)^2\pi^2+16.6576}\exp\left\{-\left[\left(i-\frac{1}{2}\right)^2\pi^2+16.6576\right]\tau\right\}$$

$$m=3 \quad Q=3.5284+2\sum_{i=1}^{\infty}\frac{\left(i-\frac{1}{2}\right)^2\pi^2}{\left(i-\frac{1}{2}\right)^{22}\pi^2+12.4921}\exp\left\{-\left[\left(i-\frac{1}{2}\right)^2\pi^2+12.4921\right]\tau\right\}$$

$$m=4 \quad Q=3.1499+2\sum_{i=1}^{\infty}\frac{\left(i-\frac{1}{2}\right)^2\pi^2}{\left(i-\frac{1}{2}\right)^2\pi^2+9.9934}\exp\left\{-\left[\left(i-\frac{1}{2}\right)^2\pi^2+9.9934\right]\tau\right\} \qquad (24)$$

For the cases of $N = 0$ and $m = 1$ ($N = 5$), the present solutions in equation (24) are the same as the exact solution obtained by the Laplace transform method.

The steady-state heat-transfer rate, Q_{ss}, can be easily acquired from equation (24) as τ approaches infinity. The error for $m=4$ does not exceed 0.385 percent, compared with the numerical solution in Fig. 1. A comparison of curves of the transient heat-transfer rates obtained by the present method and the coordinate perturbation expansion method [2] is graphically shown in Fig. 1 for different values of m. It indicates that the perturbation solutions [2] do not approach Q_{ss} as $\tau\to\infty$, and they cover the early part of the transient period only. However, the present solutions in equation (24) converge to the steady-state figures. It is observed that the accuracy of the present approximate solutions for $m = 2$ and $m = 3$ decreases during $\tau = 0.04$ to $\tau = 0.10$. However, the comparison is remarkably good since, for $m = 3$ and $\tau = 0.08$, the largest error does not exceed 3.5 percent.

The present solution matches almost exactly the numerical solution for $N = 5$. The results for $N = 1, 2, 3, 4$ or even over 5, would not be grossly in error and should be useful at least for preliminary calculation.

From the results of the analysis, it appears that the present technique is a simple, fast, and straightforward method and the obtained solution can predict quite accurately the performance of the fins with a power law type cooling process.

References

1 Haley, K. W., and Westward, J. W., "Boiling Heat Transfer from Single Fins," *Proceedings of the 3rd International Heat Transfer Conference*, Chicago, Vol. 3, 1966, pp. 245-253.

2 Aziz, A., and Na, T. Y., "Transient Response of Fins by Coordinate Perturbation Expansion," *International Journal of Heat and Mass Transfer*, Vol. 23, 1980, pp. 1695-1698.

3 Vujanovic, B., "Application of Optimal Linearization Method to the Heat Transfer Problem," *International Journal of Heat and Mass Transfer*, Vol. 16, 1973, pp. 1111-1117.

4 Bhatkar, V., and Rao, B., "Variational Embedding Method and Application to Distributed Systems Control," *International Journal of Control*, Vol. 23, 1976, pp. 805-920.

Journal of Heat Transfer

Discussion

An Exact Solution of the Sublimation Problems in a Porous Medium[1]

A. Aziz.[2] I have recently studied the paper by Sui Lin and found that the transcendental equation (32) of his paper is identical to equation (13) of the paper Churchill and Evans [3], presented a decade ago. The identity is readily established if the parameters a_{21}, v, and KT of Lin are interpreted respectively as K_s/K_L,

$L/c_S(T_F - T_W)$, and $\left(\frac{T_0 - T_F}{T_F - T_W}\right)\left(\frac{(k\ \rho\ c)_L}{(k\ \rho\ c)_S}\right)^{1/2} \Big/ \left(\frac{K_s}{K_L}\right)^{1/2}$

of Churchill and Evans.

Since Churchill and Evans tabulate the values of the root λ to four or five significant figures for a wide range of parameters, their Table 1 is more convenient and accurate to use than the graphical information on λ embodied in Figs. 1 and 2 of Lin's paper. Plotting a few representative values of λ from Churchill and Evans on Figs. 1 and 2 has confirmed the consistency of the two results (within the graphical accuracy). However, the data in Lin's paper for λ reach $v = 100$, while Churchill and Evans data go up to $v = 10$.

[1] By Sui Lin, published in the February 1981 issue of the ASME JOURNAL OF HEAT TRANSFER, Vol. 103, No. 1, pp. 165–168.

[2] Professor, Department of Mechanical Engineering, King Saud University, Riyadh, Saudi Arabia.

Authors' Closure

As indicated in paper [1], the system of equations (1,2,4,5,7) and (8), describing the temperature distributions in the frozen and vapor regions in the sublimation process in a porous medium is the same as that describing the temperature distributions in the solid and liquid regions in a melting process for a pure substance. Therefore, Neumann's solution [2] can be used to obtain the temperature distributions. In the paper by Churchill and Evans [3], equation (13) is the exact Neumann's solution. Therefore, it is obvious that equation (32) in [1] must be the same as equation (13) in [3].

For the determination of the distributions of the vapor moisture concentration, the temperatures in the frozen and vapor regions, and the limitation of the sublimation process, values of λ can be simply obtained from Figs. 1 or 2 of [1]. Certainly more accurate values of λ can be obtained from Table 1 of [3].

References

1 Lin, S., "An Exact Solution of the Sublimation Problem in a Porous Medium," ASME JOURNAL OF HEAT TRANSFER, Vol. 103, 1981, pp. 165–168.

2 Carslaw, H.S., and Jaeger, J.C., "Conduction of Heat in Solids," Oxford University Press, London, 1959, ch. 11.

3 Churchill, S.W., and Evans, L.B., "Coefficients for Calculation of Freezing in a Semi-Infinite Region," ASME JOURNAL OF HEAT TRANSFER, Vol. 93, 1971, pp. 234–236.

ERRATA

Corrections to "Effect of Fluid Carryover on Regenerator Performance," by P.J. Banks, published in the February 1982 issue of the ASME JOURNAL OF HEAT TRANSFER, pp. 215–217:

1 Line above equation (2), insert "ratio" before [2]

2 Two lines above equation (4), "0.01" is replaced by "0.1"

3 In several places, symbols "K" and "k" are replaced by "κ"